BOOK OF EXTENDED ABSTRACTS

of the 18TH European Symposium on Comminution & Classification

MISKOLCI EGYETEM

MFK

ESCC 2024

24 – 26 June 2024
Miskolc, Hungary

BOOK OF EXTENDED ABSTRACTS

of the 18th European Symposium on
Comminution & Classification

Edited by J. Faitli and Á. Rácz

24 – 26 June 2024
Miskolc, Hungary

ISBN 978-615-6018-25-0
DOI: 10.14755/escc2024

Contact Information:
Prof. Dr. József Faitli, Conference Chair
jozsef.faitli@uni-miskolc.hu

How to Cite:
Faitli J., Rácz Á. (Eds.) Book of Extended Abstracts of the 18th European Symposium on Comminution and Classification, Miskolc, Hungary, 24-26 June, 2024. Publisher: Hungarian Chemical Society. ISBN 978-615-6018-25-0, https://doi.org/10.14755/escc2024

WELCOME to the 18TH EUROPEAN SYMPOSIUM ON COMMINUTION & CLASSIFICATION

The 18th ESCC conference will be held in Miskolc, Hungary on Monday, June 24th to Wednesday, 26th, 2024 at the University of Miskolc, Hungary. We have the great pleasure of organising this event on behalf of the Working Party Comminution and Classification of the European Federation of Chemical Engineering (EFCE). This bi-annual conference has a long history of facilitating impactful discussions and networking and results dissemination among expert professionals from both academia and industry of the field since 1964. The two most recent successful events were the 16th in Leeds, UK and the 17th in Toulouse, France. This ESCC is the second one in Hungary and the first one in Miskolc. We think it is the right place, because our predecessor is the world's first technical higher education institution the "Bergakademie of Banská Štiavnica" and therefore, this institution carries within itself the cradle of mineral processing and of course its core comminution and classification roots.

This new event will further broaden the traditional scope of ESCC conferences of fundamentals of breakage, advanced modelling of fine- and coarse comminution and classification processes and applications for various industries, i.e. mineral processing, bio-refinery, food, pharmaceutical, chemical, electronic and materials industries with waste recycling and with mechanochemical-mechanofusion processes. The fundament of the circular economy is the recirculation of previously used materials (wastes) of which central elements are the first comminution and separation mechanical processes.

Altogether 80 presentations are scheduled, 3 plenary and 4 keynote speakers, parallel 2 times 7 oral sessions include 64 oral lectures and 1 poster session includes 9 posters in the Programme of ESCC 2024. After extension and a peer-review process, selected papers will be published in two special issues: a., Advances in Comminution and Classification. Special Issue of 18th ESCC in Chemical Engineering & Technology (CET); b., Comminution and Classification for the Circular Economy. Special Issue of 18th ESCC in Geosciences & Engineering.

The organisers, University of Miskolc, Faculty of Earth and Environmental Sciences and Engineering, Institute of Raw Materials Preparation and Environmental Technology and the Hungarian Chemical Society wish You a pleasant time in Miskolc, which is also useful in building professional and academic relationships and in acquiring and organizing new knowledge!

With miner's greetings: Good Luck!

Prof. Dr. József Faitli
Organising Committee Chair of ESCC 2024

INTERNATIONAL SCIENTIFIC COMMITTEE

Prof. Peter Baláž, Slovak Academy of Science
Prof. Hakan Benzer, Hacettepe University
Prof. Ecevit Bilgili, New Jersey Institute of Technology
Prof. Sandra Breitung-Faes, Technische Hochschule Nürnberg Georg Simon Ohm
Prof. Alain Chamayou, IMT Mines Albi
Prof. Magnus Evertsson, Chalmers University of Technology
Prof. József Faitli, University of Miskolc
Prof. Christine Frances, Université de Toulouse
Prof. Mojtaba Gadhiri, University of Leeds
Dr. Michael Juhnke, Novartis Pharma AG
Prof. Haim Kalman, Ben Gurion University of the Negev
Prof. Arno Kwade, Technical University of Braunschweig
Prof. Aubrey Mainza, University of Cape Town
Prof. Gabrie Meesters, TU Delft
Dr. Frank Müller, BASF SE
Dr. Priya Perumal, University of Oulu
Prof. Wolfgang Peukert, University of Erlangen
Prof. Malcolm Powell, University of Queensland
Prof. Agba Salman, University of Sheffield
Dr. Steffen Sander, Hosokawa Alpine
Prof. Luis Marcelo Tavares, Federal University of Rio de Janeiro
Prof. Yanmin Wang, South China University of Technology
Prof. Satoru Watano, Osaka Prefecture University
Dr. Mohsen Yahyaei, University of Queensland

ORGANIZING COMMITTEE

Chair

Prof. József Faitli, University of Miskolc

Members

Beáta Androsits, Hungarian Chemical Society
Prof. Gábor Mucsi, University of Miskolc
Dr. Ádám Rácz, University of Miskolc
Dr. Sándor Nagy, University of Miskolc
Dr. Beatrix Schenker, Hungarian Chemical Society

Conference secretariat and communication

Dr. Beatrix Schenker
escc2024@mke.org.hu

Acknowledgements

Partners & Sponsors

https://ins.hu

https://www.netzsch.com

https://www.fritsch-international.com

https://www.global.weir

Media partner

https://www.min-eng.com

Public Organisations

https://efce.info

https://www.mke.org.hu

https://processing.uni-miskolc.hu

UNIVERSITY OF MISKOLC
https://www.uni-miskolc.hu

https://mfk.uni-miskolc.hu

CONTENT

Session D: Comminution in recycling and classification

Session E: Fundamentals of particle breakage

Session F: Comminution and separation in recycling industries and waste processing

Session G: Stirred media milling

Session H: Coarse grinding and classification processes, especially for minerals, ores, cement and other materials

Poster Session

I: What are the limits of practical comminution energy?

Malcolm Powell

University of Queensland, Australia

Abstract. As industries utilising energy to reduce particle size to recover minerals and produce final products, we contribute an essential service to society, but at a significant energy cost. This motivates the increasing emphasis on reducing energy use in comminution processes. Theoretical calculations of minimum energy for rock breakage place industrial efficiency at somewhere between 0.1% and 1%. The value and validity of these figures are dubious, for they ignore the practicality of applying energy at industrial scale, the inherent (and irrecoverable) activation energy of crack propagation, and complexity of mineral grain boundaries in determining rock competence. Mechanical fracture is most efficiently achieved through single-particle stressing causing failure along the resultant tension planes. A relatively simple rolls breakage device was proposed in 2014 which has been developed to accurately measure this for many particles through a wide size range down to final product size below 200 µm. The results presented in the form of minimum practically achievable comminution energy by Ali et al (2003), Ali (2024) are most illuminating, indicating that the common conclusion of higher particle competence with decreasing size is incorrect. It is probable that this conclusion is a consequence of measuring increasing inefficiency of comminution at finer sizes, rather than rock competence. The results assessed against laboratory tests and industrial operations indicate that a viable target for reduction of energy in comminution circuits may be 75%. The uptake of this understanding should be via a structured approach to comminution device and circuit development. The consequences should provide a synergy of less energy with lower overall environmental impact – in terms of water use, tailings production, dust emission, contaminated waste – while enabling improved utilisation of our resources.

Short CV: Prof Malcolm Powell, Emeritus Professor University of Queensland, Honorary Professor University of Cape Town, Director of Liner Design services, Comminution & Transportation Technologies Inc., & CTO Geopyörä. Malcolm has applied fundamental comminution research to design and process improvement on over 70 mines worldwide during 40 years at Mintek, leader comminution at Centre for Minerals Research UCT, Professor of comminution at the JKMRC in Australia, and now independently. His work is published in over 240 papers and has been presented in as many conferences worldwide. Malcolm collaborates extensively, with close compatriots on 5 continents forming the Global Comminution Collaborative (GCC) – providing an expert research and consulting base covering the full comminution process chain, and developing people for our future industry. Malcolm's research vision is of integrated total process simulation as a tool for innovation – linking geology, mining, energy and size reduction, gangue rejection and recovery into flexible process design and process optimisation. Through his research companies, Malcolm is currently applying advanced modelling techniques and knowledge of fracture to the development of new highly energy-efficient, processes enhancing and lower environmental impact equipment to be integrated into flexible processing of the future.

II: Mechanochemistry in extractive metallurgy, materials science and medicine: good perspective for my followers

Peter Baláž

Institute of Geotechnics, Slovak Academy of Sciences, Košice, Slovakia

Abstract. In this retrospective lecture the overall view on my activities in mechanochemistry during more than 40 years stay at Slovak Academy of Sciences will be presented. The agenda of results in science and technology of extractive metallurgy, materials science and medicine will be incorporated. Knowledge which we obtained from treatment of nature minerals to obtain metals and application of the minerals in cancer treatment was later broaden for preparation of synthetic minerals to obtain advanced materials with the application in photovoltaics and thermoelectrics. All the mentioned approaches represent contribution to the common aim of mechanochemists: to prepare new materials with the desired properties in a reproducible way under easy-operating, environmentally friendly and essentially waste-free conditions. However, the presented results required cooperation with scientists from many foreign institutions. The great help of my followers who performed PhD studies under my supervision is strongly appreciated.

Short CV: Dr.h.c. Prof. RNDr. Peter Baláž, DrSc. is a specialist in the field of materials science, extractive metallurgy and mineral processing. He is member of Department of Mechanochemistry which is a centre of the research in mechanochemistry in Slovakia. Prof. Baláž is a member of various institutions such as IMA (International Mechanochemical Association) at IUPAC (International Union of Pure and Applied Chemistry), RFM (Reseau Francais de Mechanosynthese) and the Learned Society of Slovak Academy of Sciences. In the years 2000, 2008 and 2015 he obtained the Prizes of the Slovak Literary Foundation for his monographs "Extractive Metallurgy of Activated Minerals" (Elsevier) and "Mechanochemistry in Nanoscience and Minerals Engineering" (Springer). His SCI records in the year 2001, 2006, 2009, 2012 and 2014 has been awarded by Slovak Literary Found. During his carrier he completed long-term stays at Technical Universities in Berlin and Clausthal (Germany), University of Maryland Baltimore County (USA) and Busan National University (South Korea). He is active as PhD supervisor. Under his supervision 10 PhD thesis were successfully defended. He published 4 books, 16 chapters in monographs, 292 scientific papers in journals registered in Scopus. According to Scopus his papers have been cited more than 5500 times. His Hirsch index is 35.

III: Optimisation of compressive crushing

Magnus Evertsson

Chalmers University of Technology, Sweden

Abstract. Compressive crushing is applied in crushing plants used in mineral, mining, and aggregate industry for fragmentation of rock materials. From a global perspective, the total volume of crushed rock is massive and corresponds to several billion tons. All societies have to fulfil a daily need of rock material products and its derivatives such as metals and minerals. The market for metals and minerals is global while the aggregates production is mainly a local industry. This lecture presents a broader overview of optimisation with respect to "product yield, use of natural resources and energy consumption". High level plant optimisation of compressive crushing plants is covered as well as real-time optimisation and optimisation of single production units. Each of optimisation areas is presented and a discussion around how these three areas will be able to communicate with each other is given. Several models, e.g. process performance behaviour with respect to wear, as well as fitness functions can be common for all three areas. Well-defined and representative fitness functions are of the utmost importance in order to assure that the optimisation results reflect the production targets. It is concluded that great benefits can be achieved by linking together different areas of optimisation. The future for compressing crushing lies, without a doubt, in tailored processes both with respect to machines optimised for each customer, plant parameters and operation routines as well as an on-line adjustment, which takes into account current information and control possibilities.

Short CV: Prof. Dr. Magnus Evertsson is professor in Machine Elements at the department of Industrial and Materials Science of the Chalmers University of Technology. He received his PhD from Chalmers in 2000 and was appointed Docent in 2006. His own research is on machine elements and systems with a focus on rock processing equipment and process plants used in the aggregates producing industry and mining. He has a close collaboration with the leading manufacturers of rock processing equipment, producers of aggregates and mining companies. Several research results and patent has been implemented in industrial applications and commercial products.

IV: Mechanical Activation of Waste and Secondary Resources: Our journey of 25 years

Sanjay Kumar

CSIR-National Metallurgical Laboratory, Jamshedpur, India

Abstract. We started our activities in the area of mechanochemistry during the year 1999. The present abstract is the summary of our journey of 25 years. The activity was started to improve the resource and energy efficiency of cement production. With the use of mechanical activation, we are able to use 55% fly ash in Portland Pozzolana Cement, and 90% granulated blast furnace slag (GBFS) in Portland Slag Cement. The important learning was that fly ash and GBFS behave differently under similar condition and alteration in reactivity is mechanism specific. We have started a comprehensive program with the name of MARS (mechanical activation & reactivity of solids) under the guidance of Dr. Rakesh Kumar. This program encompasses both basic research and technology development. We were the first one to combine mechanical and chemical activation to develop geopolymer cement from fly ash. We could achieve a compressive strength of 120 MPa and 8 GPa flexural strength. With this understanding, we have developed the technology of quick road repairing material and transferred to an industry. Some of the area we studied mechanical activation are construction and demolition waste, enhancing ion exchange in gluconite, geopolymer cement from volcanic ash, and so on. Our current activities include the carbon sequestration using mechanical activation of slag, development of hybrid geopolymers, and improved recovery of metals from the black mass of lithium ion batteries.

Short CV: Prof. Dr. Sanjay Kumar is currently Chief Scientist & Head, Metal Extraction & Recycling Division, CSIR-National Metallurgical Laboratory, Jamshedpur, India and Professor, Academy of Scientific and Innovative Research (AcSIR), India. He is M.Sc & M.Phil in Geology, Ph.D in Chemical Technology (Ceramic Area), and P.G.Diploma in Cement Technology. He is currently Chairman, Indian Ceramic Society, Jamshedpur Chapter, Fellow, Indian Institute of Ceramics and Council Member, Indian Ceramic Society. He is also visiting faculty at University of Miskolc, Hungary. He is having 30 years of research experience in the area of waste utilization and recycling, low carbon cements, mechanochemistry, and circular economy. He has transferred and implemented three technologies in the industry. He is on the editorial board of two journals of repute. Dr. Kumar has edited 1 book, authored 5 book chapters, published 150 papers with more than 7000 citations, having 26 patents and delivered more than 50 keynote and invited talks. He has mentored 3 Post Doc, guided 6 Ph.D and 14 M.Tech student. Dr Kumar is in the various international and national expert advisory committees of funding and policy making bodies. He is recipient of many prestigious awards like Pro Facultate Rerum Metallicarum Award by University of Miskolc, Hungary, 2018, NMD award from Ministry of Steel 2013, Viswakarma Award by Construction Industry Development Board 2013, Sarswat Award for best Eco-Innovation project 2012, Altekar Award for Best Technology 2011, and 2016, Tamotia Award in 2006 and 2015, Nijhawan Award 2005, and many more. His current research interest is extraction of critical metals and sustainable technology from waste, secondary and byproducts.

V: Role of Comminution for Sorbent Particles Processed in Fluidised Bed Reactors Aimed at CO2 Capture, H2 Production and Solar Energy Storage

Fabio Montagnaro

Department of Chemical Sciences, University of Naples Federico II, Italy

Abstract. Fluidised bed reactors are particularly advantageous for conducting solid–gas chemical processes. Nonetheless, solid particles placed in a state of fluidisation are subject to comminution phenomena (attrition and fragmentation) with alteration of their residence time distribution and reactive performances. This contribution focuses on the comminution behaviour of limestone sorbent particles which in a fluidised bed have the ability to capture CO2, in processes of: 1) gasification for the production of syn-gas with increased H2 content ("sorption-enhanced gasification"); 2) removal of CO2 from industrial gaseous effluents ("calcium looping"); 3) thermochemical solar energy storage ("TCES"). The inter-relationships between operating conditions, tendency to comminution phenomena (e.g. surface wear and impact fragmentation) and performances of the sorbent in terms of CO2 capture capacity, in the processes listed above, will be highlighted.

Short CV: Prof. Fabio Montagnaro, Ph.D. in Chemical Engineering, is Professor of Chemical Plants and Italian Delegate at European Federation of Chemical Engineering - Working Party on Comminution and Classification. Apart from comminution of solid materials in reactive processes, other main research activities deal with: thermochemical solar energy storage; biomass thermo-conversion to produce energy vectors; purification of gaseous streams from pollutants and greenhouse agents; liquid-solid and gas-solid adsorption; synthesis of innovative/eco-sustainable binders; re-use of solid wastes of different nature; chemical processes in fluidised bed reactors; design and modelling of chemical reactors and plants; fractal dynamics in heterogeneous processes. Fabio is author of about 140 Journal-papers, with global "Hirsch index" of 37. His scientific activities have been carried out in collaboration with several public and private partners, and within international and national financed projects. Invited speaker/organiser for numerous international Conferences, Fabio has been (2015–2021) Associate Editor for Royal Society of Chemistry, and is currently Guest Editor/Member of the Editorial Board of other Journals. Contact and info: fabio.montagnaro@unina.it; www.docenti.unina.it/fabio.montagnaro.

VI: Particle shape modification by comminution in mineral and waste processing

Ádám Rácz

Institute of Raw Material Preparation and Environmental Technologies, University of Miskolc, Hungary

Abstract. The change of particle shape is a side effect in the comminution process; however in some cases the main objective of the comminution process can be the modification of particle shape as well. The particle shape modification can be achieved during the reduction of the particle size and without significant particle size decrease as well. In the presentation the different cases of targeted particle shape modification and their applications will be shown and the evaluation of the process by particle shape distribution and by efficiency parameters will be discussed for brittle and non-brittle materials as well.

Short CV: Dr. Ádám Rácz, PhD, associate professor at the Institute of Raw Material Preparation and Environmental Processing, University of Miskolc, Hungary. He has studied process engineering at University of Miskolc and received his PhD title in 2014. He has more than 15 years of experience in mineral and waste processing. His research interests are focused on the comminution processes for brittle and non-brittle materials also. In his previous work, he dealt with dry grinding and shape modification in stirred media mill, and later broadened his research area and worked in the field of design and optimization of waste preparation technologies and comminution of non-brittle materials. He has participated in many industrial research projects and in several Hungarian-European projects involving industrial and academic partners.

VII: No More Potential for Breakthrough Developments in Comminution?

Holger Lieberwirth

Institute of Mineral Processing Machines and Recycling Systems Technology (IART), TU Bergakademie Freiberg, Germany

Abstract. The number of breakthrough developments in comminution has been limited in recent decades. A recent research experimentally comparing the minimum comminution energy experimentally determined in single-particle-single-layer breakage with the specific energy consumption of the industrial circuits comminuting the same three ores reveal substantial potential for energy savings in comminution. Considering constraints by physics and technical and economical limitations the request is derived to develop new solutions in comminution to meet the growing demand for mineral resources in the future.

Short CV: Prof. Dr.-Ing. Holger Lieberwirth is currently director of the Institute of Mineral Processing Machines and Recycling Systems Technology (IART) at the TU Bergakademie Freiberg. His short professional biography includes CEO Asia, TAKRAF, Leipzig, Germany (2010 – 2013), Vice President, TAKRAF, Leipzig, Germany (2006 – 2010), Managing Director Sales, Beumer Maschinenfabrik, Beckum (2002 – 2006) Managing Director Sales and Technology, Maschinenfabrik Effing, Ahaus (2000 – 2002) Chief Engineer, Business Unit Essen, Krupp Fördertechnik (1997 – 2000) Chief Representative, China, Krupp Fördertechnik, Beijing (1996 – 1997) Project Manager Sales, Krupp Fördertechnik, Essen (1991 – 1995). Some selected projects since 2013 are selective comminution of ores, spars, slags, …; design/ application of crushers, HPGR, VRM; smart screening machines + air classifiers; briquetting, pelletizing, agglomerating machines and recirculation of secondary raw materials.

A1: Using CFD-DEM simulation to model the specific breakage rate based on a grinding media transport model in wet-operated stirred media mills

Ann-Christin Brandt[1,2 *], *Carsten Schilde*[2], and *Arno Kwade*[2]

[1]Netzsch Trockenmahltechnik GmbH, Hanau, Germany
[2]Institute for Particle Technology, TU Braunschweig, Braunschweig, Germany

Abstract. This study focuses on the description of the specific breakage rate in wet-operated stirred media mills. In previous studies, the specific breakage rate has been modelled for the wet-operated stirred media mill as an equally distributed parameter. However, CFD-DEM simulations have shown that the grinding media is not equally distributed along the mill length. Therefore, this study shows the localization of the specific breakage rate. For this, CFD-DEM simulations have been carried out with Rocky DEM and Ansys Fluent. Based on the cell model with backmixing, where each disc is surrounded by a volume defining an ideally mixed cell, the local filling degree has been determined and the dissipation rate has been calculated. This information has been correlated to the critical breakage energy measured by nanoindentation. Based on the effective stresses, a breakage rate has been calculated.

1 Introduction

Dynamic process simulation gains importance in control and regulation of mechanical processes (Skorych et al., 2017) such as grinding in stirred media mills (Fragnière et al., 2020). Furthermore, for stirred media mills the combination of complex models, necessary to simulate the device, increases the understanding of the process itself and especially of its dynamics (Böttcher, Schilde, Kwade, 2021; Böttcher, Thon et al., 2021; Fragnière et al., 2018; Kwade, 1999; Schons and Kwade, 2019). For instance, changes in particle size distribution influence the grinding efficiency, particle transport and grinding media movement. One option to simulate these dynamics is applying population balances which are based on breakage function, breakage rate, and grinding media and particle transport of the stirred media mill (Doraiswami Ramkrishna, 2000). This allows real-time simulations of the processes.

More and more advanced products need precise process control to achieve desired product requirements. Therefore, the process itself and its modelling have been improved in the past decade. One example of such improvements, often applied in industrial operation, is an installed internal deflector wheel, which influences the grinding media transport within the mill. Originally, it was installed to avoid grinding media compression at the outlet. However, the installed deflector wheel influences the overall media transport, leading to different local filling degrees. As an example, a global filling degree of 70 % leads to varying local filling degrees from 30 % up to 95 % (Schons and Kwade, 2019).

These local changes influence the performance of the mill, since the breakage is dependent on the stress intensity and the stress number.

$$SI = \frac{SE}{m_P} = \frac{\rho_{MK} d_{MK}^3 v_t^2}{m_P} \qquad (1)$$

For the process itself, it is ideal, if there is a maximum stress number with an optimal stress intensity. However, due to concentration or even packing of grinding media in a specific location, the velocity of the beads decrease and with this also their stress intensity. Reducing the number of grinding media (low local filling degree) leads to higher energies, but the stress number is reduced in those areas.

In conclusion, a compromise of grinding bead velocity and contact probability would affect the grinding positively. Furthermore, it is the aim to protect the outlet by the installed deflector wheel, but have a mostly uniform distribution of the grinding media along the length of the mill.

CFD-DEM simulation build the basis to access the information of the stress number and stress energy (Beinert et al., 2018; Fragnière et al., 2018; Jayasundara et al., 2011). In Rocky DEM, it is possible to access the dissipated energy from the contacts directly. Fragnière et al. (Fragnière et al., 2018) presented a methodology to apply CFD-DEM for the access of the specific breakage rate. Within this study, the methodology is extended to simulation of a complete wet-operated stirred media

* Corresponding author: ann-christin.brandt@netzsch.com

mill. Furthermore, it is analyzed how the local filling degree influences the specific breakage rate within each region. This localization functions build a basis for a more precise mill model which takes the effects of an internal deflector wheel into account. To analyze this localization, the mill has been divided into seven cells, each cell located around one of the six discs and the last one placed around the internal deflector wheel at the outlet.

2 CFD-DEM simulation

Within this study, a two-way coupled CFD-DEM has been set-up to model the effect of different operating conditions on the grinding media transport and the specific breakage rate derived from the simulations. For this purpose, Rocky DEM and Ansys Fluent have been used to model the grinding media motion in a surrounding fluid. For the DEM, the Hertz-Mindlin contact model and for the CFD, the drag model of Huilin & Gidaspow was used.

A broad range of operation parameters has been investigated. The study focuses on the effect of tip speed, viscosity and the geometrical influence of the deflector wheel at the outlet of the mill.

Fig. 1. CFD-DEM simulation of a wet-operated stirred media mill.

Based on the results of the CFD-DEM, the local rate for the dissipated energy has been calculated. For this purpose, for each time step the dissipated energy per particle has been extracted for two rotations of the stirrer after the mill has been in steady state. Then the energy dissipation has been clustered by the axial position of the particle. For the contact rate, the number of contacts have been extrapolated from the time the mill needs to carry out two rotations towards one second.

In Fig. 2, an example is shown for the local dissipation rate. Differences in the local dissipated energies are visible. Especially, cell 1 shows higher number of contacts per second. However, it also shows that mainly the number of small energetic contacts increased. Even though, it seems the other cells are quite close by each other, the differences in the number of contacts will affect the overall grinding process.

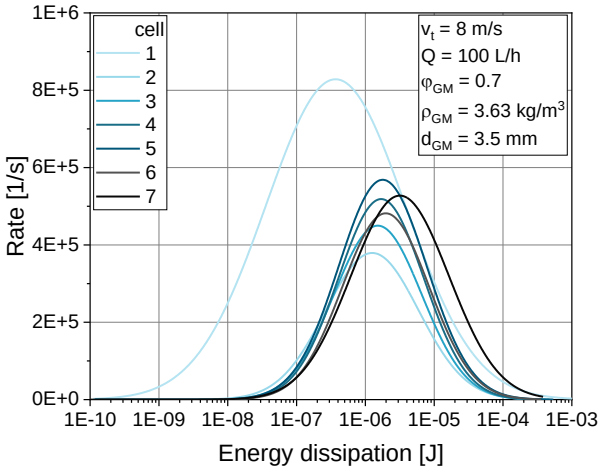

Fig. 2. An example for the rate of dissipated energy based on the results of the CFD-DEM simulation

The aforementioned collision statistics have been combined with the breakage energy of the material. This way, it was possible to calculate the local specific breakage rate for each cell separately. Based on the results a model is be derived which connects the dissipated energy towards the local filling degree which on itself is dependent on the viscosity, tip speed, volume flow and the geometry of the internal deflector wheel.

3 Conclusions

Calculations show big differences in between the dissipated energies within the cells of the mill. Furthermore, the operating parameters tip speed, viscosity and deflector wheel have a strong impact on the local distribution of the grinding media. To describe the mill process and get a better understanding on the underlying process mechanisms, it is absolutely necessary to model the local specific breakage energy. Especially for long mills with several cells, this differences within the cells will have a major impact. This method promises to be a basis for a better prediction of the grinding process in wet-operated stirred media mills.

References

Beinert, S., Fragnière, G., Schilde, C. and Kwade, A. (2018) 'Multiscale simulation of fine grinding and dispersing processes: Stressing probability, stressing energy and resultant breakage rate', Advanced Powder Technology, vol. 29, no. 3, pp. 573–583.

Böttcher, A.-C., Schilde, C. and Kwade, A. (2021) 'Experimental assessment of grinding bead velocity distributions and stressing conditions in stirred media mills', Advanced Powder Technology, vol. 32, no. 2, pp. 413–423.

Böttcher, A.-C., Thon, C., Fragnière, G., Chagas, A., Schilde, C. and Kwade, A. (2021) 'Rigidly-mounted roll mill as breakage tester for characterizing fine particle breakage', Powder Technology, vol. 383, pp. 554–563.

Doraiswami Ramkrishna (2000) Population balances: Theory and applications to particulate systems in engineering [Online], San Diego, CA, Academic Press. Available at http://www.sciencedirect.com/science/book/9780125769709.

Fragnière, G., Beinert, S., Overbeck, A., Kampen, I., Schilde, C. and Kwade, A. (2018) 'Predicting effects of operating condition variations on breakage rates in stirred media mills', Chemical Engineering Research and Design, vol. 138, pp. 433–443.

Fragnière, G., Böttcher, A.-C., Thon, C., Schilde, C. and Kwade, A. (2020) 'Dynamic Process Models for Fine Grinding and Dispersing', in Heinrich, S. (ed) Dynamic Flowsheet Simulation of Solids Processes, Cham, Springer International Publishing, pp. 199–236.

Jayasundara, C. T., Yang, R. Y., Guo, B. Y., Yu, A. B., Govender, I., Mainza, A., van der Westhuizen, A. and Rubenstein, J. (2011) 'CFD–DEM modelling of particle flow in IsaMills – Comparison between simulations and PEPT measurements', Minerals Engineering, vol. 24, 3-4, pp. 181–187.

Kwade, A. (1999) 'Determination of the most important grinding mechanism in stirred media mills by calculating stress intensity and stress number', Powder Technology, no. 105, pp. 382–388.

Schons, D. and Kwade, A. (2019) 'Determination of the axial grinding media distribution in the IsaMill using radiometric densitometry', Minerals Engineering, vol. 130, pp. 110–116.

Skorych, V., Dosta, M., Hartge, E.-U. and Heinrich, S. (2017) 'Novel system for dynamic flowsheet simulation of solids processes', Powder Technology, vol. 314, pp. 665–679.

A2: Optimisation of a new vertical roller mill by DEM modelling

Muzammil Ali, *Alejandro* López, *Mehrdad* Pasha *and Mojtaba* Ghadiri*
School of Chemical and Process Engineering, University of Leeds, Leeds, UK

Abstract. Vertical roller mills are used for milling of solids in a variety of industries. The performance of a new vertical roller mill is analysed using the DEM modelling approach. The flow of feed particles on the spreader plate and their buildup above the vertical rollers are analysed and design changes to improve the spreading of particles above the rollers are evaluated to improve the milling efficiency and throughput. Different roller designs are also evaluated to increase the shear force on particles during the milling which would increase the milling efficiency, particularly for soft materials.

1 Introduction

Vertical roller mills are used increasingly for milling solids in a variety of industries including cement, power, chemicals and mining. Particularly in the cement industry, the ball mills have largely been replaced by vertical roller mills for new plants (Harder, 2010), as they are compact, and the installation cost is smaller (Mutter, 2013). Vertical roller mills are up to 40% more energy efficient than ball mills (Simmons *et al.*, 2005), as the fines are immediately separated from fragments.

Distinct element method (DEM) modelling is applied to a new vertical roller mill (M350) (depicted in Figure 1), designed and manufactured by IIT, Gateshead, UK to evaluate its performance. The study is focused on investigating the flow and buildup of feed particles on the spreader plate and wear ring above the rollers. The spreader plate, conical feeder and roller design changes are evaluated to improve the distribution of particles on the rollers for optimum milling efficiency and increased throughput.

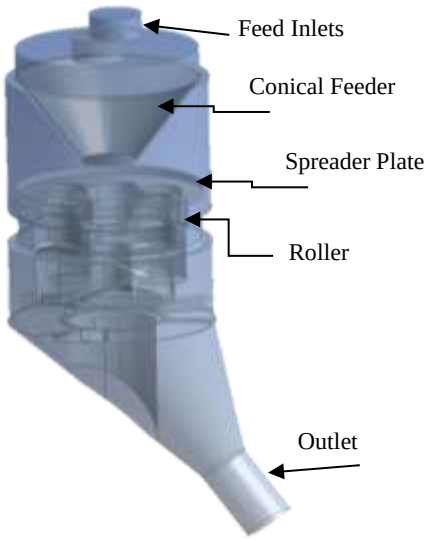

Fig. 1. Vertical Roller Mill (M350) Geometry.

2 DEM Modelling

DEM modelling is carried out using commercial DEM software EDEM provided by formerly DEM Solutions Ltd (now Altair®). Spherical glass beads are used as the feed particles, having a density of 2500 kg/m^3. The Young's modulus is specified as 100 MPa. To reduce the computation time, the geometry used for DEM modelling comprises the feeding section spreader plate, rollers rotating on their own axis in addition to the rotation with the swinging arms. The bottom outlet section is not considered as the purpose of the DEM study was only to investigate the particle flow around the spreader plate and rollers. The geometry used in DEM modelling is depicted in Figure 2. The time step specified for carrying out the DEM simulation is 20% of Rayleigh's time step. The coefficient of restitution is specified to be 0.5 for particle-wall and inter-particle collisions and the coefficient of static friction is 0.5 and rolling friction is specified as 0.01. The contact forces are modelled using the Hertz-Mindlin contact model, as reviewed by Di Renzo and Di Maio, 2004.

The feed particles comprises 3 mm to 5.5 mm particle diameters and the feed flow rate was specified to be 1 kg/s, which is on the higher end of the operating range of this mill to evaluate the performance and possible build-up of material on the spreader plate. The particles get milled to sizes typically ranging from 10 to 1000 µm. It is not practical to simulate particles of this size range at a flow rate of 1 kg/s, since it will be highly computationally expensive. Therefore, to speed up the computation time, the particles are allowed to reduce up to sizes ranging from 1.2 to 1.5 mm in diameter as they pass through the roller region. These sizes are significantly larger than the actual milled particle sizes, hence build-up of particles in the roller region may occur. In order to avoid this artificial build-up of material, the rollers are not allowed to rotate at the surface of the wear ring; instead a spacing of 8 mm is set

* Corresponding author: m.ghadiri@leeds.ac.uk

to facilitate the flow of particles between the rollers and the wear ring.

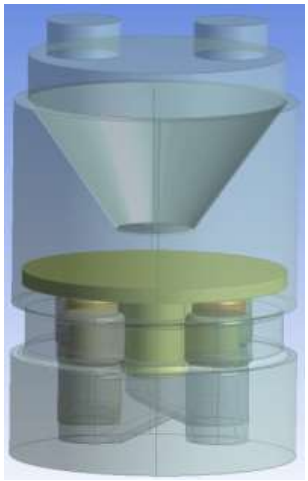

Fig. 2. Geometry used for DEM modelling of the mill.

2.1 DEM Modelling Results

2.1.1 Performance of the Existing Design of Spreader Plate

Figure 3 is a plot of the exit mass flow of particles plotted as a function of time in the vertical roller mill with the existing design. It can be observed that the particles start to exit at about 0.8 s and the outlet mass flow reaches the specified inlet mass flow (1 kg/s) at about 1.8 s. The average exit mass flow is equal to 1 kg/s, hence there is no build-up of particles in the mill.

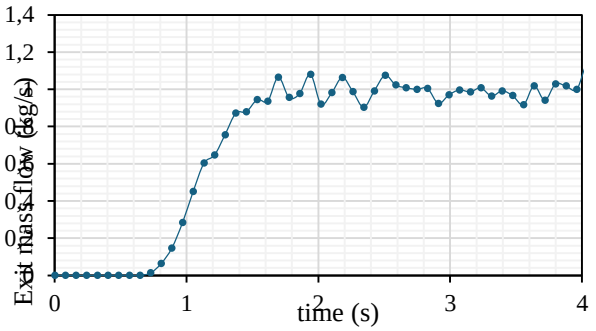

Fig. 3. Predicted particles exit mass flow as a function of time.

Figure 4 (a) depicts particles flowing in the mill coloured by mass at 5.29 s (after reaching the steady state). The feed particles are uniformly spread on the spreader plate and go towards the wear ring, where they are reduced in size due to the rotating rollers. The milled particles flow in the downward direction with a very small mixing of milled particles with the feed just above the wear ring (Figure 4 (b)). It should be noted that the simulation is carried out without considering the air flow. However, incorporating the influence of air flow and turbulence significantly impacts the particles trajectories and build-up inside the mill, particularly for the milled particles as they have a lower momentum and can get easily influenced by the air flow turbulence as predicted in the CFD study of this mill by Ali *et al.*, (2024). Our analysis of the induced air flow from the mill exit, caused by the exiting design of the spread plate, acting as a fan, showed deleterious effects on milled particle flow, necessitating improvements in the design of the spreader plate.

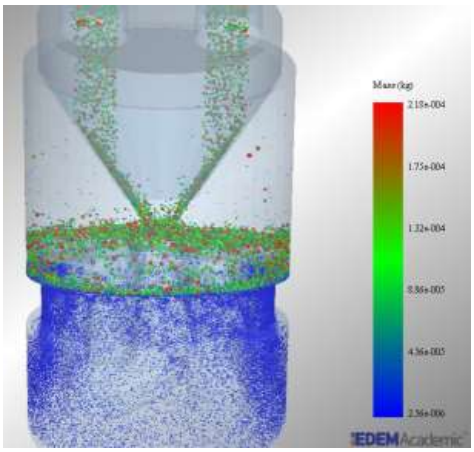

(a)

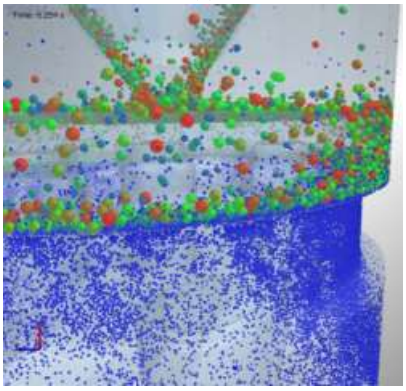

(b)

Fig. 4. Flow of particles in the mill.

2.1.2 New Spreader Plate Design Evaluation

Designs utilizing vanes and channels in the spreader plate are evaluated using DEM modelling to further facilitate the movement of particles. The designs considered for the evaluation are depicted in Figure 5. In all these designs, the flow of the particles within the spreader plate is enclosed in chambers which guide the particles towards the wear ring, where the particles exits via openings. The mass flow specified is 1 kg/s and the feed particles size ranges from 3 mm to 5.5 mm.

A B C

Fig. 5. Design modifications in the spreader plate to facilitate particles movement.

In all three designs evaluated, significant buildup of particles just above the wear ring was observed (Figure

6). This is due to the very high tangential velocity of the particles attained due to the presence of vanes that resulted in high centrifugal force and longer retention of particles above the wear ring, hence the buildup of particles in that region. Furthermore, there is a possibility that the particles may get blocked inside the channels if the feed particles are cohesive. Hence these design modifications in the spreader plate will result in reduced throughput and lower performance of the mill.

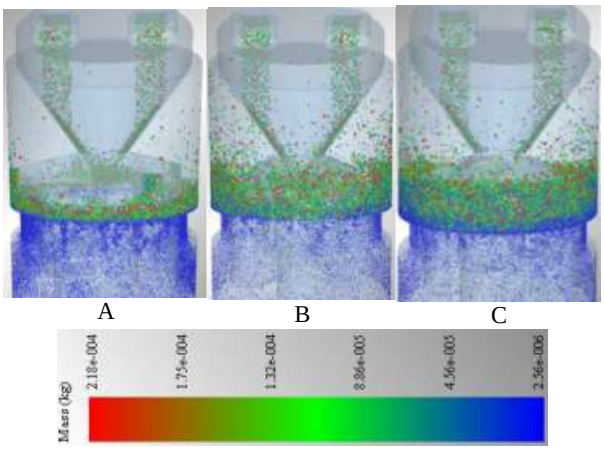

Fig. 6. DEM results of modified spreader plate designs.

2.1.3 Conical Feeder Design Evaluation

The purpose of the conical feeder is to uniformly distribute the particles onto the spreader plate. The top conical feeder is adjustable to allow control over the feed rate of particles on the spreader plate. DEM modelling is used to evaluate the effect of spacing between the conical feeder and the spreader plate on the distribution of particles. Two DEM simulation runs are carried out considering 50 mm spacing and 20 mm spacing between the spreader plate and the conical feeder (depicted as schematic in Figure (7)). The specified inlet mass flow of particles is 1 kg/s and comprises sizes ranging from 3 to 5.5 mm of glass beads.

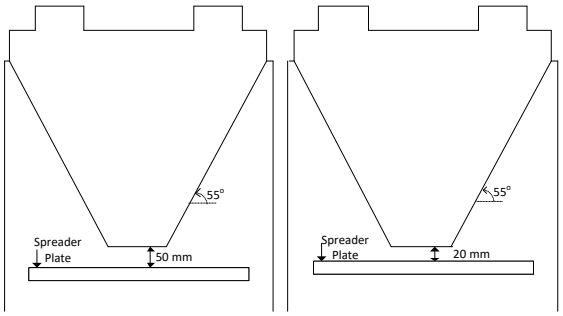

Fig. 7. Spacing between the cone and spreader plate.

Both simulation cases are run for sufficient time to allow reaching a steady state (i.e. inlet mass equals outlet mass of particles) and the spread of particles on the spreader plate is observed. The spread of particles with 50 mm spacing is given in Figure 8 (a) and that with 20 mm is given in Figure 8 (b). With 50 mm spacing, the spread of particles is more uniform over the spreader plate while in 20 mm spacing, it can be observed that the distribution of particles is non-uniform with more concentration on one side. This is expected to reduce the milling efficiency and capacity of the mill as the particles will not be uniformly distributed on the wear ring.

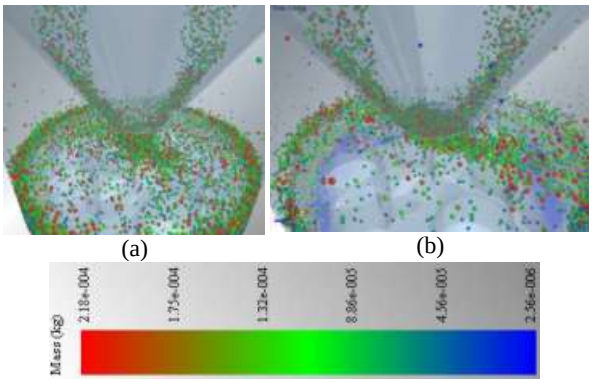

Fig. 8. Effect of cone feeder spacing on particles distribution on the spreader plate. (a): 50 mm spacing; (b): 20 mm spacing.

A new DEM simulation run with a modified conical feeder design is carried out which is depicted as a schematic in Figure 9 (a). The spacing between the feeder and the spreader plate is 50 mm. In the modified design the mixing between the two streams of particles feed is allowed to take place within the cone. The mixed stream then exits via a duct at the cone bottom. This results in a uniform distribution of particles on the spreader plate (Figure 9 (b)) and is fairly independent of the spacing between the spreader plate and the cone.

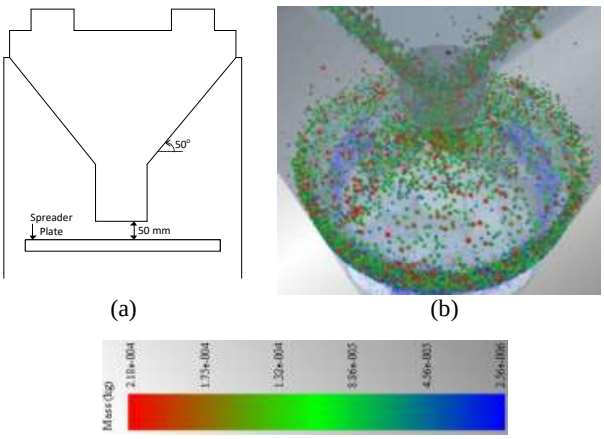

Fig. 9. Modified cone feeder design. (a): Schematic of new design; (b): DEM result.

2.1.4 Roller Design Evaluation

In the existing designs, the rollers are cylindrical, and the primary force responsible for the milling of particles resulting from this design is the compressive force. This is not very helpful in the milling of semi-brittle materials, posing a limit on the type of materials which can be milled. Shear force is more useful in the milling of soft materials. By making changes in the design of the rollers, it is possible to add shear force as the rollers rotate in addition to the compressive force. Simulations

using several roller designs are carried out to evaluate the flow of particles using the modified designs and the expected velocity distribution along the roller height. Three different designs are considered, which are depicted in Figure 10. The cone angle is 65° in all three designs.

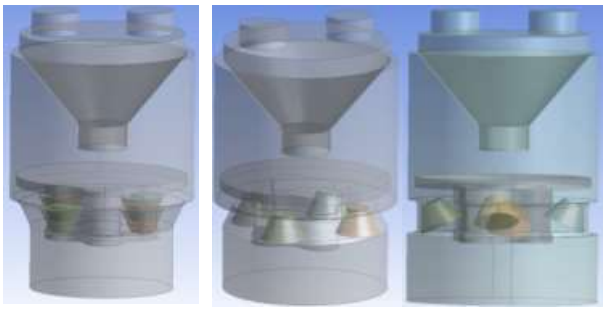

Converging Conical Rollers | Diverging Conical Rollers | Conical Rollers with Angled Axis

Fig. 10. Geometry of M350 mill with modified roller designs.

Figure 11 is a plot of the predicted exit mass flow of particles plotted as a function of time for all three designs and compared with the existing cylindrical roller design. The inlet mass flow is 1 kg/s, and the outlet mass flow becomes equal to the inlet mass flow at about 2 s except in the conical rollers diverging design. The conical rollers converging design and conical design with angled axis gives very similar exit mass flow plots compared to the existing cylindrical roller design. The conical roller diverging design results in a build-up of particles in the mill as given by a decreased mass flow at the outlet. Hence both conical rollers converging design and conical design with angled axis are suitable for this mill. The influence of air velocity on the particle flow is not considered here, hence the actual flow of particles, especially the milled particles may be significantly different as the particles will get influenced by the air flow.

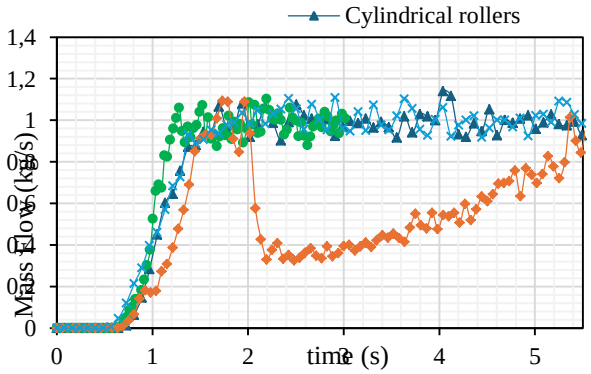

Fig. 11. Plot of exit mass flow of particles v/s time for different roller designs in M350 mill.

The particle velocity magnitude along the height of the rollers is depicted in Figure 12. In the existing cylindrical roller design, the particle velocity along the roller height is a constant value of 1 m/s. Hence the particles along the height of the roller exhibit a constant force, whereas in the conical roller designs the velocity experienced by the particles varies linearly along the height of the rollers. This velocity gradient can result in additional shear force on the particles in addition to the compressive force. Hence it will aid in the milling of particles particularly soft materials.

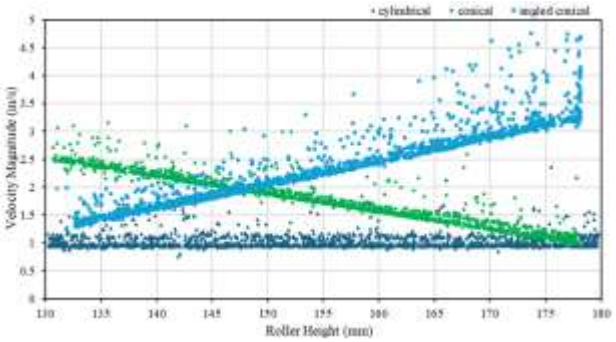

Fig. 12. Plot of velocity profiles exhibited by particles along the roller length.

3 Conclusions

Design changes in the vertical roller mill are evaluated to improve the milling performance. The existing plane spreader plate design results in a minimum particles buildup on the wear ring, while the proposed conical feeder design improves the spreading of particles on the spreader plate. Due to the presence of cylindrical rollers, the primary milling mechanism in the current design is due to compressive forces, hence it is not suitable for milling of 'soft' materials. Design evaluation using conical rollers has been carried out using DEM and the mill is expected to perform better with conical roller design for milling of ductile materials.

References

Ali, M., Lopez, A., Pasha, M. and Ghadiri, M. (2024). Optimisation of the Performance of a New Vertical Roller Mill by Computational Fluid Dynamics Simulations. Particles Technology, 433, 119282.

Di Renzo, A. and Di Maio, F. P. (2004). Comparison of contact force models for the simulation of collisions in DEM based granular flow codes. Chemical Engineering Science, 59(3), 525-541.

Harder, J. (2010). Grinding trends in the cement industry. ZKG International, issue 4-2010.

Mutter, M. (2013). Cement grinding – VRM or ball mill? World Cement, issue 3-2013.

Simmons, M., Gorby, L. and Terembula, J. (2005). Operational experience from the United States first roller mill for cement grinding. IEEE-IAS/PCA Cement Industry Conference, 15-19 May, 2005, USA.

Acknowledgements

The financial support of AMSCI for funding this project through the Chariot Programme is gratefully acknowledged.

A3: Coupled CFD-DEM simulations as a machine function to describe Wet Stirred Media Mills

Yeswanth Sai Tanneru[1,2,3,*], *Jan Henrik* Finke[1,2], *Carsten* Schilde[1,2], *Yogesh M.* Harshe[3], *Arno* Kwade[1,2]

[1]Institute for Particle Technology (iPAT), TU Braunschweig, Volkmaroder Straße 5, Braunschweig, 38104, Germany
[2]Center of Pharmaceutical Engineering (PVZ), TU Braunschweig, Franz-Liszt-Straße 35A, Braunschweig, 38106, Germany
[3]Société des Produits Nestlé SA, Nestlé Research, Route du Jorat 57, Lausanne, 1000, Switzerland

Abstract. Numerical simulations such as coupled CFD-DEM models can be used to digitally represent the multiphase systems such as Wet Stirred Media Mills (WSMMs). Once modelled accurately, the simulations can provide the detailed information about the system at different operating settings (such as, stirrer rotation speed, bead size, filling degree, etc.). The extracted information includes the quantitative description of the stress energies that occur in the system. Such quantitative description of the stress energies, i.e., the stress energy distribution can then serve as a machine function at a given operating condition. One of the advantages of such machine function is that it can serve as an input for the population balance models to predict the comminution result. One main limitation for coupled CFD-DEM modelling approach is handling the number of particles produced in the system. To overcome such computational limitation, assumptions are necessary to represent the system as accurately as possible. The current work focuses on establishing a modelling approach to simulate WSMMs using coupled CFD-DEM simulations. An immersed boundary methodology is used to emulate the impeller/stirrer rotation on the finite volume domain, and a hydrodynamic lubrication force is used to represent the bead-bead/bead-wall interactions. The operating parameter influence on the system characteristics, especially the stress energy, and stress frequency, are compared to the trends seen in literature, fostering the suitability of classic mill models. The specific outcomes of different modelling approaches such as DEM (only), coupled CFD-DEM and the cases with and without lubrication effect are also analyzed.

1 Introduction

Wet-operated Stirred Media Mills (WSMMs) are essential systems in many industrial applications such as food, pharmaceuticals, and mineral processing. These systems can reduce the particle size of materials ranging from several millimeters to nanometer scale. Mechanistic modelling of such systems helps in detailed understanding of a given system and thereby optimize it for a user-defined performance.

Tavares and Carvalho (2010) have proposed a batch grinding model for ball mills (UFRJ mechanistic model) with an input from the Discrete Element Method (DEM), that serves as a function for machine behavior. Beinert et al (2015) have investigated the usage of coupled CFD-DEM simulations to extract the stress energy distributions for wet fine grinding applications. In the present work, we adopt a similar modelling approach from Beinert et al (2015) to capture the stress energy distributions in a wet-operated stirred media mill and further improve the simulations by adopting the models such as hydrodynamic lubrication forces (Kroupa et al, 2016) for media interactions and an immersed boundary approach (IB) (Blais et al, 2016) to emulate the stirrer rotation on finite-volume mesh.

2 Coupled CFD-DEM modelling

The open-source software packages such as LIGGGHTS, OpenFOAM and CFDEMcoupling are used to simulate the grinding media motion in wet-operated stirred media mills. The unresolved coupling framework adopted in this work, is detailed in Kloss et al, (2012). In DEM, the Hertz-Mindlin contact model is used and the lubrication forces described by Kroupa et al (2016) are used in the non-contact model. Koch-Hill drag model is used, and the IB approach described by Blais et al (2016) is adopted to emulate the stirrer rotation on CFD domain. The k-ε turbulence model was chosen to model the fluid turbulence.

3 Simulation setup and post-processing

In the current work, the geometry of a bench scale pin-type wet stirred media mill, MiniCer form Netzsch (shown in Fig. 1) was considered for the coupled CFD-DEM simulations. The properties of Zirconium Oxide (ZrO_2) are taken for the mill walls and grinding beads. The grinding bead number for different filling degrees is calculated and set according to equation 1, with V_{act} and V_{gb} being the active volume for bead filling and volume of a grinding bead, respectively. ϕ and α are the filling ratio and pore fraction, respectively. The Young's

* Corresponding author: y.tanneru@tu-braunschweig.de

modulus of the material is reduced by 100 orders of magnitude for computational feasibility. A cut-off distance was chosen for the lubrication force to avoid the divergence when the surface distance between the beads and their relative velocity approaches to zero.

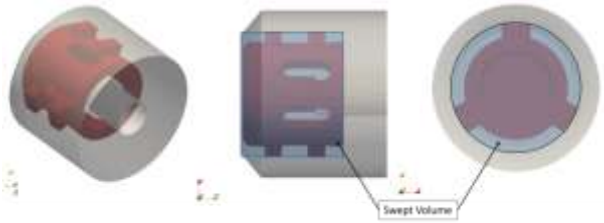

Fig. 1. Geometry of the bench scale, pin-type wet stirred media mill, MiniCer (Netzsch).

$$N_{gb} = (V_{act}/V_{gb})\ \phi\ (1-\alpha) \quad (1)$$

To satisfy the unresolved coupling of CFD-DEM, the edge lengths of the cells in finite volume mesh are maintained at 2.5 to 3 times the grinding bead diameter. The time step of DEM is chosen as 20% of the Rayleigh time step criterion, while the CFD time step is chosen to satisfy the Courant-Friedrich-Lewy (CFL < 1) criterion. Different parameter sets were assessed with combination of process parameters i.e., stirrer rotation speed (n), bead diameter (d_{gb}), and filling degree (ϕ). Also, the effect of fluid is assessed using the properties of water and glycerol mixtures.

In the post processing step, the system relevant information such as stress energy and stress frequency are captured to compare with the analytical model from Kwade (2003).

4 Results and discussion

4.1 DEM vs coupled CFD-DEM

Fig. 2 shows the comparison of the stress energy distributions from DEM and coupled CFD-DEM simulations at same operating conditions (stirrer tip speed of 9.27 m/s, a bead diameter of 1100µm, and a filling degree of 0.8). As it can be clearly seen that the simulations with DEM only have a less agitated system and doesn't yield a high stress frequency as compared to coupled CFD-DEM simulations. It can also be seen that the inclusion of the lubrication provided additional damping which resulted in a reduction in the stress frequency.

4.2 Effect of the fluid properties

Fig. 3 shows the comparison of the stress energy distributions from coupled CFD-DEM simulations with different fluid properties i.e., water and glycerol mixtures. The distribution has significant change when the percentage of glycerol is the highest. This shows that the change in fluid properties will indeed effect the system dynamics (especially for medium to high viscosities).

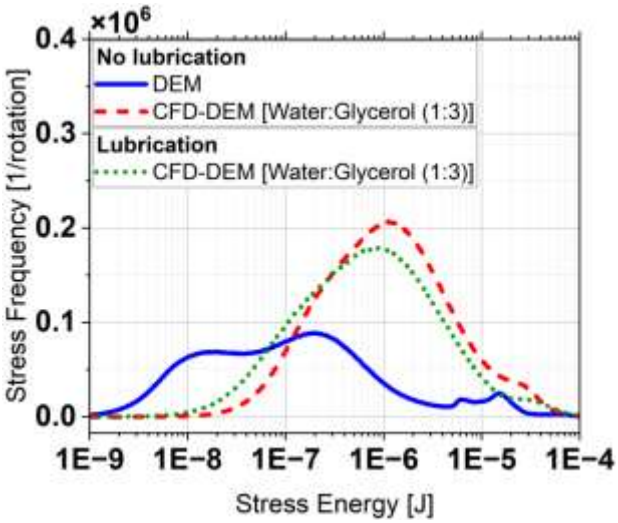

Fig. 2. Stress energy distributions from DEM and coupled CFD-DEM simulations.

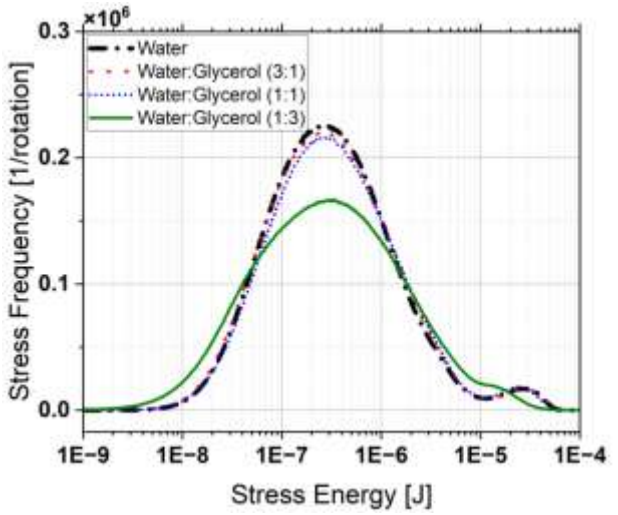

Fig. 3. Effect of fluid properties on the stress energy distribution.

4.3 Effect of operating parameters

Fig. 4 shows the system behaviour i.e., the mean stress energy and the stress frequency at different operating settings. The mean stress energy increases with the increase in stirrer tip speed. This is obvious as the increase in tip speed introduces more power or energy, respectively into the system, which transfers from stirrer to the fluid (and grinding beads), and from the fluid to the grinding beads. With the decrease in bead diameter (size), the mean stress energy is reduced, as smaller beads have less inertia compared to the larger beads, resulting in less intense collisions. The change in filling degree didn't affect the mean stress energy.

It is evident that the stress frequency is a function of both stirrer tip speed and the bead number. In contrast to the mean stress energy, the stress frequency increases with a decrease in bead diameter due to the increased number of beads in the system.

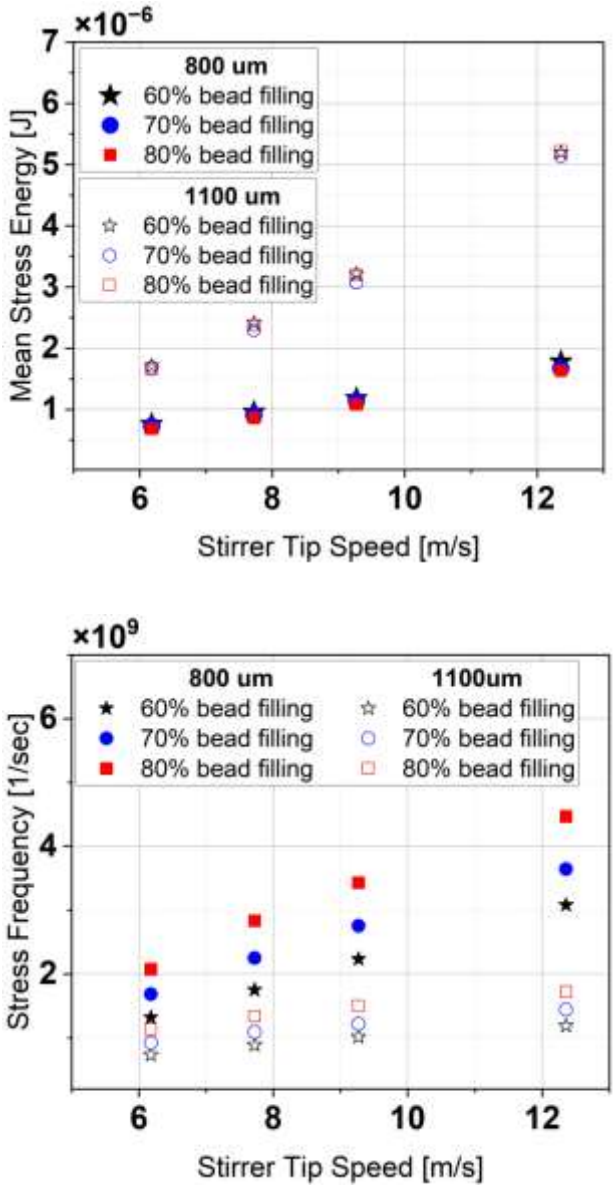

Fig. 4. System behavior at different operating conditions.

5 Conclusion

In the present work, the modelling considerations such as, the need for CFD-DEM coupling, the role of lubrication forces, and fluid properties are investigated by comparing the stress energy distributions. It was identified that the lubrication forces are needed to compensate for the unresolved CFD-DEM coupling, especially for medium to high viscous fluids.

The stress energy distributions captured from the simulations can serve as a machine function for the population balance models to provide the accurate description of the applied energies in the system.

References

Kwade, A. (2003). A stressing model for the description and optimization of grinding processes. *Chemical Engineering & Technology: Industrial Chemistry-Plant Equipment-Process Engineering-Biotechnology*, *26*(2), 199-205.

Tavares, L. M., & Carvalho, R. M. (2010). A mechanistic model of batch grinding in ball mills. In *XXV International Mineral Processing Congress* (Vol. 1, pp. 1287-1297). AUSIMM Brisbane.

Kloss, C., Goniva, C., Hager, A., Amberger, S., & Pirker, S. (2012). Models, algorithms and validation for opensource DEM and CFD–DEM. *Progress in Computational Fluid Dynamics, an International Journal*, *12*(2-3), 140-152.

Beinert, S., Fragnière, G., Schilde, C., & Kwade, A. (2015). Analysis and modelling of bead contacts in wet-operating stirred media and planetary ball mills with CFD–DEM simulations. Chemical Engineering Science, 134, 648-662.

Kroupa, M., Vonka, M., Soos, M., & Kosek, J. (2016). Utilizing the discrete element method for the modeling of viscosity in concentrated suspensions. *Langmuir*, *32*(33), 8451-8460.

Blais, B., Lassaigne, M., Goniva, C., Fradette, L., & Bertrand, F. (2016). A semi-implicit immersed boundary method and its application to viscous mixing. *Computers & Chemical Engineering*, *85*, 136-146.

A4: Autogenous stirred media milling of silicon

Marcel Filipe Möller[1*] and *Arno* Kwade[1]

[1]Institute for Particle Technology, Technical University of Braunschweig, Brunswick, Germany

Abstract. Silicon nanoparticles will take the performance of lithium-ion batteries to the next level. An attractive production method for silicon nanoparticles is wet stirred media milling. However, undesired wear of the ceramic media contaminate the silicon. Autogenous grinding media can overcome this challenge. These media are made out of coarse silicon so that the wear becomes the product. Nonetheless, the autogenous grinding media wear significantly faster than conventional grinding media. For that matter, this study addresses the properties of coarse silicon as grinding media in stirred media mills. It was found that the wear rate of the autogenous grinding media is determined by their size and shape. Larger media wear faster than smaller ones due to their stress energy. In addition, mixing different sizes showed that the wear rate of larger media can be reduced. Reduction of the wear rate was also obtained by spheroidization of the media. In terms of energy consumption, the weighted specific energy was introduced for comparing milling results with different autogenous grinding media concentrations. Spheroidized media performed more efficiently, as long as their size was not reduced significantly.

1 Introduction

With the energy transition in transportation, the demands on the range of future electric vehicles are also increasing. Current research is therefore focusing on lithium-ion battery cells with a high specific energy content and high energy density. One promising approach for increased energy density is the use of silicon as an anode material. However, the current challenge is that silicon undergoes significant volume expansion during battery charging, irreversibly damaging the electrode structure. Recent studies show that a combination of graphite and silicon nanoparticles can be used to significantly increase the mechanical integrity of the electrode and consequently the performance of a silicon-based battery. In this context, the interest in efficient methods for the production of high-quality silicon nanoparticles is increasing fast.

Wet comminution in stirred media mills provides a common method for the production of silicon nanoparticles. For example, Nöske et al. developed a fine-grinding method based on ethanol and electrostatic stabilization of the nanoparticles by adding sodium hydroxide (Nöske et al., 2019). However, comminution with stirred media mills is always accompanied by wear. The colliding grinding media, usually made out of ceramic spheres, are the main cause of wear. In order to decrease contamination and increase the purity of the nano-sized silicon, an autogenous milling method is addressed in this study. In autogenous stirred media milling, grinding media and product are made out of the same material. As a result, grinding media wear becomes the product and contamination can be decreased significantly. While this milling technology is well described for the processing of ores in ball mills, the use in stirred media mills for the production of nanoparticles is poorly investigated. Nevertheless, Kwade investigated the autogenous milling of limestone in stirred media mills (Kwade and Schwedes, 1995). It was demonstrated that product particles below 10 µm can be produced. Former studies showed that the autogenous milling of silicon and the production of nanoparticles is possible. For instance, Breitung-Faes and Kwade (2011) successfully produced alumina nanoparticles around 100 nm via autogenous milling. Nonetheless, the used autogenous grinding media (aGM) show a different wear and stressing behavior than conventionally used ceramic grinding media. This different behavior is related to the non-spherical shape and rough surface of the coarse silicon particles.

This study presents a novel autogenous stirred media milling of silicon and shows the importance of the grinding media properties. Therefore, aGM of different sizes are characterized with respect to their size and shape distribution. Then, their wear rates are analyzed and correlated with corresponding properties. The stressing efficiency is investigated by conducting autogenous milling experiments. In a second step, aGM of different sizes are mixed in order to broaden their size distribution. Again, their performance with respect to the wear rate and stressing efficiency are demonstrated. In a third step, aGM of certain size fractions are spheroidized by reusing already used aGM from older experiments. To evaluate their efficiency, the results are compared to milling with conventional grinding media. Here, the focus is put on the milling efficiency and on the shape of the final product particle size distribution.

2 Autogenous stirred media milling

* Corresponding author: marcel.moeller@tu-braunschweig.de

Coarse silicon of different size fractions around 250 µm (aGM025) and 650 µm (aGM065) were used as aGM. Fine silicon (~ 4 µm) was used as feed material. The autogenous milling experiments were conducted in the stirred media mill LabStar (Netzsch GmbH). Highly pure ethanol was used as dispersion medium. The silicon nanoparticles were stabilized by feeding ethanolic sodium hydroxide solution to the suspension during the experiments. The milling was conducted in a circuit mode.

To investigate the importance of the aGM size distribution, the initial size fractions were mixed in the ratios 30:70, 50:50 and 70:30 by mass, respectively. Furthermore, the importance of the aGM shape was investigated by comparing the performance with respect to the aGM sphericity. Different sphercities of the aGM were achieved by reusing aGM from previous milling experiments.

2.1 Wear rate

The wear rate r_{aGM} of the aGM was calculated as follows:

$$r_{aGM} = -\frac{1}{c_{v,aGM}}\frac{dc_{v,aGM}}{d_t} \quad (1)$$

For this purpose, the volumetric grinding media concentration $c_{v,aGM}$ was calculated directly from experimental data by taking into account the loss of aGM mass during one autogenous milling experiment. Figure 1 shows the wear rate for two aGM size fractions and mixtures of these with different mass ratios.

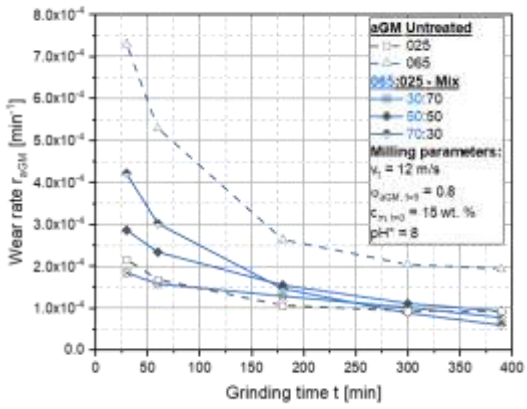

Fig. 1. Wear rate of coarse (065), fine (025) and mixtures of aGM as a function of grinding time.

It can be noticed that the wear behaviour can be divided into an exponential and a linear or constant phase. During the exponential phase, chipping predominates the wear characteristic, while abrasion mechanisms lead to the subsequent linear wear rate. Furthermore, the absolute values of the wear rate are generally higher if the used aGM size is larger. This can be attributed to the stress energy, which larger particles generate during collision. As a result, higher stress energies are available for generating higher wear rates. The wear rates of the aGM mixtures locate themselves between both starting aGM sizes, while the absolute wear rates decrease as the amount of smaller aGM sizes increases. This pattern is most distinct for the chipping phase. During the subsequent abrasion dominated phase, the wear rates of the mixtures are located around the wear rate of the sole smaller size fraction 025. This indicates that adding smaller sized aGM potentially reduces the wear rate of larger aGM by providing protection of surface abrasion.

Another way to influence the wear rate can be achieved by spheroidizing the aGM. Figure 2 shows SEM images of raw and spheroidized aGM of the size fraction 065.

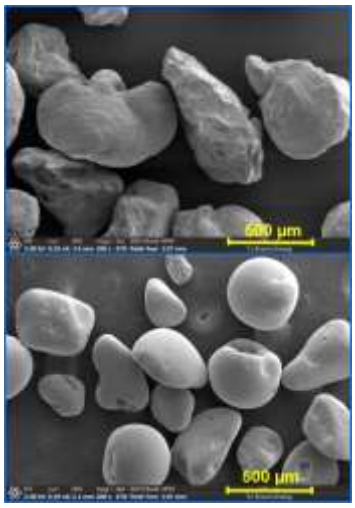

Fig. 2. SEM images of raw (upper) and spheroidized (lower) aGM065.

Using aGM in a stirred media mill leads to chipping and abrasion of the particles surfaces. Eventually, the shape becomes sphere-like as shown in Figure 2. In this context, the wear rate can be decreased significantly. As an example, this is shown for the size fraction aGM065 in Figure 3.

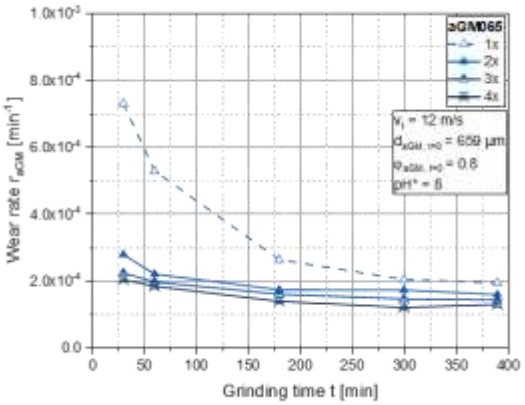

Fig. 3. Wear rate of aGM065 which were reused up to four times as a function of grinding time.

The more often the aGM are used in autogenous milling experiments, the higher the degree of spheroidization. It can be noticed that the total amount of wear can be reduced with each use. Additionally, the initial exponential chipping phase is only present during the

first use. After that, defects and weak spots of the aGM disappear and chipping becomes unlikely. In this case, surface abrasion is the only wear mechanism and, thus, the wear rate becomes almost constant.

2.2 Specific energy consumption

The grinding media concentration during autogenous milling varies due to different wear rates, size and shapes of the used aGM. For that reason, we introduce the weighted specific energy:

$$\sum_{i=0}^{t} c_{v,aGM,i} \bullet \Delta E_{m,i} = \overline{c_{aGM} \bullet E_m} \qquad (2)$$

This concentration $c_{v,aGM}$ is a measure for the energy transfer. By weighting the specific energy consumption E_m, it becomes possible to compare the milling results with different grinding media concentrations.

Besides the particle size distribution, the shape of the aGM plays a crucial role for their energy efficiency in terms of milling performance. This is demonstrated in Figure 4.

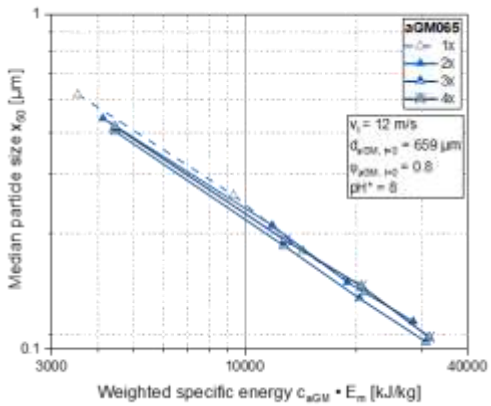

Fig. 4. Milling efficiency of aGM065. The median particle size of the product is plotted vs. the weighted specific energy obtained by Equation (2)

Analog to the results presented in Figure 3, the aGM have been used up to four times. The curves follow a power function, which is typical for stirred media milling in the submicron size range. Additionally, it can be seen that the aGM during the first use consume more specific energy than the ones that were used multiple times. The increase in efficiency can be explained by considering their shape and higher resistance against wear. As shown before, the sphericity increases and the wear rate decreases the more often the aGM are used. The greater sphericity increases the active volume so that capturing and stressing product particles becomes more likely. In addition, the lower and constant wear rate are beneficial for the milling, because otherwise too many and large wear particles can potentially protect the feed particles from stressing events. Interestingly, the four-times-used aGM seem to become less efficient. One explanation for this behaviour can be the reduced size of the aGM, which is associated with the abrasion of the surfaces (see also Figure 2). In different words, the enhanced milling efficiency caused by higher sphericity is compensated by reduced particle sizes of the aGM. This effect was not observed for the smaller sized aGM025. In this case, the reduction in particle size is negligible, while the increase in sphericity enhances the milling performance.

References

Nöske, M., Breitung-Faes, S., Kwade, A., (2019) Electrostatic Stabilization and Characterization of Fine Ground Silicon Particles in Ethanol, *Silicon*, 11, 3001 - 3010

Kwade, A. and Schwedes, J., (1995), Autogenzerkleinerung in Rührwerkmühlen, *Chemie Ingenieur Technik*, 68, 809-812

Breitung-Faes, S., Kwade, A., (2011), Production of transparent suspensions by real grinding of fused corundum, *Powder Technology*, 212, 383-389

A5: Comparison study of media dynamics in a horizontal stirred mill

Sherry Bremner[1,*], *Ann-Christin* Brandt[3], *Aubrey* Mainza[1], *Arno* Kwade[2], *Divine* Ssebunnya[1]

[1]Department of Chemical Engineering, Faculty of Engineering and the Built Environment, University of Cape Town, South Africa
[2]Institut für Partikeltechnik, Technische Universität Braunschweig, Braunschweig, Germany
[3]Netzsch Grinding & Dispersing, Germany

Abstract. This paper presents a comparative analysis of Positron Emission Particle Tracking (PEPT) and Magnetic Particle Tracking (MPT) experiments with Discrete Element Method and Smooth Particle Hydrodynamics (DEM-SPH) simulations in the context of a horizontal stirred mill. The study aims to elucidate the dynamics of grinding media within the mill and to validate experimental techniques against computational simulations. Initial quantitative comparisons of velocity distributions derived from PEPT and MPT reveal similar behaviours at corresponding velocity magnitudes. Subsequent validation through DEM-SPH simulations bridges discrepancies in operational parameters and verifies results obtained from both experimental methods. While PEPT represents a state-of-the-art yet costly tracking technique requiring strict safety protocols, MPT and DEM-SPH serve as complementary tools for exploration. This comparative analysis offers valuable insights into the effectiveness and applicability of various tracking and simulation methodologies in studying stirred media mill dynamics.

1 Introduction

Enhancing the modelling of stirred media comminution devices relies on a comprehensive understanding of the flow dynamics within them. The flow characteristics of the media vary based on the agitation speed, media size and density, and the volumetric fill of the mill. Observing the dynamics of grinding media within a shearing environment, such as a horizontal stirred mill, requires indirect observation methods due to the system's opaque nature and the intense shear forces, which makes it impossible to use internal probes to collect information.

Two experimental particle tracking techniques, Positron Emission Particle Tracking (PEPT) and Magnetic Particle Tracking (MPT), have been employed to elucidate the dynamics within a horizontal stirred mill. These techniques assume that the time-averaged behaviour of a single tracked particle represents the ensemble average of the bulk material, allowing examination of the opaque system under high shear conditions. While successful in various geometries, these techniques can only track one or a few particles in the system which necessitates observation of the ensemble using computational models.

One method to confirm that experimental data obtained by tracking one or a few particles in the system can represent the ensemble behaviour is by comparing the outs to the solution from computational simulations. This paper focuses on employing a coupled Discrete Element Method and Smooth Particle Hydrodynamics (DEM-SPH) simulation of the horizontal stirred mill. The purpose of this paper is to compare the results of PEPT and MPT experiments with a DEM-SPH simulation of a horizontal stirred mill in a wet grinding environment containing fluid flow.

2 Experimental Studies

The experimental studies were carried out separately on geometries similar to the M4 IsaMill. Both campaigns examined the effect of stirrer speed, with the PEPT adding fluid flow rate and MPT investigating fluid viscosity.

2.1 Positron Emission Particle Tracking

Positron Emission Particle Tracking (PEPT) is a non-invasive method that detects 511 keV γ-rays resulting from the annihilation of a positron with an electron. A tracer particle, labelled with a radionuclide, decays via positron emission, leading to annihilation with an electron near the tracer particle. This produces a pair of γ-rays traveling along nearly the same path but in opposite directions, defining a line where the positron source lies. Multiple coincident event detections enable triangulation of the gamma-ray source's location. Sequential detections and the associated time intervals allow calculation of the tracer particle's path and velocity (Parker et al, 1997).

Experiments were undertaken at PEPT Cape Town, a facility based at iThemba Laboratory for Accelerator Based Science (LABS) and covered variations in the mill speed and flow rate. The media filling was kept constant at 60 %. The experimental rig is shown in Figure 1.

* Corresponding author: sherry.bremner@uct.ac.za

Fig. 1. The PEPT experimental rig.

A single bead of grinding media was labelled with Ga^{68} and placed inside the mill. This tracer particle was then tracked for an extended period of time, allowing for the average velocity and bulk media density distributions to be determined. The cross-sectional velocity distribution determined for a stirrer speed of 168 rad/s is shown in Figure 2, which indicates areas where the media is subjected to high shear rates.

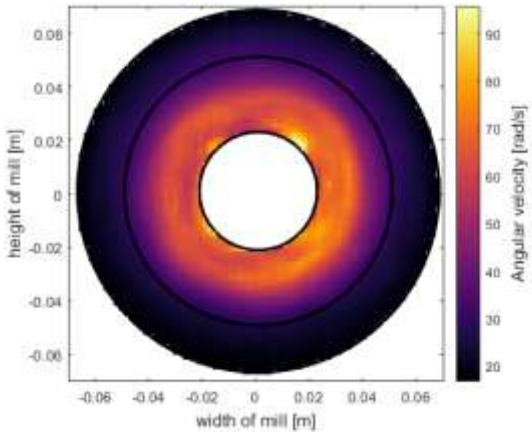

Fig. 2. The angular velocity distribution derived from PEPT experiments on a horizontal stirred mill.

2.2 Magnetic Particle Tracking

Magnetic Particle Tracking is another non-invasive tracking technique which is relatively inexpensive. The main limitation of the technique is the magnetic strength which is a function of the tracer size and the distance from the tracer to the detector. This technique was explored in Böttcher et al (2021) where a magnetic tracer was tracked in a closed system of a horizontal stirred mill.

The position, velocity and radial circulation of the grinding media was examined at different stirrer speeds and viscosities (Böttcher et al, 2021). The angular velocity distribution from a similar set of operational variables to the PEPT experiments is shown in Figure 3, reproduced from Böttcher et al (2021).

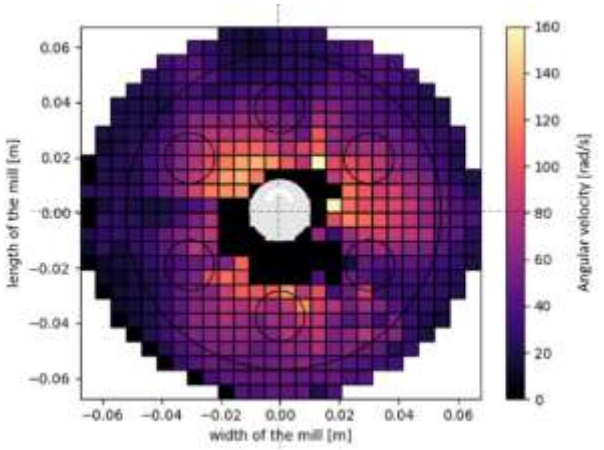

Fig. 3. The angular velocity distribution derived from MPT, reproduced from Böttcher et al (2021).

3 Computational Studies

A simultaneous two-way coupled DEM-SPH model is used to simulate media and fluid motion in the IsaMill. Within the model, DEM is used to describe the translational and rotational motion of cohesionless grinding media bodies through a non-linear soft contact model. The fluid is modelled by SPH. This defines the fluid as a homogenous mobile grid of discretized point-mass fluid particles, linked through a kernel weighted sum. The fluid particles are constrained by a discretized Navier-Stokes equation, to conserve momentum, and an equation of state to allow for slight compressibility within the fluid. The two-way coupling interface transfers the buoyancy and drag interaction forces between the solid and fluid phases of the model. The model computes its DEM and SPH components simultaneously, with the time integration regulated through separate timesteps and sub-cycling. The IsaMill is simulated in a continuous system where the media is contained in the mill while the fluid flows through it.

The DEM-SPH simulation will provide ensemble-averaged distributions of the media velocity and bulk density, which will be compared with the same results from the experimental methods. Additionally, the simulation can provide calculations of the compressive and shear force distributions, which will allow for an estimation of the energy dissipation within the mill.

4 Conclusions

An initial quantitative comparison between PEPT and MPT-derived velocity distributions reveals similar behaviour at comparable velocity magnitudes. Further comparison of these techniques will be facilitated by DEM-SPH simulations, which should reconcile differences in operational parameters between the experimental campaigns. This comparison will prove beneficial since, while PEPT represents a cutting-edge tracking technique, it comes with high costs and stringent health and safety protocols. MPT and DEM-SPH, on the other hand, can serve as exploratory tools, with PEPT being reserved for fine-tuning final results.

Additionally, the unique capabilities of DEM-SPH in this system promise to provide further insights beyond what PEPT and MPT alone can gather such as distributions of the compressive and shear forces experienced within the mill.

References

Parker, D.J., Allen, D.A., Benton, D.M., Fowles, P., McNeil, P.A., Tan, M. and Beynon, T.D., 1997. Developments in particle tracking using the Birmingham Positron Camera. *Nuclear Instruments and Methods in Physics Research Section A: Accelerators, Spectrometers, Detectors and Associated Equipment*, *392*(1-3), pp.421-426.

Böttcher, A.C., Schilde, C. and Kwade, A., 2021. Experimental assessment of grinding bead velocity distributions and stressing conditions in stirred media mills. *Advanced Powder Technology*, *32*(2), pp.413-423.

A6: Top-down production and two-dimensional size analysis of plate-like nanoparticles

Cornelia Damm[1,*], *Paola* Cardenas Lopez[1,2], *Johannes* Walter[1,2], *Moritz* Moß[1,2], *Bettina* Winzer[1] and *Wolfgang* Peukert[1,2]

[1]Institute of Particle Technology (LFG), Friedrich-Alexander-Universität Erlangen-Nürnberg (FAU), Cauerstr. 4, D-91058 Erlangen, Germany
[2]Center for Functional Particle Systems, Friedrich-Alexander-Universität Erlangen-Nürnberg (FAU), Haberstr. 9a, D-91058 Erlangen, Germany

Abstract. We present methods for production of plate-like nanoparticles in a stirred media mill. The first method, which will be discussed exemplary for few-layer-graphene and molybdenum disulfide, yields nanoplates with a thickness of few atomic layers by delamination of layered materials. In the stirred media delamination process van der Waals interactions between the layers are overcome by shear forces generated due to collisions of the layered material with milling beads. Plate-shaped two-dimensional particles with lateral diameters in the sub-µm range and a thickness of about 100-200 nm are accessible by deformation of spherical sub-µm particles in a stirred media mill. If the spherical feed material has a particle size below the brittle-ductile transition (for example 200 nm silica), no remarkable breakage, but an increasing shape-transformation from spherical to plate-like morphology is observed with increasing process time (Esper et al. (2020)). The two-dimensional size characterization of non-spherical sub-µm and nanoparticles is challenging. As molybdenum disulfide exhibits size-dependent optical properties, distributions of the nanoplate dimensions are accessible with high precision by analytical ultracentrifugation with UV/Vis/NIR detector. Moreover, we investigate the shape transformation of silica particles quantitatively by using a forward and sideward light scattering method (LUMiSpoc).

1 Nanosheet formation by stirred media delamination and 2D size analysis of molybdenum disulfide nanosheets

Layered materials exhibit an anisotropy in the strength of intermolecular interactions: within the layers there are strong covalent or ionic bonds, between the layers there are only weak van der Waals interactions. In a stirred media mill the layered material particles interact with moving beads. In this way shear forces are generated which overcome the van der Waals interactions between the layers and lead to delamination of nanosheets. If the delaminated nanosheets are sufficiently stabilized against agglomeration and re-stacking, colloidal stable nanosheet suspensions are obtained. In previous works we demonstrated for graphene (Knieke et al. (2010), Nacken et al. (2015), Damm et al. (2015)) and for hexagonal boron nitride (Damm et al. (2013)) that stirred media delamination of layered materials is a scalable top-down method for the production of nanosheets. Here we present the results of a process parameter study for few-layer-graphene. We found that the stressing energy, that means the kinetic energy of the beads, is the most crucial parameter for the product quality regarding delamination degree and defect concentration. Based on the results of statistical Raman spectroscopic investigations we could demonstrate that the stressing energy has to be kept below a critical threshold value to obtain few-layer graphene of good quality (see parameter roadmap in Figure 1).

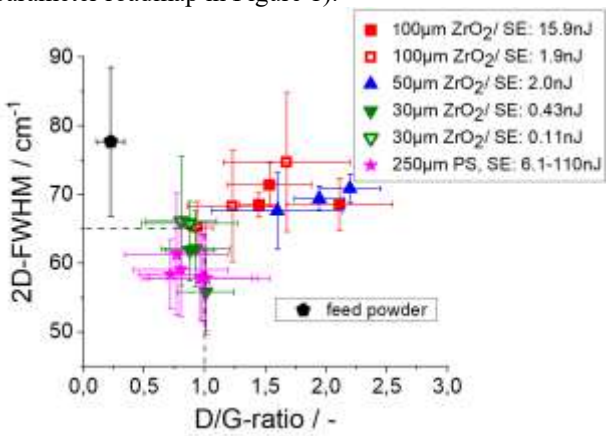

Fig. 1. Process parameter roadmap for the few-layer-graphene production by stirred media delamination (Nacken et al. 2015)).

The product exhibits good quality regarding the delamination degree (< 5 layers) and low defect concentration if the width of the 2D-Raman peak is narrower than 65 cm^{-1} and if the D/G Raman peak intensity ratio is < 1. That means, the process conditions mentioned in the legend result in good product

* Corresponding author: cornelia.damm@fau.de

quality if the data point is located within the area marked by the dashed lines.

According to the parameter roadmap in Figure 1, either very small ZrO_2 beads (30 µm in diameter) or soft polystyrene beads have to be used as delamination media to keep the stressing energy below the threshold value for defect generation. In this paper we apply stirred media delamination to molybdenum disulfide.

Nanosheets of the semiconductor molybdenum disulfide exhibit interesting size-dependent properties (Mak et al. (2010), Backes et al. (2014)) and are therefore promising for applications in visible light photocatalysis and sensing (Wang and Mi (2017)). Based on the size-dependence of the optical properties of molybdenum disulfide nanosheets (Figure 2) Backes et al. (2014) developed a method for the extraction of mean values for the lateral diameter L and the number of layers N from UV/Vis spectra based on the equations (1) and (2)

$$L = [3.5\mu m \cdot (E_B/E_{345nm})] - 0.14\mu m] / [11.5 - (E_B/E_{345nm})] \quad (1)$$

$$N = 2.3 \cdot 10^{36} \cdot exp(-54888nm/\lambda_A) \quad (2)$$

with E_{345nm}: extinction at 345 nm, E_B: extinction at the B-exciton and λ_A: wavelength of the A-exciton (see Figure 2).

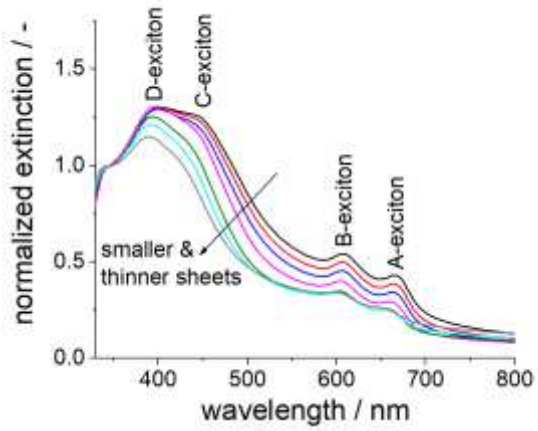

Fig. 2. Size-dependent UV/Vis spectra of molybdenum disulfide nanosheets with excitonic transitions.

We extended the method of Backes et al. (2014) to extract distributions of L and N. We demonstrate that L and N distributions are accessible by fractionation experiments. For that purpose, we classified a delaminated molybdenum disulfide suspension by preparative centrifugation to different sphere-equivalent cut sizes (from 300 to 50 nm) and measured the UV/Vis spectrum of each size fraction. Evaluation of the UV/Vis spectra by equations (1) and (2) and by Lambert-Beer's law provides values for L, N and the nanosheet concentration for each size fraction. A combination of the L and N values with the relative concentration of each fraction provides estimates for cumulative distributions of L and N of the feed material (the 300 nm fraction) and reveals that the material contains a remarkable amount of mono and bilayers.

Analytical ultracentrifugation with UV/Vis/NIR multiwavelength detector (MWL-AUC) (Walter et al. (2014), Walter et al. (2015), Wawra et al. (2018)) provides distributions of the size-dimensions of 2D-materials in one step, without need of any preparative fractionation and with high precision. MWL-AUC measures the sedimentation properties of each settling particle fraction in combination with its optical properties. The measured cumulative sedimentation coefficient distributions were subdivided in different intervals and for each interval the UV/Vis-spectrum was extracted and evaluated by equations (1) and (2). From the datasets for L, N and the quantile of the cumulative distribution Q_{ext} obtained for each sedimentation coefficient interval, cumulative distributions for L and N were constructed. The median values of the L and N distributions obtained by MWL-AUC agree well with the mean values for L and N obtained for each size fraction by the preparative centrifugation experiment.
Based on the distributions of the molybdenum disulfide nanosheet dimensions obtained from MWL-AUC the classification by preparative centrifugation was described quantitatively by determination of a separation efficiency curve for each size dimension.

2 Silica platelet formation by deformation of spherical particles

Spherical silica particles about 200 nm in diameter were processed in a stirred media mill in an organic solvent to prevent dissolution of the particles. SEM investigations reveal that the fraction of spherical particles decreases for longer process time, whereas the fraction of plate-like particles increases continuously. After about 10 h the spheres are almost completely transformed to platelets. As silica does not exhibit size and shape dependent optical features, the 2D size analysis is hampered as no size information is accessible from UV/Vis spectra. We demonstrate that for such class of material the evaluation of light scattering in two directions is helpful for measuring the shape transformation in suspension. The commercial device LUMiSpoc (LUM GmbH, Germany) measures the intensity of forward and sideward scattered light on single particles in suspension. Spherical particles scatter equally in all directions, whereas, anisotropic particles exhibit different scatter intensities in forward and sideward direction. By extracting the relative fraction of particles scattering equally in both directions the relative amount of spheres can be determined. The analysis of SEM micrographs and investigations in suspension using the LUMiSpoc yield comparable trends for the relative fraction of spherical silica particles. This gives evidence for the high potential of the LUMiSpoc for size analysis of 2D materials with dimensions in the sub µm-range.

The authors gratefully acknowledge the financial support of this work by the German Science Foundation (DFG) within the priority program PP2045 – Highly specific and multi-dimensional fractionation of particle systems with technical relevance and the collaborative research center CRC953 – Synthetical Carbon Allotropes as well as in project PE427/10-1.

References

Backes, C., Smith, R. J., McEvoy, N., Berner, N. C., McCloskey, D., Nerl, H. C., O'Neill, A., King, P. J., Higgins, T., Hanlon, D., Scheuschner, N., Maultzsch, J., Houben, L., Duesberg, G. S., Donegan, J. F., Nicolosi, V., & Coleman, J. N., (2014) Edge and confinement effects allow in situ measurement of size and thickness of liquid-exfoliated nanosheets. *Nature Communications* 5, 4576.

Damm, C., Nacken, T. J., & Peukert, W., (2015) Quantitative evaluation of delamination of graphite by wet media milling. *Carbon* 81, 284–294.

Esper, J. D., Liu, L., Willnauer, J., Strobel, A., Schwenger, J., & Peukert, W., (2020) Scalable production of glass flakes via compression in the liquid phase. *Advanced Powder Technology* 31, 4145-4156.

Knieke, C., Berger, A., Voigt, M., Taylor, R., Röhrl, J., & Peukert, W., (2010) Scalable production of graphene sheets by mechanical delamination. *Carbon* 48, 3 196–3204.

Mak, K.F., Lee, C., Hone, J., Shan, J. & Heinz, T. F., (2010) Atomically thin MoS_2: a new direct-gap semiconductor. *Physical Review Letters* 105, 136805.

Nacken, T. J., Damm, C., Xing, H., Rüger, A., & Peukert, W., (2015) Determination of quantitative structure-property and structure-process relationships for graphene production in water. *Nano Research* 8, 1865–1881.

Walter, J., Löhr, K., Karabudak, E., Reis, W., Mikhael, J., Peukert, W., Wohlleben, W., & Cölfen, H. (2014) Multidimensional analysis of nanoparticles with highly disperse properties using multiwavelength analytical ultracentrifugation. *ACS Nano* 8, 8871–8886.

Walter, J., Sherwood, P.J., Lin, W., Segets, D., Stafford, W. F., & Peukert, W. (2015) Simultaneous analysis of hydrodynamic and optical properties using analytical ultracentrifugation equipped with multiwavelength detection. *Analytical Chemistry* 87, 3396–3403.

Wang, Z. & Mi, B., (2017) Environmental applications of 2D molybdenum disulfide (MoS_2) nanosheets. *Environmental Science & Technology* 51, 8229-8244.

Wawra, S. E., Pflug, L., Thajudeen, T., Kryschi, C., Stingl, M., & Peukert, W. (2018) Determination of the two-dimensional distributions of gold nanorods by multiwavelength analytical ultracentrifugation. *Nature Communications* 9, 4898.

18th European Symposium on Comminution & Classification (ESCC 2024)
24-26 June 2024, Miskolc - Hungary

B1: Using the vertical roller mill to address different challenges in mineral processing.

Aubrey Mainza[1,*], *Hakan* Benzer[2], Carsten Gerold[3], *Megan* Becker[1], *Kirsten* C. Corin,[1]*Warren* Little,[1] *Hebert* Nyakunuhwa[1]

[1]Department of Chemical Engineering, Faculty of Engineering and the Built Environment, University of Cape Town, South Africa
[2]Department of Mining, Hacettepe University, Ankara, Turkey

[3]Loesche, Ore & Minerals Technology / Mining Division, Hansaallee 243, 40549 Duesseldorf - Germany

Abstract. This paper discusses the test work performed using the vertical roller mills to show how this technology can be used in the processing of different ore types in the minerals industry. A vertical roller mill can be configured to produce products that are achieved by one of several stages of grinding using conventional mills. The liberation profiles show the threshold beyond which further grinding would not be beneficial. The flotation response from particles prepared using the vertical roller mill was comparable to what was obtained for the material prepared using the rod mill even though the flotation method employed was optimised for rod milling but not for vertical roller mill products that exhibit fast flotation kinetics. A case study on the novel concept of using the vertical roller mill in conjunction with magnetic separation which involves intercepting and extracting a grit fraction and process it in the magnetic separator to reject non-magnetic grits to tailings and recycling magnetic grits for further grinding. The three case studies demonstrate the robustness of the vertical roller mill in addressing challenges that are encountered in mineral processing circuits.

1 Introduction

Comminution is one of the most important areas in the metal production chain from ores. The comminution step is responsible for breaking down ore particles into smaller sizes to expose the valuable minerals. When the valuable minerals are sufficiently exposed, higher recoveries are achieved in downstream concentration or extraction processes. Energy is used in the comminution devices to achieve size reduction of ore particles. Comminution is arguably one of the most energy intensive processes in the metal extraction value chain. Conventional comminution circuits employ crushers and tumbling mills in closed circuit with classifiers to prepare particles for downstream concentration and extraction processes. However, the energy usage in tumbling mills is very high because most of it is dissipated in moving the charge around with less than 5% contributing to breaking the particles. Therefore, development and testing technology that can be used in mineral processing comminution circuits is crucial to the sustainability of the industry where the grades of ores being mined are becoming leaner and plants have to process high tonnages on the plants to meet the desired metal production targets. Vertical Roller Mills (VRMs) have been used successfully to produce fine particles in the cement industry with relatively low energy requirements.

The Vertical Roller Mill is one of the grinding technologies that is of interest in the minerals processing industry because of its energy efficiency and the ability to prepare the ore for flotation or leaching in fewer comminution stages compared to conventional comminution circuits. Apart from high grinding efficiency, the recovery of valuable minerals downstream must be competitive for the comminution technology to be accepted in the minerals industry.

Several studies were performed to evaluate the performance of the Vertical Roller Mill designed and manufactured by Loesche. The VRMs used in the studies were designed to produce a classified product that can be adjusted to meet downstream requirements by adjusting operating and design variables such as the operating pressure, dam ring high, and airflow rates of the classifier. Case studies showing the grinding performance of the VRM when employed to grind different ore types are presented in this paper. Examples from tests where the product from the VRM is floated to evaluate the flotation response are included in the paper. The flotation response for VRM product was compared with material prepared using either the ball mill or rod mill. This was done to assess the recovery potential when ball mill or rod mill are replaced with the VRM. Mineralogical analysis was performed on selected tests to study the liberation profiles of particles prepared using the VRM and was compared to the ball mill or rod mill.

* Corresponding author: aubrey.mainza@uct.ac.za

2 Description of the Vertical Roller Mill

The Vertical Roller Mill is a grinding machine that uses compression and shear grinding mechanisms to produce progeny from feed. The device has conical rollers positioned to press particles placed on a rotating circular table (Erkan,et al, 2012). In conventional vertical roller mill designs the ground material is fluidised and classified in an internal air classifier. The coarse particles fall back on the grinding table while the fine particles are transported out of the grinding circuit and processed in suitable downstream processes. In industrial applications, the device can be fed particles with sizes of up to 150 mm and achieve grinds of down to 20 µm (Erkan et al., 2012), thereby performing the function of two units in traditional circuits: either the tertiary crusher and ball mill or the SAG mill and ball mill from conventional circuits.

3 Vertical Roller Mill Case Studies

Test work involving the vertical roller mill has been performed for the minerals industry for a number of years now. This paper presents three case studies showing the robustness of this technology in addressing the challenges encountered in minerals processing.

3.1 Replacing several grinding stages with VRM

Tests were performed on a mineral ore that has Bond work index values between 23 and 27 at a closing screen size of 75 µm and drop weight Axb parameter of 30-40 (Powell and Mainza, 2006). The ore with such resistance to breakage indices is difficult to process in conventional circuits consisting of either crushers and ball mills or SAG/ball mills making it a suitable choice for conducting the VRM test work. The process plants designed to treat the ore used in this test work have three grinding stages targeting P80 values of 240 µm, 75 µm, and 40 µm in the first, second and third stage, respectively. The tests performed using the VRM were designed to obtain grinds with the P80 values corresponding to the grind stages in conventional circuits. Figure 1 shows the particles size distributions achieved using the VRM in airflow mode. The VRM was able to produce products with particles size distributions close to target grinds at all three grinding pressures tested (Little, 2021).

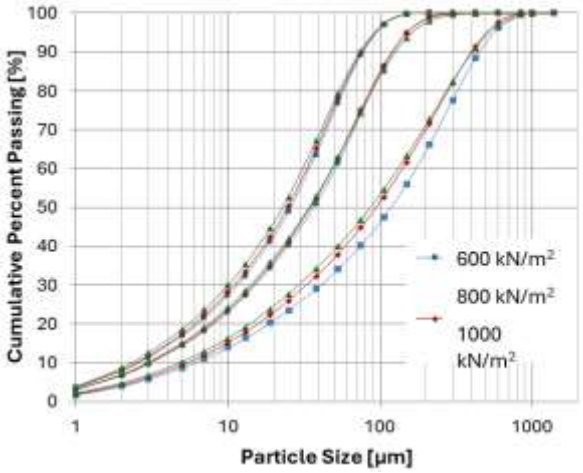

Fig. 1. Particle size distribution for different target product P80s for three grinding pressures at the intermediate dam ring height (Little, 2021).

The liberation profiles from the VRM products at the three target grinds are shown in Figure 2. At a coarse grind with the P80 values of 240 µm, 40% of the valuable minerals were liberated, 22% were in the middling fraction, and 38% were still locked (Little, 2021). A significant improvement in liberated particles were observed at a grind with a P80 value of 75 µm. At that grind, 82% of the minerals of interest were liberated, 9% in the middling fraction and the remainder in the fraction locked in the gangue. No significant change was observed in the liberation profile between the material ground with the VRM to a P80 of 75 µm and a P80 of 45 µm. This shows that there is no significant benefit to grind the material further after achieving a P80 of 75 µm. The flotation performance of material ground with the VRM was superior to that obtained from ore ground using the conventional ball mill. Grind and flotation results from the test work will be presented in the full paper to show the implications of using the vertical roller mill for this ore type.

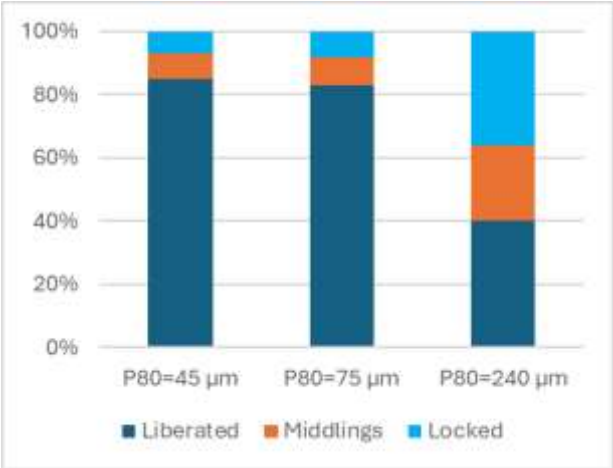

Fig. 2. The liberation profile obtained by grinding ore to different target grinds using the Loeshe VRM (Adapted from Little 2021).

3.2 VRM application on copper-lead-zinc ore

A pilot plant study was performed to evaluate the implications of using the VRM to comminute a copper-lead-zinc ore as a preparation stage for flotation. Test work was performed using the VRM to grind the ore to 65% passing 75 µm and the product subjected to flotation. Ore from the batch was also ground using a laboratory Rod mill to obtain products with 65% passing 75 µm and similar overall product size distributions. The flotation tests were performed on particles prepared using both wet and dry rod milling operation and the flotation response was compared to that of particles milled using the VRM. The VRM recovery for all three minerals of interest was comparable to those obtained from rod milling even though the flotation tests were not optimised for ore prepared using this type of equipment. The information on concentrate grades and fractions that contained losses from flotation of material prepared using the three grinding methods will be included in the paper.

Table 1. Flotation response to material prepared using different comminution methods (extracted from Nyakunuhwa, 2019).

Comminution equipment	Recovery, %		
	Copper	Lead	Zinc
VRM	96.7	94.3	96.6
Rod mill (dry)	96.3	94.3	97.4
Rod mill (wet)	96.7	92.9	97.4

3.3 VRM/grit magnetic separation

The application of a novel concept was developed by Loesche on how the VRM can be used in conjunction with magnetic separation when processing magnetite ores. The magnetite ore is ground using the VRM and a grit fraction is intercepted and extracted for dry magnetic separation. A grit fraction is an internal dry classifier oversize stream, in conventional VRM operation it is recycled to the grinding table. Magnetic grits are returned to the VRM for additional grinding and coarse dry non-magnetic grits are rejected to tailings. The final dry product is also suitable for emerging fine dry magnetic separation that would not require water addition. Results where this concept was applied successfully will be presented in the paper.

4 Conclusions

Three case studies showing the robustness of the vertical roller mill in addressing some of the challenges encountered in comminution circuits for different commodities are discussed. The test work performed showed that the vertical roller mill can be used to achieve different target grinds by tuning operating and design variables as well as the classifier. Improved liberation can be achieved by operating the vertical roller mill at high press forces. The device can be used to grind ores that are easy to float and get comparable results without optimising the flotation approach to take advantage of the fast kinetics encountered when products from the vertical roller mill are floated. The vertical roller mill in conjunction with magnetic separators provides a unique concept to process magnetite ore. In this application, the grit fraction from the air classifier is intercepted and extracted from the machine and treated in a magnetic separator where coarse non-magnetic grits are rejected to the tailings and magnetic grits are recycled to the vertical roller mill for further grinding. The paper provides a broad perspective of what can be achieved by compression machines such as vertical roller mills in the minerals industry.

References

Erkan, E., Umurhan, S., Sayiner, B., Cankurtaran, M., Benzer, H., Aydogan, N., Demir, H.K., Langel, J., Carsten, G., 2012. Comparison of the Vertical Roller Mill and Rod-Ball Mill Circuit on the Gold Extraction, in: XIII International Mineral Processing Symposium.

Little, W. Performance of the vertical roller mill in minéral processing applications when coupled with internal and external classifiers. PhD Thesis 2021.

Nyakunuhwa, S.H, 2019. Effect of VRM on a polymetallic sulfide ore and the Effect of VRM on a polymetallic sulfide ore and the flotation response as compared to conventional wet and dry rod milling.

B2: Comparison of Energy Performance of SAG and HPGR circuits for a Large Copper Mine

Bern Klein[1,*], *Chengtie* Wang[1], *Amit* Kumar[1], *Cherezade* Saud[1], *Giovanni* Pamparana[1], *Jaidar* Saud[1,*]

[1]Norman B. Keevil Institute of Mining, University of British Columbia, Vancouver, Canada

Abstract. Comminution is the most energy intensive component of mining operations. For large copper mines, the convention is to use SAG mill-based circuits followed by ball mill grinding. Alternative, circuits that use High Pressure Grinding Rolls are reported to use about 20% less energy than the SAG based circuits. As a result, despite higher capital cost for HPGR circuits, trade off studies to compare the SAG based and HPGR based circuits is common for new projects. With consideration of the improved energy efficiency of particle compression breakage as compared to attrition and impact, a study was conducted to assess the potential energy savings resulting from the replacement of ball mills with the HPGR. This paper is based on research to assess alternative comminution flowsheets for copper porphyry mine and compare energy consumption of three alternative circuits: 1. Pre-crush - SABC, 2. HPGR - Ball Mill and 3. HPGR - HPGR.

1 Introduction

For large copper porphyry mines, variations on SAG mill based circuits such SAB, SABC and Pre-crush followed by SABC are commonly applied. The SAG based circuits have high capacity and are relatively simple from a material handling perspective. However, these circuits are energy intensive and plant throughputs are susceptible to variations in ore hardness. High Pressure Grinding Roll (HPGR) based circuits report reduced operating costs, and production rates are less susceptible to variations in ore hardness (Costello et al, 2019, Wang, 2013, Lovatt et al, 2023). With goal of reducing comminution energy consumption, UBC participated in the Natural Resources Canada CrushIt! Challenge; the goal was to reduce overall comminution energy consumption by more than 20%. UBC in collaboration with COREM and a copper porphyry mine conducted a study to potentially replace secondary wet ball mill grinding with the HPGR.

This paper compiles the results of plant surveys and pilot scale HPGR test programs for the copper porphyry mine in British Columbia, Canada. The results were used as the basis for comparison of three circuit options: 1. Base Case Pre-crush followed by SABC; 2. Primary HPGR followed by Ball Mill Grinding and 3. Primary and Secondary HPGR comminution. A comparison of direct comminution energy consumption as well as consumptions including energy consumed by ancillary material handling, size classification and dewatering equipment is presented. There will also likely be reductions in embodied energy due to reduction in use of steel grinding (balls) media; however, the study will not assess the impacts on embodied energy.

2 Process Description

The three comminution circuits are described in the following section. The selected design parameters, assumptions, and energy calculations for the three circuits are summarized in Table 1.

2.1 Copper Porphyry Mine (Base Case)

The copper porphyry mine recovers copper and gold from there deposit in Canada. The mine was originally designed and commissioned in 2011 with a conventional SABC circuit. The ore was considered very competent and hard with Axb values of less than 30 and ball mill Bond work indexes (BWI) of greater than 20 kWh/t (Marks et al, 2010). In 2014, the plant added a pre-crush cone crusher ahead of the SABC circuit to increase capacity to 40,000 tpd (Westendorf et al, 2015). The ball mill generates rougher flotation feed with a target grind size (P80) of 150 microns.

In 2019, a plant survey was conducted to collect operational and energy consumption information from the comminution circuit. During the survey, samples of SAG mill feed, ball mill circuit feed, and cyclone underflow were collected for pilot scale HPGR testing at the UBC lab. In addition, the samples were used to determine SAG (drop weight test), Ball Mill (BWI) and HPGR (Piston Press test) parameters.

* Corresponding author: bklein@mining.ubc.ca

2.2 HPGR – Ball Mill Circuit

For the proposed HPGR – Ball Mill circuit, 40,000 tpd of ore is fed to a primary crusher and then to a cone crusher in closed circuit with screening to prepare HPGR feed. Testing was conducted using a Koeppern pilot scale HPGR on samples collected during a plant survey to determine specific energy requirements and throughput parameters (Wang, 2021; Pamparana, 2024). The HPGR is operated in a closed circuit with a 6 mm screen. The specific energy for the HPGR circuit with and without ancillary equipment is presented in Table 1. Including conveyor belts and screens, it is estimated that a 4.5 kWh/t energy consumption is required to reduce the particle size from the F80 of about 40 mm to a P80 of 4 mm (Pamparana et al., 2023). For the Ball Mill, a 5% reduction in BWI was assumed, although studies at UBC and the literature indicate that HPGR comminution lowers the BWI in the order of 10%.

2.3 HPGR – HPGR Circuit

For the HPGR-HPGR circuit, the primary HPGR conditions and energy consumption were assumed to be the same as in the HPGR-Ball Mill Circuit. For the secondary HPGR circuit, an extensive study was conducted at UBC in collaboration with COREM. The study was supported through the CrushIt! Challenge which was an initiative by Natural Resources Canada to evaluate novel technologies with the target of reducing overall comminution energy consumption by greater than 20%. As described, a plant survey was conducted, and samples were collected for pilot and bench scale testing. While the primary focus was on direct comparison of ball mill energy to secondary HPGR energy, the study also investigated size classification and dewatering technologies for the secondary HPGR. Several studies have demonstrated fine HPGR comminution circuits with dry air classification. However, due to the wet coastal climate, it was necessary to assess wet size classification and dewatering technologies for the selected HPGR – HPGR circuit. It was therefore necessary to determine the tolerable moisture content for the secondary HPGR. Feed particle size is much finer than feed to the primary HPGR. Therefore, the feed has a much larger specific surface area such that it was expected that the secondary HPGR could tolerate a higher moisture content than the primary HPGR (typically 2 to 5%). Pilot HPGR tests over a range of moisture contents showed that the secondary HPGR could accept feeds with up to 9% moisture (by wt.) while still achieving good gap expansion and particle size reduction (McIvor et al, 2023).

A study, including pilot scale testing, size classification and dewatering technologies was conducted (Saud, 2021). For size classification, a range of technologies were compared and ranked shortlisting hydrocyclones, high frequency vibrating screens (Derrick Stack Sizer) and screw (spiral) classifiers. The main considerations were for ranking the technologies were throughput, energy requirements and footprint. A greater challenge was to dewater the size classifier oversize to the target 9% moisture content. The main considerations were the ability to achieve the target moisture content, energy consumption and footprint. Pilot tests showed the vibrating dewatering screens were not able to achieve the target moisture levels. Thickening and filtration could achieve target moisture levels, but with large footprint and significant energy consumption. A small-scale pilot test program with a spiral classifier showed the water was released near the top of the spiral and lowered water contents to below 8%. The suitability of the spiral for large scale operations was re-enforced by the installation at Boliden's Aitik Mine in Sweden where spirals were selected due to their low energy consumption (McElroy et al, 2019). The spiral classifier was therefore selected for both size classification and dewatering for this study. The estimates of energy consumption for the size classification was conservative as more research is needed to evaluate the spiral for size classification and dewatering.

3 Comparison of Circuit Comminution Energy Consumptions

The three circuits were compared based on direct consumption of comminution energy as well as with consideration of ancillary equipment for the respective circuits. As shown in Table 1, the base specific energy consumption for comminution is 19.4 kWh/t which decreased to 16 kWh/t for the HPGR-Ball Mill circuit and to 9.5 kWh/t for the HPGR-HPGR circuit. These decreases represent 18% and 51% energy savings, respectively. With estimates of power consumed by ancillary equipment, the base case total circuit specific energy consumption is 20.8 kWh/t. This is decreased to 18.1kWh/t for the HPGR-Ball Mill Circuit and to 13.0 kWh/t for the HPGR-HPGR circuit representing 13% and 38% energy savings, respectively.

4 Conclusions

One role of research is to provide information about and advance promising technologies. First invented in 1979, the HPGR is such a technology and is only in recently gaining acceptance. The results of the study showed that significant energy savings can be achieved using existing comminution technologies. While HPGR based circuits have been and are increasingly being applied to replace SAG mills, there has been relatively few studies to assess replacing ball mills with the HPGR. Some challenges need to be addressed, however the potential energy saving benefits are substantial. The paper did not assess the impacts on embodied energy; however, an HPGR-HPGR circuit would not require grinding balls and therefore likely has less associated embodied energy. It is expected that with additional research and development, the assumptions made in this study can be verified, and energy savings can be improved further.

Table 1. Energy Comparison of three comminution circuits.

Description		Operation	Survey 2019	Case 1	Case 2
		Precrush-SABC	Precrush-SABC	HPGR+BM	HPGR+HPGR
Ore hardness					
Axb	-	25-40	29.2	29.2	29.2
BBWI on SAG/HPGR feed	kWh/t	20-25	21.5	21.5	21.5
Grind size	microns	150-212	205	192	192
SAG Mill Circuit		**One (1) 34' x 20'**	**One (1) 34' x 20'**		
Installed/operating power	kW	13,691	11,666		
Comminution specific energy	kWh/t		6.3		
Auxiliary specific energy	kWh/t		0.32		
Primary HPGR Circuit				**Pilot (open)**	**Pilot (open)**
Specific throughput constant m-dot				250	250
Net specific energy	kWh/t			2.34	2.34
Recirculating load	%			50%	60%
Comminution specific energy	kWh/t			3.51	3.74
Auxiliary specific energy	kWh/t			1	1
Secondary Ball Mill Circuit		**Two (2) 24' x 40'**	**Two (2) 24' x 40'**	**Assume/Simulate**	
Installed/operating power	kW	25,354	24,303	23,088	
Comminution specific energy	kWh/t		13.1	12.5	
Auxiliary specific energy	kWh/t		1.08	1.08	
Secondary HPGR Circuit					**Pilot (close)**
Specific throughput constant m-dot					210
Net specific energy	kWh/t				1.78
Recirculating load	%				321%
Comminution specific energy	kWh/t				5.7
Auxiliary specific energy	kWh/t				2.5
Summary					
Total comminution specific energy	kWh/t		19.4	16.0	9.5
Relative to base case	kWh/t			**18%**	**51%**
Total circuit specific energy	kWh/t		20.8	18.1	13.0
Relative to base case	**kWh/t**			**13%**	**38%**

Acknowledgements

The authors would like to acknowledge the technical and financial support from COREM, Koeppern Machinary Australia as well the financial support from Mitacs.

References

Costello, B., Brown, J., 2019, A Tabletop Cost Estimate Review of Several Large HPGR Projects, SAG Conference, 2019, Vancouver, Canada

McIvor, R., Gagnon, C., Klein, B., Kumar, A., 2023, Development of Fine High-Pressure Grinding for Mineral Processing Plans, SAG Conference 2023, Vancouver, Canada

Lovatt, I.A., Becker, M., Putland, B., Radford, R., Robinson, J., 2023, Trade-Off Realities in HPGR vs SAG Milling – A Practical Comparison of Tropicana and Gruyere Comminution Circuits, SAG Conference 2023, Vancouver, Canada

Marks, A., Sams, C., and Major, K.W., 2010, Grinding Circuit Design for Similco Mines, SAG Conference 2010, Vancouver Canada

McElroy, A., Powell, M., Tillberg, J., Hilden, M., Yahyaei, M., Linna, M., Johansson, A., 2019, An Assessment of the Energy Efficiency and Operability of the World's Largest Autogenous Grinding Mills at Boliden's Aitik Mine, SAG Conference 2023, Vancouver, Canada.

Pamparana, G., Klein, B., Bergerman, M.G., Westendorf, M., and Atutxa, I., 2023. Optimizing Energy and Throughput for HPGR: A Case Study for Copper Mountain Mine, SAG Conference 2023, Vancouver, Canada.

Pamparana, G., 2024. A Study on Compression Breakage: From Theory to Practice (unpublished Doctoral dissertation, University of British Columbia).

Saud Soto, C.K., 2021, Size classification and dewatering for fine HPGR comminution circuit, (MASc Thesis, The University of British Columbia).

Wang, C., 2013. Comparison of HPGR-ball mill and HPGR-stirred mill circuits to the existing AG/SAG mill-ball mill circuits (Master's Thesis, University of British Columbia).

Wang, C., 2021, Development of a comprehensive model using large experimental data sets, (Doctoral Thesis, The University of British Columbia).

Westendorf, M., Rose, M., Meadows, D.G., 2015, Increasing SAG Mill Capacity at the Copper Mountain Mine through the addition of a Pre-crushing Circuit, SAG Conference 2015, Vancouver, Canada

B3: Axial wear in HPGR

Felix Heinicke[1,*] and *Holger* Lieberwirth[2]

[1]Köppern Aufbereitungstechnik GmbH & Co.KG., Freiberg, Germany
[2]Institute of Mineral Processing Machine and Recycling System Technology, TU Bergakademie Freiberg, Germany

Abstract. High pressure grinding rolls (HPGR) are known for effective grinding of clinker and raw materials for clinker production since the 1980's. Modern advancements with regards to the development of roller surfaces now make HPGR operation suitable for hard rock materials in mineral processing. The physical basis of the axial wear and the determination of limiting factors of the material compounds for roller surfaces are still of high interest. This contribution addresses measurements of reaction stresses as a basis for future surface developments, including detailing of the axial wear.

1 Basis

The basis for HPGR technology was developed by Professor Schönert at the Technical University of Clausthal (Schönert, 1985). Subsequent investigation by Lubjuhn (1992) took measurements of the axial behaviour of grinding taking into account pressure, fineness of product and mass throughput on a lab machine, as per Figure 1.

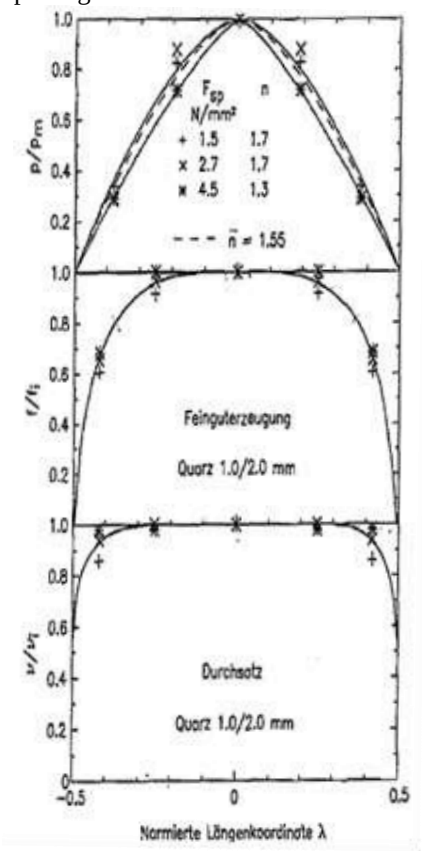

Fig. 1. Pressure, fineness and throughput of lab machine as per Lubjuhn (1992) with low value at the edges.

While large machine sizes of up to 2500 tph have been in operation for hard rock processing since 2006 (Vanderbeek 2006), more industry research has been addressed by Heinicke (2007). The research clearly shows that the behaviour of material within the HPGR is linked to the material flow by the wall friction, axial bypass and segregation of material. Modelling was developed to assess the axial stress distribution in coarse materials (Barrios, 2014). For special materials, such as very fine iron ore concentrate under moist conditions, the stress distribution was not directly accessible by measurements and was therefore a target for a research campaign at Freiberg University (Drechsel, 2020 and Kreibich, 2019). The results of piston and die measurements along with small scale HPGR test work are therefore addressed in this contribution.

2 Piston and Die Measurements

The test work was structured to replicate tests performed by Kühnel (2018) by using *Fujifilm Prescale* pressure response paper and a piston and die test as per Figure 2.

Fig. 2. Left: Die with pressure foils in one of the measurement layers; Right: piston after pressure application on wet material

The calibration was done through photo analysis of the RGB values resulting in a noticeable trend shown in Figure 3.

* Corresponding author: Holger.Lieberwirth@iart.tu-freiberg.de

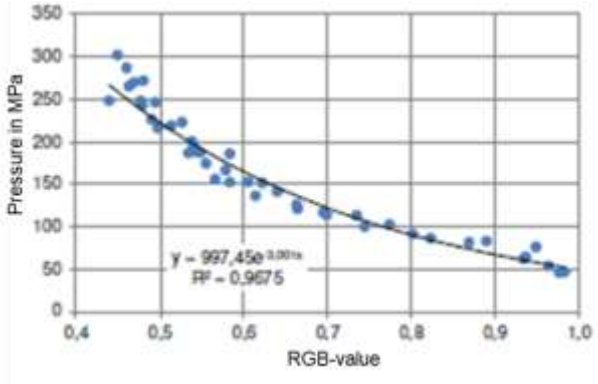

Fig. 3. Pressure vs. RGB-value for foil testing

Subsequently, a two-dimensional post-processing of the data was conducted to analyse the behaviour of the particle bed. Figure 3 shows the results of various piston and die pressures normalized to a base value.

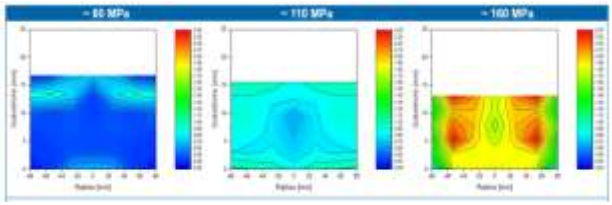

Fig. 4. Particle bed pressures for iron ore concentrate at various activation stresses

Three trends can be identified in accordance with the findings of Aziz (1979):

a) The stress intrusion from the top stresses are higher at the top than at the bottom of the material,
b) stress paths balance from the top towards the walls which isolate the center of the bulk,
c) peak stresses are 2.5 times higher than medium stress values.

An additional test series was processed to confirm the effect of the edge gap with respect to the applied stress. Therefor the die diameter was reduced to allow for a 1, 3 and 10 mm gap as per Figure 5. Pressure drops along the edge can be seen to increase by a factor of 2. The sealing at the edges of the HPGR is therefore a key target for optimization of the operation of the HPGR machines. Spring loaded cheek plates with adaptable gaps may be more valuable than edge rotating side plates, which by design have fixed axial gaps (Heinicke, 2023)

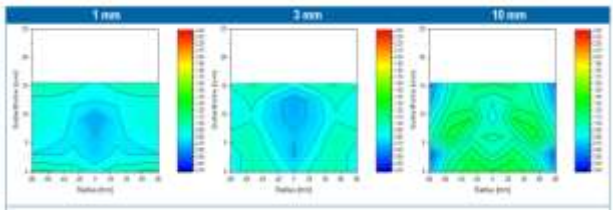

Fig. 5. Particle bed pressures for iron ore concentrate at various edge gaps

Furthermore, investigations have been conducted to verify the impact of previously compacted material or tramp metal passing within the bulk material bed, as sometimes is observed in the iron ore concentrates industry. Therefor a prepressed tablet has been embedded in the iron ore concentrate as per Figure 6. Peak pressures of up to 4 times higher than the medium stress have been measured which clearly show that a HPGR process can create stresses out of material boundaries (Figure 7, also see Kleeberg, 2007). The development of state of the art roller surfaces can use this information to adapt for better designs. However to maintain a stable operation an engineering process control or online digital helpers for tracking such events in production is a key.

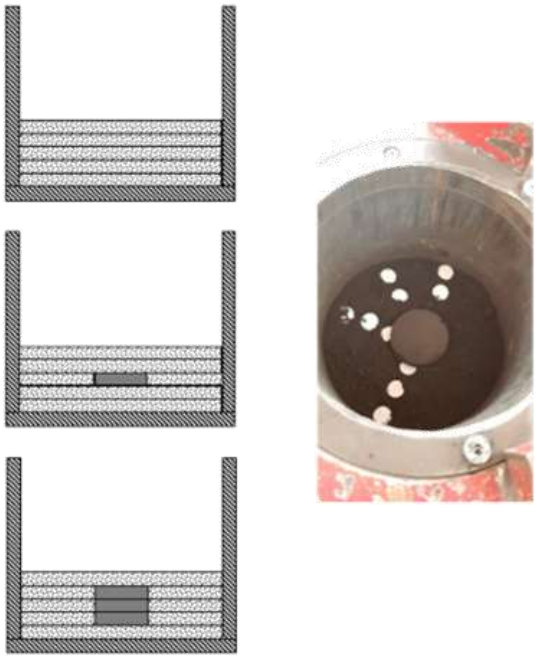

Fig. 6. Test setup for prepressed material within the bulk pressure assessment

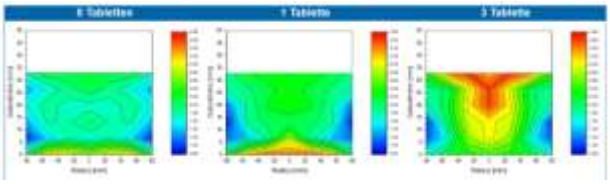

Fig. 7. Stresses of embedded prepressed materials

3 HPGR measurements

The same stress analysis methodology has been applied using a half scale HPGR test machine with 0,3 m diameter. The foil was taped to the surface of the rollers as per Figure 8. This test also produced clear trends in the RGB values.

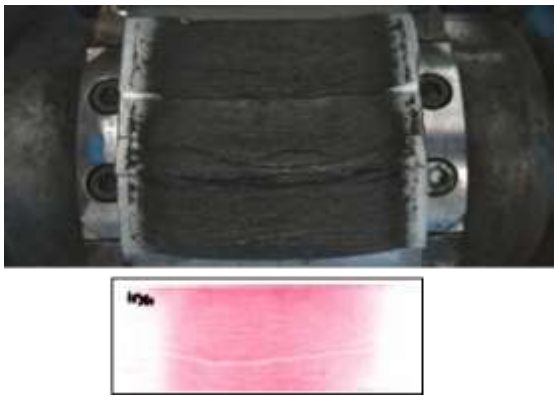

Fig. 8. Foil after test series and extracted color trend

The data was process and wear measurements were used as described by Hanstein (2001). Figure 9 shows the normalized trends for both sets of data. It can clearly be seen that the curves still deviate. This likely caused by the axial movement of iron ore concentrate, as discussed in relation to industrial presses by Odenwald (2005). Future research on the resulting edge force at the cheek plates may therefore be a basis for a more detailed understanding of the process.

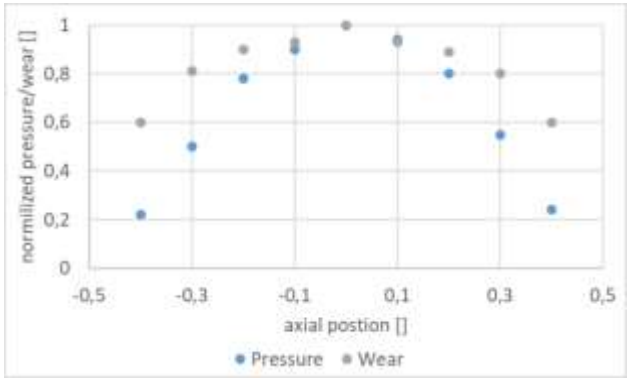

Fig. 9. Axial wear vs axial pressure

References

Aziz, M.S.J.A. (1979) Zerkleinerung von Zementklinker in Einzelkorn-Situation, Kornschichten und im Gutbett. *Dissertation. Universität Karlsruhe*

Barrios, G.K.P. (2014) A DEM model of HPGR operation using bed compression models calibrated with a piston die test. *Proceedings of Comminution in Cape Town*, 1-8

Drechsel, R. (2020) Druckmessung in Gutbetten. *Grosser Beleg. Technische Universität Bergakademie Freiberg*

Hanstein, T. (2001) Beitrag zu Erhöhung der Standzeit der Arbeitsorgane von Gutbett- Walzenmühlen. *Dissertation. Technische Universität Bergakademie Freiberg*

Heinicke, F. (2012) Beitrag zur Modellierung der Zerkleinerung in Gutbettwalzenmühlen. *Dissertation. Rheinisch-Westfälische Technische Hochschule Aachen*

Heinicke, F. (2023) Physical relations of Edgs Effects in HPGR. *Proceesing of the SAG conference in Vancouver*, 1-11

Kleeberg, J.: Untersuchungen zur Oberflächenbelastung der Walzen von Gutbett-Walzenmühlen. Dissertation. Technische Universität Bergakademie Freiberg, 2007

Kreibich, J. (2019) Druckmessung bei der Vermahlung von Eisenerzkonzentraten. *Diplomarbeit. Technische Universität Bergakademie Freiberg*

Kühnel, L. (2018) Druckverteilung im idealen Gutbett. *Dissertation. Technische Universität Bergakademie Freiberg*

Lubjuhn, U. (1992) Materialtransport und Druckverteilung im Spalt der Gutbett-Walzenmühle. *Dissertation. Technische Universität Clausthal*

Odenwald, B.H. u.a.: HPGR applications in iron ore pellet plants in Brazil. Paper at Randol Pacific conference on innovative metallurgy in Perth, 2005

Schönert, K. (1985) Zur Auslegung von Gutbett-Walzenmühlen. *Zement Kalk Gips*, Jg. 38 Nr.12, 728-730

Vanderbeek, J.L. (2006) HPGR implementation at Cerro Verde. *Proceedings of SAG*, 45-61

B4: Optimisation of vibrating mills operation – Case study: A copper processing application

Saeid Zare[1], *Mohsen Yahyaei*[2*]

[1]Shahid Bahonar University of Kerman, Iran
[2]Jullius Kruttschnitt Mineral Research Centre (JKMRC), The University of Queensland, Queensland, Australia

Abstract. As orebodies become more complex and lower grade, there's a growing demand from crushing and grinding circuits for a finer product with higher feed rates. When the grinding circuit output fails to meet downstream process requirements, production costs rise while performance declines and therefore, optimizing grinding efficiency becomes crucial. In a practical study at the Shahrood copper ore process plant, the performance of a vibrating mill in the grinding circuit was assessed. The investigation indicated subpar circuit performance. Operational solutions included reducing particle size in the vibrating mill feed, changing from series to parallel connection for vibrating mill tubes, and using a standard filling charge of balls. These modifications resulted in a 51% increase in plant throughput, along with 24% reductions in operational-specific energy consumption and the operational work index.

1 Introduction

Mineral processing plants involve stages like crushing, grinding, classification and concentration, all impacting the performance of the process. The Mining industry consumes 6% to 7% of the total world's total energy. Comminution accounts for 40-50% of the total energy consumed in a mining operation. The grinding process alone requires 90% of the energy while blasting and crushing use 3-5% and 5–7%, respectively. The comminution energy efficiency despite all research and optimisation efforts, remains low. Large ball mills in mining utilize only about 20-30% of the input energy for size reduction [Alvardo et al., 1998; BCS Incorporated, 2007; Fuerstenau and Abouzeid, 2002].

Energy analysis reveals that comminution is highly irreversible. [Alvardo et al., 1998]. Most input energy dissipates as heat (85%), electrochemical losses (12%), and noise (2%). Ancillary processes (material handling, classification) and indirect energy (grinding media and liners manufacturing) also contribute. [Musa, and Morrison, 2009]. Liner costs can be as high as 50% of operational and maintenance costs in milling [Manouchehri, 2013].

Therefore, researchers seek optimal methods for blasting and mining, crushing, and grinding to enhance energy efficiency. The goal is to transfer most energy used in comminution to particles and minimizing wastage at every stage.

Grinding within a tumbling mill is influenced by factors such as particle size, quantity, motion type, and the spaces between individual pieces of the medium. Unlike crushing, which occurs between rigid surfaces, grinding is a stochastic process. It can occur through various mechanisms, including:

- **Impact or Compression:** Sudden forces applied nearly perpendicular to the particle surface.
- **Attrition:** Steady forces that break the particle matrix.
- **Abrasion:** Forces acting parallel to and along the surfaces (shear).

Product size control depends on the properties of the mill charge, the nature of the ore feed, and the specific mill and circuit employed [Wills, 2016].

1.1 Vibrating mills

Vibration mills, akin to ball mills, operate by crushing particles between porcelain or metal balls and the mill body [Hiroaki et al., 2007; Michael and Taylor, 2013]. Specifically, twin-tube vibrating mills employ an unbalanced drive. The grinding cylinders, containing both the grinding bodies and the material to be processed, continuously experience impulses from circular vibrations within the mill body.

The grinding process itself results from the rotation of the grinding bodies in the opposite direction to the driving rotation, leading to continuous head-on collisions. The driving motor connects to the primary shaft via a propeller shaft. Centrifugal weights on the primary shaft are meticulously adjusted to achieve the optimal vibration circuit diameter for efficient grinding. Lubricated anti-friction bearings are safeguarded by a specialized labyrinth sealing.

The entire vibration system is positioned on spring elements or rubber buffers. If the transfer of vibrating power to the mill's base requires reduction, an additional counter-vibration frame supports the entire vibrating mill and its drive.

* Corresponding author: m.yahyaei@uq.edu.au

Grinding cylinders in vibrating mills feature flanged inlet and outlet caps at both ends. Separating discs hold the grinding bodies in place at the outflow heads, ensuring that only the ground material can exit. Internally, the grinding cylinders are safeguarded by replaceable wear-resistant linings.

Continuous charging occurs through vibrating feeders, rotary valves, or conveyor screws. In **Fig. 1**, the typical construction of a twin-tube vibrating mill is illustrated. The throughput depends not only on machine size but also on parameters such as frequency, vibration amplitude, material residence time, and the arrangement of grinding cylinders and media.

Fig. 1. Palla™ vibrating mill with charged grinding cylinders (Andres and Hude, 2010)

1.2 Operating Principles of Vibrating Mills

The vibrating mill belongs to the group of mills that harness impact forces. Unlike the so-called impact mill, where size reduction occurs primarily due to impact energy, vibrating mills rely on the impact energy of the grinding media. Three types of grinding media are applicable in vibrating mills, each causing distinct impulse transitions due to their geometry [Andres and Haude, 2010]:

- Rods: Impart linear impact energy.
- Balls: Deliver punctual impact energy.
- Cylpebs: Contribute linear and laminar impact as well as friction energy.

To achieve optimal energy transmission, selecting the right grinding media is critical. Generally, the largest grinding element should be capable of accommodating the largest particle in the feed material. However, using excessively large grinding media reduces the rating, subsequently diminishing the comminution outcome. Conversely, operating the vibrating mill with too small grinding media may allow the feed material to bypass size reduction or lead to accumulation and plugging within the mill.

Vibrating mills, sometimes used in closed circuits with classification equipment, enhance circuit capacity and prevent the production of excessively coarse or fine particles. Arghr (1997) established conditions to protect the elastic system of vibrating mills with spatial motions. They also proposed a driving system for efficient milling.

In vibrating mills, the feed continuously charges the grinding cylinders, and material flows into gaps among the grinding media via vibration. Simultaneously, size reduction and transportation occur. The degree of size reduction primarily depends on retention time and throughput. In-chamber screens can be installed at the end of the grinding cylinders to retain grinding media while allowing product material to pass through. For dry grinding, the following cylinder connection options are feasible which are also illustrated in **Fig. 2**.

- Series connection
- Parallel connection
- Center feeding

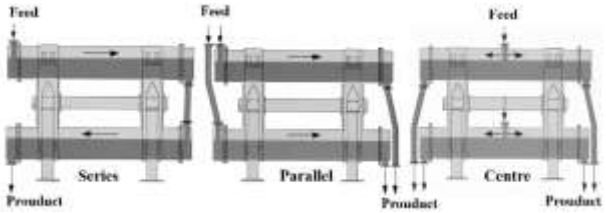

Fig. 2. Various operating configurations of two vibrating mills (Andres and Hude, 2010)

The connection of grinding cylinders in industrial mills depends on material characteristics and process requirements. In the conventional model, grinding cylinders are arranged in series, allowing the feeding material to traverse both cylinders for intensive treatment. This configuration is crucial for hard or coarse materials and fine grinding outcomes.

Alternatively, parallel cylinder arrangement enables independent operation, halving the residence time. Material treatment is less intense, resulting in higher mill output. This setup benefits soft or low-grain-size materials and situations where lower fineness suffices.

Centre feeding, with four distinct routes, maximizes capacity but shortens residence time. It suits gentle grinding processes and non-ultra-high fineness requirements.

Despite practical importance, research on vibrating mills remains limited. No published works explicitly describe their impact on efficiency and feed rates. Our industrial investigation explores operational parameters and feed rate enhancement strategies, emphasizing the advantages of this grinding equipment.

2 Materials and methods

2.1 Shahrood Copper Processing Plant

The Shahrood mineral processing plant utilizes a comprehensive five-stage process for oxide copper leaching. The operation begins with crushing and screening, where a jaw crusher followed by a hammer crusher, in a closed circuit with a double screen, prepares the ore. The second screen level features 4mm square apertures, ensuring the right size particles proceed to grinding. Subsequent stages include tank leaching and dewatering before the final cementation stage. With a feed rate of 72 tons per day, the plant processes ore with

a fresh feed grade of copper above 0.7%, moisture content above 1%, and a particle size (d80) larger than 10 cm. The malachite ore is transformed into a product with a remarkable 60% copper grade, showcasing the plant's efficiency.

2.2 Grinding circuit configuration

The twin tube vibrating mill of the Shahrood plant is in a series connection because of the characteristics of mill feed (**Fig. 3**). The speed of the mill motor drive is 1500 to 800 rpm/min and it is controlled from the control room. The mill has been operating in an open circuit. The maximum feed rate is 3.1 tons/hour. The additional technical data of this equipment are displayed in **Table 1**.

Table 1. The specifications of the Shahrood twin vibrating mill

Design specification	Value
Max ball diameter (mm)	50
Maximum power (Kw)	97
Operation power (Kw)	80
Operation speed (rpm/min)	950
Mill diameter (**c**m)	60
Mill length (EGL*) (**c**m)	285

*EGL: effective grinding length.

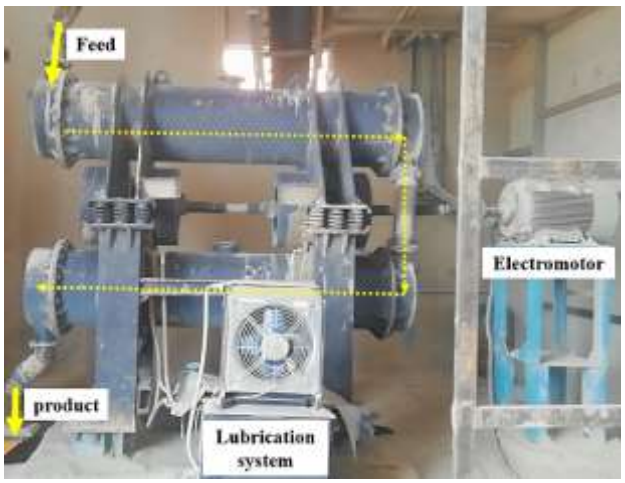

Fig. 3. Configuration of Sharood's twin vibrating mills

2.3 Mill inspection and sampling

The study of the vibrating mill's performance, focusing on particle size distribution (PSD), was conducted through meticulous monitoring over 8 hours with subsamples taken every 20 minutes. The operational parameters, such as power draw, rotational speed, feed rate, and feed particle size, were maintained consistently, ensuring the reliability of the data collected.

The results indicate a slight reduction in the P_{80} size of the product compared to the feed, showcasing the mill's ability to reduce particle size under the specified operating conditions. (**Fig. 4** and **Fig. 5**).

The particle size distribution (PSD) analysis of the vibrating mill product indicates a predominance of impact grinding mechanisms, as evidenced by the low percentage of particles under 63 µm. This finding is crucial as it correlates with reduced sulfuric acid consumption and energy savings. However, the presence of particles larger than 355 µm, constituting a quarter of the total product, suggests inefficiencies in yield recovery and potential blockages in the leaching process. These insights from the audit highlight opportunities for optimization in the vibrating mill and the associated crushing and screening circuits.

Fig. 4. Images of feed and product of the vibrating mill after sizing

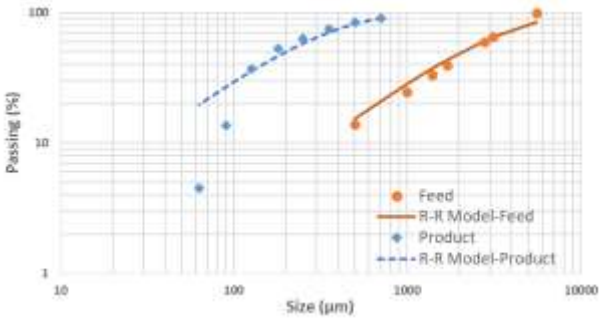

Fig. 5. Size distribution of mill feed and product in a series configuration

2.4 Mill grinding performance

The differential wear rate of balls in the top and bottom tubes is indeed influenced by the PSD of the feed. When the PSD of the feed in the top tube is larger, it necessitates the use of larger balls to accommodate the coarser material. Adhering to the recommended ball charge of 60-70% is crucial for optimal operation, as supported by the studies of Andres and Haude (2010) and Du and Wu (2015). The observed higher wear rate in the top tube compared to the bottom tube aligns with expectations due to the differences in PSD and the subsequent need for varied ball charging schedules in terms of both size and quantity. The measured ball consumption rates further validate these findings, with the top tube showing a higher consumption rate.

The optimal ball charge for tube mills is a critical factor for ensuring efficient operation. Research indicates that a filling charge of 60-70% is ideal for maximizing the grinding efficiency and longevity of the balls. The ball charge measurements for the top and bottom tubes are conducted and the results are presented in **Table 2** and **Fig. 6**. The grinding media consumption for the top and bottom tubes are 510 and 390 g/ton, respectively.

The findings suggest that the charging schedules should be adjusted not only in terms of quantity but also the size

of the balls to optimize the milling process and reduce the overall wear rate.
H_c = Vertical Height between balls level to up tube (cm)
D_M = internal diameter of the tube (cm)
V = Ball filling (%)

Table 2. The technical data of Ball filling of vibrating mill

tube	H_C	DM	Filling (%)
Top	29	58	50
Bottom	25	58	58

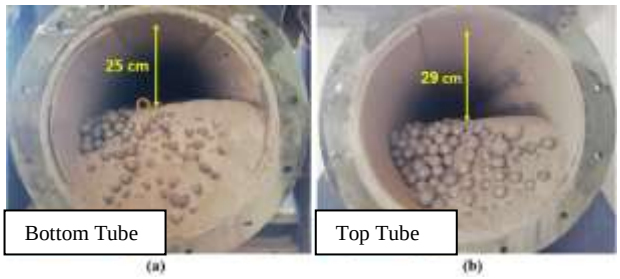

Fig. 6. Mill filling of the bottom (a) and top (b) tubes during the mill's inspection.

The plant audit indicates that the power draw of the vibrating mill varies depending on its operational state. Without feed, the mill draws 62 kW, which increases to 78 kW during operation and reaches 97 kW under nominal conditions. This suggests that the mill operates at 80% of its nominal power draw (**Table 3**).

Table 3. Powerdarw details of the mill during the inspection

	Nominal	Empty	Operational
Ampere (I/h)	165	105	131
Power (Kw/h)	97	62	78

2.6 Process optimisation

The optimization of the Shahrood copper processing plant's milling process through the installation of a roller crusher is a strategic move to enhance efficiency. By reducing the particle size of the mill feed, the plant can significantly increase the feed rate. The roller crusher, powered by dual 18 kW motors, ensures a consistent and fine feed, which is crucial for the subsequent vibrating mill operation. The investigation into the feeding mechanisms revealed that a parallel connection of cylinders is most effective for this setup, optimizing the feed rate and, ultimately, the plant's throughput.

3 Results and discussions

3.1 Effect of pre-crushing

The integration of a roller crusher before the vibrating mill, along with a series of modifications to the parallel tube connections, has increased the feed rate by 51%, from 3050 to 6200 kg/hour. Additionally, the filling charge of balls for both tubes was raised to 65%, resulting in an increase in the power draw of the vibrating mill to 90 kW, which is 93% of its nominal power draw. During an 8-hour sampling period, with subsamples taken every 20 minutes, it was observed that the critical operational parameters influencing the particle size distribution of the product remained stable. These parameters included a power draw of 90 kW, a motor rotational speed of 1400 rpm, a feed rate of 6200 kg/hour, and a P_{80} of feed at 1553 µm. Under these operational conditions, the P_{80} of the product from the vibrating mill was measured at 420 µm (**Fig. 7**).

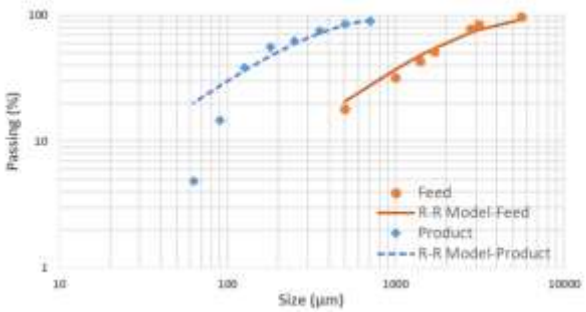

Fig. 7. PSD of feed and product of the vibrating mill in parallel configuration.

3.1 Investigating energy efficiency

The operating work index of the mill in series and parallel configurations is presented in **Table 4**.

Table 4. Comparison of operating work index before and after optimisation

Configuration	Power draw (kw)	Throughput (t/h)	Ecs (Kwh/t)	P_{80} (µm)	F_{80} (µm)	Wi (Kwh/t)
Series	80	3.05	26.2	436	4242	80.5
Parallel	126	6.2	20.3	422	4242	60.9

Operating the vibrating mill in parallel with a roller crusher led to a 51% increase in throughput and 24% reductions in specific energy consumption and operational work index. Improved energy efficiency can enhance capacity, product fineness, and reduce production costs.

4 Conclusions

The study aimed to enhance the grinding circuit efficiency at the Shahrood copper ore processing plant. Initial analysis of the vibrating mill revealed key operational parameters. Subsequent modifications, such as reducing the feed particle size, altering the mill tube connections and operational parameters led to a significant improvement in throughput and energy efficiency. These changes not only increased the plant's capacity by 51% but also reduced the specific energy consumption and operational work index by 24% each, demonstrating the potential for optimization in mineral processing operations.

5 Acknowledgement

The authors would like to express their gratitude to the Shahrood copper ore process plant management for their permission to publish this research.

References

Alvardo, S. Erno J A. Auracher, N. & Casali, A. 1998. Andres, K. and Haude, F., 2010. Application of the Palla™ vibrating mill in ultra-fine grinding circuits, *The Journal of the Southern African Institute of Mining and Metallurgy*, March 2010

Arghr, M.; 1997. the elastic system study of the vibrating mill with spatial motions for milling the metallic powders, *NonlincarAnalysis, Theory, Metti & Applications*, Vol. 30, No. 1, pp. 15-168.

BCS Incorporated, 2007. Mining Industry Energy Bandwidth Study, *U.S. Department of Energy, Industrial Technology Program*.

Du, Y., Wu, X., 2015. Experimental Study on Superfine Grind Process for the Preparation of Calcium Carbonate Particles via Vibrated Mill, *The 7th World Congress on Particle Technology (WCPT7). Procedia Engineering* 102, 424 – 434

Energy-exergy optimization of comminution, *Energy*, vol.23, no.2, pp. 153-158.

Fuerstenau, D W. & Abouzeid, A-Z., 2002. The energy efficiency of ball milling in comminution, *Int. J Mineral Processing*, vol. 67, no. 1, pp. 161-185.

Hiroaki Masuda, Ko Higashitani, and Hideto Yoshida, 2007. Powder Technology: Handling and Operations, Process Instrumentation, and Working Hazards. *CRC Press*, Taylor and Francis Group, LLC.

Manouchehri, H R., 2013. VibroconeTM, Breakthrough Crushing Technology for Sustainable Development in Mining Industry, *CIM Convention*, May 5 -8, Toronto, CANADA.

Michael E. A., and Taylor, K., 2013. Aulton's Pharmaceutics: The Design and Manufacture of Medicines (4th ed.). New York: Elsevier Ltd.

Musa, F. & Morrison, R., 2009. A more sustainable approach to assessing comminution efficiency, *Minerals Engineering*, vol. 22, pp. 593-601.

WILLS, B.A., 2016. Will's Mineral Processing Technology, 4th ed., Elsevier, 498pp.

B5: Investigation of the Effects of Material Properties on Crushing Performance Using Pilot Scale Jaw Crusher Tests

*O. Altun[1], D. Altun[*1], A. Toprak, Ö. Akın[2], Z. Dağtarla[2], E. Savaş[2]*

[1]Hacettepe University, Mining Engineering Department, Ankara, Turkey

[2]MEKA Crushing, Screening and Concrete Plant Technologies, R&D Center Department, Ankara, Turkey

Abstract. This study aims to evaluate the performance of jaw crusher based on material properties. With this aim, characterization studies of two different materials, basalt and limestone, were carried out. Within the scope of the characterization studies of the material, properties such as breakage characteristics, chemical compositions and wear were determined through tests. Afterwards, the characterized samples with similar particle size distributions were subjected to pilot scale jaw crusher tests at different closed side settings. Size distributions of the test products were determined and effect of operational parameters and material characteristics on product was evaluated.

1 Introduction

Size reduction, a crucial step in many industries, plays an important role in mining. The crushing operation, which reduces the run of mine to an appropriate size for the next operation is the first stage of size reduction. Crushers are not energy efficient in terms of transferring energy to the crushing operation, like other size reduction equipment. Compression crushers such as jaw crushers are known to be inefficient machines with idling power ranging from 30% to 50% of their nominal power (De la Vergne et al., 2003; Moray et al. 2006). So, these operations are high energy consuming in mining operations.

Given the rising energy demands of today's world, it is vital to reduce energy consumption and CO_2 emissions, while also lowering production costs. Recently, as energy efficiency has become important in many areas, studies to ensure energy efficiency and capacity increase in crushing circuits have come to the fore. In this regard, achieving energy-efficient crushing requires careful equipment selection, efficient operation of the chosen equipment, process optimization, and innovative size reduction strategies.

In recent years, there has been an increase in the number of process simulation studies conducted to improve the performance of crushing circuits (Asbjörnsson et al., 2012, 2013a, 2013b; Brown et al., 2016). Due to the complexity and many variables of the crushing circuit, mathematical optimization is a powerful tool. Since the performance of the crushing process is directly related to material properties, material characterization is also important in modelling and simulation studies. At this point, characterizing geometallurgical parameters can be used to identify and provide solutions (Walters, 2008; Jackson et al., 2016; Dominiy et al., 2018, Hunt et al., 2019).

In this study, the size reduction behaviour of two different materials in a jaw crusher was evaluated. In this context, material properties, including the breakage behaviour of the materials, were determined. Crushing tests were conducted at closed side settings (C.S.S.) for the characterized materials.

2 Materials and Methods

Basalt and limestone samples were used during the study. At the first step, samples were sieved from the top size to 25 mm. It was carried out in two phases as the first phase included sieving down to 50 mm and the second phase consisted of sampling and then completing the analyses accordingly. Then the two results were combined. Using these fractions, similar size distributions were created for basalt and limestone samples to eliminate the effect of the feed size distribution. Feed size distribution used for the crushing tests are given in Fig.1.

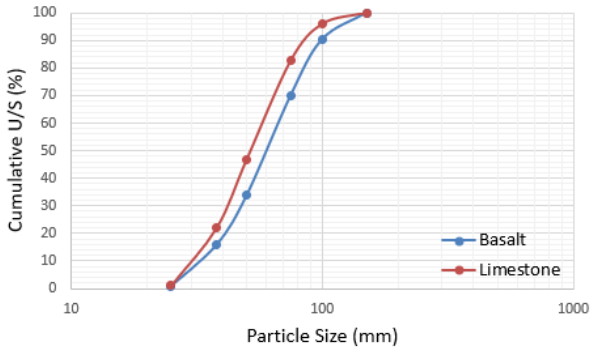

Fig. 1. Feed size distributions

* Corresponding author: deksi@hacettepe.edu.tr

Representative samples were collected from the material for characterization tests. Firstly, chemical composition of the basalt and limestone were determined by XRF technique. Composition of the materials are given in Table 1.

Basalt		Limestone			
Comp.	Content (%)	Comp.	Content (%)	Comp.	Content (%)
A.Za	5	SO_3	<0.01	P_2O_5	<0.01
Al_2O_3	17	Al_2O_3	0.11	SiO_2	0.49
CaO	10	CaO	55.89	TiO_2	0.013
Fe_2O_3	9	Fe_2O_3	0.073	Cr_2O_3	<0.01
K_2O	1	K_2O	0.01	BaO	<0.01
MgO	6	MgO	1.2	SrO	0.044
MnO	0	MnO	<0.01	LOI	42.12
Na_2O	4	Na_2O	<0.01		
P_2O_5	1				
SiO_2	46				
TiO_2	2				

Table 1. Chemical compositions of the samples

Following the characterization tests, drop weight, point load and Los Angeles tests were conducted. Summary of the test results are given in Table 2.

Table 2. Characterization test results of the samples

	Basalt	Limestone
Drop Weight Index (Axb)	55.58	74.21
Point Load Index (IS_{50})	4.56	3.64
Los Angeles Abrasion Index (L_A)	8.31	12.71

3 Pilot Scale Crushing Tests

Crushing tests were performed by jaw crusher (Figure 2) at different operating conditions. Technical properties and test conditions are summarized in Table 3. Three different closed site settings were used in the tests.

Fig. 1. Jaw crusher

Table 3. Technical specifications of jaw crusher

Feed size opening length (mm)	175
Feed size opening width (mm)	300
Flywheel Diameter (mm)	630
Motor power (kW)	11
Operating speed (rpm)	1500

After crushing tests, particle size distributions of the product were determined by sieve analysis. This information was used to evaluate the jaw crushing tests based on different operating factors. Fig.2 and Fig.3 show the effect C.S.S. on product size for basalt and limestone, respectively.

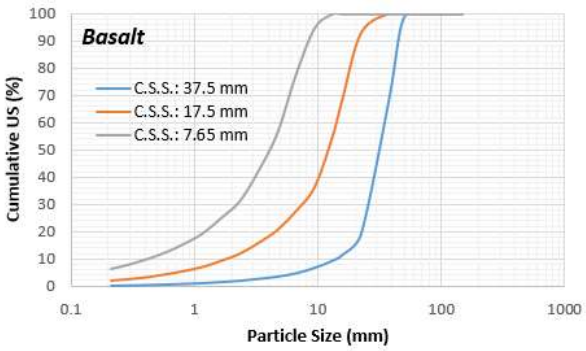

Fig. 2. Effect of C.S.S. on product size-Basalt

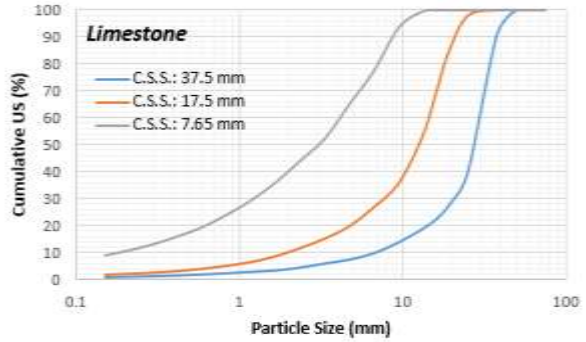

Fig. 3. Effect of C.S.S. on product size-Limestone

Within each specific type of product, increasing C.S.S. consistently results in coarser product size. When two samples were compared a difference that depended on the C.S.S. was observed. This comparison is given in Fig. 4. Large C.S.S. make equal the behaviour of various materials regardless of their breakage characteristics. Only under low C.S.S. conditions make differences in material breakage characteristics become apparent.

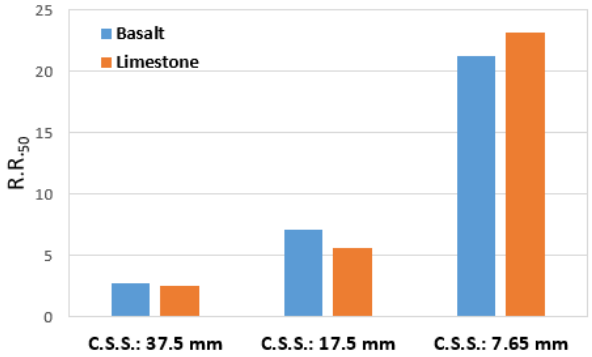

Fig. 3. Effect of C.S.S. on $R.R_{50}$

Crushing tests were conducted by feeding narrow particle size fractions as well as the full distribution. -150+100 mm, -100+75 mm, -75+50 mm size fractions were crushed at 17.5 mm and 37.5 mm C.S.S. Product size distributions of the fractional crushing tests were given in Fig.4-Fig.6. For all particle size fractions, the limestone sample with the lowest C.S.S. was broken more easily, consistent with the characterization tests. The influence of material on product size diminishes to insignificance as the C.S.S. increases.

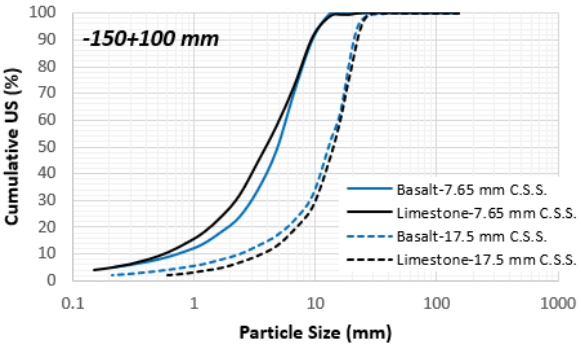

Fig. 4. Product size distributions of -150+100 mm fraction

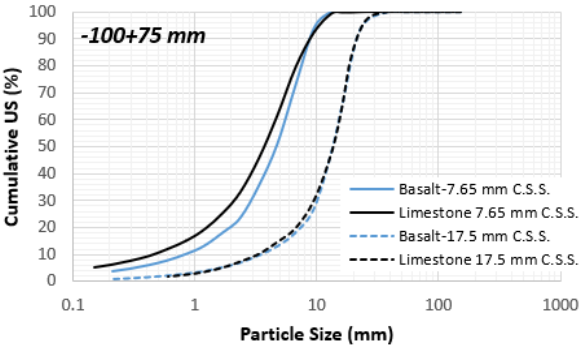

Fig. 5. Product size distributions of -100+75 mm fraction

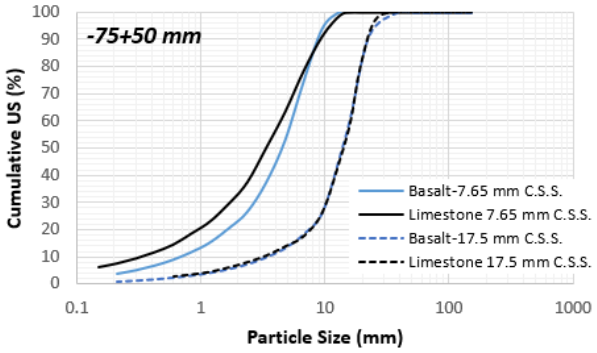

Fig. 6. Product size distributions of -75+50 mm fraction

4 Conclusion

This study successfully analysed size reduction in basalt and limestone using a pilot-scale jaw crusher. To minimize error, all the material were carefully sieved into different size fractions, creating similar feed distributions. The data obtained valuable insights into the impact of two key factors: C.S.S. and material properties. For both materials, as the C.S.S. increased, the product size became coarser. However, although the strength of the limestone is lower than basalt, material characteristic effect wasn't observed in large C.S.S.. For lowest C.S.S. 7.65 mm reduction ratio of limestone is the highest.

Additionally, narrow particle size fractions were broken at two different C.S.S., and product of the limestone at the 7.65 mm C.S.S. was finer. For the 17.5 mm C.S.S., no significant difference was observed between the products of the two materials.

References

Asbjörnsson, G., Hulth´en, E. and Evertsson, M. (2012). Modelling and dynamic simulation of gradual performance deterioration of a crushing circuit - Including time dependence and wear. *Minerals Engineering*. 33, 13-19.

Asbjörnsson, G., Hulthén, E., Evertsson, M. (2013a). Modelling and simulation of dynamic crushing plant behavior with MATLAB/Simulink. *Minerals Engineering*. 43-44, 112-120.

Asbjörnsson, G., Hulthén, E., Evertsson, M.(2013b). An on-line training simulator built on dynamic simulations of crushing plants. 16th IFAC Symposium on Automation in Mining, *Mineral and Metal Processing*. San Diego, USA.

Brown, R.P., C.W. Steyn, and R.J. Fouchee. (2016). Improving crusher performance by comparing various control strategies using a validated simulation. in *Comminution 2016*. Cape Town, RSA.

De la Vergne, J. (2003). Hard rock Miner's handbook. Arizona, United States: McIntosh Engineering Inc.

Dominy, S.C., O'Connor, L., Parbhakar-Fox, A., Glass, H.J., Purevgerel, S., 2018. Geometallurgy—a route to more resilient mine operations. *Minerals*. 8, 560.

Hunt, J. A., Berry, R. F., Becker, M., Baumgartner, R., 2019. A special issue dedicated to geometallurgy: preface. *Econ. Geol.* 114, 1473–1479.

Jackson, J., Young, M.F., 2016. Ore type – everything to someone but nothing to anyone.In: Dominy, S., O'Connor, L. (Eds.), *Proceedings of The Third AusIMM International Geometallurgy Conference*, Perth, Australia. AusIMM, Melbourne, pp. 267–274.

Moray, S., Throop, N., Seryak, J., Schmidt, C. (2006). Energy efficiency opportunities in the stone and asphalt industry. In: Proceedings of the Twenty-Eighth *Industrial Energy Technology Conference*. New Orleans, Louisiana, United States; 9-12 May.

Walters, S.G., 2008. An overview of new integrated geometallurgical research. In: Proceedings of the Ninth *International Congress for Applied Mineralogy*, Brisbane, Australia. AusIMM, Melbourne, pp. 79–82

B6: Effect of the andesite geological properties on the breakage behaviour

Izabella Rebeka Márkus[1,*], *John Kwame* Bediako[2], and Ádám Rácz[1]

[1] Faculty of Earth and Environmental Sciences and Engineering, University of Miskolc, Miskolc, HU
[2]Department of Separation Science, School of Engineering Science, Lappeenranta-Lahti University of Technology (LUT), Lappeenranta, FIN

Abstract. Crushed aggregates are the biggest branch of mining by production volume with increasing demand. The decreasing availability of good quality resources and the energy consumption of comminution processes makes inevitable the need for optimisation of production processes. For this purpose, the detailed knowledge of factors influencing the breakage process is essential, the properties of the material being one of them. Linking the material properties, including mineralogical composition, rock texture, cracks, porosity, and weathering to the breakage and product properties has significant research literature. Many a time, some general conclusions are drawn and applied in the cases of given types of materials, however, conflicting results are numerous in the literature given that different rock types with different textural properties were often examined and compared. This study thus focuses on the systematic study of andesite samples, an intrusive magmatic rock widely quarried in Europe, in this case from different Hungarian mines. Each mine quarries a single magmatic body, therefore, the produced material usually has slight variation in mineralogical composition and texture on different production levels. For the assessment of the relationship between rock and breakage properties, single particle breakage tests were conducted. Resistance to wear and fragmentation tests were applied to assess the effect of rock properties on the product mechanical properties. The results showed that in the case of andesite the mineralogical composition, texture, alteration, porosity, and the size of the sample subjected to breakage influence the breakage in a complex manner.

1 Introduction

Crushed aggregates are one of the most voluminous mineral raw materials exploited nowadays, constituting the biggest branch of mining by production volume and the second in value (Menegaki & Kaliampakos, 2010; Ayuk et al, 2020; Bendixen et al, 2021;). Most construction aggregates still come from primary natural resources (Prikryl, 2021). In 2022 in Europe, 1809 million tonnes of crushed aggregates were produced from primary sources by a total of 19174 extraction sites, whilst the quantity of recycled aggregates reached only 70 million tonnes (https://www.aggregates-europe.eu/facts-figures/figures/). With the increasing demand, the European average demand for aggregates was 5.6 tonnes per capita in 2019, the availability of good quality resources is decreasing, producing products complying with the requisite quality requirements is becoming a challenge. The energy consumption demands of comminution is another concern affecting the industry, being one of the world's most energy-intensive industrial processes. An estimated 20 billion kWh of energy is consumed annually by processing plants engaged in crushed stone production (Napier-Munn 2015). These plants are usually designed and operated at less-than-optimal energy efficiency (Napier-Munn et al., 2012; Jeswiet and Szekeres, 2016, Aditya et al. 2017). The aspirations for the optimisation of production and energy consumption leads to a need for better understanding of the comminution process and the factors influencing the quality of the product. The energy consumed in the process depends on both the mechanism of comminution and the mechanical properties of the materials being comminuted (Popov et al., 2020). Geological characteristics of rocks have a significant influence on energy consumption during crushing, the constituent minerals of the rock, relative mineral abundances, texture, fracture frequency and alteration determine the rock strength (Petruk, 2000; Korman et al., 2015; Yildirim, 2016) which has a significant influence on the energy consumption during crushing.

2 Influence of rock properties

Several researchers have examined the relationships between petrographical and mechanical properties of rocks. Some general conclusions can be drawn, however, some of the results have led to conflicting findings on the influence of the rock properties, given the fact that usually different types of rocks with different textural properties are examined and compared. The resistance to mechanical wear and fragmentation of rock is influenced by the hardness, strength, fracture toughness and

* Corresponding author: izabella.markus@uni-miskolc.hu

modulus of elasticity of the individual minerals (Lindqvist et al, 2007), Wang (2015) highlighting the importance of the mineral distribution in the breakage pattern, indicated that the breakage results depend on the proportion of minerals, especially the softest mineral. In the case of similar mineralogical composition, some authors highlighted that the effect of grain size and shape is more significant than the mineralogy itself (Oyarzún and Arévalo, 2011; Yuce, 2017), while others suggest that grain size plays a secondary role compared to mineralogy (Eberhardt et al, 1999).

The effect and type of alteration can be significant, according to Pola et al (2014). The alteration can cause either an increase or a decrease in rock strength. Other influencing factors can be material discontinuities like cracks and pores; the first one provides a path for further crack propagation whiles the second one can both facilitate and arrest crack propagation.

3 Materials and methods

The single particle breakage tests are commonly used methods in the field of mineral processing, most frequently applied for studying the energy utilization in the comminution process, the effect of particle shape, material physical properties and the energy-size reduction relationship. The classical drop-weight test (DWT) is a double impact type test in which a single particle is subjected to breakage between two solid surfaces, where the drop weight can be a steel ball or a plate. For the purpose of assessing the relationship between the geological properties and breakage properties of andesites, a drop weight tester apparatus was constructed at the Institute of Raw Material Preparation and Environmental Processing, University of Miskolc. The apparatus makes it possible to vary the breakage energy between 5.3 J and 295.7 J.

For the systematic study of the relationship between geological properties and their breakage properties, samples from two different quarries operated by Colas Északkő Ltd, Recsk quarry and Tállya quarry were collected. Both quarries are engaged in quarrying andesite from a single magmatic body, and the produced material has slight variation in the mineralogical composition and texture on different production levels within each mine. In the case of both quarries three samples were collected, from Recsk quarry, samples R_1, R_2, and R_3, and from Tállya quarry, samples T_1, T_2 and T_3, making a total of six samples. From both quarries, the samples collected were in the categories of no sign of alteration, slightly altered and strongly altered (Fig. 1).

Fig. 1. Sample types from the Recsk quarry. From left to right are samples R_1, R_2 and R_3.

For the drop weight testing, five particle size fraction ranges: 40–45 mm, 25-31.5 mm, 20–22.5 mm, 12.5–16 mm and 8–11.2 mm were produced by crushing and sieving. The tests were conducted for each sample and foreach particle size fraction range at three energy levels. The tests were repeated three times on similarly prepared andesite samples for every parameter setup. Following the breakage, the particle size distribution of each sample was determined using dry sieving method.

The size distributions of the samples after single particle breakage tests were determined by dry sieving. On the results of the particle size analysis, the Rosin-Rammler distribution function was fitted as shown in Fig. 2 a, b, and c.

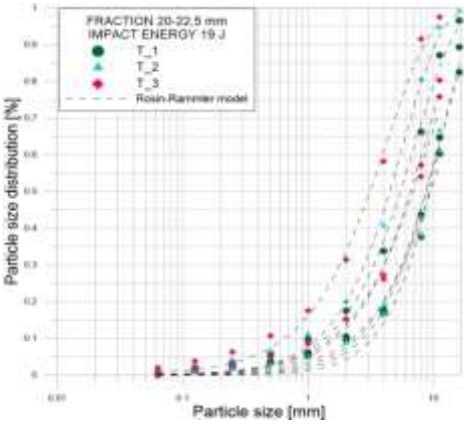

Fig. 2a. Particle size distribution of sample fraction size 20-22,5 mm from Tállya quarry at breakage energy level 19 J.

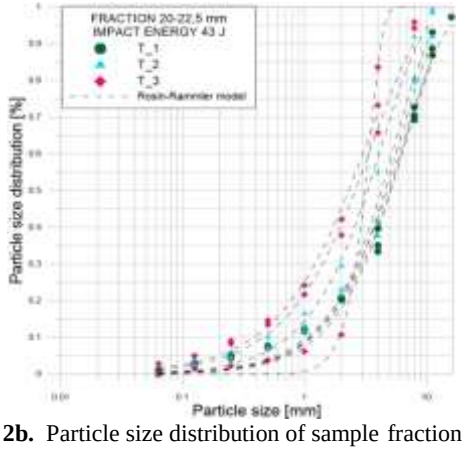

Fig. 2b. Particle size distribution of sample fraction size 20-22,5 mm from Tállya quarry at breakage energy level 43 J.

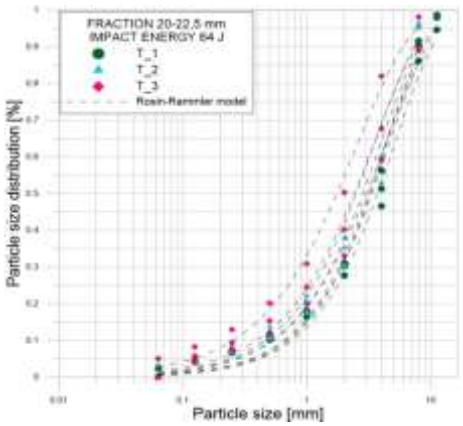

Fig. 2c. Particle size distribution of sample fraction size 20-22,5 mm from Tállya quarry at breakage energy level 64 J

From the fitted function, the average of the characteristic particle size, parameter *a*, defined as the size at which 63.2 % of the particles are smaller, was determined for each sample. The sample averages and the corrected sample standard deviation values were calculated for each type of andesite, and for each particle size fraction and energy level. The relationship between the characteristic particle size and the specific breakage energy, E_s was examined. Example of andesites from Tállya quarry with fraction size of 12.5-16 mm can be seen in Fig. 3.

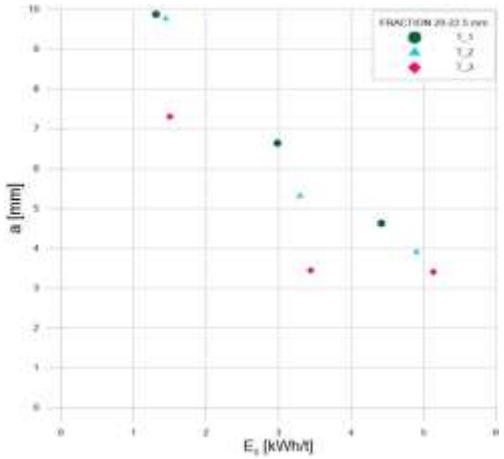

Fig. 3. Relationship of specific breakage energy E_s and parameter *a* of the fitted Rosin-Rammler functions for fraction size 20-22.5 mm for samples from Tállya quarry

The resistance to wear of each sample type was investigated in accordance with the EN 1097-1:2012 standard, and the resistance to fragmentation in accordance with the EN 1097-2:2020 standard. Description of sample preparation, test method and calculation of the results can be found in the mentioned European standards. In the case of the resistance to wear testing, the main implemented stress type is attrition, while in the case of the resistance to fragmentation the main implemented type is impact, similar to the drop weight testing.

For the description of the geological properties, the quantitative mineralogical composition was assessed using X-ray powder diffraction method (Fig. 4).

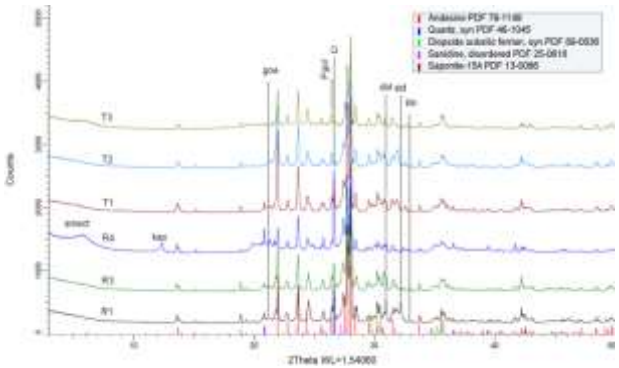

Fig. 4. Mineralogical composition of samples

The chemical composition was determined using X-ray fluorescence. From the obtained results, alteration of the samples was quantified by calculating the weathering indices of the samples. In this study, the weathering indices were calculated based on the AFB (alumina+ferric oxides/bases) index (Sergeev 2022).

The textural properties were assessed on polished rock thin sections by optical microscopical observations using an optical microscope, Zeiss AXIO Imager M2m. Digital images were captured, and grain properties were assessed using Zeiss's AxioImager software, which has an integrated Particle Size Analysis function.

The porosity of each sample type was assessed using particle density measurements with the pycnometer method. The measurements were conducted on particles in the size range of 40-45 mm, and on material comminuted below 125 µm. Consequently, the porosity was calculated using the porosity measurement results.

4 Results and discussion

The geological properties of the samples were assessed as a first step of this study. The XRD result showed that the mineralogical compositions are similar for samples within the same mine (Fig. 3), however their quantitative compositions show variations especially in the case of main constituents. The textural observations showed differences in the mineral grain sizes, and the ratio of smaller and bigger mineral grains in the samples. The calculated weathering indices showed that the samples are at different stages of weathering.

The present results highlighted that rocks with similar quantitative mineralogical compositions show different breakage properties and responses to resistance to wear and fragmentation. In the case of the breakage behaviour, the results led to the conclusion that the effect of mineralogical composition, texture parameters and porosity can compensate each other and exert their effect at the same time, leading to complex breakage behaviours. In the range of coarse particle size, texture has less significance in comparison with weakness planes like porosity and cracks, however the secondary mineral genesis can fill the pores and result in a toughening effect. With the decrease of the particle size, the influence of the texture parameters becomes more significant. The shape and size of the individual mineral grains in the micro-texture has a more significant effect on the breakage. Moreover, the mineralogical

composition and the differences between the size of mineral grains influence the breakage more than the grain size itself. In our study, the alteration was found to contribute to the increase of the material's resistance to breakage.

Based on the obtained results it is concluded that in resistance to wear, the main influencing factors are the mineralogy and alteration of the samples. The samples with higher quartz content and lowest alteration values showed the highest resistance to wear. The results of resistance to fragmentation demonstrated that other factors than mineralogical composition and alteration, most probably the textural properties, may be influencing the resistance to fragmentation. The particle size used for the Los Angeles testing is between 10–14 mm, limiting the presence and effects of faults and cracks.

Acknowledgement

This project is funded by the European Union's Horizon Europe program under grant no. 101079354.

References

Menegaki, M. E. & Kaliampakos, D. C. (2010) European aggregates production: Drivers, correlations and trends, Resources Policy, 35 (3), 235-244

Ayuk, E., Pedro, A., Ekins, P., Gatune, J., Milligan, B., Oberle, B., Christmann, P., Ali, S., Kumar, S. V., Bringezu, S., Acquatella, J., Bernaudat, L., Bodouroglou, C., Brooks, S., Burgii Bonanomi, E., Clement, J., Collins, N., Davis, K., Davy, A., & Mancini, L. (2020) Mineral Resource Governance in the 21st Century: Gearing extractive industries towards sustainable development, Nairobi, Kenya: International Resource Panel, United Nations Envio.

Bendixen M., Iversen, L. L., Best J., Franks, D. M., Hackney Latrubesse, E.M. & Tustin, L.S. (2021) Sand, gravel, and UN Sustainable Development Goals: Conflicts, synergies, and pathways forward, *One Earth*, 4 (11), 1095-1111

Napier-Munn T. (2015) Is progress in energy-efficient comminution doomed?, *Minerals Engineering*, 73, 1–6

Napier-Munn, T. J., Drinkwater, D. & Ballantyne G., (2012) The CEEC Roadmap for Eco-Efficient Comminution. 2012 Workshop 12-13 June 2012. Noosa, Queensland, 15

Jeswiet, J. & Szekeres A. (2016) Energy consumption in mining comminution, *Procedia CIRP 48*, 140-145

Aditya, S., Tapas, N. K., Samir, P. K. & Arun, M.K. (2017) Pre-treatment of rocks prior to comminution – A critical review of present practices, *International Journal of Mining Science and Technology*, 27, 339–348

Popov, O., Talovina, I., Lieberwirth, H. & Duriagina, A. (2020) Quantitative Microstructural Analysis and X-ray Computed Tomography of Ores and Rocks-Comparison of Results, *Minerals*, 10(2), 129

Petruk, W. (2000) Applied mineralogy in the mining industry, Elsevier, 268

Korman, T., Bedekovic, G., Kujundzic, T. & Kuhinek, D. (2015) Impact of physical and mechanical properties of rocks on energy consumption of jaw crusher, *Physicochem. Probl. Miner. Process*, 51(2), 461−475

Yildirim, B. G. (2016) Development of a correlation between mineralogy, rock strength measures, and breakage of Copper Porphyries, PhD thesis, The University of Queensland

Lindqvist, J. E., Akesson, U. & Malaga, K. (2007) Microstructure and functional properties of rock materials, *Materials Characterization* 58, 1183–1188

Wang, Y. (2015) Numerical modelling of heterogeneous rock breakage behaviour based on texture images, *Minerals Engineering*, 74, 130–141

Oyarzún, A., Arévalo, A. (2011) Rock Texture and BWi Relationships, El Teniente Ore Deposit, Chile, *Proceedings of The First AusIMM International Geometallurgy Conference (Geomet*, 181–186

Yuce, A. E. (2017) Grinding size estimation and beneficiation studies based on simple properties of ore components, *Physicochemical Problems of Mineral Processing*, 53(1), 541–552

Eberhardt, E., Stimpson, B. & Stead, D. (1999) Effects of Grain Size on the Initiation and Propagation Thresholds of Stress-induced Brittle Fractures, *Rock Mech. Rock Eng.*, 32, 81–99

Pola, A., Crosta, G.B., Fusi, N. & Castellanza, R. (2014) General characterization of the mechanical behaviour of different volcanic rocks with respect to alteration, *Engineering Geology*, 169, 1-13

N. Sergeev (2023) Quantifying weathering intensity using chemical proxies: a weathering index AFB, *Australian Journal of Earth Sciences*, 70(2), 260-284

https://www.aggregates-europe.eu/facts-figures/figures/ Date of information: 06.03.2024.

C1: Production of urea-gypsum co-crystals (URCASU) via mechano-chemical cocrystallisation

Würl Roman[1,*], *Lim* Zhi Shuen, *Hamad* Danial, and *Breitung-Faes* Sandra

[1]Faculty of Process Engineering, Nuremberg University of Applied Sciences, DE

Abstract. In the present work, $CaSO_4*xH_2O$ (x = 0, 0.5, 2) and urea were converted to the cocrystal URCASU in a planetary ball mill. Urea and calcium carbonate are important substances in means of agricultural fertilization, whereas especially the urea is solved by water and penetrates the earth rather quickly. The cocrystallisation of the urea with a gypsum component delivers the advantage of retarded solubility of the urea. Thus, the frequency of fertilization can be reduced, as well as the amount of urea, which is used. The possibility to synthesize URCASU was already shown in literature. Here the water amount addition, the grinding media size, the ball to powder ratio and the grinding time were varied at room temperature and their dependency on the yield were investigated. The reactant-product mixtures were mainly analysed using Raman spectroscopy, but also confirmed with XRD measurements. It was shown that, contrary to previous literature data, the anhydrite can also be quantitatively converted into URCASU.

1 Introduction

Co-crystals are a class of substances in which all components form an ordered structure in a clearly defined stoichiometric ratio, as in a salt crystal. (Rodrigues et al., 2018) So far, there is no clear consensus on the definition of a cocrystal, e.g. whether or not solvates are also included. (Aitipamula et al., 2012) It's certain that at least one component in the cocrystal needs to be uncharged (ionic cocrystal) or every component is uncharged (cocrystal). (Kumar and Nanda, 2018) In most cases, the focus is on an active pharmaceutical ingredient or a target component (API), which is converted into a new crystal structure with another substance (coformer).

In recent years, this trend has also affected products from the agricultural sector in order to develop a kind of new generation of urea fertilisers. In this way, several environmental aspects are to be addressed by reducing the solubility of the urea: Storage stability is increased by lower hygroscopicity, leaching from the soil and thus eutrophication is reduced and the release of the fertiliser is somewhat adapted to plant growth. (Barčauskaite et al., 2020) Initial studies with ionic urea-gypsum co-crystals on *Sorghum bicolor* (L.) in greenhouses showed that significantly more nitrogen was absorbed in the fruits and plant mass compared to conventional urea. Only root growth remained unchanged. (Bista et al. 2023)

These co-crystals have been researched comparatively extensively in terms of their chemical and physical properties, but no industry-relevant approach to scale-up has yet been undertaken. However, the scientific work to date is promising, as the throughput has already been increased from a few µg to up to 330 g h^{-1} (Brekalo et al., 2022)

On the basis of previous publications, an initial approach will be taken to determine relevant parameters on a laboratory scale for a better understanding of the process and the subsequent scale-up. The focus is also on the $CaSO_4$ material system in its various hydrate forms and urea.

2 Theoretical Background

2.1 Process parameters

In their work, Brekalo et al. investigated several mechanochemical production processes using the different hydrate forms of $CaSO_4*xH_2O$ (x = 0, 0.5, 2). Depending on the hydrate stage, anhydrite (x = 0), hemihydrate (x = 0.5) or dehydrate (x = 2) is used in the following. The process parameters considered in the planetary ball mill and the differences observed with regard to the kinetics of co-crystallisation of the respective hydrate form in the mixer mill using an in-situ Raman probe were of particular interest for the present work.

In the mixer mill with the Raman probe and identical process parameters, the kinetics were faster for the hemihydrate at room temperature (RT) than for the dihydrate (starting within 10 vs. 32 min). The conversion at the end of the experiment was higher for the dihydrate than for the hemihydrate. In comparison, the anhydrite could only be converted to URCASU in very small quantities. The addition of water to the reactants had no influence on the degree of conversion.

In order to test the "inert nature" of the anhydrite, the anhydrite and hemihydrate were each ground with a

* Corresponding author: roman.wuerl@th-nuernberg.de

corresponding amount of water and without urea as a control in order to convert them into their higher hydrate stage. In the case of the anhydrite, this was only possible in almost negligible quantities, but the hemihydrate could be quantitatively converted into the dihydrate.

Based on the results, the authors surmised that the water of crystallisation in the hemihydrate and dihydrate would be decisive for the conversion process. The comminution process would lead to the removal of the water from the crystal structure, resulting in defects that would subsequently facilitate or enable interaction with the urea. For a more detailed explanation, please refer to the corresponding paper.

The authors (Brekalo et al., 2022) used stainless steel grinding jars with a mixture of grinding balls of different sizes between 9 mm and 14.3 mm. The speed was either 300 or 500 rpm at RT for 60 min. The samples were then dried at 70 °C for 24 hours. A mixture of grinding beads makes it impossible to analyse the specific energy input, stress energy and stress number with the currently known methods. In order to enable a calculation at a later date, only the same size were used per patch in this work presented.

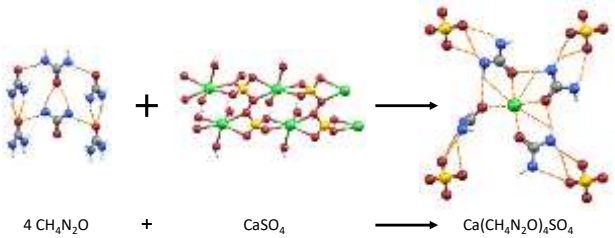

Fig. 1. Structural composition of urea, calcium sulphate and URCASU. Colors of the spheres: Hydrogen (blue), oxygen (red), carbon (gray), calcium (green), sulphur (yellow). (Brekalo et al., 2022, modified figure)

2.2 Analytics

Single-crystal XRD measurements are carried out as standard to proof the successful co-crystallisation and to investigate the crystal structure. However, these cannot be obtained in a mechanochemical process, but only from solvent based processes such as solvent evaporation. Based on the spectra obtained and comparative samples from the mechanochemical methods, further analytical methods or methods better suited to process monitoring can then be verified and used. (Brekalo et al., 2022)

Using Raman spectroscopy, it is comparatively easy to verify the conversion during the mechanochemical production process because a peak at 975 cm^{-1} appears in the spectrum that is not present in any of the reactants. Fortunately, no by-products are known so far from the co-crystallisation mentioned above or would be noticeable in the fingerprint range at this wavenumber. In addition, an in-situ Raman probe can be calibrated to quantify the powdered samples using a single crystal grown from solvents and the spectrum obtained from it. Alternatively, samples can be taken for analysis after the experiment or at specific times during the experiment and analysed in a Raman spectroscope. (Brekalo et al., 2022)

3 Materials and methods

3.1 Materials

Urea (99.5%) and $CaSO_4*2H_2O$ (98%) were obtained from Carl Roth, $CaSO_4*0.5H_2O$ (97%) from Honeywell and $CaSO_4$ (99%) from Thermo Fisher.

3.2 Methods

3.2.1 Cocrystallisation using a planetary mill

A Fritsch Pulverisette 7 planetary ball mill was used for mechanochemical production. The 80 mL grinding jars had an interior lining made of zirconium oxide, with the ZrO_2 grinding balls having a diameter of 2, 5 or 10 mm. Depending on the experiment, 250, 500 or 800 rpm were set for 30, 60 or 120 min. In relation to the mass, the ball-to-powder ratio (btpr) was 2:1, 3.33:1 or 4:1 and the amount of additional deionised water added was 1, 2, 3, 4 or 5 mL. In almost all experiments (those with a ball-to-powder ration of 3.33:1), the total amount of reactant per grinding jar was about 30 g. If one parameter was changed, the others were kept constant as follows: 5 mm ZrO_2 grinding balls, 500 rpm, 60 min, btpr 3.33:1 and 5 mL deionised water. All experiments were carried out at RT. So far, most of the tests have only been carried out once. The necessary test runs are to be carried out in the near future in order to obtain statistical significance of the measured value scatter.

A stoichiometric ratio of 4:1 (urea to $CaSO_4*xH_2O$) was always maintained for the reactants. In order to avoid caking on the edge of the grinding bowl and to enable the samples to be transferred as completely as possible to an evaporation dish after the test, 5 mL of deionised water was added to the reactant. The pasty grinding ball and product mixture was dried for 24 h at 70 °C in a drying oven, cooled in a desiccator and then separated using a mortar and pestle and a sieve. The powdered samples were stored in snap-lid jars until analysed.

3.2.2 Raman spectroscopy

The powdered samples were analysed using a LabRAM HR Evolution from Horiba Scientific calibrated via a silicon waver. The laser had a wavelength of 633 nm and a 300 grooves mm^{-1} grating was used. The spectrum was recorded between 40 and 4000 cm^{-1}.

The area of the peak at 975 cm^{-1} was calculated using the trapezoidal method, taking into account a skewed baseline between the first and last measurement points of the peak. The limits were 951 and 984 cm^{-1}. Since no single crystals were yet available as a reference for correct quantification, the area of the peak at approximately 1000 cm^{-1} (limits at 984 and 1038 cm^{-1}) was also calculated and set in relation to the former. The sample with the highest area ratio was declared with a conversion level of 100 % for better comparison, even though this was very probably not achieved and is therefore questionable. In this way, however, the results could be better compared with each other. For this

reason, the conversion is stated in this paper as the relative value X_{rel} in order to avoid confusion.

3.2.3 X-ray diffractometry

The X-ray diffractometer X'Pert PRO from PANalaytical with 45 kV, 40 mA, a copper K-α line, a Sollar aperture, a nickel sheet filter and a Bragg-Brentano geometry was used. The measurement range was between 5 and 70° and 2θ with a step size of 0.013°. For the measurement, the samples were grinded with an agate mortar and then moulded into a pellet.

4 Results and discussion

4.1 Results

Qualitative and quantitative analysis. Both Raman spectroscopy and PXRD were able to detect the cocrystal URCASU. An absolute quantification was not possible due to the lack of single crystals, which is why the conversions were given as relative values and are discussed accordingly in the following subchapters.

Variation of the additional water. Firstly, the experiments of Brekalo et al. were repeated with the company's own planetary bead mill. It was confirmed that additionally added water had no significant influence on the degree of conversion and the values fluctuated between X_{rel} = 80 % and 99 %.

Dependency of X_{rel} on the hydration state. No clear trend was found that the dihydrate (X_{rel} = 83 %) achieved a higher conversion than the hemihydrate (X_{rel} = 85 %). Furthermore, it was found that X_{rel} remained the same at all selected speeds and grinding times.

Further examination of the anhydrite. It was possible to confirm the results of Brekalo et al. that relatively little URCASU was formed at 500 rpm with less than X_{rel} = 20 %. However, at 800 rpm with X_{rel} = 85 %, a conversion was achieved which was similar to the values of hemihydrate and dihydrate at 500 rpm.

Variation of the ball to powder ratio. No significant influence was found for dihydrate. At 4:1, X_{rel} = 91 % was only four percentage points higher than at 2:1, but this could also lie within the scatter of the measurement data.

Variation of the ball size. It was found that a lower X_{rel} = 56 % was achieved with a grinding ball size of 10 mm. At 2 and 5 mm, the values were similar and at a much higher level (X_{rel} = 84 % and 83 % respectively).

4.2 Discussion

The exact mechanochemical processes involved in the production of co-crystals are generally still largely unknown. This work is therefore only intended to contribute a further piece of the puzzle to the basic understanding and the already existing hypothesis. In order to be able to formulate such an extended hypothesis, its context and the experiments still required will be explained first.

4.2.1 New findings on the existing hypothesis

Brekalo et al. proposed the hypothesis that the water of crystallisation appears to play an important role in the co-crystallisation process of URCASU. The dissolving water would lead to defects in the lattice structure, which would promote the formation of the cocrystal as a result. The anhydrite does not have this water of crystallisation, which means that no significant defects occur and therefore no or only very little URCASU can be produced. (Brekalo et al., 2022)

The hypothesis could be questioned in the present study, at least partially, because the anhydrite could very well be quantitatively converted into URCASU at 800 rpm. This would disprove, that the water of crystallisation plays a decisive or direct role in the quantitative formation of URCASU. Otherwise, no quantitative conversion should have been possible with the anhydrite (and additionally added water) at 800 rpm, at least in a broader parameter range.

4.2.2 Thoughts on an alternative hypothesis

It is assumed that the water of crystallisation influences other properties in the reactant, which ultimately enables or prevents the formation of URCASU. One indication in favour of this is the different Mohs hardness: $CaSO_4*2H_2O$ has a Mohs hardness of around 2, while the anhydrite has one of around 3 to 3.5. (Wächter 2012) The Mohs hardness of URCASU is unknown. Based on a similarly sized particle, the anhydrite therefore requires a higher stress energy to achieve the same result during comminution. However, comminution or the creation of a new surface is essential in mechanochemistry and therefore also in mechanochemical co-crystallisation from a thermodynamic point of view. (Tan and García, 2019) Due to its mechanochemical activation, it tends to enter into reactions or new (hydrogen) bonds. Since this could not be created in the harder anhydrite at 500 rpm, only little URCASU was found. It would be interesting here to consider the role of the hardness or other mechanical properties of the cocrystal, which are not yet known. Depending on whether it would be harder or softer than one of the hydrate stages, there would be even more detailed possibilities for explanation and prediction.

4.2.3 Approaches to confirm the alternative hypothesis

In order to be able to take a closer look at the aspects mentioned, a few more experiments are necessary, which will be explained below. Most of these aspects are to be tested experimentally up to the ESCC 2024.

As there are still no energetic considerations in this area for planetary ball mills, these should be sought. The theoretical basis for this has already been established. (Burmeister et al., 2018) These include the stress energies and stress numbers required for the respective hydrate stages in order to achieve the same degree of comminution. If this value has been found for each

material system, the respective hydration to the next higher hydration stage or co-crystallisation should achieve the same yields, as the same amount of new surface area would be created for conversion. Otherwise, the influence of the already formed cocrystal or the higher hydrate stage on the comminution of the $CaSO_4$*xH_2O still present as a reactant would probably have to be investigated. Depending on whether this is harder, softer than or similarly hard as the reactants, different results can be expected for comminution behaviour and conversion. Such correlations have already been investigated for some time in the field of selective comminution or are already known, depending on the material system. (Nöske et al., 2022) If this is the case, abrasion coefficients must also be taken into account. (Burmeister et al., 2017)

Furthermore, it must be clarified whether the anhydrite can be converted into the hemi- or dihydrate with a corresponding amount of added water at 800 rpm. A conversion from hemihydrate to dihydrate at 500 rpm has already been observed. If this is possible, dry grinding tests with anhydrite and urea are necessary in order to verify or exclude the influence of the additionally added water (and possibly water of crystallisation). At the very least, the extent to which a catalytic effect can be seen should be checked in the extended test matrix. However, previous work has not shown any such tendency.

In the aspects already mentioned, it is also interesting to find out whether the degree of comminution or abrasion correlates with the degree of conversion and thus the kinetics of cocrystallisation. This would require detailed analyses for the selective determination of particle size distributions and whether this can also be concluded from the overall particle size distribution of the mixture.

In addition, it should be checked whether the added water played a significant role in the observed phenomenon. This could be achieved by neat grinding, although the issue of caking would still need to be resolved. More detailed energetic considerations are necessary to determine the stress energies and/or stress numbers at which the various hydrate levels can be converted or whether the thresholds are reached at different speeds for each $CaSO_4$*xH_2O.

5 Summary

In the present work, the experiments already mentioned in the literature were extended by some parameters. These included only one grinding media size per batch instead of a mixture of several sizes, the ball to powder ratio and additional speeds in the planetary ball mill.

New findings were also added. These include the fact that the anhydrite of $CaSO_4$ could also be quantitatively converted to URCASU. Furthermore, the stress energy and stress number seem to play a role, which has not yet been quantitatively analysed. Further experiments are to follow in order to obtain a more comprehensive picture of the mechanical and mechanochemical properties in the production process of URCASU.

We would like to thank Dr. rer. Nat. Jochen Schmidt and M. Sc. Ali Massomi for making it possible for us to examine the samples using Raman spectroscopy, as well as Prof. Dr. rer. nat. Uta Helbig and Dipl.-Ing. Jessica Aumüller using their X-ray diffractometer and for their support.

References

Aakeröy, C. B., Fasulo, M. E., Desper, J. (2007) Cocrystal or salt : does it really matter? *Molecular Pharmaceutics*, 4 (3), 317-322.

Aitipamula, S., M., Banerjee, R., Bansal, A. K., Zaworotko, M. J. and more (2012) Polymorphs, Salts, and Cocrystals: What's in a Name? *Crystal Growth & -Design*, 12 (5), 2147-2152.

Barčauskaite, K. Brazienė, Z., Avižienyte D., Baltrusaitis, J. (2020) Mechanochemically synthesized gypsum and gypsum drywall waste cocrystals with urea for enhanced environmental sustainability fertilizers. *Journal of Environmental Chemical Engineering*, 8 (4), 103965.

Bista, P., Eisa, M., Ragauskaitė, D., Sapkota, S., Baltruasaitis, J., Ghimire, R. (2023) Effect of Urea-Calcium Sulfate Cocrystal Nitrogen Fertilizer on Sorghum Productivity and Soil N_2O Emissions. *Sustainability*, 15, 8010.

Brekalo, I., Martinez, V., Karadeniz, B. Baltrusaitis J. and more (2022) Scale-Up of Agrochemical Urea-Gypsum Cocrystal Synthesis Using Thermally Controlled Mechanochemistry. *ACS Sustainable Chemistry & Engineering*, 10, 6743-6754.

Burmeister, C., Titscher, L., Breitung-Faes, S., Kwade, A. (2017) Dry grinding in planetary ball mills: Evaluation of a stressing model. *Advanced Powder Technology*, 29, 191-201.

Kumar, S., Nanda, A. (2018) Pharmaceutical Cocrystals: An Overview. *Indian Journal of Pharmaceutical Sciences*, 79 (6), 858-871.

Nöske, M., Müller, J., Nowak, C., Kwade, A. and more (2022) Multicomponent Comminution within a Stirred Media Mill and Its Application for Processing a Lithium-Ion Battery Slurry. *Processes*, 10, 2309.

Rodrigues, M., Baptista, Lopes, J. A. and Sarraguça (2018) Pharmaceutical cocrystallization techniques. Advances and challenges. *International Journal of Pharmaceutics*, 547 (1-2), 404-420.

Tan, D., García (2019) Main group mechanochemistry: from curiosity to established protocols. *Chemical Society Reviews* , 48, 2274-2292.

Wächter, M., (2012) Ergänzendes Online-Angebot zu o.g. Nachschlagwerk, *Tabellenbuch zur Chemie*.

C2: Improving the carbonation of steel slags through concurrent wet milling

Anthony de Schutter[1], *Luka* Ceyssens[1], *Giuseppe* Granata[2] and *Tom* Van Gerven[1,*]

[1] Department of Chemical Engineering, Process Engineering for Sustainable Systems, KU Leuven, 3001 Leuven, Belgium
[2] Department of Materials Engineering, Sustainable Materials Processing and Recycling, KU Leuven, 3001 Leuven, Belgium

Abstract. This work studies mineral carbonation of steel slags with the aim to reduce the amount of slag that is landfilled. Besides permanently storing carbon dioxide (CO_2), carbonating the slags can improve their quality for use in beneficial applications and reduces the leaching of harmful heavy metals. Mechanochemical activation is used to improve both the mineral carbonation kinetics and yield. The milling is performed in a planetary ball mill, resulting in a fast reduction of the particle size and quick amorphization and disturbance of the crystal structure, allowing high reaction rates to be achieved. The effects of the three main processing parameters of a planetary ball mill – bead-to-powder ratio *R*, bead size *D* and milling speed *S* – are investigated. Under optimal conditions, more than 50% of the maximum CO_2 uptake is achieved in only 6 min, representing a very significant improvement over regular slurry carbonation. Quantitative XRD allows to identify the reactivity of the different crystalline phases present in the slag under different milling conditions. With the help of a mass balance, the formation of an inert outer layer consisting of silica (SiO_2) is confirmed. This explains both the shell diffusion mechanism controlling the carbonation reaction and the total conversion being limited to 50-60%.

1 Introduction

Due to the continuing increase of carbon dioxide (CO_2) concentration in the atmosphere, the need for techniques that allow for the capture and storage of CO_2 is becoming more pressing. An example of long-term storage is the natural weathering of silicate containing materials, also known as mineral carbonation. This is however limited by unfavorable kinetics (Seifritz, 1990).

Industrial steel slags are readily available waste products which contain the necessary silicate materials needed for mineral carbonation (Ragipani, Bhattacharya and K. Suresh, 2021). The current investigation focuses on two different types of slag, namely basic oxygen furnace (BOF) and argon oxygen decarburization (AOD) slags. BOF slag is produced when the carbon-rich hot metal from the blast furnace (BF) is poured into a furnace through which pure oxygen is blown in order to lower the carbon content of the steel (Kildahl *et al.*, 2023). This process, together with the blast furnace process, generated an estimated 190 – 280 million tons of slag worldwide in 2021 (Tuck, 2022). AOD slags constitute a major part of stainless steel slags, of which approximately 16 million tons was produced worldwide in 2019 (Holappa *et al.*, 2021).

To tackle the challenge of the slow kinetics of the carbonation, the current work focuses on the effects of milling on the reaction. The long term effects of milling, such as an increased specific surface area and the resulting improved carbonation kinetics and conversion, are proven by multiple studies where carbonation is carried out after milling (Li and Hitch, 2017; Rigopoulos *et al.*, 2018).

This work further investigates the mechanisms by which concurrent milling can improve the carbonation through increasing the intensity of grinding by carrying out experiments in a planetary ball mill, which introduces more impact and compression forces than a stirred media mill. Besides the long-term effects of particle size reduction and the removal of the inert outer layer, these forces also bring in short-term effects like lattice vibrations and highly excited states on the crystal level during impact (Hoffmann, Horst and Kunz, 2005). Studying the milling parameters like bead-to-powder ratio *R*, bead size *D*, milling speed *S* and milling time *t* gives greater insight into which forces are most responsible for improving the reaction. This allows to optimize the process on lab-scale and eventually scale up the process for industrial use.

2 Materials and methods

BOF and AOD slag was sieved to a particle size below 1 mm to ensure reproducibility of the experimental procedure. Carbonation experiments were conducted in a planetary ball mill using zirconia grinding jars with gassing lids and zirconia grinding beads, pressurized with 99.9% CO_2. To avoid sub-stoichiometric CO_2 conditions during carbonation, the milling experiments were stopped periodically to repressurize the grinding

* Corresponding author: tom.vangerven@kuleuven.be

jars. The solid concentration in milling was kept constant.

Three different milling parameters were investigated, namely the milling speed *S* (200 – 500 – 800 [rpm]), bead diameter *D* (2 – 3 – 5 – 10 [mm]) and bead-to-powder ratio *R* (20 – 40 – 100 [-]). Control carbonation experiments were performed in a glass reactor at the same pressure and solid concentration under constant stirring.

Laser diffraction was utilized to measure the particle size distribution of the starting and processed material. The chemical composition of the unreacted and unmilled slags was determined with ICP-OES. Thermogravimetric analysis (TGA) heating runs were carried out to measure the amount of CO_2 that was captured during the reaction. These measurements, together with the known chemical composition from ICP-OES, allow to calculate the percentage of the maximum CO_2 uptake using Equation 1 (Bodor *et al.*, 2013):

$$\mathrm{CO_2\ uptake\ (\%\ maximal)} = x = \frac{\frac{Q_{\mathrm{CO_2}}}{\mathrm{MW_{CO_2}}}}{\frac{w_{\mathrm{Ca}}}{\mathrm{MW_{Ca}}} + \frac{w_{\mathrm{Mg}}}{\mathrm{MW_{Mg}}}} \quad (1)$$

where Q_{CO2} is the amount of CO_2 released during the TGA measurement over the total material not containing CO_2, w_i the mole fraction of element *i* and MW_i the molar weight of element *i*.

In addition, XRD measurements were performed on selected samples after the addition of an internal standard. Rietveld refinement was carried out in order to quantify both the different crystalline phases present in the slag and the amorphous content in the experiment.

3 Results and discussion

3.1. Slurry carbonation of slags glass reactor without milling

The TGA results for the slurry carbonation experiment at 5 bar are shown in Figure 1. After 30 min, **Hiba! A hivatkozási forrás nem található.** 1a shows that AOD in the stirred glass reactor reaches approximately 15% of the maximum CO_2 uptake. The reaction in the stirred reactor continues for up to five hours – but the uptake only slowly grows to 20 % of the maximum. Note that in a previous study on slurry carbonation 40% of the maximum uptake was achieved for AOD after 120 min, because of more efficient stirring and a pressure of 6 bar (Santos *et al.*, 2013). Figure 1b shows that even in the absence of milling, BOF slag is able to reach a plateau carbonation level between 38% and 45% of the theoretical maximal uptake rate.

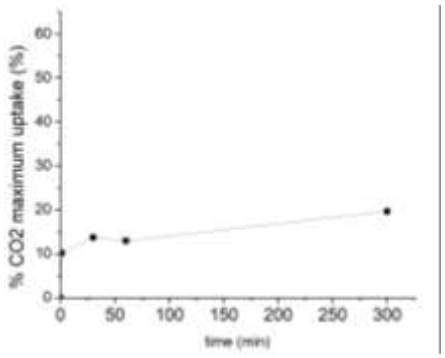

(a)

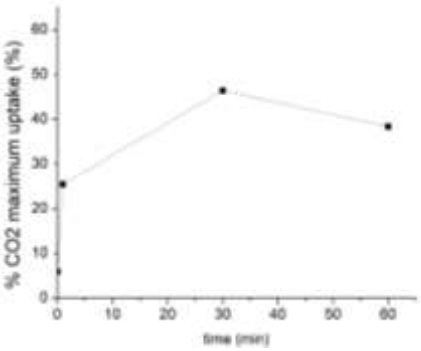

(b)

Fig. 1. Evolution of the percentage of maximum CO_2 uptake during slurry carbonation in a glass reactor for (a) AOD and (b) BOF

The results of these experiments serve as a benchmark to which the results of the concurrent wet milling carbonation can be compared.

3.2. Effect of milling parameters on carbonation rate and total CO_2 uptake

Figures 2a and 2b show the effect of milling speed on the carbonation uptake for AOD and BOF, respectively. The milling speed was found to be the parameter with the biggest impact on carbonation rate, more so than bead-to-powder ratio or bead diameter. For both slags the initial rate is greatly enhanced by increasing the speed. For example, after 1 min, the uptake only reaches 10 % of the maximum for 200 rpm, while a speed of 500 rpm manages to achieve double the amount. Moreover, quadrupling the speed from 200 to 800 rpm leads to a 4-fold increase in the uptake at 1 min. The vast majority of the carbonation happens in the first minute of this experiment with a duration of 30 min. The reason for the observed rise in initial carbonation rate is logical: increasing the speed provides more energy to the system, promoting mixing and increasing the dissolution of CO_2 in the water (which is the first step in the carbonation mechanism, and represented by Eq. S1 in the supplementary information). In addition, the larger energy input translates to higher impact forces.

In addition, the larger energy input translates to higher impact forces. As a result, the particles break more easily, increasing the specific surface area and exposing fresh surfaces to the dissolved CO_2, promoting the slag dissolution. Other, smaller effects include

disturbing the crystal lattice and amorphization which both make the material more reactive (Suryanarayana, 2001; Baláž *et al.*, 2013).

While the effect of speed on the initial carbonation rate is clear and significant, speeding up the milling process does not seem to have a positive effect on the final uptake. The behavior of BOF is very similar to AOD: increasing the speed greatly affects the initial carbonation rate, but does not enhance the final uptake at 30 min.

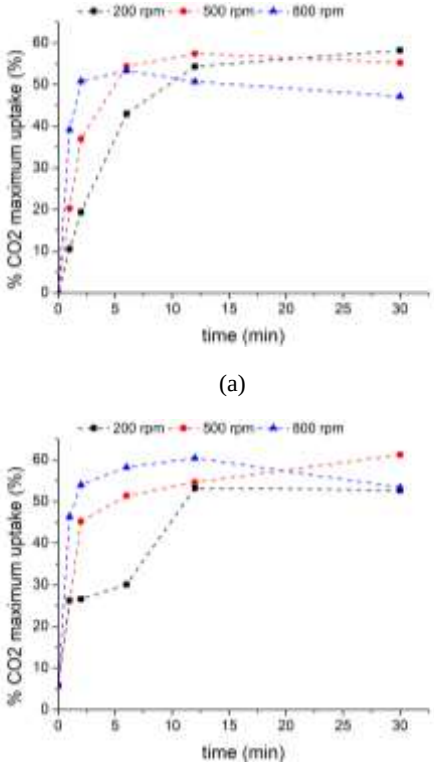

Fig. 2. Evolution of percentage of maximum CO_2 uptake during concurrent wet carbonation and milling with D = 5 mm, R = 40 and varying S for (a) AOD and (b) BOF

The results in the ball mill show much faster reaction rates compared to those from the slurry carbonation in the glass reactor, presented in Figure 1. After 30 min, for all milling experimental conditions, AOD has reached ± 50% of the maximum uptake, while Figure 1a shows that AOD in the stirred reactor barely reaches 15%. The difference between the stirred reaction in Figure 1b for BOF and the milled experiments is less pronounced than for AOD as the stirred reactor is able to reach a plateau between 38% and 45% of the maximum uptake in 30 min. Still, in the milled experiments this value is obtained in 2 min, proving that milling is certainly beneficial for the carbonation of BOF as well.

3.3. Effect of milling speed on crystalline carbonate and amorphous phase production

Figures 3a and 3b show the crystalline Ca and Si content of the total material, respectively, excluding the crystalline carbonate concentration. This is done to eliminate the diluting effect of the extra mass that comes with the formed carbonate. In other words, these graphs show the concentration of a certain element where the reference mass remains the original uncarbonated material. Figure 3c clearly shows that the increase in amorphous content is strongly correlated with the increase in amorphous silica for all milling speeds investigated.

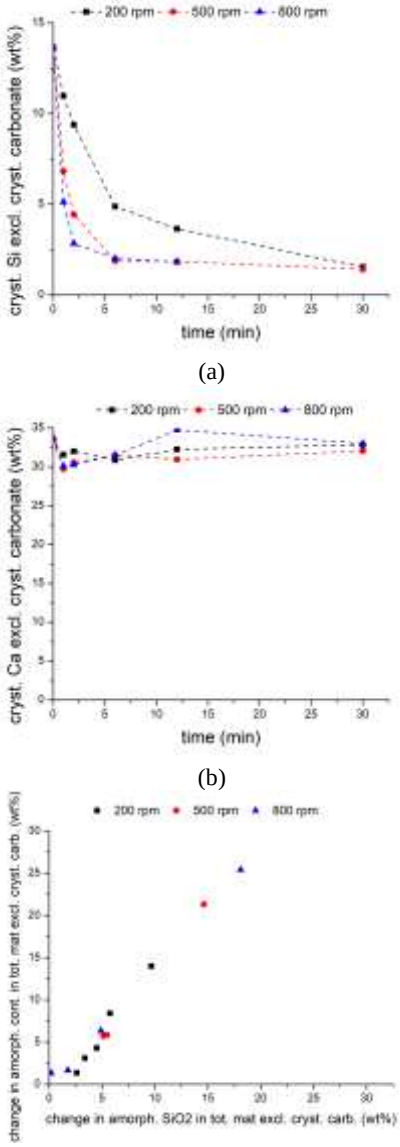

Fig. 3. Evolution of the percentage of maximum CO_2 uptake during slurry carbonation in a glass reactor for (a) AOD and (b) BOF

The reduction in crystalline silicon, combined with the constant level of crystalline calcium, suggests the formation of an inert amorphous silica outer layer.

4 Conclusion

The results show that the concurrent wet milling and carbonation of AOD slag leads to much faster carbonation on the one hand and fourfold increase in total CO_2 uptake on the other hand, when compared to

regular slurry carbonation in a pressurized stirred reactor. Having established the effectiveness of milling for carbonation in general, the effects of the three milling parameters – milling speed *S*, bead-to-powder ratio *R*, and bead size *D* – are investigated with the aim of optimizing the milling process. Increasing *S* leads to a substantial acceleration of the carbonation rate for both AOD and BOF. The higher speed leads to more impactful collisions of the grinding beads with the slag, resulting in a faster decrease in particle size, more effective removal of the outer inert layer surrounding the particles and a quicker generation of more reactive amorphous material.

None of the parameters seem to be able to elevate the total amount of CO_2 captured: a plateau between 50% and 60% of the maximum uptake is reached after 6-12 minutes depending on which combination of milling parameters is chosen. The timing of reaching this carbonation plateau coincides with the timing at which the slags stop decreasing in size, but rather start showing signs of agglomeration in the case of AOD or remain constant in size for BOF. In other words, from the moment that milling is no longer able to decrease the size of the slags or create fresh surfaces, the carbonation effectively stops. This result also shows that the influence of short-term effects like lattice vibrations are limited at this stage of the reaction.

Finally, with the help of quantitative XRD, a mass balance of Ca and Si shows that the concentration of crystalline Ca remains constant: calcium is being converted from a crystalline silicate phase to a crystalline carbonate phase, as expected. Silicon shows a clear reduction in crystalline concentration. Further analyses show that the increase in amorphous content is highly correlated to the decrease in crystalline silica, proving that the majority of the amorphous phase created during the process consists of amorphous silica, which makes up the inert outer layer surrounding the particles.

The Research Foundation – Flanders (FWO) is gratefully acknowledged for funding this research as part of the AgriCarb project (G0A4821N) and the C-Farms project (S004023N).

References

Baláž, P. *et al.* (2013) ‘Hallmarks of mechanochemistry: from nanoparticles to technology’, *Chemical Society Reviews*, 42(18), p. 7571. Available at: https://doi.org/10.1039/c3cs35468g.

Bodor, M. *et al.* (2013) ‘Susceptibility of mineral phases of steel slags towards carbonation: mineralogical, morphological and chemical assessment’, *European Journal of Mineralogy*, 25(4), pp. 533–549. Available at: https://doi.org/10.1127/0935-1221/2013/0025-2300.

Hoffmann, U., Horst, C. and Kunz, U. (2005) ‘Reactive Comminution’, in K. Sundmacher, A. Kienle, and A. Seidel-Morgenstern (eds) *Integrated Chemical Processes*. Weinheim, FRG: Wiley-VCH Verlag GmbH & Co. KGaA, pp. 407–436. Available at: https://doi.org/10.1002/3527605738.ch14.

Holappa, L. *et al.* (2021) ‘A Review of Circular Economy Prospects for Stainless Steelmaking Slags’, *Journal of Sustainable Metallurgy*, 7(3), pp. 806–817. Available at: https://doi.org/10.1007/s40831-021-00392-w.

Kildahl, H. *et al.* (2023) ‘Cost effective decarbonisation of blast furnace – basic oxygen furnace steel production through thermochemical sector coupling’, *Journal of Cleaner Production*, 389, p. 135963. Available at: https://doi.org/10.1016/j.jclepro.2023.135963.

Li, J. and Hitch, M. (2017) ‘Ultra-fine grinding and mechanical activation of mine waste rock using a planetary mill for mineral carbonation’, *International Journal of Mineral Processing*, 158, pp. 18–26. Available at: https://doi.org/10.1016/j.minpro.2016.11.016.

Ragipani, R., Bhattacharya, S. and K. Suresh, A. (2021) ‘A review on steel slag valorisation via mineral carbonation’, *Reaction Chemistry & Engineering*, 6(7), pp. 1152–1178. Available at: https://doi.org/10.1039/D1RE00035G.

Rigopoulos, I. *et al.* (2018) ‘Effect of ball milling on the carbon sequestration efficiency of serpentinized peridotites’, *Minerals Engineering*, 120, pp. 66–74. Available at: https://doi.org/10.1016/j.mineng.2018.02.011.

Santos, R.M. *et al.* (2013) ‘Accelerated mineral carbonation of stainless steel slags for CO2 storage and waste valorization: Effect of process parameters on geochemical properties’, *International Journal of Greenhouse Gas Control*, 17, pp. 32–45. Available at: https://doi.org/10.1016/j.ijggc.2013.04.004.

Seifritz, W. (1990) ‘CO2 disposal by means of silicates’, *Nature*, 345(6275), pp. 486–486. Available at: https://doi.org/10.1038/345486b0.

Suryanarayana, C. (2001) ‘Mechanical alloying and milling’, *Progress in Materials Science*, p. 184.

Tuck, C.C. (2022) *Mineral Commodity Summaries 2022 - Iron and Steel Slag*. U.S. Geological Survey. Available at: https://pubs.usgs.gov/periodicals/mcs2022/mcs2022-iron-steel-slag.pdf.

C3: Mechanochemical synthesis of sulfide-based solid electrolytes for solid-state batteries – Process investigation, characterization methods and upscaling

Michael Grube[1,*], *Sabrina Zellmer*[1,2], and *Arno Kwade*[1,2]

[1] Fraunhofer Institute for Surface Engineering and Thin Films IST, Braunschweig, Germany
[2] Institute for Particle Technology, TU Braunschweig, Braunschweig, Germany

Abstract. Mechanochemical syntheses for the compositional flexible production of new materials based on powder precursors have a high potential as environmentally friendly processes with the absence of solvents involved. As a method to synthesize solid electrolytes for solid-state batteries, mechanochemical processes are reported as highly time consuming and not easily scalable but promise superior product properties in form of high ionic conductivities compared to solvent based processes. In our study, sulfide-based solid electrolytes were successfully synthesized in much reduced times after a systematic variation of the process parameters in different ball mill types. A better understanding of the process-structure–property relations and process efficiency was achieved by variation of process parameters such as rotational speed, grinding media size and grinding media filling ratio. The different sets of investigated process parameters also exhibit systematic effects on the crystallinity and particle size distribution of the solid electrolytes. Furthermore scale-up strategies, safety aspects and subsequent process steps to further improve the material properties were investigated. As a result, a highly enhanced process with lower specific energy demand, higher throughput and increased ionic conductivity was achieved. (Hofer & Grube et al, 2023)

1 Application of mechanochemistry for sulfide-based solid-state batteries

Solid-state batteries (SSB) are regarded as a promising concept to enhance performance and capacity within the established lithium-ion battery (LIB) technology, which in the case of current liquid-based systems has already come close to its achievable performance limits. The current limitations of traditional lithium-ion batteries, such as safety concerns related to the flammable liquid electrolytes and challenges in achieving higher energy densities, have led to increased research effort on solid-state batteries. (Janek & Zeier, 2023; Schmaltz et al, 2023) SSBs aim to overcome these limitations by replacing liquid electrolytes with an ion-conducting solid electrolyte with enhanced safety potential, and increased energy density. On the way of developing and establishing SSB technologies on a larger scale – especially those based on high performance sulfide-based solid electrolytes – the demand for industrial production processes highly increases (Janek & Zeier, 2023; Robinson & Janek, 2014, Yamamoto et al, 2021). Currently, there are many challenges and the development of production processes for the solid electrolyte (SE) in sulfide-based SSB is a key challenge, due to low material availability, high cost and lack of established processes. Aiming at the availability of high-conductive SE, the focus of this work was to investigate, establish and improve the mechanochemical process for the synthesis of sulfide-based SE like Li_3PS_4 or Li_6PS_5Cl.

Sulfide-based SE are currently being researched with high effort because of their very high Li+ conductivity and suitable mechanical properties for processing in SSB electrodes, but their syntheses are mostly reported with long process times and they often require toxic and inflammable solvents (Janek & Zeier, 2023; Yamamoto et al, 2021; Kato et al, 2016; Stöffler et al 2019, Ruhl et al 2021). In a previous work (Hofer & Grube et al, 2023), the solvent-free mechanochemical synthesis of Li_3PS_4 was investigated and highly optimized in lab scale via high energy ball milling. A deeper understanding of process-structure-product-relations was gained by experiments and associated simulations of stressing conditions with the discrete-element-method (DEM). The insights of the experimental and simulation results revealed a direct correlation between the stressing conditions at different parameter sets and the obtained product properties.

In this work improved mechanochemical processes for sulfide-based solid electrolytes, suitable processing strategies in ball mills and material properties in different production atmospheres and after varied post-treatments are presented, to further facilitate the industrial production of ASSB.

Furthermore, challenges for large scale production as well as suitable processing strategies in upscaled media mills for dry mechanochemical syntheses are presented and discussed.

* Corresponding author: michael.grube@ist.fraunhofer.de

2 Method and product characterization

To investigate and improve the mechanochemical synthesis of sulfide-based solid electrolytes several process parameters such as rotational speed, grinding media size and grinding media filling ratio were varied in different ball mills in a systematic study. Furthermore, experiments were conducted under different potential production atmospheres in a dry room and in an argon filled glovebox to evaluate product qualities in upscaled scenarios. To gain insights in the mechanochemical process and to characterize the achieved product properties the following main methods were used among others, such as particle size measurements and SEM imaging.

2.1 Parameter study in media mills

In contrast to pure comminution processes, the optimization of mechanochemical processes aims at high reaction kinetics, improved product properties and chemical composition instead of an optimized specific energy input for a certain particle size distribution of the product. Nevertheless, parameters of media mills for tailored processes are similar both for comminution and mechanochemistry. In this study prior to an upscaling in media mills with larger grinding chamber volumes in the liter-scale and different stressing mechanisms (e.g. planetary ball mill compared to stirred media mill), process investigations were conducted in a cooled high energy ball mill. The variation of process parameters for the used high energy ball mill is shown in table 1. (Hofer & Grube et al, 2023)

Table 1. Example of varied process parameter for cooled high energy ball mill during lab scale process optimization (Hofer & Grube et al, 2023)

Parameter	Unit	Variation
Grinding media diameter (d_{GM})	mm	5, 7, 10
Grinding media filling ratio (φ_{GM})	-	0.2, 0.3, 0.5
Rotational speed (n)	rpm	600, 800, 1000, 1200
Process time (t_p)	h	1, 2, 3, 5, 7, 10, 15, 20

2.2 Raman spectroscopy (Reaction progress)

The Raman spectroscopy was performed with the use of a Thermo Scientific DXR 2 Raman microscope. Samples were excited at 532 nm and the presented spectra were obtained by the accumulation of 20 scans of 2 s at 1 mW laser power in the range of 55 to 1555 cm^{-1}. For auxiliary quantification of the synthesis progress by Raman spectroscopy, a relative phase ratio of $[PS_4]^{3-}$ was calculated based on three characteristic chemical phases ($[P_2S_6]^{4-}$ at 388 cm^{-1}, $[P_2S_7]^{4-}$ at 408 cm^{-1}, $[PS_4]^{3-}$ at 420 cm^{-1}) during conversion of reactants to the electrolyte Li_3PS_4. Before the calculation, Raman spectra were baseline corrected, normalized and then fitted by a gaussian function to integrate the individual phases at their characteristic wavenumbers. (Hofer & Grube et al, 2023)

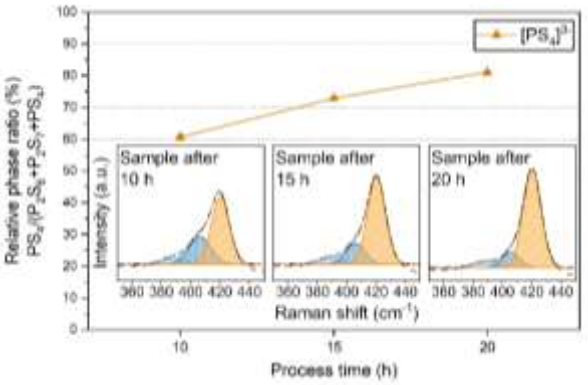

Fig. 1. Reaction progress in form of the calculated auxiliary relative phase ratio characterized by Raman spectroscopy for a reference synthesis of Li_3PS_4 (used with permission from Hofer & Grube et al, 2023).

The electrolyte samples were prepared in a glovebox where the educts and products were placed on a glass substrate and sealed by a high viscosity silicone vacuum grease under a cover glass. (Hofer & Grube et al, 2023)

2.3 X-ray diffraction (Product crystallinity)

To characterize the crystallinity of the solid electrolyte, which has a high impact on the ionic conductivity of the final product, X-ray diffraction was utilized. The diffraction patterns were obtained with a Malvern Panalytical Empyrean diffractometer with a Cu Ka (k = 0.154 nm) monochromatic source. Scans were recorded over the range from 5 to 120° 2 Θ with a step size of 0.05° 2Θ. Kapton foil was used as a top seal to prevent exposure to air. (Hofer & Grube et al, 2023)

2.4 Electrochemical impedance spectroscopy (Ionic conductivity)

The ionic conductivities were determined by electrochemical impedance spectroscopy (EIS) of powder pellets (~500–600 µm thickness, ~2.01 cm^2 electrode area). The synthesized electrolytes were placed in a Teflon tube and stainless-steel rods were used as blocking electrodes on both sides and subsequently pelletized by uniaxial pressing at 380 MPa in a two-column laboratory press. Three EIS measurements were conducted per parameter set under uniaxial pressure to maintain contacting of solids. (Hofer & Grube et al, 2023)

References

Janek, J. and Zeier, W. G. (2023) 'Challenges in speeding up solid-state battery development', Nature Energy, vol. 8, no. 3, pp. 230–240.

Schmaltz, T., Hartmann, F., Wicke, T., Weymann, L., Neef, C. and Janek, J. (2023) 'A Roadmap for Solid-State Batteries', Advanced Energy Materials, vol. 13, no. 43, p. 5.

Robinson, A. L. and Janek, J. (2014) 'Solid-state batteries enter EV fray', MRS Bulletin, vol. 39, no. 12, pp. 1046–1047.

Yamamoto, K., Yang, S., Takahashi, M., Ohara, K., Uchiyama, T., Watanabe, T., Sakuda, A., Hayashi, A., Tatsumisago, M., Muto, H., Matsuda, A. and Uchimoto, Y. (2021) 'High Ionic Conductivity of Liquid-Phase-Synthesized Li 3 PS 4 Solid Electrolyte, Comparable to That Obtained via Ball Milling', ACS Applied Energy Materials.

Kato, Y., Hori, S., Saito, T., Suzuki, K., Hirayama, M., Mitsui, A., Yonemura, M., Iba, H. and Kanno, R. (2016) 'High-power all-solid-state batteries using sulfide superionic conductors', Nature Energy, vol. 1, no. 4, p. 652.

Janek, J. and Zeier, W. G. (2016) 'A solid future for battery development', Nature Energy, vol. 1, no. 9, p. 1167.

Stöffler, H., Zinkevich, T., Yavuz, M., Hansen, A.-L., Knapp, M., Bednarčík, J., Randau, S., Richter, F. H., Janek, J., Ehrenberg, H. and Indris, S. (2019) 'Amorphous versus Crystalline Li 3 PS 4 : Local Structural Changes during Synthesis and Li Ion Mobility', The Journal of Physical Chemistry C, vol. 123, no. 16, pp. 10280–10290.

Ruhl, J., Riegger, L. M., Ghidiu, M. and Zeier, W. G. (2021) 'Impact of Solvent Treatment of the Superionic Argyrodite Li 6 PS 5 Cl on Solid-State Battery Performance', Advanced Energy and Sustainability Research, vol. 2, no. 2, p. 2000077.

Hofer, M. & Grube, M., Burmeister, C. F., Michalowski, P., Zellmer, S. and Kwade, A. (2023) 'Effective mechanochemical synthesis of sulfide solid electrolyte Li3PS4 in a high energy ball mill by process investigation', Advanced Powder Technology, vol. 34, no. 6, p. 104004.

C4: A mechanochemical reaction study on the role of stress conditions and particle properties within a mixer ball mill

Victor Marcus Oldhues[1,*], *Arno* Kwade[1], and *Sandra* Breitung-Faes[2]

[1]Institute for Particle Technology, Technische Universität Braunschweig, Brunswick, Germany
[2]Department for Mechanical Engineering / Particle Technology, Technische Hochschule Nürnberg, Nuremberg, Germany

Abstract. Mechanochemistry fulfils all principles of green chemistry making its pathways a serious alternative to conventional wet-chemical routes. To this day, the knowledge on the general mechanistic background of such reactions is still limited. The presented study helps uncovering the role of mechanical stress on a model reaction by applying a stress model on a simple setup in a mixer ball mill, which enables quantifying the stress conditions and correlating these with the reaction progress. For further insights, the influences of input particle size, reduction in particle size due to grinding, presented amount of particles and stress frequency were investigated. A general and direct influence of the stress intensity could be derived for the studied model reaction.

1 Introduction

Mechanochemistry is a sustainable and efficient alternative to conventional wet chemistry and, therefore, considered as an emerging technology of the future. Its methods enable chemical reactions by applying mechanical forces to the reactant materials, which trigger chemical and physical transformations in the stressed solids. The according chemical reactions can be conducted without the use of solvents or additional thermal energy supply. Consequently, mechanochemical pathways are oftentimes energy-efficient and promote reducing chemical waste in the future (James et al. 2012). Such reactions are often performed in different types of ball mills, in which the grinding media transfer their kinetic energy to the reactants and activate them mechanically to facilitate a reaction. The exact molecular processes are subject of current research, but it is legitimate to assume that altering the solid structures plays a crucial role in enabling mechanochemical reactions. The mechanical stress leads to deformation and surface enlargement, particle breakage and reduction in particle size, as well as formation of new surfaces. Furthermore, changes to the crystal lattice, such as amorphisation, shifts and distortion and introduction of defects supposedly decrease the activation energy of the reactant materials and, thus, increase their reactivity. Additional phenomena like frictional heat development and intensive surface contact as a result mixing effects can also support the reaction progress.

In this study, we want to focus on the correlation of certain stress conditions with the reaction progress of a mechanochemical model reaction. A simple setup of a mixer mill with a single steel ball is used as a model system, as it is easy to describe and allows modelling the mechanical energy input. The mass-specific energy as well as number, frequency and intensity of stress events are quantified and correlated with chemical conversion. Also, we emphasise the influence of certain particle properties on the reaction, namely, the input particle size, the input powder mass and the stressed powder mass per impact. We also address the occurring particle size reduction due to grinding and its role in the investigated model system. Overall, this study contributes to further enlightening the mechanistic background of mechanochemical reactions by identifying reaction-relevant parameters and separating grinding-related from reaction-related effects.

2 Experimental

In this study, a simple inorganic displacement reaction was used as a model reaction (1). The reaction was initiated and supported by mechanical energy input only and performed completely dry without providing thermal energy in addition to the milling energy.

$$Na_2CO_3 + CaCl_2 \rightarrow CaCO_3 + 2\,NaCl \qquad (1)$$

The experiments were performed in a laboratory mixer mill (CryoMill, Retsch, Germany) at 15 or 20 Hz milling frequency. The reactants were used in a molar ratio of 1:1 according to the reaction stoichiometry. A single steel ball (d = 20 mm) stressed the reactants in a steel grinding chamber (V = 25 mL).

The sodium carbonate was classified in an air classifier (Alpine 100 MZR Classifier, Hosokawa-Alpine, Germany) to use different input particle size distributions of this reactant for a series of experiments. Both reactants were also ground alone to follow the particle size reduction due to comminution without the influence of a chemical transformation of the materials.

* Corresponding author: v.oldhues@tu-braunschweig.de

Particle sizes were measured using laser diffraction (MasterSizer 3000, Malvern Panalytical, UK).

The weighted in powder mass varied in another series of experiments to investigate the influence of the presented particle amount on stress parameters and the related product yield. Finally, the increase in operation frequency of the used mixer mill allowed insights in the effect of impact energy and stress frequency on the model reaction.

3 Stress model

The simple setup of a mixer mill with a single steel ball allows modelling of the mechanical stress of the experiments effectively. The dry powder is suggested to be predominantly stressed due to impact of the grinding medium against the left and right grinding chamber wall (Blanc et al. 2020). For interpretation of the stress conditions, the stress model proposed by Kwade (Kwade and Schwedes 2002; Kwade 2003) was used. Accordingly, the grinding medium transfers the so called stress energy SE to the powder upon impact, which is dependent on the kinetic energy of the grinding medium.

$$SE \propto E_{kin,GM} \tag{2}$$

Considering the amount of product material that is captured and actively stressed in a single impact event, the stress intensity SI can be determined.

$$SI = SE / m_{P,act} \tag{3}$$

A whole grinding process includes multiple stress events, that can be described by the stress number SN. Since every impact introduces the energy amount of SE into the system, the total energy input equals the product of stress energy and number. The mass-specific energy E_m refers to the total amount of the powder in the system.

$$E_m = E / m_{P,tot} = SE \cdot SN / m_{P,tot} \tag{4}$$

For the single ball mixer mill that was used in this study, a few assumptions allow quantifying the stress energy and number and, therefore, the specific energy input (Blanc et al. 2020).

$$E_m = [8 \cdot m_{GM} \cdot (A\,\pi f)^2] \cdot [2 f t] / m_{P,tot} \tag{5}$$

4 Results and discussion

The comminution of both sodium carbonate and calcium chloride without the respective other reactant resulted in a quick particle size reduction for both materials. In only 5 min a median particle size of less than 10 µm was achieved, independent of the ground reactant and input particle size. Further grinding did not reduce the particle size significantly anymore in the used single ball mixer due to cushioning through a bed of fine material. Therefore, only a minor influence of the input particle size on the chemical conversion in an actual mixer mill reaction was expected. The according experiments did match the expectations, which can be seen in Fig. 1.

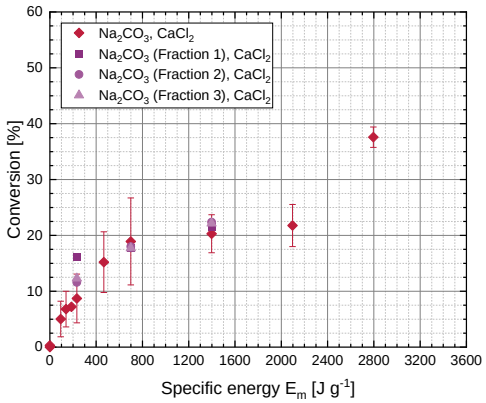

Fig. 1. Influence of input particle size on the reaction progress.

Instead, it was observed that the product yield is directly dependent on total supply of mechanical energy. The use of higher input powder masses led to the same findings, however, for the same specific energy lower yields were obtained with higher amounts of reactant material. This effect could be assigned to a decrease in the intensity of the occurring impacts in the mill as more particles were stressed per impact. Fig. 2 shows that the same number of stress events is less effective in progressing the reaction with an increase in reactant material.

Operating the mill at a higher vibrational frequency resulted in a different behaviour. It could be demonstrated that the amount of reactants had less influence on the energy efficiency of the reaction for higher vibrational frequencies although the stress intensity did still differ significantly. By increasing the frequency of the mill both the frequency of impacts and the transferred energy per impact were increased in the model system. Both phenomena are suggested to support frictional heat development and to introduce more deformation energy into the reactants due to higher mechanical forces and less relaxation time. This can be responsible for the reduced influence of the actively stressed powder masses per impact in the case of higher mill operation frequencies.

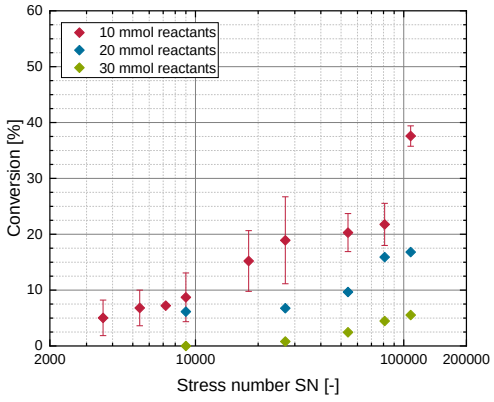

Fig. 2. Reaction efficiency due to the amount of reactants.

Overall, a direct correlation of reaction progress with the stress intensity was found. Considering all experimental series with variation of input particle sizes, amount of reactants and vibrational frequency, a general benefit of a higher stress intensity on the reaction could be observed, which can support process design and parameter choice for mechanochemical reactions in the future.

The German Research Foundation (DFG) is gratefully acknowledged for funding this research work. The cooperation with Desislava Dobreva and Lars Borchardt of the mechanochemistry group at Ruhr-Universität Bochum (RUB) is highly valued.

References

Blanc, N., Mayer-Laigle, C., Frank, X., Radjai, F. and Delenne, J.-Y. (2020) Evolution of grinding energy and particle size during dry ball-milling of silica sand. *Powder Technology*, 376, 662-667.

James, S., Adams, C., Bolm, C., Braga, D., Collier, P., Friščić, T. et al. (2012) Mechanochemistry: opportunities for new and cleaner synthesis. *Chemical Society Reviews*, 41, 413–447.

Kwade, A. (2003) A Stressing Model for the Description and Optimization of Grinding Processes. *Chemical Engineering & Technology*, 26, 199–205.

Kwade, A., Schwedes, J. (2002) Breaking characteristics of different materials and their effect on stress intensity and stress number in stirred media mills. *Powder Technol*ogy, 122, 109–121.

C5: Assessing the comminution effect of planetary ball milling parameters on the particle size of *Thymus serpyllum* L. (wild thyme) biomass by Taguchi method

Mária Kováčová[1], *Vendula* Bednaříková[2], *Michaela* Remešová[2], *Radovan* Bureš[3], *Ladislav* Čelko[2], *Matej* Baláž[1,*]

[1]Institute of Geotechnics, Slovak Academy of Sciences, Košice, Slovakia
[2] High-Performance Materials and Coatings for Industry Research Group, Central European Institute of Technology, Brno University of Technology, Brno, Czech Republic
[3]Institute of Materials Research, Slovak Academy of Sciences, Košice, Slovakia

Abstract. The mechanochemical valorisation of biomass for its transformation into valuable products (such as adsorbents or bio-alcohol) is in the research spotlight these days. The first step usually comprises particle size reduction. In the present contribution, the influence of three planetary ball milling parameters (a milling speed, the milling time and a sample mass) on the biomass powder was assessed via Taguchi orthogonal array. As a biomass, a common plant *Thymus serpyllum* L. (wild thyme) was used. An intermediate milling speed (500 rpm) and a longer milling time (120 min) was found to be most efficient in producing the finest powder. According to the Analysis of Variance, the milling time was the most important (and the only one most significant) factor influencing the outcome, its contribution being almost 68%, while the contributions of milling speed and sample mass were only around 12 and 0.05%, respectively.

1 Introduction

The mechanochemical valorisation of biomass is a hot topic today (Baláž, 2021; Hajiali et al., 2022). The beneficial effect of milling treatment on the biomass lies, among others, in facilitating the lignin extraction and the enzymatic hydrolysis to yield simple sugars and bioethanol (Shen et al., 2020; Sitotaw et al., 2023). The optimum milling conditions can be found by applying Design of Experiments (DoE) methodology, which simplifies the experiments and reduces the time required. The Taguchi method using orthogonal arrays is one of the most common DoE approaches (Taguchi et al., 2004). There are few examples of applying DoE also for the mechanochemical valorisation of biomass, including the assessment of particle size, e.g. (Arce and Krátky, 2024).

Investigating the effect of various milling pre-treatments on the particle size of the biomass is of utmost importance since it can significantly affect its suitability for the above-mentioned applications (Lomovskiy et al., 2020).

Common plants are particularly interesting examples of biomass due to their high abundance. *Thymus serpyllum* L. (wild thyme) plant definitely belongs to this category. It serves as a great source of antioxidants, such as phenols and flavonoids (Jovanovic et al., 2021). It was used as a reducing agent to produce antibacterially active bionanocomposites with the content of Ag^0 (Baláž et al., 2022), and recently also as an adsorbent of Cu(II) and Pb(II) ions by our research group (Kováčová et al., 2024).

The aim of the present study was to investigate the effect of high-energy milling treatment on the *Thymus serpyllum* L. plant via applying the DoE Taguchi methodology for assessing the effect of various milling conditions on particle size.

2 Materials and methods

2.1 Material

Thymus serpyllum L. plant (SER) was purchased from a local company Agrokarpaty, s.r.o., Slovakia concerned with the cultivation of medicinal plants. The plant was milled in a kitchen mixer and sieved to reach a particle size ≤ 1 mm.

2.2 High-energy ball milling

The *Thymus serpyllum* L. plant (SER) was milled in a Pulverisette 7 Premium line planetary ball mill (Fritsch, Idar-Oberstein, Germany) under the following conditions: air atmosphere, 25 zirconium oxide (ZrO_2) milling balls (10 mm diameter) in 80 ml zirconium oxide milling chamber. In order to optimize the milling conditions, Taguchi design was applied and three factors (a milling speed, the milling time, a mass of sample) at

* Corresponding author: balazm@saske.sk

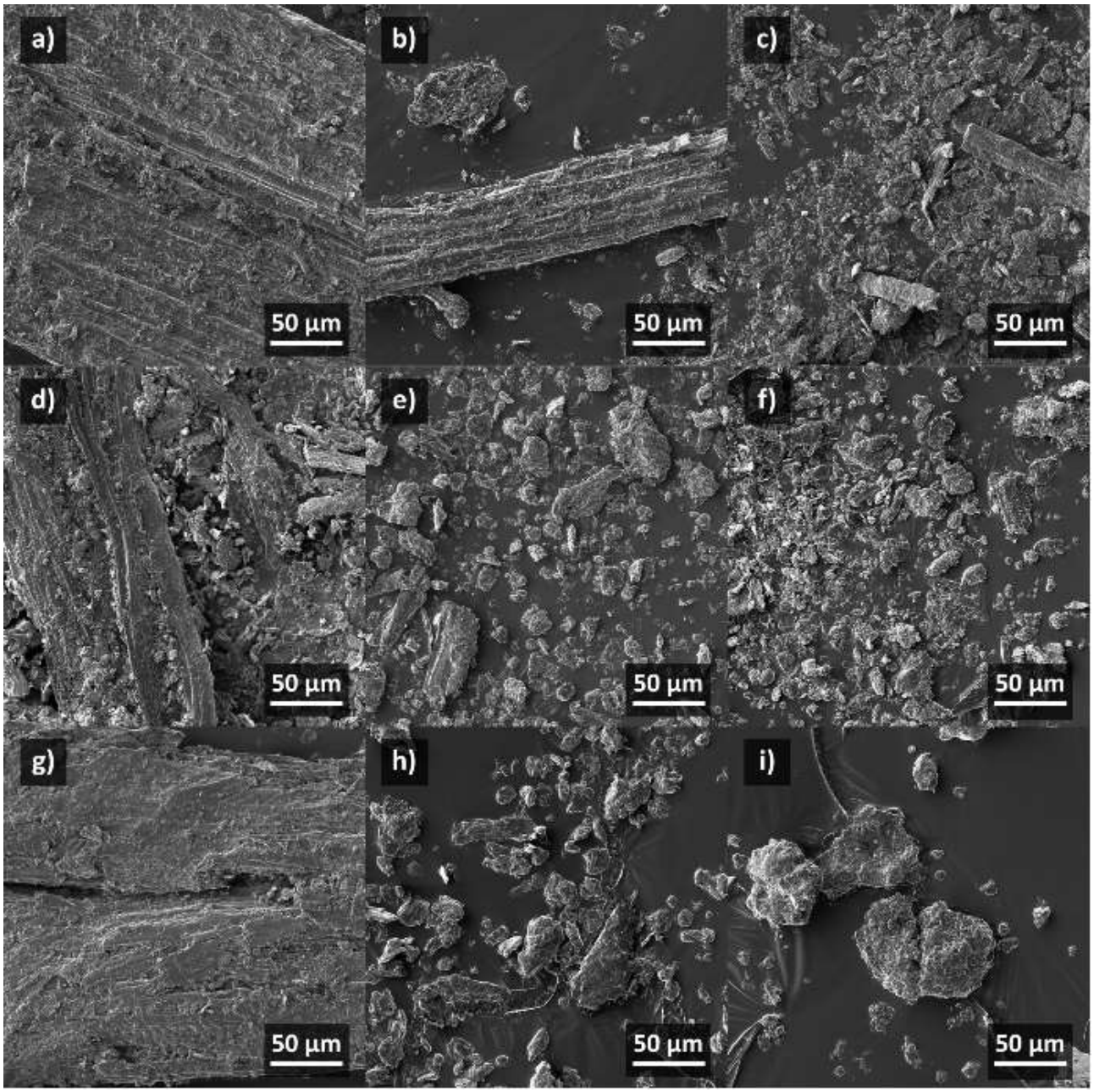

Fig. 1. SEM images of wild thyme powder treated under different conditions according to Taguchi design SER-T1 (a) – SER-T9 (i).

three levels were selected and changed (see Table 1). Taguchi orthogonal array (3^3) was created using the Minitab14 software (Minitab, Ltd., United Kingdom) and subsequently, nine experiments (SER-T1 – T9) with different combinations of parameters were planned and performed.

2.3 Characterization

2.3.1 Particle size analysis

The particle size analysis was performed using a particle size laser diffraction analysser Mastersizer 2000E (Malvern, Malvern, UK) in the dry mode. Each sample was measured three times.

2.3.2 Scanning electron microscopy

The morphology of the samples was studied by the scanning electron microscope (SEM) Lyra3 XMH (Tescan, Czech Republic). The SEM examination was carried out in secondary electron (SE) mode using an acceleration beam voltage of 3 keV. Prior to SEM examination, each dry SER sample was placed on double-sided adhesive carbon tape and coated with a 40 nm thick carbon layer using a high vacuum sputter coater Leica EM ACE600 (Leica Microsystems, Germany).

Table 5. Experimental plan based on Taguchi design for the optimization of mechanical activation conditions for *Thymus serpyllum* L. (SER) plant

Sample	Milling speed (rpm)	Milling time (min)	Mass of sample (g)
SER-T1	300	30	7.0
SER-T2	300	60	5.0
SER-T3	300	120	3.0
SER-T4	500	30	5.0
SER-T5	500	60	3.0
SER-T6	500	120	7.0
SER-T7	700	30	3.0
SER-T8	700	60	7.0
SER-T9	700	120	5.0

3 Results and Discussion

3.1 Morphology

The Fig. 1 displays the morphology of all the samples at the same magnification. The images in **Hiba! A hivatkozási forrás nem található.**a, d and g corresponds to the samples SER-T1, T4 and T7, respectively that were milled only for 30 minutes (which was the shortest milling time studied). The sample SER-T2 in Fig.1b contains a smaller culm of SER material and almost none of the plant fragments and in general its structure is different from the other 8 milled samples. The samples SER-T3, T5 and T6 (Fig.1c, e, f) contain the very fine particles and most of them with a size below 50 µm. This points to the fact that prolonged milling for 120 minutes (in case of SER-T3 sample) and increased milling speed (the samples SER-T5 and T6) led to the disintegration of SER structure and the formation of smaller particles. The samples SER-T8 and T9 in Fig.1h and Fig.1i nicely demonstrate agglomeration connected with a high milling speed (700 rpm) and an extended milling time (60 and 120 minutes for the samples SER-T8 and T9, respectively) which is more pronounced in the case of SER-T9 sample.

3.2 Particle size distribution

The summarized results of the median particle size, d_{50} values (d_{50}) for all the samples (SER-T1 – T9) and non-milled SER sample are shown in Fig. 2. As expected, the largest particles were detected for the non-milled SER sample (196 µm). Apart from the non-treated SER, the largest d_{50} values were obtained for SER-T1 (113 µm) and SER-T7 (104 µm) which were milled only for 30 minutes. The intermediate d_{50} value was achieved for both SER-T4 (55 µm) and SER-T2 sample (73 µm). The sample SER-T6 had the smallest particles (d_{50} value equal to 12 µm). Other samples with small particles (d_{50} around 20 µm) were samples SER-T3, SER-T5, SER-T8 and SER-T9, which demonstrate that the proper combination of milling time and milling speed facilitated the comminution process to reach fine particles. It seems that too intensive milling leads to agglomeration, in line with traditional theory regarding mechanical activation (Baláž, 2021).

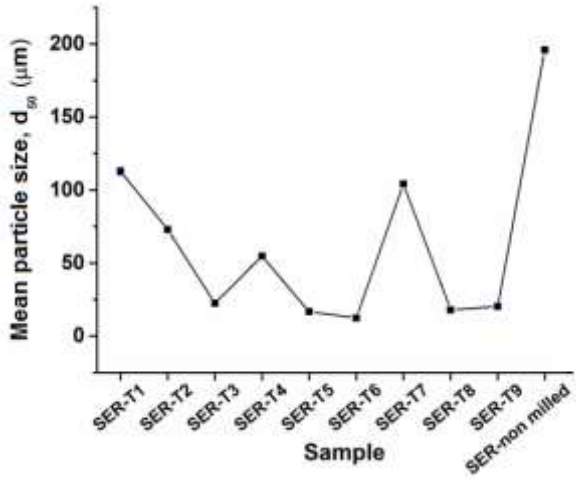

Fig. 2. d_{50} (median particle size) values for wild thyme powder treated under different conditions according to Taguchi design and the non-treated one.

3.3 Taguchi and ANOVA analysis

After measuring the particle size of all the samples, the acquired results were analysed in the Minitab14 software using Taguchi method via the "smaller is better" approach (see Fig.3a-c). The lowest d_{50} values represent the best parameters for obtaining the finest particles. According to the performed calculations, the rotation speed 500 rpm and the milling time 120 min seems to be the most beneficial. The almost straight line connecting the three d_{50} values evidenced for the sample mass shows the low significance of this parameter (Fig. 3c).

In order to determine the contribution of the selected milling parameters to the decrease in particle size, the analysis of variance (ANOVA) was applied (see Fig.3d). From all three studied parameters (a milling speed, the milling time, a mass of sample), the milling time proved to be the most significant factor for the preparation of fine particles (67.6%, p value = 0.034). A similar effect was observed in the case of classical ball milling in (Arce and Krátky, 2024), where also a response surface methodology was used. The influence of rotation speed was much less important (11.9% with p value 0.503) and the sample mass was found to be not important at all (0.4%, p value = 0.999).

Conclusions

Thymus serpyllum L. (wild thyme) plant was mechanically activated under the different milling speed, milling time and sample mass, according to 3^3 Taguchi orthogonal array. The results have shown a significant particle size reduction upon the treatment under an intermediate milling speed (500 rpm) and a longer milling time (120 min). The effect of sample mass was

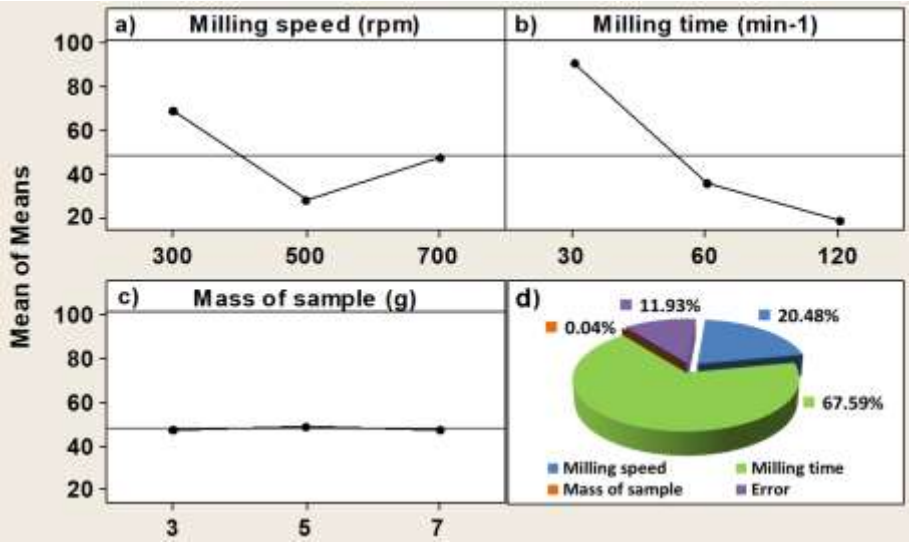

Fig. 3. Results of Taguchi (a-c) and ANOVA (d) calculations showing the influence of milling speed, milling time and mass of sample on the median particle size (d_{50}) of the wild thyme particles.

insignificant, as also proven by the Analysis of Variance. The most important influencing factor was milling time, with a p value below the limit of 0.05 and a contribution of around 68%. The obtained results show that upon proper tuning of planetary ball milling conditions, it is possible to obtain a very fine powder from the biomass, which should significantly facilitate the outcome of subsequent operations such as enzymatic hydrolysis, lignin separation or adsorption.

This work was supported by the Scientific Grant Agency of the Ministry of Education, Science, Research and Sport of the Slovak Republic (project 2/0112/22) and by the Slovak Research and Development Agency under the contract No. APVV-18-0357.

References

Arce, C. & Krátky, L. (2024) Investigating the effect of process variables for ball milling of wood chips: energy demand and particle size. *Biomass Conversion and Biorefinery*, DOI 10.1007/s13399-13024-05283-13390.

Baláž, M. (2021). Environmental Mechanochemistry: Recycling Waste into Materials Using High-Energy Ball Milling, Springer.

Baláž, M., Casas-Luna, M., Augustyniak, A., Tkáčiková, Ľ., Szmuc, K., Kováčová, M., Čelko, L. & Shpotyuk, Y. (2022) Hybrid Ag^0/Ag_2CO_3–eggshell–plant nanocomposites for antimicrobial action prepared by bio-mechanochemical synthesis. *Applied Nanoscience*, 12, 1899-1916.

Hajiali, F., Jin, T., Yang, G., Santos, M., Lam, E. & Moores, A. (2022) Mechanochemical Transformations of Biomass into Functional Materials. *Chemsuschem*, 15, e202102535.

Jovanovic, A. A., Djordjevic, V. B., Petrovic, P. M., Pljevljakusic, D. S., Zdunic, G. M., Savikin, K. P. & Bugarski, B. M. (2021) The influence of different extraction conditions on polyphenol content, antioxidant and antimicrobial activities of wild thyme. *Journal of Applied Research on Medicinal and Aromatic Plants*, 25, 100328.

Kováčová, M., Yankovych, H., Casas Luna, M., Remešová, M., FIndoráková, L., Stahorský, M., Čelko, L. & Baláž, M. (2024) Triggering antibacterial activity of a common plant by biosorption of selected heavy metals. *Journal of Biological and Inorganic Chemistry*, accepted on Jan 22, 2024.

Lomovskiy, I., Bychkov, A., Lomovsky, O. & Skripkina, T. (2020) Mechanochemical and Size Reduction Machines for Biorefining. *Molecules*, 25, 5345.

Shen, F., Xiong, X. N., Fu, J. Y., Yang, J. R., Qiu, M., Qi, X. H. & Tsang, D. C. W. (2020) Recent advances in mechanochemical production of chemicals and carbon materials from sustainable biomass resources. *Renewable & Sustainable Energy Reviews*, 130, 109944.

Sitotaw, Y. W., Habtu, N. G., Gebreyohannes, A. Y., Nunes, S. P. & Van Gerven, T. (2023) Ball milling as an important pretreatment technique in lignocellulose biorefineries: a review. *Biomass Conversion and Biorefinery*, 13, 15593-15616.

Taguchi, G., Jugulum, R. & Taguchi, S. (2004). Computer-based Robust Engineering: Essentials for DFSS. Milwaukee, MI, ASQ Quality Press.

D1: Electrodynamic fragmentation as treatment for concrete comminution: influence of limestone filler in the mix composition

Tatiane Isabel Hentges[1,*], *Margarita* Mezzeti[2], *Christine* Hecker[2], *Oleg* Popov[2], *Pierre* Landgraf[2], *Sérgio C.* Angulo[1], *Luis Marcelo* Tavares[3], and *Holger* Lieberwirth[2]

[1] Civil and Urban Construction Engineering Department, Polytechnic School of University of São Paulo, São Paulo, Brazil
[2] Institute for Mineral Processing Machines and Recycling Systems Technology, Technische Universität Bergakademie Freiberg, Freiberg, Saxony, Germany
[3] Department of Metallurgical & Materials Engineering, Federal University of Rio de Janeiro, Rio de Janeiro, Brazil

Abstract. In recent years, incorporation of limestone filler (LF) in cementitious materials has attracted great attention as a potential strategy for promoting more uniform crack propagation under load conditions. On the other hand, electrodynamic fragmentation (EDF) has been studied as an innovative approach for concrete recycling, as the electric impulses can pass along the grain boundaries of the components and separate them efficiently. However, application of EDF to concretes with LF has not yet been studied. The present work investigates the impact of LF inclusion in concrete composition subjected to electrodynamic fragmentation. Concrete samples were produced as reference and with LF, and EDF was conducted using energy inputs of 84 Joules at frequencies of 1, 10, 50, 80, and 100 impulses. Point load tests (PLT) were carried out before and after the EDF to assess its effect on the mechanical properties. Results revealed that EDF was as effective with reference concrete as with LF concrete, since nearly identical mean reductions in PLT strength (35% for LF and 33% for reference concrete) were observed. The work suggests that EDF holds promise in concrete weakening, even with the addition of LF. Future investigations should explore a broader range of energy inputs to elucidate the true impact of LF for this type of comminution treatment.

1 Introduction

Conventional crushing methods for concrete recycling often produce recycled aggregates containing adhered cement pastes, which are detrimental to their suitability for use in new concrete structures (Kim, 2022).

One promising strategy for enhance concrete recycling is electrodynamic fragmentation. In this method a discharge of electrical impulses leads to an imbalance of electrical charges at the grain boundaries due to locally differing electrical properties of the components. This creates a localized plasma combined with thermal expansion (Touzé et al., 2017).

Another approach to improve concrete recyclability involves incorporating limestone filler (LF) into the concrete mixture. The literature suggests a more uniform crack propagation in samples subjected to load conditions (Das et al., 2015). The use of LF is attractive in another way, since its use in replacement of Portland cement also reduces the CO_2 emissions of the concrete industry (John et al., 2018).

The combination of both strategies could yield even greater benefits for the circular economy of concrete. Therefore, this study aims to assess the impact of limestone filler on electrodynamic fragmentation of concrete.

2 Experimental program

The experimental program of this study was divided in four steps: i. concrete samples production, ii. strength determination by point load test, iii. electrical impulses applying (EDF treatment), and iv. determination of point load test after EDF treatment. These stages are illustrated in Figure 1.

2.1 Concrete production

For this study, the concrete was produced in the laboratory. Besides the reference, a 40%-replacement of the cement mass by LF was done in concrete mix proportioning. Water was adjusted aiming to reach total porosity and similar compressive strength, since the partial replacement of binder (cement) by an inert material (LF) with same water to solid ratio resulted in higher porosity. Based on previous studies by the research group, the mix proportions adopted for producing the concretes are presented on Table 1. The cement used was a CEM I 42.5R and the limestone filler was composed of 99% of calcite ($CaCO_3$). The

* Corresponding author: tatiane.hentges@lme.pcc.usp.br

aggregates used were river sand and gravel, which present particle sizes between 0.18 and 2.0 mm, and 2.0 and 15.0 mm, respectively.

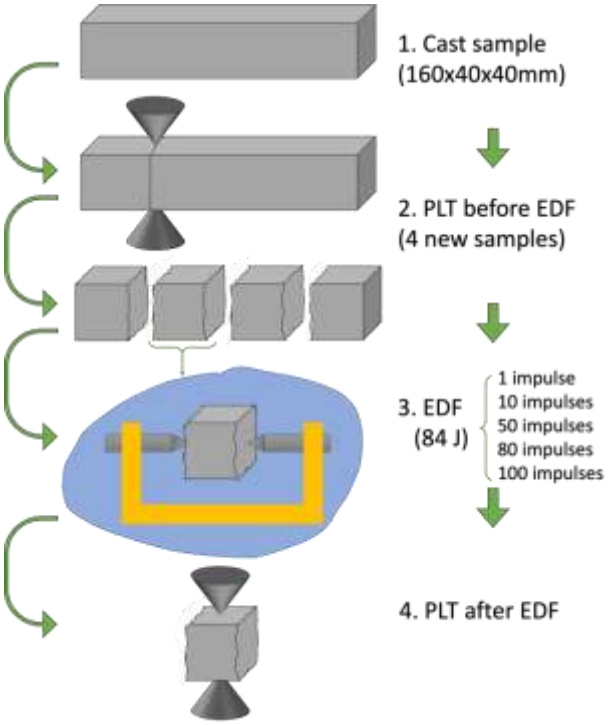

Fig. 1. Stages of the experimental program.

Table 1. Mix proportion in kg/m³ of concretes.

Materials	Reference concrete (RF)	Limestone filler concrete (LF)
Cement	310.53	211.68
Limestone filler	0	140.99
Sand	796.87	796.76
Gravel	1048.79	1049.93
Water	201.85	182.28
Mechanical properties		
Compressive strength in MPa	41.1	35.0
Flexural strength in MPa	6.73	5.52
Water absorption in %	5.75	5.79

Concrete samples measuring 160x40x40mm were casted and stored for 24 hours at high moisture (90%) and constant temperature (21°C). After that, the samples were kept underwater for 28 days and then dried in oven for 21 days at 60°C.

2.2 Methods

2.2.1 Point Load Test (PLT)

The point load test (PLT) is used as a measurement process for the classification of rock strength. A significant advantage of this process compared to the widely applied compressive and tensile strength tests is the limited demand for preparation of the rock specimens. The test can be conducted fast and simply with a portable tester either at the quarry or in the laboratory.

The strength index determined on the application of a concentrated load on a rock specimen to rock fracture can be used for classification or characterization of the rock. The strength index (*IS*) characterizes the strength of a rock specimen that breaks under a point force *P*. The introduction of the equivalent diameter *De* is useful to enable comparison of the results of the tests on irregularly shaped specimens with those of the diametral tests.

The measured strength index is largely dependent on the absolute size of the test specimen. This effect, which is also observed in all other test processes (e.g. uniaxial compression test), is generally referred to as the scale effect in rock mechanics (Thuro, 1996). As the size of the test specimen influences the strength index, the strength indices of lumps of rock of varying dimensions must be converted to a "standard rock lump" with a standard diameter *De* = 50 mm. Accordingly to Raaz (2002), the strength index IS may be converted into *IS*(50).

For the test a concentrated load (*P*) is applied to the samples and, after broken, the width and thickness of the fracture surface is measured to determine the strength index of the samples, according to equations (1) to (3):

$$D_e^2 = (W \times D) \times 4 \times \pi^{-1} \quad (1)$$

$$P = p \times 0.1 \times 1450 \quad (2)$$

$$Is = P \times D_e^2 \quad (3)$$

where *De* is the equivalent diameter (mm); *W* is the specimen width (mm); *D* is the thickness (mm); *P* is the breaking load (kN); *P* is the applied load (bar); and *Is* is the strength index (MPa). This later was determined using a test device from Fa. Wille Geotechnik.

Before EDF treatment, the PLT was determined to verify the initial strength index *Is* of the prisms and was used strategically to divide them in approximately four equal cubic samples (whenever possible due to the crack orientation). *Is* was then converted to *Is*(50).

After EDF the treated samples, whenever still maintained the appearance of a cube, were tested by PLT on the central point of the upper and bottom surfaces, i. e., in the same direction as the applied impulse. After this first split, two halves were also tested in the orthogonal direction.

In the end, *Is* and *Is*(50) were estimated, and a comparison of both *Is* and *Is*(50) before and after EDF could be made.

2.2.2 Electrodynamic fragmentation

After the initial PLT (PLT before EDF), the dry cubic samples were identified and randomly distributed in five groups. Each group, composed for 6 samples, received a different number of impulses: 1, 10, 50, 80, and 100. For the EDF treatment the cubes were fixed between the electrodes keeping constant 40 mm of spacing. Then they were immersed in water and, after one minute, the impulses were applied with 84 Joules.

The test setup of the EDF is shown schematically in Figure 1 (3. EDF). The individual particle to be tested is placed between the two electrodes. The functional principle of the EDF is based on that the dielectric strength of a material to electrical discharges is not constant. It depends on the voltage ramp rise time. In water, the dielectric strength at times in the order of, approximately, 500 ns is higher than that of rocks (Bluhm et al., 2000; Otto et al., 2021). This means that with correspondingly short voltage ramp rise time < 500 ns, it is possible to introduce pulses into the material in a targeted process (Seifert et al., 2014; Otto et al., 2021).

After the impulses, the sample was collected, dried in oven for 48 hours, its picture was captured and, then, PLT strength was measured ("PLT after").

3 Results

A noticeable reduction in the PLT *Is* becomes evident when the concretes are submitted to EDF, as depicted in Figure 2. This reduction presents a similar trend for both RF and LF concretes, whereas increasing the number of impulses leads to a decrease in *Is*. However, after 80 impulses the strength appears to reach a plateau, suggesting a potential saturation of weakening. Statistical analysis revealed no significant influence of the number of impulses on the *Is*(50), as expected by the high standard deviations. It is worth mentioning that all samples presented the original cube aspect in the "one impulse" group, 30% for "10 impulses" group, and all the samples of the other groups were broken at least in two halves on the other groups.

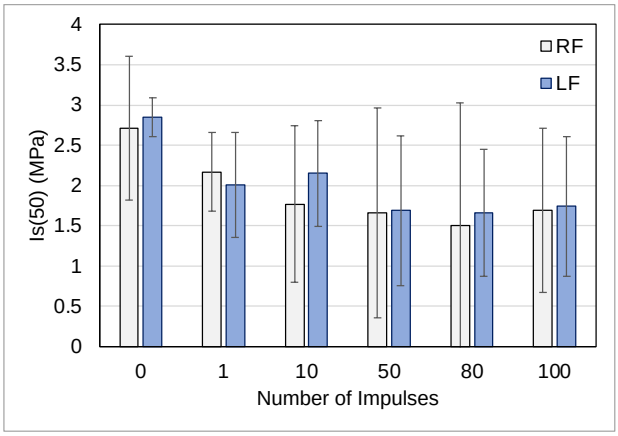

Fig. 2. Strength index of PLT before (0 impulses) and after each group of impulses from EDF.

For comparative purposes, Figure 3 presents the average of all EDF treated samples alongside those of the non-treated ones. Reduction of 33% were observed for the Reference concrete and 35% for the LF concrete. These results highlight the effectiveness of EDF in weakening concrete and facilitating the crushing process to obtain higher-quality recycled material. The 2 % difference between RF and LF concrete has so far indicated that LF does not have a major influence on crack propagation/strength at the particle size tested. However, further investigations need to be carried out in this regard to examine crack propagation and crack behaviour when impact-EDF crushing are combined to promote cement paste liberation. The influence of the proportion of LF in concrete can also play a major role. For this reason, further investigations must be conducted.

The observation that most samples fractured before reaching 10 impulses suggests that the energy applied traversed the samples too rapidly, offering minimal resistance from the concrete. A more detailed examination under lower energy conditions and further analytical methods could provide more insights into LF's role in strength decrease and crack propagation dynamics during EDF treatment.

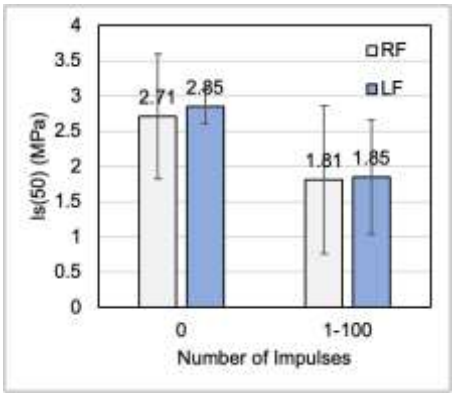

Fig. 3. Comparison of the average strength index of PLT before (0) and after (1-100) EDF impulses.

4 Conclusion

This study investigated two strategies for improving concrete recycling: the EDF as a treatment method and the incorporation of LF in the concrete composition.

After subjecting the concrete samples to EDF, reductions in 33% and 35% on the point load test index strength were observed for RF and LF concretes, respectively. Furthermore, larger numbers of electro impulses resulted in marginally more weakening.

The results indicate EDF as a promising treatment method for enhancing the concrete recycling process by facilitating the fragmentation of the material.

The effect of LF on concretes after EDF remains unclear. Further investigations employing a broader range of energy inputs and other analysis methods, such as SEM examinations of the fracture surfaces, may provide additional insights in this regard.

Overall, this study underscores the importance of continued research into innovative techniques and material compositions to advance sustainable concrete recycling practices.

Acknowledgements

The authors gratefully acknowledge: Fundação de Amparo à Pesquisa do Estado de São Paulo (Fapesp process 2023/ 08124-2) for scholarship and financial support; Technische Universität Dresden and Technische Universität Bergakademie Freiberg for the infrastructure and technical support. Special thanks go to Ms. S. Waida and the Institute for Ceramics, Refractories and Composites of Technische Universität Bergakademie Freiberg on providing materials and laboratory infrastructure for concrete production.

References

Bluhm, H., Frey, W., Giese, H., Hoppe, P., Schultheiss, C. & Strassner, R. (2000) Application of pulsed HV discharges to material fragmentation and recycling. IEEE Transactions on Dielectrics and Electrical Insulation, 7(5), 625–636. Available online: https://doi.org/10.1109/94.879358.

Das, S., Aguayo, M., Sant, G., Mobasher, B. & Neithalath, N. (2015) Fracture process zone and tensile behavior of blended binders containing limestone powder. Cement and Concrete Research, 73, 51–62. Available online: https://doi.org/10.1016/j.cemconres.2015.03.002.

John, V.M., Damineli, B.L., Quattrone, M. & Pileggi, R.G. (2018) Fillers in cementitious materials — Experience, recent advances and future potential. Cement and Concrete Research, 114, 65–78. Available online: https://doi.org/10.1016/j.cemconres.2017.09.013.

Kim, J. (2022) Influence of quality of recycled aggregates on the mechanical properties of recycled aggregate concretes: An overview. Construction and Building Materials, 328, 127071. Available online: https://doi.org/10.1016/j.conbuildmat.2022.127071.

Otto, Jens; Will, Frank; Hammel, Lukas; Lehmann, Franziska; Anders, Erik; Voigt, Matthias: Selektiver Rückbau mittels Elektro-Impuls-Verfahren: Grundlagenermittlung zur Adaption eines innovativen Abbruchverfahrens aus dem Bergbau (EIV) als neue Bautechnologie für selektiven Rückbau in sensiblen Bereichen. BBSR-Online-Publikation 30/2021, Bonn, Dezember 2021.

Raaz, V.: Charakterisierung der Gesteinsfestigkeit mit Hilfe eines modifizierten Punktlastversuches. In: Z. geol. Wiss. 30 (2002), Nr. 3, S. 213–226

Seifert, S.; Thome, V.; Karlstetter, C.: Elektrodynamische Fragmentierung – Eine Technologie zur effektiven Aufbereitung von Abfallströmen –, Aus: Recycling und Rohstoffe – Band 7, Karl J. Thomé-Kozmiensky, Daniel Goldmann. – Neuruppin: TK Verlag Karl Thomé-Kozmiensky, 2014, S. 431–438, ISBN 978-3-944310-09-1

Thuro, K.: Bohrbarkeit beim konventionellen Sprengvortrieb. Geologisch-felsmechanische Untersuchungen anhand sieben ausgewählter Tunnelprojekte. Münchner Geologische Hefte, Reihe B: Angewandte Geologie, B 1, 1–145, I–XII, 1996

Touzé, S., Bru, K., Ménard, Y., Weh, A. & Von der Weid, F. (2017) Electrical fragmentation applied to the recycling of concrete waste – Effect on aggregate liberation. International Journal of Mineral Processing, 158, 68–75. Available online: https://doi.org/10.1016/j.minpro.2016.11.009.

D2: Environmental performance of recycled aggregates from secondary sources: A case study on Norwegian site

Varun Gowda[1,*], *Kanishk Bhadani*[1], *Gauti Asbjörnsson*[1], *Hernan Mujica*[2], *and Magnus Evertsson*[1]

[1]Chalmers University of Technology, Sweden
[2] Velde Pukk AS, Norway

Abstract. Circular economy is a model of production and consumption to maximize material use repeatedly and extend the product life cycle. In the case of aggregates, this can be achieved by reducing virgin raw material consumption and waste generation. As well as by recycling aggregate materials from secondary sources such as excavation and construction and demolition (C&D) waste. Using recycled aggregates (RAs) from excavation and C&D waste can help preserve the natural environment and reduce the demand for landfill. Although it is economically feasible to recover aggregates from secondary sources, in many cases there are quality issues and lack of environmental information that inhibit their use. The focus of this study is to quantify the environmental impact of RAs recovered from excavation waste from a recycling facility in Norway. The facility is equipped with equipment such as screens, conveyors, and pumps that are specifically built to clean and separate the rock material from secondary sources to produce different fractions of aggregate products. The environmental impact is calculated by developing a process simulation-based Life Cycle Assessment (LCA). Results indicate that the environmental performance of the facility is sensitive to diesel and electricity consumption in conjunction with the operating capacity of the facility.

1. Introduction

The demand for aggregates in Europe is around 4.3 billion tonnes per year (UEPG, 2022a) out of which 93.1% (around 4.09 billion tonnes) is currently supplied by the aggregates extracted from natural sources (UEPG, 2022b) (See Fig 1). The exploitation of natural sources to satisfy such a demand has an impact on the environment, due to operations such as blasting, material handling, and production processes. The impact can be reduced by using recycled aggregates (RAs) from secondary sources such as excavation waste and construction and demolition (C&D) waste as it eliminates the environmental impact from the blasting of material. Using RAs reduces the extraction of natural resources and contributes to reducing the demand for landfilling of waste.

The waste from secondary sources that can be used as aggregates consists of concrete, sand, gravel, plastics, and even metals (Silva et al., 2014). To recover the aggregate products of certain size fractions, the waste material needs to be processed through a comminution circuit consisting of crushing, screening, and washing operations. Since these operations consume material and energy, the RAs produced from the recycling process will have a certain environmental impact. Also, there is an impact originating from the transportation of waste to recycling facilities and longer distances can result in an increased environmental impact in comparison to natural aggregates. (Atta & Bakhoum, 2024; Dias et al., 2021).

The consumption of aggregates in Norway was 91 million tonnes, out of which 3.4 million tonnes were sourced from secondary sources (UEPG, 2022b). This indicates that the construction sector in Norway is heavily dependent on naturally sourced aggregates. The reason for such a trend could be due to the availability of high-quality naturally sourced aggregates. Another

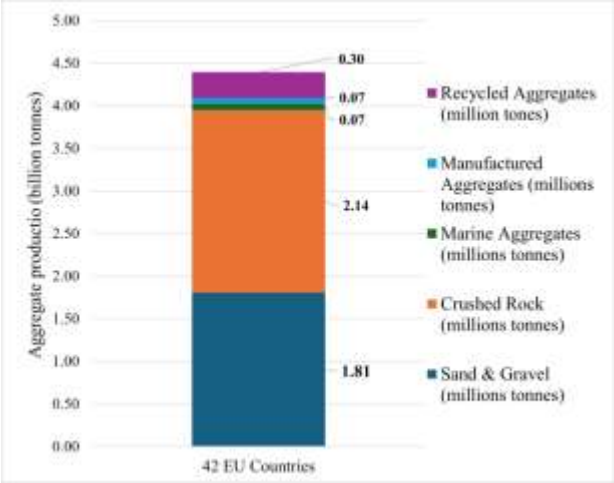

Fig. 4. Aggregate production in Europe (UEPG, 2022b)

reason is also due to challenges such as a lack of understanding of the environmental profile of RAs from excavation and C&D waste, economic and environmental costs due to transportation, lack of quality information, and lack of standards and specifications for the RAs (Silva et al., 2014).

This study focuses on one of the above-mentioned challenges i.e., addressing the lack of information on the environmental profile of RAs recovered from excavation waste. A case study is developed focusing on the recycling facility at Velde, a Norwegian aggregate producer. The recycling facility produces RAs of different size fractions such as 0/2 mm, 2/4 mm, 4/16 mm, 16/32 mm, 32/90 mm, and ultra-fine products <0.063 mm. To quantify the environmental profile of RAs, a process simulation-based Life Cycle Assessment (LCA) model is used. The model is developed on Plantsmith, an online simulation and environmental

* Corresponding author: varung@chalmers.se

platform designed for assessing the sustainability of aggregate products (Asbjörnsson et al., 2024). After configuring the process simulation, the data on different process inputs (i.e., consumables such as material and energy) and outputs (i.e., waste) of the recycling process are entered into the LCA module of Plantsmith to quantify the environmental impacts of different products from the recycling process. In addition, the study investigates the influence of transportation from the excavation site to the recycling facility on the overall environmental profile of RAs.

2. Method and Materials

2.1 Case Study – Process Layout

The recycling facility has a maximum operation capacity of processing 300 tonnes of waste materials per hour. In 2021, the facility produced 89053 tonnes of recycled aggregate products and operated for approximately 1500 hours. Fig 2 illustrates the recycling process layout that processes the excavation waste consisting of both contaminated and uncontaminated materials to produce recycled aggregate products of different size fractions.

The waste material consisting of aggregates, metals, sand, and plastics is fed to the recycling process using a wheel loader. Then the material is subjected to screening in dry screens S1 and S2, resulting in two fractions: <90 mm and >90mm. The fraction >90mm is crushed in a mobile jaw crusher and fed back into the circuit. To clean and produce the fine and coarse fractions of products, the <90 mm fraction is passed on a conveyor C3 with an in-built over-band magnet to remove any ferrous material. The <90 mm fraction is subjected to a separation process by passing it through dewatering and drain screens to remove any lightweight floating materials and separate the material stream into fine and coarse fractions. The coarse fraction is further processed in a dry screen S3 to produce coarse products 32/90 mm, 16/32 mm, 11/16 mm, and 4/11 mm. To produce a 4/16 mm product, a wheel loader is used to blend 11/16 mm and 4/16 mm. The fine fraction is passed over conveyor C4 with an in-built over-band magnet to remove the remaining ferrous material. Then the fine fraction is passed through dewatering and drain screens to produce a 2/4 mm product. The fines <2 mm from the dewatering screen DWS 5 are passed through hydrocyclones and a dewatering screen to produce 0/2 mm and ultrafine <0.063 mm products.

2.2 Process Simulation

The process simulation model is developed on Plantsmith by recreating the process layout shown in Fig 2. The model is configured by entering settings for the screens, pumps, and conveyors that represent the operating conditions at the recycling process facility during the reference year 2021. From process simulation, an automatic allocation matrix is generated based on mass and energy which is used for distinguishing the environmental profile for each product.

2.3 Life Cycle Assessment (LCA)

With respect to LCA, the following illustrates the different methodological choices and assumptions made during this study,

- **System boundary**: Cradle to Gate i.e., includes raw material acquisition, transportation to the recycling plant, and the recycling process. Activities such as transportation of RAs of different size fractions to customers have not been considered.
- **Declared unit**: 1 tonne of each recycled aggregate product.
- **Foreground data**: The data describing the recycling process is collected through site visits, sales data, and invoices. The water consumption is reported as zero even though there is water usage during the process. This is because the water used is sourced through an inbuilt rainwater harvesting system. Consumption of metals and lubricants, their quantities are both estimated.
- **Background data**: The data sets used for modelling consumables originate from the GaBi 2021 database and are representative of the geological region EU-28 and the electricity the geographical region for electricity is Nordics.
- **Allocation method**: Mass-based and Energy based allocation.
- **Impact assessment**: EN 15804+A2 reference package based on Environmental Footprint 3.0.

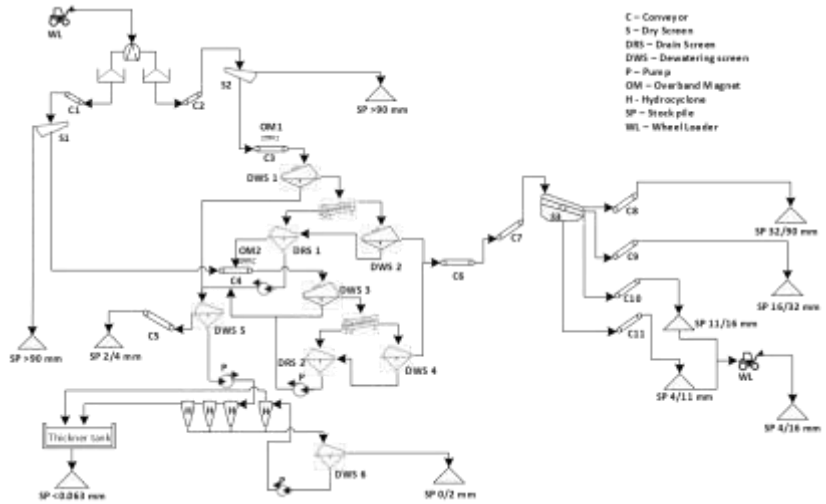

Fig. 5. Process layout of recycling facility

- **Reference year**: The production and operation data referring to the year 2021 is used for the assessment.
- **Assumptions**: The losses that occur during the recycling process are neglected. A steady-state model has been used to represent yearly production based on the annual data and localised fluctuation in production is neglected.

The foreground data concerning different process inputs (i.e., material and energy-based consumables) and outputs (i.e., waste) of the recycling process is shown in Table 1. This data is used in LCA for quantifying the environmental impacts per tonne of each product.

Table 6: Production, consumable, and waste data used in LCA.

Data	Value	Unit
Production		
<0.063 mm	22 213	tonne/year
0/2 mm	20 473	tonne/year
2/4 mm	10 287	tonne/year
4/16 mm	18 378	tonne/year
16/32 mm	10 676	tonne/year
32/90 mm	7 026	tonne/year
Consumables		
Diesel	Scenario 1 – 42 218 Scenario 2 – 26 503	l/year
Electricity	699397	kWh/year
Water	0	m3/year
Lubricants	280	l/year
Metals	8 390	kg/year
Rubber	725	kg/year
Plastics	440	kg/year
Wood	3 086	kg/year
Waste		
Non-Hazardous waste	4 856	kg/year
Hazardous waste	202	kg/year

To develop a process-simulation-based LCA, a systematic process has been followed as shown in Fig 3.

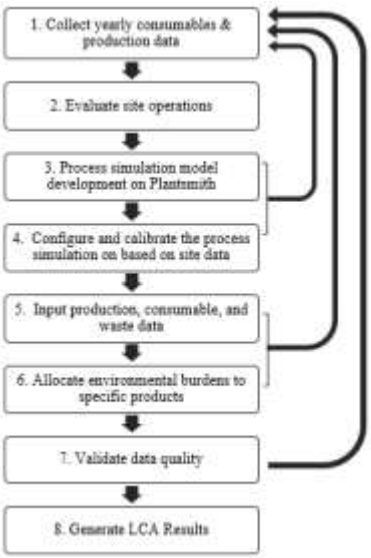

Fig. 6. Illustration of the systematic process followed during the assessment.

2.1. Scenario Analysis

In this study, two scenarios have been assessed to judge the influence of transportation on the overall environmental performance. Scenario 1 is based on the assumption that Velde is paid to treat the excavation waste, thus leading to the exclusion of impact from transportation. This means that the waste producer is transporting the material to Velde and thus excluding the material transport from the system boundary under assessment. Scenario 2 is based on the assumption that the excavation waste is purchased by Velde leading to the inclusion of the impact of the transportation from the excavation site to the recycling facility to the environmental profile of RAs produced from the recycling process.

In scenario 2, precise data on diesel consumption in transport to the site is unavailable. Hence, the consumption is diesel over a transportation distance of 20 km to the site is estimated with an assumption of 85% utilization factor for the truck with a maximum capacity of 40 tonnes. In both scenarios, the diesel consumption in the wheel loader used for feeding the waste material to the process and blending of the products 4/11 and 11/16 is estimated. The estimation is based on the number of hours that the wheel loader operates and hourly diesel consumption in liters per hour. The total diesel consumption for both scenarios is reported in Table 1.

3. Results

The LCA results are quantified and represented by following the European standard EN 15804+A2 (CEN, 2019). According to EN15804+A2, thirteen core impact categories need to be quantified and, for the scope of this study, the focus has been placed on for Global Warming Potential (GWP) - total impact category. The reason for focusing on the GWP–total is that the majority of environmental impact originates from diesel and electricity consumption which produces greenhouse gases during their production and consumption which contributes to global warming.

The results for GWP–total impact category for each product from both scenarios are shown in Fig 4. In the case of the GWP–total impact category, the majority of the impact originates during the production process in both scenarios. This is due to diesel consumed in wheel loaders during feeding of waste material to the recycling process and while blending products. In addition to diesel, electricity consumption in screens, hydrocyclones, and pumps is the second largest contributor to the overall environmental profile. The results show that the 32/90 mm product results in the highest environmental impact in comparison to other products. This is because the 32/90 product is drawn at the end of the circuit and is produced in smaller quantity in comparison to other products. This leads to higher electricity consumption to produce one tonne of 32/90 mm product. In both scenarios, as can be seen from Fig 4, the contribution of the production process (A3) to the overall environmental profile of each product remains the same.

From the results, three key insights can be drawn. Firstly, using simulation results and site-specific data helped in distinguishing the impact between different products which otherwise is difficult to manually allocate the impact to each product. Thus, indicating the need for combining the process simulation and LCA.

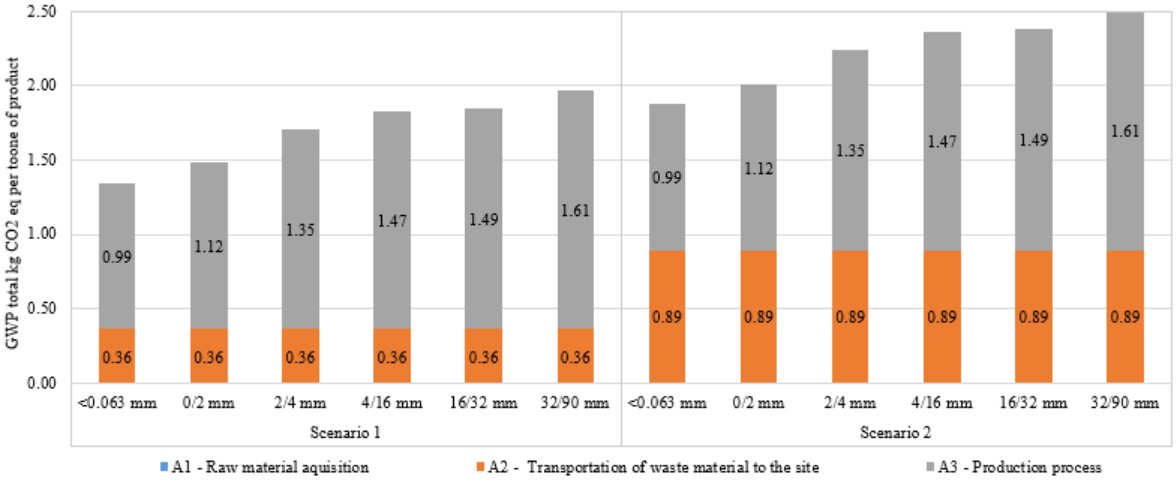

Fig. 7. Scenario 1 and Scenario 2 - Cradle to Gate results GWP-total in kg CO2 equivalent (eq) per tonne of each product

Secondly, the environmental profile of the products can be sensitive to the transportation distance between the waste generation site and the recycling facility (Atta & Bakhoum, 2024). Comparing scenarios 1 and 2, the contribution of transportation increases the GWP–total from 0.36 to 0.89 kg CO_2 eq due to the inclusion of diesel consumed during the transport of waste material to the recycling facility (See Fig 4). Longer distances can result in environmental impacts. For instance, if the transport distance is increased from 20 km to 70 km, the overall environmental profile of each product increases. In the case of a 32/90 mm product, the result for GWP total per tonne increases from 2.50 to 3.81 kg CO_2 eq. This entails a limitation on the transport distance to the facility before the products become environmentally poor in performance compared to virgin raw material extraction.

Lastly, the facility is built with an operation capacity of 300 tonnes of waste materials per hour and only processed about 60 tonnes per hour (based on the production data and production hours) which is 20 % of the installed capacity in the year 2021. This indicates that the facility is underutilised and leads to a higher impact per tonne of each product. Increasing the processing material amount can lead to reduced environmental impact per tonne since the electricity needed for processing will be lower per tonne.

4. Conclusion

The study focuses on quantifying the environmental profile of RAs produced from secondary sources such as excavation waste. To quantify the environmental profile of RAs, a process simulation-based LCA focusing on the recycling process at Velde has been developed on Plantsmith. Combining simulation and LCA facilitated distinguishing the environmental profile of the products.

Other key insights are the influence of the transport distance and operating capacity on the environmental performance of the facility. The environmental profile of the products is sensitive to the transportation distance between the waste generation site and the recycling facility. Lower operating capacity can lead to a higher environmental impact per tonne of each product.

Looking into the future, to achieve circularity, the use of recycled aggregate products in construction and infrastructure development needs to be increased. This in turn requires an increase in the number of recycling facilities in different locations. However, the environmental and economic influence of transportation distance can be a limiting factor in the feasibility of a recycling facility. Hence more studies focusing on quantifying the environmental performance of recycling processes are required.

5. Acknowledgments

This study has been performed under the project Rotate – Circular Ecological Essential & Critical Raw Materials, funded by EU Horizon Europe. This work has been performed within the Sustainable Production Initiative and the Production Area of Advance at Chalmers; this support is gratefully acknowledged.

6. References

Asbjörnsson, G., Sköld, A., Zougari, S., Yar, A.-G., Kamel, N., Turlur-Chabanon, S., Bhadani, K., Gowda, V., Lee, C., Hulthén, E., & Evertsson, M. (2024). Development of production and environmental platforms for the European aggregates and minerals industries. *Minerals Engineering*, *206*, 108519. https://doi.org/https://doi.org/10.1016/j.mineng.2023.108519

Atta, I., & Bakhoum, E. S. (2024). Environmental feasibility of recycling construction and demolition waste. *International Journal of Environmental Science and Technology*, *21*(3), 2675-2694. https://doi.org/10.1007/s13762-023-05036-y

CEN. (2019). EN 15804:2012+A2:2019 Sustainability of Construction Works - Environmental Product Declarations—Core Rules for the Product Category of Construction Products. In. Brussels, Belgium.

Dias, A. B., Pacheco, J. N., Silvestre, J. D., Martins, I. M., & de Brito, J. (2021). Environmental and economic life cycle assessment of recycled coarse aggregates: A Portuguese case study. *Materials*, *14*(18), 5452.

Silva, R. V., de Brito, J., & Dhir, R. K. (2014). Properties and composition of recycled aggregates from construction and demolition waste suitable for concrete production. *Construction and Building Materials*, *65*, 201-217. https://doi.org/https://doi.org/10.1016/j.conbuildmat.2014.04.117

UEPG. (2022a). *Current trends for the European aggregates sector*. Retrieved 14th February, 2024 from https://www.aggregates-europe.eu/facts-figures/trends/

UEPG. (2022b). *Each year, Aggregates Europe – UEPG collates best available aggregates production data from all over Europe*. Retrieved 4th March, 2024 from https://www.aggregates-europe.eu/facts-figures/figures/

D3: Crushed Concrete – Quality Issues of Concrete Recycling

Viktória Gável[1,*], *Márk* Kertész[1], and *Gábor* Radnai[1]

[1]CEMKUT Research & Development Ltd. for Cement Industry, Budapest, Hungary

Abstract. According to current practice, structural concrete is designed to last for decades, and when a concrete structure reaches the end of its life cycle, it must be recycled in accordance with the principle of the circular economic approach. The presented experimental results expand the knowledge required for the re-use of recycled concrete aggregates produced from crushed concrete in concrete and the re-use of recycled concrete fines as cement additive. They represent the importance of appropriate, selective preparation technology and the role played by the material characteristics of crushed concrete in the development of certain properties of concrete. Knowledge of these relationships is not only useful for concrete technologists, but also for recycling plants that process concrete waste, since the cooperation of these stakeholders is necessary in order for crushed concrete to become a valuable product in the construction industry, instead of ending up as waste.

1 Introduction

Concrete is actually an artificial stone. A composite material that traditionally consists of three components: aggregate (most often sanded gravel or crushed stone), cement and water. However, modern concretes can consist of up to five or six components. With admixtures, concrete additives (active or inert fine powders), fibers, etc. the properties of the concrete can be significantly influenced.

Due to its plasticity, many-sided usability and durability, concrete has become the most used construction material in the world today, and after water, concrete is the second most used material. Commonly used concrete is designed to last at least 50 years, but the lifetime of more serious structures (bridges, tunnels, valley closing dams, marine structures, etc.) can be hundreds of years.

When a building made of concrete reaches the end of its lifetime, it can be completely recycled with modern technologies available today. The processing of demolished concrete is very similar to that of natural aggregates: it is crushed and graded according to size. Based on its carefully examined characteristics, the field of use where these processed concrete wastes can be used as raw materials can be determined. By recycling, the accumulation of concrete waste can be avoided and natural raw material sources can be protected.

This approach, the idea of circular economy, waste reduction and more efficient use of resources is gaining more and more ground in the construction industry, especially in the building materials industry. Nowadays, there are no technical obstacles to the recycling of crushed concrete as aggregate and cement additive we have sufficient experience and appropriate technical regulations.

For decades, the construction industry has been striving for the largest possible proportion recycling of construction, demolition and construction material production waste, but this was not really successful for a long time because of the lack of guidance for concrete technologists that would have helped them to design the composition without a large number of concrete mixes.

Nowadays there are several technical guidelines and standards which prescribe the technical requirements of recycled concrete to use as concrete aggregate. European product standards for concrete admixtures also cover recycled aggregates from demolition waste and the Hungarian concrete standard also contains limitations concerning the maximal proportion of recycled aggregate used in ready-mixed concrete but the technical specifications cannot give exact composition of these concrete mixtures because of the differences of original properties of concrete and because of the long-term environmental effects.

Despite detailed technical regulations the rate of high-quality recycling of demolished concrete is still quite low. In Hungary the majority of demolished concrete is placed in road sub-basis and landfills. However, with the increase in construction industry output, the amount of concrete waste increases, which, in contrast to gravel quarries, is mostly generated in densely populated areas where the greatest need for concrete use occurs. One of the reasons for the low rate of high-quality recycling is the misconception that concrete made from recycled aggregates has worse characteristics than concrete with conventional aggregates. The experiments presented here prove that with proper care, regular raw material tests and precise composition planning, concrete made with recycled aggregate can have the same or even better properties than concrete made with conventional additives. And if the natural sand and gravel additive with high transport costs can be replaced at least in part, then the cost of concrete production can be reduced in addition to protecting the environment.

* Corresponding author: gavelv@cemkut.hu

However, there is another problem, the recycling of the fine (< 4 mm) part of crushed concrete, for which EN 197-6:2023 Cement Part 6: Cement with recycled building materials non-harmonized cement product standard (published in 2023) offers an option. This standard allows the use of the fine fraction of crushed recycled concrete as a cement additive. Initial experiments aimed at determining the composition and technical parameters of cements containing concrete fines with appropriate quality and application technical properties are also in progress.

2 Experimental materials and methods

The test materials were crushed road concrete made with basalt, concrete paving stones and formwork elements produced with a laboratory jaw crusher and natural aggregates from eight Hungarian gravel quarries, as well as the concretes made with them. In accordance with the technical specifications, only the part of the crushed concrete waste over 4 mm was used for the tests, classified into 4/8 and 8/16 fractions and 50 m/m% replacing the natural gravel fraction.

The following tests were performed on the crushed concrete and natural gravel fractions:

- particle density and water absorption in accordance with MSZ EN 1097-6 standard;
- resistance to wear (micro-Deval test) in accordance with MSZ EN 1097-1 standard;
- resistance to fragmentation (Los Angeles test) in accordance with MSZ EN 1097-2 standard;
- resistance to freezing and thawing in accordance with MSZ EN 1367-1 standard.

The test results of crushed concrete aggregates were compared with the average of the test results of natural gravel aggregates from eight different Hungarian quarries.

Experimental concrete mixtures were prepared with crushed concrete aggregates from different types of concrete elements, which consisted of 50 m/m% natural gravel and 50 m/m% crushed concrete per fraction of aggregate over 4 mm. The experimental concrete mixes were designed to have almost the same consistency (flow class F2), which was achieved by changing the amount of plasticizing admixture while maintaining the water/cement ratio of v/c = 0.55.

The composition of the experimental concrete mixtures was as follows:

- 325 kg of CEM II/A-S 42.5 N type Portland-slag cement
- 179 kg of water
- 896 kg of 0/4 aggregate fraction
- 573 kg of 4/8 aggregate fraction
- 386 kg of 8/16 aggregate fraction
- 50-100-110-120 g of plasticizing concrete admixture

Cube test specimens with an edge length of 150 mm were prepared from the experimental concrete mixtures for compressive strength and freeze-thaw resistance tests in accordance with the requirements of the relevant standards. The compressive strength test specimens were stored under water at 20°C until they were 28 days old, and the freeze-thaw resistance test specimens were also stored under water at 20°C for 7 days, then in a climate chamber until the beginning of the test.

The compressive strength was tested according to MSZ EN 12390-3 standard. The freeze-thaw with de-icing salts resistance test was carried out according to the reference method of MSZ CEN/TS 12390-9 standard, which is called scaling.

3 Some experimental results

The differences between the three different types of concrete elements (road concrete, paving stones and formwork elements) were already evident during crushing and classification. The yield of fractions produced in the same way depends significantly on the composition, strength, and porosity of the original concrete. The profitability of recycling mostly depends on the energy spent on crushing and the yield ratio of the 0/4 fraction to be further treated, which in this case was the highest for the formwork stone (~ 35 m/m%) and the lowest for the road concrete (~ 20 m/m%).

Of course, in the case of concrete with a heterogeneous composition, such as road concrete with crushed basalt aggregate, the crushed concrete fraction above 4 mm contained a much higher proportion of basalt fraction 11/22 than in the original concrete aggregate, and in addition, the different crushing technologies result different grain shapes, which effect the properties of both fresh and hardened concrete.

3.1 Results of aggregates

As expected, crushed concrete aggregate has much higher water absorption (Figure 1) than natural gravel, which is mostly consists of low-porosity quartz grains and fragments of volcanic rocks.

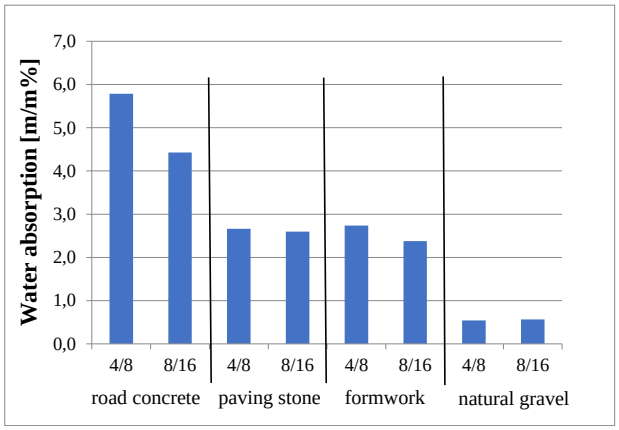

Fig. 1. Water absorption of different crushed concrete and natural gravel aggregate fractions

In the case of using crushed, recycled concrete as an aggregate, due to its significantly higher water absorption, in order to achieve the planned consistency

of the concrete, it may be necessary to use a higher w/c ratio or to use a larger amount of plasticizing admixture. The resistance to wear and fragmentation of the crushed, recycled concrete aggregate was worse than that of the harder natural quartz gravel (Figure 2).

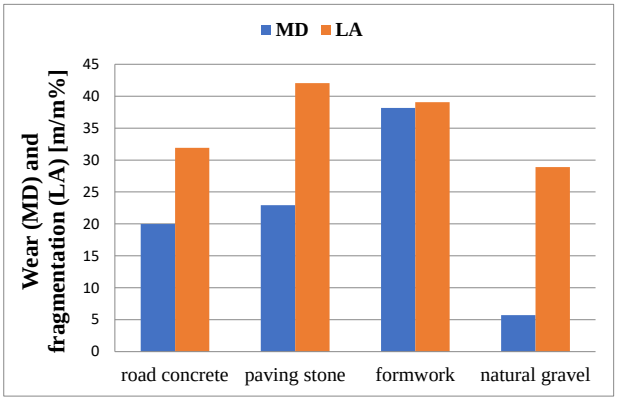

Fig. 2. Water absorption of different crushed concrete and natural gravel aggregate fractions

As a result, the recycled aggregates are not suitable for use as the wear layer of roads and paving and their use is also not recommended for making high-strength concrete.
Figure 3 shows the structure of recycled concrete aggregates.

a)

b)

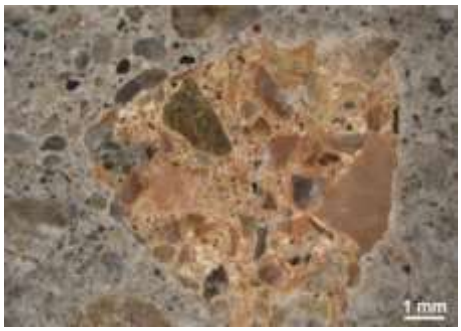

c)

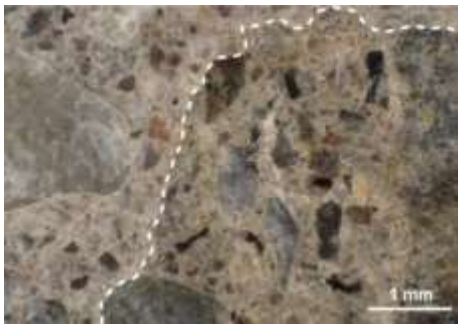

Fig. 3. Microscopic images of concretes made with different recycled concrete aggregates
a) road concrete, b) paving stone, c) formwork element

Compared to natural gravel, crushed concrete particles come into contact with the cement paste on a larger surface area. It must be taken into account when calculating the necessary paste content of concrete. During crushing, the concrete waste broke along the cracks and weak joints, cracks inside the grains were not typical.

3.2 Results of concretes

Figure 4 shows the average compressive strength at the age of 28 days of experimental concretes made with a gravel fraction and different types of crushed concrete aggregates (50-50 m/m%), and the reference concrete made with only natural gravel aggregates.

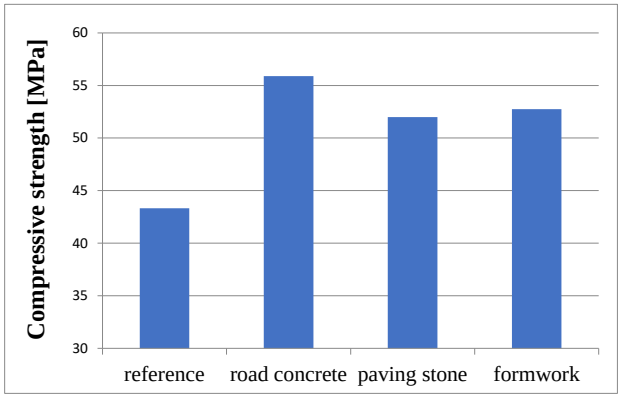

Fig. 4. Compressive strength of the experimental concretes made with 50 m/m% recycled concrete aggregate and the reference concrete without recycled concrete aggregate

The compressive strength of all experimental concretes was higher than that of the reference concrete, which, by the way, contained only natural gravel aggregate with higher particle strength based on its resistance to wear and fragmentation. In the case of the test specimens made with crushed concrete containing basalt, we measured a significant strength increase of almost 30% compared to the reference concrete. These results indicate that the size of the surface of the aggregate binding to the cement paste plays an important role in the development of the compressive strength of concrete.
Figure 5 shows the results of the freeze-thaw test (the specific amount of material scaled from the surface

exposed to the salt solution during freezing) of the experimental concretes made using different types of crushed concrete aggregates (50 m/m% in the gravel fraction) and the reference concrete after 7, 14, 21 and 28 freeze-thaw cycles (days).

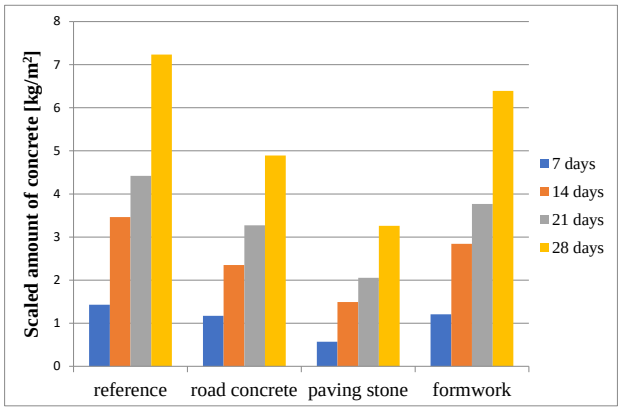

Fig. 5. Freeze-thaw resistance of the experimental concretes made with 50 m/m% recycled concrete aggregate and the reference concrete without recycled concrete aggregate

Air entraining admixture, which is required for freeze-thaw resistant concrete, was not added to the concrete mixtures, so it was expected that none of the concretes would meet the requirements of the standards. However, it is clear from the test results that the crushed road concrete and paving stones (which were originally designed to be freeze-thaw resistant) significantly improved the freeze-thaw resistance of the experimental concretes made with them compared to the reference.

4 Conclusion

Our test results indicate that, in addition to the physical characteristics of aggregates laid down in the technical specifications, it is advisable to carry out additional raw material tests before using recycled concrete as aggregate. These characteristics fundamentally influence the properties of fresh and hardened concrete, and by knowing them, it is possible to design a concrete mixture composition that can have more favourable properties than concrete that does not contain recycled concrete.

These results also draw attention to the importance of knowledge of the types of recycled concrete aggregate (crushed concrete) and of original concrete waste constituents and their limitations before use.

Satisfying these technical requirements is the task of the producers of recycled concrete aggregates, who, when choosing the required crushing machine, must pay attention to the fact that different crushing technologies result different grain shapes, which significantly affects the properties of both fresh and hardened concrete. In addition, efforts must currently be made to minimize the amount of the 0/4 fraction that cannot be used as a concrete filler. In this regard, it should be noted that the new European cement product standard published in August 2023 (EN 197-6:2023 Cement Part 6: Cement with recycled building materials) offers the opportunity to use the fine part of recycled concrete waste (0/4 fraction) as a cement additive. However, we cannot expect the mass appearance of these new types of cements in the near future, because as far as we know, suitable concrete fines are not yet available in industrial quantities, and the experiments establishing the basis for the production of these cements and the concrete technology tests that facilitate their practical use are still in their initial stages.

D4: Vibratory Screening – Practical Challenges and Production Losses

Kanishk Bhadani [1,*], *Gauti* Asbjörnsson [1] *and Magnus* Evertsson [1]

[1]Department of Industrial and Materials Science. Chalmers University of Technology, Gothenburg, Sweden

Abstract. Vibratory screening is a crucial process in crushing plants, primarily aimed at separating different sizes of crushed materials. The production performance of the crushing circuit is often highly dependent on the vibratory screen performance. Despite understanding vibratory screening performance, multiple practical application at the industrial scale suffers production losses due to low-efficiency vibratory screen operation. The following paper provides an account of various practical issues encountered by vibratory screens at crushing plants for both aggregates and minerals processing plants. The practical issues originate from different sources such as physical plant construction, operational decisions by the plant, control strategies in process operation, and maintenance choices. Multiple data from different site surveys are used to demonstrate the lack of control of the screening process. The practical challenges list provides scope for future improvements in the screening process and careful consideration required by the companies providing screening solutions.

1 INTRODUCTION

Vibrating screens are essential for material separation in industries like mining, minerals, and aggregates processing, especially for coarse particle size range. Vibratory screening is either applied in intermediate steps between size reduction equipment (crushers) or applied as the last step of the circuit controlling the final products. In an intermediate step, a vibratory screen separates the oversized material for recirculation while undersized products are transported to the next stage. Screens applied at the last stage control the overall production throughput of the circuit and product quality (in the case of aggregate production). (Soldinger, 2002; Wills and Finch, 2015)

During the design phase of a crushing plant, screens are often dimensioned according to the estimated loading condition of the circuit. Different manufacturers provide guidelines for screening selection choices. One of the central aspects of the selection process is to design/select screens to obtain an optimal range of screening efficiency. According to Napier-Munn et al. (1996), the screening efficiency is usually between 92-95% at the design phase, where the screening efficiency is defined as the percentage of undersized material in the feed that passes through the screen. The screening efficiency is a function of various phenomena such as stratification and passage of the material which is influenced by the conditioning of the screen (Soldinger, 2002). The conditioning of the screen constitutes of multiple factors related to the geometrical design (e.g., screen length, width, aperture, open area, etc.), rated capacity, screening media (e.g., steel wire mesh, polyurethane panel), feed size distribution and feed rates in the circuit.

Figure 1 shows a generic graph for screening efficiency with respect to the rated capacity. Based on the VSMA standard (CIMA, 1996), the selection of screening size depends on the loading requirements to achieve the optimum condition of high-efficiency screening.

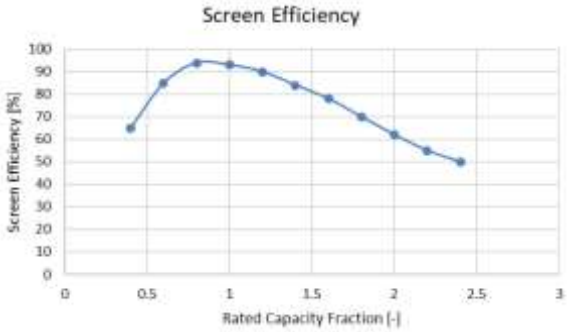

Figure 8. Generic screening efficiency.

Despite selecting the screen based on different capacity calculations at the design phase of the circuit, the practical operation of the screen often lacks the maintenance of the conditioning of high-performing screening (misses the target performance region). The practical issues originate from multiple sources such as physical plant construction, operational decisions by the plant, control strategies in process operation, and maintenance choices. These issues are encountered during the operation phase and are often limited to fixing the issue as it involves retrofitting existing engineering design. The paper presents a brief account of practical issues encountered in screen operation. The issues were observed on different industrial surveys carried out at

* Corresponding author: kanishk@chalmers.se

both aggregates and minerals processing operations. The paper focuses on the pragmatic aspects of operating the screens and can influence future comminution circuit requirements and philosophical operation strategies.

2 Practical Challenges with Screening

Screens are important production units in crushing plants to classify the aggregates into different products. Even if the screens are used to maintain a certain product quality, they are often not a focus in process improvement work. These are considered to be passive and robust equipment that leads to screens often not operating at their intended capacities.

One key aspect of screening performance is screening efficiency, i.e., the screens' ability to separate the flow into two different size classes. Eq. 1 is used for quantifying the screening efficiency (E), f refers to the fraction of material above the cut-point in the feed and c refers to the fraction of material above the cut-point in the overflow product. The formula applied for representing the recovery of the fine material is 100%, meaning the underflow of the screen does not have coarse material. (Wills and Finch, 2015)

$$E = \frac{c - f}{c(1 - f)} \tag{1}$$

The following sections briefly describe practical issues found at multiple site surveys related to screening operations which can potentially increase process performance.

2.1 Screen Feeding Issues

Feeding the screen improperly reduces the fine material probability of passing through the screen. In many cases, there is a reduction in utilized open area of the screen deck where portions of the deck, often the upper corners, are not covered by the material stream. An uneven load onto the deck or improper feeding direction can lead to excessive wear and frequent panel replacements on certain hotspots as demonstrated in Figure 2. The perpendicular feeding of the stream caused excessive wear on one side of the screen where the material hit the panels directly instead of a rock box. The wear of the lower deck of the screen was generally more even with more wear further down the screen, as shown in the frequency of replacement of screen panels in Figure 3.

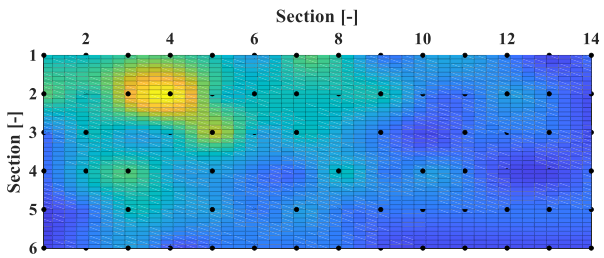

Figure 9. Heat map of the wear on the upper screen deck from panel replacements.

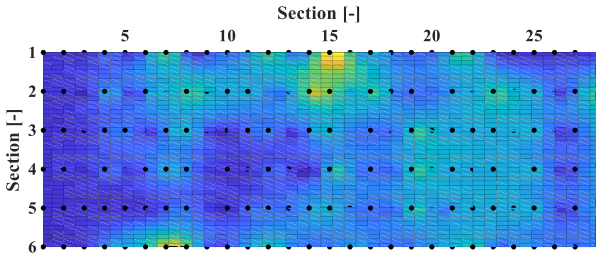

Figure 10. Heat map of the wear on the lower screen deck from panel replacements

2.2 Screen Blinding and Clogging

Another significant reason for the reduced open area is due to blockage of the screen apertures. Larger particles that are in a similar size range as the aperture (near-size particles) will risk getting lodged in apertures, also called pegging. For smaller apertures similar phenomena will happen but due to elevated moisture and the buildup of fines block the aperture. This may, be referred to as blinding. There are several solutions that can be used and most utilize either more open area or more flexible screen panels to minimize pegging and material buildup. However, regular observation is often neglected since no active process alarms are implemented to indicate a risk of blockage.

Figure 4 shows an example of a screen clogging issue found in the aggregate production for fine materials. The screening media was steel wire mesh and the environmental condition contained elevated moisture levels. In this case, the screen was manually cleaned by the operator which resulted in loss of production operation time.

Figure 11. Clogging of a lower screen deck.

Blinding of parts of the screen deck is also performed by operational decisions to prevent frequent maintenance issues. Figure 5 shows the screen panel's active blinding due to the misaligned feeding of the screen and to avoid excessive wear due to non-distributed feeding. The top deck is the relief deck while the bottom deck controls the final product of the circuit. Almost 40% of the open area for the screening in the bottom deck was not utilized.

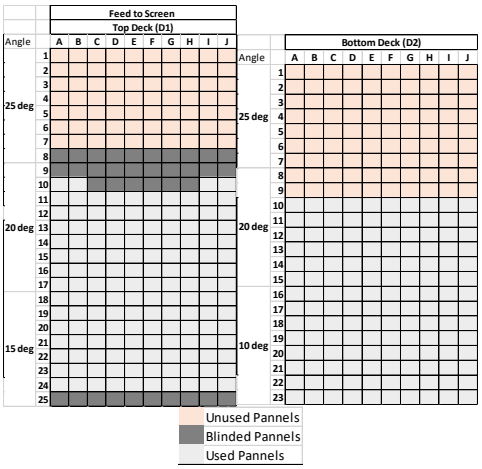

Figure 12. Active blinding of the screen due to wear and maintenance issues (Bhadani et al., 2021).

2.3 Screen Construction Design

Merging or diverting the material streams is usually not done without some complications. In a large volume minerals processing plant, the product from the crusher was fed to a screen bin where it was supposed to be split evenly between two identical screens. Due to several issues that originate from segregation in the incoming fed, the material build-up within the bin and the positions of the inlet/outlets, the circuit experiences an uneven balance for the loading of the screen to maintain a stable level in the bin.

Figure 6 shows the material distribution on the top deck of the two parallel screen operations. Figure 7 shows the estimated undersize flow rate of the parallel screens when the feed rate was varied. The two screens are loaded differently resulting in different performance levels. On top of that, since the feed to the screen was positioned perpendicular to the feed to the bin, there was also a clear difference in size distribution fed to the screens.

Figure 13. Uneven load on the parallel screens – unbalanced screen and balanced screen.

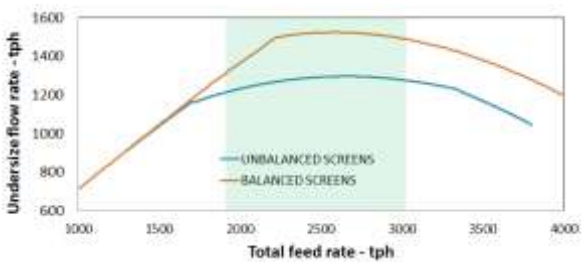

Figure 14. Undersize flow rate performance of two parallel screens with varying feed rates (Powell et al., 2012).

According to VSMA (CIMA, 1996), the amount of material below the passing size and the amount below half of the passing size are key variables to determine the required screen surface area. Increasing the percentage below the passing size increases the required screening area. While on the other hand increasing the percentage below half the passing will reduce the needed screen surface area.

Figure 8 shows an example of a construction of a conveyor feeding the bins of three parallel screens. Due to the angle of the drop of material from the conveyor to the bin together with the trouser leg construction, the material was found to be highly segregated in the bins. This further resulted in the three parallel screens receiving different feed materials both in PSD (due to segregation) as well as in capacity (due to the differential filling rate of the bin).

Figure 15. Example of parallel bin and screen placements – segregated material in bins due to the positioning of the conveyor drop angle.

2.4 Process Operation Issues – Crusher Dependency and Interlocks

In a crushing circuit, the objective of the control system is to protect and maintain a stable operation. In a closed circuit or a circuit with a parallel stream, the crusher and screen interdependencies become vital. For a closed-circuit configuration, the circuit yield is not only determined by the crusher but the performance of the screen as well. Operating the crusher at low CSS results in more size reduction and lower capacity, while larger CSS results in less size reduction and higher capacity. Usually, this happens if the crusher is not adjusted due to wear.

In a controlled experiment in aggregate production, the screening performance was evaluated over the crusher operating range, with two screens operating in a sequence (Bhadani et al., 2024). The calculated efficiency for each screen and deck at different loading conditions is illustrated in Table 1. At a higher loading, the first screen (S290) upper deck starts to lose efficiency and recirculate more finished product back to the crusher. For the lower rate, the screening performance is close to optimum. For the second screen (S330), the screening efficiency on the top deck was close to optimum, while the lower decks experienced overloading and clogging issues.

Table 1. Calculated screening efficiency for different screen decks for two consecutive screens (S290 and S330) subjected to two load levels (Bhadani et al., 2024).

S290	**Deck 1**	**Deck 2**	**Deck 3**
Low	0.952	0.948	0.945
High	0.716	0.930	0.950
S330	**Deck 1**	**Deck 2**	**Deck 3**
Low	0.899	0.833	0.582
High	0.919	0.702	0.728

Another aspect to consider in the parallel stream (multiple parallel crusher operation) is the control of the circuit. The control system aims to protect and stabilise the circuit. However, in many cases, the control system tries to maintain a fixed level in a crusher for assumed better performance (choke feed condition in the crusher). When levels get too high or too low in bins the interlocks start disrupting the flow causing the screen to operate at two distinct operating conditions. Often a high load case and a low load case. This could easily be a factor of two, given that the two streams have a similar-sized crusher. Figure 9 shows the partition of the screen for the two load cases. In this minerals processing plant, the circuit operated with either two or three crushers creating low load and high load conditions for the screen, respectively. At a higher loading, the screen starts to lose significant efficiency with more fines and near-size particles being carried over to the coarse product.

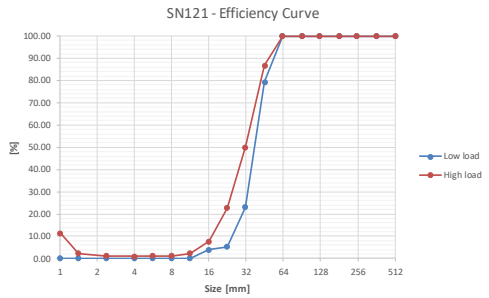

Figure 16. Partition curves for different operating conditions.

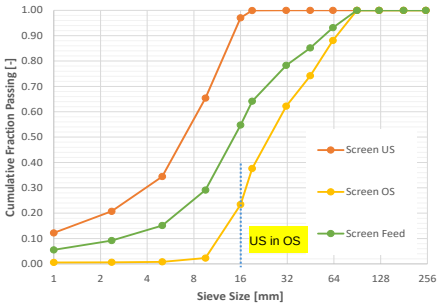

Figure 17. Belt-cut sampling of screens for variable feed scenario (combined feed and product of three parallel screens).

In another process operation of a closed loop circuit with 5 parallel crushers (3 fed from the oversize of the screen), the screen feeder frequency was actively controlled to maintain the bin levels before the crushers. This led to screen operation under variable feed rate (20% to 80%). A snapshot belt-cut sampling of the screen feed and products is shown in Figure 10. It was found that approx. 25% (at a 16 mm cut-point) of the fine material was recirculated back to the three crushers. The calculated theoretical improvement in the screening efficiency by 10% could add approximately 67 tph to the final product stockpile.

3 Discussion

One of the direct impacts of solving certain practical issues will directly result in increasing the production of the circuit. The issues highlighted in the paper represent mostly the engineering choices, physical plant construction, operational and maintenance decisions by the plant, and control strategies in process operation. Issues such as segregation of the material are possible to solve by engineering retrofitting which can further reduce uneven wear on the screens.

It can be of interest to question what happens if the process operation philosophy is changed to maintain a consistent feed to the screen. One impact will be that the crusher will not operate at the choke feed position and require more on/off if the circuit is in a closed loop. Another alternative is to design a circuit with de-coupled and controllable screens with an open loop circuit. Further, the screen can be built with more active control and sensors to steer the operation.

The critical question to be asked here is if the future comminution circuit considers active control of the screening process for manoeuvring productivity of the circuit. Today the screening process is considered as passive equipment while the operation requires it to be actively controlled for increasing productivity. There is room for innovation for future screening equipment development such as active control, sensor alert systems, and continuous condition monitoring.

References

Bhadani, K., Asbjörnsson, G., Bepswa, P., Mainza, A., Andrew, E., Philipo, J., Zulu, N., Anyimadu, A., Hulthén, E., Evertsson, M., 2021. Experimental and simulation-driven improvements for coarse comminution circuit using Plantsmith process simulator - A case study of Geita Gold Mine, Tanzania, In *Conference in Minerals Engineering (Konferens i mineralteknik)*, Luleå, Sweden.

Bhadani, K., Asbjörnsson, G., Hofling, K., Hulthén, E., Evertsson, M., Application of design of experiments (DoE) in evaluating crushing-screening performance for aggregates production. Minerals Engineering, 2024, **209**, 108616.

CIMA, 1996. VSMA Vibrating Screen Handbook by Construction Industry Manufacturers Association, Milwaukee, USA.

Napier-Munn, T.J., Morrell, S., Morrison, R.D., Kojovic, T., *Mineral Comminution Circuits: Their Operation and Optimisation*. 1996, Julius Kruttschnitt Mineral Research Centre, The University of Queensland, Indooroopilly, Qld Australia.

Powell, M.S., Hilden, M.M., Evertsson, C.M., Asbjörnsson, G., Benzer, A.H., Mainza, A.N., Tavares, L.M., Davis, B., Plint, N., Rule, C., 2012. Optimisation opportunities for HPGR circuits, In *11th AusIMM Mill Operators' Conference*.

Soldinger, M., 2002. Screening of crushed rock material, In *Machine and Vehicle Systems*. Chalmers University of Technology, Gothenburg.

Wills, B.A., Finch, J., *Wills' mineral processing technology: an introduction to the practical aspects of ore treatment and mineral recovery*. 2015, Butterworth-Heinemann.

D5: A grindability comparison between bio- and mineral calcium carbonate

Diler Katircioglu Bayel[1,*]

[1] *Nigde Omer Halisdemir University, Mining Engineering Department, 51240 Nigde, Turkey*

Abstract. One of the most widely used inorganic fillers is calcium carbonate ($CaCO_3$). This is due to its low cost, high capacity to improve mechanical properties such as hardness and good particle dispersion in a polymeric matrix. The primary mineral content in eggshell is calcium carbonate, which has become a serious solid waste problem due to excessive consumption. The rapidly developing industrialization process in the world has led individuals to consume more, and as a result, the amount of waste produced has increased very rapidly. It is possible to use these wastes as bio-fillers as it has a composition similar to conventional calcium carbonate. On the other hand, the use of filler reduces the price of the product and increases some of the physical and mechanical properties of composite materials. The main purpose of this study is to reveal the differences in the grindability of bio- and mineral calcium carbonate down to submicron sizes and to compare the efficiency of grinding aids.

1 Introduction

Calcium carbonate ($CaCO_3$) due to its low cost, high capacity to improve mechanical properties such as hardness and good particle dispersion in a polymeric matrix is widely used as a filler and pigment material not only in paper, plastics, rubbers, paints, and inks but also in pharmaceutics, cosmetics, construction materials, and asphalts and as a nutritional supplement in animal foods. While our natural resources are decreasing day by day, rapid industrialization in the world has led individuals to consume more and as a result, the amount of waste produced has increased very rapidly. For this reason, most of the bio-fillers used today are residues from primary transformation industries. It is possible to gather waste materials under two groups: industrial by-products and agro-based wastes. Eggshell is one of the agro-based wastes, and its primary mineral content is calcium carbonate, which has turned into a significant solid waste problem due to excessive consumption (Sathiparan, 2021). Managing large amounts of waste from the food processing industry from excessive consumption is a challenging problem. The sustainability of the circular economy depends on the 3R principles (reduce, reuse and recycle) defined by Russell and Burch in 1959. In this way, waste can be turned into valuable and useful resources, improving both sustainable development and adequate waste management strategies.

The use of submicron-sized products increases the desired physical properties of the product, compared to the use of micronized products, due to reasons such as the greater surface area of the submicron products and a more homogeneous particle size distribution compared to micronized products (Katircioglu-Bayel, 2023).

Maintaining the quality and health of the environment requires looking for an effective way to manage waste appropriately. The main aim of the current experimental research was to investigate the effective role of two grinding aids from two chemical classes and the differences in the grindability of bio and mineral calcium carbonate to submicron sizes.

2 Materials and methods

2.1 Material

The mineral calcite ($CaCO_3$) used in the experiments was obtained from Mertaş Company (Niğde, Turkey) The eggshell used in the experiments was obtained from various food industries and restaurants and cleaned from the residues by keeping it in a 4% NaOH solution for 24 hours after pre-washing. Afterward, the eggshell, which was cleaned from its residues, was dried in an oven for 12 hours at 103±2 °C until it reached a humidity level of 1-3%. In order to compare with the mineral calcium carbonate, it was coarsely ground in a laboratory-scale ball mill to equalize the particle size. Tables 1 and 2 present the chemical properties of the eggshell and mineral calcite samples determined by XRF.

Table 1. Chemical properties of eggshell powders used in experimental studies (wt.%).

MgO	CaO	Fe_2O_3	Al_2O_3	P_2O_5	Na_2O
0.521	51.7	0.011	1.2	0.216	0.091

* Corresponding author: dkatircioglu@ohu.edu.tr

Table 2. The chemical composition of mineral calcite measured by X-ray fluorescence analysis (wt.%)

MgO	CaO	Fe_2O_3	Al_2O_3	P_2O_5	Na_2O
0.43	54.25	0.1	0.2	0.02	0.11

Fig. 1 demonstrates the particle size distribution of the eggshell feed and mineral calcium carbonate.

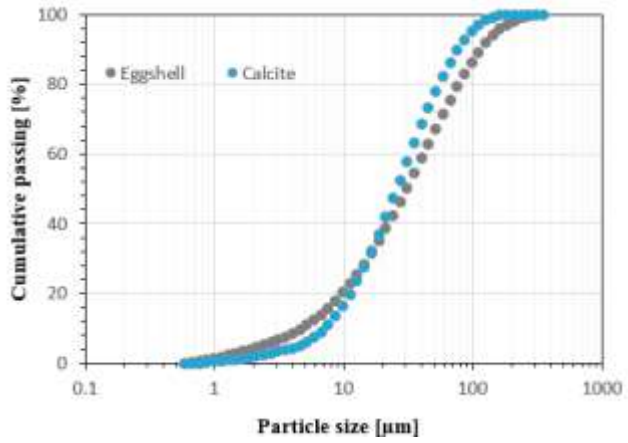

Fig. 1. Particle Size Distribution of the Eggshell and Calcite Feed.

2.2 Method

In this study, firstly, coarse grinding tests of eggshells were carried out in a laboratory scale ball mill, and experiments were carried out in a vertical stirred ball mill to determine the effects of grinding aids in two different groups on the fracture characteristics of the samples. The laboratory scale ball mill has internal dimensions of 20×20 cm and a volume of 6283 cm^3 and is made of stainless steel. Its speed is equipped with a revolution counter and it is operated at 60 rpm. After each grinding test, grinding media and product were sieved using a Retsch AS200 analytical sieve shaker. Table 3 presents the experimental conditions.

The micronized grinding of eggshell waste and calcite samples were carried out in a Standard–01 model batch-type vertical stirred media mill produced by Union Process (USA). High density (6000 kg/m^3) yttria-stabilized zirconia (ZrO_2) grinding media (chemical composition: 93% ZrO_2, 5% Y_2O_3, and 2% others) purchased from Cenotec Co., Ltd., Korea, were used for the submicron grinding experiments.

Table 3. Summary of the experimental conditions in a lab--scale conventional ball mill.

Parameters	Experimental conditions
Media filling ratio (%)	35
Powder filling ratio	0.125
Grinding time (min)	20
Mill speed (% of Nc)	60
Media size distribution of 40-32-20-12 mm (%)	10-10-40-40

Table 4 contains the experimental conditions in the vertical stirred media mill.

Table 4. Summary of the experimental conditions in the vertical stirred media mill.

Parameters	Experimental conditions
Media filling ratio (%)	70
Powder filling ratio	0.14
Grinding time (min)	75
Mill speed (rpm)	600
Media size distribution of 3- 5 mm (%)	50-50

Triethanolamine (TEA) and ethanol (EtOH) (both Sigma Aldrich) were used as grinding aids in the current study. The effects of the type and dosage (0, 0.25, 0.5, and 1 wt. %) of grinding aids on grinding efficiency were investigated.

3 Results and Discussion

3.1 Product Fineness

In dry grinding experiments, the effect of van der Waals attractive forces between molecules increases with the increased number of fine particles, and accordingly, agglomeration increases and causes in-mill flow characteristics to change. Since sufficient mixing cannot be provided in the mill as a result of this agglomeration, the product milled by the cushioning effect of particles cannot ensure sufficient contact with the grinding medium (Orumwense and Forssberg, 1992).

Suitable grinding aids should be used to eliminate or reduce this effect caused by agglomeration. To evaluate the grinding performance of the grinding aids, the findings of the experiments without grinding aids were taken as a reference. The findings are presented as a function of the d_{50} size in Fig. 2

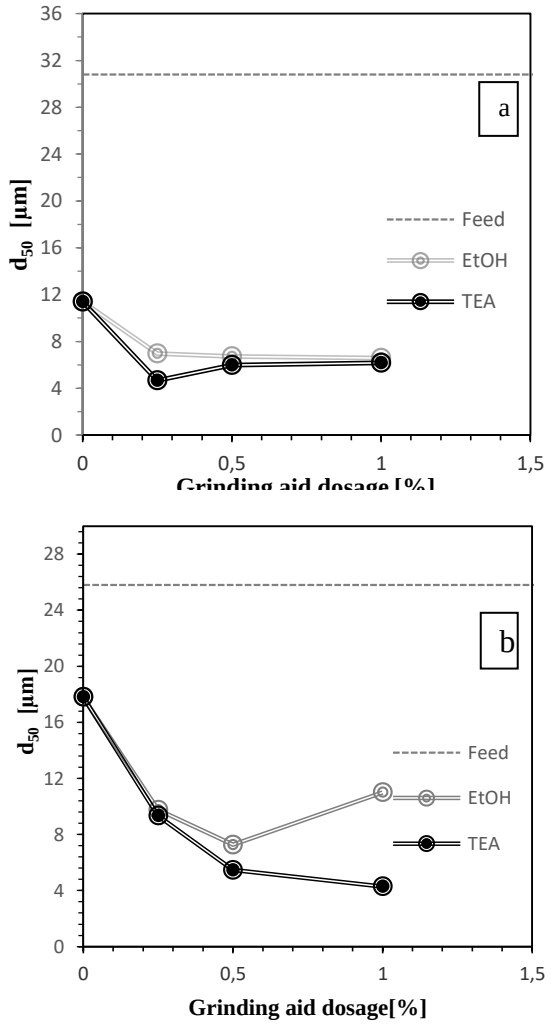

Fig. 2. The Effect of Grinding Aid Type and Dosage on d_{50} Size: (a) Eggshell Powder; (b) Calcite.

The grinding results showed that all grinding aids positively affected grinding performance compared to the no-aid condition. Upon examining the results of the experiments with TEA for eggshell, d_{50} particle size increased with the increased amount of grinding aid after a 0.25% dosage. But, for calcite, as the dosage of TEA increases, d_{50} decreases depending on the dosage. When grinding aids are used at appropriate dosages, the product size decreases quickly (Choi and Choi, 2002). The best product fineness value was acquired with TEA. Within this context, TEA is a polar compound tending to be adsorbed on a solid surface by polar functional groups. In addition, it is also a triol, which is both a tertiary amine and a molecule with three alcohol groups. These polar functional groups attached to the surface envelop the surface, preventing the fine particles from agglomeration and covering the grinding media with dust. When EtOH was examined, the d_{50} size was 6.59 µm using 1% EtOH for eggshell, while the d_{50} size was recorded as 7.27 µm using 0.5% EtOH for calcite. In the presence of small molecules such as EtOH, a highly ordered thin layer forms directly on the solid surface (Pasarin et al, 2012). But, such a monolayer may not keep the particles at a further distance, which may be necessary to reduce the effect of attractive particle-particle forces and consequently change the bulk flow behavior.

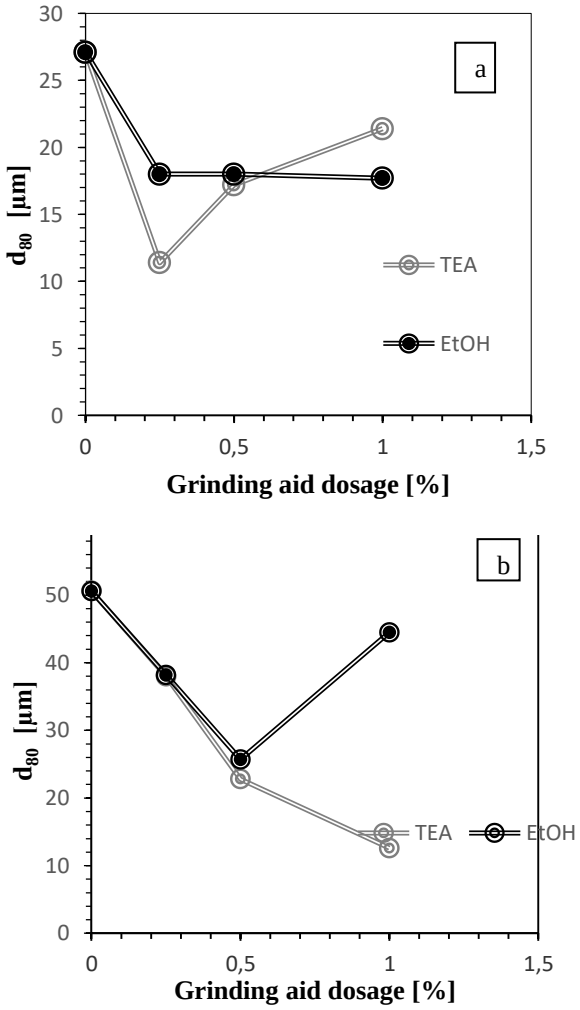

Fig. 3. The Effect of Grinding Aid Type and Dosage on d_{80} Size: (a) Eggshell Powder; (b) Calcite.

Amines and alcohols are organic compounds containing a polar functional group that tends to be adsorbed on a solid surface by -O(H) functional groups (Olsen et al, 2019). Dombrowe et al (1982) indicated that the polar group on TEA, DEG, and EtOH form tight bonds with calcite and non-polar groups pointing away from the surface form a hydrophobic layer that reduces surface energy and prevents aggregation.

Fig. 3 shows the impacts of grinding aids on the d_{80} particle size, which decreases when the correct dosages of grinding aids are added. Moreover, reasonable and the best effects are obtained with a 11.4 µm size and 0.25% TEA for eggshell and with a 12.6 µm size and 1% TEA for calcite.

3.2 Energy Consumption

Grinding aids or chemicals can be used to effectively reduce size and energy consumption. The effect of the grinding aid type and dosage on energy consumption is shown in Fig. 4.

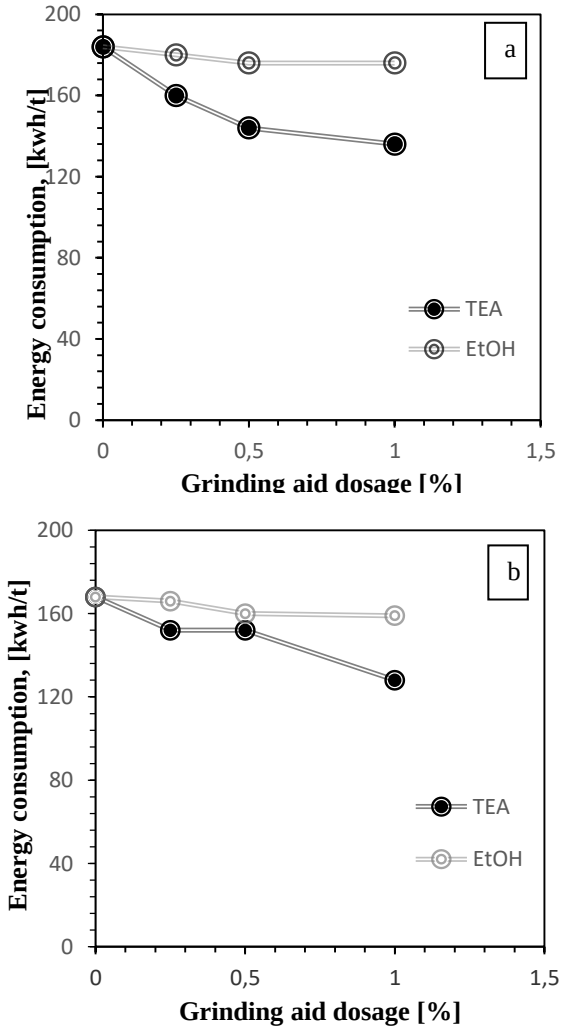

Fig. 4. The Effect of Grinding Aid Type and Dosage on Energy Consumption: (a) Eggshell Powder; (b) Calcite.

The lowest energy consumption was recorded as 136, and 128 kWh/t using 1% TEA for eggshell and calcite, respectively. This positive effect of TEA on energy consumption can be attributed to ease of powder flow. With increasing fine particles in dry grinding, the effect of intermolecular van der Waal's adhesion forces increases. As a result of this phenomenon, agglomeration increases, and flow characteristics change. However, it is seen that EtOH do not provide significant energy savings. The non-polar parts within the grinding aid molecule positively affect the powder fluidity by providing a thicker adsorption layer. Thanks to this thick adsorption layer, the distance between particles increases and the van der Waal's forces are reduced (Choi et al, 2010).

4 Conclusion

The purpose of the present work was to research the impacts of pure grinding aids from two different chemical classes on the dry grinding of bio and mineral calcium carbonate in a vertical stirred media mill. The grinding results demonstrated that two grinding aids positively affected grinding performance and energy savings compared to the no-aid condition. Additionally, coarse particle size and more energy consumption were obtained with EtOH than with TEA. When small polar molecules such as ethanol are adsorbed onto calcite, they form a self-assembled monolayer on the surface. This self-formed monolayer may not be sufficient to reduce Van der Waal's adhesion forces between fine particles and thus reduce particle size and powder flow.

When the grindability of eggshell and mineral calcite was compared, it was determined that finer sizes were obtained with TEA for calcite at higher dosage. It can be thought that this is due to the nanopores found in the structure of the egg shell.

The study revealed the grindability of eggshell. These obtained bio-$CaCO_3$ particles can be used effectively in many biotechnological applications.

References

Choi, H., Lee, W., Kim, D. U., Kumar, S., , ... & Ahn, Y. C., (2010). Effect of grinding aids on the grinding energy consumed during grinding of calcite in a stirred ball mill, *Minerals Engineering*, 23(1), 54-57.

Choi, H.K. and Choi, W.S., (2002) The ultra-fine grinding mechanism of inorganic powders in a stirred ball mill, *Journal-Korean Institute of Chemical Engineers*, 40(4), 498-506.

Dombrowe H., Hoffmann B., Scheibe W., (1982) Über Wirkungsweise und Einsatzmoglichkeiten von Mahlhilfsmitteln, *Zement-Kalk-Gips*, 11, 571–580.

Katircioglu-Bayel, D., (2023) Effective role of grinding aids in the dry grinding performance of calcite, *Powder Technology*, 426, 118675.

Olsen, R., Leirvik, K.N., Kvamme, B., (2019) Adsorption characteristics of glycols on calcite and hematite, *AIChE Journal*, 65(11), e16728.

Orumwense, O.A. and Forssberg, E., (1992) Superfine and ultrafine grinding—a literature survey, *Mineral Processing and Extractive Metullargy Review*, 11(1-2), 107-127.

Russell, W.M.S. and Burch, R.L., (1959) The principles of humane experimental technique, *Methuen.*

Sathiparan, N., (2021) Utilization prospects of eggshell powder in sustainable construction material–A review, *Construction and Building Materials*, 293, 123465.

E1: Understanding fine particle bed breakage using the Zeisel Grindability Tester

Anderson Chagas, *Shreedhara* Yasajnappa, *Sima* Hellmers and *Arno* Kwade*

Institute for Particle Technology, Technical University of Braunschweig, Braunschweig, Germany

Abstract. This work aims in further study stressing and breakage of fine particles in dry powders. A Zeisel grindability tester was selected due to the test practicality, easy control of applied stress energy and for allowing testing powders from fill millimetres down to lower microns. The torque and power measurement system was enhanced and the device was used characterize the influence of internal friction, use of flow additives and feed size distribution on grinding efficiency of dry powders.

1 Introduction

Nowadays, understanding energy utilization and dissipation during industrial processes, especially comminution operations, is of utmost importance. For instance, during ball milling operations, the fraction of total energy consumed that effectively contributes to particle grinding is known to be smaller than the fraction required during single particle breakage. In production-scale operations, far from the idealized laboratory scenario, the challenge lies not only in stressing product particles but also in efficiently transferring system energy to individual particles.

In terms of particle breakage, the majority of the characterization procedures are based on single particle stressing, being divided, as a function of the mode of stressing, in three classes, slow compression, single impact and double impact (Tavares, 2007). These procedures, although reliable in its results, typically demand extensive effort due manual handling of individual particles and are limited relatively coarse sizes (> 1 mm).

This work aims in further study stressing and breakage of fine particles in dry powders. The Zeisel grindability tester was selected due to the test practicality, easy control of applied stress energy and for allowing testing powders from fill millimetres down to lower microns in particle size.

2 Equipment and methods

The Zeisel grindability testing device features a stationary grinding bowl in which eight balls are positioned over the test powder. A rotating die apply load over the ball and powder, causing comminution of the powder due to compression. The rotating die and motor is assemble in such way as to, during testing, being supported vertically only by balls and test powder. Therefore, the load applied on the balls and test powder is determined by the mass of the rotating die axle and motor plus additional disk weights that can be added to the system.

Fig. 1. Zeisel grindability device (up) and grinding bowl with balls and test powder (bottom). Grinding bowl (1), rotating die (2), disk weights (3) and load cell for torque measurement (4).

For determination of the specific energy applied to the sample, it was installed a cantilever arm attached to base of the bowl. The steel cantilever arm was positioned

* Corresponding author: a.kwade@tu-braunschweig.de

radially to the base of the bowl and with a 90° degree angle with a second steel bin hooked to the load cell, rigidly fixed to the side of the device frame.

For the calculation of the specific energy consumption during grinding was adopted the methodology proposed by Fleiger et al. (2012). Once the torque (T_b) applied to the bowl and powder system is determined, the grinding work (W) during comminution can be obtained from the integral,

$$W = \frac{\pi n}{30} \int T_b \, dt = \frac{\pi n}{30} \sum_i \left(T_{b_i} \, \Delta t \right) \qquad (1)$$

where n is die rotation per minute (rpm) and Δt is time interval between acquired torque data. Considering now the mass of powder sample in the bowl (m/s), the specific energy consumption in kWh/t during grinding is given by:

$$E_{sp} = \frac{W}{3.6 \, m_s}. \qquad (2)$$

3 Results and discussions

Fig. 2 presents variation of both torque and powder bed particle size in relation to specific energy. In previous studies, it was observed for the material a decrease in powder flowability with particle size reduction. We observe that in the beginning of the size curve, for specific energy smaller than 10 kWh/t, the rate of grinding is relatively small. However, as the process progresses, torque reduces, more energy is dissipated in the particle bed and the rate of grinding increases. Eventually, somewhere around 20-60 kWh/t, as particle size continuously reduces, powder flowability reduces and torque on the bowl increases due to higher friction in the particle bed. From there onwards, torque continuously increases and rate of grinding also reduces.

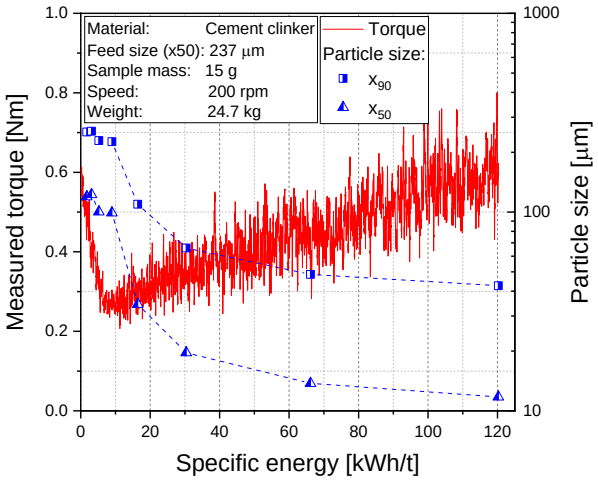

Fig. 2. Torque applied to the bowl and particle size in relation the specific energy.

Following the argumentation that reduction in grinding rate happens due to friction increase, tests were conducted using grinding aids (GA) in different dosages. Fig 3 compares the torque measured for two different GA substances. Prziwara et al. (2018a) showed that those substances present a direct impact on powder flowability, with heptanoic acid conferring higher powder flow. Indeed, low internal friction on the powder bed promoted reduction on the torque in the device bowl and increase in grinding efficiency.

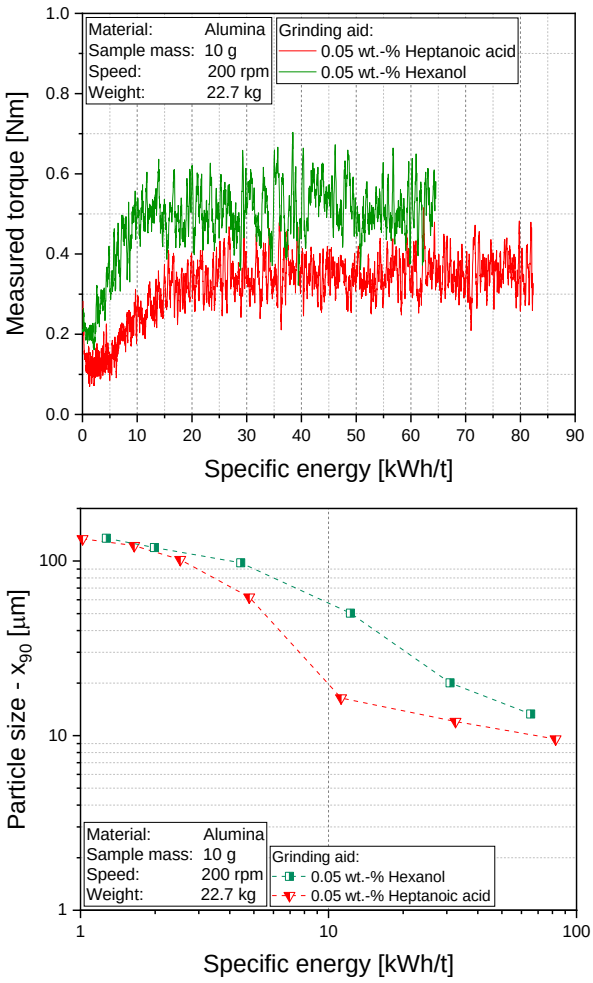

Fig. 3. Impact of grinding aid substance on torque and grinding

It was also compared the impact of GA dosage on powder grinding efficiency in the Zeisel grindability tester, shown in Fig 4. Here, it was observed an increase in efficiency with increase on dosage up to a certain point. However, as also observed by Prziwara et al. (2018b) on a dry stirred media mill, excessive high dosage of GA can become detrimental for grinding.

Another interesting observation made was the preferential breakage of coarser particles in the powder over smaller particles. Fig 5 presents the grinding results of a bimodal feed size distribution in relation to number of die rotations. As can be observed, during grinding, the coarser peak reduces due to breakage while finer peak barely changes. Lieberwirth & Kühnel (2021) previously observed preferential selectivity for breakage of coarser particles in confined particle bed compression of binary mixtures and Nöske et al. (2022) also observed similar preferential breakage of coarser particles in wet stirred media milling.

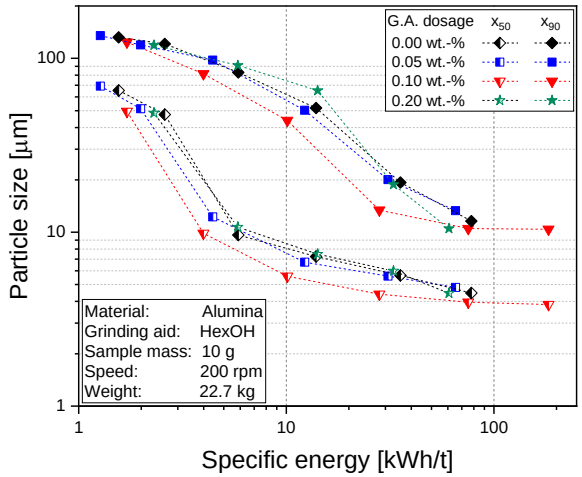

Fig. 4. Impact of grinding aid substance and dosage on the grinding efficiency in the Zeisel grindability tester.

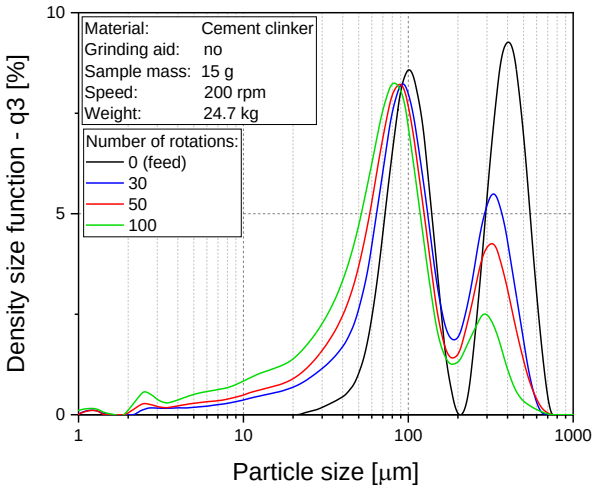

Fig. 5. Variation of the particle size distribution during particle bed grinding for a bimodal distribution

3 Conclusions

The main results observed in this work in terms of particle breakage are:

1) Increase in powder flowability changes, by means of the use of grinding aids, promotes reduction in internal friction among particle in a bed, resulting in more relative motion among the particles and a likely higher amount of stressing events. Therefore, a more intense grinding occurs with less energy.

2) A preferential breakage of coarser particles in a bed was observed, presumably due to less internal mobility of such size classes and higher difficulty escaping the path of the approaching balls. Is possible to assume that such behaviour occurs also in dry ball mills.

3) Based on previous indicators from the literature and results shown here, the Zeisel grindability tester can be used, assumed stress energy could be reliably measured, to characterize the breakage function of particles in dry powders. Additionally, considering that this type of device is already present in the production routine in the cement industry, its application for this purpose is facilitated

References

Tavares, L.M., (2007) Breakage of single particles: quasi-static, in: A.D. Salman, M. Ghadiri, M.J. Hounslow (Eds.), *Handbook of Particle Breakage*, vol. 12 (2007), 3–69. Elsevier

Prziwara, P., Breitung-Faes, S., Kwade, A. (2018a) Impact of grinding aids on dry grinding performance, bulk properties and surface energy. *Advanced Powder Technology*, 29, 416-425.

Prziwara, P., Breitung-Faes, S., Kwade, A. (2018b) Impact of the powder flow behavior on continuous fine grinding in dry operated stirred media mills. *Minerals Engineering*, 128, 215-223.

Lieberwirth, H., Kühnel, L. (2021) Particle Size Effects on Selectivity in Confined Bed Comminution. *Minerals* 11, 342

Nöske, M., Müller, J., Nowak, C., Li, K., Xu, X., Breitung-Faes, S., Kwade, A. (2022) Multicomponent Comminution within a Stirred Media Mill and Its Application for Processing a Lithium-Ion Battery Slurry. *Processes* No. 10, 2309

E2: Compression breakage of particle assemblies

Túlio M. Campos[1,*], *Magnus* Evertsson[2], *Malcolm* Powell[3], and *Luís Marcelo* Tavares[1]

[1]Department of Metallurgical and Materials Engineering, Universidade Federal do Rio de Janeiro – COPPE/UFRJ, Brazil
[2]Department of Industrial and Materials Science, Chalmers University of Technology, SE-412 96 Gothenburg, Sweden
[3]Comminution Reimagined Ltd., Brisbane, Australia

Abstract. Particle breakage by compression has been widely investigated to map the effect of different modes of application of stresses, particle shape and deformation rates, while investigations on particle assemblies are not as common. Yet, works analysing different particle assemblies commonly assess breakage by controlling the applied compressive force, even though often in comminution machines deformation is the variable that is directly controlled. The present work analyses breakage of a polymetallic ore in a piston-and-die system under different bed occupancies and by controlling the level of bed deformation. The term occupancy is defined to quantify the amount of material and the bed configuration used in the different particle assemblies. Results demonstrated large variabilities in the force-deformation profiles and a reduction in the specific energy absorbed by the particle assembly with the increase in occupancy and, therefore, particle interaction. No clear reduction in breakage efficiency was observed when assessing particle breakage from an individual particle to full packed layer of particles.

1 Introduction

Great attention has been dedicated to understanding fundamentals of particle fracture by compression since the 1960s, which includes analysis on the effect of different rates of deformation (Arbiter et al., 1969; Schönert, 1972), changes in particle shape (Rumpf, 1973; Schubert, 1987; Campos et al., 2024), different modes of application of stresses (Campos et al., 2024), breakage efficiency under different conditions (Rumpf, 1973) and comparison between single-particle and particle-bed breakage (Schönert, 1979).

Crushing minerals under compression usually relies on a particle assembly stressed between two hard surfaces, where the geometrical condition of the particle arrangement varies significantly. In this regard, Schönert (1996) investigated the transition in size reduction efficiency when moving from a single-particle breakage to a particle-bed breakage environment. His work was key to show that friction strongly influences the stress distribution under confinement, thus reducing breakage efficiency when compressing particles in a confined bed when compared to single-particle breakage (Schönert, 1996).

Tests performed by Schönert (1996) attempted not only to map the transition between single particle and bed breakage, but also to propose a reliable approach that enables analysis of particle fracture in an ideal particle bed (Schönert, 1996). This situation forced him to do all tests by using the applied force to control fracture, even though it is recognized that deformation is the variable that is directly controlled during breakage by compression (Fuerstenau et al., 1990; Gutsche and Fuerstenau, 2004). As such, it should be mentioned that classification of particles according to their size and shape (Campos et al., 2024), which is a key phenomenon involved in particle breakage by compression, has not been accounted so far in earlier studies, even though it is critical to assess and understand the size reduction efficiency.

The present work investigates particle breakage by compression of a polymetallic ore under different bed arrangements with breakage controlled by deformations of the bed. Tests served as the basis to understand the transition in breakage efficiency when moving from individual particles to a single layer full of particles.

2 Materials and methods

Samples of a polymetallic ore, investigated elsewhere (Campos et al., 2024), were used in this investigation. Specific gravity of the material is 2.9 t/m³ (Campos et al., 2024) and particles in the narrow size range of 16.0–22.4 mm, 11.2–16.0 mm and 8.00–11.2 mm were carefully prepared for testing.

Tests were performed with the aim of analysing the size reduction efficiency in particle breakage by compression when changing the bed configuration in a cylindrical piston-and-die apparatus. To quantify the relative amount of material in the different particle assemblies, the present work defines the term occupancy, which represents the ratio between the effective projected area of the particle assembly filling a given the area of a cylindrical piston-and-die apparatus (Figure 1).

* Corresponding author: tulio.campos@coppe.ufrj.br

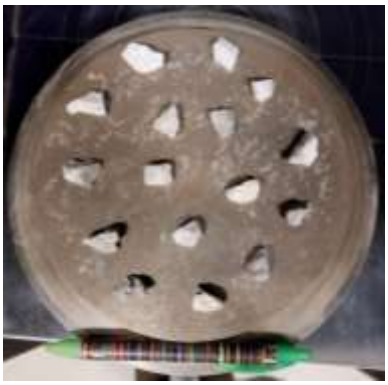

Figure 1. Single layer configuration with particles in the narrow size range of 11.2–16.0 mm and occupancy of 20%. Piston-and-die apparatus with 170 mm with 16 particles.

The present work analyses occupancies varying from 10% to a single full layer of particles by using a piston-and-die apparatus with 170 mm of diameter. Tests were controlled by fixed maximum deformation (Δ_m) calculated as (Campos et al., 2024):

$$\Delta_m = h\alpha \quad (1)$$

where h is the maximum height of the particle assembly and α is the deformation ratio. Deformation ratios varied from 0.1 (10%) to 0.3 (30%). Deformation rate was 15 mm/min, which approximately corresponds to strain rates from 0.01 to 0.05 s^{-1}, while the data acquisition rate was 0.01 s^{-1}.

Occupancy was estimated for each test by collecting pictures of the different particle assemblies for further image analysis. Indeed, all pictures relied on placing the particles on a 170 mm diameter cardboard circle (Figure 2a) to allow good contrast during analysis, besides a calliper as a reference measurement. The Java based software Fiji was used to estimate the area of the circle covered by particles (Figure 2b).

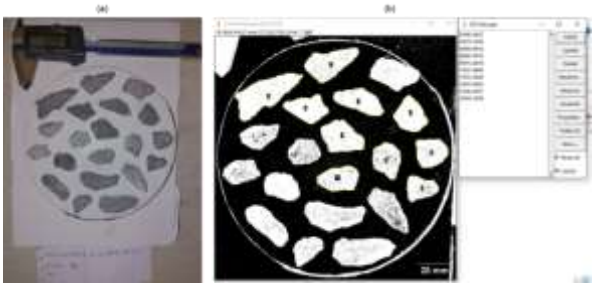

Figure 2. Single layer configuration with particles in the narrow size range of 16.0–11.2 mm on the 170 mm diameter cardboard (a) and picture analysed using the software Fiji (b).

As an output of the compression test, force-deformation profiles were recorded, and the specific energy absorbed by the particle assembly was calculated by integrating them and dividing by the total mass tested. Fragments collected after each test were then analysed by dry sieving.

3 Results and discussions

Force-deformation profiles are presented in Figure 3 for different occupancies in the narrow size ranges of 16.0–22.4 mm (a) and 11.2–16.0 mm. Results from Figure 3 did not show a clear trend between the different occupancies and size ranges tested. Noisy profiles, which are characteristic of slow compression tests (Rumpf, 1973; Tavares, 2007; Campos et al., 2024), also demonstrate the spread between the different conditions tested. Further analysis of Figure 3 also indicates high variability in the force-deformation profiles for small deformations, which may be partially explained by the effect of particles being classified for breakage according to their thickness and maximum level of deformation.

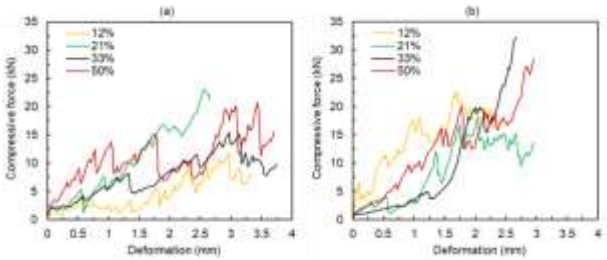

Figure 3. Force-deformation profiles for different tests carried out with occupancies varying from 10% to 50% with particles in the narrow size range of 16.0–22.4 mm (a) and 11.2–16.0 mm (b).

Specific energy absorbed by the particle assembly is obtained by integrating the force-deformation profiles (Figure 3) and results are presented in Figure 4, according to different occupancies for the narrow size ranges of 16.0–22.4 mm (a) and 11.2–16.0 mm. A reduction in specific energy absorbed is clear with an increment in the occupancy, with values varying from 1000 to 200 J/kg in the coarser size range with 20% deformation ratio (Figure 4a).

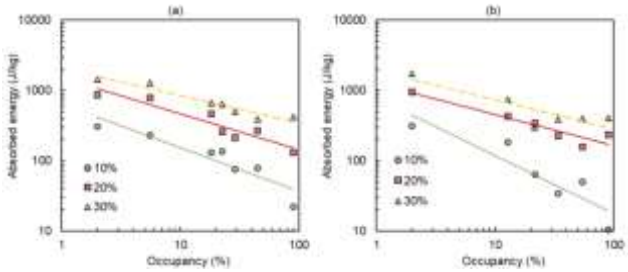

Figure 4. Variation of the specific energy absorbed in the layer of particles according to different occupancies for particles tested in the narrow size range of 16.0–22.4 mm (a) and 11.2–16.0 mm (b).

Results on size reduction are summarized in Figure 5 using the t_{10} index (Narayanan and Whiten, 1988) in respect to the specific energy absorbed by the particle assembly for the narrow size range of 16.0–22.4 mm and all occupancies tested. No clear difference was observed when testing occupancies from 10% to a single layer of particles, demonstrating that, unlike the results presented by Schönert (1996), no reduction in the energy

efficiency was observed when increasing the number of particles up to a single full layer of particles. Up to this point it is worth mentioning that current analysis considered the classification of particles for breakage once particle fracture was controlled by setting a fixed applied deformation. Schönert (1996), on the other hand, controlled compression tests by the applied force, which partially minimizes the effect of particles classification and particle assembly rearrangement at the beginning of the compression. This likely explains, at least partially, the differences between the current approach and the one adopted by Schönert (Schönert, 1996).

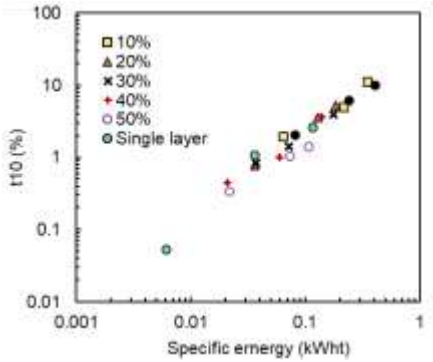

Figure 5. Variation of the t_{10} breakage index according to different specific energies for particles tested in the narrow size range of 16.0–22.4 mm with different occupancies.

4 Conclusions

The work investigated particle breakage by compression of a polymetallic ore under different particle arrangements.

Force-deformation profiles were characterized by the well-known noisy profile. High variability of these profiles for low deformations was partially associated with the particles being classified for breakage according to their different shapes (thickness).

Specific energy absorbed by the particles reduced with the increase in occupancy. Despite this reduction in specific energy absorbed, no significant differences were observed in the size reduction energy efficiency when going from individual particles to a single layer full of particles.

References

Arbiter, N. (1969). Single fracture of brittle spheres. Soc. Min. Eng. AIME, Trans., 244, 118-133.

Campos, T. M., Andersson, C., Evertsson, M., Powell, M., & Tavares, L. M. (2024). Energy-based modelling of single-particle breakage by slow compression. Minerals Engineering, 208, 108585.

Fuerstenau, D. W., Kapur, P. C., Schoenert, K., & Marktscheffel, M. (1990). Comparison of energy consumption in the breakage of single particles in a rigidly mounted roll mill with ball mill grinding. International Journal of Mineral Processing, 28(1-2), 109-125.

Gutsche, O., & Fuerstenau, D. W. (2004). Influence of particle size and shape on the comminution of single particles in a rigidly mounted roll mill. Powder technology, 143, 186-195.

Narayanan, S. S. (1988). Determination of comminution characteristics from single particle breakage tests and its application to ball mill scale-up. Trans. Inst. Min. Metall.(Sec. C), 97, 115-124.

Rumpf, H. (1973). Physical aspects of comminution and new formulation of a law of comminution. Powder Technology, 7(3), 145-159.

Schonert, K. (1972). Role of fracture physics in understanding comminution phenomena. Trans. AIME, 252, 21-26.

Schönert, K. (1979). Aspects of the physics of breakage relevant to comminution. In Fourth Tewksbury Symposium, University of Melbourne (Vol. 3, No. 1, pp. 3-30).

Schönert, K. (1996). The influence of particle bed configurations and confinements on particle breakage. International Journal of Mineral Processing, 44, 1-16.

Schubert, H. (1987). On the microprocesses of comminution. Aufbereit.-Tech, 5, 237-246.

Tavares, L. M. (2007). Breakage of single particles: quasi-static. Handbook of powder technology, 12, 3-68.

E3: The effect of non-ideal particle bed breakage on the particle shape of white fused corundum

László Tamás[1,2], *Ádám Rácz*[2]

[1]Refra-System Ltd., Újrónafő, Hungary
[2]Institute of Raw Material Preparation and Environmental Technology, University of Miskolc, Miskolc, Hungary

Abstract. The comminution of corundum is a challenging task, as it has outstanding mechanical strength and is highly abrasive and is consequently applied as a blasting and polishing agent in the abrasive industry. Thus, the selection of the best comminution methods to achieve the required dispersity properties has great importance. For this, first we must understand the effects of different type of stresses and their influence on the corundum particle fractions. Laboratory scale particle bed compression experiments in a piston press and laboratory scale HPGR tests were carried out to examine the effect of non-ideal particle bed comminution method and its effects on the product's particle size distribution, bulk density, and particle shape. The effects of the applied pressure and particle bed height on the progeny particles were investigated. The results showed that outstanding yield, high bulk density, and appropriate particle shape can be achieved by non-ideal particle bed breakage mechanisms. This transient comminution process possesses the energy efficiency of single particle breakage with a favourable particle shape associated to the particle bed breakage.

1 Introduction

In terms of energy utilisation, the most efficient compressive stress related comminution method is single particle breakage by compression loading, the second is the loading the bed of particles by compressive stress, and then comes the unconfined particle-bed comminution stated by Schönert (1979). Single particle breakage can easily be carried out in continuous operation in roller crushers. Compressive stress on a bed of particles can be achieved by high-pressure grinding rolls (HPGR) and unconfined particle-bed comminution by ball mills, also in continuous operation mode. While roller crushers and ball mills have been widely used starting several decades ago, continuous operation for particle bed related comminution is a relatively new technology. During the last decades, due to the extraordinarily energy intensive processes of raw material preparation industry, conventional comminution and classification processes have been studied to decrease the energy requirements to reduce the environmental impact and save money. To meet these requirements fundamental experiments were carried out by German scientist Schönert (1979) to understand the particle-particle interactions under compressive stress in a particle bed with his coworker (Schönert and Flügel, 1980). These experiments were conducted by piston press and the results led directly to the continuously operating HPGR equipment patented by Schönert (1982). In 1984, the HPGR technology was not yet used in industrial scale comminution processes, although Schönert and Knobloch (1984) proposed it as an alternative particle size reduction technology, with several benefits such as energy efficiency and less wear rate of plates, furthermore it is an optimal way to avoid overgrinding. Due to the high throughput rate and energy sensitivity requirements, the first commercial application was introduced in the cement industry in 1985 stated by (Schönert, 1988; Kellerwessel 1990; and Fiege 1993). Several authors have published about the general benefits of HPGR technology in the cement industry. Wüstner (1986) stated that a 30 % energy reduction can be achieved by the application of HPGR in a closed circuit with a ball mill, compared to a simple step comminution by ball mill for cement grinding. A similar finding was made by Patzelt (1992) for an HPGR-ball mill arrangement in case of clinker comminution, where the specific energy consumption decreased by 30 % compared to the simple ball mill comminution method. Ellerbrock (1994) identified a 20 % increase in throughput and 15 % energy savings using HPGR for clinker comminution. While the energy efficiency of ball mills for clinker grinding is highly limited and the specific grinding work requirement is 30–42 kWh/t depending on the product fineness according to Marchal (1997), HPGR technology can reduce it to 20–30 kWh/t in a HPGR-ball mill comminution system published by (Alsop and Post, 1995; Cembureau, 1997; and Seebach et al. 1996). Madlool et al. (2011) also described different HPGR-ball mill configurations, where the energy requirement for comminution of clinker was reduced by 10-50 % depending on the comminution process configurations. In 2007 Daniel (2007) estimated there were around 400 high-throughput HPGR machines operating globally for clinker comminution. Although the preliminary industrial scale applications of HPGR

* Corresponding author: laszlo.tamas@refra-system.hu

machines were limited to the initial comminution stages, subsequently the comminution technology was introduced in different segments of particle size reduction, such as pre-grinding, hybrid-grinding, semi-finish grinding and finished products grinding stated by (Kellerwessel, 1993 and Kellerwessel, 1996). According to Plath (2005), in 2005 there were 29 diamond, 21 iron ore and 2 copper-gold mines using HPGR, provided by only one manufacturer. In 2013 Sesemann et al. (2013) estimated around 130 HPGR machines had been installed in ore and mineral processing plants.

There are a limited number of articles and scientific studies related to HPGR or particle bed comminution with the most abrasive minerals like silicon-carbide or corundum. Piston-die press experiments were conducted by Cooper and Eaton (1962) to examine the compaction mechanism of ceramics such as fine alumina, which is the raw material of the electro-fused corundum. Reichardt and Schönert (2003) also used piston-die press experiments to evaluate single and multiple compression on fine fractions of limestone, quartz, zircon-silicate, fused corundum, and silicon-carbide. Karimi and Djokoto (2012) carried out experiments with silicon-carbide in a laboratory scale HPGR system to describe the modelling, simulation, and instrumentation to produce silicon carbide grains. Pedrosa et al. (2019) conducted an assessment for the circuit simplification of the comminution processes with HPGR machine to produce fused and tabular alumina ground particles. The research group concluded that 13 roll crushers can be replaced with only one HPGR to reduce operational costs. The article also stated there was no record of HPGR used in fused alumina (corundum) comminution. The application of HPGRs started in the cement industry, through the mining industry and nowadays for the comminution of the most abrasive minerals due to the higher quality of machine materials. The tungsten carbide studs, and more wear resistance roll surfaces applied with the hydraulic control system and sensors are more advanced to regulate the rollers surfaces completely parallel, to avoid inconsistent wear rate.

The fundamental particle bed comminution experiments conducted by Schönert in 1979 with a piston press is still a basic and standard research methodology to examine particle breakage by particle-particle interaction in a particle bed, also for the evaluation and sizing of HPGR equipment for different applications. While the most energy efficient fracturing mechanism by compression loading is single particle breakage, the product particles have several disadvantageous properties for the high-end consumers processing methods, such as low bulk density and a sharp, needle-like elongated particle shape on white fused corundum published by Tamas and Racz (2022).

According to Schönert (1996), the particle bed configuration and confinement have a remarkable effect on particle breakage. Particle arrangement and confinement were proposed to be classified as: Single particle situation, one particle layer, closely and widely confined particle bed and the ideal particle bed. The ideal particle bed and its requirements were determined as follows: 1. Stochastically homogeneous structure of particle bed. 2. Homogeneous compaction of the particle bed. 3. Known volume or mass of the stressed particles. 4. Wall effects are negligible in respect to the overall size reduction process stated by Schönert, (1996). The requirements can be satisfied by two parallel stressing surfaces, while the particle bed height in a cylindrical bed must be at least 6 times thicker than the maximal particle size of the feed and also the diameter of the stressed particle bed has to be 3 times more than the height of the bed proposed by Schönert (1996). To achieve the required material parameters like high bulk density, a blocky and rounded particle shape, high yield for the target fraction and lower wear to reduce contamination of the product, piston-die press experiments were carried out to determine the particle bed related stress conditions in white fused corundum comminution. Transient particle bed conditions between the single particle situation and ideal particle bed breakage mechanism were applied in the study to achieve the desired corundum particle properties.

2 Materials and methods

Artificial white fused corundum is an excellent advanced abrasive material with a different additional value depending on miscellaneous applications in industrial fields like medical and dental technology, the space and aerospace industry, the optical industry and the laminate industry. The average and moderate additional value application fields – refractory mineral, sand blasting agent, polishing agent – should be mentioned as well, because those fields consume a large quantity of white fused corundum and have a major part of the global market too. The basic technology of the production is the electrical arc furnace, where high-grade (min 98.5 %) Al2O3 containing alumina is melted at 2040 °C, with specific smelting work of 1.2 MWh/t. After melting the white fused corundum is cast in a mold, then a special solidification and cooling process takes place. The cooled material is crushed and classified in many steps to produce the different size fractions for various applications.

The comminution test's feed of white fused corundum (hereafter corundum) 1–3 mm fraction was produced by 3-step comminution by two jaw crushers and one roller crusher in line without any reflux. The 0–3 mm particles were classified to 1–3 mm. The classification was performed in Sieve Shaker AS 200 TAP equipment for 5 minutes for the feed and until constant sieve mass residual under 1 mm. The remaining 0-1 mm fractions were separated into 0–0.15, 0.15–0.3, 0.3–0.5, and 0.5–1 mm fractions and provided the base numbers for the evaluation of particle shape examination.

The chemical composition of corundum could vary with the particle size, depending on the fault points inside the particles. Chemical analysis was carried out by an independent laboratory with XRF spectrometry according to the MSZ-EN-ISO 12677:2012 standard with ARL 9900 equipment. The bulk density of the corundum 1-3 mm was 1.83 g/cm^3.

The laboratory scale hydraulic piston press was built by the Institute of Raw Material Preparation and Environmental Technology, University of Miskolc. Two pistons are situated in the equipment, one for the pressing force transmission, the other for sample discharge. The piston pressure can be adjusted to a maximum value of 275 MPa by the piston's oil pressure. During the material bed compression experiments a die with 25 mm diameter was used, the piston velocity was 34.5 mm/s. Different series of experiments were carried out with pressure of 125, 175, 225 and 250 MPa, while the applied material bed height was 5, 10, 15, 20 and 25 mm. To achieve the required products for the measurements, with each experimental adjustments, at least 20 piston press events were conducted. Every pressing event was carried out with fresh feed material.

After the material bed compression tests, the product was sieved to <0.15, 0.15–0.3, 0.3–0.5, 0.5–1 and >1 mm size fractions by a Retsch TAP sieve shaker AS 200 for the later tests. The bulk density of the feed and product fractions (1) was measured according to the MSZ 6506-84 standard, where at least 1200 g of dry test material is fed from a conical feeder through a 20 mm diameter outlet to a container. The measuring container takes place 76 ± 0.05 mm below the conical feeder outlet, on the same vertical axis line. Just as the mechanical lock is opened in the feeder, the material fills up the container and the rest of the particles are peeled off from its top by a cutting-edge ruler with 4 hand movements. It must be done to two mutually perpendicular axes. The accuracy of mass measurement is 0.1 g by the balance. During the procedure the vibration and collision must be avoided due to its effect to the compaction. The arithmetic mean of two parallel measurements provide the result of the procedure.

$$\rho_{bulk} = \frac{m_1 - m_0}{V} \quad (1)$$

Where: ρbulk= bulk density [g/cm3]; m1= mass of container and particles [g]; m0= mass of container [g]; V= volume of container [cm3]

The particle shape analysis was carried out by a RETSCH CAMSIZER X2 dynamic image analyser device with a dry jet dispersion module. The Xc_{min} parameter was applied to determine the particle size distribution. The chord Xc is defined as the maximum distance between two boundary points perpendicular to the scanning direction. Xc_{min} shows the particle width, which is determined from the narrowest of all measured chords Xc. The device can calculate several parameters describing particle shape and their distribution, based on particle number, particle area or particle volume.

For the characterisation of particle shape, volume-based sphericity values (2) were determined for each product fractions and pre-crushed fractions were also determined to provide the base value for the evaluation.

$$SPHT = \frac{4\pi \times A}{P^2} \quad (2)$$

The sphericity value (hereafter SPHT) displays the roundness, which is determined from the particle perimeter (P) and the particle area (A). A perfect circle or sphere has a SPHT equal to 1. All other particle shapes will result in SPHT <1.

3 Results

Piston press experiments were carried out to examine two major parameters - piston pressure and particle bed height - and their influences on the product dispersity. The results showed high effective yield (58-80%) for the 0–1 mm fraction from the 1–3 mm feed, increased sphericity and bulk density also occurred. Figure 1. shows that higher applied piston pressure resulted more effective yield for the 0-1 mm fraction, in case of every examined particle bed height. At a certain pressure level, better comminution occurred in a thinner particle bed resulting in higher effective yield of 0-1 mm. The transition from a closely ideal particle bed to the single particle crushing method and it's more energy efficient breakage mechanism can explain the experienced phenomenon. The experiments and conclusions point to the successful application of HPGR technology for comminution of highly abrasive materials. The product properties fulfilled the requirements for product yield, high bulk density and favourable particle shape for high-end consumers in the abrasives industry.

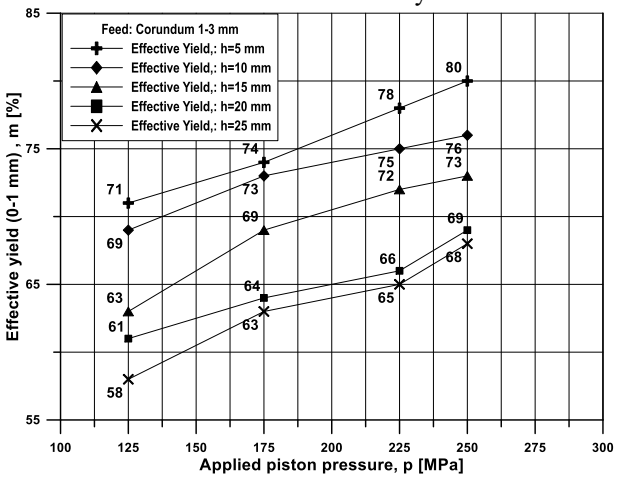

Fig. 1. Effect of applied piston pressure and particle bed height on the effective yield

Acknowledgement

Project no. 1012971 has been implemented with the support provided by the Ministry of Culture and Innovation of Hungary from the National Research, Development and Innovation Fund, financed under the KDP 2020 funding scheme.

References

Schönert, K. (1979) Energetische aspekte des Zerkleinerns spröder Stoffe. Zement-Kalk-Gibs, v. 32. p. 1-9.

Schönert, K. and Flügel, F. (1980) Zerkleinerung spröder Minerale im hochkomprimierten Gut-bett. European Symposium, Particle Technology, Preprints Vol. A, Dechema, Frankfurt, pp. 82-95.

Method of fine and very fine comminution of materials having brittle behavior; Patent number: US4357287A

Schönert, K., Knobloch, O. (1984) Cement grinding in the twin-roll mill. Zement-Kalk-Gips 11, 563–568.

Kellerwessel, H. (1990) High pressure material bed comminution in practice. Zement-Kalk-Gips , 2, 57–64.

Feige, F. (1993) Current state of development in high compression. Zement-Kalk-Gips 11, 305–312.

Wüstner, H. (1986) Energy-saving with the roller press comminution process. World Cement, 94–96.

Patzelt, N. (1992) High pressure grinding rolls, a survey of experience. IEEE Cement Industry Technical Conference, Dallas/Texas 10 (14), 180

Ellerbrock, H.-G. (1994) Gutbett-Walzenmuhlen, Zement-Kalk-Gips 2 75–82.

Marchal, G. (1997) Industrial Experience with Clinker Grinding in the Horomill Proc.1997 IEEE/PCA Cement Industry Technical Conference XXXIX Conference Record, Institute of Electrical and Electronics Engineers: New Jersey.

Alsop, P.A., and J.W. Post. (1995) The Cement Plant Operations Handbook, Tradeship Publications Ltd., Dorking, UK

Cembureau. (1997) Best Available Techniques for the Cement Industry, Brussels: Cembureau.

Von Seebach, H. M., E. Neumann, and L. Lohnherr. (1996) State-of-the-art of energy-efficient grinding systems. Zement-Kalk-Gips 49(2):61–67.

Madlool, N.A, Saidur, R., Hossain, M.S. and Rahim, N.A. (2011) A critical review on energy use and savings in the cement industries, Renewable and Sustainble Energy Reviews 15, 2042–2060.

Daniel, M. J. (2007) Energy efficient mineral liberation using HPGR technology. Doctoral dissertation, University of Queensland.

Kellerwessel, H. (1993) High pressure particle bed comminution of mineral raw materials. Aufbereitungs-Technik 34 (5), 243–249.

Kellerwessel, H. (February 1996) High pressure particle bed comminution, state of the art, application, recent developments. Minerals Engineering Journal, 45–52.

Plath, H. (2005) High pressure grinding rolls for copper–gold ores and other mineral applications. McGill Professional Development Seminar Notes.

Sesemann, Y., Broeckmann, C., & Höfter, A. (2013) A new laboratory test for the estimation of wear in high pressure grinding rolls. Wear, 302(1-2), 1088–1097. doi:10.1016/j.wear.2012.10.022

COOPER, A. R., EATON, L. E. (1962) Compaction Behavior of Several Ceramic Powders. Journal of the American Ceramic Society, 45(3), 97–101. doi:10.1111/j.1151-2916.1962.tb11092.x

Reichardt, Y., & Schönert, K. (2003) Interpartical Breakage on Fine Hard Materials by Single and Multiple Compression. Chemical Engineering & Technology, 26(2), 191–197. doi:10.1002/ceat.200390028

Karimi, H. R., & Djokoto, S. S. (2012) Instrumentation and modeling of high-pressure roller crusher for silicon carbide production. The International Journal of Advanced Manufacturing Technology, 62(9-12), 1107–1113. doi:10.1007/s00170-011-3871-8

Pedrosa, F. J. B., Bergerman M. G., Segura-Salazar, J., Junior H., D. (2019) HPGR as alternative to fused alumina comminution route: an assessment of circuit simplification potential, REM, International Engineering Journal, Ouro Preto, 72(3), 543-551, http://dx.doi.org/10.1590/0370-44672018720193

László, Tamás; Ádám, Rácz. (2022) Material bed compression experiments and the examination of the bulk density of the product, Geosciences and Engineering: 10 : 15 pp. 97-109.

Schönert, K. (1988) A First Survey of Grinding with High-Compression Roller Mills, International Journal of Mineral Processing, 22 (1988) 401-412.

Schönert, K. (1996) The: influence of particle bed configurations and confinements on particle breakage, Int. J. Miner. Process. 44-45 (1996) I – 16.

E4: Unlocking the Potential of HPGR: Predictive Insights from the Piston-and-Die Press Test Suite at UBC

Giovanni Pamparana[1,*], and *Bern* Klein[1]

[1] The Norman B. Keevil Institute of Mining Engineering, University of British Columbia, Vancouver, Canada

Abstract. In the evolving landscape of mineral processing, High-Pressure Grinding Rolls (HPGR) have emerged as a forefront technology, promising significant energy savings and operational efficiencies. This paper introduces a suite of innovative tests developed at the University of British Columbia (UBC), designed to accurately predict HPGR specific energy consumption, size reduction, and specific throughput. Leveraging the piston-and-die press test (PPT) as a laboratory-scale proxy of HPGR conditions, this research presents a breakthrough in pre-emptive HPGR performance assessment using a small quantity of material. The methodology integrates either direct calibration with actual HPGR performance data or with the comprehensive database of pilot scale HPGR tests available at UBC, offering a multidimensional analysis of different kinds of ores behaviour under HPGR conditions. This predictive capability is crucial for sizing and optimizing comminution circuit design and enhancing the energy efficiency of mineral processing operations. The findings not only underscore the practical application of the PPT in various stages of project development, from pre-feasibility to geometallurgical modelling, but also highlight the potential for significant advancements in the field of comminution. By providing a reliable, scalable, and efficient method for predicting HPGR performance, this research contributes to the broader pursuit of sustainable and optimized mineral processing solutions.

1 Introduction

High-Pressure Grinding Rolls (HPGR) represent a significant advancement in the efficiency and effectiveness of the comminution process in mineral processing. The HPGR technology, recognized for its ability to reduce energy consumption and increase throughput, has necessitated the development of reliable predictive models for its operation (Schönert, 1988). In response to this need, the University of British Columbia has developed a suite of predictive tests utilizing the piston-and-die press test (PPT). This set of methodologies allows for accurately predicting HPGR performance metrics, such as specific energy consumption, size reduction, and throughput, based on small-scale laboratory tests. The significance of this development lies in its ability to facilitate the optimal design and operation of comminution circuits, thereby enhancing the overall efficiency and sustainability of mineral processing operations.

The methodologies developed are grounded in rigorous experimental work and have been validated through comprehensive studies. Davaanyam et al. (2015) introduced the piston press tests as a means for determining the optimal energy input for HPGR operations, highlighting the direct calibration methodology's effectiveness in bridging lab-scale observations with pilot-scale HPGR performance. Pamparana et al. (2022) further expanded on this foundation by presenting a model to predict HPGR throughput based on piston press testing, offering a robust circuit design and optimization tool. Together, these studies underscore the potential of piston press tests in advancing the efficiency and predictive capability of HPGR technology in mineral processing (Wang, 2021).

2 Methodologies

The methodology encompasses three core components: the PPT for simulating HPGR conditions, the force-displacement curve analysis for energy consumption prediction and comparison of PPT outcomes with actual HPGR performance data. This approach involves direct calibration with pilot scale HPGR tests, database calibration against a comprehensive HPGR database at UBC, and a simulation methodology for circuit prediction. Each method's accuracy and applicability in different project stages are discussed, emphasizing the practical implications of the test suite in pre-feasibility studies, feasibility studies, and geometallurgical modelling.

These methodologies highlight a comprehensive approach to predicting and optimizing HPGR performance, utilizing both experimental data and advanced simulation techniques to provide accurate estimations of specific energy consumption, size reduction, and throughput in mineral processing applications.

* Corresponding author: giovannipamparana@gmail.com

2.1 Specific Energy Consumption and Size Reduction Prediction

There are three methodologies that can be used to predict the specific energy consumption and size reduction relationships using the PPT for the HPGR (Davaanyam, 2015).

2.1.1 Direct Calibration Methodology

This technique involves conducting piston press tests on sample materials and directly correlating the comminution properties observed with HPGR performance data. The study emphasizes the importance of understanding the ore's comminution behaviour under pressure to accurately estimate the specific energy requirements. The process entails calibrating the outcomes derived from the piston press tests against the pilot-scale HPGR results on a composite sample that represents the deposit. The piston press test results can be used to obtain the correlation between energy consumption and size reduction for various ore types within the deposit and make predictions on the HPGR behaviour.

Pilot scale HPGR is the standard approach used to determine operating and design parameters for full scale HPGR operations. Due to the requirement of performing pilot-scale HPGR tests, more than 1000 kg of material is needed to conduct this methodology, which can be prohibitive.

Figure 1 shows how the energy consumption predictions with the piston press test fit the HPGR results for the same ore, whereas Figure 2 shows the reduction ratio prediction.

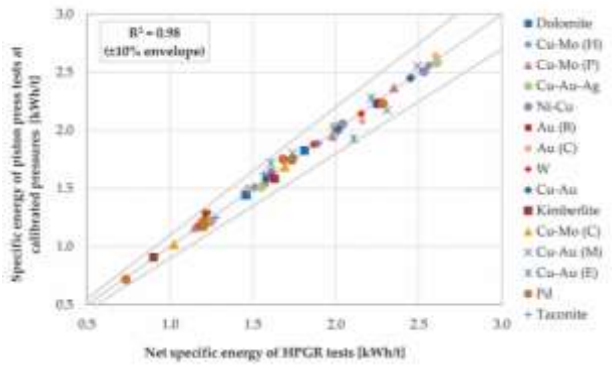

Fig. 1. Specific energy consumption prediction using the direct calibration methodology (Davaanyam et al., 2015).

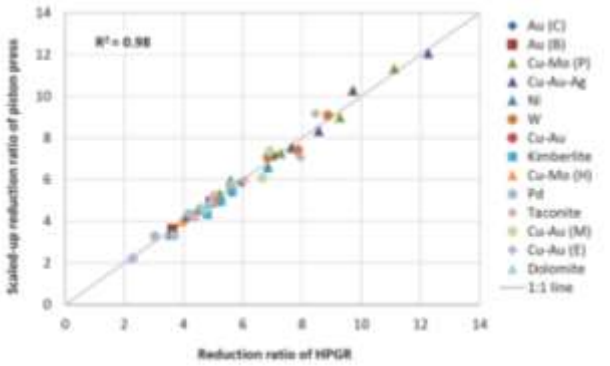

Fig. 2. Reduction ratio prediction using the direct calibration methodology (Davaanyam et al., 2015).

2.1.2 Database Calibration Methodology

A broad database comprising various ore types and their corresponding HPGR test results allows for comparative analysis. This method leverages historical data to refine predictions for new ore samples, offering a more comprehensive understanding of expected performance. Similarly to the direct calibration methodology, the piston press results can be compared against the database to obtain the energy consumption and size reduction capabilities of the ore in the HPGR.

Since no pilot-scale HPGR tests are needed, it is possible to conduct this methodology utilizing approximately 10 kg of material.

Figure 3 shows how the energy consumption predictions with the piston press test fit the HPGR results for the same ore, whereas Figure 4 shows the reduction ratio prediction.

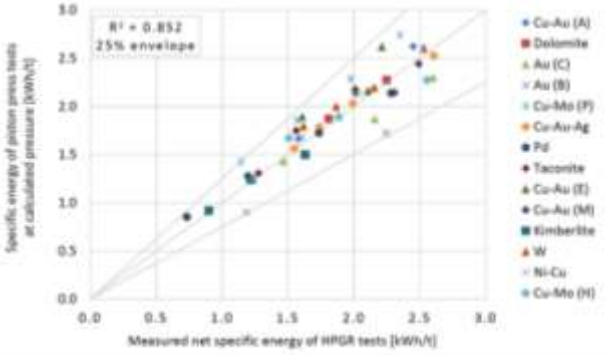

Fig. 3. Specific energy consumption prediction using the database calibration methodology (Davaanyam et al., 2015).

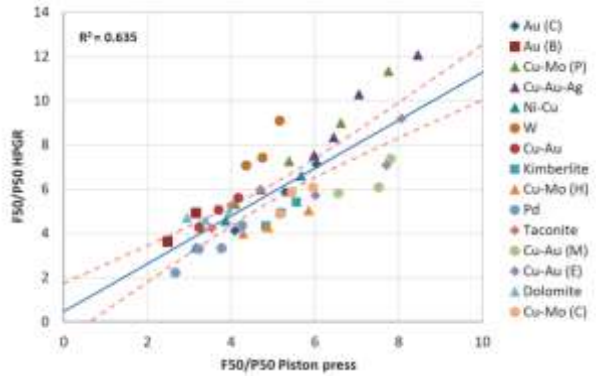

Fig. 4. Reduction ratio prediction using the database calibration methodology (Davaanyam et al., 2015).

2.1.2 Simulation Methodology

The Simulation Methodology involves conducting piston press tests across five distinct particle size ranges within a mineral sample at three different energy settings. These tests are designed to establish a relationship between energy application and particle breakage, which is then utilized in circuit simulations to predict processing outcomes.

Figure 5 shows the accuracy of predicting the particle size using the simulation methodology for a closed-circuit HPGR.

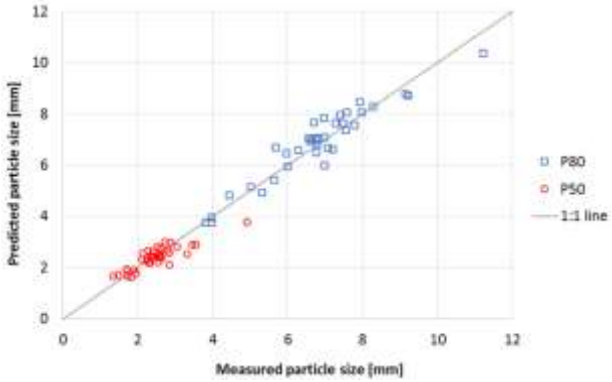

Fig. 5. Particle size prediction using the simulation methodology (Davaanyam et al., 2015).

2.2 Throughput Prediction

The throughput prediction utilizes the findings from the direct calibration and database-calibrated methods. By understanding the relationship between specific energy consumption, size reduction, and the ore's mechanical properties, the models can predict the volume of material that can be processed within a specific timeframe. This approach is crucial for optimizing the operational efficiency of HPGR circuits, ensuring that throughput targets align with energy and size reduction goals.

By compressing several volumes of material at different force levels, it is possible to derive information that can be used to predict the specific throughput constant (m-dot) for the HPGR (Pamparana et al., 2022). The specific throughput is the capacity of an HPGR with a roll diameter of 1 m, a width of 1 m and a roller speed of 1 m/s. The information obtained from the PPT is introduced into a previously fit linear regression? equation to predict m-dot.

From the parameters required for the specific throughput prediction, the moisture, roller speed, and specific pressing force are selected as targets for the HPGR operation. The specific energy consumption used for the modelling can be obtained directly from the HPGR pilot-scale testing or can be predicted using the database-calibrated methodology. The sample bulk density is measured from the PPT samples. Once the model is developed, the method can be used to predict throughputs for a range of samples (Fig 6).

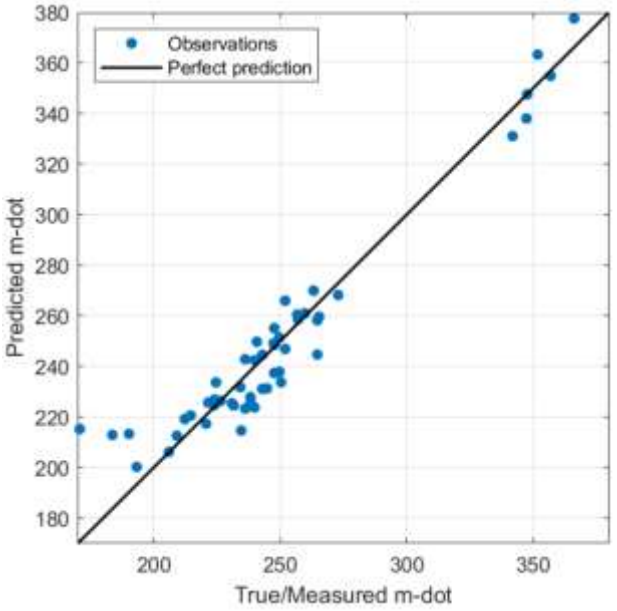

Fig. 6. Specific throughput prediction model prediction results vs measured values for different ore types (Pamparana et al., 2022).

3. Conclusions

Piston press test methodologies described for predicting the HPGR performance encompassing specific energy consumption, particle size reduction, and throughput. The direct calibration, database calibrated, and simulation methods provide a comprehensive framework for understanding and optimizing HPGR operations.

The development of the throughput model represents an important enhancement in HPGR performance prediction. This model, leveraging the outcomes from piston press tests, allows for a nuanced prediction of material processing rates, integrating the complex interplay between energy consumption, material properties, and particle size reduction. The throughput model enhances the ability to design and optimize HPGR circuits more effectively, ensuring not only energy efficiency but also the operational capacity to meet production targets.

The ability to accurately predict HPGR performance parameters from small-scale tests offers considerable benefits in circuit design and operational optimization,

leading to energy savings and improved processing outcomes. This research underscores the importance of integrating experimental data with simulation techniques for enhancing the predictability and efficiency of comminution circuits in the mineral processing industry.

The authors would like to acknowledge Koeppern Machinery Australia for the use of the pilot-scale HPGR equipment at UBC as well as the financial support from Mitacs, Geoscience BC and ANID Becas Chile.

References

Schönert, K., (1988) A first survey of grinding with high-compression roller mills. *International Journal of Mineral Processing* 22, 401–412.

Davaanyam, Z., Klein, B., and Nadolski, S., (2015) Using piston press tests for determining optimal energy input for an HPGR operation. *SAG Conference*, Vancouver, Canada.

Davaanyam, Z. (2015). Piston press test procedures for predicting energy-size reduction of high pressure grinding rolls. *Doctoral dissertation, University of British Columbia*.

Pamparana, G., Klein, B., Bergerman, M.G., (2022) Methodology and Model to Predict HPGR Throughput Based on Piston Press Testing. *Minerals* 12, 1377.

Wang, C., (2021), Development of a comprehensive HPGR model using large experimental data sets. *Doctoral dissertation, University of British Columbia*.

E5: Characterisation of breakage of crystals by aerodynamic dispersion

Wei Pin Goh*, *Saba* Saifoori, *Muzammil* Ali *and Mojtaba* Ghadiri

School of Chemical and Process Engineering, University of Leeds, Leeds, UK

Abstract. In the pharmaceutical industry, particle attrition is of paramount importance as this process could change the size and shape of particles and their crystalline structure, thereby leading to a significant change in the properties of the drug product, affecting its dissolution rate, bioavailability, stability, and processability. Attrition can occur during various stages of drug manufacturing. Understanding and controlling attrition is therefore crucial in ensuring the quality and efficacy of the final product. This study presents a novel approach to characterising the attrition of particles using the aerodynamic dispersion unit of Malvern Panalytical Morphologi G3. The particles are dispersed by an air pressure pulse, causing particle breakage, which is characterised by image processing and analysis. A number of pharmaceutical ingredients are selected for this study. They are dispersed using four different dispersion pressures and the particle impact velocities are estimated using Computational Fluid Dynamics (CFD) and Lagrangian particle tracking method. The breakage propensity is then established by adopting a mechanistic impact breakage model. The findings from this study contribute to the understanding of particle attrition and offer a practical tool for attrition characterisation in the early stages of drug development.

1 Introduction

A wide range of industrial processes involve processing and handling of particulate solids like crystals, granules and agglomerates. Particle breakage may be induced desirably or undesirably, thereby altering particle properties, namely size distribution, shape, surface area, and other physical and chemical attributes, such as dissolution. Breakage by impact is commonly encountered in a wide range of process equipment, such as fluidised beds, cyclones, stirred vessels, and of course in milling operations (Kalman, 2000). In cases that the sample supply is scarce, e.g. early stages of drug development, characterisation of particle impact breakage using a method that requires only a small amount of sample becomes valuable. The current work addresses this topic by a combination of experimental impact testing, using Malvern Panalytical Morphologi G3 disperser and CFD simulations for calculating the particle impact velocity. The objective is to quantitatively characterise the breakability of various crystals due to impact with the walls of the dispersion spool. To this end, crystals of different materials are dispersed by Morphologi G3 at different pressure pulses and their extent of breakage is determined by quantifying the shift in the particle size distribution, analysed using the Morphologi G3 microscope and image analysis system. Then, three-dimensional multiphase computational fluid dynamic simulations of the dispersion chamber of Morphologi G3 are carried out to calculate the particle trajectories and impact velocities induced by the compressed air pulse. The extent of breakage along with the calculated impact velocity of the particles in the instrument are then used to determine the breakability of the test particles. The breakage of lath-shaped crystals has previously been addressed by Goh et al. (2019) and Saifoori et al. (2020). Here we present the outcome of the work on equant particle shape.

2 Methodology

A range of common crystals (sodium chloride, paracetamol and α-lactose monohydrate, see Fig. 1) with equant-shaped morphology are used in this study. The breakage of these crystals is analysed using Morphologi G3 (Malvern Panalytical Ltd, Worcestershire, UK), which has a dispersion system and an optical microscope with a built-in software package used to measure the morphological characteristics of particles. The dispersion chamber of the instrument consists of a dispersion capsule with a spool, into which a small amount of sample (typically a few mm^3) is placed. A pulse of compressed air with adjustable pressure and duration of 20 ms is injected into the dispersion chamber. The particles are then dispersed by the air pressure pulse, as a result of which they impact onto the walls of the dispersion spool causing their potential breakage. They land onto a glass slide placed at the base of the dispersion chamber for microscopy and image analysis. The optical unit then scans across the dispersed sample on the slide, capturing 2D images of the projected view of individual particles lying on their plane of maximum stability. Morphologi G3 software translates the images into a binary format and calculates a range of measures of particle sizes, such as area, circle-equivalent diameter, length, width, aspect ratio, etc.

* Corresponding author: W.P.Goh@leeds.ac.uk

The experiments are carried out at several dispersion pressures in order to impact the particles at different velocities. The extent of breakage R^* is determined by comparing the size distribution curve of the particles dispersed at each dispersion pressure to that of the particles dispersed at 0.5 barg (taken as the reference distribution, i.e. assuming little/no crystal breakage at this pressure pulse). The area of positive difference (in percentage) between the probability density distribution curve of the reference particles and that of the data of interest, when subtracting the former from the latter, can represent the R^* caused by the corresponding dispersion pressure. Ghadiri and Zhang (2002) model is then used to analyse the breakage of the crystals, as shown below:

$$R^* = \alpha \frac{H}{K_c^2} \rho D V^2 = \psi \rho D V^2 \qquad (1)$$

where α is a proportionality constant and ρ is the density of the particle. D denotes a linear dimension of the particle, whereas V, H and K_c represent the impact velocity, the hardness and the fracture toughness of the particles, respectively. ψ ($\alpha H/K_c^2$) is a lumped parameter describing the mechanical properties of the particle that are responsible for plastic deformation and fracture toughness, known as the breakability. This parameter reflects the ease with which the particle breaks. Considering Eq. (1), if R^* is plotted as a function of ρDV^2, a unification of data is expected with the slope of the line indicating ψ. The impact velocity of the feed particles dispersed at different pressures is determined by CFD calculations. The outcome of the experimental work will be presented at the conference.

3 CFD Modelling

Three-dimensional Computational Fluid Dynamics (CFD) modelling method is used with transient, compressible flow assumption to predict gas velocity profiles in the disperser. Turbulence modelling is carried out using scale adaptive simulation method (Ali & Ghadiri, 2017). The continuous and discrete phase equations are solved using commercial CFD software Ansys Fluent (2018). The time step for particles tracking and for the continuous phase is set at 5.0×10^{-6} s. The simulation is run at the specified inlet pressure for 20 ms; thereafter the pulse is stopped by changing the pressure to 0 barg. Details of the CFD modelling methodology and the mesh used in the CFD simulations can be found in a recent work carried out by Ali and Ghadiri (2017), in which they studied triboelectric charging of particles in G3 disperser using CFD modelling. The discrete phase is considered to comprise truncated polyhedral, cubic and tomahawk-shaped particles. The particles are initially placed in the sample well and are dispersed by a pulse of pressurised air. The trajectories of particles are computed by solving the equation of motion of particles considering the drag and gravitational forces. For these particle shapes, the drag coefficient is calculated using correlations given by Ganser (1993). The rotation of particles is not considered. One-way coupling is assumed between the particles and the air, i.e. the air flow influences the trajectories of particles, but the momentum exerted by the particles on the air is ignored.

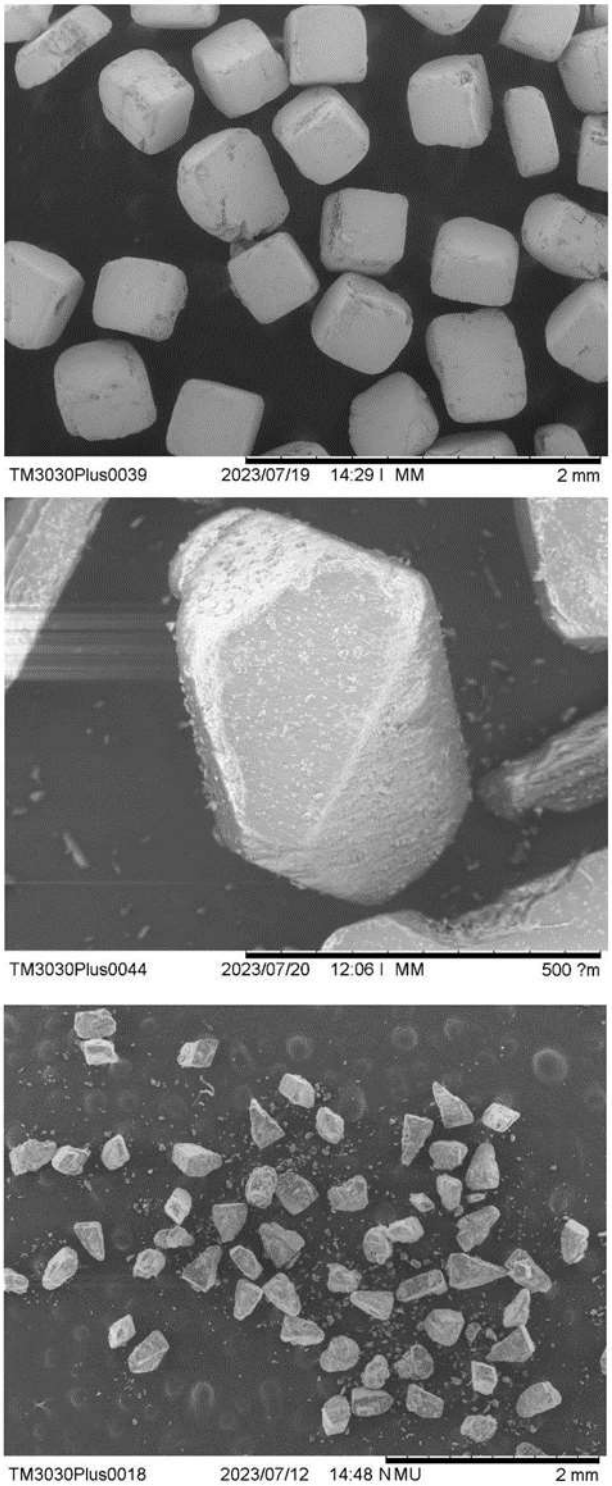

Fig. 1. SEM micrographs of (a) sodium chloride (b) paracetamol and (c) α-lactose monohydrate

The interaction between the particles, i.e. particle-particle collisions is also not considered. In a previous study by Ali and Ghadiri (2017), it was found that the maximum impact velocity of particles in the disperser took place at the wall just above the sample well. For the purpose of predicting the impact velocity, the velocity of

particles colliding with the walls in this region is recorded and the impacted particles are eliminated from the computational domain. To get a statistically representative impact velocity, 1000 particles are tracked for each size. For each case, the simulation is continued until all the particles exit the domain. A general correlation has been developed to predict the impact velocity of equant particles, taking into account of the fluid and material properties.

4 CFD Results

The CFD prediction (lines) of average impact velocity of the three materials, along with the prediction made using the correlation developed (dots) are shown in Fig. 2. There is a general trend of decreasing impact velocity as the particles get bigger in size. Increasing the dispersion pressure increases the impact velocity. Under the same dispersion pressure and particle size, lactose monohydrate particles get accelerated the most, followed by paracetamol and sodium chloride. This difference is due to the combined effect of material density and particle shape. The prediction of the average impact velocity made from the general correlation shows a good degree of agreement with the impact velocity predicted by the CFD. However, there are cases where the correlation developed slightly over/underestimate the impact velocity.

4 Conclusions

A new method has been developed to quantitatively determine the breakability of particles. Application of image analysis and post-processing and manipulation of the raw data allow various size and shape analyses to be conducted, facilitating observation of how particles undergo size reduction. Based on the model of Ghadiri and Zhang together with CFD simulations for calculating particle impact velocity, a breakability index is characterised. The outcome of the analysis for equant particle shape will be presented.

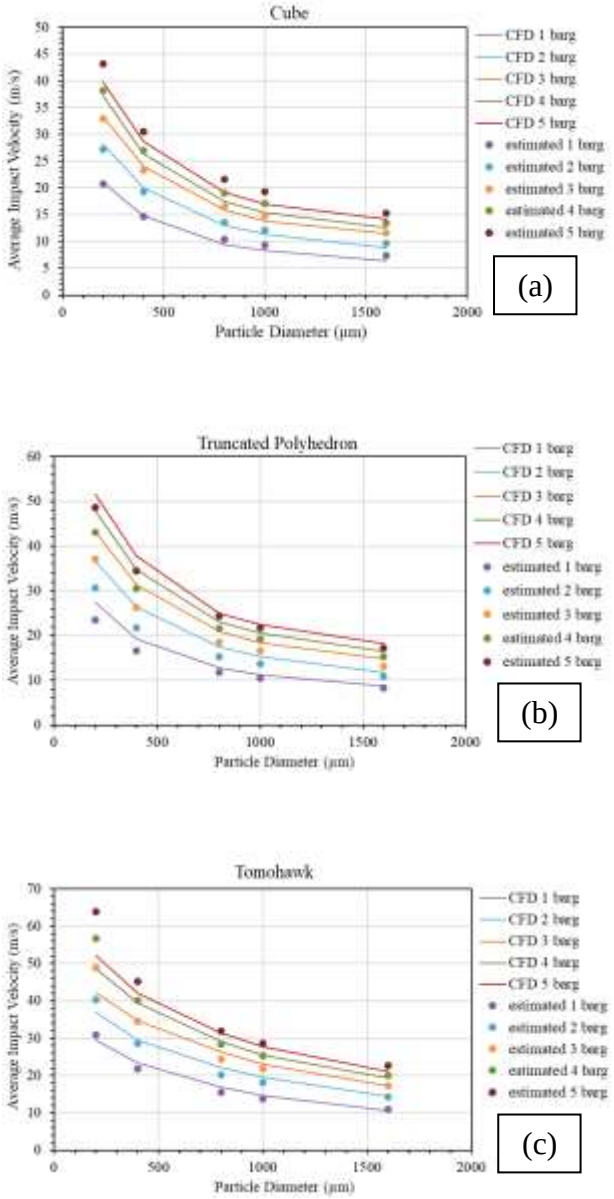

Fig. 2. CFD prediction (lines) and prediction based on the developed correlation (dots) of the average normal impact velocity of (a) sodium chloride (cubic), (b) paracetamol (truncated polyhedral) and (c) lactose monohydrate (tomahawk)

References

Ali, M., & Ghadiri, M. (2017). Analysis of triboelectric charging of particles due to aerodynamic dispersion by a pulse of pressurised air jet. *Advanced Powder Technology*, *28*(10), 2735–2740. https://doi.org/10.1016/J.APT.2017.07.026

Ganser, G. H. (1993). A rational approach to drag prediction of spherical and nonspherical particles. *Powder Technology*, *77*(2), 143–152. https://doi.org/10.1016/0032-5910(93)80051-B

Ghadiri, M., & Zhang, Z. (2002). Impact attrition of particulate solids. Part 1: A theoretical model of chipping. *Chemical Engineering Science*, *57*(17), 3659–3669. https://doi.org/10.1016/S0009-2509(02)00240-3

Goh, W.-P., Ali, M., Sinha, K., Nere, N. K., Ho, R., Bordawekar, S., Sheikh, A., & Ghadiri, M. (2019). Assessment of impact breakage of carbamazepine dihydrate due to aerodynamic dispersion. *International Journal of Pharmaceutics*, *572*. https://doi.org/10.1016/j.ijpharm.2019.118780

Kalman, H. (2000). Particle Breakage and Attrition. *KONA Powder and Particle Journal*, *18*(May), 108–120. https://doi.org/10.14356/KONA.2000017

Saifoori, S., Goh, W.-P. W. P., Ali, M., & Ghadiri, M. (2020). Impact breakage of acicular crystals. *Powder Technology*, *361*, 651–662. https://doi.org/10.1016/j.powtec.2019.11.061

F1: Fine Comminution and Classification, and Spheronization in the Value Chain of Lithium-Ion Batteries

Daniel-Christian Karhoff[1,*], *Fabian* Mertens[1], and *Marc* Giersemehl[1]

[1]NEUMAN & ESSER Process Technology GmbH, Übach-Palenberg, GERMANY

Abstract. Anode graphite micronization and spheronization using a novel technique is demonstrated. The system's primary goal is to accomplish effective micronization and spheronization in two phases at a low specific energy consumption, high yield, and high throughput. The Impact Classifier Mill eXtra (ICX) and the Impact Classifier Spheronizer (ICS) are two novel impact system designs that are intended to reduce size and achieve spheronization. With the NEA Deflector Classifier eXtra (DCX), additional classification steps are implemented to avoid overloading of the comminution and classification apparatuses and overstressing of the product.

1 Introduction

One of the current major concerns of both politics and society is energy transition and commitment for renewable energies. These are currently experiencing a rapid growth, which in turn leads to an increasing demand of electro mobility and thus of lithium-ion batteries, where graphite is used for the manufacturing of electrodes. Despite their appellation, graphite content in a lithium-ion battery is between 10 and 15 times larger than the amount of lithium contained in a battery cell.

To be suitable for the application as anode material in batteries, the purity, the size, and the shape of the graphite have to fulfil certain requirements. The graphite particles should ideally be perfect spheres. The spherical form has the smallest specific area of all possible shapes, leading to a very low flaking propensity and extended battery life due to improved charging properties. Furthermore, the spherical shape leads to a high tap density and thus to a high energy density of the cell.

2 Design Approach

The overall development goal for the NEUMAN & ESSER spheronization system was to increase both yield and throughput in comparison to conventional plants, and to offer a system that can easily be adapted to different final product requirements and offers an easy scale-up. The resulting NEA system for the spheronization comprises merely two units. The micronization occurs in the NEA ICX (Impact Classifier Mill eXtra) with an internal dynamic air classifier. The actual spheronization is conducted downstream of the NEA ICX in a NEA ICS (Impact Classifier Spheronization). Both machine types are available in various sizes offering a suitable plant size for any required output capacity.

Superfine comminution requires increased grinding intensity; therefore the grinding zone geometry was designed accordingly. The size of the final product is determined by the intensity as well as the frequency of the mechanical stress during the grinding process. These factors are both strongly influenced by the fluid dynamics in the mill [1] [2] [3].

The same applies to the development of the NEA ICS for spheronization. Grinding intensity must be adjusted carefully to ensure shaping within as few internal circulations as possible, without overstressing the product.

* Corresponding author: daniel.karhoff@neuman-esser.de

Figure 18: Impact Classifier Mill Extra ICX

The routing of the particles from the grinding zone towards the classifier wheel is of the same importance: The ground material must be distributed homogenously to the classifier wheel flow cross-section.

For good classification results, both the radial and tangential velocity component of the process gas have to correspond to the desired cut condition at the outer circumference of the classifier wheel. The classification efficiency strongly depends on the inflow conditions of the dynamic classifier wheel [4] [5] [6] [7] [8]. The guide ring design takes this requirement into account. Furthermore, the classifier wheel was designed for superfine cuts. The design principle of both the classifier wheel and the guide ring correspond to the design of the NEA Deflector Classifier Extra (DCX) [9], and the NEA Guide Ring Classifier (GRC) [10].

Production lines include the classifier NEA DCX. With additional classification steps in the production line, both residual dust as well as final product can be separated from the particle stream to avoid overloading the comminution and spheronization apparatuses, and overstressing of the product. This leads to an increase in final product yield.

Figure 19: Deflector Classifier eXtra

3 Results

The NEA spheronization system has been tested extensively in the NEA test center and successfully put into commercial operation. Key parameters determining the final product quality are particle shape (e.g., determined by flow cytometry), tap density, particle size distribution, combined with high yield and throughput. All of those can be adjusted by applying appropriate settings of the process parameters.
Spheronized product with a d_{50} between 5 µm and 20 µm and tap densities > 1 g/cm³ can be produced reliably at yields of 55 %.

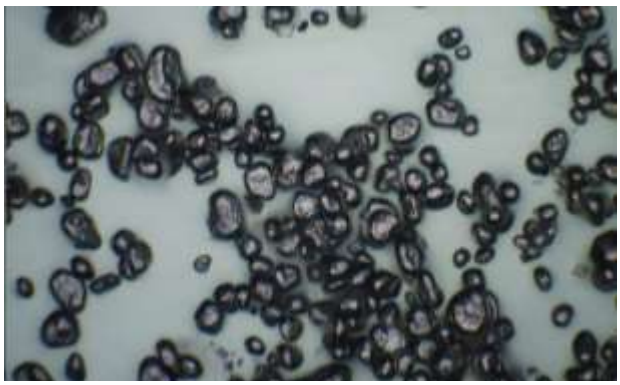

Figure 20: Shaped Natural Grafite

Figure 21: Synthetic graphite precursor; green/calcined coke

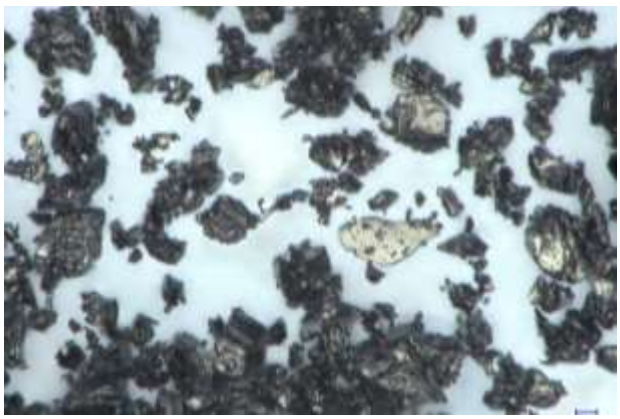

Figure 22: Hard carbons from biomass, suitable for Na-Ion battery

References

[1] P. Toneva, K.-E. Wirth and W. Peukert, “Grinding in an air classifier mill — Part II: Characterisation of the two-phase flow,” *Powder Technology,* vol. 211, no. 1, pp. 28-37, 2011.

[2] J. Galk, “New Comminution Plant for the Production of Narrow Particle Size Distributions – The Link between Laboratory Mill and Production Plant,” *Powder Handling & Processing,* vol. 12, no. 2, pp. 204-205, 2000.

[3] M. Giersemehl and G. Plihal, “Fine Grinding System with Impact Classifier Mill and Cyclone Classifier,” *Powder Handling & Processing,* vol. 11, no. 3, pp. 269-279, 1999.

[4] J. Galk, Feinsttrennung in Abweiseradsichtern, Köln: Botermann und Botermann, 1996.

[5] J. Galk, W. Peukert and J. Krahnen, “Industrial classification in a new impeller wheel classifier,” *Powder Technology,* vol. 105, no. 1-3, pp. 189-189, 1999.

[6] K. Leschonski, “Classification of particles in gases,” IFPRI-Report, Clausthal, 1981.

[7] K. Leschonski, “Das Klassieren disperser Feststoffe in gasförmigen Medien,” *Chemie Ingenieur Technik 49 (9),* vol. 49, no. 9, pp. 708-719, 1977.

[8] H. Rumpf and K. Leschonski, “Prinzipien und neuere Verfahren der Windsichtung,” *Chemie-Ingenieur-Technik 39,* vol. 39, no. 21, p. 1231–1241, 1967.

[9] D.-C. Karhoff, F. Mertens and M. Giersemehl, "Development of a Deflector Wheel Classifier for Fine Classification," in *16th European Symposium on Comminution & Classification*, Leeds, UK, 2019.

[10] D.-C. Karhoff, F. Mertens and M. Giersemehl, "Development of a Guide Ring Classifier for Fine Classification," in *17th European Symposium on Comminution & Classification*, Toulouse, FR, 2022.

F2: Modelling and flow sheet simulation of comminution and separation processes for Li-ion battery recycling

Franziska Punt[1,*], *Harald* Zetzener[1], and *Arno* Kwade[1]

[1]Institute for particle technology, Technische Universität Braunschweig, Braunschweig, Germany

Abstract. Li-ion batteries can be recycled in a number of different ways. Flow sheet simulations are a good way to efficiently compare these different routes. These simulations can help to investigate the unit processes and the interdependencies in the process chain. The first step in simulation is to develop models for the different unit processes. These models must include the complex material behaviour of the shredded battery materials. For example, materials in air classifiers cannot be treated as compact particles. In addition, the primary particle size distribution of the individual materials within the battery prior to initial shredding in the shredder is not known. The models developed, which take these factors into account, can then be used to perform process chain simulations. These simulations can show the effects of parameter variations on mass recovery and energy requirements, both for single unit processes and for linked process chains.

1 Introduction

The recycling of Li-ion batteries becomes increasingly important due to the rising demand of electric cars and the request for more independence from global raw materials markets. Therefore, various recycling process routes have already been established in industry. Especially for the recycling of end-of-life batteries, there are several ways to recover the valuable materials via mechanical, hydrometallurgical or pyro-metallurgical process routes. The processing via a mechanical process chain contains several comminution and separation steps, which can be varied. One way of recycling Li-ion batteries is based on the LithoRec process (Kwade & Diekmann, 2018) shown in Fig. 1. First, the cells or modules are fragmented in a shredder. The shredded battery fragments are than dried in a mixing and drying unit bevor the heavy parts of the cells such as the casing are removed using a zig-zag-separator. The remaining fragments consist mostly coated and uncoated electrode foils as well as separator foils and the detached black mass. These fragments are stressed a second time to increase the yield of black mass in the subsequent screening step. A cutting mill or an impact mill can be used for the second comminution. At the end of the process chain the separator foils are removed from the copper and aluminum foils using a second air classification.

A high process understanding and a large database are important to optimize this process chain and compare it with other recycling routes. To get this large database, the dynamic flowsheet simulation is beneficial. With this simulation it is possible to investigate the influence of several operating parameters of the single processes as well as the influence of these parameter changes on the subsequent processes and finally on the mass recovery of the different battery materials and the energy consumption.

2 Modelling

Before such dynamic flowsheet simulations can be performed, the individual processes have to be modelled first. In this work, simulation models for the shredder, zig-zag-sifter and cutting mill were developed and adapted to the material system. These models can be used to determine the mass recovery of each material. In addition to the particle level models described below, energy measurements were taken for each process to model the influence of parameter variations on energy requirements.

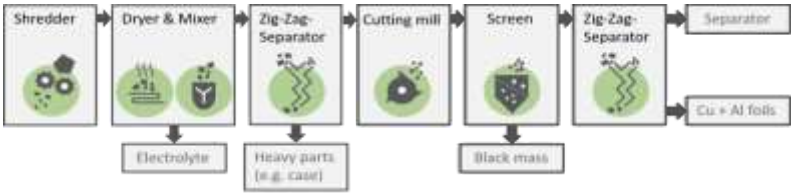

Fig. 1. Mechanical process chain based on LithoRec

* Corresponding author: franziska.punt@tu-braunschweig.de

2.1 Shredder

The shredder model was first developed at a lab scale by using a cutting mill instead of a real shredder. In the cutting mill the cylindrical cells were fragmented into foil fragments and metal parts. Since the process starts with shredding entire battery cells, the primary particle size distribution of the battery materials inside is not known. Therefore, the model is based on a Weibull-Distribution, which calculates the resulting particle size distributions.

$$Q_3(x/d_s) = 1 - \exp(-(\lambda*(x/d_s))\hat{}k) \qquad (1)$$

These Weibull-Distributions have two material specific parameters λ and k. Furthermore, it includes the bottom screen size of the mill. This allows calculating the resulting particle size distribution for each material component depending on the used bottom screen size. In Fig. 2 these results are shown for Al foil compared to the experimental data. In the following, this model should be transferred to a shredder in pilot scale.

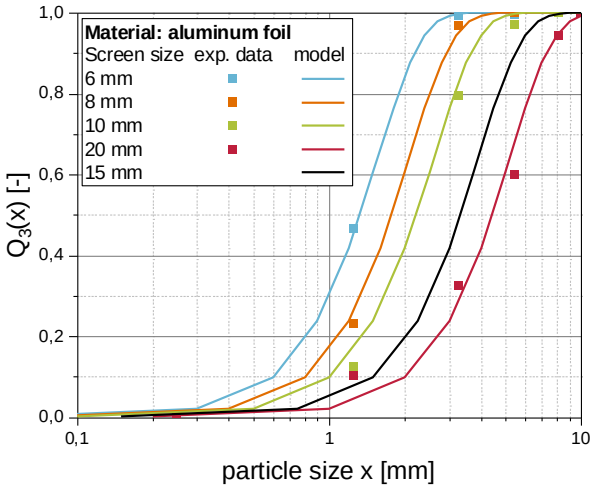

Fig. 2. PSDs for Al foil, experimental data and Weibull-model (Punt et al., 2023)

2.2 Cutting mill

In contrast to the shredder, the primary particle size distributions of the second comminution step are known. Therefore, the model of the cutting mill for the second comminution is based on a population balance model.

$$dm_i/d_t = \sum S_j * b_{ij} * m_j - S_i * m_i - P_s * m_i \qquad (2)$$

This population balance describes the particle comminution using a breakage function and a selection function. These functions were determined based on experimental data and a comminution matrix for each input material. The input materials for the second comminution are mainly Cu foil (coated and uncoated), Al foil (coated and uncoated) and separator foil. Besides the particle breakage, the material passage through the bottom screen also influences the population balance. The probability of a particle to leave the mill in a certain time interval is taken into account by the parameter P_s. The calculated particle size distributions for Cu foil using this model compared to the experimental data are presented in Fig. 3 for a bottom screen size of 8 and 10 mm.

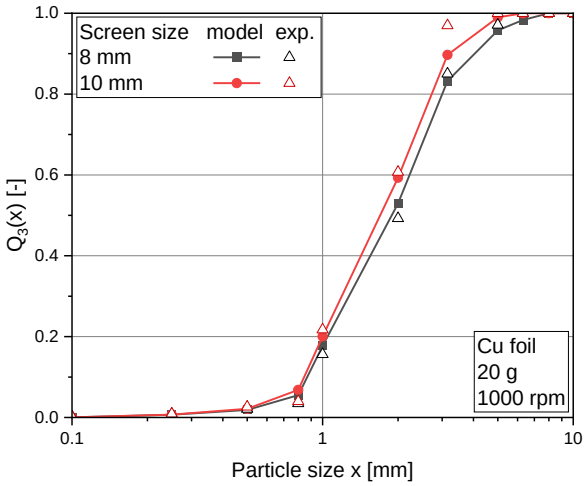

Fig. 3. PSDs for Cu foil, experimental data and population-balance-model

2.3 Zig-zag-sifter

The zig-zag-sifter model is based on the literature approach by Tomas and Gröger (2000). However, this model cannot be applied directly to the material system presented here. In this model, compact particles are considered. However, the present battery particles are made of foils, which are deformed during the processing. Thereby complex particle shapes with inclusions of air and other materials like black mass arise. To fit this literature approach to the present material system, the parameter β was added to the separation function.

$$T(x) = 1/\{1 + (\beta * (\dot{V}_F/\dot{V}_C))\hat{}[(1 - (x/x_T)^{\alpha})*z]\} \qquad (3)$$

The separation function for particles smaller than 10 mm could be approximated well to the experimental values. However, the experimental data also show that for larger particles the probability to end up in the coarse fraction decreases in contrast to the course of the separation curve. Therefore, the parameter β cannot be constant. A decreasing β with increasing particle size leads to a separation function similar to the experimental data (Fig. 4).

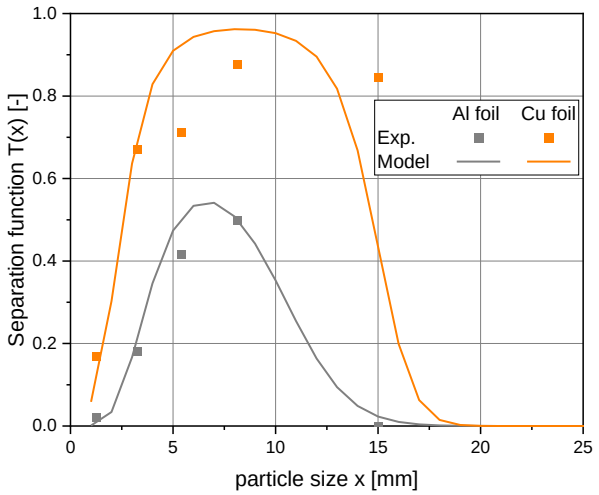

Fig. 4. Separation function for Cu and Al foil

3 Simulation

3.1 Flowsheet simulation

In this work, the dynamic flowsheet simulation software Dyssol was used. With this software, complex solid processes and process chains can be simulated. In Dyssol, it is possible to use models that have already been implemented, such as the Plitt model for sieving, as well as individually developed models. Therefore, Dyssol is well suited for the considered process chain, since standard literature models cannot be used in many cases due to the complicated material system.
During the simulation, the various sub processes are connected using material and energy streams (Skorych et al, 2017). In the context of mechanical recycling the different battery materials, have to be simulated for several interlinked comminution and separation processes. This means that changes in the boundary conditions and parameters of the first processes, such as varying the feed mass flow of the shredder, will affect the subsequent processes.

3.2 Simulation results

The presented models can be used to simulate the individual processes as well as process chains. The simulation of single processes helps to optimize the corresponding process regarding the mass recovery and energy consumption. By linking the processes, these two factors can also be optimized by varying the parameters of the previous processes. This can be shown by varying the bottom screen size of the cutting mill during the second comminution. The change in screen size directly affects the mass recovery in the subsequent screening step. This is shown in Tab. 1. The smaller the screen size, the higher the mass recovery of black mass. However, it can also be seen, that the smaller screen sizes lead to a higher energy demand during the cutting process. The change in screen sizes does not only influence the directly following process, but also the separation of the separator foil from the electrode foils in the last air classification depends on the particle size distribution. The smaller the particle sizes, the higher the probability that the electrode foil particles are also been carried out in the light fraction with the separator foils.

Table 1. Influence of screen size on specific energy and black mass recovery

Screen size	Specific energy	Black mass recovery
6 mm	4.61 Wh/kg	43 %
8 mm	2.43 Wh/kg	35 %
10 mm	2.27 Wh/kg	26 %
20 mm	1.22 Wh/kg	23 %

Summary

The mechanical recycling of Li-Ion batteries consists of several comminution and separation steps. Due to the complicated material behaviour, it is not possible to use literature models for most process steps. Thus, models must be developed or existing models must be adapted to the material system. Based on these models, corresponding simulations can then be performed for the mechanical process chain. This shows the interdependence of the different processes, for example the change in black mass recovery depending on the bottom screen size of the cutting mill.

The project on which this report is based was funded by the Federal Ministry of Education and Research (Germany) under the funding code 03XP0331A. The author is responsible for the content of this publication.

References

Kwade, A. and Diekmann, J., (2018) Recycling of Lithium-Ion Batteries. *Springer*, Cham, Switzerland.

Punt, F., Doose, S., Böttcher, A., Breitung-Faes, S., Kwade, A., (2023) Modeling and Flow Sheet Simulation of Selected Mechanical Recycling Processes for Li-Ion Batteries. *Chem. Ing. Tech.*, 95, No. 1–2, 59–67.

Tomas, J., Gröger, T., (2000) Verfahrenstechnische Bewertung einer mehrstufigen Querstrom-Aerosortierung mineralischer Stoffe, Otto-von-Guericke-Universität Magdeburg, Magdeburg.

Skorych, V., Dosta, M., Hartge, E.-U., Heinrich, S., (2017) Novel system for dynamic flowsheet simulation of solids processes, *Powder Technol.,* 314, 665–679. DOI: https://doi.org/10.1016/j.powtec.2017.01.061

F3: Liberation evaluation for compressive comminution of synthetic lithium-ion-battery slag

Sima Hellmers[1*], *Marko Ranneberg*[2], *Somayeh Hosseinhashemi*[1], Harald Zetzener[1] and *Arno Kwade*[1]

[1]Institute for Particle Technology, Technical University of Braunschweig, Braunschweig, Germany
[2]Federal Institute for Geosciences and Natural Resources, Hannover, Germany

Abstract. The rising demand for raw materials for lithium-ion batteries emphasizes the importance of recovering from secondary sources, mainly due to geopolitical factors. Thus, lithium recovery from recycling slags through optimized comminution and hydrometallurgical processes has gained high significance. The milling processes and their parameters affect the particle size and phases appearing on the surface, influencing the efficiency of the subsequent processes. This study focused on compressive stress in a double-roll mill, investigating the impact of varied milling parameters on the breakage and liberation of γ-lithium aluminate. The investigated parameters were rotational speed, gap size of the rolls, and the feed mass flow and their influence on the phases appearing on the surface of milled particles. The effect of milling parameters on breakage and distribution of different phases was investigated using SEM-Mineral liberation analysis. The results showed that decreased gap size produced finer particles with narrow distribution. The rotational speed lower than the particles' falling speed caused the formation of particle beds. The multiple stressing events from these particle beds resulted in finer particles with broader distribution. In conclusion, varying milling parameters caused different breakage mechanisms, producing particles of varying sizes and the appearance of diverse phases on the surface, affecting separation.

1 Introduction

One possible recycling route for lithium-ion batteries involves pyrometallurgy, offering adaptability, substantial processing capacity, and compatibility with various battery types. However, lithium often ends up in slag, leading to its loss for further use in batteries. Recovering lithium from the slag is challenging due to low efficiency and costly beneficiation processes. A promising approach involves using the engineered artificial mineral (EnAM) concept to enrich lithium in a synthetic slag phase, γ-$LiAlO_2$, which can be treated as a new source of lithium (Wittkowski et al. 2021). Comminution is a critical step in preparing these new synthetic ores for hydrometallurgical processes.

Dry grinding is chosen for its efficiency and environmental benefits, and a double-roll mill is preferred for its ease of handling and low contamination due to the lack of use of grinding media or additives.

Understanding particle breakage and strength is crucial for successful grinding events with specific energy as an influential factor. The specific energy in a double roll mill, $E_{m,}$ is calculated using torque measurements and the sample mass m_p. Böttcher et al. (2021) calculated and subtracted a non-active torque as a no-load component from the measured torque M. The specific energy is shown in equation 1, with m_p being the particle's weight.

$$E_m = \frac{2\pi n_{rolls} \int_{t_0}^{t_1} (M - M_0) dt}{m_p} \quad (1)$$

Deep knowledge of milling parameters becomes essential for effective separation and recovery, reducing energy consumption and costs. The double-roll mill proves to be a practical choice for achieving multi-level grinding with sieving steps influencing the subsequent flotation processes.

2 Material and methods

2.1. Synthetic slag

The material used in this study was a synthetic slag produced by the Institute of Process Metallurgy and Metal Recycling (IME) in Aachen, Germany. The feed material for this slag was a combination of lithium, aluminium, calcium, silicon, and manganese oxides, heated to 1500°C in an electric furnace using clay-graphite crucibles. A modified thermodynamic model from Li et al. (2023) with a controlled cooling rate of 25°C/h and a 6-hour holding time at 1150°C was employed.

Table 1. Rietveld quantitative phase analysis of the slag.

$Ca_2Al_2SiO_7$	γ-$LiAlO_2$	Li_2MnSiO_4	amorphous and other phases
43	27	6	24

* Corresponding author: s.hellmers@tu-braunschweig.de

The optimized production of this slag resulted in the formation of over 80% of the lithium content into γ-$LiAlO_2$ as the final phase. Table 2 presents a comprehensive mineralogical composition analysis of the slag.

2.2. Comminution

This research focused on milling slag particles, specifically those under 500 µm. The process involved initial crushing in a cone crusher, followed by extensive grinding in a double-roll mill to achieve the desired particle size. Four distinct fractions were obtained through sieving, ranging from 32-100 µm to 350-500 µm. For a rigidly mounted double-roll mill critical milling parameters were investigated: gap size, rotational speed, and mass flow.

Gap size variations were examined within the range of 30% to 60% of the measured x_{50} of each fraction. The study excluded gap sizes larger than 60% and smaller than 30% based on prior experiments demonstrating minimal grinding or mill malfunctioning, respectively. Adjustments for the largest fraction (350-500 µm) were limited due to the maximum possible gap size of the rolls and practical considerations.

Rotational speed adjustments were explored at approximately 35% slower and 35% faster than the falling velocity of the tested fraction, with gap size maintained constant. The mass flow was set to a steady feed of the material.

The last parameter studied was the mass flow of the feeding process. Initial feeding rates were adjusted for each fraction to ensure a uniform material flow. Mass flow variations of 20% lower and 20% higher than the set mass flow were implemented, modifying the frequency of the feeding unit. Table 2 and table 3 present some of the applied parameters.

Table 2. Variation of gap sizes for the fractions of the slag.

Fraction	32-100	100-200	200-350	350-500
x_{50} of reference (µm)	61	156	299	482
Gap size (µm)	18	47	90	140
	25	62	120	160
	30	78	150	180
	37	94	180	-

Table 3. Constant milling parameters with gap size variations.

Fraction	32-100	100-200	200-350	350-500
x50 (µm)	61	156	206	358
Rotational speed (m/s)	0.7	1.0	1.5	2.0
Mass flow (g/s)	0.04	0.18	0.25	0.40

2.3. Analytical methods

The study employed a Mastersizer 3000 laser diffraction particle size analyzer by Malvern Panalytical to measure the particle size distribution for each experiment. After each grinding process, measurements were performed in water, and the x_{50} values were used to examine the correlation between specific energy and particle size.

To understand the samples' phase distribution, electron microscopic analyses were conducted using a Fei MLA 650 F Quanta FEG ESEM under high vacuum conditions at 15-25 kV. A backscattered electron images (BSE) detector and two EDS (Energy Dispersive Spectroscopy) detectors were applied. The results were analysed with the SEM-MLA software, enabling automated quantitative analysis of the phases on the surface.

3 Results and discussion

3.1. Milling parameters

The particle size resulting from grinding is a function of material and mill properties. Therefore, changing the mill settings can produce different products.

3.1.1. Gap size

Gap size variations were tested across the four fractions, and results showed a consistent trend of coarser particles with increased gap size. The contact angle between the particles and the rolls' surface varied with the application of different gap sizes, influencing the applied forces on the particles. This, in return, affected the specific energy and degree of grinding. Figure 1. shows the particle size distribution of one of the fractions with four variations of the gap size.

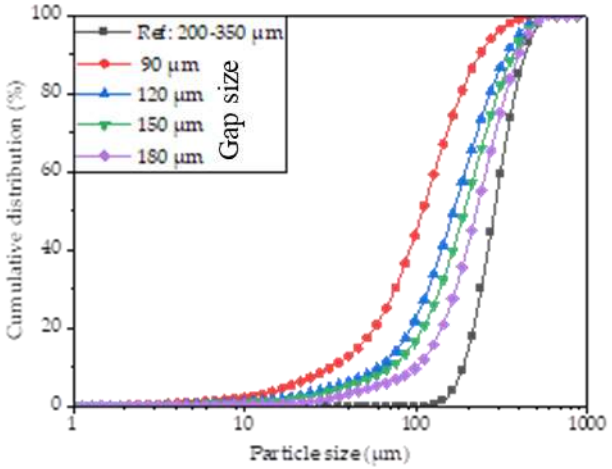

Fig. 1. Particle size distribution for different gap sizes.

The findings show that smaller gap sizes led to higher grinding degrees but at a higher specific energy. This aspect emphasized the importance of understanding the relationship between particle size and the specific energy to minimize energy consumption in comminution processes by optimizing the milling parameters.

3.1.2. Rotational speed of the rolls

The rotational speed of the rolls was studied at different speeds relative to the falling speed of particles. Findings revealed that decreasing roll speed produced finer

particles, while exceeding particle falling speed resulted in coarser milling products. Slower rotation allowed particle accumulation between the gap and surface of the rolls. The particles in the formed particle bed underwent multiple compression events before falling through the gap. The stressing events also influenced the specific energy consumption negatively. The study highlighted the intricate interplay between rotational speed, particle breakage, and energy consumption.

3.1.3. Mass flow of the feed

The investigation of variation of feeding rates variations indicated that, while x_{50} values did not significantly affect particle size in the 32-350 µm fractions, milling time and energy varied intensely. Lower feeding rates showed lower forces during the grinding. This could indicate fewer particles available on rolls simultaneously. Accordingly, higher rates showed higher forces in the load line, which could be due to the formation of a particle bed for a short time. It should be mentioned higher feeding rates could result in higher absolute energy consumption due to friction; therefore, grinding with higher feeding rate was inefficient. Remarkably, despite similar x_{50} values for different feeding rates in the same fraction, comparing x_{10} and x_{90} values revealed differences, indicating potential protective effects of fine particles in the bed.

In conclusion, the study demonstrated that gap size and rotational speed were crucial factors influencing particle size distribution and specific energy, while mass flow variations exhibited subtler effects.

3.2. Specific energy

In this study, manipulating milling parameters, such as gap size and rotational speed, led to production of finer particles by increased specific energy across all investigated fractions. The critical factor influencing specific energy was identified as the degree of grinding (ratio of feed to product particle size); a higher value of this parameter resulted in a higher specific energy consumption. For instance, with a gap size of 140 µm, the degree of grinding (Z) was 3.5 for the 350-500 µm fraction. This value was 1.4 for the 32-100 µm fraction with a gap size of 40 µm, both pointing to the highest specific energy in their respective fractions. The high degree of grinding in the coarser fractions led to generally high specific energies, however had a more efficiency in energy utilization. With decreasing the fraction size, this value was reduced. Thus, lower specific energy in products with the same x_{50} values.

Another noteworthy finding in the grinding process was the observed limitation in further grinding for particles with x_{50} smaller than 40 µm. This is presented in Figure 2 with variations of milling parameters in different fractions. Increasing the specific energy did not significantly contribute to further grinding in this size range. Based on these results, to minimize specific energy while maintaining the target size of below 50 µm, it is recommended to adjust the gap size to 40% of the x_{50} of the input fraction for coarser particles (above 100 µm) and avoid the formation of a particle bed leading to higher specific energies. For finer fractions (under 100 µm), it is suggested to use a wider gap size with a lower rotational speed to leverage the benefits of multiple stressing in a particle bed.

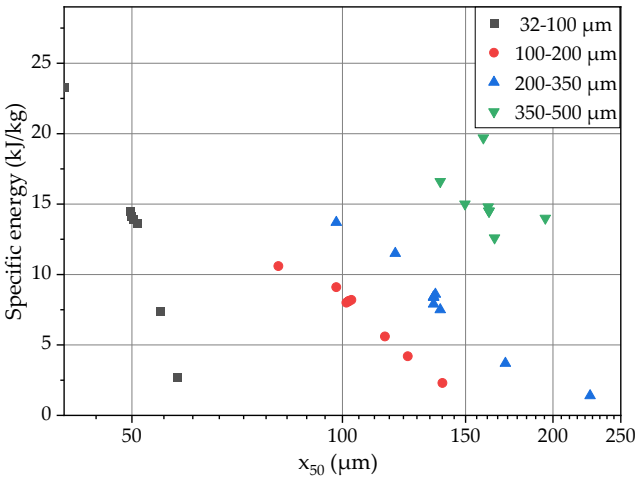

Fig. 2. Correlation of x_{50} in grinding products with specific energy at various milling parameters

3.3. Mineral liberation analysis

A comparison of SEM-BSE and SEM-MLA was conducted to better understand the breakage in different fractions under various parameters. The BSE analyses were used to detect the cracks and fractures appearing on the surface of the milledparticles to predict if the breakages were formed randomly or if they were dominated by the milling and material properties. Figure 3 shows a sample of gap variation from 200-350 µm fraction.

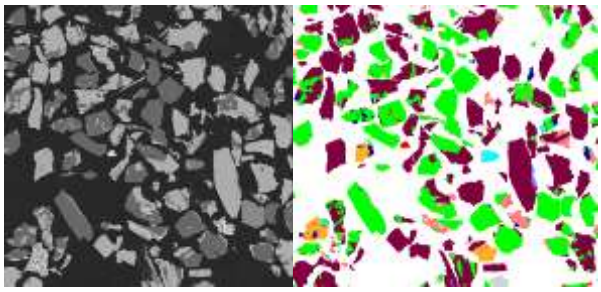

Fig. 3. Comparison of SEM-BSE and SEM-MLA analysis.

From the SEM-MLA analysis, the phases on the surface could be studied. It was possible to find the settings where more γ-lithium aluminate was exposed on the surface. This was especially important as a flotation efficiency factor in separating the target phase, γ-lithium aluminate, from the gangue material, gehlenite, in this slag.

4 Conclusion

The comminution process's design has a key role in minimizing waste and energy consumption in hydrometallurgical processes, especially in optimizing

froth flotation for separating lithium-rich phases from silicate matrices in LiB-slags. Therefore, this study focused on understanding the relationship between milling parameters of a double-roll mill and the breakage in particles below 500 µm. Key findings and recommendations are:

Gap size: Decreasing gap size reduced particle size but increased specific energy, impacting finer fractions more significantly. Further exploration is needed to understand the relationship between grinding degree, influenced by gap size, and specific energy applied in several multiple stressing events to reach a predefined particle size and optimizing the energy utilization.

Rotational speed: Adjusting rotational speed to speeds below the falling speed resulted in the formation of a particle bed, and thus, reducing particle size. Matching falling speed to rolls' speed in coarser particle milling is advised, while lower speed and particle bed formation enhance comminution efficiency for finer particles.

Mass flow: Changes in mass flow did not notably impact particle size but negatively influenced throughput. Therefore, maintaining consistent material feed is preferable.

Qiu, et al. (2024) showed the best flotation γ-lithium aluminate formed in this slag was achievable for particles finer than 32 µm. To reach this particle size with an optimized comminution, understanding the relationship between the number of grinding events, degree of grinding, and cumulative specific energy is crucial for optimization.

References

Wittkowski, A., et al., 2021. Speciation of Manganese in a Synthetic Recycling Slag Relevant for Lithium Recycling from Lithium-Ion Batteries. Metals, 11 (2), 188.

Böttcher, A.-C., et al., 2021. A rigidly-mounted roll mill is used as a breakage tester for characterizing acceptable particle breakage. Powder Technology, 383, 554–563.

References

Li, H., Ranneberg, M., and Fischlschweiger, M., 2023. High-Temperature Phase Behavior of Li2O-MnO with a Focus on the Liquid-to-Solid Transition. JOM, 75 (12), 5796–5807.

Qui, H., et al. 2024. Valorisation of Lithium Containing Slags from Pyrometallurgical Recycling Route of Spent LIBs: the Enrichment of γ-LiAlO2 Phase from Thermodynamic Controlled and Modified Slags. Mineral processing technology (submitted).

F4: Recycling of composite components made of metal and polymers

Sandra Boekhoff[1,*], *Harald* Zetzener[1], and *Arno* Kwade[1]

[1]Institute for Particle Technology, TU Braunschweig, Volkmaroder Str. 5, 38104 Braunschweig, Germany

Abstract. In this work, the comminution of metal-polymer composites is investigated regarding the influence of the joining principles of the composites. Therefore different types of joining processes are used to manufacture a component out of polymer and metal. The components are crushed at different temperatures in an impact mill and in a hammer mill to determine the influence on the degree of digestion. The polymers Polypropylene and Polyamide 6 are compared. It can be seen, that different materials lead to a different comminution behaviour and the hammer rotor leads to better results in this case than the impact rotor of the mill. In addition the results show that the joining process of composite components influence the crushing results and a force closure is preferred for a successful recycling.

1 Introduction

The focus in battery recycling is currently on high-quality cell materials such as the black mass. However, numerous construction materials such as steel and aluminium alloys, copper and different polymers in the immediate vicinity of the battery cell, are processed in large quantities. Despite their sometimes low unit costs, these add-on parts, such as connector strips or connecting components, are also recyclable materials in the recycling process, containing a metal insert and a polymer housing. The connection between both materials can be made by form-fit, force-fit or material-fit. The connection makes it difficult to recycle the components. In order to be able to recycle the polymer components, the different materials must be completely separated from each other and sorted by type.

In order to separate the metal a break at the metal-polymer phase interphases is ideal. Moreover a brittle fracture is favoured. To achieve a brittle fracture, low temperatures can be used as in the cryogenic cable recycling (Martens, Goldmann, 2016). Through the lower temperatures, the mechanical properties change and polymers behave more brittle as Young's modulus and stiffness increases (Shrivastava, 2018).

The aim for this work is to figure out how different joining processes influence the comminution of composite components.

2 Materials and Methods

2.1 Materials

For the recycling of composite components, demonstrator components have been designed and manufactured. It is possible to produce them with form closure and force closure mechanisms. Figure 1 shows the three variants which were used in this work.

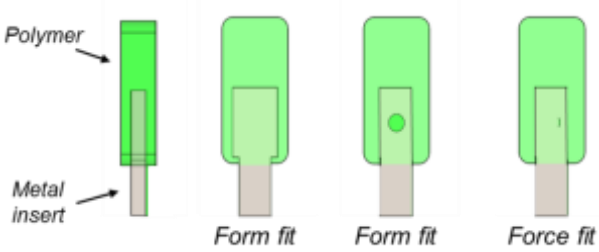

Fig.1. Demonstrator component with different joining processes

The first mechanism is the form fit connection which was used in two different ways. For the first variant, the form fit was achieved through an undercut in the metal insert; for the second variant, a hole in the metal insert was used to create the form fit. A straight metal piece was used to create a force fit, so that only frictional forces keep the connection (variant 3).

The polymer materials used are Polypropylene (PP) and Polyamide 6 (PA6). The used metal for the insert is steel, differently shaped with undercuts or holes, as in Fig. 1. The component has a dimension of 35 mm*12 mm*3.5 mm. The material of the metal insert is commercially available steel.

2.2 Methods

2.1.2 Mechanical comminution

The samples were stressed in a impact/hammer mill from Hazemag. Two different types of rotors were used. Fig. 2

* Corresponding author: s.boekhoff@tu-braunschweig.de

shows the hammer rotor (left) and the impact rotor (right). The material is stressed differently and therefore, different results can be expected.

Fig. 2. Hammer rotor and impact rotor used in the mill

Some polymer samples were pretreated before comminution to see how the result could be influenced. The comminution of the references took place at an outside temperature of 10°C. As a pretreatment, liquid nitrogen was used, to cool the samples down to -90°C.

2.1.2 Presentation of the results

After comminution, the metal and the polymer fraction were weighed to calculate the degree of digestion. It is determined as follows:

$$D = m_D / m_T * 100 \qquad (1)$$

with the degree of digestion (D), the total mass (m_T) and the digested mass (m_D). Therefore, a degree of 100% means that the different materials are fully separated from each other. This value is calculated here to compare the comminution results of the different joining processes.

3 Results

The different rotors used led to different comminution results with the demonstrator component. Figure 1 shows the results for the material PP and a comminution temperature of 10°C. The degree of digestion is shown for the different joining processes.

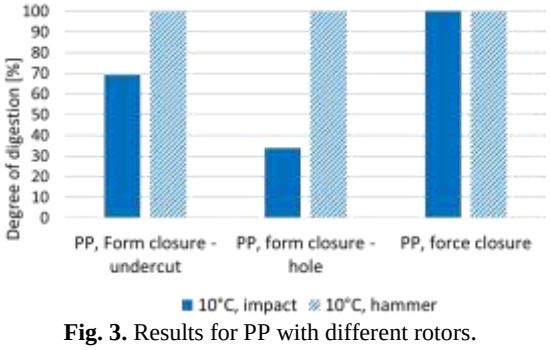

Fig. 3. Results for PP with different rotors.

The comminution with the hammer rotor leads to a complete separation of metal and polymer for all three joining processes. If we look at the comminution results with the impact rotor, there are differences regarding the degree of digestion. The force fit connected sample also reached 100% separation with the impact rotor. Comminution of the form fit connected samples shows, that polymer remained at the metal insert. The most difficult was the form closure through a hole in the metal insert. The nesting here was too strong that the polymer could not be released from the hole and the strength of the bond was too strong. Best results can be achieved with the hammer rotor; using the impact rotor shows that force fit connected composites are the best for recycling. Liquid nitrogen was used to change the mechanical properties of the polymer to increase the degree of digestion. The components were cooled down to -90°C before feeding into the mill. The following figure shows the results for the form fit connected composites trough an undercut, ground with the impact mill to see a difference.

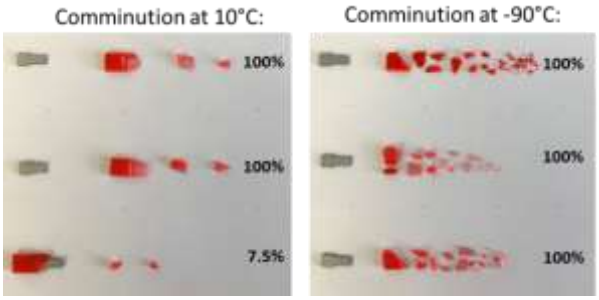

Fig. 4. Pictures of the ground material **at 10°C and -90°C**

Two of the three samples ground at 10°C could be completely separated. The third sample only has a degree of digestion of 7.5%. With the cooling of the samples the degree of digestion increased. For all three samples the comminution led to a ful separation of metal and polymer.

Cooling below the glass transition temperature led to a brittle behaviour of the polymer. Figure 2 also shows, that there are more and smaller polymer particles at a comminution at -90°C. The brittle behaviour of the polymer leads to a more uniform grain spectrum, which may be positive considering the flow behaviour.

In order to compare this results with another polymer, the same samples were manufactured with Polyamide 6 instead of Polypropylene. Figure 3 shows the result of the comminution at a temperature of 10°C, using the hammer rotor and the impact rotor of the mill.

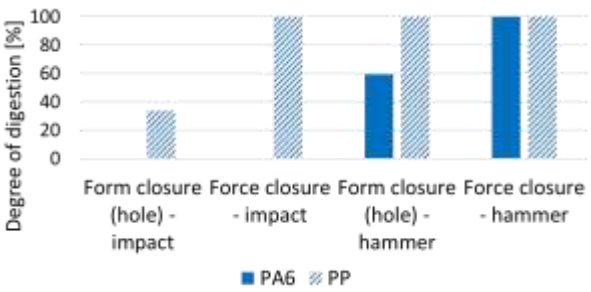

Fig. 5. Comparison of results of two different polymers

PA6 has a similar Young's modulus than PP (both 1.4 MPa), but has a higher notch impact strength (PA6: 6,46 kJ/m2; PP: 5 kJ/m2) and the crystallinity of PP is higher than that of PA6. All these parameters indicate that the comminution of PP should be easier than of

PA6. Figure 3 shows that, in fact, the degree of digestion for PP is higher for all variations except the comminution of the force closure connected samples with the hammer mill. Here a full separation of PA6 and PP was achieved. It is also noticeable, that no breakage events occurred with the material PA6 using the impact rotor. The energy input was insufficient for the form fit connected composites as well as for the force fit connected composites.

The better results achieved with the hammer rotor result in a higher residence time of the material in the mill.

Regarding recycling, it can be stated that different materials show a different comminution behaviour which should be considered when designing the process for different components. In addition the joining process through a force fit connection should be preferred to enable a high degree of digestion.

4 Conclusion and Outlook

The experiments in this work showed that the joining process of composite components affects the comminution properties and, therefore, the degree of digestion. While the hammer rotor tended to lead to a higher degree of digestion in comparison to the impact rotor, the force fit connected components were easier to comminute. Using liquid nitrogen to cool the samples increased the degree of digestion for the form fit connected components.

Further experiments will take a look at the energy consumption required by each pretreatment and the used rotor, so the results of this work can be explained much better. Moreover samples containing glass fibre in the polymer component should be considered, as they are often used in industry.

We are grateful for the financial support of BMBF (German Federal Ministry of Education and Research, Support code 02J21E040). The author is responsible for the content.

References

Martens, H., Goldmann, D., (2016) Recyclingtechnik. 2nd ed., Springer Fachmedien, Wiesbaden.

Shrivastava, A., (2018) Introduction to Plastics Engineering, Elsevier Inc., Cambridge.

Netzsch (2024) Kristallinität/Kristallinitätsgrad. Available at: https://analyzing-testing.netzsch.com/de/training-know-how/glossar/kristallinitaet-kristallinitaetsgrad (Accessed: 17th January 2024).

F5: Flow through porous media developed using concrete waste fractions

Sanduni Jayasekara[1, *], *Nazila Bolourieh*[1], *József Faitli*[2] *and, Teemu Kinnarinen*[1]

[1] LUT School of Engineering Sciences, Lappeenranta-Lahti University of Technology LUT, Lappeenranta, Finland
[2]Institute of Raw Materials Preparation and Environmental Technology, University of Miskolc, Hungary

Abstract. As environmental awareness and sustainability concerns continue to rise, there is a growing emphasis on finding innovative ways to manage and repurpose construction waste materials. Among these innovative ideas, construction, and demolition waste has increasingly attracted research interest in using it as a filter medium and an adsorption material to treat wastewater and stormwater. This research aims to reprocess the construction and demolition waste as a filter media to treat stormwater with respect to suspended and dissolved solids. In the first phase of the research, this study investigates the feasibility of utilizing concrete waste as a sustainable material for developing porous media for the purpose of filtration.

1 Introduction

Construction and demolition waste (CDW) represents a significant environmental challenge, accounting for a substantial portion of total global waste generation. The Environmental Protection Agency (EPA) of the USA defined CDW as "waste materials that are autonomous from the municipal solid wastes which primarily consist of concrete, steel, asphalt, brick, clay tiles, wood, and plasters, applied in buildings, roads, and infrastructures" (Pallewatta et al., 2023; Kabirifar et al., 2020). In 2014, the European Union (EU) produced approximately 333 million tons of CDW without soils, comprising 300 million tons of inert waste, 30 million tons of non-inert waste, and 3 million tons of hazardous waste. It is estimated that CDW accounts for around 46 % of total waste generated in the EU (Xu et al., 2019).

Waste generated from new construction activities contains fewer components, and its waste-to-material recovery potential is comparatively higher than that of demolition waste. In contrast, demolition and rehabilitation waste is more contaminated and, therefore, more difficult to recover (European Commission, 2011). A study conducted by Menegaki and Damigos. 2018, categorized CDW into nine different streams, including ferrous metals, non-ferrous metals, mixed ferrous and non-ferrous metals, plastic, wood, glass, mineral waste containing asbestos, waste containing Polychlorinated Biphenyl (PCBs), and other CDW. Crushed concrete is among the most available CDW types, containing cement, sand, gravel, water, and stones (Egemose et al., 2012). Masonry wastes are generated from building or renovating civil infrastructure and demolition activities (Grace et al., 2016). It is a waste mixture that includes bricks, ceramics, tiles, roof elements, and other masonry debris. Typically, drywall or plasterboard is constructed using gypsum wallboards, and offcuts are left once the drywall is completed. In Europe, 2.35 million tons of waste plasterboard is produced annually from construction and demolition projects (Grace et al., 2016). Mineral wool is a term used to describe a range of inorganic insulation materials, including rock wool, glass wool, and slag wool (Väntsi & Kärki, 2014). It is commonly used in the construction industry to provide insulation against heat, cold, fire, and noise, and 2.54 million tons of waste is generated annually (Yap et al., 2021).

When considering individual countries or regions, the numbers may vary, but globally, it is estimated that 35 % of CDW ends up in landfills (Menegaki & Damigos, 2018; Kabirifar et al., 2020; Pallewatta et al., 2023). A study conducted by Molla et al. (2021) stated that about 1-10 % of purchased materials by weight turned out to be CDW, responsible for 50 % of total waste sent to landfills. As CDW is usually disposed in unlined landfills, several contaminants such as organics, inorganics, pesticides, and heavy metals that are present in the CDW may cause a risk of leaching them into water bodies and soil in the vicinity of the landfill (Pallewatta et al., 2023). Therefore, the requirement of considering the value added to amply available CDW is identified, and efforts are being made to recycle and reuse. The benefits of recycling CDW include saving natural resources, decreasing the need for landfill spaces, adhering to national regulatory requirements, and reducing the negative health impacts of landfilling CDW. Meanwhile, many researchers have shown interest in transforming CDW materials into eco-friendly products (Menegaki & Damigos, 2018).

* Sanduni Jayasekara: sanduni.jayasekara@lut.fi

2 Deep bed filtration

The separation of solid particles in in-depth filtration primarily occurs through the deposition process within the pores of the filter medium. When a particle moves through a pore, depth straining occurs until it reaches a point where the pore is too small, and the particle is retained entirely due to its size. When particles move through a complex path caused by an irregular pore, they can get stuck on the pore surface due to mechanisms like direct interception, inertial interception, or diffusion. However, some particles settle under gravity within the filtration bed, while a few are captured through electrostatic precipitation (Sparks & Chase, 2016).

2.1. Filtration models

Ergun's equation is widely used to correlate pressure drop and flow rate to porous media structural characteristics (Castro & Radilla, 2017).

$$\Delta p/l = 150\frac{(1-\varepsilon)^2 \mu u}{\varepsilon^3 d^2} + 1.75\frac{(1-\varepsilon)\rho u^2}{\varepsilon^3 d} \quad (1)$$

where ε is porosity, l (m) is the bed depth, d is the medium particle diameter (m), μ (Pa·s) is the fluid's dynamic viscosity, ρ fluid density (kg/m^3), and u (m/s) is the superficial velocity.

The numerical coefficients 150 and 1.75 correspond to the viscous resistance coefficient and the inertial resistance coefficient, respectively, determined using a regular spherical particle bed (Huang et al., 2023). The constants in Eq. (1) were determined based on 640 experiments conducted using beds of small (less than 1.5 mm), mono-sized, spherical, and nearly spherical particles (glass spheres, sand, pulverized coke) and a few pure gases (H_2, CO_2, N_2, CH_4) or air. It is also highlighted that Ergun's equation is applicable for fluid flows that have Reynold's number less than 1000 (Koekemoer & Luckos, 2015).

3 Material and method

3.1. Sample preparation

The experiment setup involved a column packed with different fractions of construction and demolition concrete waste collected from Finland. The raw material was obtained from a local supplier in Finland and marked as FLSC. The preparation of the samples involved crushing and sieving of the raw material. Particles smaller than 100 μm were separated from the raw sample. The remaining material was divided into six fractions based on particle size: x > 2.5 mm, 2.5 mm < x < 1.25 mm, 1.25 mm < x < 0.8 mm, 0.8 mm < x < 0.5 mm, 0.5 mm < x < 0.3 mm, 0.3 mm < x < 0.1 mm. The fractionation process was carried out using the HAVER EML 450 Digital Plus Test Sieve Shaker. The shaker contained 13 sieves with aperture sizes ranging from 25 to 5000 μm and a pan positioned beneath the bottom sieve stack. The particles larger than 2.5 mm were crushed using the Cross Beater Mill SK 300 and then sieved again using the same set of sieves mentioned above to obtain 6-8 L of each size fraction. The glass beads bulk sample (25 kg) is in the range of 0.3 mm -0.6 mm. These glass beads were also sieved using the HAVER EML 450 Digital Plus Test Sieve Shaker to get 8 L of 0.3 mm - 0.5 mm sample.

3.2 Column Experiments

For column experiments, the bed materials made with concrete waste fractions were inserted into a column with an inner diameter of 9.5 cm and a total height of 168 cm (Fig.1). It features eleven overflow valves, which are utilized to regulate the water level above the bed. The filtrate is collected at the bottom of the column, and water enters uniformly from the top. To get a uniform bed surface and to avoid water channelling, a semi-wet state of the solids was used when the column was packed up to a certain height. After weighing the dry samples, the additional materials required to increase the bed height were added to the wet bed, with only 2-5 cm of water on top of the bed. Initially, the experiment was carried out using two size fractions of FLSC separately: 0.3 mm- 0.5 mm and 0.5 mm- 0.8 mm, and each fraction had four different bed heights: 35 cm, 45 cm,50 cm, and 60 cm. Filtering experiment was then carried out using glass beads to compare the results.

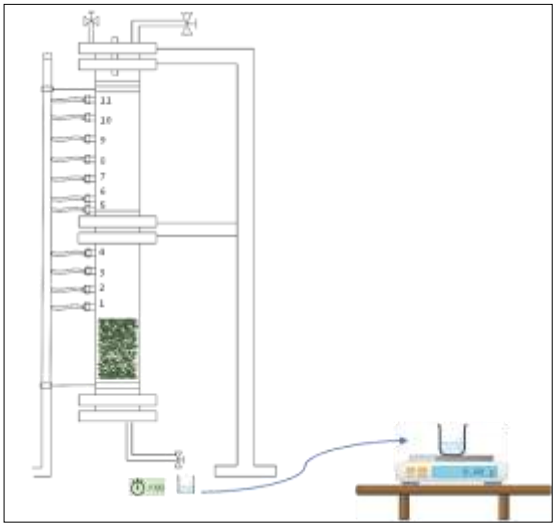

Fig. 1. Filtration column experimental setup

4 Results and discussion

The column experiments conducted using FLSC samples demonstrated that increasing the pressure drop across the bed while keeping the bed height constant increased the superficial velocity. On the other hand, increasing the bed height reduced the flow velocity throughout the bed.

Table 1 summarizes the characteristics of bed materials used for the column experiments.

Table 1: Sample characteristics (a - García-González, et al., 2015; b - Říha et al., 2018)

	FLSC	FLSC	Glass beads
Particle size range (mm)	0.3–0.5	0.5–0.8	0.3–0.5
Median Diameter (m)	0.0004	0.0007	0.0003
Bulk density (g/cm^3)	1.307	1.309	1.29
Porosity (%)	0.31[a]	0.30[a]	0.437[b]

Fig. 2 compares the pressure drops (Δp) given by Ergun's equation. Superficial velocities collected from the column experiments were used to calculate the Δp values. The results emphasize that increasing the bed heights directly impacts the Δp. When considering one superficial velocity, the higher the bed height, the higher the Δp, irrespective of the particle sizes of the bed material. Filter media depth is a crucial indicator of water filtration. The higher the depth, the higher the resistance to water flow. For FLSC 0.3-0.5 mm bed, when the superficial velocity is 400 cm/h, the pressure drops for 35 cm, 45 cm, 50 cm, and 60 cm are 44 mmH_2O, 56 mmH_2O, 64 mmH_2O, and 76 mmH_2O respectively. Similarly, for FLSC 0.5 mm- 0.8 mm bed, when the superficial velocity is 600 cm/h, the Δp of 35 cm, 45 cm, 50 cm, and 60 cm beds are 28 mmH_2O, 36 mmH_2O, 40 mmH_2O, and 48 mmH_2O respectively.

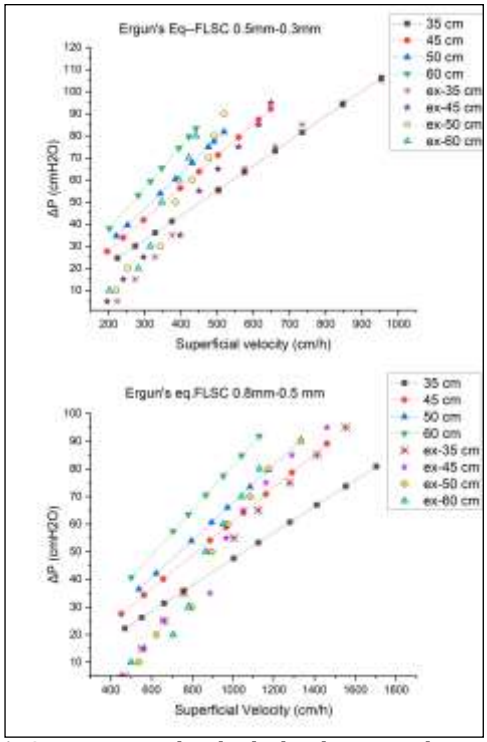

Fig 2: Experimental and calculated pressure drops vs Superficial velocity for two fractions of concrete waste

On the other hand, increasing the size range of the particles increases the superficial velocity within the same bed heights. For instance, when the bed height is 50 cm, the superficial velocities of FLSC 0.3 mm – 0.5 mm bed changed in the range of 221 cm/h – 518 cm/h, while for the same bed height of 50 cm for FLSC 0.5 mm- 0.8 mm, the superficial velocities changed in the range of 538 cm/h- 1333 cm/h. The particle size distribution of selected filter media can significantly impact the stormwater filtration process. Fine particles can penetrate deeper into the filter bed, increasing the likelihood of retention within the filter media. Also, a wide particle size distribution leads to denser packing of particles. This will eventually reduce the porosity of the filter, reducing the superficial velocities through the packed bed.

The results from the column experiments with glass beads (Fig.3) also demonstrate that increasing the bed heights reduced the superficial velocities across the bed. For a bed height of 35 cm, the velocities change from 697 cm/h to 1812 cm/h, while for a bed height of 60 cm, they change from 543 cm/h to 1083 cm/h.

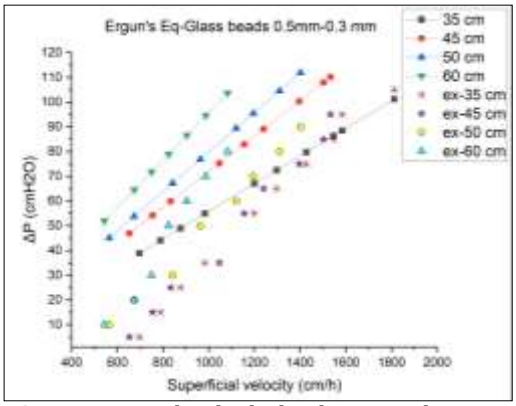

Fig 3 : Experimental and calculated pressure drops vs. Superficial velocity for glass beads.

In addition, the experimental Δp values collected as waterheads can be compared with the calculated Δp values using Ergun's equation (Fig.1, Fig.2, and Table 2). The experimental and calculated Δp values are closely similar when the waterheads are high. However, at lower waterheads, calculated Δp values are higher than the actual waterhead above the bed.

Table 2: Comparison of Δp across the packed bed when bed height is 50 cm

	Experimental Value (cmH_2O)	Ergun's Eq values (cmH_2O)
FLSC 0.5 mm – 0.8mm	90	90.38
	80	79.51
	70	73.46
	60	65.98
	50	60.66
	40	53.95
	20	42.18
	10	36.45
FLSC 0.3 mm – 0.5 mm	90	81.84
	80	77.36
	70	74.93
	60	67.78
	50	60.47
	40	53.81
	20	39.53
	10	34.65

Glass beads 0.3 mm – 0.5 mm	90	11188
	80	104.57
	70	95.39
	60	89.41
	50	76.85
	40	67.18
	20	53.78
	10	45.12

4 Conclusion

The reduction of the range of particle sizes in the concrete waste-packed bed has led to a decrease in flow velocities. This phenomenon can be attributed to the impact of both particle size distribution and particle diameter. On the other hand, increasing the bed heights also reduces the superficial velocities through the bed material for all three kinds of samples that have been experimented with. It is, therefore, essential to consider the effects of particle size distribution, diameter, and bed length when designing concrete waste-packed beds. If the waste concrete is going to be used to treat stormwater, it is recommended to use fractions below 0.5 mm so that the flow velocities are sufficiently low to allow proper removal of contaminants. However, future studies may include using the recommended fractions to treat stormwater in terms of TSS.

This research project is funded by the Interreg Central Baltic Programme and co-funded by the European Union. The authors want to acknowledge the StopWa team's support throughout the research. Publication is funded by the European Union's Horizon Europe program under grant no. 101079354.

References

Castro, A.R &, Radilla, G. 2017. Non-Darcian flow of shear-thinning fluids through packed beads: Experiments and predictions using Forchheimer's law and Ergun's equation. Advances in Water Resources.100, 35-47.

Egemose, S., Sønderup, M.J., Beinthin, M.V., Reitzel, K., Hoffmann, C.C., Flindt, M.R., 2012. Crushed concrete as a phosphate binding material: a potential new management tool. Journal of Environmental Quality. 41, 647–653.

European Commission, 2011. Service Contract on Management of Construction and Demolition Waste - SR1. Final Report Task 2. Paris, France.

García-González, J., Rodríguez-Robles, D., Juan-Valdés, A., Poz, M., Guerra-Romero, M.I, 2015. Porosity and pore size distribution in recycled concrete. Magazine of Concrete Research. ICE Publishing.

Grace, M.A., Clifford, E., Healy, M.G., 2016. The potential for the use of waste products from a variety of sectors in water treatment processes. Journal of Cleaner Production.137, 788–802

Huang, H., Ma, H., Liu, B., Yang, S., Wei, Q., Zhang, Y, Lv, 2023. Bed filtration pressure drop prediction and accuracy evaluation using the Ergun equation with optimized dynamic parameters in industrial wastewater treatment. Journal of Water Process Engineering.53, 103776

Koekemoer, A & Luckos, A., 2015. Effect of material type and particle size distribution on pressure drop in packed beds of large particles: Extending the Ergun equation. Fuel. 158, 232-238.

Kabirifar, K., Mojtahedi, M., Wang, C., Tam, V.W.Y., 2020. Construction and demolition waste management contributing factors coupled with reduce, reuse, and recycle strategies for effective waste management: a review. *Journal of Cleaner Production*, 263, 121265

Menegaki, M., & Damigos, D., 2018. A review on current situation and challenges of construction and demolition waste management. *Current opinion in green and sustainable chemistry*. 13, 8-15

Molla, A.S., Tang, P., Sher, W., Bekele, D.N., (2021).Chemicals of concern in construction and demolition waste fine residues: a systematic literature review. *Journal of Environmental Management*. 299, 113654.

Pallewatta, S., Weerasooriyagedara, M., Bordoloi, S., Sarmah, A., Vithanage, M., 2023. Reprocessed construction and demolition waste as an adsorbent: An appraisal. *Science of the total environment*. 882, 1633

Říha, J., Petrula, L., Hala, M., Alhasan, Z., 2018. Assessment of empirical formulae for determining the hydraulic conductivity of glass beads. Journal of Hydrology and Hydromechanics.66, 337–347.

Sparks, T., & Chase, G., 2013. Filters and Filtration Handbook (6th Edition). *Elsevier.*

Väntsi, O & Kärki, T., 2014. Mineral wool waste in Europe: a review of mineral wool waste quantity, quality, and current recycling methods. Journal of Material Cycles and Waste Management.16, 62-72.

Yap, Z.S., Khalid, N.H.A., Haron, Z., Mohamed, A., Tahir, M.M., Hasyim, S., Saggaff, A., 2021. Waste Mineral Wool and Its Opportunities—A Review. Materials.14, 5777

Xu, J., Shi, Y., Xie, Y., Zhao, S., 2019. A BIM-based construction and demolition waste information management system for greenhouse gas quantification and reduction. *Journal of Cleaner Production*. 229, 308–324

G1: Excellent stress model prediction of stirred media mill results by integration of mean, viscosity dependent grinding media velocities

David Sterling[1], *Sandra* Breitung-Faes[2], and *Arno* Kwade[1,*]

[1]Institute for Particle Technology, Technische Universität Braunschweig, Braunschweig, Germany
[2]University of Applied Science Nürnberg, Nürnberg, Germany

Abstract. Wet-operated stirred media mills are commonly used for fine and ultrafine grinding. Depending on the application, there are different mill geometries and materials as polyurethane and ceramics used for the grinding chamber lining and the agitator. In addition to process-related effects such as cooling and wear prevention, energy-efficient mill operation is desired, which can be achieved by applying mechanistic stress models. In addition to mill geometry and volume, process parameters and various energy transfer coefficients are of importance. In this work, the effect of different mill equipment materials, which affect the mill-related energy transfer coefficients, on performance prediction and scale-up using an improved stress model is investigated. Especially the viscosity dependent grinding media velocities have to be included into the determination of the characteristic parameters stress intensity and stress number. By that and by using both mill-related energy transfer coefficients and improved grinding media energy transfer coefficients, grinding times and specific energies for selected target particle sizes can be well predicted.

1 Motivation

Fine and ultra-fine comminution using stirred media mills is a very popular process in many industries like mineral, ore, battery, ceramic, pharmaceutical and chemical industry (Kwade et.al. 2022). Stirred media mills offer the tuning of the process by several operating parameters like tip speed, size, density and filling ratio of grinding media and product formulation. Moreover, several geometrical designs, sizes from a few millilitre up to several cubic meter and different stirrer and grinding chamber materials are available. Therefore, a relatively large parameter field exists which makes it difficult to find the best process and machine condition. Consequently, task of improving the well-known stress model is to improve the predictive performance of the mill in a way, that comminution results for new operating points and new mill geometries, sizes and materials can be predicted.

2 Stress model improvement

Basis for the improvement is the so-called advanced stress model according to Breitung-Faes and Kwade (20??). The advanced stress model uses energy transfer factors to describe the energy transfer from the stirrer to the product particles. Up to know the so-called mill related transfer factor is calculated as ratio of the product of mean stress energy and stress frequency to net power input during milling. However, the so-defined transfer factor includes not only energy dissipations by friction of the grinding media at the grinding chamber wall, but also a difference in the grinding media velocity. For the model improvement the energy transfer factor is now calculated solely on basis of an ideal operation only with water as low-viscosity medium, and the effect of the slurry rheological properties on the grinding media velocity is determined separately as ratio of the ideal net power consumption to the actual net power consumption. Using this ratio and the procedure of Stender et. al. to determine the mean stress energy or mean grinding media velocity, respectively, the characteristic values for stress intensity and stress number as well as the energy transfer factors for bead damping can be corrected.

3 Experimental

Various wet-operated stirred media mills with perforated disc stirrer geometry were used for the experiments within the scope of this publication. The mills differ in terms of the grinding chamber volume (0,24 to 3,5 l), the type of grinding media separation and the stirrer orientation (horizontal and vertical). Quartz flour was ground using grinding media of different sizes out of yttrium stabilized zirconium oxide and alumina at different tip speeds ranging from 1.5 m/s up to 14 m/s. The mills are equipped with different grinding media separation devices and different stirrer and chamber materials.

* Corresponding author: a.kwade@tu-bs.de

4 Results

From the experimental results the relationships between product fineness and specific energy requirement were determined. Beside the net specific energy input of the stirrer also the specific energy transferred to the product particles, i.e. the active specific energy was estimated using different energy transfer factors. From this relations, the specific energy required for a certain product fineness was determined and related to the characteristic parameters of the stress model, stress energy or stress energy as well as stress number. It could be shown that by considering the energy transfer from the stirrer to the product particles for a water based operation and additionally the change in grinding media velocity based on the rheological properties of the product suspension for the calculation of the stress intensity and the energy transfer factor for damping of grinding media collisions, an excellent prediction of the grinding results becomes possible. Accordingly Fig. 1 top shows the prediction of an entire relationship between product fineness (here median size) and net specific energy input, whereas Fig. 1 bottom presents the comparison of predicted and measured specific energies for different mill configurations to achieve a median size of 20 µm.

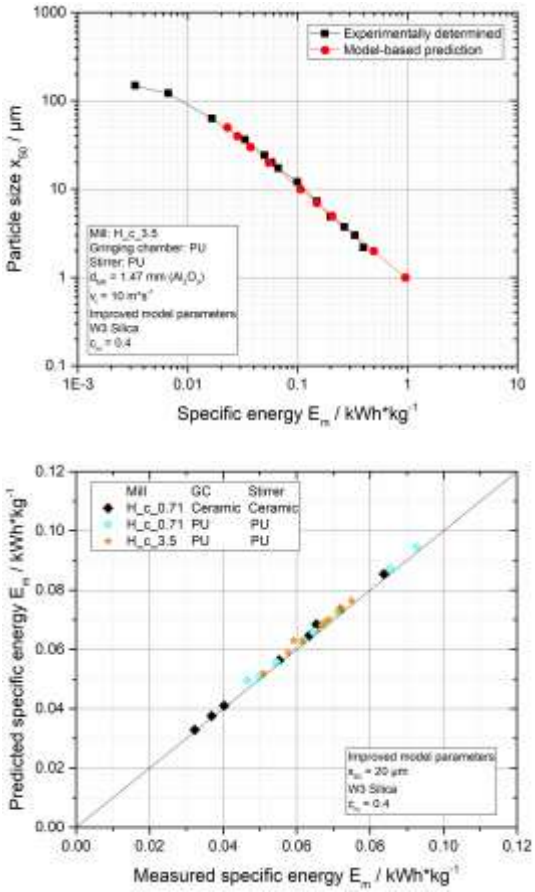

Fig. 1. Caption of the Figure 1. Below the figure.

A central role within the prediction plays the master curve which describes the product of stress intensity and stress number, i.e. the active specific energy, as function of the optimum stress intensity at which a certain product fineness can be achieved with a minimum of specific energy input.

5 Conclusions

With the so-called advanced stress model a rough prediction of the relationship between product fineness and specific energy consumption is possible. Within this work it was shown that the prediction accuracy can be much improved if the effect of the rheological suspension properties on the grinding media velocity is considered for the determination of the mean stress intensity, the stress frequency and the energy transfer factor for collision damping. Moreover, the different mill designs as well as mill and stirrer materials are well described by the stress model with improved determination of characteristic parameters stress intensity and stress number.

Leigh Duncan Hamilton, Christoph Peppersack and Victor Oldhues are thanked for proofreading and supporting. Erik Kariger, Jonas Jestel and Leon Therfer are thanked for their support in the experimental work.

Glencore plc is gratefully acknowledged for providing equipment and partially funding this research work.

References

Breitung-Faes, S. & Kwade, A. (2019) Mill, material, and process parameters – A mechanistic model for the set-up of wet-stirred media milling processes, *Advanced Powder Technology* 30, 1425–1433

Kwade, A., Möller, M., Müller, J., Hesselbach, J., Zellmer, S., Doose, S., Mayer, J., Michalowski, P., Powell, M., Breitung-Faes, S. (2023) Comminution and Classification as Important Process Steps for the Circular Production of Lithium Batteries, *KONA* 40, 50–73

G2: Vertical Wet Stirred Media Mill (HIGMill); Plant Optimization, Modelling and Scaling-Up

Okay Altun[1,*], *Alper* Toprak[1], *Deniz* Altun[1], *Arno* Kwade[2], and *Ecevit* Bilgili[3]

[1]Department of Mining Engineering, Hacettepe University, 06800 Beytepe, Ankara, Turkey
[2]Technische Universitat Braunschweig, Institute for Particle Technology, Volkmaroder Strasse 5, 38104 Braunschweig, Germany
[3]Department of Chemical and Materials Engineering, New Jersey Institute of Technology, 07102, Newark, NJ, USA

Abstract. Stirred media milling is becoming more prominent therefore deep understanding of its plant optimization, modelling and scaling-up is a never-ending subject. This study investigates these topics for HIGMill application, which is a recent technology demanding significant industrial knowledge. In the context of plant optimization, surveys at different operating and design conditions were performed. Some adjustments were recommended, and energy efficiency was improved by 18%. Within the scope of modelling, PBM incorporating 1-large–2-small-tanks model and power-law specific breakage rate function Si was formulated. Parameters of Si and three non-normalized cumulative breakage functions B_{ij} were estimated by back-calculation method with global optimization. In a hybrid method, breakage index tn-based B_{ij}, obtained from laboratory drop-weight tests, were input to the optimizer to estimate Si. The modified Tavares B_{ij} achieved the best fits. For the scale-up studies, the focus was given on lab-scale test works to predict the product d80, energy consumption by using signature plots, stress analyses and well-known energy equations. The investigations showed that the procedures can be utilized to predict both the required energy and volume required for the milling application. The developed methodologies may be helpful for basic engineering purposes requiring sizing the mill.

1 Introduction

Minerals industry desires fine grinding operation to improve the liberation degrees of the minerals of interest. Thus, the overall economy of the mine is improved, and resource management is done efficiently. Depending on the developments in the field of fine grinding, the number of installed units has been increasing gradually (Wills and Finch, 2016). Although there are alternatives in the range of fine grinding, stirred media milling is the option coming forward with its energy efficiency when compared to competitor ball milling technology (Jankovic, 2003; Shi et al., 2009).

HIGMill is a recent stirred mill technology that is in serve of the minerals industry requiring regrind/fine grinding/coarse grinding applications having p 80sof 100 µm and sub 20 µm. The launch of the HIGMill dates back to 2012 and it was reported that over 200 units had been installed with the largest installed power of 5 MW (Lehto et al., 2016). HIGMill lacks industrial knowledge compared to its competitors, IsaMill, Ball Mill, etc. This study aimed at fulfilling the gap regarding to the subjects of plant optimization, modelling and scale-up.

2 Materials and methods

HIGMill studied had installed motor power of 2.65 MW with inner height and diameter of 6.8 m and 1.66 m respectively. There exist 16 agitators having diameter of 1.36 m. The operation is held at a copper plant regrind circuit and middlings together with the rougher flotation concentrate is processed to achieve the target p_{80} of 20 µm. The feed to HIGMill is pre-cycloned to remove the fine particles in advance.

Series of sampling campaigns were organized around the mill to provide a deep-understanding on its operation. In the scope, the parameters of tip speed, solids content, media type, agitator material were changed and in total 5 surveys (S1-S5) and 30 tests were completed. The bead filling of Survey 1 to 4 was at 64% and Survey 5 was run at 70%. Table 1 summarizes the conditions.

Table 1. Scope of the sampling.

	S1	S2	S3	S4	S5 (higher bead filling)
	Media #1	Media #2	Media #3	Media #1	Media #1
Agitator config (castellated +flat)	11+5	10+6	10+6	10+6	10+6
Agitator material	Steel	Steel	Steel	Rubber	Rubber
Bead size and SG	4; 3.8	4; 3.7	3-4; 3.7	4; 3.8	4; 3.8

For the modelling of the mill, PBM approach was preferred. The form given in Eq. 1 was used to calculate

* Corresponding author: okyaltun@hacettepe.edu.tr

S_i of the given Surveys. Here, we use an RTD formalism that allows for consideration of 1L2ST model as well as other simpler RTD models as subcases. Let us consider a mill with volume V_m that consists of one tank with volume V1 and two small tanks with equal volumes ($V_2 = V_3$) placed in series. Defining a volume fraction $f = V_1/V_m$, we record that the mean residence time in tank 1 τ_1 is given by $\tau_1 = f\tau$ and the mean residence times in tanks 2 and 3 are given by $\tau_2 = \tau_3 = (1- f)\tau/2$. One can rewrite Eq.1 for well-mixed tanks 1, and 2, as follows (Eq. 2):

$$p_{1,i} = \left[f_i + f\tau \sum_{j=1}^{j=i-1} b_{ij}\, S_j\, p_{1,j} \right] \Big/ (1 + f\tau S_i) \tag{1}$$

$$p_{2,i} = \left[p_{1,i} + (1-f)(\tau/2) \sum_{j=1}^{j=i-1} b_{ij}\, S_j p_{2,j} \right] \Big/ [1 + (1-f)(\tau/2) S_i] \tag{2}$$

Throughout the modelling S_i form given in Eq. 3 was used.

$$S_i = k_s \left(\frac{n}{n_{\max}} \right)^{a_1} \left(\frac{w_p}{w_{p\max}} \right)^{a_2} \left(\frac{x_i}{x_{\max}} \right)^{\alpha} \tag{3}$$

The breakage indices t_2, t_4, and t_{10} were determined using laboratory drop-weight tests and plotted against $f_{mat}xE_{cs}$. The fits by the Shi–Kojovic (2007) model were also shown along with the fitted equations and R^2 values; the fits were reasonably good ($R^2 \geq 0.9$) with t_2 having the most deviation from the experimental data. Next, the t_n equations were used to generate the t_n-based cumulative breakage distribution B_{ij} matrix. Austin I and Austin II are given in Eqs. 4,5 and 6,7, Tavares in Eqs. 8,9.

$$B_{ij} = \left(\frac{x_{i-1}}{x_j} \right)^{\gamma} \text{ for } \phi_0 \left(\frac{x_{\max}}{x_j} \right)^{\theta} \geq 1 \tag{4}$$

$$B_{ij} = \phi_0 \left(\frac{x_{\max}}{x_j} \right)^{\theta} \left(\frac{x_{i-1}}{x_j} \right)^{\gamma} + \left[1 - \phi_0 \left(\frac{x_{\max}}{x_j} \right)^{\theta} \right] \left(\frac{x_{i-1}}{x_j} \right)^{\beta} \text{ for } \phi_0 \left(\frac{x_{\max}}{x_j} \right)^{\theta} < 1 \tag{5}$$

$$B_{ij} = \frac{1 - \exp\left[-\left(\frac{x_{i-1}/x_j}{\lambda} \right)^{\gamma} \right]}{1 - \exp\left[-\left(\frac{1}{\lambda} \right)^{\gamma} \right]} \text{ for } \phi_0 \left(\frac{x_{\max}}{x_j} \right)^{\theta} \geq 1 \tag{6}$$

$$B_{ij} = \phi_0 \left(\frac{x_{\max}}{x_j} \right)^{\theta} \frac{1 - \exp\left[-\left(\frac{x_{i-1}/x_j}{\lambda} \right)^{\gamma} \right]}{1 - \exp\left[-\left(\frac{1}{\lambda} \right)^{\gamma} \right]} + \left[1 - \phi_0 \left(\frac{x_{\max}}{x_j} \right)^{\theta} \right] \left(\frac{x_{i-1}}{x_j} \right)^{\beta} \text{ for } \phi_0 \left(\frac{x_{\max}}{x_j} \right)^{\theta} < 1 \tag{7}$$

$$B_{ij} = \phi_0 \left(\frac{x_{i-1}}{x_j} \right)^{\gamma} + (1 - \phi_0) \left(\frac{x_{i-1}}{x_j} \right)^{\beta} \text{ for } x_{i-1} \geq D \tag{8}$$

$$B_{ij} = \phi_0 \left(\frac{x_{i-1}}{D} \right)^{\theta} \left(\frac{x_{i-1}}{x_j} \right)^{\gamma} + \left[1 - \phi_0 \left(\frac{x_{i-1}}{D} \right)^{\theta} \right] \left(\frac{x_{i-1}}{x_j} \right)^{\beta} \text{ for } x_{i-1} < D \tag{9}$$

In the scope of the modelling, B_{ij}s and S_i back-calculated by minimizing the following sum-of-squared residuals SSR. For the B_{ij} the forms of modified Tavares and two different Austin equations were used. In a separate hybrid method, t_n-based B_{ij}, obtained from laboratory drop-weight tests, were input to the optimizer to estimate S_i solely. Back-calculations were held via Generalized Reduced Gradient algorithm that used a multi-start scheme (Abadie, Carpentie, 1969) to attain a probable globally optimal solution. Such comparison between the hybrid method and the well-known B_{ij} equations have not been undertaken for the wet vertical stirred media milling.

For the scale-up studies laboratory scale dry milling tests were performed with vertical stirred media mill having diameter and height of 118 mm and 192 mm respectively. The results of the tests were used to assess both the wear of the beads and scaling-up of the milling. For the scale-up studies, signature plots, stress analyses and energy equations were used. Signature plots correlate net specific energy consumption with p_{80} or reduction ratio. Stress analyses (Eqs. 10,11) benefit from the milling conditions to undertake the necessary calculations. e

$$SE = v_t^2\, d^3_{GM}\, \rho_{GM} \tag{10}$$

$$SN = n_{stirrer}\, t_g\, m_{GM} / (\pi/6\, d^3_{GM}\, \rho_{GM}) \tag{11}$$

Where,

v_t : tip speed (m/s); d_{GM} : diameter of grinding media (m); ρ_{GM} : density of grinding media (kg/ m^3); $n_{stirrer}$: stirrer speed (rpm); t_g : time of grind (h) m_{GM} : amount of grinding media (kg)

In terms of the energy equations the focus was given on Rittinger, Walker and Bond theories. As a methodology, the parameters obtained from lab-scale and industrial scale works were correlated (Lewis Taylor et al., 2020).

3 Results and discussions

3.1. Effects of operating parameters and optimization of HIGMill

This section summarizes the studies conducted by Altun et al. (2023). Solids concentration was the initial focus. Fig. 1 and 2 depict some of the results. The results imply that 30% solid has the lowest efficiency whereas 50% had the improved performance. The literature reports that the milling environment with higher solid content increases the grinding performance up to a certain point and beyond that the performance decreases (Faria et al. 2019).

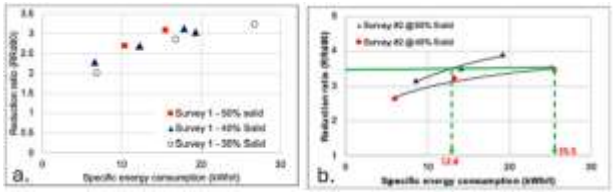

Fig. 1. The variation of reduction ratio with solids content (Altun et al. 2023).

The tests on the bead filling showed that higher size reduction is achieved when the filling was increased (Fig. 1). However, it should also be emphasized that the impact of bead filling was almost disappeared at higher solids content. Fig. 2 illustrates the impact of agitator

material on the milling performance. The results implied that steel made agitator had improved energy efficiency.

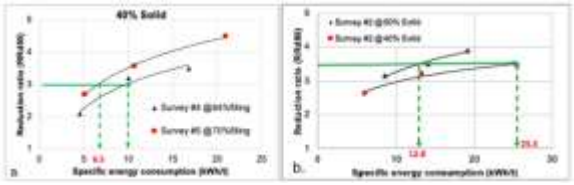

Fig. 2. The impact of bead filling (a) and agitator material (b) on comminution results.

Following the assessments, the optimized HIGMill parameters were adjusted at the plant and its long-term performance was observed. These were compared with the previous periods. Fig. 3 depicts the energy figures and the obtained energy efficiency of HIGMill.

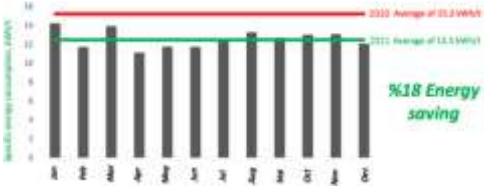

Fig. 3. The long-term benefit of optimized HIGMill parameters.

3.2. Modelling of HIGMill

Within the scope of the modelling some of the surveys were chosen. The emphasis was given on having the same bead filling but varied design conditions i.e., media type and agitator material. The model fitting was performed with the data set of S2, S3, S4. Another sampling campaign was arranged to validate the developed model structure in the real case.

Table 2. The results of model fits.

	Modified Tavares	Austin I	Austin II	Hybrid method
ϕ_0	0.597	1.000	1.00	
γ	0.003	0.920	4.33	
β	0.592	0.621	0.000	
θ	4.01	-4.48	-0.421	
D (μm)	36.6	–	–	
λ	–	–	0.298	
f	0.853	1.00	0.993	0.814
k_1 (h^{-1})	2220	23100	17200	421
k_2 (h^{-1})	1510	13800	10400	376
k_3 (h^{-1})	1070	9600	7100	297
a_1	2.51	3.09	3.04	1.41
a_2	-1.05	-1.09	-0.987	-0.949
α	2.42	3.57	3.65	0.983
SSR ($\%^2$)	322	596	384	475

Table 2 compares the results obtained from the back-calculation method with the three empirical B_{ij} functions and hybrid method. The Austin I B_{ij} yielded significantly higher *SSR* values than the modified Tavares B_{ij}. Austin I with f = 1 corresponds to perfect mixing, which is unrealistic in view of RTD studies on both horizontal and vertical WSMMs. The Austin II B_{ij} led to slightly higher *SSR* values than the modified Tavares B_{ij}. Hybrid method overcame Austin I.

After the fitting the variations in the S_i parameters with the operating conditions were discussed. The rotation rate of the rotor n and the particle size x_i had the most significant positive impacts on the specific breakage rate; the magnitude of their impact was similarly high. In contrast, the solids loading w_p had a weaker, albeit significant, negative impact. Our findings regarding the impacts of n and w_p on the breakage kinetics accord well with those observed in previous batch, continuous, and recirculation WSMM studies using vertical and horizontal mills (Navarrete et al., 2022; Afolabi et al., 2014). The rank-ordering of the breakage rate constant $k_1 > k_2 > k_3$ can be attributed to the different rotor materials and types/sizes of ceramic beads used. The results suggest that the steel rotor (S1 and S2) led to faster breakage than the rubber rotor (S3).

The monotonic increase of S_i with x_i for each survey–test is illustrated in Fig. 4 in terms log–log plots, which exhibits straight parallel lines with identical slope α = 2.35. The strong positive impact of n, which was modulated by ω in the experiments, was signified by the upward shifting lines (T1–T2–T3 and T4–T5–T6 in each survey for 600–800–1000 rpm) at similar or close values of Q_s and w_P.

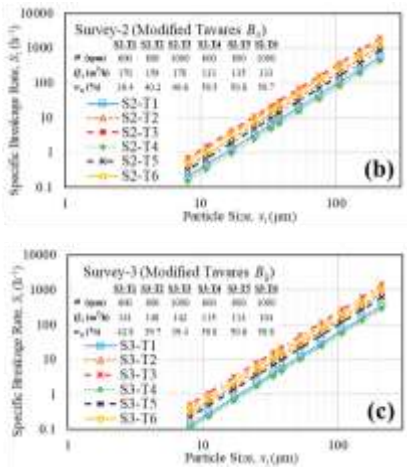

Fig. 4. Variation of the specific breakage rate Si with the particle size

The PBM was successfully validated by the good predictions of the cumulative product PSDs in P1, P2, and P3 tests, which had not been used in the parameter estimation (see Fig. 5). The root-mean-squared-error (RMSE) values were of similar order-of-magnitude to the *SER* values of the fits, which suggests the PBM performed well and reasonable predictive capability.

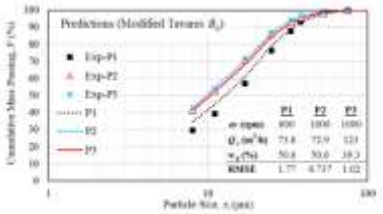

Fig. 5. Predictions of the cumulative product PSDs of Survey 6.

3.3. Scale-up of HIGMill

Within the context of the study, scaling-up via developing the signature plots, energy equation fitting, and stress analyses were considered (Altun et al. 2024).

Signature plots obtained from laboratory stirred mill and HIGMill of one of the surveys is illustrated in Fig. 6.

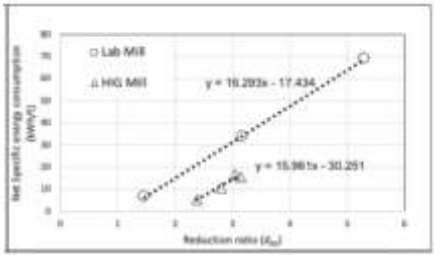

Fig. 6. The signature plots of lab mill and HIGMill.

The similar plots to that of Fig. 6 were obtained for the rest of the test works and as a result it was found that the two trends are almost parallel to each other. The assessments showed that signature plot of industrial scale HIGmill can be developed accordingly once a laboratory test is performed.

Stress analyses were the other approach tested in the scale-up. In these assessments stress energy (SE) and stress number (SN) parameters were considered, and the correlations were developed accordingly. By taking the operating and design conditions into consideration, SE and SN of both mills were calculated and divided by the volumes. The plots are depicted in Fig. 7.

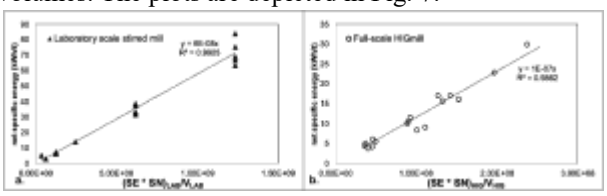

Fig. 7. Stress analyses of the mills.

In the final stage of the calculation, the two plots were combined as illustrated in Fig. 8. Such a finding has two important outcomes. It may be used to predict both the energy requirement of the milling once the operating and design variables known, or volume required can be calculated when the energy required for the grinding is known (i.e., from signature plots).

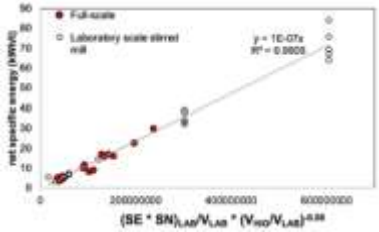

Fig. 8. Scale-up from stress analyses.

In the context of energy predictions, the Walker's expression was found to have the best estimate when compared to Bond and Rittinger hence it may be used in correlating the parameters of Kn and n of laboratory and full-scale mills, which are illustrated in Figs. 9 and 10

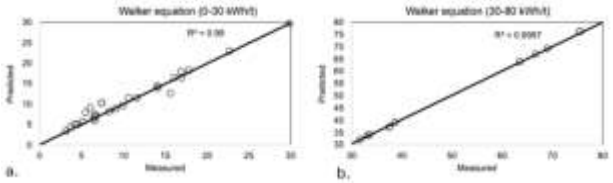

Fig. 9. The measured and predicted specific energies from different equations.

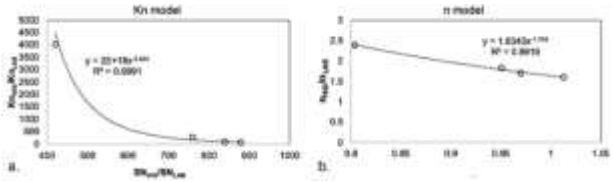

Fig. 10. Scale-up from energy equations.

4 Conclusions

The study aimed at providing a deep understanding on HIGMill operation by considering its plant optimization, modelling and scaling-up. Plant surveys and the latter analyses improved the energy efficiency of the mill by 18% when a year-long operation is observed. In modelling, PBM incorporating 1L2S model and power-law specific breakage rate function Si was formulated. In the calculations well-known Bij functions and experimental drop weight results were used and the fitting accuracies were compared. Modified Tavares function had the best fit and the developed model structure was validated with untrained set of data. In the scaling-up from the lab-scale tests, signature plots, stress analyses and energy equations were evaluated. The developed methodology enabled using stress analyses with the signature plots in sizing the HIGMill from lab tests, which is an important outcome. Walker's expression had the best energy fits and its model parameters were also scaled-up.

The authors would like to acknowledge contributions of Tolga Sert, Özgün Darılmaz, Anıl Hür, Cumhur Erdem Karahan.

References

B.A. Wills, J. Finch, (2016) Wills' Mineral Processing Technology: An Introduction to the Practical Aspects of Ore Treatment and Mineral Recovery, 8th Ed., Elsevier Science.

A. Jankovic, (2003) Variables affecting the fine grinding of minerals using stirred mills. *Miner. Eng*. 16 (2003) 337–345.

Shi, F., Morrison, R., Cervellin, A., Burns, F., Musa, F., 2009. Comparison of energy efficiency between ball mills and stirred mills in coarse grinding. *Miner. Eng*. 22, 673–680.

Lehto, H., Musuku, B., Keikkala, V., Kurki, P., Paz, A., 2016. Developments in stirred media milling test work and scale performance of Outotec HIG mill. In: *Comminution Conference*, South Africa, Cape Town.

F. N. Shi, T. Kojovic, (2007) Validation of a model for impact breakage incorporating particle size effect, Int. J. Miner. Process. 82, 156–163.

J. Abadie, J. Carpentie, (1969) Generalization of the Wolfe reduced gradient method to the case of nonlinear constraints, in: *R. Fletcher (Ed.), Optimization, Academic Press*, New York, USA, 1969, 37–47.

Lewis Taylor, D.S., Blackburn, S., Greenwood, R., (2020) Stirred media mills in the mining industry: Material grindability, energy-size relationships, and operating conditions. *Powder Technol*. 369, 1–16.

Faria, P.M.C., Rajamani, R.K., Tavares, L.M., (2019) Optimization of solids concentration in iron ore ball milling through modeling and simulation. *Minerals* 9, 366, 1–17.

Altun, O., Darılmaz, O., Karahan, E., Sert, T., Altun, D., Toprak, A., Hur, A., 2023. Understanding HIGMill operation at copper regrind application; operating parameters, wear and mineral liberation, *Minerals Engineering* 191, 107964

P. Navarrete, Segado, M. Tourbin, D. Grossin, C. Frances (2022) Tailoring hydroxyapatite suspensions by stirred bead milling, *Ceram. Int.* 48 (2022) 24953–24964.

Afolabi, A., Akinlabi O., Bilgili, E. (2014) Impact of process parameters on the breakage kinetics of poorly water–soluble drugs during wet stirred media milling: A microhydrodynamic view. *Eur. J. Pharm. Sci.* 51 (2014) 75–86.

Altun, O., Sert, T., Altun, D., Toprak, A., Kwade, A., 2024. Scale-up of Vertical Wet Stirred Media Mill (HIGmill) via Signature Plots, Stress Analyses and Energy Equations, *Minerals Engineering* 205, 108460

G3: Degradation of Y-TZP grinding media during wet milling

Arthur Pacquelet [1,2], *Vincent* Garnier[1], *Laurent* Gremillard[1], *Jérôme* Chevalier[1], *David* Bouttes[2], *Nassira* Benameur[2], *Samuel* Marlin[2] and *Helen* Reveron[1]

[1] INSA Lyon, Universite Claude Bernard Lyon 1, CNRS, MATEIS, UMR5510, 69621Villeurbanne, France
[2] Saint-Gobain Research Provence, Cavaillon, France

Abstract. Wet milling process is widely used in the industry to reach very fine particle size of products by using grinding media, often made of Yttria-stabilized-zirconia (Y-TZP). It is known that milling efficiency is affected by many operational parameters such as temperature of the suspension, viscosity etc. However, relatively few works were performed to evaluate the impact of these parameters on the grinding media degradation. In fact, during milling and due to the large number of shocks and friction events, grinding media wear out, generating issues such as pollution of the product and reduction of media size. In this work, we evaluate the effect of wet milling parameters on the degradation of Y-TZP beads of 0.8mm, in a stirred media mill. We show that varying the suspension temperature from 30°C to 55°C significantly increases wear. The pH of the suspension also plays a major role on beads degradation, the basic conditions being identified as the more degrading. Another aspect of this work was to investigate the relevance of water milling tests often use to select a grinding media. We revealed that these water tests generate a very low wear compared to what is observed during milling tests performed with solid-containing suspensions.

1 Introduction

During the milling process, many shocks and contacts occur between grinding medias. These are responsible for the decrease of the particles size of the ground product. However, it generates wear of the grinding media which depends on many operational parameters. It was shown (Mende et al. 2003; Becker et al, 1999) that suspension characteristics such as the hardness of the material to be milled or the pH highly affect the wear of the beads.

Furthermore, the large number of collisions between grinding media increases the temperature of the suspension (Guner et al, 2022). This elevation of temperature is responsible for an acceleration of the degradation of the grinding media (Ohnishi et al. 2009). In the industry, water milling tests (i.e. without powder to be ground) are performed to choose which grinding media will be used for a given application. However, this type of test generates very low wear of the grinding media (Ohnishi et al. 2009).

This study will evaluate the pertinence of the water tests in wet milling process and determine the effect of the temperature and the pH of a suspension on the wear of grinding media.

2 Material & methods

In order to study the effect of temperature and pH on grinding media wear, a stirred media mill (model Labstar from Netzsch) was used in circulation mode. Two independent cooling systems were installed to regulate the temperature of the agitation and grinding chambers, with temperature recording at the entry and exit of both chambers. The set-up is presented in Figure 23.

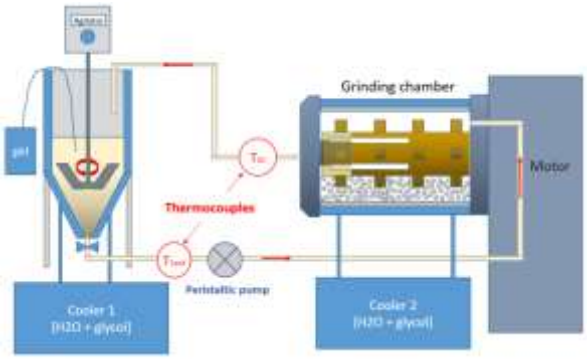

Figure 23: Experimental set-up used for milling tests

Two linings were available for the grinding chamber. The first one in polyurethane (PU) which cannot be cooled, the other in silicon carbide (SiC) allowing the regulation of the suspension temperature by means of coolers 1 and 2 (see Figure 1).

* Corresponding author: escc2024@mke.org.hu

The Y-TZP grinding media (*Zirmil-Y*) used in this work were manufactured by Saint-Gobain with a chosen diameter of 0.8mm.

A suspension of monoclinic zirconia (CC10 Saint-Gobain) or demineralized water were used in milling tests. Interrupted milling was performed until a total time of 15h (CC10; 3 steps of 5h each) or 27h (water; steps at 7, 17 and 27 h). The wear of Y-TZP beads during the milling process was evaluated by following their weight loss. These tests were performed in the chamber with PU lining.

The effect of the zirconia CC10 suspension pH (a basic around 11 and a neutral around 7) were studied in PU chamber at 55°C. To obtain equivalent viscosity of the slurry at both pH, dispersant was added to the neutral suspension.

In order to control the temperature of the suspension during grinding, additional CC10 milling experiments were performed using SiC lining. The effect of the temperature of suspensions (30°C, 45°C and 55°C as measured at the exit of grinding chamber) was thus studied.

3 Results & Discussion

The beads wear significantly increases with temperature as it is shown in Figure 2. SEM observations of the beads (not shown here) also revealed a more degraded surface at higher temperature.

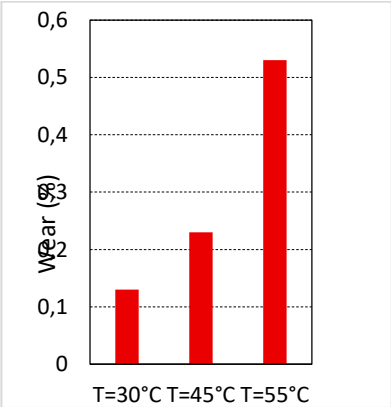

Figure 24: Evolution of the wear rate of Zirmil-Y beads at different temperatures after 15h of milling (CC10 suspension) using a SiC lining chamber

Regarding the pH effect at 55°C, the wear rates plotted in Figure 3 shows that basic conditions remove more material from the surface of the beads, leading to higher contamination of the suspension.

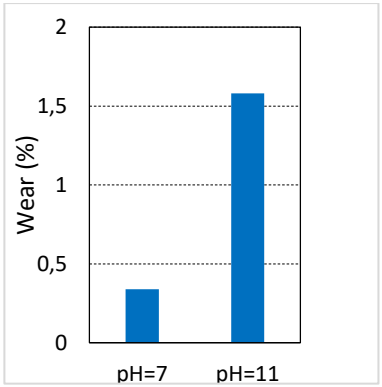

Figure 25: Evolution of the wear rate of Zirmil-Y beads at different pH and 55°C, after 15h of milling (CC10 suspension) using a PU lining chamber

The effect of performing grinding using CC10 zirconia suspension (i.e. with powder) or only water (i.e. without powder) is shown in Figure 4. Without powder to be milled, the wear of the grinding media is significantly lower than in the presence of CC10 zirconia particles.

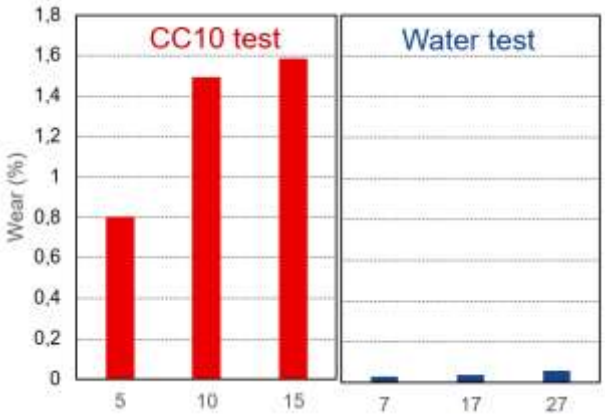

Figure 26: Comparison of grinding media wear in milling tests with or without powder to be milled (at natural pH and at 55°C) using a PU lining chamber

SEM observations (not shown here) revealed that without powder to be milled, polishing occurs at the surface of the beads during the first 7 hours of use and that zirconia grains begin to be removed from the surface of beads from 14h of milling. Therefore, this so-called "water" test does not appear to be suitable for evaluating the overall or bulk properties of the beads, but rather their surface characteristics.

4 Conclusion

This study underlines the significant effect of the pH of a suspension on the wear of Y-TZP grinding media. Basic conditions degrade these beads more than neutral ones. The temperature of the suspension also affects the Y-TZP grinding media degradation: the higher the temperature, the higher the degradation of the beads. Modifying the nature of the grinding chamber lining is a way of limiting the temperature rise during milling. However, it should be noted that it also affects the wear behaviour of the grinding media. The water tests, often used in the industry to discriminate different grinding

media, lead to a much lower wear of Y-TZP beads than that observed when milling a suspension of monoclinic zirconia powders. Although this study highlighted the most degrading conditions for Y-TZP beads in wet grinding tests, Y-TZP remains an excellent material for grinding media when used under more suitable conditions.

References

Becker, M. and J. Schwedes (1999). Comminution of ceramics in stirred media mills and wear of grinding beads. *Powder Technology* 105(1-3): 374-381.

Mende, S., et al. (2003). "Mechanical production and stabilization of submicron particles in stirred media mills." *Powder Technology* 132(1): 64-73.

Becker, M. and J. Schwedes (1999). Comminution of ceramics in stirred media mills and wear of grinding beads. *Powder Technology* 105(1-3): 374-381.

Guner, G., et al. (2022). "Analysis of Heat Generation During the Production of Drug Nanosuspensions in a Wet Stirred Media Mill." *International Journal of Pharmaceutics* 624(2): 122020.

Ohnishi, H., et al. (2009). "Wear Resistance of SiO_2-Doped Y-TZP Grinding Media During Wet Milling." *International Journal of Applied Ceramic Technology* 7(4): 502-511.

G4: Fine grinding of rhyolite tuff and the on-line monitoring of the rheological behaviour of the ground suspension by a tube rheometer

Katalin Bohács[1], Ádám Rácz[1], Izabella Márkus[1], Ferenc Kristály[2], Teemu Kinnarinen[3], Nazila Bolourieh[3], József Faitli[1]*

[1]Institute of Raw Materials Preparation and Environmental Technology, University of Miskolc, Hungary
[2]Institute of Exploration Geosciences, University of Miskolc, Hungary
[3]LUT School of Engineering Sciences, Lappeenranta-Lahti University of Technology LUT, Lappeenranta, Finland

Abstract. In this research, a Hungarian rhyolite tuff was mechanically activated in a stirred media mill in order to develop a product for agricultural use. Stress intensities and concentrations were altered during the systematic experiments; meanwhile, the particle size distribution and the grinding energy were measured. Additionally, an on-line tube rheometer and an off-line rotational rheometer were used to study the rheology of the ground suspension during the grinding process. Authors had developed a tube rheometer to supplement a Netzsch MiniCer (Netzsch GmbH, Germany) stirred media mill in order to monitor online the rheological characteristics of the suspension and therefore the result of grinding during the process. The product related stress model was applied for the evaluation of the grinding results. Besides that the mineralogical composition was off-line monitored by an XRD powder diffractometer.

1 Introduction and aim

Stirred media milling is a widely applied process in both mineral- and waste processing. However, the optimisation of this type of fine grinding is still challenging. There are two well-known and fundamentally different stirred media milling models in the literature, namely the stressing model (Kwade, 2003; Flach et. al., 2018) and the micro-hydrodynamic model (Eskin et. al., 2005). There are many parameters that affect the results of an actual grinding application. The parameters can be characterised as material, process and mill related parameters. This paper does not deal with the simulation or modelling of this process, rather it focuses on the experimental investigation of the changes in material features that occur during grinding. The two most important examined features are the mineralogical changes of the ground solid and the rheological behavioural changes of the ground suspension. For these systematic experiments a model material was selected, it is the rhyolite tuff. This is mined in many places in Hungary and its agricultural and ceramic industry applications are the most common. This research is part of an agricultural product development.

It is well known that the rheological properties of the ground suspensions can vary continuously during grinding, because the born finer particles might behave totally different, forming a new structure with the grinding medium, typically with the water. Because of the mechanical activation the mineralogical composition of the ground solids might also be changing. The viscous dampening of fine grinding is also well-known. According to both the stressing and the micro-hydrodynamic model, the speed of the grinding media is crucial for grinding. Higher speed means higher stress intensity; therefore the velocity decrease because of the viscous dampening greatly spoils the grinding efficiency. If the ground suspension remains still Newtonian during grinding, but its absolute viscosity might increase because of the finer particulate system which results in viscous dampening. If the ground suspension becomes Bingham Plastics the rising yield stress can result an even higher viscous dampening. If the ground suspension becomes shear-thinning, that is a lucky situation, because this cases the relative viscous dampening decreases for high grinding media velocities. However, for shear-thickening suspension the situation is just the opposite, and it is rather unfavourable. Regarding the capacity of the mill, the solids concentration of the feed suspension is really important. It is also well-known that generally low feed concentration leads to low capacity but a better grinding, namely finer ground product. Higher feed concentration results the opposite, at extreme high concentrations the mill can become clogged. However this general situation might not be valid for stirred media milling in a given solids concentration range of the feed, because if there are more particles in between the grinding beads they can escape less (Breitung-Faes and Kwade, 2014).

The suspension rheology strongly depends on the solids concentration and this effect might not be well taken care in the literature. The rheological behaviour of a suspension is a material feature and a wide variety can be found in the industry. According to a simple rule of

* Corresponding author: katalin.bohacs@uni-miskolc.hu

thumb, many suspensions without grinding become non-Newtonian at above 20 % volumetric solids concentration. This introduction illustrates why the monitoring of the rheological behavioural changes of the ground suspension is important. It is widely examined in the literature, but typically the rheology is measured off-line with rotational rheometers, - and many times by the re-dispersing of the ground solids - but according to Shi & Napier-Munn (2002) the on-line measurement is really important for plant-scale production and control, therefore it is also important for laboratory testing. Therefore an on-line tube rheometer was developed (Figures 2 and 3). Development issues and features of this device have been published (Faitli et. al., 2015 and 2016).

During grinding the result of the process can be monitored by the well-known methods in the literature. According to the product related stress model (Kwade & Schwedes, 2007) stress number can be calculated for grinding of crystalline materials as follows (eq. 1):

$$SN \propto \frac{\varphi_{GM}\cdot(1-\varepsilon)}{(1-\varphi_{GM}\cdot(1-\varepsilon))\cdot c_v} \cdot \frac{n\cdot t}{d_{GM}^2} \qquad (1)$$

Where φ_{GM} is grinding media fill volumetric ratio, ε is porosity, c_v is volumetric concentration of the ground suspension, n is revolution number of mill rotor and t is time. After certain grinding time the median particle size and the produced new specific surface area characterise the efficiency of grinding.

The purpose of the research carried out was to measure the rheological behaviour and mineralogical composition during stirred media milling of the selected rhyolite tuff model material when the effectiveness of grinding was also gradually monitored. Two different feed solids concentration were tested: 20 m/m% (equivalent to 10.2 V/V%) and 30 m/m% (equivalent to 16.3 V/V%). Only one mill parameter setup was used and that was determined by optimisation research carried our earlier.

2 Materials and Methods

Rhyolite tuff with a material density of 2210 kg/m^3 (measured by liquid pycnometer) was used for the grinding-rheological experiments in this study. The measured empirical particle size – distribution function and the particle size - histogram of the raw rhyolite tuff are presented in Figure 2. It can be seen from Figure 1 that the model material has a relatively wide particle size range from 0.2 µm up to 100 µm. The empirical particle size – distribution function (PSD) of the raw material and the ground samples was determined by a Horiba LA-950V2 laser particle size analyser (LPSA) in distilled water. Before PSD laser scattering measurement, ultrasonic dispersing was applied for 1 min and 0.5 mL sodium pyrophosphate was used in 50 g/L concentration as dispersant. Furthermore, during the experiments the „outer" (geometric) specific surface area (SSA) of the ground samples were measured and calculated by the same LPSA. The energy consumption of the mill was measured online by the Netzsch measuring system and data were registered in a computer. In this way the specific grinding energy could be calculated.

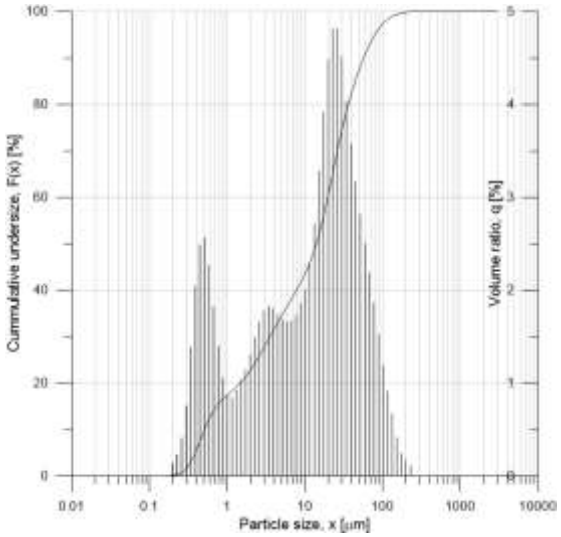

Fig. 1. Particle size distribution of the raw rhyolite tuff sample (feed).

The quantitative mineralogical composition of the samples was assessed using X-ray powder diffraction (XRD) method. The measurements were conducted with a Bruker D8 Discover XRD powder diffractometer (Cu-Kα radiation, 40 kV, 40 mA, Bregg-Brentano geometry, LynxEye XE-T detector). The powder specimen obtained from the samples was dried at 105 °C and pulverized and it was arranged in a top loaded shallow low background Si single crystal sample holder. Identification of crystalline components was done by Search/Match, on ICDD PDF2 (2005) database in the Bruker DiffracPlus EVA software. Quantitative composition was calculated with Rietveld refinement in Bruker TOPAS4. The mineralogical composition of the raw rhyolite tuff sample can be seen in Table 1.

Table 1. Quantitative mineralogical composition of the raw rhyolite tuff sample (feed)

Phase Name	Quartz	Orthoclase	Albite (K)	Sanidine	Mordenite	Andesine	Illite 2M1	Quartz nano	amorphous
m/m%	25.1	26.4	21.4	3.2	0.2	3.5	5.9	2.9	11.5

Grinding experiments were carried out in a stirred media mill (Netzsch MiniCer, Netzsch GmbH, Germany) in circular mode. The liners of the grinding chamber and the stirrer rotors were made of high wear resistant ZrO (zirconia). The range of the revolution number of the drive motor is between 1000 and 4200 min-1. The mill capacity is 140 – 500 ml suspension.

Figure 2 shows the schematic of the developed on-line tube rheometer and Figure 3 shows a photo about the built test setup. The original peristaltic pump of the Netzsch MiniCer was used as the main pump to drive the suspension through the measuring pipe sections. Two

measuring pipe sections made by stainless steel were connected serially (D1=10 mm, L1=1.6 m, D2=9 mm, L2=1.6 m). If we have two measured pressure loss - flow rate points for a given operational condition, two parameters non-Newtonian rheological model can be fit. The flow rate can also be changed and many points of the pseudo shear curve can be measured. Pressure losses on the test pipe sections were measured by no dead space gauge pressure transducers (Δp1=p1-p2; Δp2=p3-p4).

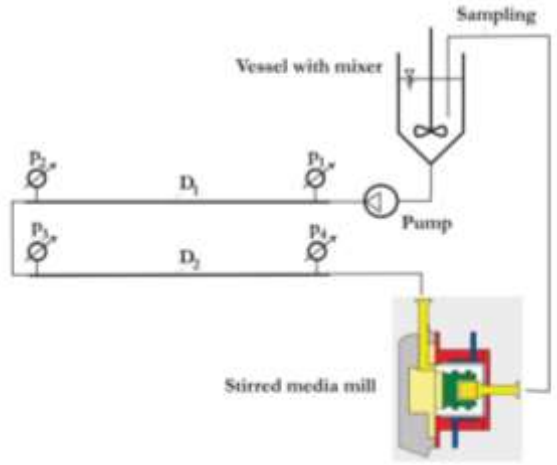

Fig. 2. Stirred media mill with the on-line tube rheometer.

Fig. 3. Photo of the test rig with the on-line tube rheometer.

Flow rate was determined indirectly. The applied peristaltic pump is a positive displacement pump. Therefore, the flow rate was assumed to be constant for a given revolution number. The capacity of the peristaltic pump was calibrated by the simple method by measuring the volume of the outflowing water by a vessel and a weight and measuring the time with a stopwatch. Pump performance had been tested by viscous suspensions as well. For the tube rheometer a separate computer data acquisition system was developed and signals of the pressure transducers No. 1-4 were measured by this auxiliary system with 100 Pa sensitivity. The traditional off-line rheological test method was also used for comparison. After sampling the ground suspensions were measured in an Anton-Paar MCR51 rotational rheometer with a cylinder-cylinder measuring system with 0.5 mm Couette width gap.

3 Results and Discussion

Grinding experiments were carried out in the described Netzsch MiniCer mill with the on-line tube rheometer in wet mode. Two experimental series were carried out. Only the suspension concentration (20 and 30 m/m%) was varied, all the other grinding parameters were kept constant. Maximum grinding time was 120 min. The circumferential velocity of the mill rotor edge was 7.8 m/s, the grinding media was ZY Premium 0.8-1.0 mm (ZrO). Samples were taken after 5, 10, 20, 30, 45, 60, 90, 120 min grinding times then were analysed using LPSA. Figure 4 shows the median particle size as a function of stress number and Figure 5 shows the produced specific surface area as a function of specific surface area.

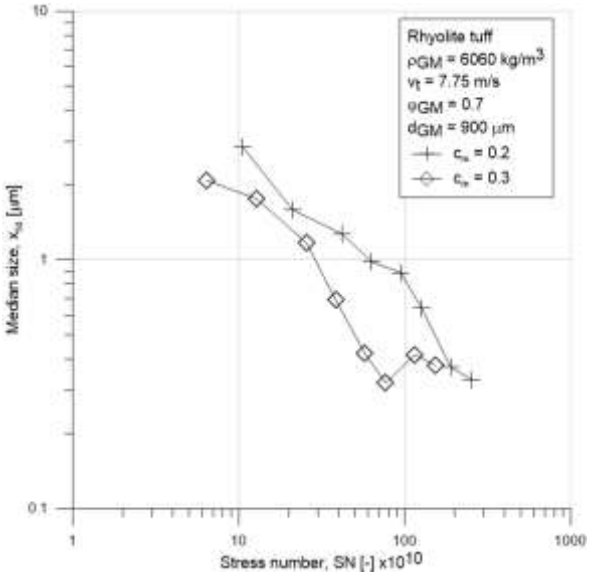

Fig. 4. Median particle size as a function of Stress number.

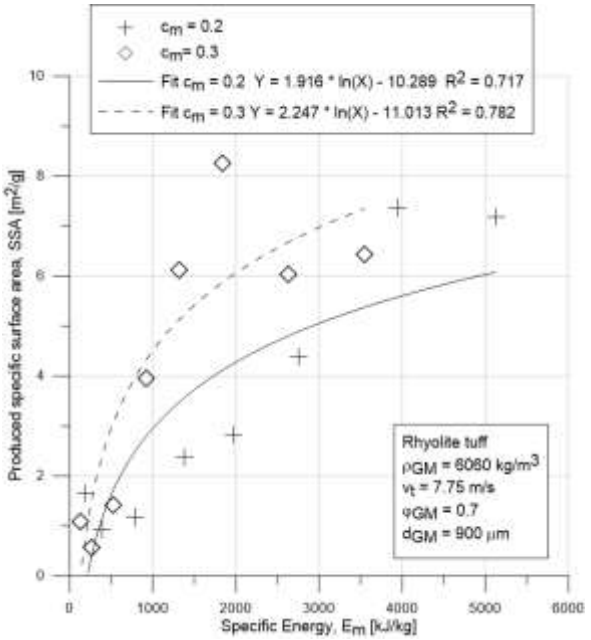

Fig. 5. Produced specific surface area as a function of specific surface area.

After 30, 60, 90 and 120 minutes continuous peristaltic pump speed grinding, the mill motor was switched off for a short time. During these milling breaks, standard tube rheometer testing was performed, namely the pump speed was changed, and five discrete speed values were set. This procedure resulted five pseudo shear points for both pipes for all the two series.

Mineralogical composition analysis was carried out only with the 20 m/m% solids feed concentration grinding. The change in the quantitative mineralogical composition was measured after 120 minutes continuous grinding. A significant increase in the amorphous phase was observed, while the quantity of feldspars albite and orthoclase decreased. A significant decrease of almost 10 % could also be observed in the case of quartz (Figures 6 and 7).

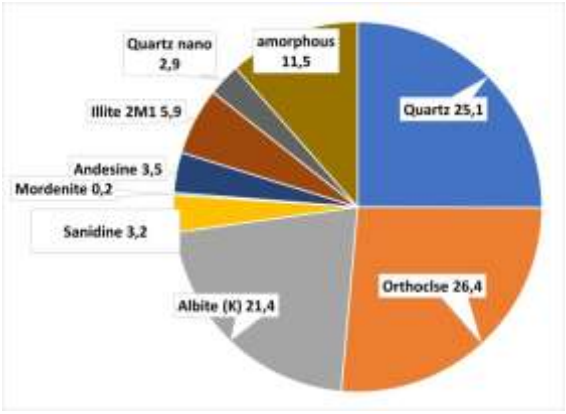

Fig. 6. Quantitative mineralogical composition of the raw rhyolite tuff sample (feed)

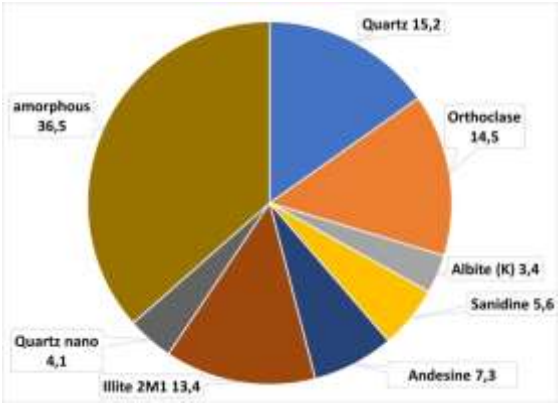

Fig. 7. Quantitative mineralogical composition of the rhyolite tuff samples after 120 min grinding.

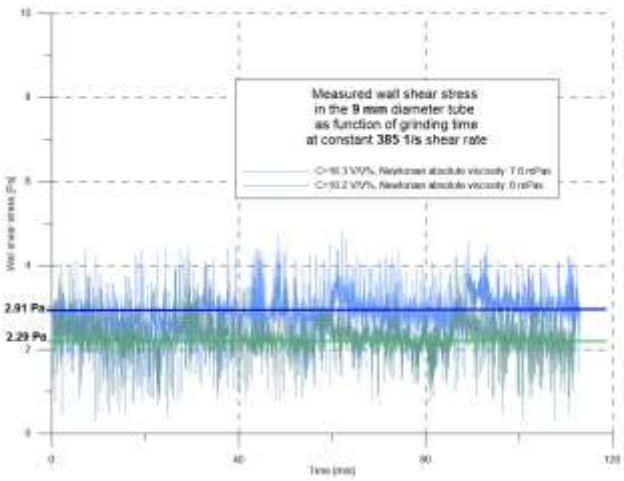

Fig. 8. The wall shear stress as function of grinding time.

Regarding to the rheological testing the pseudo shear curves of all the tube and the rotational rheometer tests have been evaluated. The ground suspensions only after the complete 120 min grinding were tested in the rotational rheometer, simply because of the necessary sample volume. All the materials were needed for the continuous grinding. Figure 8 shows the measured wall shear stress on the 9 mm test tube as function of time for the two different concentration rhyolite tuff suspensions. The revolution number of the peristaltic pump was kept constant; therefore, the flow velocity and the pseudo shear rate (385 1/s) were also constant. It is very well seen that the wall shear stress and therefore the absolute viscosity were also constant. It cannot be seen on Figure 8 but according to the pseudo shear curves (not shown here) of the tube- and the rotational rheometer the tested rhyolite tuff suspensions were Newtonian fluids. The absolute viscosity of the more dilute 20 m/m% suspension was 6 mPas, while the thicker 30 m/m% one was 7.6 mPas. According to Figure 4 the particle size evidently decreased, the medium particle size decreased from about 2 to 0.3 μm after 120 min grinding for both concentrations. The created new surface also increased according to Figure 5 and the higher feed solids concentration resulted some more new surface generation at the end of identical grinding time. The absolute viscosity of the 30 m/m% suspension is just slightly higher than the 20 m/m% one, so the higher viscous dampening was negligible; the already mentioned solids effect on grinding (if there are more ground solids in between the beads, solids can escape less) was more dominant.

As it was described earlier the rheology of the 120 min grinded suspensions were measured parallel by two different devices. It was concluded that the measured rheological model (Newtonian) and the absolute viscosity values were identical in ±0.2 mPas accuracy.

4 Conclusion

A comparative grinding experiment has been carried out with a stirred media mill with a selected model material (rhyolite tuff). Only one grinding parameter setup and two solids concentrations were tested and the rheological behaviour and the mineralogical composition were monitored during and after 120 min grinding. Grinding was effective because the median particle size decreased from about 2 to 0.3 μm, significant quantity of new surfaces was created and the mineralogical composition changed significantly as well. Quantity of the amorphous phase increased; the one of quartz, feldspars albite and orthoclase decreased. However, the normally viscous Newtonian ground suspension rheology did not change, even the absolute viscosity was constant during the 120 min grinding. It indicates that for this material and this particle size range the particles behave as neutral particles related to rheology and therefore the resultant fine suspension do not change its rheological behaviour (Newtonian) and rheological parameter (absolute viscosity).

This project is funded by the European Union's Horizon Europe program under grant no. 101079354.

References

Breitung-Faes S., Kwade A. (2014) Use of an Enhanced Stress Model for the Optimization of Wet Stirred Media Milling Processes. *Chemical Engineering and Technology*. Vol. 37. Issue 5. pp. 819-826. DOI: 10.1002/ceat.201300686

Bilgili E., Alfolabi A. (2012) A combined microhydrodynamics-polymer adsorption analysis for elucidation of the role of stabilizers in wet stirred media milling. *Int. J. Pharm*., Vol. 439, pp. 193-206. DOI: 10.1016/j.ijpharm.2012.09.040

Eskin D., Zhupanska O., Hamey R., Moudgil B., Scarlett B. (2005) Microhydrodynamics of stirred media milling. *Powder Technology*, Vol. 156, pp. 95-102. DOI: 10.1016/j.powtec.2005.04.004

Faitli J., Bohács K., Mucsi G. (2015) Online Rheological Behaviour Testing of Stirred Media Milled Suspensions. In Proceedings of the 14th European Symposium on Comminution and Classification, eds. Magnus Evertsson, Erik Hulthén, and Johannes Quist. Gothenburg, Sweden, 87–93.

Faitli J., Bohács K., Mucsi G. (2016) Online Rheological Monitoring of Stirred Media Milling. *Powder Technology*. Vol. 308. pp. 20-29. DOI: 10.1016/j.powtec.2016.12.021

Faitli J. (2017) Continuity theory and settling model for spheres falling in non-Newtonian one- and two-phase media. *International Journal of Mineral Processing*. Vol. 169, pp. 16–26. DOI: 10.1016/j.minpro.2017.09.010

Flach F., Breitung-Faes S., Kwade A. (2018) Model based process optimization of nanosuspension preparation via wet stirred media milling. *Powder Technology*. Vol. 331, pp. 146-154. DOI: 10.1016/j.powtec.2018.03.011

Kwade A. (2003) A Stressing Model for the Description and Optimization of Grinding Processes. *Chemical Engineering and Technology*. Vol. 26. Issue 2. pp. 199-205. DOI: 10.1002/ceat.200390029

G5: Modelling of multi-component fine grinding processes in stirred media mills

Maximilian Tobaben[1,*], *Arno* Kwade[1]

[1]Institute for Particle Technology, TU Braunschweig, Braunschweig, Germany

Abstract. The fine grinding of multi-component systems finds applications across various industries. The fine grinding processes often aim at increasing the selectivity, which enables optimized separation of valuable and non-valuable components in subsequent process steps. One challenge is the identification of suitable process parameters, as selectivity depends on both process parameters and the properties of the multi-component system. In order to address this challenge, the present work focuses on modelling multi-component fine grinding processes based on population balances. The results demonstrate that, with knowledge of the fine grinding behaviour of individual components and an energy split factor, the reduction in particle size and changes in selectivity during the fine grinding process can be represented with satisfactory accuracy.

1 Introduction

The fine grinding of multi-component systems is of high importance in numerous industries. Especially in the fields of minerals engineering and building material production, multi-component systems are omnipresent. Furthermore, they are gaining increasing importance in the recycling area, where stricter regulations make the comminution and subsequent separation of multi-component systems indispensable. While the fine grinding of single components in stirred media mills has already been extensively studied and optimized in previous papers (Kwade, 2003; Breitung-Faes and Kwade, 2013), there is a lack of systematic studies describing the fine grinding behaviour of multi-component systems. In particular, the interaction of individual components does not appear to be fully understood, resulting in the necessity for comprehensive experimental investigations for process optimization (Nöske et al., 2020). In order to address this challenge, current studies increasingly focus on modelling the comminution of multi-component systems mostly at laboratory scale using population balances (Rocha et al., 2022; Zhao et al., 2017). A crucial part of population balance equations is the implementation of an energy split factor, as described in the paper of Kapur and Fuerstenau (1988), which characterizes the variation in the breakage rate of a material with changes in the composition of the multi-component system. In the context of the present work, the utilization of the energy split factor is employed for modelling the fine grinding of an ideal mixture of quartz and limestone in a stirred media mill. Based on experiments, the model aims to describe the evolution of individual particles sizes during the fine grinding process and evaluate the selectivity and energy efficiency under varying stress energies.

2 Materials and methods

2.1 Experimental investigations

As a basis for modelling the multi-component fine grinding process, batch experiments were carried out in a horizontal stirred media mill on laboratory scale. The mill was equipped with a disc stirrer and a cooled grinding chamber ($V = 0.67\ l$). The grinding media stress energy SE_{GM} was systematically varied by adjusting the grinding media size d_{GM} and the stirrer tip speed v_t. The grinding media density ρ_{GM} was set to 6050 kg/m³. According to the model approach of Kwade (2003) in Eq. (1) and the specifications of test parameters in Table 1, seven different grinding media stress energies between 0.014 mJ and 0.81 mJ were realised.

$$SE \propto SE_{GM} = d_{GM}^3 \cdot v_t^2 \cdot \rho_{GM} \quad (1)$$

Table 1. Test parameters of fine grinding experiments.

Parameter	Symbol	Variation
Grinding media size	d_{GM}	530 – 1100 µm
Grinding media density	ρ_{GM}	6050 kg/m³
Stirrer tip speed	v_t	4 – 12 m/s
Grinding media stress energy	SE_{GM}	0.014 – 0.81 mJ
Grinding media filling ratio	φ_{GM}	80 %

* Corresponding author: m.tobaben@tu-braunschweig.de

Quartz and limestone were used as test materials. Both materials were classified in the range of 50 µm to 71 µm using an air jet sieve. The fine grinding experiments were carried out using both the single components and binary mixtures of the two materials in a ratio of 50/50 rel. wt. % and 20/80 rel. wt. %. The grinding time was varied between 30 seconds and 480 seconds. After each test, the stirred media mill was completely emptied and the product particle size was measured using laser diffraction. A selective analysis of the particle size was realised by dissolving limestone in hydrochloride acid analogy to the investigations by Nöske et al. (2020). The selectivity of fine grinding tests was evaluated using the approach of Hesse et al. (2017), whereby the selectivity S is calculated as the normalized difference between integrated particle size distributions Q_3 of both components using Eq. (2)

$$S = \frac{\int_{x_l}^{x_u} Q_{3,Limestone}(x)dx - \int_{x_l}^{x_u} Q_{3,Quartz}(x)dx}{x_u - x_l} \qquad (2)$$

where x_l and x_u are the lower and upper limit of the respective particle size range. Based on the selectivity values of the feed (S_F) and the product (S_P) the selective comminution value SC can be calculated according to Eq. (3).

$$SC = S_P - S_F \qquad (3)$$

2.2 Modelling

The modelling of fine grinding processes in the stirred media mill is based on the population balance equation of Herbst and Fuerstenau (1980) which considers the mass balance of both materials in each particle size class i as a function of the energy input E. Taking the energy split factor proposed by Kapur and Fuerstenau (1988) into account, the population balance model is given by the following equation:

$$\frac{dm_{i,k}(E)}{dE} = -k_k \cdot S_{i,k}^E \cdot m_{i,k}(E) + \sum_{j=1}^{i-1} k_k \cdot S_{j,k}^E \cdot b_{ij,k} \cdot m_{j,k}(E) \qquad (4)$$

where m_i is the mass fraction in the particle size class i, S_i^E denotes the specific breakage rate in particle size class i, b_{ij} represents the breakage function, and k is the energy split factor. The index k describes each component of the binary mixture. The breakage rate was calculated using the model by Herbst and Fuerstenau (1980), while the breakage function was based on the approach by Austin and Luckie (1972). All model parameters were determined based on the batch experiments conducted beforehand.

3 Results and discussion

The experimental fine grinding tests indicate that the optimal grinding media stress energy increases with a higher proportion of quartz particles, which can be attributed to its higher material hardness and breakage strength. While the fine grinding of pure limestone is most energy-efficient at a grinding media stress energy of approximately 0.03 mJ, processing quartz requires a grinding media stress energy of 0.5 mJ to prevent elevated energy dissipation.

Unlike the design of fine grinding processes for single components, the processing of multi-component systems often aims for selective comminution. As illustrated in Fig. 1, the selectivity depends on both the process parameters and the mixing ratio of the multi-component system. It is evident that relatively low grinding media stress energies $SE_{GM} \leq 0.1$ mJ enable selective limestone comminution of 20 % to 30 %. In contrast, increased grinding media stress energies result in uniform fine grinding of both components, leading to a significant decrease in selective limestone comminution. Generally, it is noticeable that a limestone content of 80 rel. wt.% allows for increased selective comminution, attributed to the higher capture probability of limestone particles.

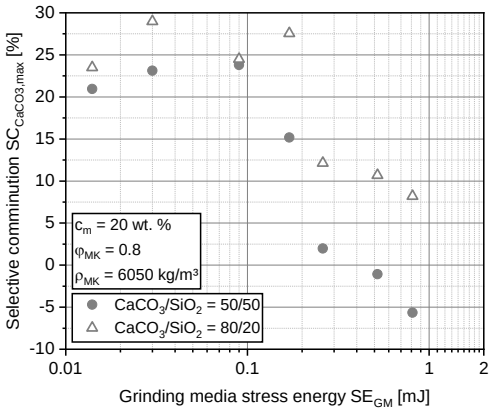

Fig. 1. Selective comminution of limestone for varying grinding media stress energies.

In terms of modelling the fine grinding behaviour of multi-component systems with population balances, the implementation of the energy split factor enables description of particle size distributions with satisfactory accuracy. For a mixing ratio of 50/50 rel. wt.%, the modelled selective comminution values for investigated grinding media stress energies are shown and compared to the experimental data in Fig. 2. It is evident that, except for a grinding media stress energy of 0.26 mJ, the trends and levels of selective limestone comminution can be described correctly.

Furthermore, the evaluation of the energy split factor indicates that fine grinding of limestone in a mixture with quartz is less energy-efficient than grinding limestone as a single component, whereby the efficiency decreases with increasing grinding media stress energy. This is attributed to the so-called protection effect, where

the harder quartz particles protect the softer limestone particles from being stressed by the grinding media.

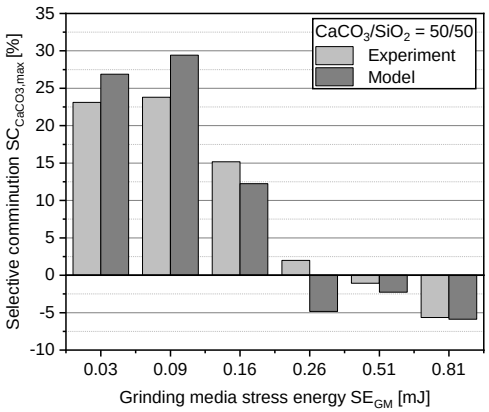

Fig. 2. Comparison of modelled, selective limestone comminution with experimental data.

4 Conclusion

In the scope of the present work, the fine grinding of a binary multi-component system consisting of limestone and quartz with a stirred media mill was experimentally investigated and modelled by using population balances. The results indicate that a selective comminution of the softer limestone is achievable when a suitable grinding media stress energy is chosen. Population balances and implementation of an energy split factor can adequately model the fine grinding behaviour of the multi-component systems. The insights gained from this study can aid in selecting process parameters to ensure both selective and energy-efficient fine grinding processes.

5 Acknowledgments

The authors gratefully acknowledge the financial support of the German Research Foundation (DFG).

References

Austin, L.G., Luckie, P.T. (1972) The estimation of non normalized breakage distribution parameters from batch grinding tests. *Powder Technology*, 5, 267-271.

Breitung-Faes, S., Kwade, A. (2013) Prediction of energy efficient grinding conditions. *Minerals Engineering*, 43-44, 36-43.

Herbst, J.A., Fuerstenau, D.W. (1980) Scale-up procedure for continuous grinding mill design using PBM. *International Journal of Mineral Processing*, 7(1), 1-31.

Hesse, M., Popov O., Lieberwirth, H. (2017) Increasing efficiency by selective comminution. *Minerals Engineering*, 103-104, 112-126.

Kapur, P.C., Fuerstenau, D.W. (1988) Energy Split in Multicomponent Grinding. International Journal of Minerals Processing, 24(1-2), 125-142.

Kwade, A. (2003) A Stressing Model for the Description and Optimization of Grinding Processes. *Chemical Engineering & Technology*, 28(2), 199-205.

Nöske, M., Li, K., Brüning, K., Breitung-Faes, S., Kwade, A. (2020) Impact of stress conditions on stirred media milling of a two component mixture. *Minerals Engineering*, 146.

Rocha, B.K.N., Campos, T.M., Alves, L.P., Silva, J., Turrer, H.D.G., Lichter, J., Tavares, L.M. (2022) Multicomponent modelling and simulation of the Minas Rio iron ore grinding circuit. *IMPC Asia-Pacific*, 313-324.

Zhao, R., Han, Y., He, M., Li, Y. (2017) Grinding kinetics of quartz and chlorite in wet ball milling. *Powder Technology*, 305, 418-425.

G6: Effect of Grinding Aid Mixtures on Dry Grinding of Calcite

Serkan Cayirli[1,*] and *İbtesam* Manla[2]

[1]Faculty of Engineering, Nigde Ömer Halisdemir University, Turkey
[2]Faculty of Engineering, Nigde Ömer Halisdemir University, Turkey

Abstract. Current experimental work aims to examine the effect(s) of micronized dry grinding of calcite by using grinding aids and liquid materials with their mixtures. The determination/optimization of the appropriate conditions and the quantities of suitable grinding aids and mixtures were carried out through experiments and analyses carried out in the stirred ball mill in the laboratory environment. Looking at the background of this study, the usability of waste and by-products as a grinding aid in calcite grinding was examined (Cayirli et al, 2023a). Thus, the motivation for the current study is the mixture of waste and by-products with pure grinding aid, based on the results obtained from this background. In this context, mixtures of olive pomace oil, olive black water and molasses with triisopropanolamine at certain concentrations were tested. The results were evaluated based on particle size analysis and powder flowability.

1 Introduction

Grinding aids function by altering the interfacial forces between particles, reducing agglomeration, enhancing the dispersion of particles within the grinding medium, and chancing flow properties. Traditional grinding aids have been extensively utilized in industries to address specific challenges associated with grinding, such as increased throughput, reduced energy consumption, and improved product fineness. However, the pursuit of further optimization in grinding processes has led to the exploration of novel approaches, including the development of mixture-based grinding aids. These mixtures typically combine two or more distinct additives, each contributing unique functionalities that synergistically enhance the overall grinding performance. The rationale behind using mixture-based grinding aids lies in the potential for achieving superior outcomes compared to individual additives alone, as well as the opportunity to tailor the composition to suit specific grinding requirements and material characteristics. The most important examples of mixture-based grinding aids are seen in commercial mixtures (Toprak et al, 2014; Gokcen et al, 2015). On the other hand, its usability as a grinding aid for waste materials as well as pure and commercial grinding aids has been investigated in the literature (Li et al, 2015; Cayirli et al, 2023a; Katircioglu-Bayel, 2024). In this article, we explored the concept of mixed grinding aids through the approach of combining waste, by-products and pure grinding aids.

2 Experimental procedures

It was employed a calcite sample in the dry experiments, sourced from Mikron'S Inc., Turkey, the calcite sample is highly pure, consisting of 98.838% $CaCO_3$, with a median particle size of 83.77 µm (d_{50}) and a specific density of 2.71 g/cm^3. In this study, olive pomace oil (OPO)–triisopropanolamine (TIPA) (Acros Organics, 98%, 1.02 g/cm^3), olive black water (OWW)–triisopropanolamine and molasess (CM)–triisopropanolamine mixtures were used as grinding aids and compared with their individual uses.

The grinding tests were performed using a vertical batch-type laboratory stirred ball mill (Fig. 1). Particle size analysis (d_{50}) and powder flowability (ffp) assessments were conducted using a wet laser diffraction particle sizer (Malvern Co., Ltd., UK) and a powder flow tester (230VAC-Brookfield, UK) (Fig. 2), respectively.

Figure 1. Pin type vertical stirred ball mill

* Corresponding author: scayirli@ohu.edu.tr

Figure 2. Powder flow tester

2.1 Results and discussion

2.1.1 The tests with TIPA-OPO mixtures

The effect of variations in grinding aids on the d_{50} and ffp is illustrated in Fig. 1, based on the tested grinding times. In preliminary studies, it was understood that the equal mixture of TIPA-OPO did not affect the grinding performance in 9.5 minutes. Thereupon, other mixture ratios were tested. According to the findings, it was determined that the other mixtures showed better performance at all grinding times compared to the no-aid condition. It has been understood that mixing the grinding aids, especially in the early grinding times, is beneficial compared to using individual TIPA and OPO. The grinding performance obtained also coincides with the powder flowability index.

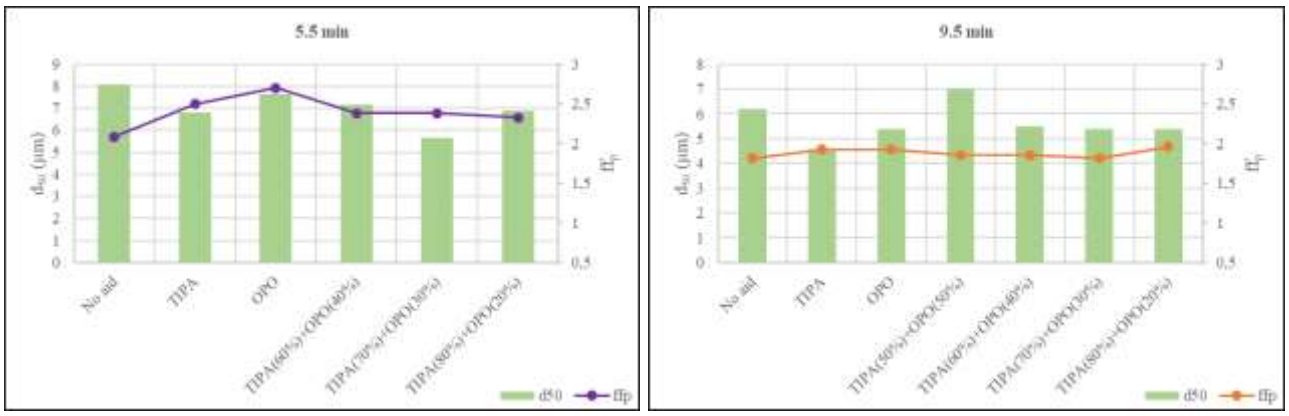

Figure 3. The variation of grinding performance with TIPA, OPO and the mixture series.

2.1.2 The tests with TIPA-OWW mixtures

Fig. 2 shows the effect of the grinding aids on d_{50} and ffp at two grinding times. It can be stated that Although OWW discussed in former study (Cayirli et al, 2023b) does not improve flowability, it contributes to grinding performance.

On the other hand, TIPA has the most effective performance in terms of both flowability and grinding performance. Regarding the mixture-based grinding aids tested, d_{50} values close to those of TIPA were obtained at both grinding times. Additionally, ffp values also increased due to TIPA, unlike OWW. Also, both graphs in Fig. 2 clearly show that all grinding aids lead to smaller particle sizes compared to the no-aid condition.

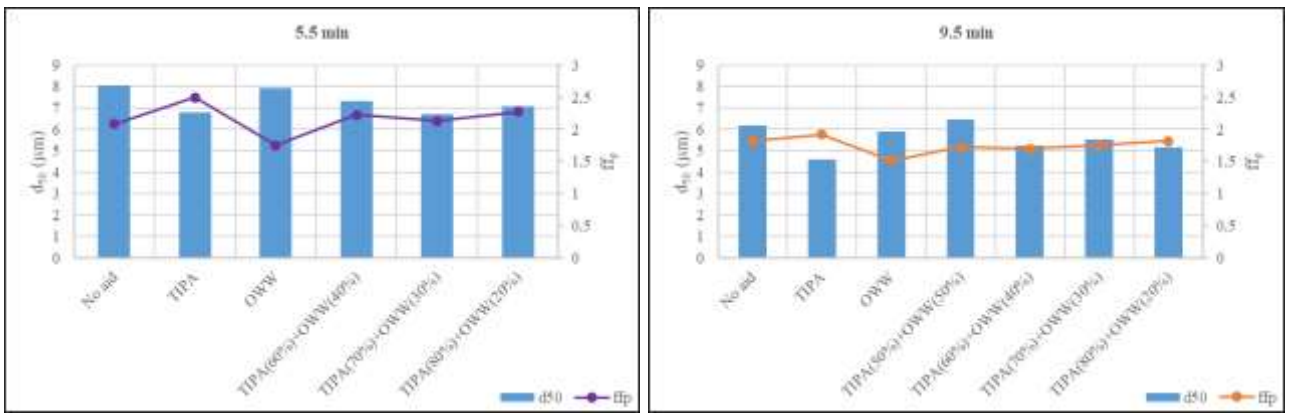

Figure 4. The variation of grinding performance with TIPA, OPO and the mixture series.

2.1.3 The tests with TIPA-CM mixtures

Fig. 3 illustrates the variation trends in grinding performance (particle size and powder flowability) of TIPA, CM with the mixture series. According to the figure, It was determined that all variations of grinding aids tested (except for TIPA(50%)+CM(50%) at 9.5 min) showed better performance compared to the no-aid condition. The effectiveness of CM in the early grinding period was noticeable, even though its powder flowability index was low. In addition to its standalone effect, it also exhibited better performance than TIPA in mixtures (70%+30% and 80%+20%). Regarding mixtures, powder flowability also increased compared to CM. It can be said that CM affects size in mixtures, while TIPA affects fluidity. Li et al. (2015) explained the effectiveness of molasses in clinker tests as the gel or colloidal structure having high viscosity, helps strengthen the stability of the coating layer. It turns out that TIPA is more effective after 9.5 grinding times. As a matter of fact, the mixture test results were between TIPA and CM.

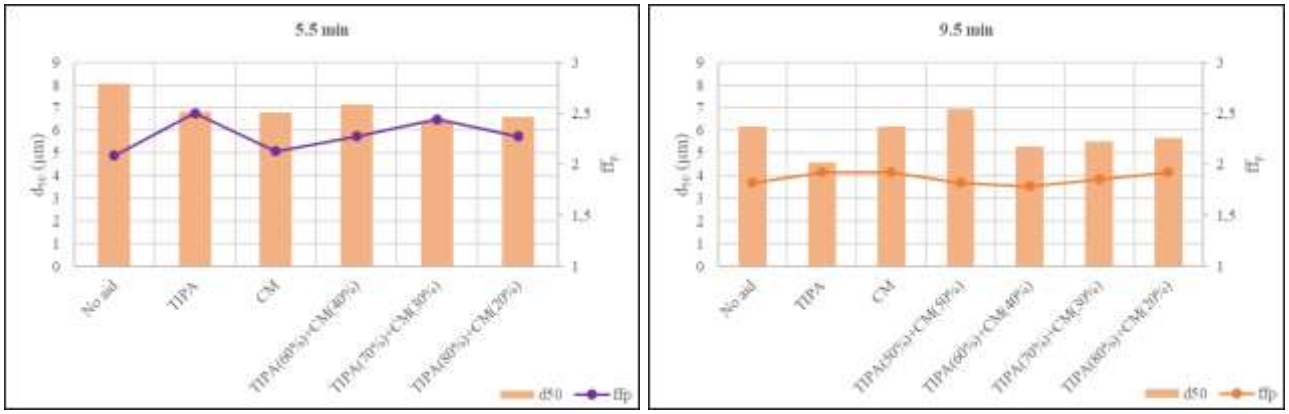

Figure 5. The variation of grinding performance with TIPA, CM and the mixture series.

2 Conclusions

Within this experimental work, the effects of individual and mixture grinding aids on particle size and powder flowability of ground calcite were identified. Although the highest product fineness and powder flowability were achieved with pure grinding aid (TIPA), it turned out that similar values could be obtained with the use of waste and by-products. In fact, it can be seen as promising that effective results can be obtained in the tested mixtures, depending on the grinding time and mixture ratio.

This work is still ongoing and different chemicals and mixing ratios will be added.

Acknowledgements

The authors express their gratitude for the contributions of the Scientific and Technological Research Council of Turkey (Grant No. 119M216), which funded a part of this research. The authors would also like to extend their thanks to Mikron'S Inc. for providing calcite samples, Eskişehir Sugar Factory for supplying molasses, and Dalan Chemistry for supplying olive pomace oil and olive black water.

References

Cayirli, S., Gokcen, H. S., Yuce, N., & Elchi, O. (2023a) Investigation of the usage of waste materials and by-products as grinding aids in calcite grinding. *Minerals Engineering*, 202, 108267.

Cayirli, S., Gokcen, H. S., Yuce, N., Elchi, O. (2023b) Utilization of wastes/by-products as grinding additives. *Scientific Mining Journal*, 62 (3), 123 – 130.

Gokcen, H. S., Cayirli, S., Ucbas, Y., & Kayaci, K. (2015) The effect of grinding aids on drymicro fine grinding of feldspar. *Int. J. Miner. Process.*, 136, 42–44.

Li, H., Jiang, Z., Yang, X., Yu, L., Zhang, G., Wu, J., Liu, X. (2015) Sustainable resource opportunity for cane molasses: use of cane molasses as a grinding aid in the production of Portland cement. *J. Clean. Prod.*, 93, 56–64.

Katircioglu-Bayel, D. (2024) Investigation of the use of glycerin as a by-product, pomace oil and paper wastewater as grinding aids in marble dust wastes. *Advanced Powder Technology*, 35 (3), 104366.

Toprak, N. A., Altun, O., Aydogan, N., & Benzer, H. (2014) The influences and selection of grinding chemicals in cement grinding circuits. *Construction and Building Materials*, 68, 199–205.

H1: Separate ultra-fine grinding and blending of cements

Jonas Knappert[1], *Kevin* Treiber[1], *Stefan* Seemann[1]

[1]VDZ Technology gGmbH, Düsseldorf, Germany

Abstract. The fineness of cements has steadily increased in recent years. Modern cement contains correspondingly higher portions of ultra-fine particles, which essentially determine the cement properties. Although ultra-fine particles make up only a small amount within the cement in absolute terms, they are of decisive importance for its quality e.g., for early strength development. Considering conventional grinding using a closed-circuit ball mill, the measures to influence the proportion of fines within the particle size distribution are very limited.

Typically, ball mills are predominantly used for grinding cement which produce a desirable wide particle size distribution on the one hand, but are characterised by low energy efficiency on the other. Vertical roller mills and high-pressure grinding rollers work much more efficiently. However, wide particle size distributions cannot be produced efficiently in all cases. Therefore, it was investigated how the missing fines of the products from the high-pressure comminution can be produced in a separate ultra-fine grinding unit (in this case a stirred media mill). This led to the approach of separate ultra-fine grinding and subsequent blending of cements (hereafter referred to as 'separate ultra-fine grinding'). It was further determined to what extend this multi-stage grinding approach affects the cement quality.

The cement properties of the mortar samples produced by separate ultra-fine grinding do not deviate significantly from those of a reference material ground in a ball mill. This of cause can only be stated, if the particle size distributions are not significantly different. The cement properties can be influenced by adjusting the particle size distribution, particularly by changing the portion of ultra-fine fractions. Separate ultra-fine grinding can therefore provide a further degree of freedom to control the cement properties. The entire product portfolio of cements available in the cement plant can be reproduced by mixing different materials of various fineness. This must also include clinker- and CO2-efficient multi-composite cements, which will become increasingly important in the future. To generally reduce CO2-emissions per ton of cement, ground limestone or granulated blast furnace slag is usually used to replace a certain portion of clinker in cements. The production of multi-composite cements is currently realised by means of inter- or separate grinding and subsequent mixing with conventional grinding equipment. However, even in the case of conventional separate grinding and mixing, the availability of products with varying fineness is limited. However, this is an essential factor for a demand-oriented utilisation of the main constituents in the cement. Using the approach of separate ultra-fine grinding, a demand-based production of cements is possible. Several materials of different fineness will be blended to a final product with a specific particle size distribution. This enables a further degree of freedom to control the cement properties. In the ideal case, this procedure allows a further reduction of the necessary amount of clinker in the cement without negatively affecting the cement properties. This optimisation approach of efficiently produced multi-composite cements is subject of current research.

To evaluate the specific energy demand of cements produced by separate ultra-fine grinding, grinding tests were carried out. This was realised using a semi-industrial high-pressure grinding roller and a subsequently used vertical stirred media mill. The energy saving potential derived from the results was 15-25% in direct comparison to an industrial production using a closed-circuit ball mill. Separate ultra-fine grinding and blending can therefore help to produce energetically optimised cements. This potential directly leads to a valuable contribution of reducing CO2-emissions. This means that a demand-oriented, high-performance product can be produced more sustainably and efficiently at the same time..

H2: A Study of The Effect of Grinding Conditions on Pyrite Flotation under Varied Reagent Schemes

Tokcan Isil,[1*], *Gokcen* Hasan Serkan[1], and *Bozkurt* Murat Mumtaz Volkan[1]

[1]Faculty of Engineering, Eskisehir Osmangazi University, Eskisehir, TÜRKİYE

Abstract. The flotation process plays a crucial role in separating valuable minerals from gangue, especially in the concentration of sulfide ores, where pyrite is a common gangue mineral. It is also well known that different grinding conditions may result in different flotation responses. Hence, it is essential to establish the flotation behavior of pyrite following different grinding schemes for optimizing sulfide ore processing strategies. This study investigates the effects of varying grinding conditions, specifically dry and wet grinding, on the flotation behavior of pyrite under different reagent schemes and pH values. The experimental methodology involved systematic alteration of grinding conditions and collector concentrations while maintaining a comprehensive pH spectrum. Both dry and wet grinding conditions were examined to evaluate their distinct effects on pyrite surface properties, particle size distribution, and subsequent flotation response. The study aimed to clarify the relationship between grinding conditions, pH, and collector dosage in determining the flotation behavior of pyrite, with a specific focus on conditions where no pyrite flotation response was recognized. The results obtained from this research provide valuable insights into the effect of grinding conditions to designate the pyrite flotation behavior, considering the entire pH range used in the experiments. The findings may contribute to increasing the flotation efficiency of complex sulfide ores by providing the conditions where the lowest pyrite recovery is obtained.

* Corresponding author: ikilickaplan@ogu.edu.tr

H3: Applicability of two-roll crusher models for modelling comminution in potash fertilizer compaction granulation circuits

Johannes Müller[1*], *Felix* Heinicke[2] and *Holger* Lieberwirth[1]

[1]Institute of Mineral Processing Machines and Recycling Systems Technology, TU Bergakademie Freiberg, Germany
[2]Köppern Aufbereitungstechnik GmbH und Co. KG, Freiberg, Germany

Abstract. Two-roll crushers are well suited for the comminution processes in potash fertilizer compaction granulation circuits. For investigating optimal machine settings, modelling of the comminution behaviour of these crushers can be useful. In this work, two of the models published in literature are reviewed. The approach by Campbell et al. and Austin et al. are used to predict the product particle size distributions based on experimental test work with varying machine settings. The Austin approach showed especially good agreement with the experimental data and can therefore be used in the field of potash compaction granulation.

1 Motivation

Different processing methodologies can be used in the production of fertilizer granules. Typical examples of such processes are compaction-granulation circuits. These mainly consist of the four major processes of mixing, agglomeration, comminution and classification. The main goal of this procedure is to process finely dispersed potash powder into granules of a product particle size, e.g., in the range of 2 – 4 mm. To obtain this product, the material is first fed to a roller press where it is compacted into solid, flat agglomerates, commonly called flakes. In the downstream process, these flakes are then carefully comminuted and screened to obtain a high yield of the desired product fraction. Material finer than the product fraction is transported back into the process where it is compacted again. The coarser compact, however, is further crushed in a second comminution stage.

For these comminution processes, a variety of machines can be used. Typical examples of equipment used in compaction granulation are hammer mills, cage mills or two-roll crushers, often with differential roll speeds. Particularly the latter are well suited for the application in this circuit type as the machine settings can be finely adjusted to achieve the optimum product yield for a given material. As a consequence of this, the need for modelling the comminution process of potash fertilizer flakes in two-roll crushers arises. Multiple authors already described models for the comminution in two-roll crushers. For instance, Austin et al. (1980 and 1981) developed a model for coal and solid rocks. This approach was further used and modified by other authors for more feed materials, such as limestone or urea (Rogers 1983, Rogers and Shoji 1983, Cotabarren et al. 2008). Another method developed for two-roll crushers was introduced by Campbell et al. (2001a and 2001b) for roller milling of wheat. There, differential speeds of the rolls are commonly used, which might make it suitable for potash. Both methodologies will be implemented and compared to analyse experimental values obtained from the comminution process in potash granulation.

2 Description of the used models

The Campbell model gives a simplified relationship between the input feed and output material of a two-roll crusher, written as a matrix equation (Campbell et al. 2001a) in eq. 1:

$$\mathrm{B} \cdot f = o \tag{1}$$

Where B is a breakage matrix, f is the input vector of the feed particle sizes and o describes the output vector of the model. The values for the elements of the breakage matrix can be obtained either from experimental data collected after milling individual material fractions (Campbell et al. 2001a) or by using a calculated breakage function (Campbell et al. 2001b). In this case, the breakage function presented by Campbell shall be used as described in eq. 2:

$$\rho(x,D) = b_0 + 2c_0x + (b_1 + 2c_1x)\left(\frac{s}{D}\right) + (b_2 + 2c_2x)\left(\frac{s}{D}\right)^2 \tag{2}$$

Where $\rho(x,D)$ is the breakage function that simulates the behavioural dependence between the output particles x and the input feed particles D while considering the roller gap s and fitting parameters b and c.

Austin et al. (1980) uses a more complex model equation, which can also be given in a matrix form according to Broadbent and Callcott (1956) as seen in equation 3 (Schönfeld 2023):

$$P_M = (B - B \cdot S_2) \cdot (I - B \cdot S_2)^{-1} \cdot S_1 \cdot F + (I - S_1) \cdot F \tag{3}$$

Where B is the breakage matrix, S_1 and S_2 are breakage rates, F is the feed particle size distribution and P_M is the model output. The breakage matrix or breakage function

* Corresponding author: Johannes.Mueller2@iart.tu-freiberg.de

itself is described by a combined Gates-Gaudin-Schumann distribution (Austin et al. 1980) in eq. 4:

$$B_{i-j} = \begin{cases} 1 & i \leq j \\ \varphi\left(\frac{x_{i-1}}{x_j}\right)^{\gamma} + (1-\varphi)\left(\frac{x_{i-1}}{x_j}\right)^{\beta} & i > j \end{cases} \quad (4)$$

The breakage rate S_1 described in eq. 5 is dependent upon the particle size x_i, the roller gap s, and the fitting parameters μ and λ (Rogers and Shoji 1983).

$$S_{1,i} = \frac{1}{1 + \left(\frac{x_i \cdot s^{-1}}{\mu}\right)^{\lambda}} \quad (5)$$

The breakage rate S_2 is defined by the empirical eq. 6, where the variable i_s is a size variable dependent on the size fraction corresponding to the roller gap s (Rogers and Shoji 1983, Schönfeld 2023):

$$S_{2,i} = \begin{cases} S_{1,i-1} & i < i_{s-1} \\ \frac{S_{1,i_s-1} + S_{1,i_s-2}}{2} & i = i_{s-1} \\ S_{1,i} & i \geq i_s \end{cases} \quad (6)$$

3 Material and Methodology

For the conducted test work, roller-compacted potash with particle sizes below 40 mm was used. The test material was crushed on a double roll crusher with profiled rolls and adjustable gap sizes. Each roll can be independently driven, enabling testing of a range of roll speeds while allowing for differential speeds between them. Roll speed ratios can be varied within a range of 1:1 up to 1:6. **Fig. 1** shows the two-roll crusher used to perform the tests. The experiments were carried out by Schönfeld (2023) as part of their doctoral research studies.

Fig. 8. Two-roll crusher

For one part of the test series, the gap size was varied within the range of 0.12 to 0.2, and data was normalized to the maximum feed particle size x_{max}. Furthermore, the speed ratio between the rolls was varied between 1:1.4 to 1:5.6 with a constant gap size of s_{norm} = 0.14 and 0.16. Thirteen settings were examined in total.
The resulting product particle size distributions were then used to obtain the fitting parameters for the modelling of the comminution process. To acquire accurate estimates, the residual sum of squares was minimized via a non-linear optimization algorithm.

4 Results and Discussion

As an example, **Fig. 2** depicts the resulting product particle size distributions of feed material subjected to three different gap sizes. The differential speed was maintained at a constant value of 1:2. With a decreasing gap size, finer distributions are achieved. Furthermore, the yield of material within the desired product size range (black dotted lines) increases. As a result, this setting can be seen as preferable.

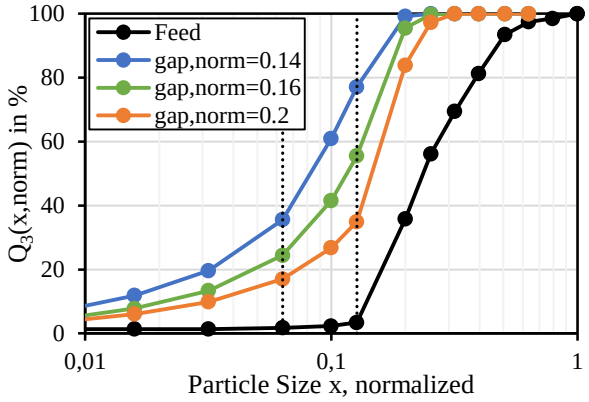

Fig. 9. Normalised particle size distribution for varying gap sizes, differential speed = 1:2

Every conducted test was then modelled both with the Campbell et al. and the Austin et al. approach. **Fig. 10** shows all calculated particle size distributions in comparison with the experimental distributions for the Campbell et al. method. The closer the individual points are to the ideal dotted line, the better the model agrees to the experiments. While good results were obtained for smaller and bigger particle sizes, for some test runs, significant deviations can be seen in the medium particle size range.

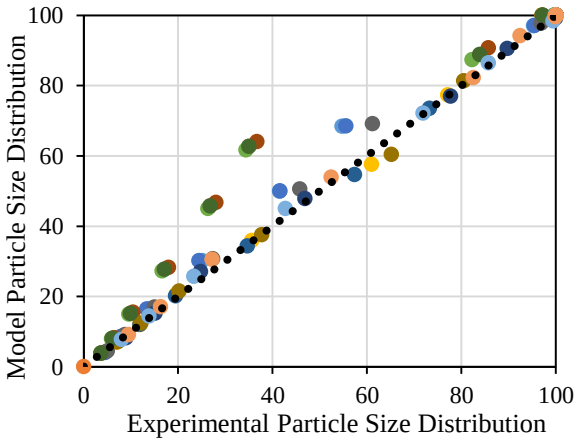

Fig. 10. Modelled particle size distributions plotted against the experimental values, Campbell et al. model

When investigating the models, it is noticeable that the tests with the highest deviations were those with steep

product particle size distributions in that particle size range. An example would be the test run with gap_{norm} = 0.2 seen in **Fig. 9**. A cause for this can be seen in the model's origin in wheat milling, as the wheats used by Campbell et al. for this approach show more evenly distributed product sizes. Additionally, being 2 mm and below, the total size range of the milled product is much smaller. Thus, it can be argued that the comminution characteristics of potash granules are in some cases not within the applicable range for this model.

Fig. 11 shows the calculated and experimental particle size distributions of the same experiments using the Austin et al. approach. The calculations showed good agreement to the experimental results over the entire particle size range. This leads to the assumption that Austin's two-roll crusher model is better suited for modelling the comminution of potash compacts within the applied test conditions.

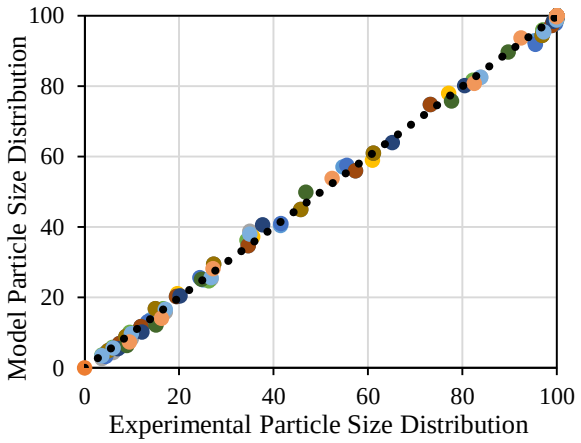

Fig. 11. Modelled particle size distributions plotted against the experimental values, Austin et al. model

5 Conclusions

Based on the test work using varying gap sizes and differential speeds, the applicability of the Campbell et al. as well as the Austin et al. two-roll crusher models for potash fertilizer comminution were investigated.

Calculated results show that while being in good agreement for some test runs, Campbell's model shows deviations for steeper product particle size distributions. Austin's approach was able to portray the entirety of conducted experiments well and can thus be used for further modelling work in potash comminution.

We thank Köppern for the support of this work and the right to publish this paper.

References

Austin, L.G., Van Orden, D.R., Perez, J.W. (1980) A Preliminary analysis of smooth roll crushers. *International Journal of Mineral Processing*, 6, 321 – 336.

Austin, L.G., Van Orden, D.R., Perez, J.W., McWilliams, B. (1981) Breakage Parameters of some Materials in Smooth Roll Crushers. *Powder Technology*, 28, 245 - 251.

Broadbent, S.R. and Callcott, T.G. (1956) A Matrix Analysis of Processes Involving Particle Assemblies. *Philosophical Transactions of the Royal Society of London. Series A, Mathematical and Physical Sciences*, 249, 99-123.

Campbell, G.M. and Webb, C. (2001a) On predicting roller milling performance. Part I: the breakage equation. *Powder Technology*, 115, 234-242.

Campbell, G.M., Bunn, P.J., Webb, C., Hook, S.C.W. (2001b) On predicting roller milling performance. Part II: the breakage function. *Powder Technology*, 115, 243-255.

Cotabarren, I., Schulz, P.G., Bucala, V., Pina, J (2008) Modeling of an industrial double-roll crusher of a urea granualtion circuit. *Powder Technology*, 183, 224 - 230.

Rogers, R.S.C. (1983) The Double Roll Crusher Model Applied to a Two-Component Feed Material. *Powder Technology*, 35, 131 - 134.

Rogers, R.S.C. and Shoji, K. (1983) A double roll Crusher Model Applied to a Full Scale Crusher. *Powder Technology*, 35, 123 - 129.

Schönfeld, P. (2023) *Beitrag zur Beschreibung des Betriebsverhaltens und der Modellierung von Kompaktier-Granulierkreisläufen*. Dissertation, TU Bergakademie Freiberg.

H4: Characterisation of the breakage behaviour of multi-component systems

Simon Bahnmüller[1,*], *Arno Kwade* [1]and *Carsten Schilde*[1]

[1]Institute for particle technology (iPAT), Technical University Braunschweig, Braunschweig, Germany

Abstract. Slags, which are by-products of metallurgical processes, have considerable recycling and utilisation potential that can contribute to the conservation of natural resources and the reduction of environmental pollution. This study focuses on the characterisation of the breakage behaviour of slags in order to better exploit their recycling potential. Firstly, two different types of slag are analysed: LD ferrous slag and S2 lithium aluminate slag. A systematic analysis of the comminution behaviour of these materials using a two-roller crushing tester (compressive stress) provides important insights into the particle size distribution and the specific energy required for comminution. Furthermore, the influence of the structural properties of the slags on the breakage behaviour will be investigated by analysing four artificially produced lithium aluminate slags with different compositions and crystal structures. The results of these investigations not only enables a deeper understanding of the material behaviour, but also contribute to the development of processes that promote efficient processing and usage of the slags in various industrial applications. The study thus makes an important contribution to promote the circular economy and sustainability in materials management.

1 Motivation

Slags, which are by-products of metallurgical processes, consist of a variety of metals and minerals whose composition is highly dependent on the type of ore processed and the specific manufacturing process. Although these multi-component systems are often regarded as waste, they harbour considerable potential for recycling and reuse, which can help to conserve natural resources and reduce environmental impact. The effective utilisation of slags can not only reduce dependence on raw material imports, but also contribute to the circular economy by providing valuable raw materials for the construction, chemical and metal industries. The key to realising this potential lies in the development of advanced extraction techniques and processes for separating and purifying the valuable materials contained in bottom ash. Through targeted research and innovation, valuable raw materials can be obtained from a supposed waste product, increasing industrial efficiency and contributing to environmental protection. The importance of slag as a resource therefore requires a reassessment of its role in the industrial sector and greater integration into sustainable economic cycles. (Jian-long Guo, Y. Bao, Min Wang 2018; N. Piatak, M. Parsons, R. Seal 2015)

The SPP2315 EnAM priority programme, which is funded by the German Research Foundation, is tackling precisely this challenge. The SPP research project deals with the breakage behaviour of slags. This will initially be demonstrated using two different types of slag. The breakage characteristics gained are then demonstrated on various artificial slag types that are specifically produced within the SPP, thus demonstrating the dependencies on structural parameters.

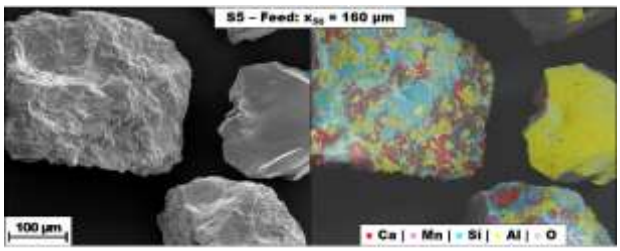

Fig. 12 : Structure of a lithium aluminate slag

2 Characterisation of the breakage behaviour using different types of slag

In this work, the breakage behaviour of slags is first characterised using an LD iron slag and an S2 lithium aluminate slag. For this purpose, the slags, which are initially present in larger blocks of several centimetres, are pre-crushed and classified using an air jet sieve. Each slag is then classified into five particle size classes between 250 µm and 25 µm. This is shown in Fig. 3 as an example for the LD slag.

* Corresponding author: simon.bahnmueller@tu-braunschweig.de

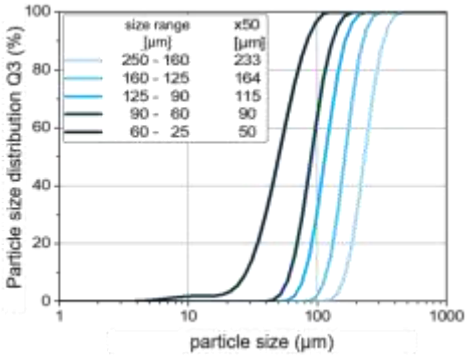

Fig. 13. Particle size distribution of the LD-slag

The breakage behaviour is then investigated using a two-roller (Böttcher et al. 2022; Böttcher et al. 2021) breakage tester developed at the institute. This offers the possibility of setting a specific gap between roller 1 and roller 2 (Fig. 2) between 5 µm and 180 µm and feeding the particles as a uniform particle bed via a hopper feed. For the tests, gap width ratios to the x50 value of the feed size of 30%, 40%, 50%, 60% and 70% are tested. Each test setting is determined three times. A total of 75 samples per slag type are therefore analysed, which corresponds to a particle quantity of over 225 million particles. On the one hand, the two-roller breakage tester offers the possibility of determining the particle size distribution of the broken particles collected with the aid of a hoover. In addition, sensors are also installed to record the force acting on the particles in the respective rollers and a torque sensor on a third roller coupled via gear wheels, which can be used to calculate the specific energy introduced.

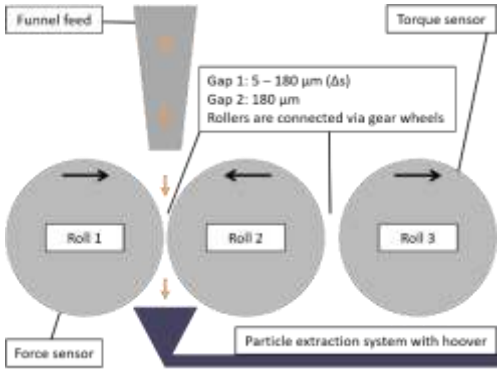

Fig. 14. Schematic construction of the two-roller breakage tester

Analysis of the fragments can provide initial insights into the breakage behaviour. On the one hand, the particle size distributions of the broken particles can be used to gain initial insights into the breakage behaviour of the respective slag. By comparing this with the feed particle size distribution, it is possible to gain insights into the specific energy input at which comminution can take place, as well as the range in which comminution occurs.

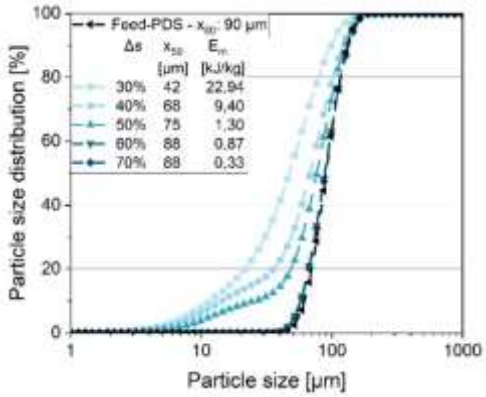

Fig. 15. Particle size distribution after five different gap width ratios of the comminuted samples of LD slag with a feed size of 90 µm

In the Fig. 4, for example, it can be shown that a strong increase is initially perceived in the area of the fines content and no major change is initially perceived in the x_{90} range. The comminution in the x_{90} range only changes at higher energies. Furthermore, information about the behaviour of particle shape and particle size can also be shown with the aid of optical particle size measurement devices.

In a further evaluation step, the determined size values x_{10}, x_{50} and x_{90} of all analysis settings (5 size classes – 5 different gap widths in each case) can be plotted in a diagram against the specific energy introduced. This is shown in Fig. 5 as an example for the LD slag. The graphic opposite makes it possible to characterise and describe the breakage behaviour of slags in more detail. Two phases with different breakage behaviour can be distinguished. In the first phase, the effects of the multi-component systems dominate, in the second phase the effects of the individual components in the slag. Four characteristic points are highlighted:

1. minimum specific energy which must be applied to cause a breakage event
2. first breakage-characteristic phase in which the slag is comminuted to varying degrees
3. transition point between the first breakage-characteristic phase and the second breakage-characteristic phase
4. second breakage-characteristic phase, in which the slag particles are not further comminuted under the energy applied

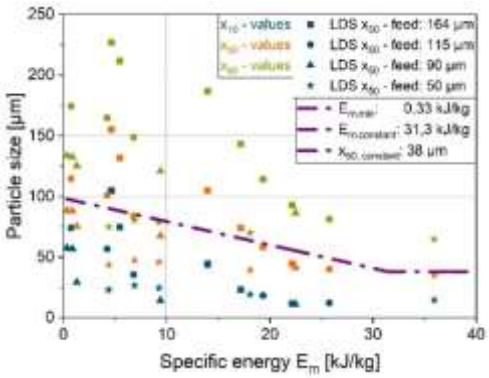

Fig. 16. Applied x_{10}, x_{50} and x_{90} values and breakage characteristics of the LD slag analysed

For further analysis, especially with regard to the degree of digestion, the particles are also analysed under the SEM/EDEX (Fig. 6). The aim is to identify structural anomalies in the starting particles as well as structural anomalies and changes in comparison with the feed particles. On the one hand, these findings can be analysed optically and quantitatively. On the other hand, as part of the research work, the images obtained should also be analysed or conclusions about the degree of digestion should be drawn using further analysis methods (e.g. MLA) in order to gain important insights for a possible recovery strategy.

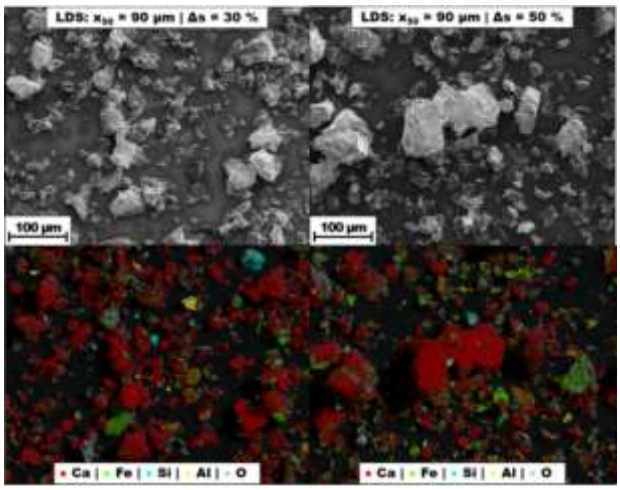

Fig. 17. SEM/EDEX images of the LD-S slag from the 90 µm breakage after comminution at a gap width ratio of 30% and 50%

3 Investigation of the structural influence on the breakage behaviour of a slag type

With the knowledge gained so far about the characterisation possibilities of the breakage behaviour of slags, the dependence of the breakage behaviour on the structural properties of the slag can be shown more precisely. For this purpose, four artificially produced lithium aluminate slags are available within the framework of the SPP (Rachmawati et al. 2024). These are produced under different conditions and therefore differ at least in composition but also in the crystalline structure. This can be controlled, for example, by the cooling rate during the production process (Rachmawati et al. 2024). The different structural properties of four artificial slags are shown and their influence on the breakage characteristics is transferred.

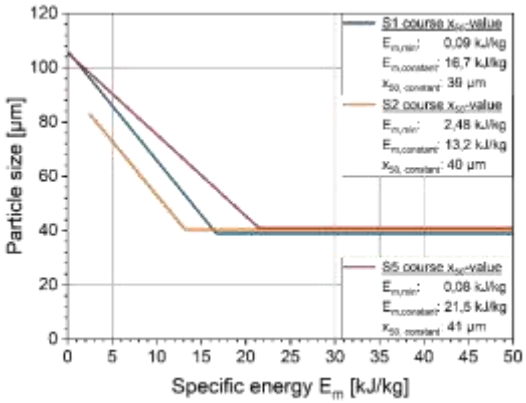

Fig. 18. Analysed breakage characteristics of three differently produced lithium aluminate slags in comparison

In this way, initial findings are shown in this work, on which the breakage behaviour depends, and can be used to predict the breakage behaviour with the help of a semi-mechanistic model.

Funded by the German Research Foundation (DFG) - SPP 2315 "Engineered Artificial Minerals (EnAM) - a geo-metallurgical tool to recycle critical elements from waste streams". The authors would also like to thank the German Research Foundation as part of the Heisenberg Programme SCHI 1265/19-1 "Digital Methods for Complex Systems in Process and Production Engineering".

References

Böttcher, Ann-Christin/Beusen, Dennis/Lüddecke, Arne/Overbeck, Achim/Schilde, Carsten/Kwade, Arno (2022). Single and multiple breakage events in fine particle breakage testing with a rigidly-mounted roll mill. Minerals Engineering 178, 107390. https://doi.org/10.1016/j.mineng.2021.107390.

Böttcher, Ann-Christin/Thon, Christoph/Fragnière, Greta/Chagas, Anderson/Schilde, Carsten/Kwade, Arno (2021). Rigidly-mounted roll mill as breakage tester for characterizing fine particle breakage. Powder Technology 383, 554–563. https://doi.org/10.1016/j.powtec.2021.01.055.

Jian-long Guo, Y. Bao, Min Wang (2018). Steel slag in China: Treatment, recycling, and management. Waste management 78, 318–330. https://doi.org/10.1016/J.WASMAN.2018.04.045.

N. Piatak, M. Parsons, R. Seal (2015). Characteristics and environmental aspects of slag: A review. Applied Geochemistry 57, 236–266. https://doi.org/10.1016/J.APGEOCHEM.2014.04.009.

Rachmawati, Cindytami/Weiss, Joao/Lucas, Hugo Ignacio/Löwer, Erik/Leißner, Thomas/Ebert, Doreen/Möckel, Robert/Friedrich, Bernd/Peuker, Urs Alexander (2024). Characterisation of the Grain Morphology of Artificial Minerals (EnAMs) in Lithium Slags by Correlating Multi-Dimensional 2D and 3D Methods. Minerals 14 (2), 130. https://doi.org/10.3390/min14020130.

H5: Assessing the influence of different mills on particle size distribution in steel slags for carbonation applications

Nina Miladinovic[1,*], *Luka* Ceyssens[1], *Giuseppe* Granata[1,2], and *Tom* Van Gerven[1]

[1]Process Engineering for Sustainable Systems (ProcESS), Department of Chemical Engineering, KU Leuven, Leuven, Belgium
[2]Sustainable Materials Processing and Recycling (SeMPeR), Department of Materials Engineering, KU Leuven, Leuven, Belgium

Abstract. In order to reduce carbon-dioxide pollution, steel slags are found a promising material for its capture. Mechanical activation of steel slags is one of the ways to activate material for carbonation. For that purpose, an examination of three different types of mills (ball mill, McCrone mill and vibratory mill) on the particle size distribution of AOD steel slag was performed. The most effective mill in milling for a shorter time was the ball mill, while the McCrone mill achieved the smallest particle size of steel slag after eight minutes, however, the McCrone mill showed the narrowest distribution of particles which led to the conclusion that less agglomerates are formed. The vibratory mill shows the least impact on the particle size of steel slag. It was concluded that processing AOD in the McCrone mill shows the greatest potential for further carbonation of slag.

1 Introduction

Steel slags represent promising material for capturing carbon dioxide from the air. In terms of improving the carbonation rate in argon oxygen decarburization (AOD) steel slag, applying mechanical activation is a well-researched field. From the work of Tao et al. (2021), it can be concluded that carbonation of this type of steel slag achieves its maximum over time. Limitations for further carbonation of AOD are the formation of an outer layer around particles or the agglomeration of particles. To overcome these obstacles, this research is based on investigating the impacts of different mills on particle size distribution, as particle size and carbonation rate are proven correlated (Tu et al., 2015). Moreover, in terms of reducing the formation of the outer layer or decreasing agglomeration, the influence of different operational conditions of mills on particle size distribution is investigated.

2 Methodology and results

2.1 Experimental

AOD steel slag obtained from Aperam (Belgium) is sieved through a 1 mm sieve. For each experiment, 1.5 g of AOD and 30 g of ethanol 99%+ (Fisher Scientific B.V., Belgium) were used. The proportion of beads in the planetary ball mill (Planetary Micro Mill PULVERISETTE 7 premium line Fritsch) was 40 beads for 1 g of steel slag. In the McCrone mill (XRD-Mill McCrone Retsch), beads were filled to the top. In the vibratory mill (Vibratory disc mill RS 200 Retsch) grinding tools were used. Particle size analysis based on volume percentage was obtained with Malvern Mastersizer 3000 - Hydro EV for each sample. Samples in the ball mill were examined at two different speeds (200 rpm and 1000 rpm) at various times, in vibratory mills at speeds 100 rpm and 1200 rpm at various times and in the McCrone, mill speed was fixed at 1000 rpm for all examined times.

2.2 Results

Average particle size distributions (PSD) of five measurements of particles ground in a planetary ball mill with different operating conditions in comparison with raw AOD are given in Figure 1.

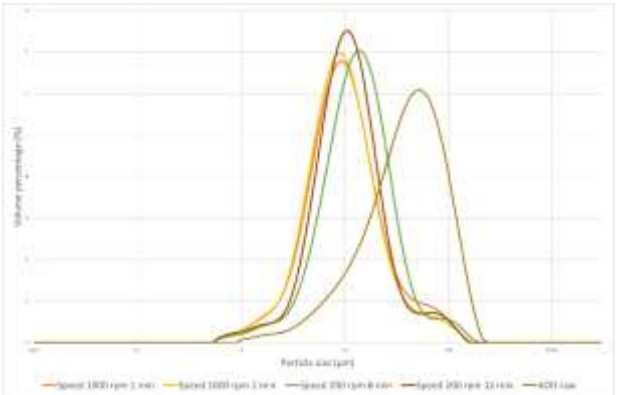

Fig. 1. Comparison of PSD of AOD samples ground in planetary ball mill

Based on five measurements of every milled sample, the average volume-weighted mean diameter and standard error for each are given in Table 1.

* Corresponding author: nina.miladinovic@kuleuven.be

Table 1. Comparison of volume-weighted mean diameter in planetary ball mill

Speed (rpm)	*Time (min)*	*D [4;3]*
1000	1	16.34 ± 0.16
1000	2	15.24 ± 0.10
200	8	19.78 ± 0.18
200	12	16.46 ± 0.07

It can be concluded that milling samples at high speed/shorter time gives similar results as milling at low speed/longer time, which was expected as time and energy involved are reciprocal values.

A similar design of the experiment was conducted in the vibratory mill, and the average PSD of five measurements of particles milled in comparison with raw AOD is given in Figure 2.

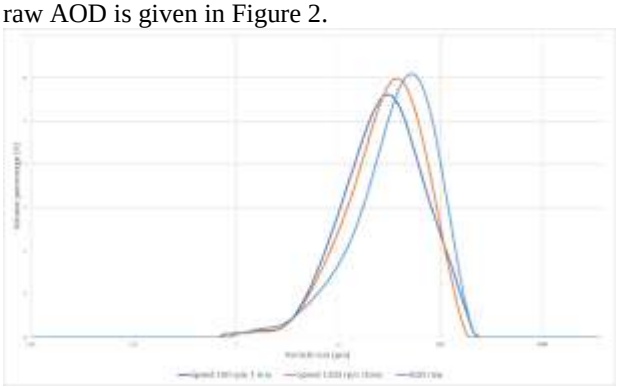

Fig. 2. Comparison of PSD of AOD samples ground in a vibratory mill

The average volume-weighted mean diameter and standard error for samples from the vibratory mill are given in Table 2.

Table 2. Comparison of volume-weighted mean diameter in a vibratory mill

Speed (rpm)	*Time (sec)*	*D [4;3]*
100	60	42.16 ± 0.39
1200	10	42.42 ± 0.55

It can be seen that the implemented conditions in the vibratory mill do not impact particle size diameter to a large degree.

In terms of the McCrone mill, changing speed was not technically feasible, so experiments were conducted only with changes in time. The evolution of average values of D10, D50, D90 and D [4;3] over time is given in Figure 3.

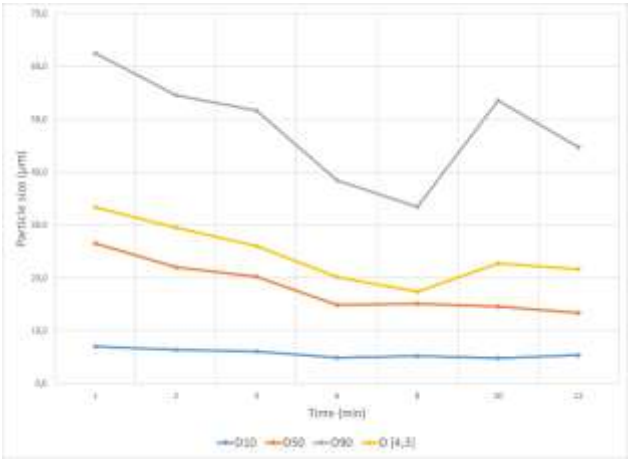

Fig. 3. Comparison of characteristic parameters from particle size analysis of samples ground in a McCrone mill over time

Average values of volume-weighted mean diameter over time in the McCrone mill are given in Table 3.

Table 3. Comparison of volume-weighted mean diameter in McCrone mill

Time of milling (min)	*D [4;3]*
1	33.36 ± 0.22
2	29.47 ± 0.47
3	26.00 ± 0.59
6	20.12 ± 0.32
8	17.42 ± 0.07
10	22.72 ± 0.29
12	21.48 ± 0.12

From the obtained results it can be concluded, that particles of AOD slag achieve their minimal diameter after 8 minutes, while after that time particles become bigger. The potential reason for that is an agglomeration of particles (Tao et al., 2021).

In terms of comparison of different mills, operating time was fixed and the average PSD of particles after grinding in different mills for 1 minute compared to the average particle size distribution of raw AOD are presented in Figure 4.

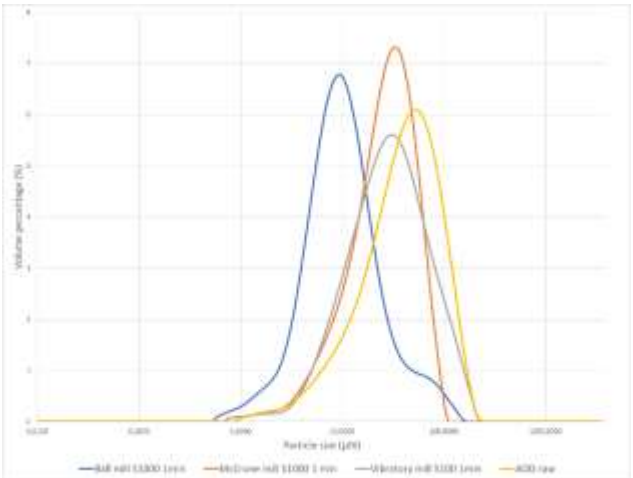

Fig. 4. Comparison of PSD of raw AOD sample and after grinding for 1 minute in different mills

From the obtained results from five measurements for every sample, a comparison of average volume-weighted mean diameter is given in Table 4.

Table 4. Comparison of volume-weighted mean diameter

Name of sample	*D [4;3]*
Ball mill S1000 1 min	16.34 ± 0.16
McCrone mill S1000 1 min	32.58 ± 0.12
Vibratory mill S100 1 min	42.16 ± 0.39
AOD raw	53.69 ± 0.52

Comparing values of volume-weighted mean diameter, the effectiveness of mills in reducing particle size is concluded in the given order: planetary ball mill, McCrone mill and vibratory mill, from most effective to least effective. In terms of the width of distributions, from Figure 4, it can be concluded that the McCrone mill gives the narrowest distribution of particles i.e. agglomeration of particles is reduced compared with other mills.

However, to better quantitively compare the different impacts all three mills have on particle size, breakage potential is calculated (Han et al., 2021). Breakage potential (BP) is defined as:

$$BP = \frac{D[4;3]_{initial} - D[4;3]_{broken}}{D[4;3]_{inital}} \quad (1)$$

where $D[4;3]_{initial}$ is the volume-weighted mean diameter of initial particles, in this case, raw AOD, and $D[4;3]_{broken}$ is the volume-weighted mean diameter of broken particles after milling. A comparison of BP over time for the experiments above is given in Figure 5. The planetary ball mill is abbreviated with BM, the vibratory mill with VM, and the McCrone mill is labelled with McCrone. Different speeds are presented as SX, where X represents speed in rpm.

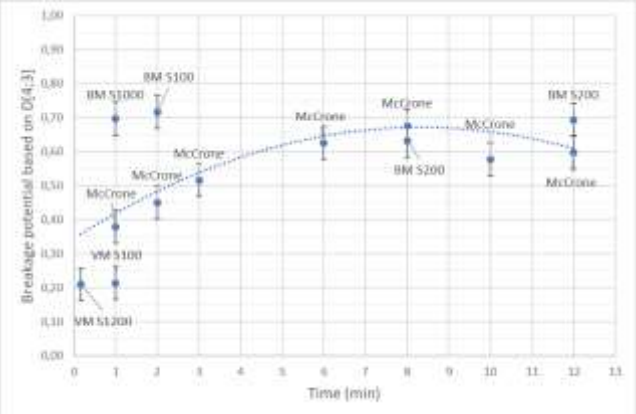

Fig. 5. Breakage potential of mills over time

From Figure 5, it can be seen that the highest breakage potential after 1 minute is achieved with a ball mill at a speed of 1000 rpm. However, over time, the McCrone mill after 8 minutes and the ball mill at a lower speed (200 rpm) after 12 minutes, show similar breakage potential. Moreover, it is important to say that samples in the ball mill at high speed (1000 rpm) are heated during milling, and even if a high breakage potential is achieved after only one minute, conducting experiments at this speed leads to the heating of ethanol and its evaporation. Heating was not noticed for other samples. The dotted line in Figure 5 is set for results obtained with the McCrone mill, from which it can be seen that breakage potential over time achieves its maximum and that a general trend for breakage potential over time exists.

3 Conclusion

Assessment of the effectiveness of different operating conditions of three different mills (ball mill, McCrone mill and vibratory mill) on the particle size of AOD steel slag is performed. In terms of reduction of particle size, the planetary ball mill shows as the most effective one at a shorter time, but due to the heating of samples processing of it is difficult. On the other hand, the McCrone mill showed a similar effect on particle size after 8 minutes and the distribution of particles was narrower compared to other mills, which means it led to less agglomeration. Less agglomeration in AOD slag is beneficial for further carbonating steps. Nevertheless, the vibratory mill showed the least impact on the particle size of slag and its distribution. Overall, milling AOD slag in the McCrone mill for 8 minutes shows the biggest potential for further carbonation. Further investigation would include using different solvents at the same operating conditions to determine if a trend in the impact of mills exists as well as carbonation of samples obtained from different mills to correlate the impact of mills with carbonation rate.

The Research Foundation – Flanders (FWO) is gratefully acknowledged for funding this research as part of the AgriCarb project (G0A4821N). The authors would like to acknowledge Yashwanth Ramesh for operating with the vibratory mill.

References

Tao, M.-J., Wang, Y.-J., Zeng, Y.-N., Liu, S.-H. & Qin, S. (2021) Slurry-Phase Carbonation Reaction Characteristics of AOD Stainless Steel Slag, *Processes*, 9(12), p. 2266.

Tu, M., Zhao, H., Lei, Z., Wang, L., Chen, D., Yu, H., & Qi. T. (2015) Aqueous Carbonation of Steel Slag: A Kinetics Study, *ISIJ International*, 55(11), pp. 2509–2514.

Han, J., Fitzpatrick, J., Cronin. K., Maidannyk, V., & Miao, S. (2021) Particle size, powder properties and the breakage behaviour of infant milk formula, *Journal of Food Engineering*, 292, p. 110367

H6: Modeling the effects of grinding and gypsum quality on the factors influencing the setting time of hemihydrate

Áron Földesi[1,*], *László* Győry[2], and *József* Faitli[3]

[1]Faculty of Earth ant Environmental Sciences and Engineering, University of Miskolc, Miskolc, HU
[2]Baumit Kft., Dorog, HU
[3]Faculty of Earth ant Environmental Sciences and Engineering, University of Miskolc, Miskolc, HU

Abstract. In the technology investigated in the study, bricks are pressed from raw gypsum, then recrystallized in an autoclave by removing most of the crystal water, and then a α-hemihydrate binder is obtained by grinding the bricks. The aim of the study is to model the effect of grinding and gypsum quality on the factors influencing the setting time of hemihydrate. The setting time of the binder as the most important product property is determined by the hemihydrate content and the particle size distribution, but other calcium sulfate impurities, such as the anhydrite and dihydrate content, also have an important influence on the binding reaction. The relationship between the properties was determined using the design of experiments method (DoE). In the first part of the study, the change in particle size of the hemihydrate was observed by varying the crystal water content of raw material gypsum, autoclaving time and grinding intensity as model parameters. In the second part of the paper, we have used the results of the previous part of the study to model the setting time, choosing the values of the particle size distribution of the hemihydrate and the crystal water content of the hemihydrate as model parameters.

1 Introduction

Gypsum is a type of mineral that belongs to the group of hydrous sulfate minerals, the dihydrate of calcium sulfate ($CaSO_4 \cdot 2H_2O$). Calcium and sulfate ions are bound together in ring-shaped units whose three-dimensional arrangement results in tubular structures. The water molecules of the crystal water are incorporated into these tubes. As this water is only loosely bound by adsorption, dehydration is possible in all stoichiometric ratios (Feldmann and Demopoulos, 2012).

When gypsum is heat treated at a temperature of over 90°C a calcium sulfate-hemihydrate is formed by removing three quarters of the crystal water, with the following reaction (Van Driessche et al, 2016):

$$CaSO4 \cdot 2H_2O + dQ \rightarrow CaSO_4 \cdot 1/2H_2O + 3/2H_2O$$

A distinction is made between two types, the α-hemihydrate, which is produced by wet processes (e.g. autoclaving) and represents a fully formed hexagonal crystal form, and the β-hemihydrate, which is produced by dry methods (e.g. calcination) which is a fine crystalline formation due to the rapid transformation of the dehydrate (Yin and Yang, 2020). Above 120 °C, all crystal water is removed and anhydrite is formed, of which two forms are known: the reducible anhydrite II modification, which is stabilized by heat treatment, and the still reactive, soluble anhydrite III phase (Van Driessche et al, 2016, Singh and Middendorf 2007).

Due to the hydraulic properties of the hemihydrate, a setting reaction (rehydration) takes place when it is mixed with water, which is the opposite of the previous equation:

$$CaSO4 \cdot 1/2H_2O + 3/2H_2O \rightarrow CaSO_4 \cdot 2H_2O + dQ$$

The reaction proceeds in three phases, first the hemihydrate crystals dissolve and form a supersaturated solution, then it enters the nucleation and crystal growth phase, as the hemihydrate interlocks, a compact dihydrate crystal system begins to form, and at the end of the setting time the reaction stops due to the exhaustion of the hemihydrate. The hemihydrate dissolves moderately in water (0.65 g/100 ml) and quickly reaches saturation. The solubility of the dihydrate (0.24 g/100 ml) is only a fraction of the solubility of the hemihydrate, but they form crystallization nuclei during the binding reaction, then precipitate and grow rapidly into an interlocking crystalline mass, significantly accelerating the setting time (Lewry and Williamson, 1996).

The influence of the particle size of the plaster is also important for the setting time. According to the literature, the fractions 0–20 μm and 20–50 μm have a negative, accelerating effect on the setting time due to the larger specific surface area, while the grain fractions 50–90 μm and 90–140 μm have a positive, retarding effect (Baohong et al, 2010, Pan et al, 2019).

* Corresponding author: a.foldesi@baumit.com

2 Materials and Methods

The experiments were carried out in a laboratory equipped for the production and testing of an α-hemihydrate. The equipment of the experimental laboratory is identical to the production technology for industrial α-hemihydrate, the steps of the process are presented in Figure 1.

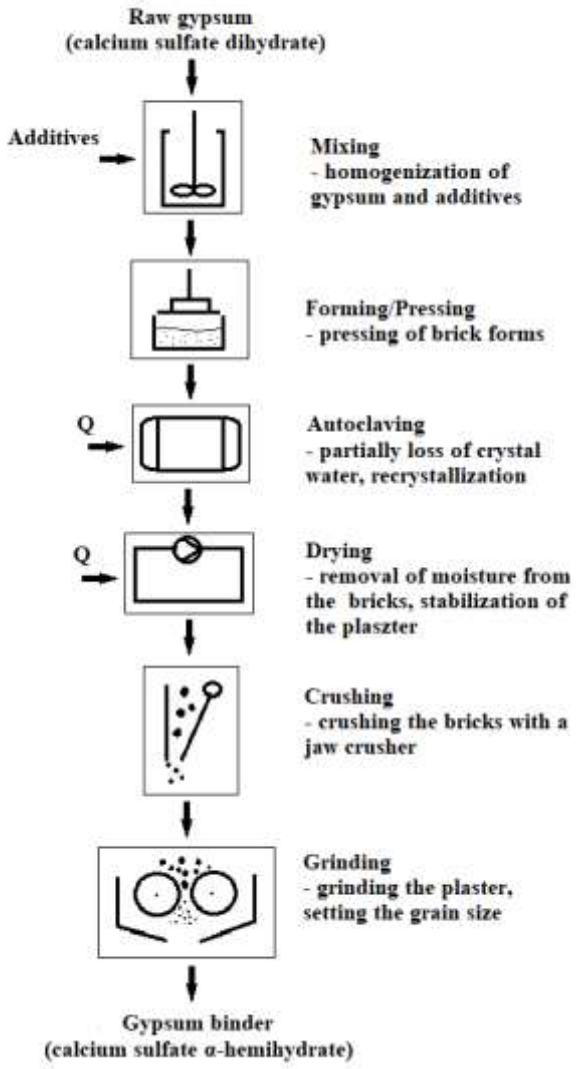

Fig. 1. The technology of the laboratory production trials of α-hemihydrate (Guan et al., 2021).

The aim of the first section of the study is to investigate the influence of raw gypsum quality, autoclaving time and grinding intensity on the particle size distribution and the crystal water content of the hemihydrate. The crystal water content of the gypsum was chosen because it represents the gypsum content of the raw material and thus the gypsum quality. During the test, the hemihydrate product was ground at different speeds in a centrifugal mill, which changed the intensity of the fragmentation.

In the second part of the paper, we have used the results of first section to model the setting time, choosing the values of the particle size distribution and the crystal water content of the hemihydrate as model parameters. To model the relationship between the selected parameters, we used the generally accepted design of experiments method (DoE).

2.1 Design of experiments

2.1.1 Planning and execution

The raw material for the model experiments was flue gas desulfurization gypsum in three different raw material qualities, which originates from the Mátra Power Plant.

In the first part of the DoE, the change in the particle size distribution of the plaster was observed by varying the raw gypsum crystal water content, the autoclaving time and the grinding intensity as three model parameters in three levels. Important step of the planning phase was the determination of these levels. These levels determine whether the variables will have a significant influence on the target values. If the repeatability of these measurements is poor, the error within one setting (between runs) will be greater than between the two settings. Therefore, it was important to perform at least two measurements (runs) for each setting. If there is no significant difference between settings in relation to the target values, then we cannot say anything about the effect of these input variables. The structure of the DoE is summarized in Table 1 with the defined parameter levels. In the second step, the laser granulometry values d10, d50, d90 of the particle size distribution and the crystal water content of the plaster measured during the tests were selected as parameters for modeling the setting time as target value.

Table 1. Structure of DoE.

	Crystal water (FGD) (%)	Autoclaving time (h)	grinding intensity (rpm)
Level -1	19.60	6.5	8000
Level 0	20.10	7.5	12000
Level 1	20.40	8.5	1600

A total of 9 settings were determined to create the model and each run was repeated 1 time, and then 4 runs were repeated 3 times in order to create exact model equations. For this reason, we completed a total of 22 runs. For this reason, 22 experimental bricks and binders were produced at the end of the study.

2.1.2 Measurement methods

The crystal water was determined using an UltraX moisture meter. The advantage of this device is that it has two heating lamps, a radiant lamp for measuring free moisture and a quartz lamp that can be heated to 360 °C, which can also be used to remove and measure bound crystal water.

Since both the raw gypsum and the hemihydrate plaster are fine powders, the particle size distribution was determined using laser diffraction. The setting times were determined using the standard Vicat method. The Vicat needle is cylindrical and moves in a vertical, scaled guide, penetrating a plaster mass located in a mold. Initial cure is defined as the time at which the needle penetrates no further than a certain distance from the top of the sample. Final hardening is defined as the time at which the needle no longer penetrates at all. A software-supported automatic Vicat was used in the tests so that the start and end of the setting time can be precisely determined from the setting curve (Sleiman et al., 2010).

2.1.2 Evaluation of the experiments

After all the experiments have been carried out, a linear mathematical model is fitted to the target values as a function of the three parameters and their interaction. The model equation was as follows:

$$y = b + a_0 * x_0 + a_1 * x_1 + a_2 * x_2$$

The first step of the evaluation was to check the significance of the shifts in the model, whether we see a meaningful change or just the noise of our measurements. To do this, we used a simplified method. We plotted the average standard deviation of the two replicate runs and used a two-sample t-test to see if there was a significant difference between the results. The aim was to perform the regression calculations and determine the best fit using the analytical solution. It has an analytical solution given by the equation below:

$$(X^T * X)^{-1} * X^T * y$$

Where X is the matrix of the values in the table (the three input parameters) and y is the target values. The calculations provide the values b and ai of the model equation for the given target variable. These steps are then repeated with the next target variable. After calculating the b and a_i values, we can make a prediction for each run in the table. These predicted values and the measured values can then be used to determine the performance of the model. By calculating the values for the total, external and internal variance (residual error), the coefficient of determination of the model can also be determined. This value provides information about the performance of the model, how well or how poorly it describes the test series under our conditions. The proportion of the total variance that can be explained by the regression was calculated using the explained variance (external variance/total variance).

3 Results

3.1 Modell of crystal water and particle size

Based on the results of the first section the crystal water of the plaster followed the length of the heat treatment in the autoclave in all cases, and the effect of the gypsum quality was also significant according to the model. This explains the very good coefficient of determination (CoD=0,97 see Fig. 2.). The model proved to be significant, which means that at least one of its parameters is significant.

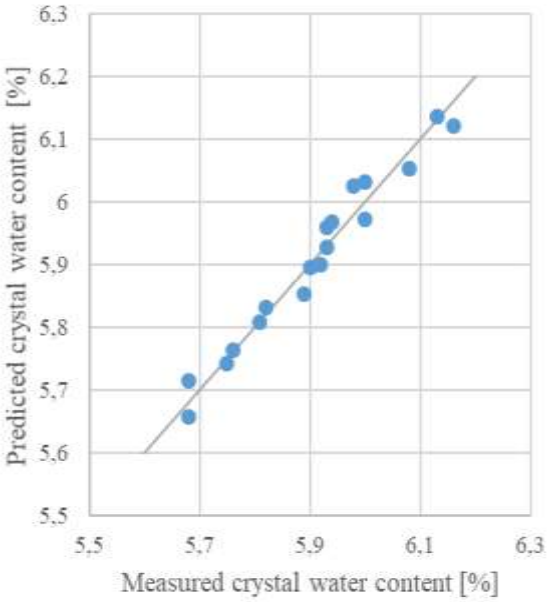

Fig. 2. The performance of the crystal water (CoD=0,97)

After grinding, the particle size distribution of the hemihydrate followed the grinding intensity, and the influence of raw material gypsum quality was also significant. The equation states that the higher the crystal water content of the raw gypsum and the higher the grinding intensity, the lower the grain size values. The autoclaving time parameter was not significant in the model, but since this is the heat treatment step, the equation is logical even without it.

3.1 Modell of setting time

To model the setting time, the particle sizes (d10, d50, d90) and the crystal water of the plaster were determined as model parameters. As the binding of the hemihydrate is a complex system, it can be said that the coefficient of determination of the model equation (initial set: CoD=0.93, see Fig. 3) is very good. The model also proved to be significant in this case. The effect of the crystal water content is related to the phases of the gypsum, in this case if the crystal water in the binder increases, the dihydrate content appears, which can accelerate the binding reaction.

It is interesting to note that increasing the d10 and d90 values prolongs the setting time, while increasing the d50 grain size accelerates the setting.

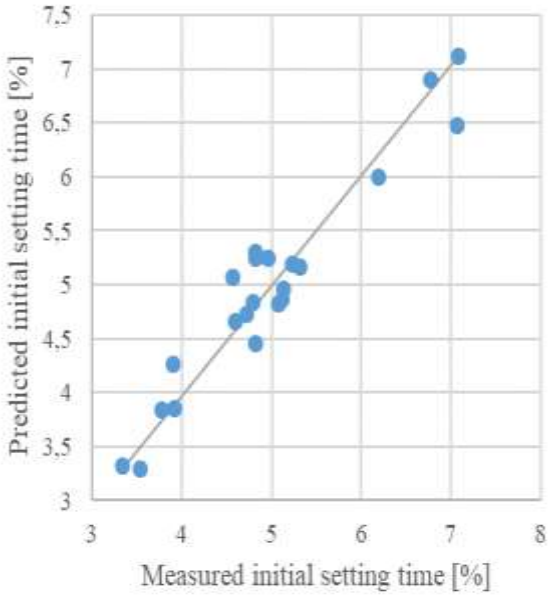

Fig. 3. The performance of the setting time model (CoD=0,93)

4 Conclusion

As part of the DoE, a total of 9 settings were determined to create the model and each run was repeated 1 time, and then 4 runs were repeated 3 times in order to create the most accurate model equations. For this reason, we completed a total of 22 runs.

We tested the models to see whether they were significant or not (F-test) and tested the parameters in the model equation itself to see whether they contributed to the predictions or not (t-test). The models created are significant according to the F-test, and the equations contain those parameters which also have a significant influence on the target parameters according to the t-test.

In the first section of the paper, reliable model equations were established. According to the model, the higher crystal water content (better quality) of the raw material gypsum and the longer the autoclaving time, the higher the crystal water. According to the equations, the quality of the raw material and the grinding intensity (grinding speed) have a significant effect on the particle size distribution formed after grinding.

In the second part of the study we were able to model the setting time with a good correlation with the values of the grain size distribution and crystal water content of the binder. The model equation for the setting time showed that the crystal water of the binder has the greatest influence, but that the particle size distribution also plays an important role.

References

Van Driessche, A , Stawski, M. , Benning, L, & Kellermeier M. (2016) Calcium Sulfate Precipitation Throughout Its Phase Diagram, *New Perspectives on Mineral Nucleation and Growth, Springer*, 227-231.

Lewry, A.J. and Williamson, J. (1994) The setting of gypsum plaster Part I The hydration of calcium sulphate hemihydrate, The setting of gypsum plaster Part III The effect of additives and impurities, *Journal of Materials Science*, 29, 5279-5284., 6085-6090.

Yin, S. and Yang, L. (2020) α or β?-hemihydrates transformed from dihydrate calcium sulfate in a salt-mediated glycerol–water solution, *Journal of Crystal Growth*, 5050, 125885

Baohong, G., Qingqing, Y., Zhongbiao, B., Wenbin, L., & Liuchun, Y. (2010) Analysis of the relationship between particle size distribution of α-calcium sulfate hemihydrate and compressive strength of set plaster-Using grey model, *Powder Technology*, 200, 136–143.

Pan, H., Deng-xing, L., Peng-sheng, W., & Zhi-ming, T (2019) Effect of Particle Size Ratios on the Physical and Chemical Properties of Surgical-Grade Calcium Sulfate Hemihydrate, *Orthopaedic Surgery Volume*, 12, 1-7.

Singh, N.B and Middendorf, B. (2007) Calcium sulphate hemihydrate hydration leading to gypsum crystallization, *Progress in Crystal Growth and Characterization of Materials*, 53, 57-77.

Sleiman, H., Perrot, A., & Amziane, S. (2010) A new look at the measurement of cementitious paste setting by Vicat test, *Cement and Concrete Research*, 40, 681-686.

Guan, Q., , Sui, Y., Zhang, F., Yu, W., Bo, Y., Wang, P., Peng, W., & Jin, J. (2021) Preparation of α-calcium sulfate hemihydrate from industrial byproduct gypsum: a review, *Physicochemical Problems of Mineral Processing*, 57, 168-181.

Feldmann, T. and Demopoulos, G.P. (2012) Phase transformation kinetics of calcium sulfate phases in strong CaCl2-HCl solutions, *Hydrometallurgy*, 129, 126-134.

I1: White fields in comminution and classification research – a personal perspective

Wolfgang Peukert*, *Cornelia* Damm

Institute of Particle Technology, Friedrich-Alexander University Erlangen-Nürnberg, Cauerstr. 4, D-91058 Erlangen, Germany

Abstract. White unexplored fields in communition and classification are discussed with a particular focus on fine particles. Key questions are related to the influence of material properties on fracture mechanisms and kinetics. Defect structures inside of particles play a major role and require more attention both in case of liberation of valuable phases in minerals processing and in grinding at the nanoscale. Here and also for the much needed characterization of unknown material properties a joint venture with materials science would be beneficial. Production of new materials including 2D nanosheets by delamination of layered materials, shape-selective deformation and mechano-chemical transformations open fascinating new prospects. Limits in multiscale modelling still exist in tackling highly turbulent two-phase flows. Their understanding is important for process models at all scales. Large scale applications contribute considerably to climate change and CO_2 emissions. Major steps in energy efficiency are urgently needed. The multidimensional description of classification processes allows to tackle the complexity of particle systems in a much better way. New prospects for fractionation of ultrafines by nanoparticle chromatography already show outstanding performance. An important next step is certainly the upscaling of these highly promising approaches.

1 Introduction

Comminution and classification of particles belong to the oldest cultural techniques of mankind. Wind sifting of grains in old Egypt or bread "factories" of the Romans in Pompeij are just two examples of their application. Over many centuries, empirical approaches lead to the development of many different types of mills and classifiers, such as ball or hammer mills for size reduction as well as cyclones and deflector wheels for classification. With the advent of systematic research in particle technology from the end of the fifties of the last century, the basic understanding of the underlying mechanisms largely improved and led to the development of first relatively simple and now highly sophisticated numerical models.

Based on more than 30 years of experience first in industry and then at universities, I will present my personal view on the current status and open white fields in comminution and classification research. In a first general view, any grinding operation as part of a larger process (described by a process function) can be understood in terms of a mill and a material function. The mill function depends on operational parameters and describes the applied stress energy distribution to particles through the prevailing stressing mechanisms and the stress number distribution, i.e. how often the particles are stressed in the mill per unit time. The reaction of the particles to the applied stress is condensed in the material function, which includes elastic and inelastic deformation. Fracture events are described by fracture probability and breakage function, i.e. the size distribution of the fragments. The latter is directly linked to size-dependent particle properties.

Many different types of machines and apparatus exist for size reduction and dispersion of particles. It is helpful to distinguish the applied machinery according to types of acting stresses on the particles: i.) one-sided impact stressing, ii.) two- or more-sided compression, iii.) fluid forces, which are applied for the dispersion of agglomerates with soft physical bonds and iv.) electrical forces, which may become more important in future for the separation of different materials in recycling applications. In the following, I will focus on cases i.) and ii.).

Interestingly, scaling laws for size reduction by grinding (as well as for emulsification and spraying) are very similar, i.e. the mass median particle size $x_{50,3}$ scales with the energy per volume E_V (or per mass): $x_{50,3} \sim E_V^{-b}$ with b between 0.3 and 0.8 for most material systems (e.g. grinding of limestone, alumina and lateral size reduction of graphene oxide) in stirred media mills. This correlation is also applicable for colloid mills and even ultrasound (see Peukert et al. (2015) and literature cited therein). Breakage kinetics strongly depend on the process parameters, i.e. the machine function, as long as the grinding limit is not reached: Proper choice of process parameters saves not only up to 90 % of the energy input to reach the grinding limit, it also leads to a higher product quality in terms of crystallinity and less milling bead wear (Knieke et al. (2011)). In contrast, the grinding limit is only dependent on material properties.

* Corresponding author: wolfgang.peukert@fau.de

Starting from this general picture, I will discuss in the following selected aspects of fundamentals of fracture, transport of particles in the mill (and in the classifier) and a few interesting novel applications.

2 Fine grinding

Nanoparticles can be produced by wet comminution in stirred media mills. Grinding in bead mills leads to multiple stress events acting on the particles inducing internal defect formation and finally particle fracture. The prevention of agglomeration of the nanoparticles in the suspension during the milling process requires careful control of the interparticle interactions, which also influence suspension rheology. Too high viscosities may terminate any progress in size reduction. A steady state between agglomeration and des-agglomeration forms. These competing phenomena often lead to a plateau in the evolution of particle size, the so called apparent grinding limit. The degree of agglomeration and therefore the observable particle size can be controlled by selection of stabilizers and by the applied shear forces.

In contrast to the apparent grinding limit, the true grinding limit is reached when the particles cannot store defects anymore. Breakage occurs for ceramic particles even down to a size range of 10 nm (e.g. alumina, zirconia and tin oxide). For organic materials similar effects also lead to minimal particle sizes in the range of few 10 nm (Maar et al. (2022)). X-ray diffraction and the application of the Rietveld refinement method revealed that defects are generated during mechanical stressing of the particles in the mill. These defects enhance the elastically stored energy in the crystalline lattice and weaken the material. Below a critical size, defects cannot be stored within the crystallites and the overall limit of grinding is reached. By comparison of the internal crystallite and particle sizes derived from gas sorption measurement, different grinding behaviors of nanoparticles are distinguished: fracture through grains and fracture along grain boundaries (Knieke et al. (2011)). The grinding limit is strongly influenced by material properties, whereas process conditions analyzed in a practically relevant range hardly affected the limit. Based on these findings, several fundamental questions arise:

The defect structure inside of a particle belongs to the least understood phenomena in particle science and technology. It is not only important for a better understanding of grinding at the nanoscale, but is also highly relevant for liberation of valuable materials in minerals processing. Which defects develop in a specific material? How can one distinguish between fracture through grains and along grain boundaries? Which material parameters determine the stability of defects inside of a small particle? Deeper insights may evolve from high resolution transmission electron microscopy (HR-TEM) and from modelling and simulation, in particular molecular simulations coupled to continuum models promise novel insights.

Fig.1: Phase transformation and defects observed in compressed nanoparticles by means of MD simulations (from left to right): Phase transition in ZnS (from wurtzite (red) to cubic (green) structure), dislocations in CaF_2, shear planes in SnO_2.

Answers to these questions may evolve from micro- and nanomechanics. Mechanical elastic and inelastic particle properties are often unknown. Compression experiments applied to single particles can provide some of the needed properties. For instance, a nanoindentation device installed within an electron microscope measures force-displacement curves and provides optical images of deformed and broken particles. Systematic studies on different materials and in dependency of particle size are needed to better understand the mechanical material behavior at all scales. This way, material functions could be derived which are highly relevant for modeling of grinding processes but may serve also as input for DEM models.

3 Shape-selective size reduction

Triggered by the Nobel prize for the discovery of graphene, a monolayer of graphite, many different layered materials (2D materials) with outstanding mechanical and electronic properties were discovered. While graphene was originally delaminated via a simple scotch tape, technical solutions are needed for industrial application. In case of particles with highly anisotropic structures such as graphite, hexagonal BN or MoS_2, delamination can be induced by mild stressing conditions leading to free standing only nm-thin graphene-like platelets in dispersion. While in chemistry labs often ultrasound is used for delamination, stirred media mills and high pressure homogenizers are better suited for scalable production. More systematic studies are needed to fully explore the production of this highly interesting new class of materials. In particular, process-structure relationships are still not sufficiently understood.

Delamination of these molecular thin platelets requires high shear forces and simultaneously small normal forces to avoid in-plane fracture. In contrast, thin platelets with thicknesses down to 100 nm can be produced by compression of feed particles between the beads of a stirred media mill (Esper et al. (2022)). Stressing of metal particles or glass particles with size below their brittle-to-ductile transition leads to irreversible plastic deformation. Oxides show a brittle-to-ductile transition in the micron-size range. Such shape-selective deformation of particles can be used to produce innovative materials for diverse applications including bioactive glasses and oxides (e.g. based on SiO_2 and GeO_2) interesting for anodes of Li-ion batteries (Esper et al. (2022)).

Related challenges are i.) a comprehensive understanding of the material properties, ii.) fast and reliable characterization of such plate-like materials, iii.) the effective shape-selective separation of the platelets (see section of classification). Since the plastic deformation can be modelled by FEM, the effect can be used for the model-based determination of stress energy and stress number distributions in mills (Strobel et al. (2017)), see Fig. 2, which are largely unknown in mills.

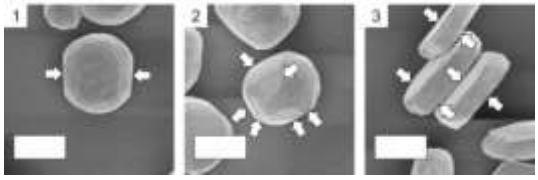

Fig. 2: Stressed copper particles inside of a stirred media mill. The indents are used to calculate the absorbed stress energy as derived from stress-strain measurements of compressed single particles (Strobel et al. (2017)).

4 Mechanochemical effects

Currently, the increased interest in industry on mechano-chemical reactions in the dry state is driven by need for "greener" production to mitigate climate change, for instance by avoiding solvents. Several reviews show the interesting possibilities (Balaz et al. (2013)).

High energy input can induce phase transitions, radical formation at the particle surface and interactions of the solvent with the particles shedding new light on mechano-chemical reactions in liquid phase. Despite the vast field of mechanochemistry which encompasses an increase in reactivity due to the effect of mechanical energy input, there is still no clear picture of the involved mechanisms. The mechanical energy input is thermodynamically rooted on the Gibbs fundamental equation

$$dF = -SdT - pdV + \sum_i^n \mu_i dn_i + \gamma dA + \vee \sum_{l,m=1}^3 E_{l,m} de_{l,m}$$

where the free energy dF depends on temperature T, pressure p, volume V, entropy S, chemical potential μ, interfacial energy γ and surface area A, and on the last term - the stress tensor. The effect of the acting stress on temperature increase and on the chemical potential as driving force for chemical reactions is poorly understood. External stress may also rise the surface energy and enhance solubility considerably. In wet grinding the situation is further complicated by the presence of the solvent: reactions of the stressed solid with the surrounding liquid phase can occur. For instance, the complex interactions of drug molecules with stabilizers enhances solubilization, impairing the formation of particles below a few 100 nm.

A key to the understanding of the underlying phenomena lies in the comprehensive product characterization and on the role of the liquid phase. The liquid phase may influence product properties like particle size, porosity, particle shape, structure, chemical composition and the molecular termination of the surface opening many unexplored options. An increase in the reactivity of glass particles is manifested by a significant increase in dissolution in the aqueous phase during processing in water (Romeis et al. (2016)). Fig.3 shows the manifold mechano-chemical effects in the liquid phase.

Fig. 3: Mechano-chemical effects at interfaces (from left to right): Radical formation, surface charges and double layers, adsorption, mass transport to and from the surface (incl. dissolution and uptake of solvents).

5 Multiscale modelling

Large scale applications contribute considerably to climate change, e.g. cement production produces as much as 8 % to worldwide CO_2 emissions. Major steps in improving the energy efficiency are urgently needed. Optimization with respect to both, product quality and environmental impact, is only possible by improved simulations.

This requires an overall modelling strategy, which must include a continuum description of the two-phase flow as well as models for fracture. Deeper insights of the fracture mechanism might come from computational continuum fracture modelling coupled to the molecular structure and respective molecular models based on force fields derived from DFT. Such comprehensive combination of models across several length are currently still out of reach.

Currently a combined CFD-DEM approach is the best and most advanced choice for description of particle motion. Limits exist for highly turbulent two-phase flows. The dynamic formation and decay of cluster-like structures is a major challenge in the modelling of gas-solid flows. Hierarchical multiphase models must take into account the local distribution of particles which depends on drag and particle-particle impacts as well as on friction. Coarse graining is a necessity to keep computational time and cost within reasonable limits. The challenge is to include more and more realistic material functions, i.e. to understand and model particle-particle interactions. This requires hierarchical optimization with clever chosen homogenization and error estimates between the scales. For instance, the observed cluster formation in the gas phase may influence particle stressing and impair separation of particles by a classifier. Recent experimental results in opposed fluidized jet mills indicate that the particles collide at surprisingly smaller velocities even when high speed (close to sonic velocity) jets are applied.

The outcome of the two-phase simulation would be, in case of an impact mill, the distribution of impact velocities and impact angles on the hammers of the mills. For sufficiently dilute systems (some 10 g solid/m^3 air) Toneva et al. derived distributions of impact velocities by using CFD coupled to Lagrangian particle tracking in a air classifier mills from Hosokawa Alpine

(Toneva et al. (2011)). The most probable impact velocity was found to be 85% of the hammer speed for particles larger than roughly 100 µm. These data serve as input for modelling fracture probability and size distribution of the fragments, which were derived earlier and found to be applicable for many different materials (Vogel et al. (2005)). On this basis, the operational behaviour could be modelled for air classifier and sieve hammer mills, i.e. the particle size distribution (PSD) could be predicted for various operating conditions such as hammer speed or screen openings.

Currently, the use of artificial intelligence (AI) becomes very popular. The availability of sufficient reliable experimental data is a key pre-condition. Hybrid approaches, which narrow the solution space by physically reasonable conditions derived from mass, momentum and energy balances and kinetic laws, in combination with the model-based determination of unknown and hard to measure parameters seem to be most promising approach.

6 Classification of multidimensional particle systems

Particle science and technology evolve towards ever increasing complexity with respect to the multidimensional particle properties of size, shape, surface, internal structure, and composition. From the application side, recycling requires the liberation and classification of different materials from multicomponent devices such as batteries.

The theoretical background for multidimensional particle property distributions was only recently developed by transferring the concepts well known from 1D PSDs to multidimensional PSDs comprising of at least two different properties such as size and shape or size and composition (Frank et al. (2023). These new possibilities evolve from advances in efficient multidimensional characterization tools, e.g. analytical (ultra-)centrifugation as well TEM or XRD tomography. In general, particles are classified according to external force and velocity fields, e.g. external gravitational, centrifugal, electric or magnetic fields. The acting field forces control particle motion, i.e. particles of differing properties move on different trajectories, which allow their separation into different fractions. In addition, force fields induced by particle interactions can be employed as well and used for fractionation. In this special case of short-range interactions, the particles interact either selectively with external surfaces, e.g. in flotation with bubbles, in particle interaction chromatography with the stationary phase material, or with themselves for property-selective agglomeration.

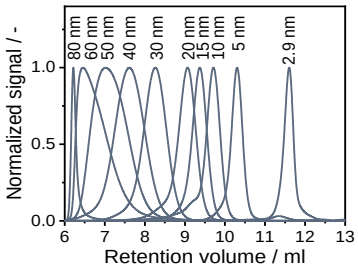

Fig. 4: Baseline separation of gold nanoparticles by size exclusion chromatography.

Nanoparticle chromatography is a promising novel approach for the highly efficient classification of particles below 100 nm (Gromotka 2022), see Fig.4. Size exclusion chromatography is based on repulsive interactions of the particles with stationary phase material. In this case, the fractionation depends on the diffusion coefficient and is independent of the type of core material. Scale-up is in principle possible as known from the industrial production of proteins and other biomaterials.

Acknowledgement

Support of DFG for funding the projects CRC1411, CRC953, PP2945 and PE427/40-1 is gratefully acknowledged.

References

Balaz P. et al., (2013) Hallmarks of mechanochemistry: from nanoparticles to technology. *Chem. Soc. Rev.* 42, 7571-7637.

Esper J., Maußner F., Romeis S., Zhuo Y., Baar M., Yokosawa T., Spiecker E., Bachmann J., Peukert W., (2022) SiO_2-GeO_2 glass-ceramic flakes as an anode material for high performance lithium-ion batteries. *Energy Technology* 2200072.

Frank U., Dienstbier J., Tischer F., Wawra S.E., Gromotka L., Walter J., Liers F., Peukert W., (2023), Multidimensional fractionation of particles. *Separations* 10, 252.

Gromotka L., Uttinger M.J., Schlumberger C., Thommes M., Peukert W., (2022) Classification and characterization of multimodal nanoparticle size distributions by size-exclusion chromatography**.** *Nanoscale* 14, 17354-17364.

Knieke C., Sommer M., Peukert W., (2009) Identifying the apparent and true grinding limit. *Powder Technology* 195, 25-31.

Knieke C., Romeis S., Peukert W., (2011) Influence of process parameters on breakage kinetics and grinding limit at the nanoscale. *AIChE J.* 57, 7, 1751-1758.

Maar S., Damm C.,Peukert W., (2022) Wet nanomilling of naproxen using a novel stabilization mechanism via Zirconium complexation. *Advanced Powder Technology* 33, 103723.

Peukert W., Segets D., Pflug L., Leugering G., (2015) Unified design strategies for particulate products. In Jinghai Li, Guy B. Marin (eds.) Mesoscale Modeling in Chemical Engineering Part I, *Advances in Chemical Engineering* 46, pages 1-81, Academic Press.

Romeis S., Schmidt J. Peukert W., (2016) Mechanochemical aspects in wet stirred media milling. *International Journal of Minerals Processing* 156, 24-31.

Strobel A., Romeis S., Wittpahl S., Schmidt J., Peukert W., (2017) Characterization of stressing conditions in mills - a comprehensive research strategy based on well-characterized model particles. *Powder Technology* 205, 652-661.

Toneva P., Wirth K.-E., Peukert W., (2011) Grinding in an air classifier mill. *Powder Technology* 211, 28-37.

Vogel L., Peukert W., (2005) From single particle impact behaviour to modelling of impact mills. *Chem. Eng. Sci.* 60, 5164-5176.

I2: DEM surrogate modelling in the context of comminution

Christoph Thon[1,*], *Kostas Giannis*[1], *Arno Kwade* [1]and *Carsten Schilde*[1]

[1]Institute for particle technology (iPAT), Technical University Braunschweig, Braunschweig, Germany

Abstract. Surrogate models can allow for substantially faster numerical investigations compared to classical approaches, as was demonstrated already by Alphafold or GNoME in material science. Applying such an approach on discrete elements method (DEM), by training quick to apply neural network based AI models that emulate DEM simulations, substantial speed-ups and investigations of much larger simulation domains can be achieved while keeping the inherent flexibility of simulation software, compared to customized predictive models of more specific systems. In this work, a scalable surrogate model is established and demonstrated on two different simulation cases, compression and free particle flow as they occur in various comminution aggregates such as crushers or stirred media mills. The approach is compared to classical simulations as well as to customized predictive models of mills. Model scale up, time advantages, accuracy, required preliminary efforts and respective characteristics will be discussed in detail.

1 Surrogate models in general

Artificial Intelligence (AI) is increasingly establishing itself as an important tool next to experimentation, and classical numerical simulation and modelling techniques. Mostly it is used for predictive modelling, that allows the leveraging of existing data in order to derive generalized predictions. Such models allow for great speed-ups in the modelling endeavour and reduce time and effort, as was previously shown (Thon et al, 2022a, 2022b) for predictive models of wet and dry stirred media mills and other systems from comminution.

A next logical step is to train more generalized systems that not only predict the result of specific simulations but emulate the simulation itself in order to join the time advantages of predictive models with the flexibility of simulation software. Similar approaches have previously been demonstrated with Alphafold by google for protein folding, which previously failed for more complex structures in classical MD simulations, within 3 years the number of known structures with comparable accuracy increased from 150000 in 2019 to over 600 million in 2022. (Jumper et al, 2021) More recently, GNoME (Merchant et al, 2023) achieved a similar success in stable inorganic crystal predictions, relevant throughout industries like batteries, chips, solar panels etc. Predictive accuracy reached 80 percent, increasing the amount of known materials by a factor of 10, an equivalent of around 800 years of conventional advances in material science before that breakthrough.

2 Discrete elements method surrogate

In this work, an AI model is trained to accurately predict the temporal and spatial interactions between particles and with walls and the free particle flow, emulating discrete elements method simulations.

Training data is generated with LIGGGHTS for particles in unit cells, see figure 1. In subsequent AI inference a larger domain is subdivided into discretized unit cells in which the motion and interaction patterns of variable particles are predicted over time with cyclic mesh updates to allow particle migration across unit cells throughout the entire domain and to enable scale up to large simulation domains. Training on a diverse range of unit cell interactions allows the neural network based AI model to capture most interaction patterns of particles and to generalize and predict novel interaction patterns.

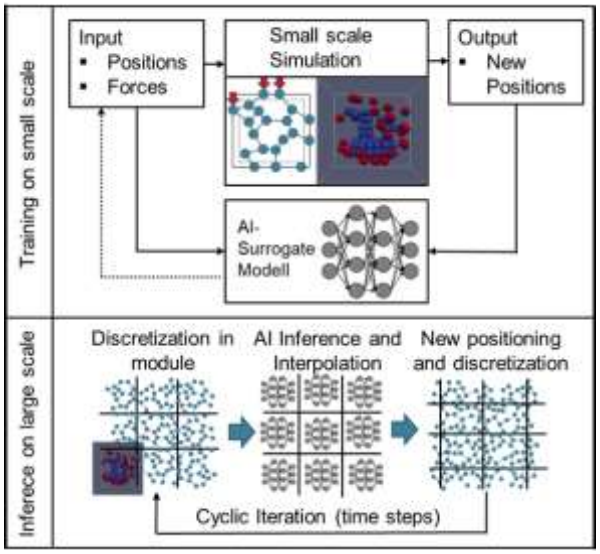

Fig. 1. Training and inference of the surrogate DEM model. Particle interaction patterns are captured and trained into a neural network architecture to predict the temporal and spatial interactions in large domains of communicating unit cells.

The framework is demonstrated on a particle compression scheme with a novel multi contact model, which was previously published by Giannis et al. (2021a,

* Corresponding author: c.thon@tu-braunschweig.de

2021b), see figure 2. Particle positions and stresses acting on them are compared with independent cases, not used in training.

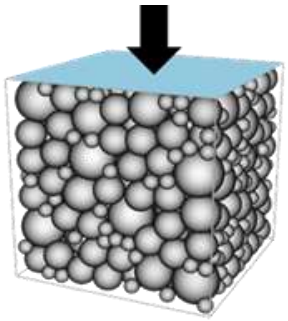

Fig. 2. Uniaxial compression of a particle bed with varying particle sizes and an implemented multi-contact contact model. Positions and stresses are compared for independent simulations not used in training. Highly accurate results could be obtained around 1000x faster than in LIGGGHTS.

The resulting AI predictions have the same data format as the simulations, allowing for consistency in post processing and visualization in Paraview or other typical visualization tools, without the need for custom adaptations. Orders of magnitude faster DEM emulations of these novel simulations could be obtained (around a factor of 1000x faster), with high degrees of accuracy for both particle positions over time as well as acting stresses, as can be seen in figure 3 for a parity plot of stresses in compression dimension z.

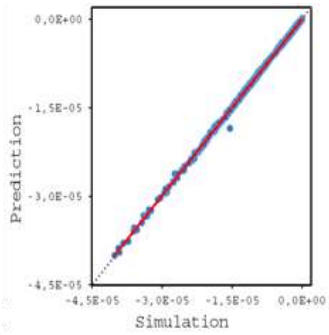

Fig. 3. Parity plot of stresses acting on the particles in compression dimension z with a high degree of accuracy. Being the most challenging parameter to predict, x and y dimensions and particle positions showed in comparison even higher accuracy then z stresses.

Furthermore, the framework has been extended to emulate the more complex free flow of particles. This is demonstrated on a vertical rotor system, with the generalizing capabilities to be investigated at a later point by comparing with another geometry of a vertical stirred media mill, already investigated in a prior publication (Thon et al, 2023) with a classical predictive model, see figure 4. This and a similar study for a horizontal wet stirred media mill (Thon et al, 2022a, 2022b) required distinct training runs, showing the motivation for generalized models in the form of surrogate models.

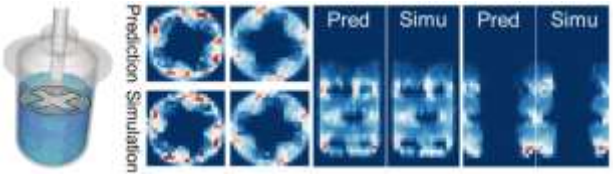

Fig. 4. Predictive model of a dry vertical stirred media mill for the prediction of grinding bread energy and collision velocity next to the evaluation simulations. (Thon et al, 2022a, 2022b)

As can be seen in figure 5, a rotor is composed of particles for reasons of simplicity to later be replaced by importable geometries. Different aspects of the simulations can be implemented by parallel running models, e.g. for demonstration cases a separate model was trained for the prediction of the rotor as alternative to mathematically accurate position updates, while the free flow of surrounding particles was implemented via a separate running surrogate model. Thus, a higher level of customization can be achieved, allowing as a long-term perspective for the implementation of model libraries with varying contact models, capabilities or levels of compute performance and accuracy.

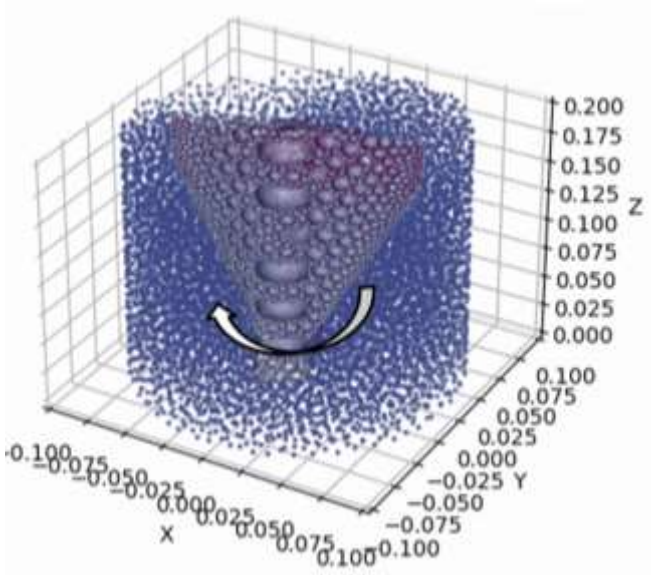

Fig. 5. A surrogate model of free particle flow in a rotor case. The rotor is at present composed of particles for reasons of implementation simplicity to later be replaced by geometries.

Variations in the meshing scheme will be elaborated on, such as dynamic remeshing and periodic mesh overlays as well as variations in training data generation like randomized approaches vs. sampling in training simulation cases and subsequent data augmentation.

The advantages of the approaches, classical DEM simulations, customized predictive models surrogate models are compared with regard to training effort, accuracies, flexibility, inference times and scalability. As an outlook, acting as quick to apply, cheap and flexible digital twin these models allow for quick iteration. Long-term opportunities for optimization, e.g. of stirrer geometries via approaches such as genetic algorithms and virtual rapid prototyping or for process control will be elaborated on.

Acknowledgements

Funded by the Deutsche Forschungsgemeinschaft (DFG, German Research Foundation) – SPP 2364 "Autonomous Processes in Particle Technology". The authors also want to thank the Deutsche Forschungsgemeinschaft in the context of the Heisenberg Program SCHI 1265/19-1 "Digital methods for complex systems in process and production engineering". Furthermore, we would like to thank the company ESSS (Florianópolis, Brasil) as developer of Rocky DEM for the close research cooperation and the provision of the research license. We especially thank Jan-Phillipp Fürstenau of CADFEM GmbH (Hannover, Germany) for the technical support.

References

Giannis, K., Schilde, C., Finke, J.H. & Kwade, A. (2021) Modeling of High-Density Compaction of Pharmaceutical Tablets Using Multi-Contact Discrete Element Method. *Pharmaceutics*, 13(12). Available from: https://doi.org/10.3390/pharmaceutics13122194.

Giannis, K., Schilde, C., Finke, J.H., Kwade, A., Celigueta, M.A. & Taghizadeh, K. et al. (2021) Stress based multi-contact model for discrete-element simulations. *Granular Matter*, 23(2), 17. Available from: https://doi.org/10.1007/s10035-020-01060-8.

Jumper, J., Evans, R., Pritzel, A., Green, T., Figurnov, M. & Ronneberger, O. et al. (2021) Highly accurate protein structure prediction with AlphaFold. *Nature*, 596(7873), 583–589.

Merchant, A., Batzner, S., Schoenholz, S.S., Aykol, M., Cheon, G. & Cubuk, E.D. (2023) Scaling deep learning for materials discovery. *Nature*, 1–6.

Thon, C., Böttcher, A.-C., Möhlen, F., Yu, M., Kwade, A. & Schilde, C. (2022a) Multi-modal framework to model wet milling through numerical simulations and artificial intelligence (part 1). *Chemical Engineering Journal*, 449, 137794.

Thon, C., Böttcher, A.-C., Möhlen, F., Yu, M., Kwade, A. & Schilde, C. (2022b) Multi-modal framework to model wet milling through numerical simulations and artificial intelligence (part 2). *Chemical Engineering Journal*, 450, 137947.

Thon, C., Röhl, M., Hosseinhashemi, S., Kwade, A. & Schilde, C. (2023) Artificial Intelligence and Evolutionary Approaches in Particle Technology. *KONA Powder and Particle Journal*, advpub, 2024011.

I3: Enhancing comprehension of grinding and mixing phenomena in nuclear applications through advanced instrumentation of a ball mill

Bastien FOSSE[1], *Christophe* ROUBAUD[1], *Nicolas* BLANC[1,*], and *Anne-Charlotte* ROBISSON[1]

[1]CEA.DES.IRESNE.DEC, Cadarache F-13108 Saint-Paul-Lez-Durance, France

Abstract. This study focuses on the development and qualification of an instrumentation suitable for acquiring key information on the grinding/mixing stages of nuclear powder. Indeed, one of the key stage in nuclear fuel production is the mixing and the grinding of powders by ball milling. A thorough understanding of this phase is essential to optimize the manufacturing of pellets, involved into the nuclear fission reaction. To meet this challenge, CEA has developed three interdependent strategies: modelling and simulation, data assimilation enhanced by artificial intelligence (AI), and experimental data acquisition through multi-sensor instrumentation. This paper focuses on the latter approach.

1. Introduction

Ball mills are essential pieces of equipment in several industrial applications, including mineral processing, chemistry, cement production, advanced material synthesis and notably, the nuclear field (Schnatz, 2004; Erdem and Ergün, 2009; Ellart *et al.*, 2020; Giraud *et al.*, 2021). Their primary function is to reduce particle size and facilitate the mixing of different components at a granular level (Canakci *et al.*, 2013; Razavi-Tousi and Szpunar, 2015). The performance and efficiency of a ball mill can significantly affect the product's quality, and consequently, the profitability and safety of the entire industrial process (Ellart *et al.*, 2020). Over the years, research on ball mills has aimed to optimize their operation and gain a deeper understanding of the complex phenomena occurring within (Shoji, 1982; Erdem and Ergün, 2009). Variables such as ball size (Austin, Shoji and Luckie, 1976; Schnatz, 2004; Erdem and Ergün, 2009; Kuziora *et al.*, 2014; Razavi-Tousi and Szpunar, 2015; Giraud *et al.*, 2021), ball material (Canakci *et al.*, 2013), ball filling (Shoji, 1982; Schnatz, 2004; Kuziora *et al.*, 2014; Cayirli, 2018), powder feed size (Cayirli, 2018; Giraud *et al.*, 2021), powder filling (Shoji, 1982; Deniz and Onur, 2002; Tangsathitkulchai, 2003), ball-to-powder ratio (Canakci *et al.*, 2013; Kuziora *et al.*, 2014), milling speed (Canakci *et al.*, 2013; Cayirli, 2018), milling time (Canakci *et al.*, 2013; Cayirli, 2018), and drum volume (L/D ratio) (Schnatz, 2004; Kuziora *et al.*, 2014) have been identified as critical factors influencing milling performance.

These studies have highlighted the complex interactions between these parameters and the way in which they collectively affect the characteristics of the final product, underlining the importance of optimising each factor for specific applications (Cayirli, 2018; Giraud *et al.*, 2021). However, it is essential to note that, despite considerable advances, there are still gaps in our understanding of the ball mill. The complex interactions between particles and pebbles, scale effects and variations introduced by different grinding parameters require further study.

A major challenge in this respect is that industrial ball mills are generally non-transparent, making it difficult to directly observe the internal dynamics during the grinding process (Wang *et al.*, 2021). This opacity adds a layer of complexity to the understanding of the phenomena that take place, underlining the need for advanced instrumentation and indirect methods to obtain information. By equipping these machines with various sensors and measuring devices, researchers are seeking to gather more precise data on these internal processes (Tano, 2005; Owusu *et al.*, 2021; Wang *et al.*, 2021). This is all the more important as grinding in ball mills is often energy-intensive and inefficient: much of the energy is wasted in impacts that do not necessarily break up the particles. These observations have stimulated interest in precise, direct measurements of charge behaviour in the mill (Tano, 2005). As load movement is closely linked to particle breakage and wear of linings or grinding media, it is essential to use a method capable of providing accurate, real-time information on the state of grinding/mixing (Wang *et al.*, 2021).
A multi-sensory approach, combined with modern techniques like artificial intelligence, promises to revolutionize our understanding of grinding and mixing (Kuziora *et al.*, 2014). In this context, the present work seeks to introduce the development of a multi-sensor instrumentation, which will allow the study of the comminution of matter in a nuclear environment.

Mixing/grinding mechanisms are highly dependent on mill operating conditions. There are several forms of transverse bed motion, all depending on the following conditions:

* Corresponding author: nicolas.blanc@cea.fr

- drum rotation speed
- drum volume
- volume of grinding media
- volume of powder to be mixed/ground

As shown in Fig. 1. below, the different types of the transverse bed motion may be subdivided into seven main forms:

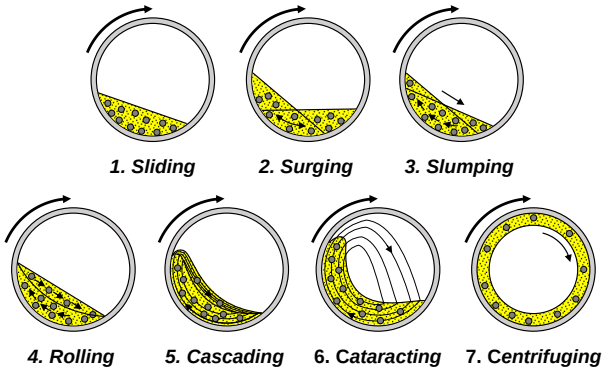

Fig. 1. Forms of transverse motion of solids in rotating cylinders (adapted from (Mellmann, 2001))

Among all the forms of transverse movement, rolling, cascading and cataracting are the most efficient in contributing to the fragmentation mechanism. In fact, they provide sufficient wall friction to enable a dynamic tumbling motion that ensures efficient mixing. At higher rotation speeds, particles can even break away from the bed and be thrown into the air, resulting in cataract motion. This movement is distinguished by the trajectories the particles take as they are thrown from the bed surface, with variations such as pure cataract and centrifugation, depending on the intensity of the movement and the particles' adhesion to the cylinder wall.

Understanding the forms of transverse movement and their transitions is essential for achieving the desired powder qualities. In fact, by controlling operational parameters (rotation speed, filling degree, etc.), bed movement can be optimized.

2. Materials & Methods

Considering the stringent environment associated with nuclear materials, studies were initially done using an experimental ball mill in a non-nuclear setting. The mill's design, adaptable to various drum sizes, facilitates the examination of scale effects from laboratory to industrial sizes using pebbles as grinding media. The focus is on understanding the physical phenomena during grinding/mixing, with detailed analysis through multi-sensor instrumentation. This includes discussing sensor types and signal processing techniques, aiming to improve process control by offering insights into material characteristics like particle size and surface area, and feeding data into simulation models for validation.

3.1 High speed camera

3.1.1 Set-up and device

A Photron FASTCAM SA4 camera is used to take images of the mixing/grinding process. This camera is equipped with a 12-bit CCD sensor with a resolution of 1024x1024 pixels and a maximum frequency of 3.6 kHz, at this resolution. The mill is observed through a Tamron macro lens with a focal length of 100 mm and a maximum aperture of 2.8. To ensure sufficiently bright images, a 4000K neutral light was used (Fig. 2.).

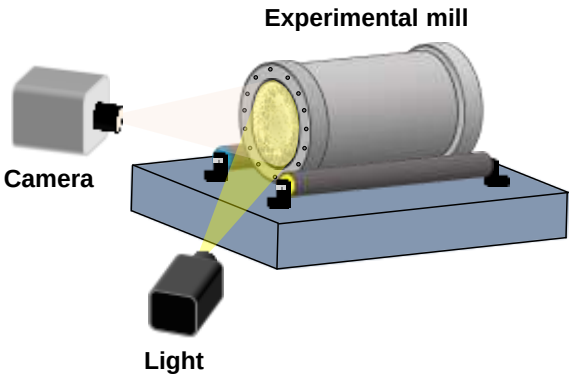

Fig. 2. Illustration of camera set-up for imaging

3.1.2 Image analysis and extracted data

Python code using OpenCV and OpenPIV was developed to analyze the captured images and extract valuable information such as velocity fields. Fig. 3. and Fig. 4. give an example of these data, used for the analysis of grinding mechanisms, and to link with fragmentation energy and the identification of specific zones. This information is crucial for validating models and enriching databases, facilitating the use of artificial intelligence to improve understanding and optimization of the grinding process.

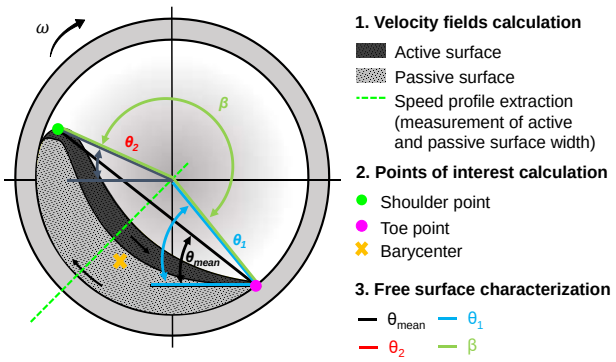

Fig. 3. Illustration of the main characteristic extracted from an image during the mixing/grinding process

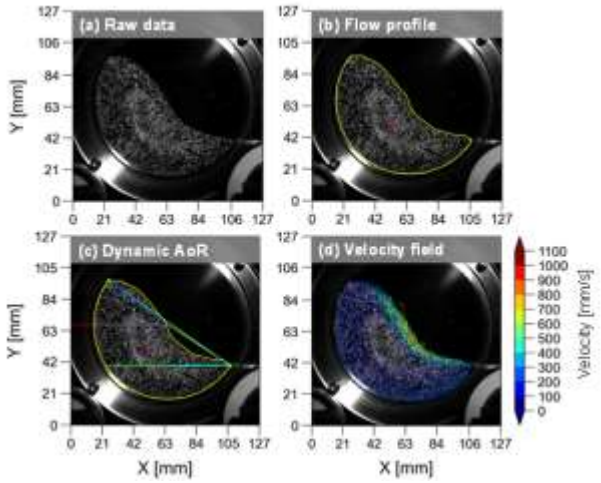

Fig. 4. Example of data extracted from python code: (a) raw data, (b) charge flow profile, (c) dynamic angles of reposes and (d) velocity fields.

3.2 Acoustic Emission sensor

In addition to camera observations, a wide-band acoustic emission sensor was used. Acoustic emission sensors would appear to be excellent tools for studying the comminution of materials. They record the mechanical waves generated by the fracturing process, providing valuable data on material decomposition. However, implementing this type of sensor presents several challenges. As the sensor is connected by a cable, modifications to the drum were required to avoid cable winding, including the installation of a rotating slip ring (Fig. 5.). As for signal processing, careful calibration was essential to adjust the sensor's sensitivity so as to accurately detect emissions specifically linked to the grinding process, while ruling out interference from ambient noise that could mask or alter the signals. A thorough analysis of the data was required to extract the relevant information.

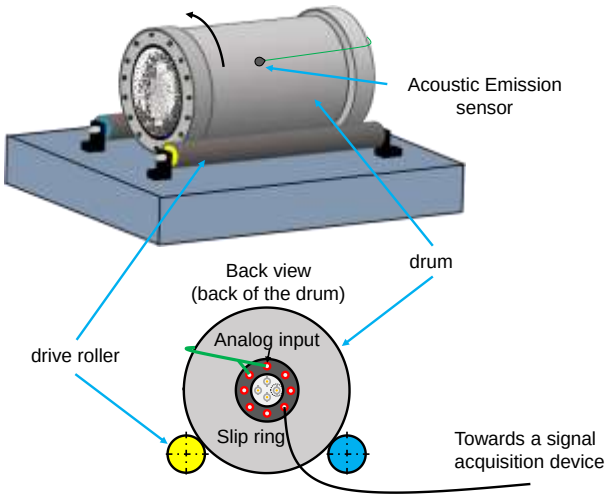

Fig. 5. Illustration of the installation of an acoustic emission sensor on a rotating drum

3. Results and discussion

In this section, we examine how the tools developed can provide valuable information for the study of materials, highlighting the contributions of acoustic and imaging analyses, as well as the incorporation of particle image velocimetry (PIV) data.

Monitoring the evolution of the dynamic angles of repose (AoR) over time can shed light on the comminution mechanisms. In Fig. 6. it can be observed that the average dynamic angle of repose tends towards the experimentally determined static resting angle for the material under study. This information provides valuable insights into the behaviour of materials under dynamic conditions and can be used to estimate the particle fragmentation energy through calculation. Also, the velocity fields obtained through Particle Image Velocimetry (PIV) reveal the material's shearing behaviour. This is accomplished by studying the active and passive surfaces, including their thickness, through the extraction of transverse profiles. Thus, PIV offers a valuable opportunity to observe and understand the internal dynamics of the material under stress.

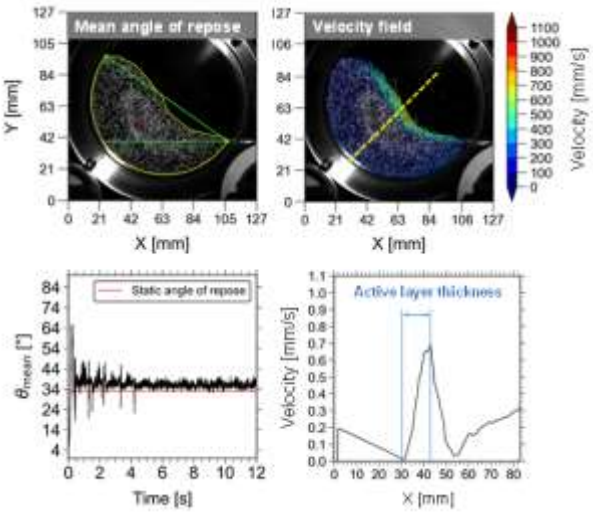

Fig. 6. Example of dynamic angle of repose and active layer thickness calculation from image processing

In terms of acoustics, the interpretation of data can significantly vary depending on the analysed parameters. Focusing solely on the frequency domain might fail to uncover clear trends or relevant information about the material's state. However, exploring the energy domain reveals promising trends. This distinction emphasizes the importance of selecting an appropriate analytical framework to uncover meaningful insights into material behaviour. In Fig. 7. below, it can be observed that measuring the absolute energy of the signal clearly helps to identify the mixing/grinding regimes as well as the comminution of the material. Indeed, the energy level allows for the differentiation between cascade and cataract modes. The observed slope in the signal indicates that the material undergoes comminution. Indeed, during the grinding the particles become smaller and smaller, increasing the bulk density of the powder and therefore changing the interaction between the pebbles and the granular bed, probably leading to fewer

collisions between the pebbles, the particles, and the inner surface of the drum, thereby reducing the presence of mechanical waves and thus acoustic energy.

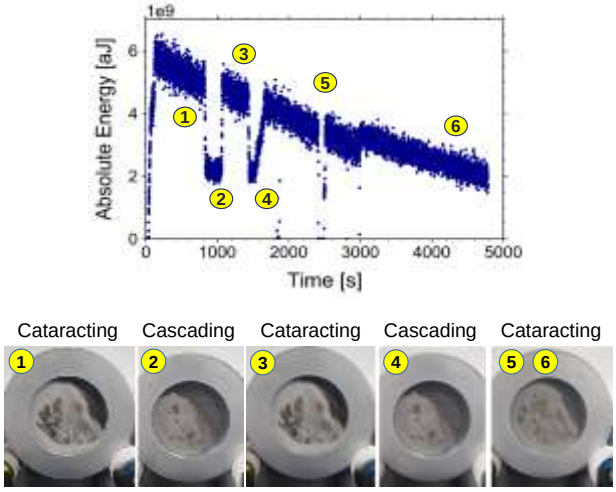

Fig. 7. Illustration of camera set-up for imaging

5 Conclusion

The tools and methods presented offer several significant advantages:

- enable observation of dynamic processes during mixing/grinding stages.
- provide quantitative metrics for a deeper analysis of mixing and grinding.
- offer insights into grinding mechanisms and material behaviour under stress.
- generate data for simulation models and databases, facilitating AI applications and digital twin development.

Looking ahead, the integration of additional sensors (such as microphones and accelerometers) promises to cover a broader frequency range, enriching the data collected. The use of machine data (such as speed and torque) opens possibilities for process control, further expanding the application scope of this instrumentation.

References

Austin, L.G., Shoji, K. and Luckie, P.T. (1976) 'The effect of ball size on mill performance', *Powder Technology*, 14(1), pp. 71–79.

Canakci, A. *et al.* (2013) 'Determining the effect of process parameters on particle size in mechanical milling using the Taguchi method: Measurement and analysis', *Measurement*, 46(9), pp. 3532–3540.

Cayirli, S. (2018) 'Influences of operating parameters on dry ball mill performance', *Physicochemical Problems of Mineral Processing; ISSN 2084-4735* [Preprint].

Deniz, V. and Onur, T. (2002) 'Investigation of the breakage kinetics of pumice samples as dependent on powder filling in a ball mill', *International Journal of Mineral Processing*, 67(1–4), pp. 71–78.

Ellart, M. *et al.* (2020) 'Influence of ball milling on the characteristics of uranium powders and on the resistance of pressed green pellets', *Ceramics International*, 46(13), pp. 21402–21409.

Erdem, A.S. and Ergün, Ş.L. (2009) 'The effect of ball size on breakage rate parameter in a pilot scale ball mill', *Minerals Engineering*, 22(7–8), pp. 660–664.

Giraud, M. *et al.* (2021) 'Investigating grinding mechanisms and scaling criteria in a ball mill by dimensional analysis', *Advanced Powder Technology*, 32(8), pp. 2988–3001.

Kuziora, P. *et al.* (2014) 'Why the ball to powder ratio (BPR) is insufficient for describing the mechanical ball milling process', *International Journal of Hydrogen Energy*, 39(18), pp. 9883–9887.

Mellmann, J. (2001) 'The transverse motion of solids in rotating cylinders—forms of motion and transition behavior', *Powder Technology*, 118(3), pp. 251–270.

Owusu, K.B. *et al.* (2021) 'AG/SAG mill acoustic emissions characterisation under different operating conditions', *Minerals Engineering*, 171, p. 107098.

Razavi-Tousi, S.S. and Szpunar, J.A. (2015) 'Effect of ball size on steady state of aluminum powder and efficiency of impacts during milling', *Powder Technology*, 284, pp. 149–158.

Schnatz, R. (2004) 'Optimization of continuous ball mills used for finish-grinding of cement by varying the L/D ratio, ball charge filling ratio, ball size and residence time', *International Journal of Mineral Processing*, 74, pp. S55–S63.

Seiss, M. (1995) *Etude du broyage de poudre d oxydes nucleaires*.

Shoji, K. (1982) 'Further Studies of Ball and Powder Filling Effects in Ball Milling'.

Tangsathitkulchai, C. (2003) 'Effects of slurry concentration and powder filling on the net mill power of a laboratory ball mill', *Powder Technology*, 137(3), pp. 131–138.

Tano, K. (2005) *Continuous Monitoring of Mineral Processes with Special Focus on Tumbling Mills – A Multivariate Approach*. Luleå University of Technology.

Wang, T. *et al.* (2021) 'Assessing load in ball mill using instrumented grinding media', *Minerals Engineering*, 173, p. 107198.

J1: Comminution and classification technological applications in the field of urban mining. A review.

József Faitli[1], *Miia* John[2], *Evelina* Repo[3], *Imre* Gombkötő[4]

[1,4] Institute of Raw Materials Preparation and Environmental Technology, University of Miskolc, Hungary
[2,3]LUT School of Engineering Sciences, Lappeenranta-Lahti University of Technology LUT, Lappeenranta, Finland

Abstract. The concept of urban mining means the mining and processing, therefore reclaiming compounds and elements from any kind of anthropogenic origin stocks, including buildings, infrastructure, industries and products (in and out of use). This review paper compiles examples from the literature showcasing industrial applications of urban mining waste-to-material recycling, focusing on cases where mechanical processing of man-made raw materials is essential, thus necessitating comminution and classification processes. Flow types of anthropogenic raw materials are reported to EU authorities regularly, therefore subcategorization of waste types follows the EU nomenclature. Characteristic comminution machines and main types of stressing and some cases characterising separation units are presented which are illustrated by a few selected application examples.

1 Introduction and aim

The challenges to the sustainability of human life on earth have intensified in recent times, as it has now become generally evident that it is under threat. As an answer, the concept of the circular economy and urban mining was born. The scientific vocabulary of these relatively new areas was clarified probably by Cossu and Williams (2015). According to Cossu and Williams (2015) the terminology Landfill Mining represents the activities involved in extracting and processing wastes which have been previously stocked in particular kinds of deposits (municipal landfills, mine tailings, etc.). Urban Mining extends landfill mining to the process of reclaiming compounds and elements from any kind of anthropogenic stocks, including buildings, infrastructure, industries, products (in and out of use), and environmental media receiving anthropogenic emissions. Circular Economy is even a much wider term, because it covers all the economic and social impacts too, including how to design fully recyclable products and so on, meaning everything that facilitates the real material circular flow. Still we think that the most important part of the circular economy is how we can gain raw materials from anthropogenic resources by urban mining and inside this the real challenge is not the waste mining but rather how the waste is processed. The stocked materials may represent a significant source of resources, with concentrations of elements often comparable to or exceeding natural stocks. A definition distinguishing between “stock” and “flow” resources, either anthropogenic or natural is necessary. The origin of natural stocks can be either geogenic or biogenic and many times geogenic natural stocks are called “virgin” (Winterstetter et. al. 2016). Annual stocks of materials held in geological deposits, groundwater reservoirs, household and industrial buildings, infrastructure and scrap products may not vary much over time. However, annual flows of materials may change considerably from year to year, depending upon the prevailing economic situation, fashion, technical innovations, etc. Nevertheless, from both anthropogenic stock and flow resources, secondary raw materials are produced. Resource Recovery includes materials recycling as well as the energy that can be generated by treating and managing wastes (waste-to-energy recovery). Materials Recycling (or waste-to-material recycling) aims to transform selected wastes into materials that can be used again in the manufacture of new products. The mining and processing of virgin geogenic raw materials have always been with us for as long as humans have lived, since without materials there can be no civilized life on earth. Therefore, the current task is to transfer the known technologies of mining and mineral processing to the field of urban mining including waste processing. The first comprehensive paper applying this concept was probably written by Ambros (2023). Ambros (2023) reviewed the typical gravity concentration units and their applications in mineral processing and then investigated the possible applications of that mechanical process for waste upgrading. Another new scientific term we have to learn is the Distinct Urban Mine (DUM). The materials and resources recoverable from individual urban spaces differ. The uniqueness of an urban mine is due to factors such as the composition and concentration of post-production and post-consumption materials of interest as well as the demographic profile of the urban space. This delimited space, unique in its material composition and concentration is called a Distinct Urban Mine (DUM) (Ongondo et. al. 2015). As with a traditional mine, a DUM requires prospection to determine its viability. Information such as size, concentration of materials and

* Corresponding author: jozsef.faitli@uni-miskolc.hu

grade of resources of interest and its location within the wider anthroposphere is necessary. According to Ambros (2023) the miners of the present will gradually become recyclers in the future since there will be more copper, iron, and zinc (and other metals) in the cities than in the earth's crust after 2050 (considering current known reserves).

Taking this introduction into account it was concluded that a review of technological applications of comminution and classification in the field of urban mining could be useful for the scientific community. Data of the continuously generating wastes, by-products and other residues, namely the flow types of anthropogenic raw materials are reported to the national and EU authorities regularly, therefore it is aimed first to give a summary of these statistical waste categories and sub-categories according to EU nomenclature. Then focusing only on the waste-to-material recycling the characteristic comminution machines and main types of stressing and some cases characterising separation units are presented which are illustrated by a few selected application examples. The typical upgrading concept is well-known in mineral processing. Every time mechanical pre-processing is needed, namely comminution and classification are necessary to release the valuable components and generate narrowly distributed particle size or shape fractions, as they enable effective upgrading. Then if there is a difference in any intrinsic feature of the component materials, the materials can be upgraded by physical separation when different particles go into products because of forces, namely concentrates - rich in the useful components - and tailings - hopefully poor in the useful components - can be produced. If the particles of the feed of different materials are sorted by manual- or sensor based sorting (SBS), this kind of upgrading requires mechanical pre-treatment also. After the mechanical pre-upgrading - when the big mass of non-useful components has been discarded - mechanical-, chemical-, thermal- or biological processes can be used for the extraction of the useful components. Without mechanical pre-concentration, it is certain that no subsequent non-mechanical waste recycling process can be economically viable. Therefore, the role of comminution is very important for urban mining.

Before going further, let's review the conclusions of Ambros (2023) about the competing three upgrading processes (upgrading at density, SBS and froth flotation), because similar conclusions are expected for the comminution. Most plastics, due to their low density and hydrophobic properties, may be considered as the urban mining equivalent of coal in mineral processing. Therefore, methods like jigging, counter-current flow separation and dense media separation can effectively separate polymers when the material feed is adequately liberated. Centrifuge gravity separation also shows potential for isolating microplastics from soil and sediments (Ambros, 2023). Gravity concentration is promising for producing recycled aggregates from construction and demolition waste (CDW), especially for coarse aggregates (>4.75 mm). However, processing fine CDW (<4.75 mm) remains underexplored, possibly due to direct applications in backfilling and geotechnical fields (Ambros, 2023). And most importantly gravity separation is increasingly challenged by two fronts: sensor-based sorting (SBS) in the processing of coarse materials and froth flotation in the treatment of fine-sized materials. However, there is an intermediate size range (about 0.75–5 mm) where these techniques face technical difficulties and in which gravity separation typically excels, particularly for treating construction and demolition waste (CDW) and microplastics. Also, SBS (sensor based sorting) typically can effectively sort particles within a limited range of sizes, with a recommended maximum size ratio of about 3 between the smallest and largest particles (Ambros, 2023). This is why classification is important.

2 Flow types of secondary raw material stocks

According to EU statistics, 776.3 million tons of waste was generated, excluding major mineral waste in the EU in 2020 (Eurostat online data code: env_wasgen). At the time of generation, this whole mass of waste can be considered as a flow type of anthropogenic secondary resource. It consists of solid wastes as 25.2% households wastes; 21.5% manufacturing wastes; 11.5% other sectors wastes; 5.9% energy wastes; 5% construction wastes; 2.7% agriculture, forestry and fishing wastes; 1% mining and quarrying wastes and non-solid 27.4% wastewater;. Some of this waste mass will be charged in deposits and landfills and later that will become a stock type of resource. Table 1 shows comminution and classification waste-to-material recycling application examples according to the subcategorization of the generated solid wastes.

Table 1. Summary of waste sub-categories and examples for their recycling options and applied comminution equipment.

Waste category	Waste sub-category	Recycling option examples	Comminution and classification equipment	Types of stressing
Agriculture, forestry and fishing wastes	Agriculture (crop) waste	Composting. Biogas generation. Biomass conversion (thermo- and biochemical conversion)	Hammer crushers Hammer mills	Beating impacting shearing
	Agriculture (animal)	Using the useful parts and disposing of the residues	Axial-gap rotary shears	Shearing tearing
	Forestry	Mulching (solid waste can be used as mulch to protect the soil) Waste-to energy recovery Decomposition	Swing hammer mills Cutting mills (tip point speed can reach 100 m/s)	Cutting shearing

	Fishing	Producing value-added products e.g., peptides, proteins, collagen, chitin, oil. Procedures as acid extraction, enzymatic hydrolysis and fermentation.	The role of mechanical pre-processing by comminution and classification is not so important for this waste stream.	
Mining and quarrying wastes and metallurgical slags	Mining and quarrying wastes	Waste rock (materials overlying), Overburden (low grade minerals) and Beneficiation wastes (residues of mineral processing) Primary aim: producing secondary raw materials.	Full spectrum of brittle materials comminution equipment. Crushers: Jaw, gyratory, cone, roll, impact, pin mill, hammer, hammer shredder. Mills: ring, media, planetary, vibrated, stirred media, jet, cutting, rotary-shear.	Pressing beating impacting shearing
	Metallurgical dusts and slags	Recovery of the valuable metals by hydro-, pyro- or bio-metallurgical processes after mechanical pre-processing. Complex utilisation. Producing cement additives.	Grinding; media mills, namely ball mills, autogenous mills (AG) and pebble mills. Ring mills for blast furnace slag.	Pressing, shearing
Manufacturing	Production specific, non-production specific	Quality assurance discarded. Technological (e.g. red mud of alumina production), Amortization wastes. Non-production-specific wastes.	Bring these materials back into their own production system. All types of wastes so all types of comm. equipment.	
Wastes of energy production	Residues of fuels incineration. (coal combustion-CCR, waste incineration residues)	CCRs is being used in cement, cellular concrete, fly ash lime bricks, fly ash lime gypsum block, building tiles; as admixture in cement concrete, timber substitute products; as aggregate in concrete, road and building block; as pozzolana.	Tumbling ball mill or high energy density mill (HEM) like the planetary ball mill, vibratory mill or stirred media mill.	Pressing shearing
	Residues of solar energy generation	c-Si PV modules: dismantling, shredding, SBS upgrading, pre-concentrates go to distinct waste recycler. FirstSolar and ANTEC Solar GmbH technologies for CdTe PVmodules. Shredding, slow leaching drum, glass separation, sodium hydroxide precipitation of metal compounds.	Specialised hammer crushers hammer mills	Beating impacting shearing
	Residues of wind energy generation	100 % waste-to-material recycling is possible.	Suitable comminution eq. for steel, Al, Cu, polymer materials, concrete, etc…	
	Residues of nuclear energy generation	Reprocessing of Spent nuclear fuel (SNF) by fission and activation products, and so-called minor actinides producing high-level solid packed waste (HLW).	Comminution is not applied typically	
Construction & Demolition wastes (CDW)	Excavated soil	Processed CDW and composted eucalyptus bark (CEB) were used at lab scale to make new soil.	Typically on-site handling with normal soil excavators.	
	Concrete aggregate	Producing recycled concrete aggregate (RCA). Producing controlled Low-Strength Materials (CLSM). Producing new binders.	Multiple stages. 1st stage: horizontal axis jaw crushers and beater rolls.2nd stage: Cone crushers, impact crushers	1·Pressing bending. 2·Pressing impact.
	Asphalt aggregate	Producing Recycled asphalt aggregate (RAA) or Pyrolysis RAA.	Toothed rolls and hammer crushers	Shearing beating
	Wood waste	See forestry waste		
	Metal waste	Metallurgical processing	Guillotine shears, alligator shears	Shearing
	Mixed CDW	Removing contamination. Production of new construction materials. Production of lower utilization fill materials.	Crushers for brittle materials comminution.	Pressing shearing
Post-consumer wastes	Municipal solid wastes (MSW)	Waste-to-material recycling of SMSW and some RMSW. Waste-to-energy recovery, RDF (refuse derived fuel). Biomass conversion.	Axial gap rotary shear and swing type hammer shredder. For RMSW: Low-speed rotary shredders for pre-shredding and radial gap shears for final.	Shear and complex tearing and shredding
	EoL Rubber tyres	Waste-to-material-recycling or energy recovery	Multiple stages: Steel cords removing by hook, axial gap shears, then radial gap shears and finally cutting mills.	Shearing cutting
	EoL Batteries	Extracting precious and structural components	Hammer shredders. Issues: fire and explosion hazard, hazardous dust emission	Shredding

	EoL Refrigerators	Waste-to-material recycling. Issue: Freon gases.	Hammer shredders. Chains can serve as hammers. Nitrogen atmosphere.	Shredding
	EoL Vehicles	Waste-to-material recycling. Waste-to-energy recovery.	High mass swinging hammer shredders	Shredding
	WEEE (electric and electronic waste), EoL TV devices. EoL Computers.	Extracting precious and structural components	Hammer shredders and hammer crushers. PCB - high-speed hammer crusher and beater mill.	Shredding shearing beating

3 Stock types of secondary raw materials

In a recent paper Mirletz et.al. (2023) projected the cumulative mass of different waste streams, namely many of the stock types of anthropogenic secondary raw materials are listed. According to this projection 70,350 mill. tons of municipal solid wastes, 45,500 mill. tons of coal ash, 12,355 mill. tons of plastic waste, 1876 mill. tons of E-waste, 249 mill. tons oily sludge and about 120 mill. tons of solar panels will be deposited somewhere by 2050. If we take into account the mineral deposits, namely gangue and tailing stockpiles and tailing ponds and the entire built infrastructure (buildings, roads) we can feel the huge amount of stocked anthropogenic materials. According to our vision there is no waste, just secondary raw materials; so the possibilities of urban mining are really promising.

4 Conclusion

This extended abstract offers only a brief glimpse into the findings of our literature survey. However, we believe that our systematic approach enhances comprehension and provides insight into the potential urban mining applications of mineral processing. Additionally, a comprehensive overview and categorization of flow and stock types of anthropogenic secondary raw material sources is provided.

This project is funded by the European Union's Horizon Europe program under grant no. 101079354.

References

Alwaeli M., Mannheim V. (2022) Investigation into the Current State of Nuclear Energy and Nuclear Waste Management - A State-of-the-Art Review. Energies 15(12) p. 4275. DOI: 10.3390/en15124275

Ambros W.M. (2023) Gravity Concentration in Urban Mining Applications - A Review. Recycling. Vol. 8. No. 85. DOI: 10.3390/recycling8060085

Cossu R., Williams I. D. (2015) Urban mining: Concepts, terminology, challenges. Waste Management. Vol. 45:1-3. DOI: 10.1016/j.wasman.2015.09.040.

Cristelo N., Segadães L., Coelho J., Chaves B., Sousa N.R., de Lurdes Lopes M. (2020) Recycling municipal solid waste incineration slag and fly ash as precursors in low-range alkaline cements. Waste Management. Vol. 104. pp. 60-73. DOI: 10.1016/j.wasman.2020.01.013

Eisenlauer M., Teipel U. (2020) Comminution of Wood – Influence of Process Parameters. Chemical Engineering & Technology, Vol. 43, Issue 5. pp. 838-847. DOI: 10.1002/ceat.201900488

Lunardi M.M., Alvarez-Gaitan J.P., Bilbao J.I., Corkish R. (2017) A Review of Recycling Processes for Photovoltaic Modules. InTechOpen. DOI: 10.5772/intechopen.74390

Matinde E., Simate G.S., Ndlovu I. S. (2018) Mining and metallurgical wastes: a review of recycling and re-use practices. J. S. Afr. Inst. Min. Metall. Vol. 118. No. 8. DOI: 10.17159/2411-9717/2018/v118n8a5

McNeil K., Kang T.H.K. (2013) Recycled Concrete Aggregates: A Review. International Journal of Concrete Structures and Materials. Vol. 7. No. 1. pp. 61–69. DOI: 10.1007/s40069-013-0032-5

Mirletz H., Hieslmair H., Ovaitt S. (2023) Unfounded concerns about photovoltaic module toxicity and waste are slowing decarbonization. Nat. Phys. Vol. 19, pp. 1376–1378. DOI: 10.1038/s41567-023-02230-0

Mucsi G. (2016) Mechanical activation of power station fly ash by grinding – A review. Journal of Silicate Based and Composite Materials. Vol. 68. No. 2. pp. 56-61. DOI: 10.14382/epitoanyag-jsbcm.2016.10

Ongondo F.O., Williams I.D., Whitlock G. (2015) Distinct Urban Mines: Exploiting secondary resources in unique anthropogenic spaces. Waste Management. Vol. 45. pp. 4-9. DOI: 10.1016/j.wasman.2015.05.026

Rácz Á., Csőke B. (2021) Comminution of single real waste particles in a swing-hammer shredder and axial gap rotary shear. Powder Technology. Vol. 390. pp. 182-189. DOI: 10.1016/j.powtec.2021.05.064

Schubert G. (1991) Aufbereitung der NE-Metallschrotte und NE-metallhaltigen Abfälle - Teil 1. Aufbereitungs-Technik 32. Nr. 2. pp. 78-89.

Winterstetter A., Laner D., Rechberger H., Fellner J. (2016) Integrating anthropogenic material stocks and flows into UNFC-2009 – Challenges and potentials. 7th session, UNECE Expert Group on Resource Classification, Geneva, 26 – 29 April 2016.

J2: Stormwater purification with construction and demolition waste (StoPWa)

Nazila Bolourieh[1, *], *Teemu* Kinnarinen[1], *Sanduni* Jayasekara[1], *Roland* Romenda[2], and *Jutta* Nuortila-Jokinen[1]

[1] LUT School of Engineering Sciences, Lappeenranta-Lahti University of Technology LUT, Lappeenranta, Finland
[2] Institute of Raw Materials Preparation and Environmental Technology, University of Miskolc, Hungary

Abstract. The paper discusses an initiative to recycle construction and demolition waste (CDW), such as bricks and concrete, as a way to reduce landfilling and promote resource conservation. It introduces the EU-funded StoPWa project focusing on efforts to reduce stormwater runoff pollution. The project aims to develop a filtration system using CDW to purify stormwater, thus integrating CDW recycling with environmental sustainability efforts. The research begins with characterization of different CDW size fractions, including difficult-to-recycle materials like bricks and insulation wool. In the next phase, laboratory experiments are used to assess the ability of CDW to retain harmful substances following pretreatment with methods like crushing, grinding, and sieving. Field trials will later test the most promising filter media for stormwater purification. The project also involves developing various filter structures using CDW-based materials. The final phase includes implementing and evaluating the developed stormwater filter systems in operational ponds in Finland, Estonia, and Latvia. The ongoing study has completed material characterization and analysis, with the next steps focusing on designing filter media for pilot testing based on pollutant removal potential.

1 Introduction

The international StopWa project focuses on the development and testing of stormwater filters to prevent harmful runoff polluting natural water bodies. The aim of the material characterization phase within the StoPWa project is to gather insights into the attributes of construction and demolition waste (CDW). Such information is essential for crafting new sustainable CDW-based filter materials for stormwater purification. Key material characteristics, including particle size distribution, specific surface area, and elemental composition, significantly influence filter material structure and capacity for adsorption, which, in turn, shape the properties of the final filter product. This paper presents a summary of the characterization findings of mixed CDW samples examined in the StoPWa project.

2 Materials and methods

To identify the most suitable CDW streams and characterization methods for the study, discussions were first held with industrial product managers and extensive information searches undertaken. Factors such as availability at project locations (Lahti, Finland; Harju County, Estonia; Smiltene, Latvia), initial particle size, hardness, and asbestos-free status were deemed crucial for sample selection, and the choice of the most effective characterization methods was guided by a thorough examination of published works and a comprehensive review of existing literature.

2.1 Sample preparation

2.1.1 Sample selection

The methodology used for selection of CDW for the characterization study is shown in Fig.1. CDW available within the project locations was prioritized.

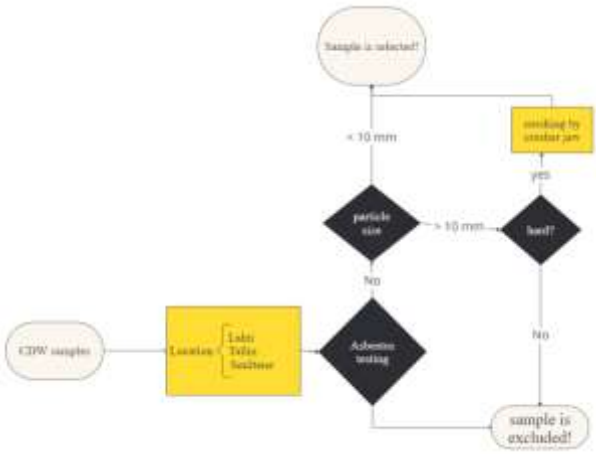

Fig. 27. Process of sample selection for characterization study in the StoPWa project

CDW recycling companies were requested to provide samples with an initial particle size less than 10 mm, and efforts were made to obtain both soft (including plastic, insulation materials, textiles, fabrics, etc.) and hard (concrete, brick, cement, ceramic, glass, clay, etc.)

* Corresponding author: nazila.bolourieh@lut.fi

samples from each location. Subsequently, approximately 5-6 increments, each weighing between 100-200 g were taken from each batch and combined to form a gross sample and sent to an asbestos testing lab to ascertain the absence of asbestos. Samples containing asbestos were excluded from the study, and only asbestos-free wastes were considered further.

2.1.2 Characteristics of the selected samples

The samples examined during the characterization study of the StoPWa project are detailed in Table 1. Each sample is accompanied by a code assigned for streamlined data management, along with descriptions, original particle size, and primary content. Two gross samples had been selected from recycling companies in the Lahti region, for the characterization study. Additionally, our partners in Estonia provided us with several samples, from which we chose one sample representing mixed waste comprising minerals, insulation materials, wood, and plastic. We also tested a sample from Latvia consisting of a mixture of hard and soft materials.

Table 7. Characteristics of construction and demolition waste gross samples selected for study

Sample code	Original particle size (mm)	Main content
FLSM	0-12	Concrete, bricks, ceramics
FLKM	0-20	Wood, foam, soil, plastic, minerals
EPM	0-5	Mineral components, Wood, Plastic
LSZM	0-20	Aerated concrete, plaster, tiles, concrete, clay, asphalt, stone mass tiles, insulation materials, brick

2.2 Construction and demolition waste characterization and analysis methods

Particle size distribution measurement and fractionation were performed using a test sieve shaker manufactured by Haver & Boecker. The shaker consisted of 13 sieves with aperture sizes ranging from 25 to 5000 µm with a pan positioned beneath the bottom sieve stack. Samples weighing between 500 and 1000 grams were placed on the uppermost sieve (5mm). An alternative method employed for particle size determination was automated image analysis with a Morphologi G3 (Malvern Instruments, UK) microscope system. Automated image analysis of microscope images of the sample was employed to assess different attributes describing particle shape. The analysis included evaluating the morphology of particles based on mean circularity and elongation. Information on the shape of particles will help predict the flow of stormwater through the designed filter and enable improvement of the filtration system. Particle size distribution measurement for fine particles (<25 µm) involves using laser diffraction particle size analyzer by Malvern Mastersizer 3000 featuring the Hydro EV particle dispersing unit and water as the dispersant liquid (Malvern Instruments, UK). The specific surface area (SSA) of solids was determined using a fully automated Micromeritics 3Flex surface characterization analyser (Micromeritics Instrument Corp., USA), which employed the Bennett-Emmett-Teller (BET) method. The material's elemental composition was assessed using energy-dispersive X-ray spectroscopy (EDS) to illustrate element distribution. The SEM-EDS apparatus employed for these measurements was the Hitachi SU3500. The mineral composition of the samples was investigated using powder X-ray diffraction (XRD, Bruker D8 Advance, Bruker Corp., Germany). The goal of the XRD analysis was to identify the main mineral phases in the sample and compare them with those in other CDW studies. Thermogravimetric analysis (TGA) was conducted to examine how a sample behaves under high temperatures. This analytical technique relies on measuring the weight loss of a material as it undergoes programmed heating. In this study, the temperature was gradually increased from room temperature to 700 °C. The thermographic analysis was performed using a Netzsch STA 449 C Jupiter thermo-microbalance. The samples underwent pretreatment prior to analysis. The particle size fraction in the range of 2.5–5 mm was separated by sieving for SSA and morphology analyses. Additional pretreatment, including grinding of the samples, was necessary for SEM-EDS, XRD, and TGA analyses to reduce particle size, as these instruments are designed to analyse small sample quantities.

3 Results and discussion

This section provides an overview of the particle properties and composition of the samples, focusing on aspects such as size, shape, elemental composition, mineralogy, and thermal behaviour.

3.1 Particle size distribution (PSD)

As it can be seen in Fig. 2, sample EPM exhibits a notably consistent particle size distribution, whereas the other samples display steep slope curves, indicative of elevated levels of coarse material content. Laser diffraction was used for particle size distribution (PSD) measurement of fine particles in samples containing particles smaller than 25 µm.

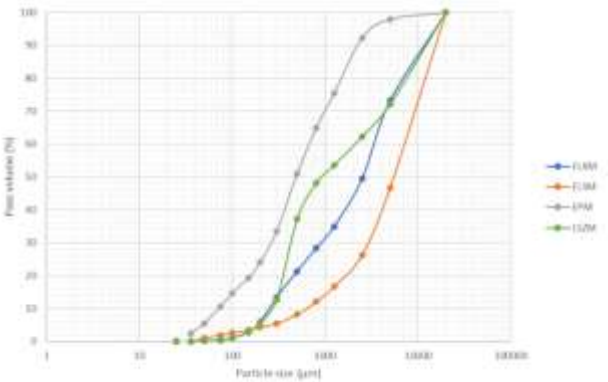

Fig. 28. Cumulative particle size distribution of the mixed CDW samples studied

Sample EPM contained such fine particles, and the PSD is plotted as per laser diffraction analysis in Fig. 3, where it can be seen that 10% of the particles have sizes below 5 µm, 50% have sizes below 17.2 µm, and 90% have sizes below 29.4 µm as determined by reading the D10, D50, and D90 values in the master sizer reports.

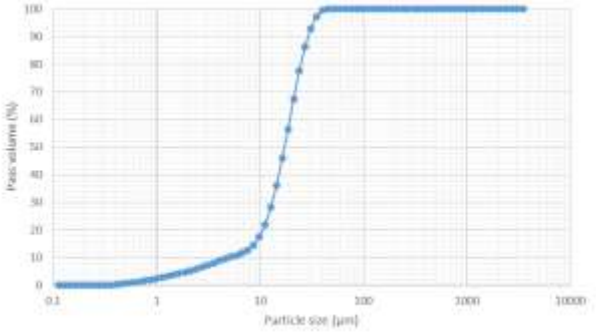

Fig. 29. Cumulative particle size distribution of fine particles present in sample EPM

3.2 Specific surface area measurement using the Bennett-Emmett-Teller (BET) method.

The conducted specific surface area measurements using the Bennett-Emmett-Teller (BET) method revealed that sample EPM had the highest specific surface area: 7.4 m^2/g, indicating its potential as a favourable raw material for filter media from a particle-level perspective. In contrast, sample LSZM had the lowest specific area (1.2 m^2/g) which means that this material may not be suitable for filtration media development. Nevertheless, the behaviour of particles in an agglomerated state can vary, potentially leading to distinct adsorption properties when these materials are employed in filter media applications (Roger et al., 2008). Specific surface area measurement results are presented in Table 2.

Table 8. Specific surface area measured using BET method

Sample code	Size fraction (µm)	BET SSA (m2/g)
FLSM	2500-5000	4.3
FLKM	2500-5000	7.1
LSZM	2500-5000	1.2
EPM	2500-5000	7.4

3.3 Morphology analysis

The findings of the morphology analysis to identify the particle shapes of the samples are presented in Table 3. Circularity refers to how close an object's shape is to a perfect circle, with a value of 1 indicating a perfect circle. Elongation, on the other hand, measures how stretched or elongated an object is compared to a perfect circle, with higher values indicating greater elongation. The results show that the majority of the samples exhibit a more circular morphology than elongated morphology. Specifically, sample LSZM demonstrates the most circular shape, while sample EPM displays the least circular shape. Conversely, sample EPM exhibits the most elongated shape, with sample FLSM having the least elongated morphology.

Table 9. Average circularity and elongation of particles in the samples examined

Sample code	Size range (µm)	Circularity (-)	Elongation (-)
EPM	2500-5000	0.56	0.41
FLKM	2500-5000	0.66	0.37
FLSM	2500-5000	0.59	0.32
LSZM	2500-5000	0.75	0.36

3.4 Elemental composition analysis using energy-dispersive X-ray spectroscopy (EDS).

Elemental composition analysis of the samples under investigation was carried out using energy dispersive X-ray spectroscopy (EDS), and the outcomes are outlined in Table 4. The results indicate the presence of O, Mg, Al, Si, Fe, and Ca in all samples, suggesting the existence of compounds such as calcium carbonate, calcium hydroxides, or other compounds derived from calcium, silicon, aluminium, and iron. Consequently, supplementary analyses were conducted to ascertain the specific mineral or chemical compounds present in the samples.

Table 10. Elemental composition of samples analysed by EDS method

Sample code		FLSM	FLKM	LSZM	EPM
Fraction		2.5-5 mm	2.5-5 mm	2.5-5 mm	2.5-5 mm
Element (Wt%)	C	-	-	27.3	7.4
	O	29.8	35.7	33.6	4.2
	Na	1.7	2.7	0.7	-
	Mg	0.5	0.8	0.4	0.2
	Al	1.7	4.7	2.2	0.9
	Si	5.6	21.9	23.2	3.9
	S	-	4.8	-	-
	Cl	4.6	-	-	-
	K	-	-	1	0.2
	Ca	2.6	13.3	7.1	3.6
	Ti	-	-	0.1	-
	Cr	-	0.9	0.4	9.9
	Fe	51.3	7.3	3.5	68.1

3.5 Mineral composition analysis using X-ray diffraction (XRD) method.

XRD analysis showed quartz and calcite in all samples. Albite was only found in samples FLKM and FLSM, and portlandite exclusively in FLKM. The absence of portlandite reflections in other samples suggests cement aging, with CaCO3 indicating portlandite carbonation. (Villaquirán-Caicedo and Mejía de Gutiérrez, 2021).

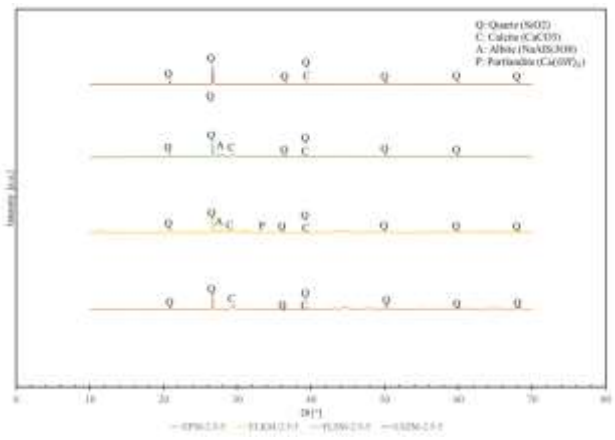

Fig. 30. XRD diffractograms of the CDW samples studied

3.6 Thermogravimetric analysis (TGA) for understanding of the thermal behaviour of material.

Thermogravimetric analysis of the mixed waste samples revealed the decomposition rates of the CDW components, with specific peaks indicating cellulose, plastic, and CaCO3 degradation, as it can be seen in Fig. 5. The FLKM and FLSM samples exhibited multiple peaks related to cellulosic and plastic degradation at specific temperature ranges (Gerassimidou et al., 2020), while a peak between 550 and 700 °C indicated CaCO3 decomposition (Wang et al., 2024). The presence of biomass materials and plastics in FLKM, and FLSM led to distinct peaks representing cellulose and plastic polymer degradation. The overlapping reactions in the heterogeneous mixtures posed challenges in distinguishing individual components.

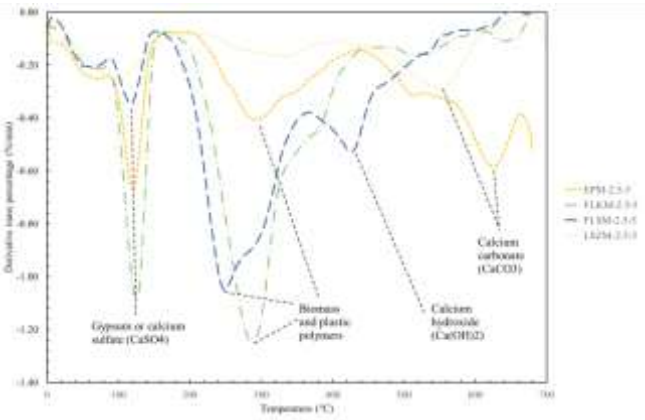

Fig. 31. Derivative thermogravimetric (DTG) curves of the mixed CDW samples studied

4 Conclusions

The flow and filtration properties of a material depend largely on its characteristics. In this study, particle size distribution, specific surface area, and particle morphology measurements revealed the physical properties of CDW samples for better understanding of potential filter performance in terms of flowability and filtration of stormwater. Materials that consist of very evenly distributed particles are presumed to let stormwater flow through more easily (Sileshi et al., 2019). Moreover, higher specific surface area enhances adsorption properties and helps filter media remove pollution (Shariatmadar Tehrani et al., 2021). Particle morphology can also give ideas about filter behaviour with respect to stormwater flow (Byungsik et al., 2018). In this study, characterization of the CDW samples with elemental and mineral composition measured by SEM-EDS and XRD as well as thermal behaviour analysed by TGA identified the chemical composition of the CDW samples, giving information about potentially hazardous elements, pollution, and the organic/inorganic ratio.

This extended abstract was supported as part of StoPWa, an Interreg Central Baltic Programme 2021-2027 project co-funded by the European Union. Throughout the research, the authors would like to acknowledge the support provided by the StoPWa team. This publication is funded by the European Union's Horizon Europe program under grant no. 101079354.

References

Byungsik, Lee., Lee-Hyung, Kim., Bonhong, Goo. (2018). Clogging Characteristics of Stormwater Infiltration System According to Filter Media Conditions. Korean Society of Hazard Mitigation, 18(3), 391-398.

Gerassimidou, S., Velis, C.A., Williams, P.T., Komilis, D., (2020) Characterisation and composition identification of waste-derived fuels obtained from municipal solid waste using thermogravimetry: A review. Waste Management & Research, 38(9) 942–965.

Redahegn, Sileshi., Robert, Pitt., Shirley, E., Clark., (2019). Statistical analyses of flow rates of stormwater treatment bioretention media. Water Environment Research, 91, 877–887.
Roger, P., Reid., Bruce, Saaski., (2008). Method of making a granular media water filter.

Shariatmadar Tehrani, F., Ahmadian, H. & Aliannezhadi, M., (2021). High specific surface area micro-mesoporous WO3 nanostructures synthesized with facile hydrothermal method. European Physical Journal Plus, 136(38), 1-11.

Villaquirán-Caicedo MA, Mejía De Gutiérrez R., (2021) Comparison of different activators for alkaline activation of construction and demolition wastes. Construction and Building Materials 281, 1-13.

Wang C, Chazallon C, Braymand S, Hornych P., (2024) Thermogravimetric analysis (TGA) for characterization of self-cementation of recycled concrete aggregates in pavement. Thermochimica Acta 733, 1-8.

J3: Mechanical preparation of End-of-Life Lithium-ion batteries

Sándor Nagy[1], Tamás Kurusta[1*], Tege Ficsór[1], S. Butylina[2] and M. Sethurajan[2]*

[1]Faculty of Earth and Environmental Sciences and Engineering, University of Miskolc, HU
[2]Faculty of Separation Science, LUT School of Engineering Sciences, LUT University, 53810 Lappeenranta, Finland

Abstract. Lithium-ion batteries (LiBs) are part of our life, from the smallest button cells size to the largest energy station. Some of the used cells can have a second life in energy storage system, but all of them should be processed at the end of battery life. Shape, structure, and chemical composition of Li-ion batteries varies that, makes their processing challenging. A mechanical preparation is the first step of battery processing. The exact structure of EoL LiBs should be investigated, and proper mechanical processing should be designed, involving the liberation in more comminution steps, separation of parts, removal of hazardous materials, and the classification step for Black Mass removal.

1 Introduction

There are several technical difficulties and obstacles for recycling and processing Li-ion batteries:

- a large number of types of Li-ion batteries (e.g., LCO, LFP, LMO, NMC, and NCA), requires appropriate pre-classification and sorting of batteries,
- larger size of battery packs and cells makes dismantling of them time-consuming and difficult,
- Li-ion batteries are flammable; they can catch fire or explode due to mechanical action (possibly even in case of improper storage),
- these batteries contain substances harmful to the human health and the environment, which must be separated, disposed of, and possibly recycled during mechanical preparation (closed technology/ circular economy approach).

The EoL LiB processing technologies in the EU have a capacity in the range of few hundred tons to 20 000 t/year. There are several methods proposed for metal recovery from LIBs including pyrometallurgical, hydrometallurgical and bio metallurgical (Roy et al. 2021).

The LiB processing technologies, which include mechanical pretreatment, can be considered environmentally friendly since the downstream operations to ensure the separation of pure metal in the later stages of the process are reduced. Mechanical processes can be implemented at relatively low cost and usually without special requirements (Javorsky da Costa et al. 2015). In the case of hydrometallurgy, the first step is the mechanical processing, which includes a comminution of the batteries, a separation of structural materials and the black mass (Brückner et al., 2020).

The technical problems mentioned, could be solved by implementation of special processes. For example, discharging of batteries is usually necessary before shredding this waste stream, to avoid the short circuit and fire hazards (Mádainé, 2020). In the case of wet shredding and freezing, the discharging is not necessary. Inert gas (CO_2, Nitrogen) or vacuum can be used for the shredding process, and there are wet technologies. Other problem is the electrolyte removal, which can be done by thermal treatment, or by application of vacuum (Greenwood et al., 2020).

The primary aim of this research is to extract the black mass from the battery cell. A material balance of the whole hybrid system in addition to the processing of the battery cells was prepared to be able to use our results as a basis for practical implementation.

2 Material and Methods

2.1 Material

The experiments were carried out on Ford Transit mild hybrid car battery pack, from Auto Mandy Car Kft., Budapest (Hungary). The battery package weighed 16.02 kg and included the battery cells, inverter, battery management system, connection circuits, and cooling system.

2.2 Methods

The battery pack was manually dismantled using hand tools, which involved removal of the releasable connection. After this, the battery cells were discharged by connecting them directly to a resistance (Kwade and Diekman, 2018), followed by manual and mechanical processing.

The battery cell was opened using a two-axis rotary shear shredder. Once opened, the electrolyte solvent was removed by heat treatment (Colledani et al, 2023) using the Memmert UFE 400 type drying oven at 60°C for 24 hours.

After the electrolyte was removed, the battery cell was mechanically crushed using a hammer crusher with a 20 mm sieve. The crushed battery cell material was sorted using an airflow separator with an air speed of

* Corresponding author: sandor.nagy@uni-miskolc.hu

2.54 m/s. Separation was carried out into the following particle size fractions: >16; 16-12; 12-8; 8-4mm. Particles smaller than 1 mm are referred to as black mass.

The qualitative analysis of materials and their identification was carried out on the FT/IR-4200 type A Fourier Transformed Infrared Spectrometer (JASCO) with a diamond ATR accessory. The spectra were obtained in a reflection mode.

The leached metals were analyzed using Varian Inc.'s 720-ES inductively coupled plasma (ICP) spectrometry. For the calibration of the device, a series of solutions were prepared from the certified multielement standard solutions, Certipur (distributed by Merck Ltd). and the Spectrascan (distributed by Teknolab).

3 Results

3.1. The manual dismantling of the hybrid system

The material balance after dismantling is shown in Table 1. The system could be split into 5 units without destroying. The largest part was the battery pack (40.60 wt%). Battery pack was treated separately and is, therefore, not included in the table. This is followed by the system case, which consists of an iron base plate (2.64 kg) to which the hybrid system is attached, and a plastic cover (2.06 kg) held together by screws and weighs 5.29 kg. The air cooling fans, and the aluminium-copper heat exchanger of the inverter are integrated in the plastic cover. Next to it is the inverter, which consists of a large aluminium heat exchanger, an AC/DC converter, and control electronics. During disassembly, the removed screws, cables, connectors, and sensors, were collected; together these weighed approx. 1.2 kg.

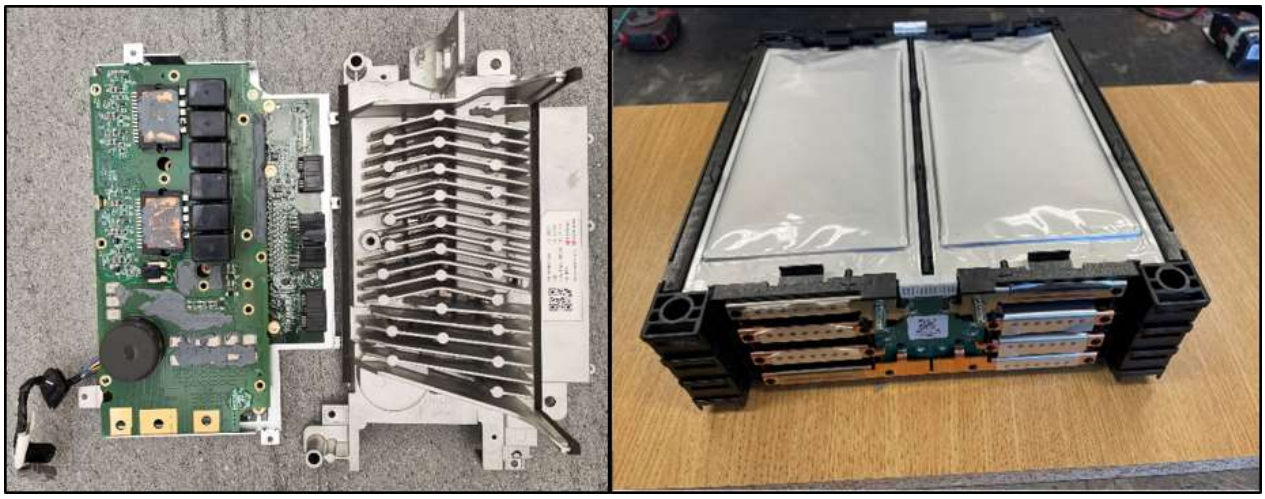

(a) **(b)**

Fig. 1. Main units of the hybrid system, (a) inverter and (b) battery pack.

Table 11. Hybrid system units and their component materials (unit: wt%)

Material	Units name (**wt%**)			
	System case	Inverter	Cooling system	Other parts (screws, plugs, sensors)
Plastic	39.06	5.00	63.46	4.10
Iron	49.83	0.00	0.00	47.39
Aluminum	6.44	46.29	23.27	1.46
Glass	4.68	9.08	0.00	0.00
PCB	0.00	38.41	0.00	0.00
Rubber	0.00	0.00	3.24	7.23
Copper	0.00	1.21	10.04	24.04
Zinc	0.00	0.00	0.00	15.78
Unit/Battery system	33.38	17.13	1.22	7.67

3.2. Processing of the battery cells

During the research, not only the mechanical processing of the battery cell was carried out, but also the manual disassembly of a cell.

3.2.1. Results of manual dismantling

Manual disassembly of the battery cell structure and its quantitative and qualitative composition were investigated. In terms of construction, the battery is

coated with a cellular composite casing, in which the anode, separator foil and cathode are layered.

According to the FT-IR measurements, the cell coating is a composite material consisting of polyethylene terephthalate-aluminium-polypropylene, PET-Al-PP. The cell casing provides 16.19 wt% of the total mass, with an aluminium content of 19-25 wt% based on volume concentration. The cathode foil consists of 28 aluminium plates, each 0.005 mm thick. It accounts for 2.51 wt% of the total cell mass. The anode foil consists of 29 copper plates, each 0.004 mm thick, making up 6.48 wt% of the cell. The separator foil between the anode and cathode plates provided 4.49 wt% of the total mass. Since the anode and cathode active materials could not be separated by the used technology, their mass fraction was determined as one, which amounted to 54.1 wt% of black mass.

During disassembly, the electrolyte content was determined by measuring the mass loss of the cells. The electrolyte content is 16.3 wt%, with a significant portion (10 wt%) removed shortly after opening the cell. The gas that is initially released contains mainly organic solvents (ethyl methyl carbonate [EMC]; dimethyl carbonate [DMC]) and CO_2 (Vetter et al, 2005; Aurbach et al, 2002).

3.2.2. Results of mechanical processing

Mechanical processing was carried out on electrically discharged batteries. The first stage of the process was to open the batteries and remove the electrolyte solvent with heat treatment. The 15.8 wt% electrolyte solvent left the cell, which is almost the same value as measured during manual dismantling. Since with this technology the electrolyte cannot be recovered, 100 wt% of the solid sample was used.

The particle size distribution and fractional composition of the battery cell after crushing in the hammer crusher are shown in Figure 2. According to the analysis, particles above 4 mm make up 60% of the sample's composition. Of these, 3/4 are metals with a partial black mass coating and 1/3 is separator foil. The fraction between 1 and 4 mm was composed of anode and cathode particles that were almost completely free of separator foil, with a significant coating of black mass. No further processing was done for particles between 1 and 4 mm.

The fraction below 1 mm, considered as a black mass, represented ~40 wt% of the sample. The composition of the extracted black mass, analyzed by ICP, is shown in Table 2. According to the results of the analysis, it has been determined that the battery that was processed is of NMC type. Upon analyzing the extracted black mass, it has been observed that it contains some amount of aluminum and copper foil fragments.

Table 12. Chemical composition of black mass

Chem.	**Ni**	**Mn**	**Cu**	**Ti**	**Al**	**Co**	**Fe**	**Li**
wt%	17.3	3.49	3.95	0.98	0.91	4.53	0.07	3.39

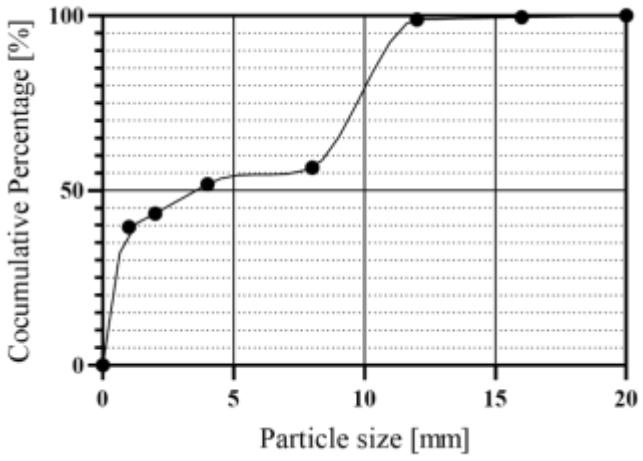

Material	4-8 mm	8-12 mm	12-16 mm
Composite case	3.43%	31.34%	40.43%
Cathode foil	26.52%	4.38%	23.40%
Anode foil	50.30%	3.60%	1.06%
Separator foil	19.78%	15.52%	35.11%
Weight ratio	34.69%	12.38%	0.94%

Figure 2. Crushed battery cell: particle size distribution and particle composition

3.2.3. Extraction of copper and aluminium

Valuable metals (aluminium and copper foil) with minor black mass coating were enriched in particle size fraction 4-16 mm. However, this fraction consisted of 70% separator foil by volume. The separation of metal and plastic was carried out in an airflow separator, with particle size fractions of 12-16- and 8-12-mm. Results of the separation is shown in Table 3. Based on the measurement results, the optimal airflow velocity is 2.68 m/s. At this velocity, the metal content loss is at its minimal, but 95 wt% of the separator film will be transferred to the product with low settling velocity.

Table 13. Material recovery in the high settling velocity products in air separator by airspeed (unit: wt%)

Particle size faction							
Particle size between 12-16 mm				Particle size between 8-12 mm			
Air velocity [m/s]	Separator foil	Copper	Aluminum	Air velocity [m/s]	Separator foil	Copper	Aluminum
1.96	40.28	100.00	100.00	1.96	43.31	100.00	100.00
2.16	30.11	100.00	98.86	2.16	19.76	100.00	100.00
2.35	18.87	100.00	95.68	2.35	12.02	100.00	98.92
2.52	10.30	99.83	95.85	2.52	12.32	100.00	96.70
2.68	5.81	99.83	92.29	2.68	9.34	100.00	98.75
2.83	8.77	100.00	94.71	2.83	8.13	100.00	98.68
2.97	2.92	97.87	87.15	2.97	4.00	100.00	95.06

4 Conclusions and future directions

The cells can be well opened with a rotary shear crusher, after which the electrolyte can be completely removed by heat treatment at 60 ℃ for 48 hours.

It was found that the technology used can recover approximately 74 % of the black mass. Results show that more than 90% pure black mass can be obtained by mechanical processes. Further black mass is also found in the coating moulds of the product with a high settling velocity and on the surface of the 1 to 4 mm particles from the hammer crusher.

As the research progresses, we plan to classify the anode and cathode grains, and to remove and recover the black mass adhered to the surface of the particles.

Funding

The research was funded by the Sustainable Development and Technologies National Programme of the Hungarian Academy of Sciences (FFT NP FTA). This publication is funded by the European Union's Horizon Europe program under grant no. 101079354.

References

Aurbach D., Markovsky B.,. Rodkin A,. Cojocaru M, Levi E, Hyeong-Jin K., (2002): An analysis of rechargeable lithium-ion batteries after prolonged cycling. *Electrochimica Acta*, 47, 1899-1911

Brückner L., Frank J., Elwert T., (2020): Industrial Recycling of Lithium-Ion Batteries - A Critical Review of Metallurgical Process Routes. *Metals*, 10(8), 1107

Colledani M., Gentilinic L., Mossalib E., Picone N., (2023): A novel mechanical pre-treatment process-chain for the recycling of LiIon batteries. *CIRP Annals*, 72, 17-20

Greenwood D., Dowson M., Unadkat P., (2020): Automotive Lithium-ion Battery Recycling in the UK. Based on a feasibility study by Anwar Sattar, University of Warwick

Javorsky da Costa A., Matos J.F., Bernardes A.M., Müller I.L., (2015): Beneficiation of cobalt, copper and aluminum from wasted lithium-ion batteries by mechanical processing. *International Journal of Mineral Processing*, 145, 77-82

Kwade A., Diekmann J., (2018): Recycling of Lithium-Ion Batteries. *Springer*

Mádainé Üveges V., Bokányi L., Papp R. Z., Szamosi Z., Romenda R. R., Nagy S., (2020): Valuable elements in waste electrical & electronic equipment (WEEE) and their possible recovery methods introduction. *Geosciences and engineering: a publication of the University of Miskolc*, 8, 71-83

Roy J.J., Cao B., Madhavi S., (2021): A review on the recycling of spent lithium-ion batteries (LIBs) by the biobleaching approach. *Chemosphere*, 282, 130944.

Vetter J., Novák P., Wagner M.R., Veit C., Möller K.C., Besenhard J.O., Winter M.,. Wohlfahrt-Mehrens M,

Vogler C., Hammouche A., (2005): Ageing mechanisms in lithium-ion batteries. *Journal of Power Sources*, 147, 269–281

K1: Simulation of Size Reduction of Iron Ore in Laboratory-scale Jaw Crusher using the Tavares Breakage Model in Rocky-DEM

Alan A. Tino[1], *Gabriel* Barrios[2] and *Luís Marcelo* Tavares[2*]

[1]Department of Metallurgical and Materials Engineering, Federal University of Rio de Janeiro, Rio de Janeiro, Brazil
[2]Universidade Federal do Oeste do Pará, Buritis, Brazil

Abstract. Although various crusher types are available, jaw crushers remain widely used in quarries and small to mid-scale plants, given their mechanical simplicity and cost. Selection of a proper primary jaw crusher to a particular application can be a challenge in the design of comminution circuits, given the impossibility of conducting tests at full scale and the limited representativity of small-scale tests. An alternative that became only recently available is the use of computer simulation using the Discrete Element Model (DEM) using suitable particle breakage models. The present work presents results of a competent low-grade iron ore from Brazil (Super Compact Itabirite) which were used to characterize particle shapes, Tavares Breakage Model parameters, besides contact parameters for DEM simulations in the software Rocky-DEM. Validation of the approach was carried out by comparing the predictions to results from crushing tests in a laboratory jaw crusher, which showed good agreement.

1 Introduction

Primary crushing refers to the initial stage of reducing large rocks into smaller pieces, typically done by mechanical means using either compression or impact. Large-scale crushing operations are generally performed by machines such as jaw crushers, gyratory crushers and roll crushers (Gupta and Yan, 2016).

Typically, the selection and scale-up of primary crushers relies in manufacturer catalogs, software and previous experience, often lacking an insightful understanding of the response of the ore to the crushing process and the effect of operating parameters on the particle flow and crushing behavior. In addition, describing the crushing phenomena with particles at full scale is a challenge using the current experimental techniques (Lindqvist and Evertsson, 2003; Naziemiec *et al.*, 2006; Li *et al.*, 2019).

Fortunately, numerical methods based on the discrete element Method (DEM) are now evolving as powerful tools to simulate primary crushers, accounting for machine geometry (Fusheng *et al.*, 2013; Guo *et al.*, 2024), crushing mechanism (Refahi and Aghazadeh Mohandesi and Rezai, 2010; Cleary and Sinnott, 2015), ore characteristics (Tavares *et al.*, 2020), and power requirements (Moncada *et al.*, 2021). However, prediction of the primary crusher performance using DEM will depend centrally on the fidelity of the particle breakage model (Tino and Tavares, 2022), on how realistically particle shapes are described (Delaney *et al.*, 2015), and how well model parameters were calibrated (Jiang *et al.*, 2023).

The present work describes the methodology of particle shape 3D modeling, material breakage characterization and DEM contact parameters calibration of an Itabirite iron ore. The DEM model parameters were validated by comparing simulations of a lab-scale jaw crusher using Rocky-DEM software to experiments.

2 Methodology

The material used in the present study was the Super Compact Itabirite iron ore, which represents the dominant ore type corresponding to the coarsest particles feeding to the primary crushing stage at the plant of interest. Coarse particles in the size range 50 to 450 mm were characterized regarding their size distribution, besides their characteristic dimensions using a digital image analysis software (Fig. 1), in which L is the length, W the width and T the thickness of the particles.

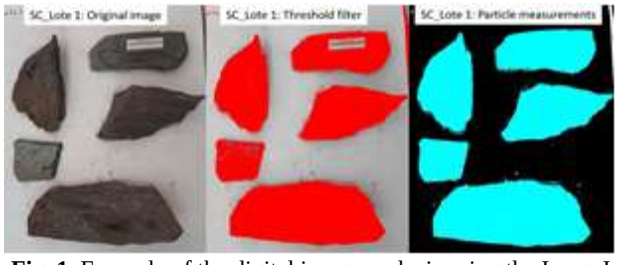

Fig. 1. Example of the digital image analysis using the ImageJ software.

Several tests were conducted to estimate the breakage parameters required for the simulation using the Tavares Breakage Model in Rocky DEM. Table 1 summarizes the tests and the corresponding particle size ranges.

* Corresponding author: tavares@ufrj.br

Table 1. Particle breakage tests used in calibrating the Tavares Breakage Model

Test	Size range (mm)
Single particle compression	212 – 75
Impact Wi	75 – 50
Drop Weight Tests	63.0 – 13.3
Repeated impact tests	45.0 – 37.5
Single particle impact ILC	19.0 – 4.75

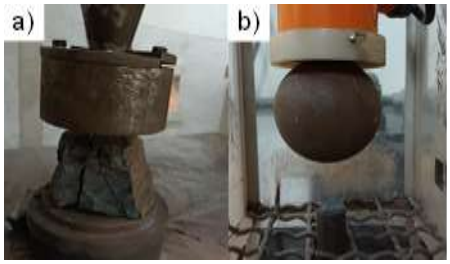

Fig. 2. Slow compression press system a), and impact load cell device b) prior to testing.

An indirect approach was used to calibrate the contact parameters, through which bulk material properties were measured and the simulation parameters are fitted until the output of the DEM simulation of the test matched the measurement results. Fig. 3 presents test results on angle of repose and particle rolling on an inclined surface.

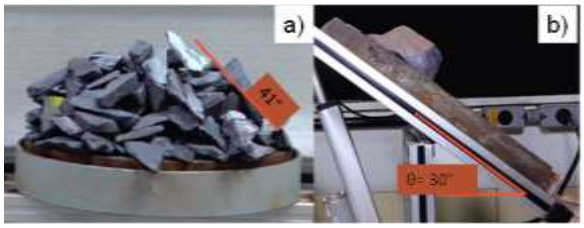

Fig. 3. The angle of repose a), and particle rolling b) DEM parameters calibration tests.

Crushing tests were carried out using a Denver laboratory scale Jaw crusher (Fig. 4). The operating parameters used in the tests are shown in Table 2.

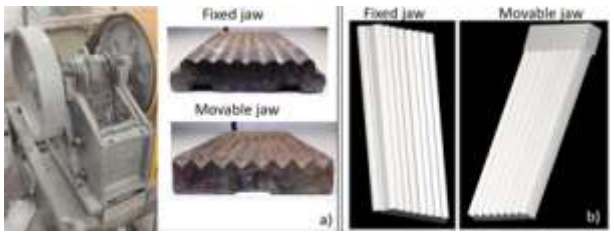

Fig. 4. Laboratory-scale jaw crusher and detail of the geometry of the fixed jaw and movable jaw (a) and CAD of the jaws (b).

Table 2. Denver laboratory-scale jaw crusher operating parameters.

Parameter	Value
Feed opening (mm)	155
Close side setting (mm)	25
Stroke (mm)	10
Frequency (Hz)	6
Feed particle range (mm)	75 - 63
Nominal motor Power (hp)	5

Power consumed by the laboratory jaw crusher during the test was measured using the DMI P100 power analyzer (ISO Telecom). Throughput was measured using a load cell coupled to and Arduino UNO board, which acquired the cumulative mass of the crushed material as a function of the test time. Product particle size distribution was measured using Tyler series sieves.

With the objective of validating the DEM contact and the breakage model parameters of the iron ore particles and assessing the capability of the simulation to predict throughput, power and product size of the laboratory jaw crusher, simulations using the Rocky DEM® software were performed, using a workstation equipped with an Intel® core i7-4590-3 GHz, 16 Gb of RAM. The contact model used to calculate normal forces was the hysteretic linear spring model, whereas the tangential forces were calculated using the linear spring Coulomb model. Breakage and contact model parameters were obtained from fitting to experiments. However, the static-dynamic friction coefficient was tuned to match the capacity measured experimentally.

3 Results

Based on the particle characteristic dimensions measured from the Itabirite particles, groups or families of shapes were proposed, and the mass percent of particles contained in each group was defined (Table 3).

Table 3. Mass percent of Super compact particles on each aspect ratio W/L and T/W families.

		W/L ratio			
		<0.5	0.5-0.7	0.7-0.9	>0.9
T/W ratio	<0.4	2%	11%	3%	0%
	0.4-0.6	8%	29%	13%	0%
	0.6-0.8	3%	21%	2%	0%
	>0.8	2%	5%	3%	0%

3D particle shape models were created using SketchUp software, resulting in a rough 3D particle in stereolithography format (STL). The 3D model was then imported to the software Mesh Lab and processed to obtain a smoothed particle. Finally, the Rocky DEM software returns a convex 3D particle shape model. Fig. 5 shows the result of the 3D modelled particles for some of the characteristic shapes defined.

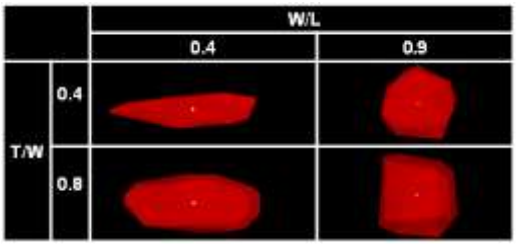

Fig. 5. Representatives of different particle shape classes for itabirite.

In Rocky DEM, the breakage model has been implemented considering a constant value of the variance of the distribution of particle fracture energies.

Fig. 6a, shows that the data approximately collapse into a single curve. This curve is characterized by the absence of an upper truncation (resulting in a selection of the ratio *Emax/E50* of 100) and by a constant variance σ^2. Fig. 6b shows the measured results of the of median particle fracture energies (E_{50}) as a function of particle size and the model fitted from the estimated values of parameters E_∞, d_o and ϕ.

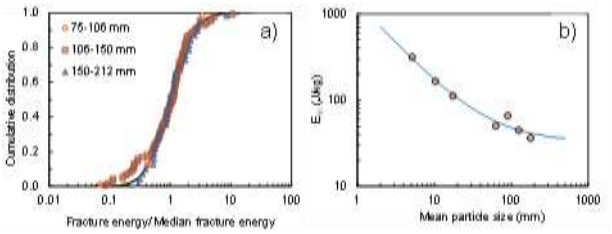

Fig. 6. Normalized particle fracture energies distribution for the slow compression tests a), E_{50} as a function of particle size for the iron ore sample b).

Fig. 7a shows the fitted distribution of particle fracture energies and results from the repeated impact tests used to estimate the parameter that controls weakening by repeated stressing events, that is, the coefficient of damage accumulation γ (Tino and Tavares, 2022). Fig.7b shows the model of the t_{10} as function of the normalized impact energy, fitting the experimental results of the Drop Weight Tester.

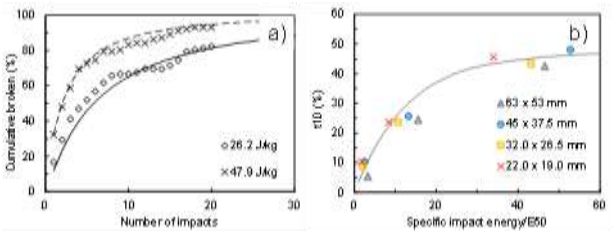

Fig. 7. Repeated impact test results and damage parameter modelling a), and t_{10} model fitting for the DWT test results b).

The complete list of DEM material properties, DEM contact parameters, and Tavares breakage model used in the simulation is presented in Table 4. Fig. 8 illustrates results from the laboratory-scale jaw crusher simulation.

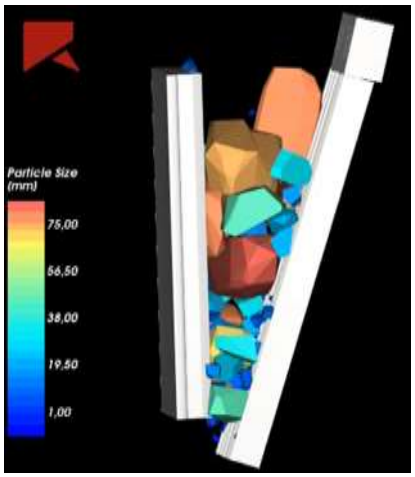

Fig. 8. Lateral view of the laboratory-scale jaw crusher simulation in Rocky DEM

Table 4. Summary of DEM material, contact and Tavares Breakage Model parameters.

DEM material properties			
	Iron ore	Steel	
Particle size (mm)	75-63 mm		
W/L and T/W aspect ratios	3D shape model		
# of corners/superquadratic °			
Density (kg/m³)	3262	7850	
Young's Modulus (GPa)	7.7	160	
DEM contact parameters			
	Steel-Particle	Particle-Particle	
Friction coeff.	0.138	0.400	
Restitution coeff.	0.300	0.300	
Tavares breakage model parameters			
σ (-)	0.552	γ (-)	4.07
Emax/E50 (-)	100	A (%)	0.470
Emin (J/kg)	1	b´ (-)	0.0768
E∞ (J/kg)	32.51	Min. absolute size (mm)	2.75 (1/25)
d0 (mm)	46.09	Min. size ratio (-)	0.2 (1/5)
Φ (-)	0.9665	Min. vol. fraction disabling	0.5

In analogy to the experimental tests, the DEM simulations show a variation in performance when the simulations are repeated. This is explained by the variability of the fracture energies of the particles simulated in DEM and the shape of particles contained in the jaw crusher feed. The predicted values of throughput, power and product size distribution, are then reported from an average of four simulations of the crusher operating for 60 seconds.

Figs. 9 and 10 compare the jaw crusher capacity and power obtained experimentally and by DEM simulation. While good agreement was observed in the case of throughput (Fig. 8), predicted values of power underestimated the measured values (Fig. 10). Fig. 11 compares the measured and predicted product size distributions, including the post processing addition of the fine fraction (<2.75 mm) that is implicit in the simulation. A good agreement of the simulations to the experimental data is observed, although simulations slightly overestimated the fineness of the measured product. This may be explained, at least partially, by the lack of control of the shapes of particles in the product during the simulation using the simulation approach.

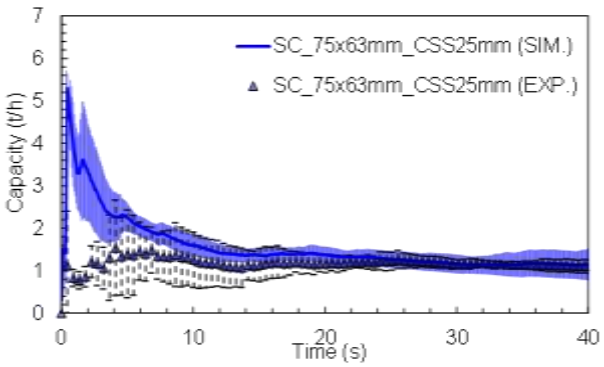

Fig. 9. Laboratory-scale jaw crusher throughput from experiments and DEM simulations (mean values and standard deviations).

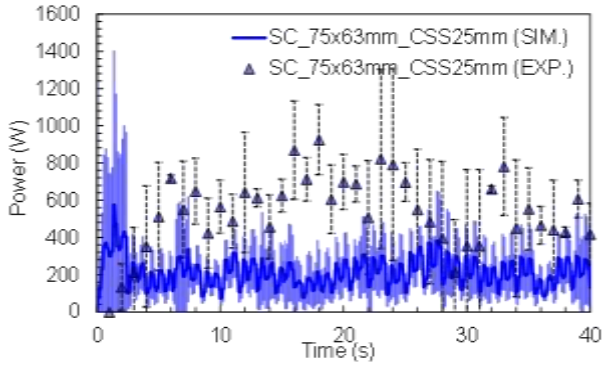

Fig. 10. Laboratory-scale jaw crusher power from experiments and DEM simulations (mean values and standard deviations).

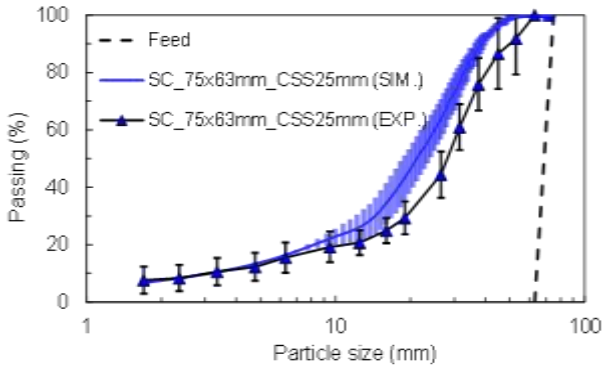

Fig. 11. Laboratory-scale jaw crusher product size distribution from experiments and DEM simulations (mean values and standard deviations).

Table 5 summarizes the experimental and simulated performance variables of the laboratory-scale Jaw crusher, showing good general agreement, with the exception of power and, as a consequence, specific energy.

Table 5. Summary of experimental and DEM performance variables of the laboratory-scale jaw crusher.

Parameter	Experimental	Simulated
Power (kW)	0.46	0.23
Crushing ratio	2.2	3.2
Product top size (mm)	53	53
Specific energy consumption (kWh/t)	0.41	0.20

4 Conclusions

Results from tests and simulations with a laboratory-scale jaw crusher, it can be stated that the simulations using Rocky DEM® provided valid predictions of product size distributions, down to fine sizes, besides throughput, within the variability already observed for the different test using the iron ore studied. However, the simulated power was underestimated when compared to the experimental data. Therefore, adequate power prediction in simulation is still a challenge that must be explored.

References

Cleary, P. W. and Sinnott, M. D. (2015) 'Simulation of particle flows and breakage in crushers using DEM: Part 1 – Compression crushers', Minerals Engineering, 74, pp. 178–197.

Delaney, G. W. et al. (2015) 'DEM modelling of non-spherical particle breakage and flow in an industrial scale cone crusher', Minerals Engineering, 74, pp. 112–122.

Fusheng, M. et al. (2013) 'Jaw crusher based on discrete element method', Applied Mechanics and Materials, 312, pp. 101–105.

Guo, J. et al. (2024) 'DEM simulation and optimization of crushing chamber shape of gyratory crusher based on Ab-t10 model', Minerals Engineering, 209, p. 108606.

Gupta, A and Yan, D. (2016) 'Chapter 4 - Jaw Crusher', in Gupta, Ashok and Yan, D. B. T.-M. P. D. and O. (Second E. (eds) Mineral Processing Design and Operations - 2nd Edition. Amsterdam: Elsevier, pp. 123–152.

Jiang, C. et al. (2023) 'Crushing characteristics and performance evaluation of iron ore in a cone crusher: A numerical study', Minerals Engineering, 204, p. 108429.

Li, Y. W. et al. (2019) 'Laboratory-scale validation of a DEM model of a toothed double-roll crusher and numerical studies', Powder Technology, 356, pp. 60–72.

Lindqvist, M. and Evertsson, C. M. (2003) 'Linear wear in jaw crushers', Minerals Engineering, 16(1), pp. 1–12.

Moncada, M. et al. (2021) 'Torque analysis of a gyratory crusher with the discrete element method', Minerals, 11(8), pp. 1–28.

Naziemiec, Z. et al. (2006) 'The influence of transverse profile of crusher jaws on comminution effects', in IMPC 2006 - Proceedings of 23rd International Mineral Processing Congress, pp. 69–74.

Refahi, A., Aghazadeh Mohandesi, J. and Rezai, B. (2010) 'Discrete element modeling for predicting breakage behavior and fracture energy of a single particle in a jaw crusher', International Journal of Mineral Processing, 94(1–2), pp. 83–91.

Tavares, L. M. et al. (2020) 'Adapting a breakage model to discrete elements using polyhedral particles', Powder Technology, 362, pp. 208–220.

Tino, A. A. De and Tavares, L. M. (2022) 'Simulating breakage tests using the discrete element method with polyhedral particles', Computational Particle Mechanics, 9(4), pp. 811–823.

K2: Challenging our understanding of rock strength with size

Malcolm Powell

Director, liner Design Services, Brisbane, Australia
Emeritus Professor, JKMRC, SMI, University of Queensland, Brisbane, Australia

Abstract. The understanding that the strength of particles increases as the size is reduced, is based on Griffiths crack theory being applied to rock breakage data. Recent data challenges the basis of the deduction that crack density decreases with the progressive elimination of the in-situ cracking. The tests apply three different modes of consistent single-particle breakage mechanism from 10 mm down to 60 µm, which provides the unexpected result that the specific energy required to produce a final desired product, expressed as size specific energy (SSE), reduces with decreasing particle size. The SSE measure provides the mineral processing measure of energy to produce a desired product size, which is the key driver in comminution energy use. The results point to particles 'weakening' with size reduction, indicated by reducing SSE, and highlight the probability that the historic data has been based on measuring the increasing inefficiency of comminution at finer sizes, rather than rock competence.

1 Introduction

It is well accepted in comminution modelling and the understanding of particle fracture that particle competence increases as size decreases. Evidence for this abounds in a number of forms, based on force to fracture in compression breakage, and on energy to progress size reduction. These measures are based on specific measures in terms of particle volume, more usually quoted in terms of particle mass. Thus, fracture force is measured as kN/g and energy as specific energy in J/g, J/kg, kWh/t (common in mineral processing).

A famous representation of this used in the mineral processing literature is the Hukki Curve, reproduced in Figure 32 (Hukki, 1961).

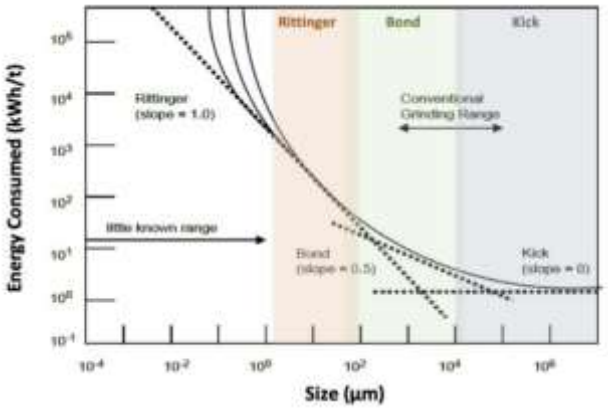

Figure 32 Hukki curve (Hukki, 1961)

This data is derived from crushing and milling tests, mainly in the laboratory, with the type of equipment changing as the particle size decreases. Principally jaw crushing followed by ball milling. However, it is not clear what milling conditions were used to derive the fine breakage data, likely small ball mills.

Data on force to fracture and mean fracture energy have been meticulously measured in single particle fracture tests, with the work of Tavares (2007) used here to illustrate this effect in Figure 33. It is clear that for a number of minerals that the specific force to fracture, kN/g, increases as particle size decreases.

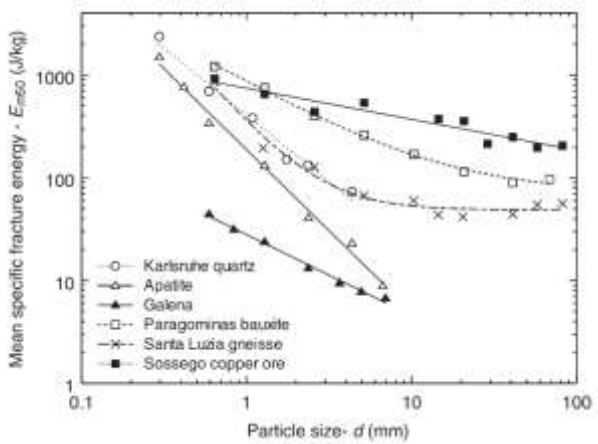

Figure 33 Force to fracture with decreasing particle size (Tavares, 2007)

The understanding that the strength of particles increases as the size is reduced, is based on Griffiths crack theory (Griffith, 1921) being applied to rock breakage data. Assuming that a bulk material has a population of pre-existing cracks, as the particle is conceptually divided into smaller pieces (breakage fragments) there is a reducing population of the cracks. The reduced crack density with decreasing fragment size leads the particle towards native material strength,

* Corresponding author: malcolm@milltraj.com

explaining the continuing increase in particle strength. Mathematically, the crack density can be back-fitted to match the experimental data, apparently proving the hypothesis. Certainly. natural rock materials have significant in-situ pre-existing macro-cracks, i.e. visible to the naked eye, and smaller ones visible under magnification. Rocks can be observed to preferentially break along these planes of weakness, and this in turn related to low energy or force required to break larger rocks.

However, at small particle sizes, below a few centimetres, the presence of minute sub-micron cracks could not be detected when these theories were developed, and remains challenging. The author was involved in work with microtomography, with the objective of tracking crack propagation around minerals during compression breakage studies. No cracks were visible in the detailed tomographic images for the sub-centimetre particles.

What is also apparent from the measures of the energy required to reduce particle size over orders of magnitude, is that the breakage method had to be changed to manage this wide size range. Being aware that every test method is a comminution device in its own right, the efficiency of the devices will vary both between devices and within a single device as the particle size changes.

2 New data

It has long been the author's desire to develop a consistent measure of particle strength across the full size range, from fist-sized rocks to the fine powder of milling products.

The basis of the bodies of work upon which this paper is based, was to progressively break particles from a parent size down to fine product with a consistent breakage method.

The term size specific energy (SSE) was coined by Powell (Powell et al, 2010), based on measures used in the industry for many years (Davis (1919), Hukki (1979), Levin (1992) but not formally defined. In essence, SSE is an approximation of required cumulative fracture energy being a function of increasing total particles surface area with progressive breakage, a fine marker size being linearly related to increasing surface area. A marker size is chosen that captures 50% to 85% of the progeny and of sufficiently fine size to be approximately linear with surface area. The chosen marker size is dependent on the desired product size, which can be specified in the SSE by placing the size as a subscript, such as SSE_{75} referring to a 75 µm marker size.

The SSE was experimentally investigated in some detail by Ballantyne, Peukert and Powell (2015). Rocks of a narrow original size class were progressively broken through kinetic impact breakage, initially with the JKRBT (Shi et al, 2009) and then at the fine sizes with the original Schönert breakage device, at the laboratories of Erlangen University. This approach ensured a consistent breakage method from 35 mm down to 200 µm.

Figure 37 shows how the SSE_{75} consistently reduced with reducing feed particle size for two different ores.

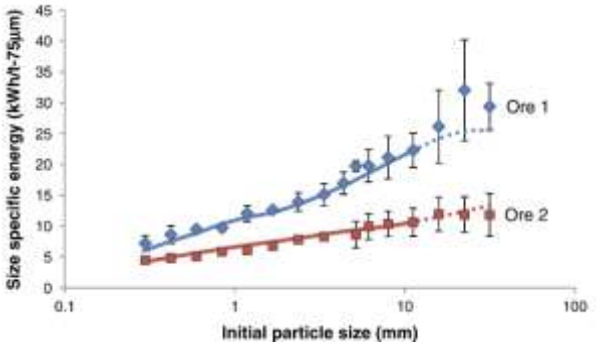

Figure 34 Decreasing SSE_{75} with particle size (Ballantyne, Peukert and Powell, 2015).

It was hypothesised by the authors that the SSE decreases with size due to the reduction ratio relative to the target size steadily reducing.

In a continuation of this work, Reja (2016) applied meticulous progressive breakage of particles in an instrumented drop-weight SILC device. He utilised dispersed monolayers of particles, sliding bars and a carefully aligned drop weight to progress single-particle impact breakage down to small size particles of 200 µm. The outcome of SSE with particle size is presented in Figure 35. The breakage was conducted for a range of four input energies, with 1.5 kWh/t providing the widest range of feed particle size and most consistent data.

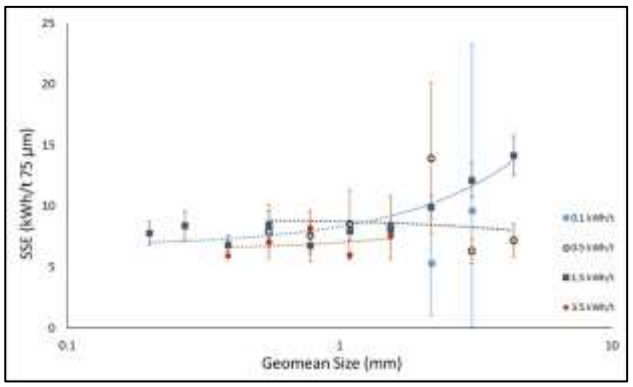

Figure 35 SSE with particle size from monolayer breakage in a drop-weight SILC test (Reja, 2016)

The results align with the prior work of Ballantyne, Peukert and Powell (2015), with the SSE decreasing with particle size.

Recent work of Ali (2024) and Ali et al (2023, 2022) utilised precision aligned rolls to break particles in a monolayer, while accurately measuring energy input with torque sensors. The particles were progressively broken with decreasing gap size, providing a breakage method of fixed reduction ratio between progressive stages, representing a maximum compression of particles for each breakage event. A key output is presented in Figure 36, for three different ore types. This shows the SSE for a range of marker sizes chosen for tracking the SSE.

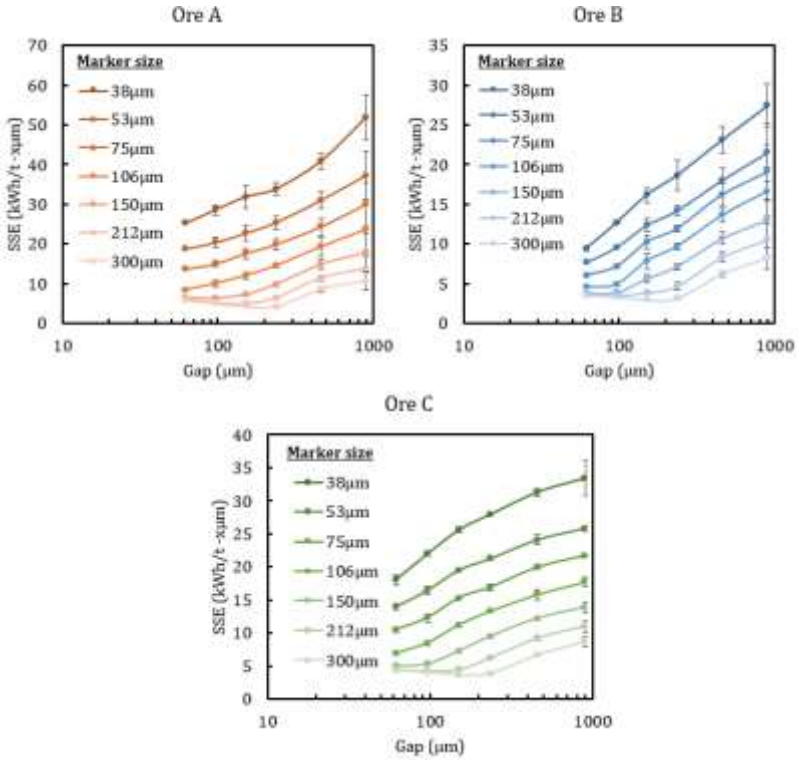

Figure 36 Reducing cumulative SSE with decreasing gap width

The breakage gap represents the maximum product particle size after that stage of breakage, the previous gap giving the top-size of feed to that gap. Maximum particle feed size thus tracks the gap setting. For marker sizes markedly larger than the breakage gap, the SSE no longer has meaning, as all the product already passes that gap, hence the coarser marker sizes show an artificial increase in SSE at low gaps. However, for valid gaps, as with the previous two sets of experimental data, the SSE steadily decreases with feed particle size.

3 Results and discussions

It has interested the author that it is accepted as unquestionable that particle strength is quoted as a measurement in terms of specific strength or competence based on particle volume. It is not clear that this is an intrinsic or fundamental basis of measure, rather being one of convenience. Unsurprisingly, the measures are derived from what can be measured, however, this does not imply a fundamental truth in these derived parameters of particle strength. We have possibly been mislead by the ease of measure rather than seeking the underlying physical relationship that represent the properties we are endeavouring to derive.

Taking a pragmatic view of the purpose of comminuting particles, the author is of the view that the reverse of common-held theory is true. The objective of comminuting particles is to produce a desired finer particle size. This size can be based on a top-size or a distribution - usually with a desired maximum particle size or a small fraction above this target maximum size.

Based on this definition, the energy required for particle breakage should be based on energy to produce this target size. The SSE is just such a measure, though not a unique manner of measuring required energy and particle competence. The SSE is established against a size that best defines the desired product size, generally seeking a value that gives 50% to 85% of the cumulative percent passing of the target progeny size distribution.

Indeed, certainly in mineral processing, the competence of an ore is measured in terms of specific energy required to produce a target size, often quoted by the P80 value. If the value is lower for a given ore, then it is clearly softer. The SSE also follows the norm, with lower SSE indicating that less grinding energy is required, and correlating to a softer rock or ore type, such as the examples in Figure 37 for production site data. The SSE is the inverse gradient of each line. Taking the SSE as a useful measure of particle strength, we would immediately relate a softer rock with a lower SSE.

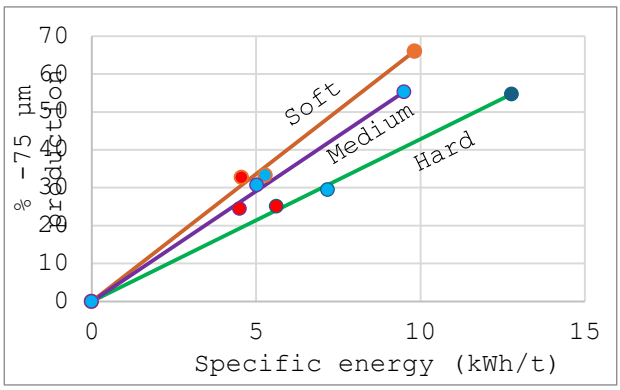

Figure 37 SSE plots for different ores

The three sets of meticulously gathered experimental data presented here provide three different breakage methods: kinetic impact, crushing in a drop-weight test,

* Corresponding author: malcolm@milltraj.com

and breakage to a fixed degree of compression. All three methods were used to progressively break a feed sample in a stage-wise manner, each using an identical mechanism over the full breakage size range. For all three, the outcome is consistent, with the SSE reducing as the feed size is reduced.

4 Conclusions

Prior data used to develop relationships between particle size and specific breakage energy relied on inefficient devices especially at the finer end of breakage. It is well-understood through measurement, that the efficiency of a ball mill drops off dramatically as the product size becomes progressively too small relative to the grinding media, leading to the introduction of finer grinding media in stirred mills. The theory of Kwade, Blecher and Schwedes (1996) defines a minimum stress intensity, that amply illustrates the interplay of the size and stiffness of grinding media and of the applied stress energy to the grinding energy in fine stirred mills. The required energy varies by orders of magnitude with changes in milling conditions for products below 10 µm.

It is asserted that each set of data underlying this work is derived from experiments that apply a consistent mode and efficiency of breakage. Furthermore, with three different modes of testing, the results, and thus conclusion is consistent.

In the work of Ballantyne, Peukert and Powell (2015), it was hypothesised that the SSE decreases with size due to the reduction ratio relative to the target size steadily reducing. This appears to be self-evidently true, as the fracture of a particle that is closer to the target final size will lead to an increasing fraction being produced at that size. But what is overlooked, is that the last few stages of fracture are producing a far greater total surface area, i.e. more fracture work is being conducted.

The irrefutable measures of a number of researchers that specific fracture force increases with decreasing particle size, is not contradictory to the deductions of this work. The simple measure of breakage force does not provide a measure of how much final product is produced. This in fact becomes the crux of the argument for decreasing particle strength, a higher specific force may be required to break the particle, but it produces a disproportionate amount of final product, resulting in a lower specific energy per unit fine product produced.

The author is not aware of any measures of decreasing crack density as particle size decreases that can detect the nano-cracks that undoubtedly exist in both in-situ rock and rock that has been progressively broken down to a fine size. This data is required to validate the assumption that the Griffiths crack theory does indeed apply to progressive particle fracture. It should be remembered that to obtain fine particles, the original large rock is progressively broken in multiple fracture events though a series of stressing events. These events induce cracking, that does not necessarily lead to fragmentation of the particle, and even when it fragments into progeny particles, these progenies are most likely to carry residual cracking and internal stress.

Reviewing the sets of carefully measured data presented in this paper, the conclusion appears to be clear:

During progressive breakage of a rock, as particle size decreases the particles become less competent.

References

Ali, S., 2024. Development of a novel ore characterisation method for the precise measurement of practical minimum comminution energy. Submitted in fulfilment of PhD, University of Queensland, February.

Ali, S., Powell, M.S., Yahyaei, M., Ballantyne, G.R. and Weatherley, D.K., 2023. Assessing comminution circuit performance using precision measurement of size specific energy. Proc. Int. autogenous and semi-autogenous grinding and high pressure grinding roll technology 2023, Sep. 25-28, Ed. Simonian et al, Published CIM.

Ali, S., Powell, M.S., Yahyaei, M., Weatherley, D.K and Ballantyne, G.R. (2022) A standardised method for the precise quantification of practical minimum comminution energy. Proc IMPC 2022: XXXI International Mineral Processing Congress, Melbourne, Australia, Australia.

22-24 Aug. Publ. Australasian Institute of Mining and Metallurgy. ISBN 978-1-922295-08-5.

Ballantyne, G.R., Peukert, W. and Powell, M.S., 2015. Size Specific Energy (SSE) – Energy Required to Generate Minus 75 Micron Material. International J. Mineral Processing vol. 139, pp. 2-6.

Bonfils, B., Ballantyne, G.R. and Powell, M.S., 2016, Developments in incremental rock breakage testing methodologies and modelling. International Journal of Mineral Processing, 10 July. Vol.152, pp.16-25.

Griffith, A. A., 1921. VI. The phenomena of rupture and flow in solids. Philosophical transactions of the royal society of London. Series A, 221(582-593), 163-198.

Hukki, R. T. 1961. Proposal for a solomnic settlement between the theories of von Rittinger, Kick and Bond. Trans. AIME, 220, 403-408.

Kwade, A., blecher, L. and Schwedes, J., 1996. Motion and stress intensity of grinding beads in a stirred media mill. Part 2: Stress intensity and its effect on comminution. Powder Technology vol. 86, pp 69-76.

Powell, M., Morrison, R., Djordjevic, N., Hilden, M., Cleary, P., Owen, P., . . . Bbosa, L., 2010. Eco-efficient liberation: outcomes and benefits, In Centre for Sustainable Resource Processing (CSRP) final report. CRC for Sustainable Resource Processing.

Reja, Y. 2016. Development of a standard methodology for energy efficiency measurement in comminution processes. Thesis submitted for the degree of Master of Philosophy at The University of Queensland.

Shi, F., Kojovic, T., Larbi-Bram, S., Manlapig, E., 2009. Development of a rapid particle breakage characterisation device – The JKRBT. Minerals Engineering 22, 602-612.

Tavares, L. M. 2007. Breakage of single particles: quasi-static. Handbook of powder technology, 12, 3-68.

K3: Breakage behavior of renewable raw materials

Patrick Walther[1], *Sebastian* Wolf[1], *Ulrich* Teipel[1,2]

[1]Faculty of Process Engineering, Technische Hochschule Nürnberg Georg Simon Ohm, Germany
[2]Faculty of Chemical Engineering, University Ulm, Germany

Abstract. Results are presented on the comminution behavior of renewable raw materials, using the example of wood. To determine the fracture behavior and fracture phenomena of these complex materials, tests were carried out on single particle comminution by impact, cutting and compression stress. Spherical beech wood particles were used as model particles. These were subjected to pressure using a test device and it was possible to determine how much force is required to cause a fracture. The results were used to calculate the mass-related comminution work. Further beech particles were tested using a shot device with impact and cutting stress and their fracture behavior was examined. A high-speed camera was used to record the trajectory of the particles and then evaluated. The mass-related impact energy of the particles was determined and, as a function of this, the probability of breakage. The particles were examined for their particulate properties using an imaging method; in particular, the particle size distribution of the different types of stress was evaluated. The experimentally determined data on the fracture probability as a function of the mass-specific comminution energy was compared with breakage probability functions from Weichert and Vogel & Peukert.

1 Introduction

Renewable raw materials have become an important commodity in the circular economy. For example, chipboard is obtained from waste wood, or it is thermally utilized as wood chips. The comminution of wood is a crucial process step in this circular economy. This is because mechanical comminution is a major energy driver. It is estimated that around 4 % of global energy requirements are used for comminution (Jeswiet and Szekeres, 2016). It is therefore of interest to keep this energy as low as possible to make the process of comminution of renewable raw materials as efficient as possible.

In the past a lot of research has been carried out to understand the mechanisms of comminution of different materials. Reichhardt and Schönert (2004) were already working on comminution using a cross piston press to comminute lime stone, quartz and corundum.

The impact comminution of brittle materials such as barite, lime stone and quartz sand was also investigated by Behrens (1965).

Breakage probability models have also been developed. These include Weichert (1988), who dealt with the stressing of glass spheres. Models were also developed by Vogel & Peukert (Vogel and Peukert, 2003), who investigated the stress and crushing of polymethyl methacrylate (PMMA), polystyrene (PS), limestone and glass.

In the field of renewable raw materials, Eisenlauer and Teipel (2021) investigated the effects of comminuting different types of wood in different types of mills. He also investigated the extent to which particle size and water content affects the single particle breakage (Eisenlauer and Teipel, 2021).

This is also where this project comes in, as single particle comminution is a method in which the breakage behavior of particles can be easily investigated without the mills having any influence on the comminution result. In particular, the aim is to investigate how the comminution of renewable raw materials by means of pressure, impact and cutting stress on the individual particle behaves.

2 Materials and methods

2.1 Experimental setup

2.1.1 Pressure stress

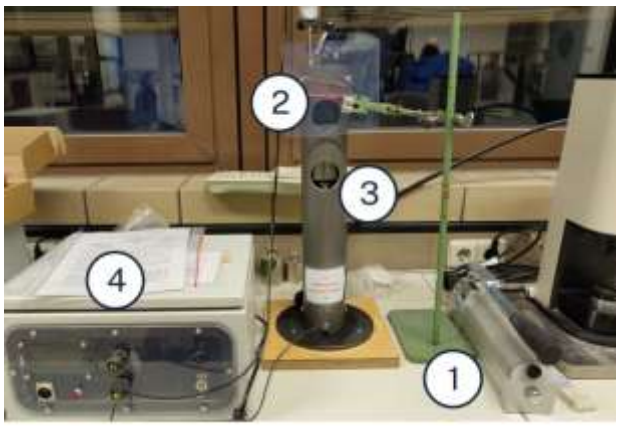

Fig. 19. Testing device for pressure stress.

Fig. 19 shows the device for the pressure stress. The pressure is increased manually using a hydraulic press

* Corresponding author: ulrich.teipel@th-nuernberg.de

(1). The particle to be stressed is placed in the sample shaft (2) of the pressure stress device (3). The data generated by the stress is recorded with a data recorder (4) and then analyzed on the computer. The device can be stress up to a force F_{max} = 25 kN. To prevent damage to the device, 80 % of this force ($F_{80\%max}$ = 20kN) was used as a safety measure.

2.1.2 Impact and cutting stress

The impact and cutting stress are applied using a shooting device, which can be seen in Fig. 20.

The testing device is based on a paintball marker in which the particle is put into the sample chamber (1). A pressurized gas cylinder with p = 200 bar is available for the shot. The particle is shot through the barrel (3) into the testing chamber (4), where it impacts against a target, which is interchangeable depending on whether impact or cutting stress is to be investigated. For all tests, it was of paramount importance that the energy did not exceed 7.5 Joule.

The trajectories from the barrel to impact on the target were recorded with the KEYENCE VW-600M high-speed camera. The analysis (5) of the particle breakages was carried out with the KEYENCE VW-9000 MotionAnalyzer software.

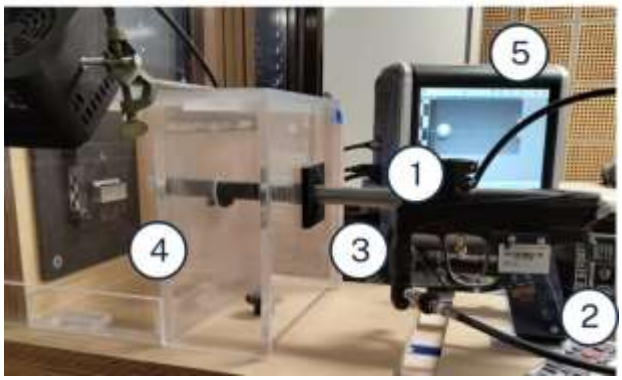

Fig. 20. Shooting device for impact and cutting stress.

2.1.3 Particle size distribution

To examine the particle size distribution after the particles have been stressed, an optical method has been applied. The Camsizer P4 (Retsch) was used as the device for determining the particle size distribution.

2.2 Material

Spherical particles of beech wood were selected as the material for testing the different types of stresses. All particles were dried at ϑ = 100 °C in a climate chamber before stressing. So that the water content was then w = 0.1 %. Particles with a diameter x = 12 mm were tested for compression stress and x = 15 mm for impact and cutting stress.

2.3 Methods

To test the particles for compressive stress, the force F exerted and the distance Δs travelled by the plunger of the pressure device were recorded every 0.25 seconds using the force transducer shown in Fig. 19.

Pressure was applied until the particle was broken or $F_{80\%max}$ was reached. The work W required to break the particle was determined as the sum product of the increments of the force F_i and the distance Δs_i. If this work is divided by the particle mass m_p, the mass-specific comminution work $W_{m,press}$ for the pressure stress is obtained, as shown in Eq. (1).

$$W_{m,press} = \frac{1}{m_p} \sum_i F_i \Delta s_i \tag{1}$$

The KEYENCE VW-600M high-speed camera was used to evaluate the speed of the particles. It was important that the frame rate was sufficiently high so that the frames could be selected in such a way that the particle hat just left the gun barrel and had not yet touched the target to be able to determine the velocity v as precisely as possible. The kinetic comminution W_{kin} could be determined via the velocity v (see Eq.(2)) and with division of the particle mass m_p, the mass-specific kinetic comminution energy $W_{m,kin}$ (Eq.(3)).

$$W_{kin} = \frac{1}{2} m_p v^2 \tag{2}$$

$$W_{m,kin} = \frac{1}{2} v^2 \tag{3}$$

The breakage probability P_B could be derived by dividing the number of all broken particles $n_{i,break}$ of a class i by the number of particles of the class n_i as shown in Eq.(4).

$$P_B = \frac{n_{i,break}}{n_i} \tag{4}$$

The models according to Weichert (1988) and from Vogel & Peukert (2003) were used to model the breakage probability functions (Eq.(5) and (6)).

In Eq.(5) c and z are material-specific model parameters. In Eq.(6) is f_{mat} the material-specific constant, x is the particle diameter, k the number of stresses and $W_{m,min}$ is the specific threshold energy required to break a particle.

$$P_B = 1 - \exp\left(-cx^2 W_{m,kin}^z\right) \tag{5}$$

$$P_B = 1 - \exp\left[-f_{mat} x k \left(W_{m,kin} - W_{m,min}\right)\right] \tag{6}$$

3 Results

3.1 Pressure stress

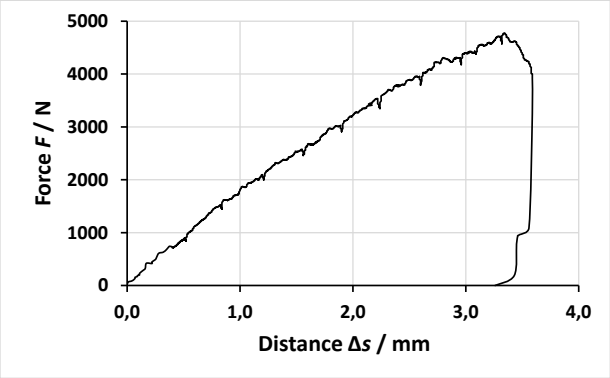

Fig. 21. Applied Force on the beech particle with x = 12 mm.

As shown in Fig. 21, the pressure stress caused the particle to break. A force peak of F_{max} = 4772 N occurred and a maximum plastic deformation of Δs_{max} = 3.6 mm. This results in a mass-specific comminution work $W_{m,press}$ = 14444 J kg^{-1}. Furthermore, it was observed that a part of the energy could be recovered by elastic deformation when the load was removed.

3.2 Visual comparison: impact vs cutting stress

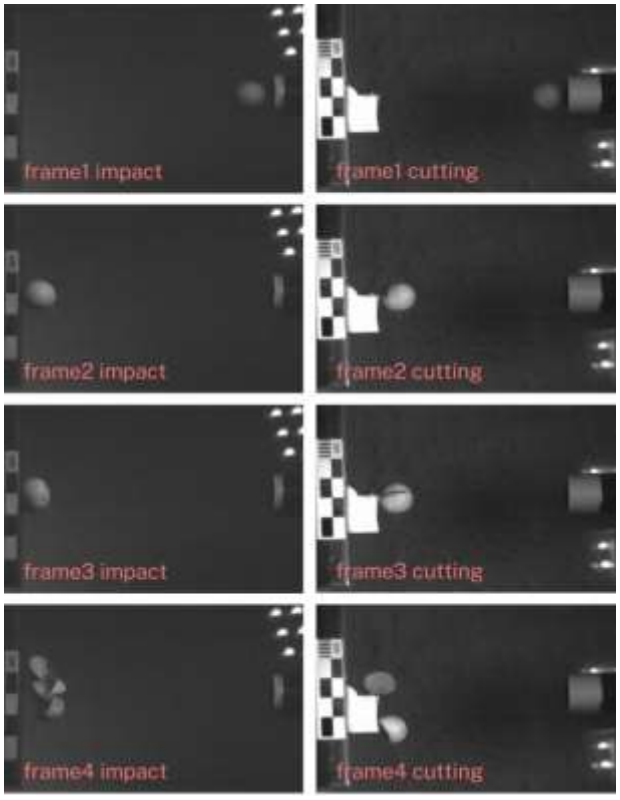

Fig. 22. Images taken from the high-speed camera (during the stressing events of the particles with x = 15 mm. Left-hand side impact stress, right-hand side cutting stress.

Four frames were extracted from the video records to visualize the trajectory from a particle during the stressing event as shown in Fig. 22 for impact and cutting stress.

The particle has just left the gun barrel in frame1. The second frame shows the particle before it hits the target. These two frames are the crucial ones for obtaining the velocity v. In this case the velocity for the impact stress was v_{imp} = 60 m s^{-1} resulting in $W_{m,kin,imp}$ = 2177 J kg^{-1} and for the cutting stress v_{cut} = 20 m s^{-1} with $W_{m,kin,cut}$ = 207 J kg^{-1}.

Frame 3 shows the particles just after the stressing event with clearly visible crack propagation. In Frame 4 the particles are comminuted, and the mother particle fell into several daughter particles.

3.3 Results impact and cutting stress

The experiments with impact stress carried out by Eisenlauer et. al. (2023) were repeated for comparisons sake and his findings could be confirmed. The model of Vogel & Peukert (2005) was consistent with the experimental data. For the spherical beech wood particles, a material factor f_{mat} = 0.038 kg J^{-1} m^{-1} was found and a threshold energy $W_{m,min}$ = 210 J kg^{-1}.

For the cutting stress it was found that the experimental data also corresponded to the model of Vogel & Peukert. The material factor for the cutting stress was f_{mat} = 0.276 kg J^{-1} m^{-1} and the threshold energy could be determined as $W_{m,min}$ = 55 J kg^{-1}.

As shown in Fig. 23 the experimental data for impact stress as well as the experimental data for cutting stress matched with the probability breakage model of Vogel & Peukert. Anyway, it is worth mentioning, that the Mass-specific energy $W_{m,kin}$ to reach a certain breakage probability P_B comparing impact and cutting stress differs considerably. To reach a breakage probability of P_B = 0.57 a mass-specific energy $W_{m,kin}$ = 264 J kg^{-1} is needed for cutting stress. To get a similar P_B = 0.60 for impact stress it would take a $W_{m,kin}$ = 1676 J kg^{-1}. The ladder is almost six times higher than for the cutting stress.

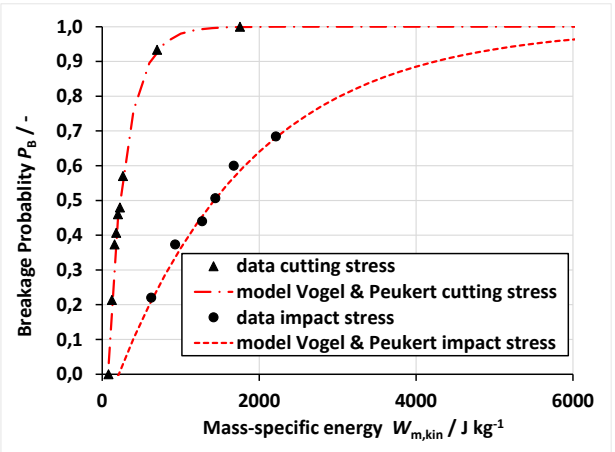

Fig. 23. Breakage Probability vs Mass-specific energy for impact stress and cutting stress and modelling the breakage probability model Vogel & Peukert with x = 15 mm.

3.4 Particle-size distribution

Fig. 24 shows that the particle-size distribution of both, the cutting and the impact events do have similar progression. However, it can be stated that the particle-size gets smaller and particle-size distribution of the cutting stress has a wider range than the impact stress one.

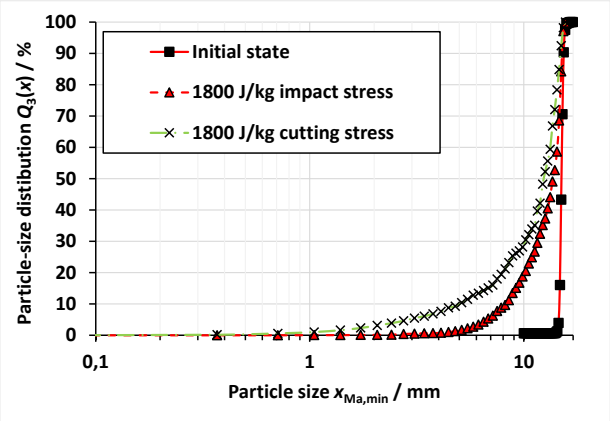

Fig. 24. Particle-size distribution for impact stress and cutting stress applied with the same mass-specific energy $W_{m,kin}$ = 1800 J kg^{-1} and an initial diameter x = 15 mm.

4 Discussion and conclusion

This work investigated the comminution of beech wood particles using different types of single particle loading. The pressure stress required the greatest mass-specific comminution energy. However, the results must be seen in the context that the operation of the apparatus can lead to fluctuations in the results.

The results of the impact comminution could be confirmed, and the Vogel & Peukert model could also be applied as a breakage probability model with good agreement. If pressure is compared with impact stress, it can be determined that a minimum mass-related energy $W_{m,break}$ = 1046 J kg^{-1} is required to induce a fracture. In the case of impact stress, on the other hand, the limit energy is significantly lower at $W_{m,min}$ = 210 J kg^{-1}.

The lowest limit energy of the three types of stress is the cutting stress with $W_{m,min}$ = 55 J kg^{-1}. It has been experimentally proven that the cutting stress consumes the least energy for the comminution of spherical beech wood particles.

List of symbols

F_{max}	Maximal appliable Force
ϑ	Temperature
w	Water content
x	Particle diameter
Δs	Distance of the pressure
m_p	Particle mass
$W_{m,press}$	Mass-specific work
v	Velocity
$W_{m,kin}$	Mass-specific energy
P_B	Breakage probability
$n_{i,break}$	Broken particles per class i
n_i	Total particles in class i
c	Material-specific model parameter
z	Material-specific model parameter
f_{mat}	Material-specific constant
k	Number of impacts
$W_{m,min}$	Threshold energy

References

Behrens, D., 1965. Prallzerkleinerung von Glas-Kugeln und unregelmäßig geformten Teilchen aus Schwerspat, Kalkstein und Quarzsand. *Chemie Ingenieur Technik*. 37, 473–483. https://doi.org/10.1002/cite.330370503

Eisenlauer, M., Steinhauer, D., Klotz, A., Jost-Kovács, A., Wolf, S., Teipel, U., 2023. Comminution of Wood:Single-Particle Breakage. *Chemical Engineering & Technology* 46, 1494–1501. https://doi.org/10.1002/ceat.202200310

Eisenlauer, M., Teipel, U., 2021. Comminution energy and particulate properties of cutting and hammer-milled beech, oak, and spruce wood. *Powder Technology* 394, 685–704. https://doi.org/10.1016/j.powtec.2021.03.072

Jeswiet, J., Szekeres, A., 2016. Energy Consumption in Mining Comminution. *Procedia CIRP* 48, 140–145. https://doi.org/10.1016/j.procir.2016.03.250

Reichardt, Y., Schönert, K., 2004. Cross piston press for high pressure comminution of fine brittle materials. *International Journal of Mineral Processing* 74, S249–S254. https://doi.org/10.1016/j.minpro.2004.07.015

Vogel, L., Peukert, W., 2005. From single particle impact behaviour to modelling of impact mills. *Chemical Engineering Science* 60, 5164–5176. https://doi.org/10.1016/j.ces.2005.03.064

Vogel, L., Peukert, W., 2003. Breakage behaviour of different materials—construction of a mastercurve for the breakage probability. *Powder Technology* 129, 101–110. https://doi.org/10.1016/S0032-5910(02)00217-6

Weichert, R., 1988. Correlation between probability of breakage and fragment size distribution of mineral particles. *International Journal of Mineral Processing*. 22, 1–8. https://doi.org/10.1016/0301-7516(88)90052-X

L1: Comparative investigation of eggshell's particle size distribution as foaming agent for manufacturing glass foam

Ildikó Fóris[1*], *Thomas* Mütze[2], *Miia* John[3], and *Gábor* Mucsi[1]

[1]Faculty of Earth and Environmental Sciences and Engineering, University of Miskolc, HU
[2]BASF Schwarzheide GmbH, Germany
[3]LUT School of Engineering Science, LUT University, Finland

Abstract. A wide range of waste types has been used as secondary raw materials to produce environmentally friendly building materials. One type is glass foam which is a thermal insulation material. To produce glass foams, glass powder is mixed with a foaming agent and treated at temperatures higher than 600 °C to inflict gas formation. One step during raw material preparation is the grinding of the raw materials to the optimum size range. One type of foaming agent can be eggshell. Due to its plate-like structure, the definition of its relevant size parameters is challenging. In this work, a comparison of two different analyzers is shown, namely laser diffraction (LD) and dynamic image analysis (DIA).

1 Introduction

Due to urbanization, the consumption of non-renewable raw materials is continuously rising causing huge environmental problems if disposed improperly. (Cheng et al., 2016, Liu et al., 2019, Shelby, 2017). Waste treatment can improve the sustainable development of mankind.

Glass foams are environmentally friendly materials made from secondary raw materials (Fóris and Mucsi.,2023, Scarinci et al., 2005, Souza et al. 2017, Assefi et al., 2021, Cengizler et al., 2021). They can be used as aggregate, heat insulation, or filler because of their many positive features like being lightweight, highly porous, chemically neutral, non-flammable, and frost resistant. With relatively low thermal conductivity, glass foams effectively prevent heat transfer (Goltsman and Yatsenko, 2023). Those foams are opening new opportunities for using waste materials such as glass and eggshell powder to make a high-value product that easily fits into the circular economy concept. A key disadvantage of glass foams is the production cost which is attributed to high raw material expenses (using SiC as a foaming agent) and energy-intensive processes like milling and thermal treatment.

To produce glass foams, foaming agents are necessary to create pores. The foaming agents release gas in the molten glass during decomposition. Carbonates are cost-effective types of foaming agents (Vaddi and Padmanabhan, 2023). One example of this is eggshell (Fóris and Mucsi, 2023) due to its high calcium carbonate content. Eggshells are one of the most abundant food wastes through everyday egg consumption. Annually 50.000 tonnes of ES waste generates approximately (Das et al., 2022). Eggshells main constituent is calcium carbonate (94-96 %) or more specifically calcite in crystalline form (Baláž, 2018). It is suitable for forming a porous structure in glass foams because CO_2 is generated during the thermal decomposition of calcium carbonate at high temperatures (Souza et al., 2017, Ibrahim et al., 2022).

One of the most important steps during glass foam production is the grinding of the raw materials to the optimum size. Overall, it can be said that the raw materials must be ground generally below 100 µm to be suitable for the foaming process (Guo et al., 2013, Xia et al., Bueno et al., 2020). The particle size of the foaming agent influences the pore size and the foaming behavior. If the particle size of the foaming agent falls in the same size range, the structure of the finished glass foams is most homogeneous, so it is necessary to grind it below 100 µm also (Spence and Kultermann, 2016).

The main difficulty of eggshells is that the shape of the particles is plate-like, so it is challenging to determine the particle size distribution. The objective of the study was to investigate how the grinding affects the particle size distribution and shape parameters of eggshells with two different methods, namely laser diffraction and dynamic image analysis.

2 Materials and methods

The raw material for the experimental procedure was chicken eggshell waste, which was grounded in a ball mill with different grinding times (1 to 60 min). The general description of the chicken eggshell can be seen in Figure 2. The grinding media were 10 mm and 20 mm stainless steel balls. The eggshell sample material is called here ES.

Before milling, ES waste was heat treated in boiling water for 30 minutes to remove the organic content, then dried at 105 °C for 2 hours until mass consistency. Before milling, the ES was kept in a desiccator at room temperature (25°C).

* Corresponding author: ildiko.foris@uni-miskolc.hu

The eggshell's thickness was measured with a digital gauge. The average thickness was 401 +/- 28.29 µm.

Fig. 1. ES powder after 60 minutes grinding

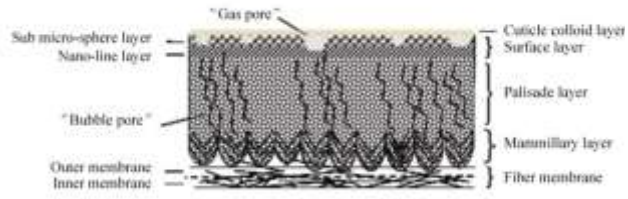

Fig. 2. Description of ES (chicken ES) (Zhou et al, 2011)

2.1 Methods for raw material characterization

The chemical compositions of eggshells were measured by a Rigaku Supermini 200-type wave-length X-ray fluorescence spectroscope (XRF). The loss of ignition (LOI) was measured at 950 °C with 90 min heating time, and 60 min holding time in a static furnace. The XRF and LOI experiments were carried out from the original sample (before ES was heat-treated in boiling water). Table 1 shows the results of XRF and LOI measurements. Calcium oxide can be found in the highest amount in ES which can help to form the porous structure of the glass foams. The loss of ignition was relatively high due to the organic content.

Table 1. Chemical composition and loss of ignition of ES

	$(^{m}/_{m}\%)$
SiO_2	0.3
Al_2O_3	0
MgO	0.62
CaO	54.4
Na_2O	0.13
K_2O	0.13
Fe_2O_3	0.03
MnO	0.001
TiO_2	0.002
P_2O_5	0.499
S	0.21
F	<0.3
LOI	45.71

2.2 Methods for ES powder characterization

The ground powders were analyzed with two different methods. For the first method LD, a Horiba LA-950 V2 laser diffraction particle size analyzer was used in wet conditions using distilled water as dispersing media applying the Fraunhofer theory. For the second method DIA, Retsch Camsizer XT dynamic image analyzer was used in dry conditions. To evaluate the influence of milling on the shape properties, the parameter sphericity (surface rounding of grains) SPHT was selected (Equation 1).

$$\text{SPHT} = 4\,\pi\,(\text{particle area}) / (\text{particle perimeter})^2 \quad (1)$$

For the sphericity, the mean value, and the confidence interval of a 95 % level of confidence were calculated (Equation 2-4).

$$\alpha_{bottom} = \bar{X} - t_{0,95} * \frac{S_n^*}{\sqrt{n}} \quad (2)$$

$$\alpha_{\text{top}} = \bar{X} + t_{0,95} * \frac{S_n^*}{\sqrt{n}} \quad (3)$$

$$\alpha_{top} - \alpha_{bottom} \quad (4)$$

where, $\bar{x}$= mean value, $t_{0.95}$= t-distribution table 95 % level of confidence, S_n^*= standard deviation and n= number of values.

3 Results

Particle size distributions are provided in Figures 3 and 4 in volume distribution (Q_3) with the two different devices (Horiba LA-950 V2 and Retsch Camsizer X2).

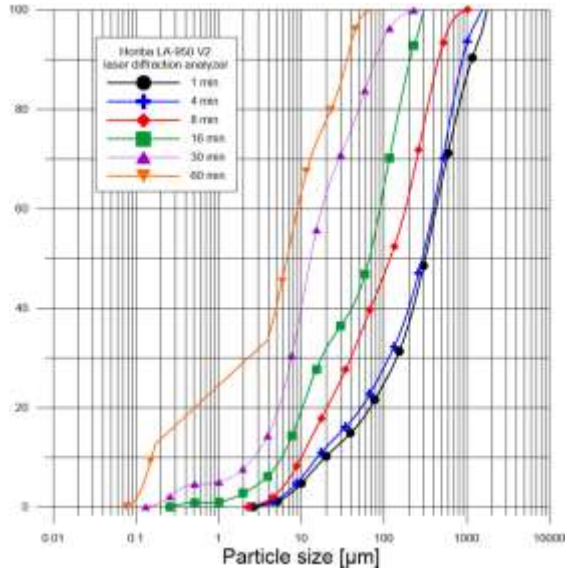

Fig. 3. Particle size distribution with Horiba LA-950 V2 laser diffraction analyzer at different grinding times

In Figure 3 the LD results showed no major size reduction at 1 and 4 min of grinding. At 8 minutes, the particle size starts to decrease significantly. After 30 minutes the < 100 µm range is reached continuing the

size reduction further on to 60 minutes. The product of 60 minutes of grinding can be seen in Figure 1.

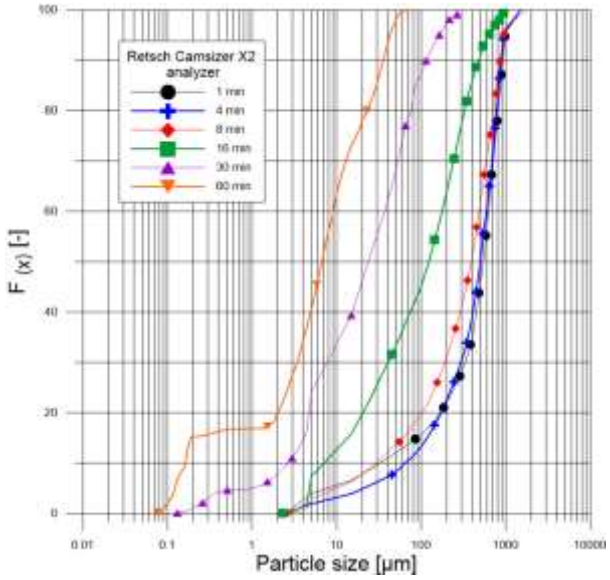

Fig. 4. Particle size distribution with Retsch Camsizer X2 dynamic image analyzer at different grinding times

At 1-8 minutes of grinding no significant size reduction can be observed in the case of DIA method (Figure 4). The major breaking point in particle size can be after 16 minutes of grinding. From that point, the particle size decreased respectively and the < 100 µm range reached at 30 minutes, too. Compared to the two methods, the major size reduction occurred from 16 minutes of grinding. With the increasing grinding time the particle size reduces respectively, this trend can be seen in the case of both methods. However minor oscillations can be seen between the methods during lower grinding time.

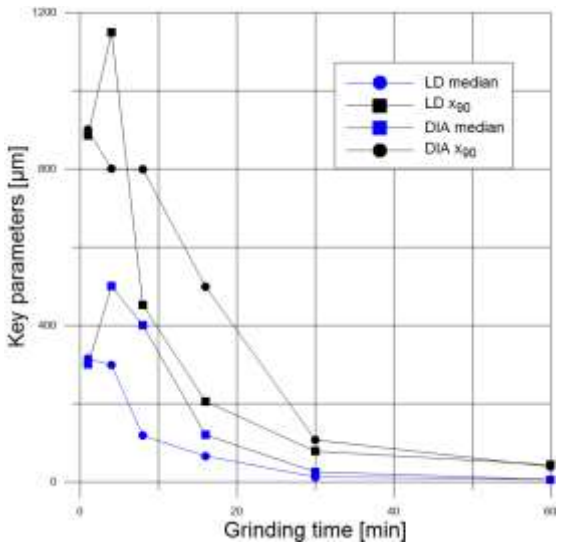

Fig.5. Key parameters measured by Camsizer (DIA) and Horiba LA-950 V2 laser diffraction analyzer (LD)

In Figure 5 it can be noticed that the key parameter values (median and x_{90}) decrease in proportion to the grinding time. An increase from 1 to 4 minutes of grinding can be observed in x_{90} parameter which can be an artefact due to particle shape. At 30 and 60 minutes of grinding LD and DIA showed almost the same results. However, during lower grinding times more significant differences occurred between the measured values except in the 1-minute grinding which was similar in both methods. At 16 minutes when the particles started to break and the compaction began, the difference between the two methods decreased.

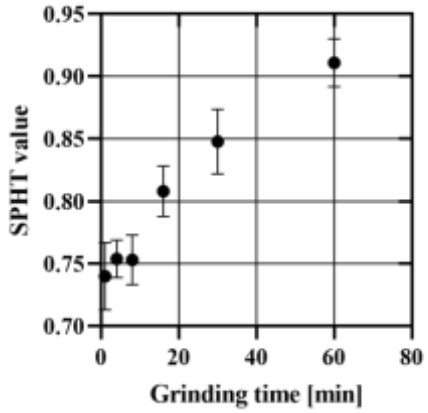

Fig. 6. Sphericity results measured by Camsizer analyzer at different grinding times

In Figure 6 the SPHT values showed that the sphericity of the particles increases with the grinding time. With increasing grinding time, the compactness of the particles increases due to a loss of the plate-like structure of ES. It can be seen that the SPHT increases gradually with the grinding time. No significant change in sphericity was observed below 8 minutes, similar to the particle size distribution measured by DIA. It can be concluded that compared to the 1-minute grinding, the sphericity rate increased significantly at the 60-minute grinding.

This tendency correlates to the two different methods. Laser diffraction makes the convenient assumption that every particle is a sphere so where the SPHT values are close to 1 the LD and DIA methods show similar results. This means that the 30 and 60 minutes of grinding are alike. However, for shorter grinding times there are significant differences in the results. It can be seen that the particles keep their size and shape at the beginning of the grinding until 8 minutes. Only after 16 minutes of grinding do they start to break, being reduced in size. Also, they lose their plate-like shape at the same time it can be seen from the sphericity results a major increase occurs towards value 1.

4 Conclusion

During the experiments systematic grinding tests were carried out and particle size distribution and particle shape distribution were investigated. The following conclusions were observed from the measurements:

- The breakage of the particles occurs at 16 minutes, before that the size and shape parameters does not change a lot in the earlier stage of grinding (1-8 minutes).
- As the grinding time increases, a gradual decrease in particle size can be seen, with an optimal size range of 100 μm being achieved after 30 minutes of grinding.
- With the increasing grinding time the particle size decreases and the particles' sphericity value increases because of more compact particles.
- With shorter grinding times, the two results are not correlated, which is due to the plate-like shape and thickness of the particles, as more energy is invested and longer grinding times are needed to break the particles.
- The two methods used to evaluate particle size distribution show similar results according to the sphericity values at the 60-minute grinding period.
- Due to the plate-like nature of eggshells the particle's behavior during grinding can be observed in more detail with SEM (scanning electron microscope) method.
- Due to the plate-like nature of eggshells at shorter grinding times DIA method is suggested to investigate particle size distribution, but at longer grinding times (60 minutes of grinding) LD analyses can give reliable results because the particles become more compact and spherical the effect of grinding.

This project is funded by the European Union's Horizon Europe program under grant no. 101079354.

References

Assefi, M., Maroufi, S., Mansuri, I. and Sahajwalla, V. (2021) High strength glass foams recycled from LCD waste screens for insulation application. *Journal of Cleaner Production*, 280, 124311-124320.

Baláž, M. (2018) Ball milling of eggshell waste as a green and sustainable approach: A review. *Advances in Colloid and Interface Science*, 256, 256-275.

Bueno, E. T., Paris, J. M., Clavier, K. A., Spreadbury, C., Ferraro, C. C. and Townsend, T. G. (2020) A review of ground waste glass as a supplementary cementitious material: A focus on alkali-silica reaction. *Journal of Cleaner Production*, 257, 120180.

Cengizler, H., Koç, M. and Şan, O. (2021) Production of ceramic glass foam of low thermal conductivity by a simple method entirely from fly ash. *Ceramics International*, 47, 28460-28470.

Cheng, J.H., Dai, S. and Ye, X.Y. (2016) Spatiotemporal heterogeneity of industrial pollution in China. *China Economic Review.*, 40, 179-191.

Da Costa, F. P., Da Silva Morais, C. R., and Rodrigues, A. M. (2020) Sustainable glass-ceramic foams manufactured from waste glass bottles and bentonite. *Ceramics International*, 46, 17957-17961.

Liu, T., Zhang, J., Wu, J., Liu, J., Li, C., Ning, T., Lou, Z., Zhou, X., Yang, Q. and Lu, A. (2019) The utilization of electrical insulators waste and red mud for fabrication of partially vitrified ceramic materials with high porosity and high strength. *Journal of Cleaner Production*, 223, 790-800.

Shelby, J. E. (2017) Introduction to Glass Science and Technology. *Royal Society of Chemistry*, 1-3.

Scarinci, G., Brusatin, G., and Bernardo, E. (2005) Glass foams**,** In Scheffler, M., Colombo, P. (eds.): Cellular Ceramics: Structure, Manufacturing, Properties and Applications. Wiley-VCH, Weinheim, 158-176.

Souza, M. T., Maia, B. G. O., Teixeira, L. B., de Oliveira, K. G., Teixeira, A. H. B. and Novaes de Oliveira, A. P. (2017) Glass foams produced from glass bottles and eggshell wastes. *Process Safety and Environmental Protection*, 111, 60-64.

Vaddi Thulasikanth and R. Padmanabhan (2023) Fabrication of sustainable closed-cell aluminium foams using recycled fly ash and eggshell powder. *Materialstoday Communications*, 37, 107302

J. Zhou, S. Wang, F. Nie, L. Feng, G. Zhu, L. Jiang (2011) Elaborate architecture of the hierarchical hen's eggshell, *Nano Res.* 4, 171-179

Fóris, I., Mucsi, G. (2023) Glass foam experiment with eggshell as a foaming agent and red mud as additive material. *Journal of Silicate Based and Composite Materials*, 75, 132-135.

Fóris, I., Mucsi, G. (2023) Influence of raw material properties on waste-based glass foam. Mining Geological Petroleum Engineering Bulletin, 38, 75-83.

Das, S., Mohanty, P. K., Mallik, B. K. (2022) Agricultural and pharmaceutical applications of eggshells: a comprehensive review of eggshell waste value-added products. *Journal of Pharmaceutical Negative Results*, 13, 3979-3784.

Spence, W. P. and Kultermann, E. (2016) Construction Materials, Methods and Techniques. *Cengage Learning*, 510-526.

L2: Mechanical preparation of end of life car light-emitting diodes (LED) front lights

Sándor Nagy[1], M. Dojcsák[1], S. Butylina[2] and M. Sethurajan[2]*

[1]Faculty of Earth and Environmental Sciences and Engineering, University of Miskolc, HU
[2]Department of Separation Science, LUT School of Engineering Sciences, LUT University, 53810 Lappeenranta, Finland

Abstract. Number of cars commonly estimated in the EU member states is 400-700 vehicle per 1000 inhabitants. Electronic units applied in cars include computers printed circuit boards (PCB), light crystal displays (LCD), light-emitting diodes (LED), and sensors. Nowadays large percentage of the new cars are available only equipped with LED lights. The End of Life (EoL) car lights are generated as a result of accident or at the end service time of car. The EoL car lights contain valuable materials, however, as a rule they occur in small concentrations. Structure of EoL car lights and the chemical composition were determined in this study. Also the mechanical processing possibilities were investigated in the case of this lights.

1 Introduction

The number of cars on the roads as well as the amount of waste materials generated at the end of their lifetime is constantly increasing. Distribution of motorisation rate in between EU member states is shown in Figure 1. On the average, the European Union counts 567 passenger cars per 1,000 inhabitants, and some 83 commercial vehicles and buses (ACEA, 2023).

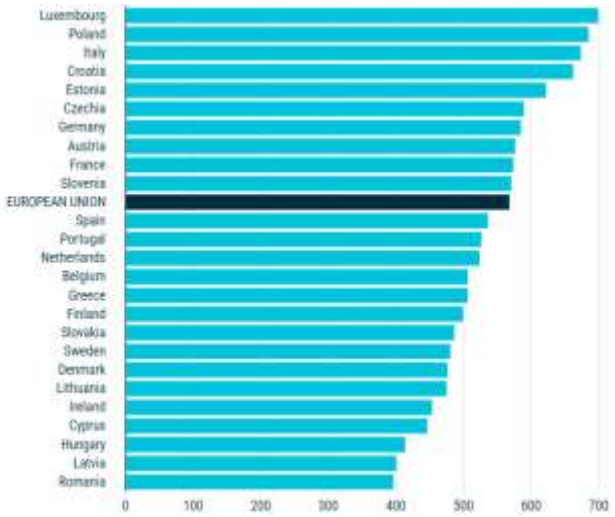

Fig. 1. Motorisation rates in the EU (ACEA, 2023)

The number of electronic parts in the cars and vehicles is increasing; modern cars and vehicles contains more "new" electronic parts. These electronic parts include sensors, computers, printed circuit boards (PCB), liquid crystal displays (LCD) (with light-emitting diodes (LED) backlight), LED lights, and Lithium ion batteries (LiB) (Dojcsák, 2022; Mazurek, 2022). If to count the ratio of vehicles equipped with LED front and taillights to the total number of vehicles, it will show the stable growth. Advantage of LED lights are their high light power at lower power consumption. However, their structure is much more complicated (containing WEEE-type parts), that makes them much more expensive (Thiago, 2020; Rahman, 2021).

The electronic parts contain valuable metals and materials, belonging to the class of critical materials (Fig. 2.), although their concentrations are small (Nagy, 2017, Illés, 2021).

Figure 2. EU Critical Raw Materials (Grohol and Veeh, 2023)

The EoL or waste streams are generated by different ways: production waste, failure component or road accident during the lifetime of the vehicle or end of life of the car. Standard processing of EoL cars by means of shredder technology does not focus on the separated processing of the "new" parts and so on the recovery of valuable materials from them. The possible solutions could be a removal of these parts before the shredding, or an investigation of by products (e.g.: shredder light residues) for content of the valuable materials. The removal of these parts by hand demand large human work.

The primary aim of our research is to determinate the structure and composition of full LED front lights, and to investigate the possible mechanical treatment methods.

* Corresponding author: sandor.nagy@uni-miskolc.hu

2 Materials and Methods

2.1 Materials

The experiments were carried out on full LED front lights originated from vehicles, named "A" and "B" car producer. The industrial waste management partner was Auto Mandy Car Ltd., Budapest (Hungary).

Fig. 3. A) Front light „A", and B) „B"

The mass of "A" light was 4.9 kg, and of "B" 10.8 kg.

2.2 Methods

Front light "A" was manually dismantled using first angle grinder for the opening of the covering, after that screwdriver was applied to dismantle the main parts. Front light "B" was crushed in a RT 60/35 type impact shredder (at the site of NHSZ Miskolc Ltd.) having the 600×350 mm rotor, max rev. number of 960/min, electric power of 30 kW. An AGH 40/20 hammer shredder with 20 m/s rotor speed was applied for the second and third steps of comminution.
X-ray fluorescence, XRF, (Olympus Vanta) was used to analyse metals, and Fourier transform infrared spectrometer, FT/IR-4200type A (JASCO) was used for analysis of plastic parts. Zeiss AXIO Imager.M2m optical microscope was used to show the LEDs.

3.1. The manual dismantling of "A" front light

3.2.1. Results of manual dismantling of front light

After opening the cover and dismantling the parts (Fig. 4), the masses of different components were measured and presented in Table 1.

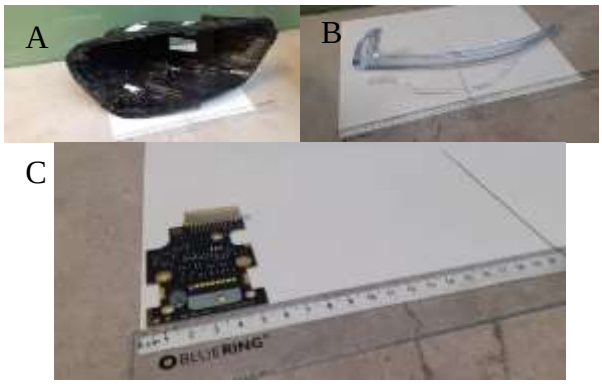

Fig. 4. Parts after dismantling (examples): back cover (A), optical plastic parts (B), and PCB with LEDs (C)

Table 1. Front light "A" composition (main parts)

Main part	**Mass [g]**	**Ratio [%]**
Optical parts	*350.03*	*7.16*
Glass	*381.53*	*7.81*
Cooling system parts (metal)	*817.46*	*16.73*
Screws	*113.16*	*2.31*
PCB	*85.85*	*1.75*
Plastic parts	*2477.88*	*50.71*
Al cooling plates	*12.70*	*0.26*
Plastic connectors	*60.00*	*1.23*
Plastic from cables	*20.39*	*0.41*
Cu from cable	*63.72*	*1.30*
Front covering (PC)	*504.00*	*10.33*
Sum	***4886.72***	***100.00***

Results show that more than 50 % of the front light is plastic, and the printed circuit boards (PCBs) are less than 2 %.

3.1.2. LEDs in front light "A"

The LEDs (Fig. 5) were removed from front light "A" by mechanical methods. Detailed analysis of LEDs is demonstrated in Table 2. For the future experiments, the removal of LEDs by heat could be a good solution.

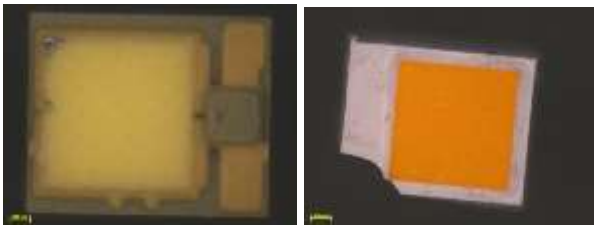

Fig. 5. Images of LED for main-beam headlight and LED for direction indicator obtained with optical microscopy (Zeiss AXIO)

Table 2. LEDs in front light "A"

LED type	Mass of one LED [mg]	Number of LEDs on PCB	Sum mass [mg]
Main-beam (a)	10	9	90
Main-beam (b)	10	9	90
Daytime running lamp and direction indicator	5	13	65
Dipped-beam (a)	20	4	80
Dipped-beam (b)	10	6	60
Curnering lamp	6	2	12
Sum		**43**	**397**

According to the results shown in Table 2, the number of LEDs was high (43 pieces), but their masses were extreme low (between 5 and 20 mg), meaning the mass of the LEDs in one front light ("A") is less than 0.4 g.

3.2. Comminution of "B" front light

3.2.2. Results of mechanical processing

Mechanical processing was carried out on front light "B". The first stage of the process was to open the front light cover by an impact crusher. It was realised, that this equipment was able to open the cover, and liberate the main parts. The particles produced by impact crusher are shown in Fig. 6 and Table 3 demonstrates their size distribution.

Fig. 6. 40-56 mm and 8-16 mm size fractions (mainly plastic)

Table 3. Particle size distribution after impact crusher

Particle size [mm]	m_i [g]	Δm_i [-]	F(x) [%]
125-200	4272.91	47.06	100.00
90-125	166.27	1.83	52.94
63-90	836.03	9.21	51.11
56-63	59.05	0.65	41.90
40-56	837.22	9.22	41.25
31.5-40	417.35	4.59	32.03
22.4-31.5	777.58	8.56	27.44
16-22.4	630.68	6.95	18.88
8-16	690.26	7.60	11.93
4-8	229.68	2.53	4.33
2-4	41.05	0.45	1.80
<2	122.78	1.35	1.35

Larger fraction (47.06%) belongs to the 125-200 mm size fraction. The LEDs components were present in main parts, which are consisting of the >63 mm fraction. Plastics (PP, PC, PE, etc.) are mainly seen in the 40-56 mm fraction size and 8-16 mm fraction size (Figure 6.).

3.2.3. Liberation of LEDs

Larger parts (Fig. 7) produced by the impact crusher required further size decreasing (liberation of LEDs).

Fig. 7. Larger parts used for further liberation

One of such larger parts was manually disassembled, to see its structure (Fig. 8A). Alternatively, the hammer shredder was used without screen; the product of mechanical processing can be seen on Fig. 8B. In this case, the LEDs were not destroyed.

It was found that the LEDs were partially removed from PCBs, and so they went to the fine fraction (it means they were lost) in the case when the 30 mm screen was used in hammer shredder.

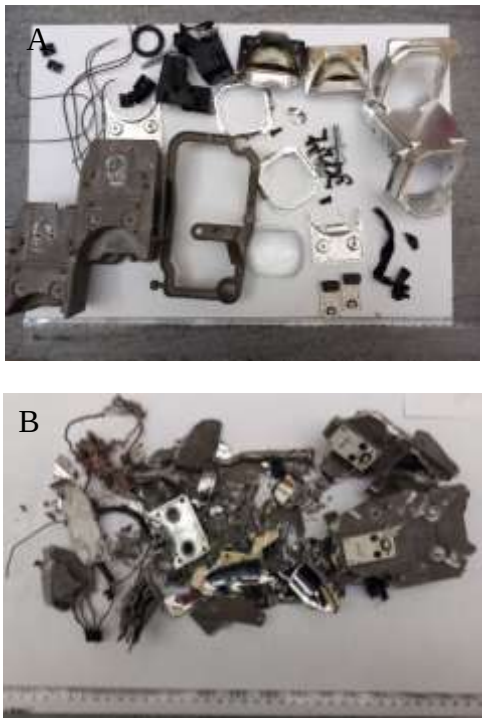

Fig. 8. Manually disasembled part (A) and product of hammer shredder (without screen) (B)

Table 4 shows the number and mass of LEDs determined in the front light "B". Although, it is worth to note that not all of LEDs were removed, because some of them were strongly mounted on or in the surface. Large part of LEDs was easy to remove by a heat gun (600 °C, 30 s).

Table 4. LEDs in front light "B"

LED type	Mass of one LED [mg]	Number of LEDs on PCB	Sum mass [mg]
SK3_DRL_LAM	10.0	16	160.0
SK3_EV_LOW	-	16	-
SK3_SUB_LOW_LAM	-	12	-
Direction light LED	10.0	4	40.0
Sum		**48**	**200.0***

** without the mass of SK3_EV_LOW and SK3_SUB_LOW_LAM*

4 Conclusion

The LED vehicle lights contain WEEE similar parts, such as PCB, LED and cable. This research results revealed that how mechanical processing help to remove them from the vehicles before the shredder technology. According to the circular economy directive, the proper processing after removal of lights from the cars is important. It was found that the mechanical processing of them should contain the following steps: (i) comminution (or opening of the cover), (ii) classification, (iii) further comminution for larger parts, separation of metals and (iv) removal of LEDs from PCB. The results showed, that the amount of the LEDs is small, below 1 g per light. Even if the LEDs contain valuable materials, it is matter in hand if it is economical to focus on LED recycling. The PCB content was below 2 % (type "A" front light).

Funding

The research was funded by the Sustainable Development and Technologies National Programme of the Hungarian Academy of Sciences (FFT NP FTA). This publication is funded by the European Union's Horizon Europe program under grant no. 101079354.

References

ACEA: Motorisation rates in the EU, by country and vehicle type. 2 May 2023. link : https://www.acea.auto/figure/motorisation-rates-in-the-eu-by-country-and-vehicle-type/ (downloaded: 04/04/2024)

Dojcsák M., Nagy S., Csiszár T., (2022): Examination of the processing of end-of-life railway towing vehicles. *In: Pomberger, R. et al. (szerk.) Vorträge-Konferenzband zur 16. Recy & DepoTech-Konferenz Leoben, Ausztria: Montanuniversität Leoben, Leoben Institute of Mechanical Engineering*, 197-202

Grohol, M., Veeh, C., (2023) : Study on the critical raw materials for the EU 2023 – Final report. *Publications Office of the European Union, 2023*

Illés I.B., Nagy S., Kékesi T., (2021): The possibility of Rare Metal Recovery from white LED Bulbs. *Materials Science And Engineering: A Publication Of The University of Miskolc*, 46, 43-53

Martins T.R., Tanabe E.H., Bertuol D.A., (2020): Innovative method for the recycling of end-of-life LED bulbs by mechanical processing. *Resources, Conservation and Recycling*, 161

Mazurek M., Bačo P., Bőhm, J., Bokányi Lj., Borska I., Csőke, B., Csomor Á.T., Czeglédi B., Faitli J., Földessy J. et al., (2022): Critical raw materials in the economies of the V4 countries. *Główny Instytut Górnictwa (Katowice)*

Nagy S., Bokányi L., Gombkötő I., Magyar T., (2017): Recycling of Gallium from End-of-Life Light Emitting Diodes. *Archives of metallurgy and materials*, 62, 1161-1166

Rahman Sm.M., Pompidou S., Alix T., Laratte B. (2021): A review of LED lamp recycling process from the 10 R strategy perspective. *Sustainable Production and Consumption*, 28, 1178-1191

L3: CO_2 sequestration experiments by producing geopolymer specimens from lignite fly ash

Tamás Kurusta[1*], *Kitti Patrícia Klaj*[1], Teemu Kinnarine[2], Nazila Bolourieh[2], and Gábor Mucsi[1]

[1]Faculty of Earth and Environmental Sciences and Engineering, University of Miskolc, HU
[2] LUT School of Engineering Sciences, Lappeenranta-Lahti University of Technology LUT, Lappeenranta, FI

Abstract. Carbonate sequestration of CO_2 as a mineral is an option to permanently and safely store CO_2 captured from flue gas. In this process, CO_2 reacts with calcium and/or magnesium-containing materials to form thermodynamically stable, environmentally friendly carbonate minerals. In a research project, CO_2 sequestration was performed on deposited fly ash from Visonta (Hungary), combined with mechanical activation. The new carbonate phases' samples were analyzed for their potential use as geopolymer-based building materials. CO_2 sequestration and mechanical activation were carried out in a Fritsch Pulverisette 5 planetary ball mill under wet conditions. After CO_2 sequestration, the samples were dried, and 20x20x20 mm geopolymer specimens were prepared and measured for compressive strength at seven days of age. It was found that the primary Ca source in fly ash is bassanite, which reacts with CO_2 only in the presence of NaOH. Furthermore, it was revealed that the addition of low NaOH concentrations (0,5 M) during the grinding phase, positively affects the compressive strength of the geopolymer. In contrast, using higher NaOH concentrations, the strength of the specimen is reduced; at a concentration of 2 M, the specimen does not completely consolidate and deforms plastically under pressure. As a result of the experiment the maximum geopolymer compressive strength reached 16.1 MPa using 0.5 M NaOH.

1 Introduction

Global warming is a significant issue that the world is facing today. The Earth's atmospheric temperature has risen due to the increase of greenhouse gases. These gases are naturally present in the atmosphere, but anthropogenic greenhouse gases, such as CO_2, have been added to them, mainly after the Second Industrial Revolution. Mineral CO_2 sequestration is one possible technique to prevent these gases from being released into the atmosphere. This technique involves the reaction of CO_2 with non-carbonate minerals containing alkali metals like sodium or potassium and alkaline earth metals like calcium or magnesium. Following the carbonate reactions, CO_2 will be present in the system as different carbonate minerals (anhydrous or bound, OH- or H_2O-containing), such as calcite [$CaCO_3$], magnesite [$MgCO_3$], siderite [Fe_2CO_3] (Turvey et al., 2018).

The mineralogical requirement for effective CO_2 sequestration is that the host material must contain high amounts of non-carbonate Ca and/or Mg minerals. On this basis, natural silicate minerals with high serpentinite, forsterite, or olivine content (Inês. Romão 2014) or industrial by-products with mineralogically similar composition and properties, such as construction and demolition waste (Ghacham et al., 2017), red mud (Mucsi et al., 2021), steel slag (Bonenfant et al., 2008), fly ash (Montes-Hernandez et al., 2009) can be used for CO_2 sequestration.

In this research work, fly ash-based CO_2 sequestration was investigated through promoted by mechanical activation. The experiments aim for CO_2 capture and sequestration (CCS) in stable form by mineral carbonation. In addition to CO_2 sequestration, we investigated the potential of using fly ash containing new mineral phases as a geopolymer building material. We have used the direct carbonation method, where the reactivity of the ash was increased by high-energy milling in wet media.

2 Material and Methods

2.1. Material

The experiments were carried out on lignite fly ash from MVM Mátra Energia Zrt, Visonta (Hungary). The analysis of the particle size distribution of the sample reveals that the sample primarily comprises particles below 400 µm, with 66 µm median particle size. The initial moisture content was found to be 24.1 wt%. The fly ash particle density was 1.92 g/cm^3, and the bulk density was 0.58 g/cm^3. Biogon-C CO_2 gas (95.5% purity) was used for carbonate reactions without future purification.

2.2. Methods

2.2.1. Mechanical activation and CCS

The experiment conducted CO_2 sequestration and mechanical activation simultaneously in a Fritch Pulverisette 5 planetary ball mill under wet conditions,

* Corresponding author: tamas.kurusta@uni-miskolc.hu

using NaOH solution of varying concentrations (0.1, 0.25, 0.5, 1, and 2 M) as the grinding fluid. The milling was carried out using 500 ml steel jars and grinding media. The jars were filled with 54.3 g of dry sample and 543 g of 20 mm diameter grinding balls. The grinding was carried out at 200 rpm for 180 min, and the free grinding chamber was filled with CO_2 gas at up to 5.5 bar pressure and refilled every 15 min to the initial CO_2 pressure.

2.2.2. Production of geopolymer

Fly ash treated with CO_2 was used to create geopolymer specimens in the size of 20x20x20 mm. To achieve the ideal Al_2O_3/Na_2O ratio of 1, various concentrations of NaOH were used as activating solution. The mixtures were prepared with a liquid-to-solid ratio of 1, with half of the liquid of Betol93 sodium silicate.

2.2.3. Characteristics measurements

WD-XRF measurement was performed using a RIGAKU Supermini 200 type WDXRF. The radiation source was an air-cooled 200 W palladium (Pd) X-ray tube with an excitation voltage of 50 kV and 4.0 mA. Quantitative analysis requires the calibration of standards for identified elements. Calibration is performed element-by-element, with 8-12 pcs for main elements and 6-10 pcs for trace elements (the number of standards used is not constant, determined by the concentration in the standards for each component). Each element is measured seven times (two background points 10-10, peak position 40 sec), so the errors can be reduced statistically, and the measurement also gives a better average value.

The mineralogy of the fly ash was determined by X-ray powder diffraction (XRD) with a Bruker D8 Advance diffractometer using Cu K-alpha radiation (40 kV, 40 mA) in parallel beam geometry obtained with Göbel mirror, in the 2°–70° (2θ) range with a 0.007° (2θ) step interval and a 24 s step counting time. The crystalline phases were identified by Bruker DiffracPlus software package in its EVA module ICDD PDF-2 (2005) database for search/matching of phases. The quantitative evaluation was carried out by Rietveld refinement in TOPAS4 software, where the amorphous content was determined by the amorphous hump method.

Stretching and bending vibrations of chemical bonds in the samples before and after CO_2 sequestration were detected by a JASCO FT-IR 4200 type Fourier Transformed Infrared Spectrometer in reflection mode with a diamond ATR. The infrared transmission spectra of samples were recorded for 400-4000 cm^{-1} with a resolution of 4 cm^{-1}. The observed spectra are plotted in the function of wavenumber and transmittance. Observed FTIR bands were interpreted based on the handbook by Chukanov and Chervonny (2014).

The Controls C250Kn uniaxial compression machine was used to measure the compressive strength of the prepared specimens. The test involved placing the specimens between parallel steel plates and subjecting them to axial compression up to the breaking load, with a load increment of 300 N/min.

3 Results

3.1. Chemical and mineral properties of fly ash

According to the XRF measurement (Table 1.) the major component of the fly ash is CaO, proving it a suitable material for CCS. The sample contains a total of 15.51 wt% of CaO and MgO, which is relatively low for CO_2 sequestration. The utilization of CO_2-treated fly ash will play an important role.

Table 14. Oxidic components of fly ash (weight percent, error +/- 0.01 relative percent, LOI 0,05 wt%).

Oxidic components	wt%
Al_2O_3	14
Fe_2O_3	11.2
SiO_2	39.8
TiO_2	0.50
Na_2O	**0.54**
MgO	**3.41**
CaO	**12.1**
P_2O_5	0.35
K_2O	1.61
MnO	0.18
S	6.5
F	<0.3

The Table 2 shows the mineral composition of fly ash. Among the minerals present in the sample, bassanite, bytownite, galenite, and magnesioferrite can react with CO_2. The calculated oxide breakdown for each mineral phase is based on the amorphous material that still contains around 5-6 wt% of Ca and MgO. Portlandite, lime, brucite, and periclase are the mineral phases typically found in typical fly ashes (Monasterio et al., 2020), and they possess good CO_2 sequestration capacity. However, these minerals are not present in the Visonta lignite fly ash.

Table 15. Mineral components of fly ash (weight percent, error +/- 0.01 relative percent)

Mineral phase	Formula	
Calcite	$CaCO_3$	6.2
Quartz	SiO_2	17.6
Bassanite	$Ca[SO_4]\cdot 0{,}5\ H_2O$	9.5
Hematite	Fe_2O_3	4.1
Maghemite	$Fe^{3+}{}_2O_3$	4.9
Bytownite	$Na_{0.2}Ca_{0.8}Al_{1.8}Si_{2.2}O_8$	6.7
Galenite	PbS	3.9
Albite	$NaAlSi_3O_8$	7.6
Mg-Ferrite	$MgFe_2O_4$	1.9
Amorf		38

3.2. Structural changes during carbonation and geopolymerization

In Figure 1, the spectral images of FTIR measurements on CO_2 treated samples. After CO_2 sequestration, significant differences can be observed in the -C=O peaks at 1460 cm^{-1} and the C-O peaks at 880 cm^{-1} for calcite. Both peaks increase with NaOH concentration up to a concentration of 1 M and then remain constant. A slight change is observed in the Al-O-Si peak at 1010 cm^{-1}, which decreases slightly in intensity and shifts towards 980 cm^{-1}, indicating that geopolymerization has already started during grinding.

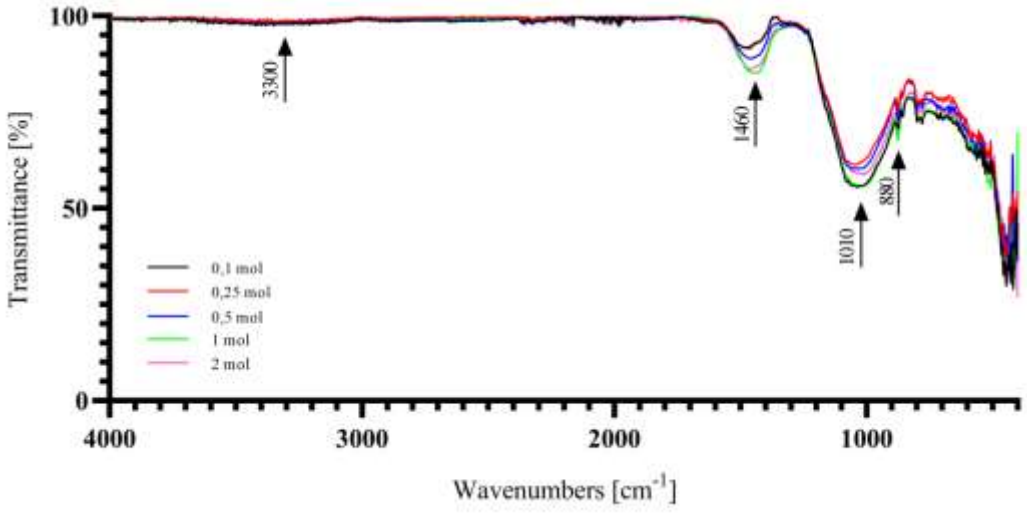

Figure 38. FTIR spectrum of the CO_2 treated sample

After the process of geopolymerization, it can be observed that there is a slight decrease in peak intensities up to 0.5 M, and a significant decrease at 1 and 2 M in the full FTIR spectrum (Figure 2) with increasing NaOH concentration. The most significant changes are visible in the OH-HOH and 1645 cm^{-1} bonds at 3300 cm^{-1} for bound water, and in the silicate band around 980 cm^{-1}, which is crucial for geopolymerization. The latter increase shows a higher degree of polymerization (Rattanasak and Chindaprasirt 2009), which is inconsistent with the strength study. Therefore, it can be assumed that the formation of clay-like hydrosilicates in the non-bonded state is taking place. Also, there is a decrease in intensity of the -C=O peak at 1390 cm^{-1} and the C-O peak at 880 cm^{-1}, suggesting that carbonate reactions are taking place in addition to polymerization.

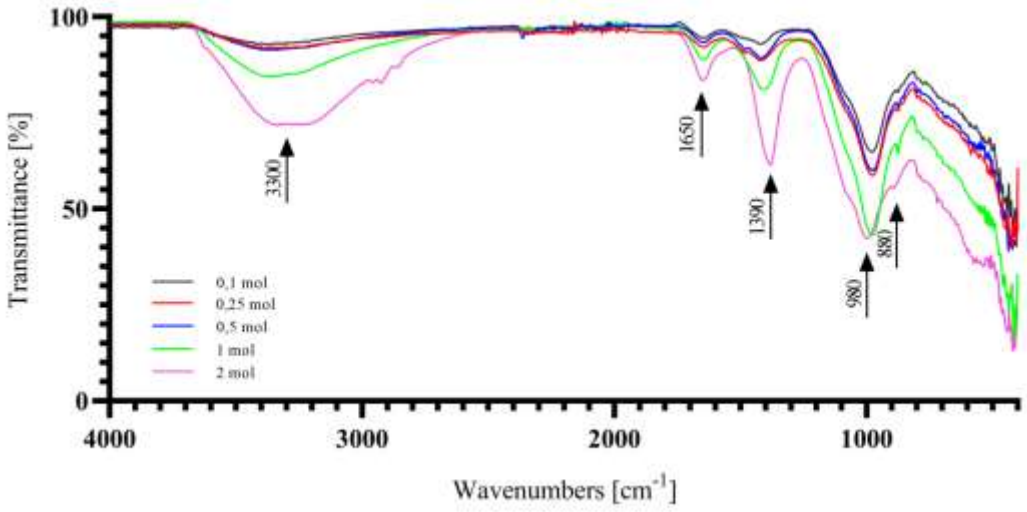

Figure 39. FTIR spectrum of the geopolymer samples

3.3. Result of the axial load test

The compressive strength of geopolymer specimens improved as the concentration of the added NaOH solution during grinding increased up to 0.5 M, the compressive strength of the specimens increased from 9.5 MPa to 16.1 MPa. However, a significant loss of strength was observed when the NaOH concentration was further increased to 1 and 2 M. At a concentration of 1 M, the strength of the specimens was only 5.68 MPa, which is approx. 60 % of the reference sample. At 2 M, the specimen did not fully solidified, leading to plastic deformation during measurement.

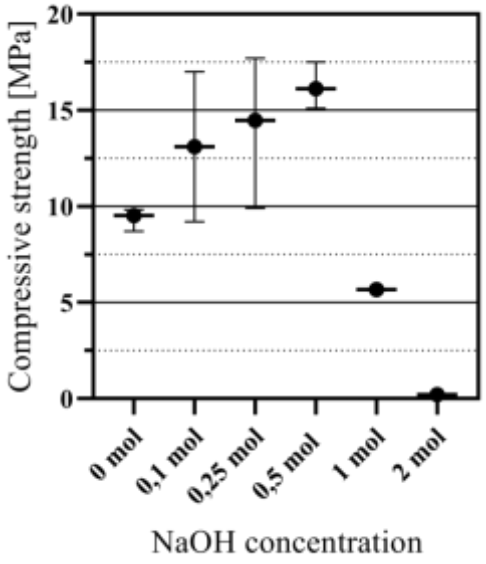

Figure 40. Compressive strength of the test specimens

4 Conclusion

By increasing the concentration of added NaOH, we can enhance the CO_2 absorption capacity of the sample material. This can be explained by the fact that the primary source of Ca in the fly ash, bassanite, decomposes into sodium sulphate, calcium hydroxide, and water after reacting with NaOH. Only then it can react with CO_2 in the system. Furthermore, adding low concentrations of NaOH (up to 0.5 M) during grinding positively affects the compressive strength of the specimens. Geopolymers prepared this way achieve 40.1% higher strength than specimens subjected only to mechanical activation. This is presumably due to the strength-increasing effect of the resulting microcrystalline calcite (Itam et al., 2020). However, it is observed that high NaOH concentration (1, 2 M) added during grinding already causes strength loss. At 2 M solution, the specimens still need to be fully solidified.

The sample prepared in 0.5 M NaOH meets the 7-day strength requirement for 32.5 strength class standard batch cements. In the next phase of the research, we will extend the strength testing to 2 and 28 days and investigate the role of different bonds (carbonate and geopolymeric bonds) in the setting process.

This project is funded by the European Union's Horizon Europe program under grant no. 101079354.

References

Turvey C.C., Wilson S.A.,. Hamilton J.L,. Tait A.W, McCutcheon J., Beinlich A., Fallon S.J., Dipple G.M., Southam G. (2018): Hydrotalcites and hydrated Mg-carbonates as carbon sinks in serpentinite mineral wastes from the Woodsreef chrysotile mine, New South Wales, Australia: Controls on carbonate mineralogy and efficiency of CO_2 air capture in mine tailings. International. *Journal of Greenhouse Gas Control,* 79, 38-60

Romão I., Slotte M., Gando-Ferreira L.M.,. Zevenhoven R. (2014): CO_2 sequestration with magnesium silicates—Exergetic performance assessment, *Chemical Engineering Research and Design*, 3072-3082

Ghacham A.B., Pasquier L., Cecchi E., Blais J., Mercier G. (2017): Valorization of waste concrete through CO_2 mineral carbonation: Optimizing parameters and improving reactivity using concrete separation, Journal of Cleaner Production 166, 869-878

Mucsi G., Halyag N., Kurusta T., Kristály F. (2021) Control of Carbon Dioxide Sequestration by Mechanical Activation of Red Mud. *Waste and Biomass Valorization*, 12, 6481–6495

Bonenfant D., Kharoune L., Sauve S., Hausler R., Niquette P., Mimeault M., Kharoune M. (2008) CO_2 sequestration potential of steel slags at ambient pressure and temperature. *Ind. Eng. Chem. Re,*. 47, 7610–7616

Montes-Hernandez G., Pérez-López R., Renard F., Nieto M., Charlet L. (2009): Mineral sequestration of CO_2 by aqueous carbonation of coal combustion fly-ash. *Journal of Hazardous Materials* 161, 1347-1354

Chukanov, V.N., Chervonnyi, D.A. (2014): Infrared Spectroscopy of Minerals and Related Compounds. *Springer*

Monasterio-Guillot L., Alvarez-Lloret P., Ibañez-Velasco A., Fernandez-Martinez A., Ruiz-Agudo E., Rodriguez-Navarro C. (2020) CO_2 sequestration and simultaneous zeolite production by carbonation of coal fly ash: Impact on the trapping of toxic element. *Journal of CO_2 Utilization*, 40, 101263

Rattanasak U., Chindaprasirt P. (2009): Influence of NaOH solution on the synthesis of fly ash geopolymer. *Minerals Engineering*, 22, 1073–1078

Kamal N.L, Itam Z., Sivaganese Y., Beddu S., (2020) Carbon dioxide sequestration in concrete and its effects on concrete compressive strength. *Materials Today: Proceedings,* 31, A18-A21

M1: Process modelling for real-time process prediction and control of grinding circuits

Mohsen Yahyaei[1,*]

[1]Julius Kruttschnitt Mineral Research Centre, The University of Queensland, Australia

Abstract. Automation and advanced process control are key technologies for increasing mineral processing plants' sustainability. Despite significant technological advances and investment in digitalization, a fully autonomous operation still is a distant target for the minerals industry. The main barrier to the effective automation of processing plants, particularly implementing advanced process control, is the reliability of measurements and sensor data. Soft sensors are a credible way to improve the reliability of measurements and data quality and therefore play an important role in developing an effective autonomous system. Process modelling can enhance data reliability of measurement from instrumentation by utilising a phenomenological understanding of the processes. Process modelling and data analytics effectively enhance the reliability of autonomous systems. The Julius Kruttschnitt Mineral Research Centre (JKMRC) Mill Filling Inference Tool (JK Mill FIT) and JKMRC CycloPS are two soft sensors developed and implemented in the industry. Those soft sensors proved to provide measurements which are practically hard to measure directly but they are important for decision-making to operate grinding circuits.

1 Introduction

The integration of automation and autonomous systems in mining operations has significantly enhanced safety and productivity (Farrelly & Records, 2007; Harris, 2019; McNab & Garcia-Vasquez, 2011; Torbin, 1989; Yahyaei, 2023). By stabilizing operational processes, these technologies ensure consistent quality and higher throughput, which translates to increased productivity. Moreover, maintaining mining equipment within optimal operating parameters extends its lifespan and reduces both operational costs and downtime required for maintenance, further contributing to the efficiency and cost-effectiveness of mining projects.

1.1 Process automation for comminution and classification circuits

Automation plays a crucial role in the efficiency of comminution and classification units. It achieves this by monitoring real-time data and applying control actions to mitigate the effects of disturbances. Thus, automation of comminution and classification units is integral in optimizing processes and safeguarding them against the emerging environmental, social and governance constraints.

In the context of mineral processing, the SAG mill, ball mill, and pebble crushing circuit (SABC) is a common comminution configuration. The circuit utilizes various signals for monitoring, such as power draw, acoustic emissions, and particle size distribution, to assess the circuit's condition (**Fig. 1**). These signals are integral to the automation system, which, depending on its maturity level, can make real-time adjustments to optimize performance. Advanced data processing techniques are employed to analyze the sensor data, providing a comprehensive understanding of the circuit's dynamics, which is crucial for maintaining optimal operation and improving efficiency.

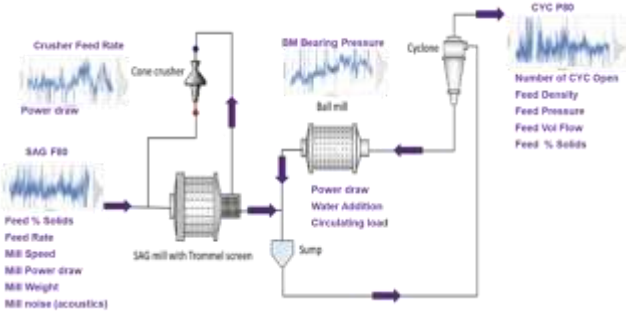

Fig. 25. Flow diagram of a standard SABC circuit with some of the primary signals used in process control (Yahyaei et al., 2023)

1.2 Data processing and modelling for automation

The integrity of sensor data is fundamental to the performance of automation systems in comminution and classification units. Regular calibration, maintenance, and redundancy are key practices to ensure data quality. However, challenges such as high costs and the complexity of validating and processing data persist. Addressing these issues is essential for the advancement of reliable and trustworthy automated systems in mineral processing and other industries (Lee & See, 2004; Schaefer et al., 2018)..

Semi-phenomenological models indeed play a crucial role in enhancing the trustworthiness of

* Corresponding author: m.yahyaei@uq.edu.au

autonomous systems. By integrating empirical data with fundamental physical laws, these models provide a comprehensive understanding of system behaviour, which is essential for validating sensor data. Furthermore, the ability to quantify uncertainties helps in risk assessment and management, ensuring that autonomous systems can be relied upon even in the presence of inherent measurement variabilities.

2 Process modelling for soft sensors

Soft sensors represent a significant advancement in process control, utilizing computational models to infer parameters that are challenging or impossible to measure directly. These virtual sensors combine various data sources, including measurements from physical sensors, to provide real-time predictions of process variables. The integration of machine learning and artificial intelligence has further enhanced their capabilities, allowing for the development of sophisticated neural network-based models. This innovation not only improves the reliability and accuracy of process monitoring but also facilitates more efficient control strategies, particularly in industrial settings where certain parameters, such as ore hardness in grinding circuits, cannot be continuously measured due to practical constraints (Cao et al., 2020; Fu & Aldrich, 2020; Hodouin, 2011).

2.1 Mill Filling Inference Soft Sensor

The Julius Kruttschnitt Mineral Research Centre (JKMRC) Mill Filling Inference Tool (JK Mill FIT) is a soft sensor for monitoring and optimization of the grinding media and total charge filling of Autogenous Grinding (AG), Semi-Autogenous Grinding (SAG) and Ball mills. The soft sensor employs a suite of mathematical models to provide real-time data on mill conditions, surpassing traditional methods in accuracy and efficiency. This tool not only enhances the performance of grinding mills but also contributes to the energy efficiency and stability of comminution and classification circuits. The JK Mill FIT is delivered in various forms based on the operation's preferred implementation platform. **Fig. 26** presents the interface of the Microsoft Excel-based JK Mill FIT.

Fig. 26. Interface of the Microsoft Excel-based JK Mill FIT (Yahyaei et al., 2021)

2.2 Cyclone Performance Soft Sensor

The JKMRC Cyclone Performance Sensor (JK CycloPS), represents a significant advancement in the monitoring and optimization of hydrocyclone performance. This soft sensor technology enables real-time predictions of various key performance indicators, such as the cyclone's cut size and the overflow P_{80}, which is a measure of particle size distribution. Additionally, it can estimate the water and mass split in the cyclone and the circulating load by size. The adaptability of JK CycloPS extends to dense medium cyclones used in coal operations, enhancing its utility across different mineral processing applications. By providing essential data, CycloPS aids plant operators in fine-tuning the operation of hydrocyclones and grinding circuits. This optimization is vital for maintaining the desired product size for downstream flotation processes and minimizing the bypass of fines back to the grinding circuits, thus ensuring efficiency and cost-effectiveness in mineral processing operations.

Fig. 27 presents the interface of an implementation of JK CycloPS for a regrinding circuit which utilises two Vertical Stirred Media Mills in a closed circuit with a cluster of cyclones for a copper/gold processing plant.

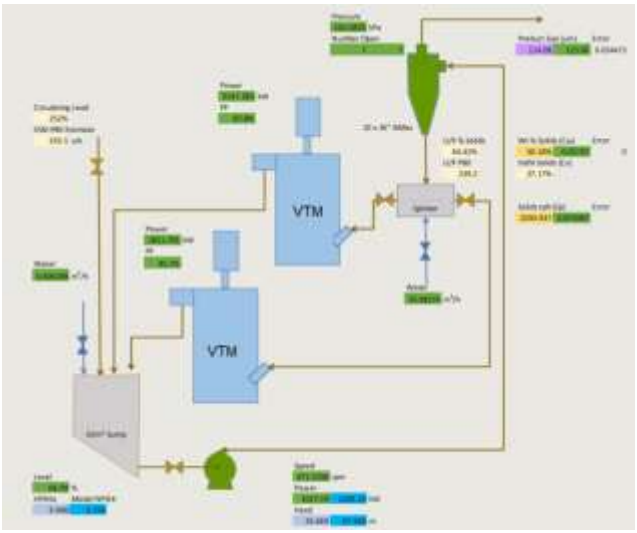

Fig. 27. Prototype of cyclone and VTM soft sensors

3 Soft sensor applications

The operation of grinding circuits in mineral processing is indeed a sophisticated task, requiring advanced process control systems to manage the variability in ore characteristics.

Soft sensors play a pivotal role in monitoring these complex systems, providing essential data that cannot be measured directly, such as the conditions inside AG, SAG or ball mills. Real-time prediction of the performance of classification units such as hydrocyclone can guide plant operators to focus their optimisation efforts on grinding or classification units based on the operational state of comminution and classification units. The development and validation of these sensors, are critical steps towards achieving autonomous, reliable, and efficient operations in SABC circuits, ensuring that the grinding process is optimized for both immediate and long-term performance. **Fig. 28** presents the validation of JK Mill FIT ball charge prediction across various operations indicating the soft sensor accuracy is a maximum of 0.8% of absolute ball filling. Given that the

ball-filling measurement has inherent errors, this accuracy is acceptable for industrial applications.

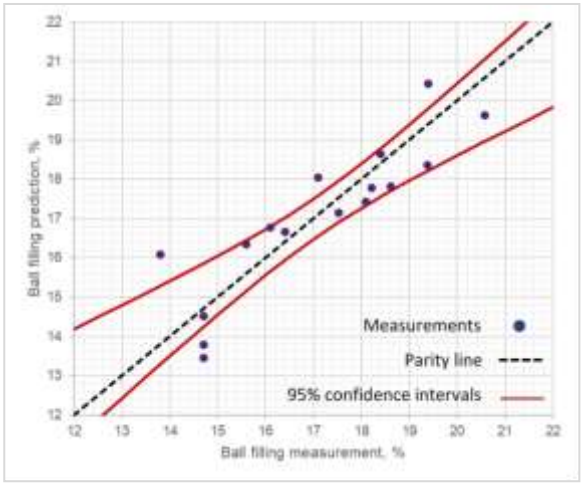

Fig. 28. Validation of JK Mill FIT prediction of ball filling based on data collected from various operations (Yahyaei et al., 2021)

3.1 Process stability using JK Mill FIT

The JK Mill FIT, a soft sensor developed for real-time monitoring of tumbling mill content, has significantly enhanced plant stability and increased throughput in mineral processing operations. By providing accurate, real-time data on mill charge levels, the JK Mill FIT allows for improved process control, leading to more stable operation of grinding mills. This stability is crucial for maintaining optimal grinding conditions, which, in turn, increases throughput.

Moreover, the sensor's ability to reduce operational costs contributes to its overall positive impact on plant performance. The implementation of JK Mill FIT across various operations globally has demonstrated an average increase between 1% to 5% in throughput or energy efficiency.

Additionally, the JK Mill FIT helps reduce grinding media consumption and liner wear by assisting operators in running their mills at a suitable rock-ball ratio over an extended period. This preventive measure prevents excessive wear of grinding media and liners. The authors are currently collecting more industrial data to precisely measure the reduction in grinding media and liner wear.

3.2 Managing grinding circuit using JK CycloPS

The JK CycloPS plays an important role in aiding plant operators to maintain efficient grinding circuits through real-time monitoring of the grinding circuit's cut size, specifically the hydrocyclone's overflow P_{80}. This continuous oversight of the cut size ensures that the cyclone functions within its optimal parameters. Any deviation from the established target cut size can adversely affect the efficiency of subsequent flotation processes and the stability of the entire circuit.

Real-time data on cyclone performance is provided to operators, enabling them to swiftly adjust variables such as feed pressure or pulp density to preserve the desired cut size. Additionally, the CycloPS offers insights into water and mass splits, as well as circulating load data segmented by size. The circulating load, which denotes the mass of material moving within the grinding circuit, plays a pivotal role in influencing both the grinding efficiency and the circuit's stability.

Comprehending the volume of circulating load and the nature of the materials in circulation—whether fines or coarse particles—allows operators to determine the stability of the grinding circuit. For instance, if fines circumvent the grinding process, it may signal poor cyclone performance. Conversely, a high circulating load of coarse particles suggests an overburdened grinding process, potentially leading to unstable operations and diminished throughput.

Fine-tuning the cyclone's settings to strike a balance between fresh feed and recirculated material, or optimizing the grinding process, aids in stabilizing the grinding circuit and reducing energy waste due to excessive recirculation. A consistent circulating load is key to uniform grinding performance and the overall stability of the circuit. Moreover, maintaining a stable cut size is crucial to ensure that downstream processes, such as flotation or leaching, receive the correct particle size distribution, thereby optimizing their efficiency.

3.3 Sensors fusion to enhance data quality

The integration of soft sensors into grinding circuits represents a significant advancement in process control systems.

These soft sensing technologies enable the monitoring of parameters that are challenging to measure directly, such as the internal load of a grinding mill or the particle size distribution in a hydrocyclone overflow. By leveraging semi-fundamental models, soft sensors can infer these critical parameters from accessible data, facilitating real-time adjustments and enhancing the overall efficiency of the circuit.

This approach not only improves the accuracy and reliability of the process control system but also contributes to the concept of trusted autonomy in industrial processes.

The predictive capabilities of soft sensors allow for the preemptive identification of anomalies, ensuring consistent quality and performance in grinding operations.

As a result, the adoption of soft sensors is poised to revolutionize the management of complex industrial systems, leading to more robust and responsive process control systems.

3.4 Development of trusted autonomous systems

The integration of soft sensors in mineral processing plants represents a significant advancement in the automation and optimization of these facilities.

By utilizing validated models, soft sensors provide a more reliable and less subjective analysis of the plant's operational state, leading to improved consistency in predictions. This technology not only verifies the accuracy of instrumentation data but also identifies discrepancies, thereby bolstering real-time data

validation and quality assurance. Consequently, this enhances the credibility of advanced control systems.
In the context of comminution circuits, the development of dynamic models informed by verified measurements allows for accurate predictions of the circuit's behaviour in response to varying feed properties and operational parameter adjustments. The transformation of spatial or data into a temporal format through post-blast material movement models and load and haul management solutions is pivotal. Furthermore, dynamic stockpile models facilitate the tracking of material properties, thereby enriching the ore-tracking process from extraction to primary crushing stages.

Despite the lack of robust models for certain operational behaviours, such as the wear-related performance variability in SAG mills, existing process insights and tools offer substantial benefits. For instance, the grind curve response analysis provides a framework for refining dynamic models and setting advanced control optimization targets. The overarching goal is to achieve a comprehensive optimization of the grinding circuit, tailored to the demands of the separation circuit and the desired plant throughput. This holistic approach is underpinned by the insights gained from each comminution unit's workload and the models' ability to determine the optimal operating conditions for achieving the set performance objectives.

4 Conclusions

The advancement of real-time monitoring systems in comminution and classification circuits is a significant step in mineral processing technology.

Utilizing semi-phenomenological models, it is possible to develop soft sensors like JK Mill FIT and JK CycloPS to provide accurate, real-time data on the performance of grinding and classification units. These soft sensors are essential for the validation of hard sensor data, ensuring the integrity of the monitoring process and process automation.

The implementation of soft sensors based on semi-phenomenological models not only enhances the performance of grinding circuits, it ensures the quality of the final product and contributes to energy efficiency by identifying and rectifying process inefficiencies. The continuous monitoring and optimization capabilities offered by these systems are pivotal for the sustainable and economical operation of mineral processing plants.

Acknowledgement

The authors express gratitude for the funding and support provided by the Australian Research Council under the ARC Centre of Excellence for Enabling Eco-Efficient Beneficiation of Minerals (CE200100009).

The authors extend their heartfelt gratitude to The University of Queensland, JKTech Pty. Ltd. and industry partners for their technical support of the project and permission to publish the results.

References

Cao, L. , Yu, F. , Yang, F. , Cao, Y. , & Gopaluni, R. B. , 2020. Data-driven dynamic inferential sensors based on causality analysis. Control Engineering Practice, 104, 104626.

Farrelly, C. , Records, L. R. , 2007. Remote operations centres – Lessons from other industries, Australian Mining Technology Conference, AusIMM, WA, Australia.

Fu, Y. , & Aldrich, C. , 2020. Deep Learning in Mining and Mineral Processing Operations: A Review. IFAC-PapersOnLine, 53(2), 11920–11925.

Harris, F. , 2019. Guideline for the implementation of autonomous systems in mining, Global Mining Guidelines Group, Accessed April 2023: https://gmggroup.org/projects/implementation-of-autonomous-systems/

Hodouin, D. , 2011. Methods for automatic control, observation, and optimization in mineral processing plants. Journal of Process Control, 21(2), 211–225.

Lee, J. D. , See, K. A. , (2004). Trust in automation: designing for appropriate reliance. Hum Factors, Spring;46(1):50-80. doi: 10.1518/hfes.46.1.50_30392. PMID: 15151155.

McNab, K. L. , Garcia-Vasquez, M., (2011). Autonomous and remote operation technologies in Australian mining, Prepared for CSIRO Minerals Down Under Flagship, Minerals Futures Cluster Collaboration, by the Centre for Social Responsibility in Mining, Sustainable Minerals Institute, The University of Queensland. Brisbane.

Schaefer, K. E. , Hill, S. G. , & Jentsch, F. G. , (2018, 21-25 July). Trust in human-autonomy teaming: A review of trust research from the US Army research laboratory robotics collaborative technology alliance. In Advances in Human Factors in Robots and Unmanned Systems: Proceedings of the AHFE 2018 International Conference on Human Factors in Robots and Unmanned Systems, Loews Sapphire Falls Resort at Universal Studios, Orlando, Florida, USA 9 (102-114). Springer International Publishing.

Torbin, R. , (1989). Application of remote control to mining equipment, SME annual meeting, Las Vegas, Nevada, February 27-March 2, 1989.

Yahyaei, M. , (2023). Automation in ESG framework: How automation can contribute to the sustainability of mineral resources supply, Mining Magazine, Issue 2, Autumn 2023, 32-37.

Yahyaei, M. , Hilden, M. , Reyes, F. , Forbes, G. , (2021, October 20-22). Soft sensors and their application in advanced process control of mineral processing plants, 17th International Conference on Mineral Processing and Geometallurgy (Procemin-Geomet 2021), Santiago, Chile.

M2: Dynamic Simulation of an Iron Ore Comminution Circuit with Mineral Components Tracking

Rodrigo de A. Prates[1], *Rodrigo M.* de Carvalho[2,*], and *Luís Marcelo* Tavares[1]

[1]Department of Metallurgical and Materials Engineering, Federal University of Rio de Janeiro, Rio de Janeiro, Brazil

Abstract Simulation of comminution circuits has been an important topic in the last couple of decades. However, there are still challenges to be faced. In Brazil, several iron ore operations are dealing with the continuous decrease of ore grade and the push for processing ore from tailings dams. One way to deal with such demand is to process blends of different ore lithologies, therefore subjecting the plant to fluctuations in several ore characteristics such as size distribution, grade, grindability and particle shapes. This work proposes implementation of dynamic multicomponent models of an iron ore grinding circuit using Dyssol, a process flowsheet simulator that has an embedded multicomponent structure that allows tracking iron ore components along the circuit. Results show that dynamic simulation has allowed to describe the dynamics of a ball mill operating in closed circuit with a hydrocyclone cluster.

1 Introduction

Dynamic simulation approaches have been successfully used to describe comminution circuits, including crushing, classification and grinding operations (Asbjörnsson et al., 2022; Légaré et al., 2016; Gama et al., 2023). However, a simplification often used in process simulation in the minerals industry is to assume ores may be represented by a single component. However, for some operations this representation can lead to a poor understanding of the process. For instance, in iron ore operations, separately defining and parameterizing each of the major mineral species that compose the ore allows a much deeper analysis. This multicomponent approach can be used to capture the effect of changes in Run-of-Mine composition and, therefore, competence of the ore, a common occurrence after years of operation. It is also key to model mineral liberation.

Dyssol is a process simulator that allows using this complex multicomponent approach, defining material streams as interdependent distributed parameters in the form of a tree structure, as shown in Fig. 1 (Skorych et al., 2017, 2020). With this structure it is mathematically possible to represent material streams in a more complex way via new distributions, like shape, moisture, and porosity along the process from ROM to concentrate, while maintaining the same structure.

The present work explores Dyssol capabilities on dealing with multicomponent structures allowing for tracking of individual ore streams and components. To do so, a hypothetical iron ore comminution circuit was analysed by emulating current challenges faced by some Brazilian iron ore processing plants. The feed to the circuit is made up by a mixture of ores, each of which composed of individual minerals representing a fully liberated particles, middlings and gangue.

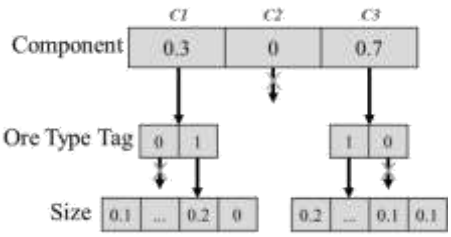

Fig 1. Example of tree structure for multicomponent stream implemented in Dyssol (Skorych et al., 2017, 2020)

2 Methodology

The proposed comminution circuit is composed of a two separate feed streams representing hypothetical iron ores, Iron Ore 1 (IO1) and Iron Ore 2 (IO2), each of which with their own grades, or components, particle size distributions and grindabilities that are mixed and fed to a ball mill. In this work IO1 represents the most friable ore between the two, therefore containing higher grade of liberated hematite particles (Tavares et al., 2022). The grinding circuit contains a cluster with six hydrocyclones that classify the discharge of a 5.1 m (internal diameter) x 10.31 m (length) overflow ball mill equipped with two 4.5 MW motors (Fig. 1). The mean residence time of material in the mill for this operation is about 34 min.

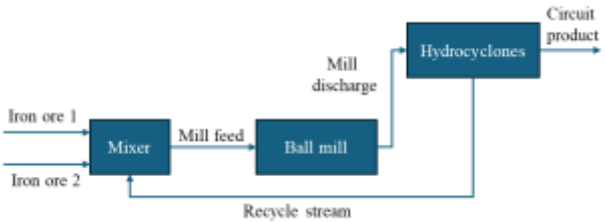

Fig. 2. Grinding circuit considered in the simulations

* Corresponding author: rodrigo@metalmat.ufrj.br

In the simulation, material streams were defined with three components, being hematite, middling particles and quartz, represented by H, M and Q respectively. Additionally, each stream contained 22 size classes and an additional component class that carries the ore type information throughout the circuit for each component.

Classification is performed in a cluster of 33'' Krebs hydrocyclones. In the simulation, each component has been assumed to be classified with a different partition curve, as shown in Fig. 3, where the cutsize is a function of the component density ($d50c \propto \rho^{0.22}$), following Nageswararao model (Nageswararao et al., 2004). The partition curves for each component, H, M and Q are illustrated in Fig 3.

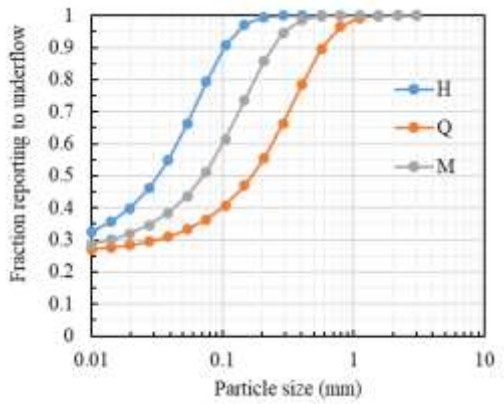

Fig. 3. Partition curves for each of the components in the simulation

The ball mill model has been implemented as a perfect mixing reactor which contains a given mass of material being ground inside, referred to as hold-up. The comminution response in the mill is governed by the classic population balance model (PBM) (Ramkrishna & Borwanker, 1973; Carvalho et al., 2024), expressed in its version that associates mass fractions with particle size classes given by system of integro-differential equations (Muanpaong et al., 2022). The mass transport is modelled as power relationship between mill discharge rate (W_{out}) and its hold-up mass (M_h) (Austin et al., 1984), given in Eq. 1, where a and c are fitting parameters.

$$Wout(t) = aM_h(t)^c \quad (1)$$

For simulation case studies, initially the fresh feed is consisted of 70% of IO1 and 30% of IO2. The simulation begins from guessed particle size distributions and recycle streams calculated automatically by Dyssol. The simulation is run until steady state conditions are reached, then the composition of the feed is gradually changed until IO2 represents the majority of the feed (55%). For simplicity, the feed size distribution for both ores are equal. Details on the composition of each hypothetical ore is given in Table 1, in which the data has been based on França et al. (2020) work.

Table 1. Ore composition (in mass) used in the simulations.

Ore type	H (ρ=5.2 t/m³)	M (ρ=3.4 t/m³)	Q (ρ=2.7 t/m³)	ρ (t/m³)
IO1	0.64	0.20	0.16	4.52
IO2	0.37	0.15	0.48	3.79

Finally, the individual breakage and selection functions are presented in Fig 4. The data was based on Rocha et al. (2022). Since Austin's selection function can be affected by mill hold-up, mill efficiency is expected to vary due to changes in ore composition that may disturb the recycle stream.

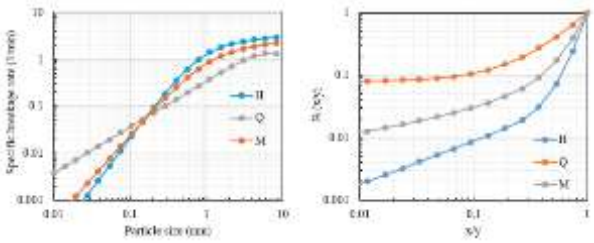

Fig. 4. Selection function (left) and breakage function (right) for each component

3 Results

The implementation of the multicomponent stream variables in Dyssol, including the 22 particle size classes distribution classes and the ore type tag (IO1 and IO2), is shown in Fig 5.

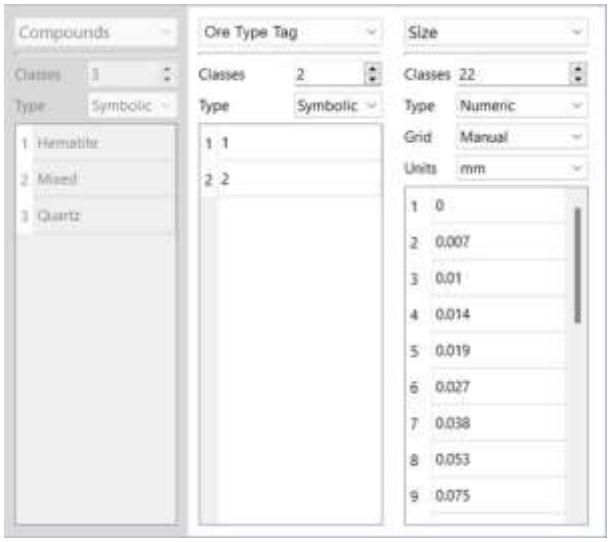

Fig. 5. Multicomponent stream as implemented in Dyssol

The first simulation case considering 70% of IO1 and 30% of IO2 in the fresh feed showed that the system reached steady state in 160 minutes. Fig 6 shows the particle size distribution of main streams of the circuit. From the mass balance of the circuit, shown in Table 2, it can be seen that the recycle stream was richer in IO1, and contained 74.7% of liberated Hematite and 11.3% of Quartz. Even though hematite particles are more brittle than quartz particles, most of them is directed to the

underflow of the hydrocyclones, returning to the mill, owing to their higher specific gravity.

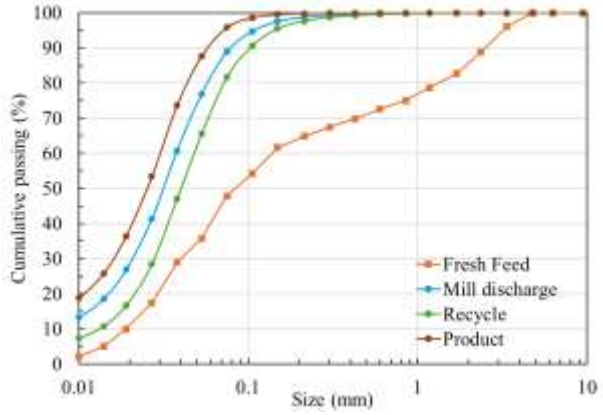

Fig. 6. Size distributions of selected streams at steady state

Table 2. Mass balance of the simulated grinding circuit as function of component and ore contents

Stream	Rate	Component (%)			Ore type (%)	
	t/h	H	M	Q	IO1	IO2
Fresh feed	36.0	56.0	18.5	25.5	70.0	30.0
Recycle stream	33.8	74.7	13.9	11.3	75.3	24.7
Mill discharge	69.8	65.1	16.3	18.6	72.6	27.4

After the system reached the steady state considering the feed composed of 70% IO1 and 30%IO2, a step change was introduced in the feed composition. The resulting composition of the mill hold-up is presented in Fig. 7 which shows that the percentage of hematite dropped from 65% to 59%. Although a smaller amount of brittle material is now present in the mill holdup, there was no significant change in the mill product P80 (55 µm). As a result of an increased quantity of quartz particles entering the hydrocyclones, which are more likely to be carried out of the circuit via the overflow, there has been a gradual drop in the circulating load from 193% to 188%. Consequently, this has led to a slight reduction in the workload of the mill.

The evolution of the recycle stream contents can be seen in Fig. 8, whch shows the gradual decrease in the percentage of IO1 (richer in H) until it reaches the steady state, with a larger contribution than the one in the fresh feed given its higher hematite content.

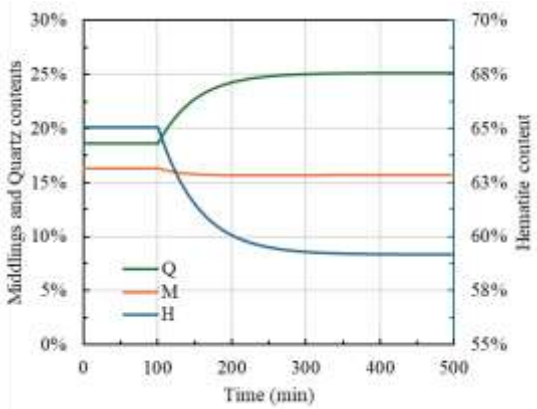

Fig. 7. Evolution of mill hold-up composition after change in feed composition

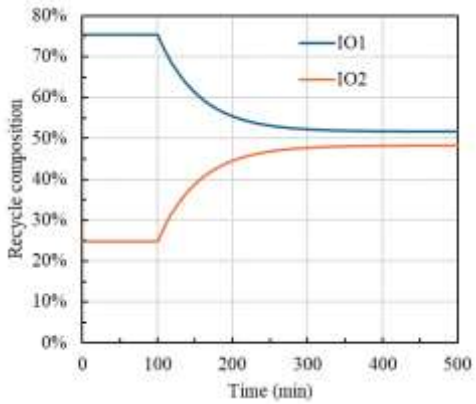

Fig. 8. Evolution of the recycle stream contents per ore type

4 Conclusions

It was possible to implement a multicomponent dynamic simulation of an iron ore grinding circuit in Dyssol. The simulations considered two different iron ores in terms of composition where each composition has been described considering three hypothetical components, hematite, quartz and middlings.

The simulation was able to reach steady-state conditions for multiple initial conditions and process disturbances such as changes on the fresh feed composition. It was also possible to implement component tracking and a multicomponent structure that presents coupled effects, such as different breakage parameters for each component and sensitivity to changes on operational conditions. The ability to work with a set of interdependent distributions presented by Dyssol will potentially allow future implementation of liberation models, thus allowing full circuit integration, from primary crushing to concentration processes.

Acknowledgements

The authors would like to thank Dr. Vasyl Skorych from DyssolTEC for the technical support. This study was financed in part by the Coordenação de Aperfeiçoamento de Pessoal de Nível Superior - Brasil (CAPES) - Finance Code 001.

References

Asbjörnsson, G., Tavares, L. M., Mainza, A., & Yahyaei, M. (2022). Different perspectives of dynamics in comminution processes. *Minerals Engineering, 176*, 107326.

Rocha, B. K. N., Campos, T. M., França, J. R. O., Turrer, H. D. G., & Tavares, L. M. (2022). Comportamento de quebra multicomponente na prensagem de minério de ferro itabirítico. In *21st Mining Symposium*, pp. 212-225. São Paulo.

França, J. R., Barrios, G. K., Turrer, H. D., & Tavares, L. M. (2020). Comminution and liberation response of iron ore types in a low-grade deposit. *Minerals Engineering*, 158, 106590.

Gama, T. S., de Carvalho, R. M., da Silva, B. P., & Tavares, L. M. (2023). Modeling and simulation of dry grinding of coke breeze in rod mills. *Minerals Engineering*, *204*, 108432.

Légaré, B., Bouchard, J., & Poulin, É. (2016). A modular dynamic simulation model for comminution circuits. *IFAC-PapersOnLine*, *49*(20), 19-24.

Nageswararao, K., Wiseman, D. M., & Napier-Munn, T. J. (2004). Two empirical hydrocyclone models revisited. Minerals Engineering, 17(5), 671-687.

Rajamani, R. K., & Herbst, J. A. (1991). Optimal control of a ball mill grinding circuit—I. Grinding circuit modeling and dynamic simulation. *Chemical Engineering Science*, *46*(3), 861-870.

Skorych, V., Dosta, M., Hartge, E. U., & Heinrich, S. (2017). Novel system for dynamic flowsheet simulation of solids processes. *Powder technology*, *314*, 665-679.

Skorych, V., Dosta, M., & Heinrich, S. (2020). Dyssol—An open-source flowsheet simulation framework for particulate materials. *SoftwareX*, *12*, 100572.

Whiten, W. J. (1972). The simulation of crushing plants with models developed using multiple spline regression. *Journal of the Southern African Institute of Mining and Metallurgy*, *72*(10), 257-264.

M3: Process optimization of fluidized bed opposed jet mills based on a soft sensor for the particle size

Steffen Sander*, *Ergün* Altin and *Tobias* Fuchs

Hosokawa Alpine AG, Augsburg, Germany

Abstract. Measuring the particle size distribution in real time is usually difficult and expensive. Therefore, a soft sensor was developed to predict the fineness of a grinding process in classifier mills. The soft sensor uses machine and process data and helps to detect deviations from the PSD targets in real time. Based on this soft sensor as well as models for the mill and adjacent equipment, optimization of the process conditions becomes possible resulting in maximum throughput and reduced specific energy consumption, respectively.

1 Soft sensor for the particle size

1.1 Background

The particle size distribution of products from grinding and classifying processes is a key parameter in mechanical process engineering and serves as an important quality criterion for the bulk materials produced. The main objective of a comminution process is therefore generally to operate it in such a way that a product with a specified target fineness is produced, ideally with maximum efficiency and the highest possible throughput.

For particle size analysis, offline devices are typically used in laboratories. Therefore, deviations from the specified fineness target can be recognised with a delay only. Alternatively, online, at-line or inline measuring devices can determine the particle size in real time but are expensive, vulnerable for malfunction and often require a high effort for maintenance and calibration.

An interesting alternative for determining the particle size in comminution processes are therefore soft sensors that enable the particle size to be predicted in real time and incur only low procurement and operating costs. In contrast to the soft sensors described in the literature making use of grey box or black box models, the soft sensor for the particle size used here utilises a physical white box model to determine the particle size in real time. The particle size is predicted using a two-stage calculation in which the physical cut size limit determined from the process data is corrected with a calibration curve learnt from the application and dependent on the cut particle diameter.

1.2 Determination of the particle size

The presented HOSOKAWA ALPINE soft sensor for the particle size can always be used if the size reduction process includes a dynamic classification step. In a first calculation step, the cut particle diameter of the classifier is determined utilizing geometrical and process data.

In a second step, the particle size can be calculated using the cut particle diameter and a correction function. This function can be computed using the process data and off-line particle size analysis results of 3-5 process settings. This is one of the biggest advantages of the concept, as black box models require significantly higher number of data sets to achieve a high accuracy for predicting the desired particle size.

1.3 Accuracy of the results

In various campaigns utilizing impact classifier mills of several designs (ACM, ZPS) as well as fluidized bed opposed jet mills (AFG, TDG), it was successfully demonstrated that the particle size determined using the soft sensor in real time agrees with the fineness analyses measured in the laboratory with an average accuracy of nearly 97% (Fig. 1).

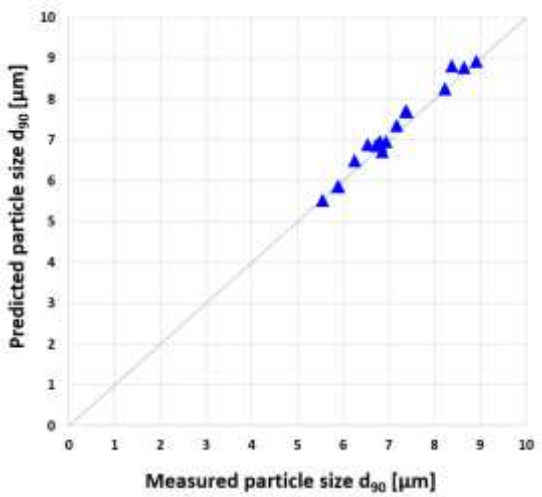

Fig. 1. Comparison of predicted and measured particle sizes for the comminution of talc on an AFG 400

* Corresponding author: s.sander@alpine.hosokawa.com

2 Process optimization of fluidized bed opposed jet mills

2.1 Modelling

Having now access to one of the most important product quality criteria, namely the particle size, it becomes possible to develop process optimisation strategies with respect to the highest throughput and energy efficiency for the desired particle size specification.

For fluidized bed opposed jet mills, such as the HOSOKAWA ALPINE AFG and TDG, the energy available for the comminution process can be computed from the geometry of the nozzles and the process parameters. It can be linked to the throughput, which is determined at the same process parameter sets that are used to train the soft sensor for the particle size. If a measurement of the power draw of the compressor is not available, it can be predicted using the characteristic of the compressor. A statistic model is used to determine the power draw of the fan.

2.2 Validation

In several test trials at the HOSOKAWA ALPINE technical centre using different materials a model could be validated to describe main process output parameters in dependency of the cut size. This could be done for the throughput and blower energy. The grinding gas temperature is one of the parameters of the models. Therefore, they are suitable for operation at ambient and high temperatures.

In the second step, optimization strategies could be determined for a given particle size target with respect to maximum throughput and minimum specific energy consumption, respectively.

2.3 Results

To validate the models and optimization strategies trials were carried out using the parameter sets suggested by the models. As can be seen in fig.2 the throughput and fineness d_{90} obtained with the AFG fluidized bed opposed jet mill are similar to the predicted values.

Moreover, the predictions were challenged by our experienced test centre engineers, who are experts in optimizing the HOSOKAWA ALPINE AFG and TDG fluidized bed opposed jet mills.

The task was to achieve a maximum capacity for two different target particle sizes. Fig. 2 illustrates that the soft sensor-based models obtained apparently similar results to the test centre engineers.

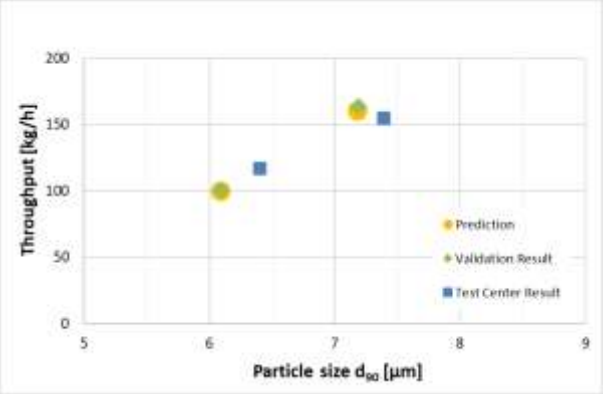

Fig. 2. Validation of predicted and measured throughput in comparison to the results of the experienced test centre engineers.

3 Conclusions

By using process and machine parameters it was shown that it is possible to describe models for the particle size with a high accuracy for classifier mills.

Based on this soft sensor it is also possible to optimize the process conditions such as the throughput and specific total energy consumption for the fluidized bed opposed jet mills.

The main advantages of modelling grinding processes are:

- Real time information on particle size and reduced demand for lab measurements
- Real time process control and fast identification of favourable process conditions
- In future, automated recipes could close knowledge gaps regarding the impending shortage of skilled labour
- New process conditions (recipes) for changing particle size requirements could be easier and faster obtained, resulting in reduced losses for off-spec material.

M4: Closed milling circuit with innovative vertical roller mill for dry and wet comminution

Oliver Schindler[1,*]; *Thomas* Zinke[1]; *Holger* Lieberwirth[1]

[1]Institute for Mineral Processing Machines and Recycling Systems Technology;
TU Bergakademie Freiberg, Freiberg, Saxony, Germany

Abstract. Comminution within confined beds is widely deployed in the dry milling process for cement and ore processing on High-Pressure Grinding Rolls (HPGR) and Vertical Roller Mills (VRM). It shows notable energy efficiency advantages compared to conventional tumbling mills. However, the presence of moisture in the feed material escalates the energy consumption required for drying, thereby mitigating these advantages. A pioneering approach involves the utilization of VRM in an overflow configuration for wet milling purposes. Through collaborative efforts between TU Bergakademie Freiberg and Loesche, a pilot-scale circuit comprising the new type of mill, a vibrating screen, hydro-cyclones, and a centrifuge for solid/liquid separation was developed. This initiative holds promise for enhancing ore liberation efficiency via wet grinding methodologies. The report delineates investigations into the plant operations as well as a first comparison between dry and wet milling utilizing the aforementioned pilot plant setup.

1 Introduction

The current century is characterized by a drive to reduce energy demand, promote e-mobility, and generate energy from renewable resources. This trend significantly impacts the primary raw materials sector. Specifically, the production of electric vehicles and renewable energy exacerbates the demand for key metals (International Energy Agency, 2021). Population growth and increased GDP per capita further contribute to the demand for raw materials (Krausmann et al., 2009). Additionally, the industry faces challenges such as declining ore grades and higher production costs (Schodde, 2019). Primary metal producers aim to reduce costs and emissions, necessitating a reduction in energy consumption. Approximately 1-2 % of global electrical energy is currently consumed by various comminution processes (Segura-Salazar et al., 2021). Especially the commonly used tumbling mills in wet grinding are not known for their energy efficiency. With high-grade deposits depleting, new ones often have lower ore grades and require finer milling (Harder, 2022). The need for the development of a more efficient ore liberation method is given (Peuker et al., 2012).

2 Comminution of ores

The target of every ore processing plant is to recover the contained value minerals. Because of the small mineral size, a comminution to a certain particle size has to take place before the mineral specific sorting can be carried out. SAG and ball mills are prevalent in ore grinding due to their reliability and high capacity, but they are not highly energy-efficient. Efforts have intensified to adopt more efficient technologies, such as HPGR and VRM, especially in dry grinding applications (Segura-Salazar et al., 2021).

HPGR technology has shown promising results, with energy savings of up to 62 % compared to traditional ball mills for gold and copper ore processing (Gagnon et al., 2021). However, HPGR applicability is limited by material moisture content.

Currently, VRMs are mostly operating in airflow mode. Various roller geometries, such as conical rollers with adjustable angles, allow VRMs to adjust achieved shear stresses based on feed material characteristics and comminution targets. When a material with a higher moisture is fed, fine particles tend to agglomerate and adhere to the parts of the dynamic classifier. This has a negative influence to the efficiency of the separation process. Therefore, drying of the material becomes necessary for higher moisture content, thus reducing energy savings. In some climatic regions with high humidity, frequently raining and temperatures below zero, the circumstances are quite challenging to dry the material without additional energy input (Ballantyne and Lane, 2022; Leonida, 2020). Additionally, the airflow mode becomes less effective when the processed ore has a higher density (Reichert, 2016). LOESCHE developed a pilot VRM operating in overflow mode with external air sifting as an energy-efficient alternative to internal classification. Comparisons between internal and external sifting showed similar size reduction ratios and specific energy consumption when dynamic classifiers were used. Energy savings ranging from 19.8 kWh/t to 24.2 kWh/t were achieved compared to conventional rod and ball mill circuits (Altun et al., 2015).

While dry grinding may seem advantageous, studies show wet grinding can be in some cases more efficient (Ogonowski et al., 2018). Furthermore, some mineral sorting technologies can only be carried out as

* Corresponding author: Holger.Lieberwirth@iart.tu-freiberg.de

wet process today. This makes additional drying of the material undesirable for the milling process. Therefore, exploring both wet and dry grinding technologies is essential for optimizing ore comminution processes.

3 The milling circuit

The German Research Foundation (DFG) supported the construction of a comminution circuit for both dry and wet milling of ores using a Vertical Roller Mill. The facility, located at the Institute for Mineral Processing Machines and Recycling Systems Technology (IART) in Saxony, Germany, was built in collaboration with LOESCHE and AKW, representing a closed-circuit system for both wet and dry milling operations. The plant encompasses controlled material feeding considering recirculating load, multi-stage screening, and dewatering via a centrifuge on a pilot scale. Figure 41 shows a simplified flowsheet of the plant.

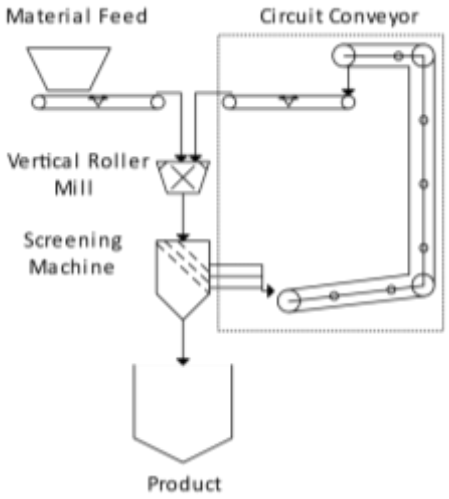

Figure 41: Simplified flowsheet of the milling plant

The plant offers one dry milling and two different wet milling modes. Central components include the new VRM (LM 3.6/3w) developed by LOESCHE and a vibrating round screen (VRS 1500/3) from Allgaier. Designed for a nominal throughput of up to 500 kg/h with a circuit load of up to 5,000 kg/h, separation is achieved at 200 µm, facilitated by relieving decks in the screening machine.

In the circuit, coarse material classified by the screening machine is recirculated to the mill via a tube chain conveyor to ensure a continuous flow. Fresh feed material is added to the mill via a belt feeder equipped with a weighing scale. Material feed is regulated based on recirculated material mass flow and target throughput, enabling consistent mill throughput as desired by the operator.

Routing of fines (< 200 µm) differs in various operating modes. In dry operation, the product is discharged directly after screening. Conversely, in wet milling, the product is transformed into a suspension and pumped through tubes. In the "coarse mode", the suspension undergoes hydro cyclone and centrifuge separation, while in the "fine mode," a flat-bottom hydro cyclone is used as an additional separation step. Process water recovery is recirculated.

Water injection points are included in the mill feed chute, primarily for moistening dry feed material to adjust flowability. Additionally, water spraying onto individual screen decks in wet milling is possible, allowing precise dosage at all water outlets.

4 Performed experiments

Initial milling tests aimed to assess the processing plant's response to various combinations of milling parameters, employing simplifications to establish process boundaries. Granodiorite from the nearby Kindisch quarry is chosen as the test material for its resemblance to ore host rocks and widespread availability. Characterized by mica, feldspar, and quartz, the granodiorite has a Bond-Work-Index of 16.3 kWh/t and a Point-Load-Index of 7.0 MPa (Reichert, 2016). The material was fed as a fraction of 0/8 mm to the plant with mostly constant particle size distribution.

The primary milling parameters investigated in the initial tests include milling pressure (in kN/m²), milling table speed (in m/s), and mill throughput (in kg/h), all controllable via the programmable logic controller (PLC). The experiments commenced with a mill throughput of 1625 kg/h. Additionally, the input parameter of added water flow or moisture was considered for wet milling operations. An initial feed moisture of approximately 15 % was set for wet milling tests, based on findings by (Ballantyne and Lane, 2022). Wet milling tests were conducted solely in the coarse mode, wherein product classification at 200 µm was consistent for both dry and wet milling, facilitating comparability. In reference to the maximum feed size, a size reduction ratio of $\varepsilon = 40$ was assumed for simplicity.

Within the PLC, milling parameters are continuously monitored and recorded. Currently, the determination of the processes stationary point is primarily left to the operator's discretion. This decision is typically based on observations of feed and mill throughput, power consumption and milling bed height. Once the decision is made, a fixed ten-minute interval is allocated to calculate the mean values of the signals followed by sampling of the material flows.

Various tests have been conducted, some with fixed settings and others with varying milling parameter configurations to assess the stability of the process and the impact of milling parameters. Given that fresh material is continuously fed, each sample and calculated mean is considered independent of the others. This contribution focuses solely on the analysis of continuously logged data with particular emphasis on feed throughput. Among the continuously logged data, feed throughput was found to be the most unstable parameter. Moreover, it significantly influences the operator's perception of whether the process is stable or not.

5 Achieved results

To assess the stability of the process, tests involving only the same milling parameter are considered. A number of sample intervals of one ongoing test were then subjected to a t-test against the current gross mean of the corresponding parameter setting according to (Napier-Munn, 2020). The diagram in Figure 42 illustrates the ratio of the t-value to the critical t-value (t*) over the time difference from the first observation time. A ratio of one or greater signifies rejection of the null hypothesis, indicating a significant difference from the gross mean at a significance level (α) of 0.05. The diagram presented only encompasses dry milling tests and is conducted using a two-sided t-test.

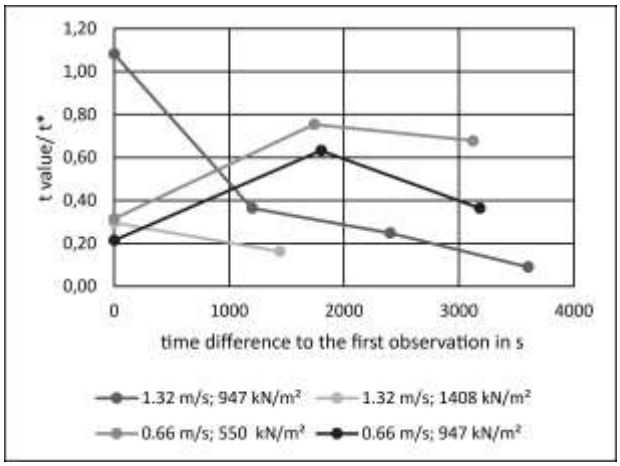

Figure 42: t-value ratio to critical t-value over time; dry milling

Only one observation displays a ratio greater than 1.0, indicating a significant difference from the gross mean of its corresponding mill setting. However, the remaining observations do not show any notable difference to their respective gross means. Furthermore, there is no discernible overall pattern. This suggests that the initially made assumption for the stability condition is generally applicable. Further analysis of the observed significantly different data point reveals that in this specific case, the decision regarding the stationary point was made prematurely. Consequently, the calculated mean was still affected by the preceding start-up process.

Figure 43 depicts a diagram illustrating the comparison of achieved feed material throughputs as a function of milling pressure and milling table speed. In addition to various dry milling tests, a wet milling trial run with a feed moisture of 15 % is plotted at its corresponding parameter setting. Due to the PLC design and the obligatory mass balance in stationary plant operation, the feed throughput can be assumed to be the same as the product throughput.

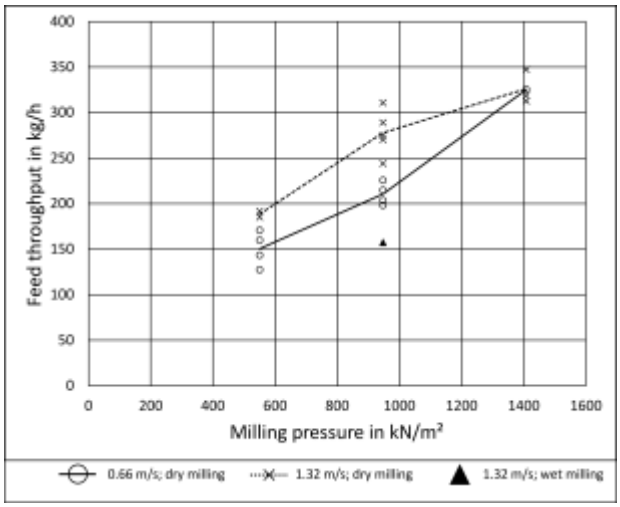

Figure 43: Feed throughput in dependence of the milling parameters

The milling pressure exerts a significant influence on the feed throughput, whereas the milling table speed has a lesser impact. In contrast, the wet milling test exhibits a considerable deviation from the corresponding dry tests. This variance could be attributed to various factors, e.g., differences in the particle size distribution of the feed material.

Specific energy consumption is primarily affected by the milling table speed. Specifically, at a speed of 1.32 m/s, the energy consumption ranges between 12 and 14 kWh/t, whereas at 0.66 m/s, it falls between 8 and 10 kWh/t. Interestingly, within these test conditions the milling pressure appears to have minimal impact on specific energy consumption. The wet milling test demonstrates a specific energy consumption of 11.27 kWh/t at 947 kN/m² and 1.32 m/s. While this represents only a minor difference compared to dry milling, the reduction in energy consumption seems disproportionate to the lower feed throughput observed during wet milling.

6 Discussion and Outlook

The tests presented here mark just the beginning of a comprehensive exploration of the VRM wet grinding plant. Special attention should be given to the wet grinding trials. It is crucial to rigorously examine the sampling methodology to ensure the independence of consecutive samples. Moreover, the particle size distributions, which have not been addressed yet, require attention. After completing trials with the granodiorite test material, milling processes involving ores will follow, taking into account the mineral liberation effects of milling parameters.

As it already can be observed from the few presented data, it is quite complicated to obtain a statistically correct impression of the ongoing process and the subsequent analysis. Therefore, more statistic considerations should be applied for the data analysis.

References

Altun, D., Gerold, C., Benzer, H., Altun, O. and Aydogan, N. (2015) 'Copper ore grinding in a mobile vertical roller mill pilot plant', *International Journal of Mineral Processing*, vol. 136, pp. 32–36.

Ballantyne, G. R. and Lane, G. (2022) 'Comparison of dry VRM or HPGR circuits to wet milling circuits', *IMPC Asia-Pacific 2022.* Melbourne, 22.08.2022, pp. 93–99.

Gagnon, C., Rosa, A., Makni, S., McIvor, R., Klein, B., Kumar, A., Fisher, W., Gong, D. and Saud, C. (2021) *REPLACEMENT OF WET BALL MILLING WITH HIGH-PRESSURE GRINDING AHEAD OF MINERAL SEPERATION,* Corem and University of British Columbia.

Harder, J. (2022) *Trends in the mining industry - Aufbereitungstechnik* [Online]. Available at https://www.at-minerals.com/de/artikel/at_Trends_in_the_mining_industry_3596020.html (Accessed 4 July 2022).

International Energy Agency (2021) *The Role of Critical Minerals in Clean Energy Transitions: World Energy Outlook Special Report*.

Krausmann, F., Gringrich, S., Eisenmenger, N., Erb, K.-H., Haberl, H. and Fischer-Kowalski, M. (2009) 'Growth in global meaterial use: GDP and population during the 20th century', *Ecological Economics*, vol. 68, no. 10, pp. 2696–2705.

Leonida, C. (2020) *Mining to Energy Efficiency and Beyond* [Online]. Available at https://www.e-mj.com/features/mining-to-energy-efficiency-and-beyond/ (Accessed 5 August 2022).

Napier-Munn, T. J. (2020) *Statistical methods for mineral engineers: How to design experiments and analyse data*, 2020th edn, Indooroopilly, Queensland, JKMRC Julius Kruttschnitt Mineral Research Centre.

Ogonowski, S., Wołosiewicz-Głąb, M., Ogonowski, Z., Foszcz, D. and Pawełczyk, M. (2018) 'Comparison of Wet and Dry Grinding in Electromagnetic Mill', *Minerals*, vol. 8, no. 4, p. 138.

Peuker, U. A., Kwade, A., Teipel, U., Jäckel, H.-G. and Mütze, T. (2012) 'Aufbereitungstechnik: Aktuelle verfahrenstechnische Fragestellungen für die Aufbereitung von mineralischen, nachwachsenden und sekundären Rohstoffen ; Positionspapier der ProcessNet-Fachgruppen "Zerkleinern/Klassieren", "Grenzflächenbestimmte Systeme", "Mechanische Flüssigkeitsabtrennung"'.

Reichert, M. (2016) *Erzmahlung in Wälzmühlen*, Dissertation, Freiberg, TU Bergakademie Freiberg.

Schodde, R. (2019) 'Role of Technology and Innovation for Identifying and Growing Economic Resources', in *AMIRA International's 12th Biennial Exploration Managers Conference*.

Segura-Salazar, J., Santos, N. d. S. L. and Tavares, L. M. (2021) 'Holistic Pre-Feasibility Study of Comminution Routes for a Brazilian Itabirite Ore', *Minerals*, vol. 11, no. 8, p. 894.

N1: Bioleaching of valuable metals from black mass originated from LFP and NMC Li-ion batteries

Mádainé-Üveges V.[1], Butylina S.[2], Sethurajan M[2], Nouaili A. [1], Spekker, D.[3] and Bokányi L. [1]

[1]Faculty of Earth and Environmental Sciences and Engineering, University of Miskolc, Miskolc, Hungary
[2] Department of Separation Science, LUT University, Finland
[3]Metal Shredder PLC, Miskolc, Hungary

Abstract. Li-Ni-Mn-Co-Oxide (NMC) and $LiFePO_4$ (LFP) batteries are gaining ground in electric vehicles and their recycling is expected to become a hot topic over the next decade at industrial size. Among the possible processing methods, this research focuses on the bioleaching of lithium and other metals, assisted by the *Acidithiobacillus ferrooxidans* bacteria, and *Acidithibacillus ferridurans* strain. Inhibition analysis and laboratory-scale biosolubilisation experiments were carried out with the two types of black mass materials. The results show that the LFP battery black mass has an overall positive effect on the growth of both bacteria at the concentrations tested (up to 2 g/L). Bioleaching experiments were carried out at 28 ^{o}C, for two weeks at different solid/liquid ratios, and as a result, it was established, that the inhibitory behaviour of the NMC battery materials is a barrier to the application of higher (>5 g/L) solid content, while increasing the solid content from 5 to 10g/L in case of LFP black mass, resulted higher recovery values. These findings narrow down the possible recycling routes for NMC-type batteries, but opens the way for bio-recovery in the LFP line. For such considerations, the production and use of LFP can be declared as preferable from point of view of their recycling by bioleaching.

1 Introduction

The world market size of LIBs grows unstoppable in the last 10 years, and undoubtedly the reason of this tendency, especially for the last 5 years can be found in their application in electric vehicles. Circular economy and sustainability goals give clear tasks to industry to find the most economical and environmental friendly way and build capacities for battery recycling (Chen et al, 2020). The first challenge to overcome is to identify the type of battery, especially in case of electric car originated ones. The composition varies with the producer and because of continuous developments, with production date as well, and from the side of recycling industry it has a big importance, whether a NMC (nickel, manganese, cobalt) or LFP (lithium, ferro-phosphate) battery to be processed. Regarding the economic aspects, big differences can be directed from the approximate value of the components, for example, while cobalt price was around 30,000 USD/ton in 2023-2024, iron ore was about 120USD/ton according to the data from source: web1. Besides, different recycling methods can be appropriate and methods such as mechanical, thermal, hydrometallurgical, or even mechano-chemical treatment and their combination of these can work (Tawonezvi et al, 2023). A promising method to obtain metals recovery under the egis of green chemistry called bioleaching is getting increasing attention in the last decade for electronic wastes (Roy et al, 2021).

Bioleaching is the process, when metals from primary or secondary raw material sources are recovered by microorganisms assisted mechanisms, so metal dissolution carried out under less vigorous circumstances compared to conventional chemical leaching. Species of the genus *Acidithiobacillus* can be used for this purpose (Mádainé, 2022). There are already many results reported in scientific literature, for example Xin et al, 2016, found that metals can be extracted with more than 95% recovery from spent electric vehicle LIBs, but industrial application still hindered by low solid concentration (1% w/v) and elongated residence time. *Acidithiobacillus* bacteria are acidophilic, Gram-negative, rod-shaped, facultative anaerobe bacteria that obtain the carbon for autotrophic growth from the atmospheric CO_2 and energy from the oxidation of elemental sulphur and sulphur compounds, or iron and iron compounds. *Acidithiobacillus ferrooxidans*, which oxidises Fe^{2+} ions to Fe^{3+} ions and produces sulphuric acid from sulphur compounds (S^0, $S_2O_3^{2-}$, H_2S or polysulphides) is the best-known species, the less commonly used *Acidithiobacillus ferridurans* has similar characteristics, being able to use elemental sulphur (S^0) and Fe^{2+} and $S_4O_6^{2-}$ ions, or hydrogen, as electron donors (Hedrich and Johnson 2013). The mechanisms of bioleaching by *A. ferrooxidans* are usually discussed in terms of direct bacterial attack on sulphide minerals and indirect oxidative dissolution of minerals by Fe^{3+}.

Initially the application of these microorganisms for metal recovery was performed from low-grade ores, but as such streams have expanded, research turned to waste side. Although the bacteria have high tolerance against metals and can be adopted to different wastes, it is shown for NMC type battery, that above 10g/L, a sharp reduction was reported in leaching efficiency (Roy

* Corresponding author: valeria.uveges@uni-miskolc.hu

et al., 2021). Jarosite formation, lower oxygen levels due to elevated viscosity and metal toxicity were the identified reasons. So, it was revealed, that especially in case of Li-ion battery, Co, Ni and Mn content can limit the application of higher pulp density during leaching. To predict the behaviour of the bacteria before performing bioleaching tests, it is recommended to monitor bacterial growth in the presence of waste. Moreover, it would be advisable to be able to interact in real time when growth curve shows undesired behaviour. By monitoring the growth condition of a bacterial culture from the beginning of the cultivation, some basic malfunctions, like bad timing can be avoided. The age of the cells at the time bioleaching starts, is very important, for instance lag-phase cells are more sensitive to inhibition than log-phase cells (Kovalenko et al., 1982). There are limitations to the methods known from the literature for monitoring the growth of microorganisms, particularly in the case of *A. ferroxidans* and *A. ferridurans*, which are 1.5 microns in size and produce a jarosite precipitate in their culture medium as the population grows. The hoped-for future role of these bacteria in the biosolubilisation of electronic waste justifies the need to monitor their growth in real time, even in the presence of fine powdery waste. This will also allow the determination of toxic limit concentrations.

The aim of our preliminary research in the field of bioleaching of LIBs was to investigate the possibility of lithium and other valuable metals recovery from the black mass of two different type of waste LIBs: NMC and LFP.

2 Materials and methods

2.1. Battery samples

Batteries (LFP and NMC type) were collected and discharged to remove any residual charge. In order for the separation of black mass a series of unit operations were carried out. Initially, a two stage shredding was done followed by thermal treatment at 60°C to remove the electrolyte solvent and finally size separation by hand sieving was carried out. In case of LFP battery, black mass was separated at 1mm, while for the NMC, 0.5mm was chosen.

2.2 Acid digestion

Black masses (BM) were water washed and dried before experiments and samples were dissolved from each type of BM in strong hydrochloric acid to analyse the solutions by atomic absorption spectroscopy (AAS, PerkinElmer Analyst 400). Solutions after bioleaching experiments were also analysed by AAS to calculate the metal recovery.

2.3 Microorganisms and growth

2.3.1. Inhibition analysis

The inhibition analysis prior bioleaching can serve information about limitations for tolerable pulp density. These measurements were carried out by Hamilton Bonaduz on-line cell monitoring system at Institute of Raw Materials Preparation and Environmental Technology. The system is equipped with four measuring rods, the two main sensors besides the pH and dissolved oxygen meters are the so-called Incyte and Dencyte sensors. Our attempt to use this device for *Acidithiobacillus ferridurans* is the first one in the history of Hamilton. Hamilton sensors during work are shown in Fig. 1. Inhibition analysis for LFP battery black mass was carried out with *A. ferrooxidans* and *A. ferridurans* at 0.5, 1 and 2 g/L concentration, the waste powder (x<1mm) was added at late log phase and suspension was agitated 8hours/day.

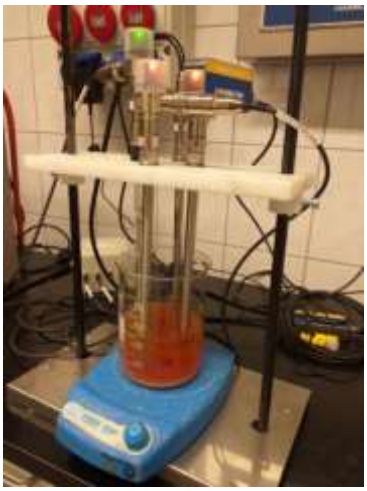

Fig. 1**.** Hamilton sensors during bacterial growth analysis

2.3.2 Growth medium

During the experiments, *Acidithiobacillus ferrooxidans* ATCC 23270 and *Acidithiobacillus ferridurans* ATCC 33020 bacteria were used. Both were isolated from acid mine drainage in Slovakia and kindly provided by the Geotechnical Research Institute of the Slovak Academy of Sciences. The composition of the nutrient solution used for cultivation per 1 litre total volume is as follows. Solution 'A' consists of 3g $(NH_4)_2SO_4$, 0.1g KCl, 0.5g K_2HPO_4, 0.5g $MgSO_4$*7 H_2O, 0.0144g $Ca(NO_3)_2$*4 H_2O and 700 ml deionized water. The iron (II) sulphate solution 'B' (consists of 44.24g $FeSO_4$*7 H_2O, 10ml 1N H_2SO_4 and 300 ml deionized water) is not autoclavable, because the Fe^{2+} ion would be oxidised, so this solution was filter-sterilised before being mixed with the autoclaved sterilised and cooled solution 'A'. The pH of the solution was adjusted to 2.3-2.5 by further addition of sulphuric acid, and 10% inoculum (old culture) was used for inoculation. Equal age of bacteria was provided by 2fold inoculation with 1 week frequency before each experiment.

2.2 Bioleaching experiments

The bioleaching experiments were carried out using Wise Cube shaker at 28°C for 14 days at a rate of 150rpm. For the bioleaching experiments of NMC type battery, 3 solid concentrations of BM were used: 5g/L, 20g/L and 52.5g/L to evaluate the effect of black mass on the bacterial activity and thus on the solubilisation of metals. For LFP type battery, it was decided to investigate at this preliminary experiment phase lower concentrations, such as: 2, 5 and 10g/L, since to the best of our knowledge there was no data available for the bioleaching of this substrate with *Acidithiobacillus ferrooxidans* or *A. ferridurans*.

After 14 days, suspensions were filtrated and subjected to AAS analysis.

3 Results

Soluble metal content of LFP and NMC batteries black masses were determined by chemical leaching. Based on the results of solution analysis, the Li content of LFP battery was 2.89%. The soluble Li content of BM of NMC type battery was 1.41%, while Mn, Ni and Co content were 12.28%, 4.72% and 1.07% respectively. These data serve as basis for the calculation of recovery results of bioleaching experiments.

3.1 Inhibition analysis

Before LFP bioleaching experiments, inhibiton analysis was performed to determine the possible solid concentration for leaching using Hamilton on-line cell monitoring system. Incyte sensor works on the principle of permittivity measurement, the number of living cells can be deduced from the measured values and conductivity values can also be read. Permittivity is measured at the frequency specific to the cell type, which for bacteria is 1MHz. Direct bacterial count under microscope to evaluate number of cells is hindered by the formation of precipitate during bacterial growth, as it is reported by several researchers (Roy et al, 2021), so permittivity results from Hamilton in pF/cm units were accepted by us as an indicator of the condition of bacterial population. The growth curve of the echte cultures in 9K solution and the permittivity results for sterile 9K can be seen in Fig. 2 (Mádainé, 2022).

It was revealed, that both bacterial straines were able to take nutrients from this source, but especially *A. ferridurans* interacted well for the elevated solid concentrations, as can be seen from Fig.3, where growth curves of this bacteria with the presence of LFP black mass at different solid concentrations are presented.

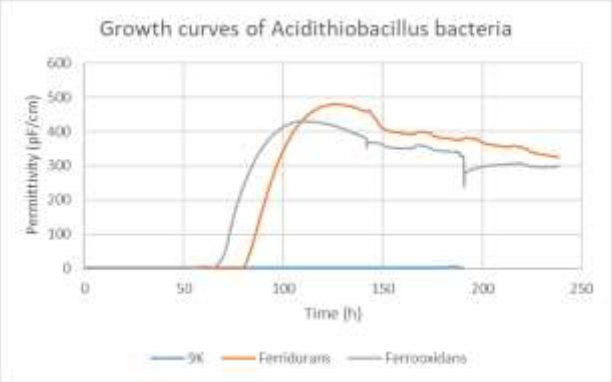

Fig.2. Growth curves of *Acidithiobacillus ferrooxidans* and *Acidithiobacillus ferridurans* in 9K solution plotted by data from Hamilton Bonaduz Incyte sensor (Mádainé, 2022).

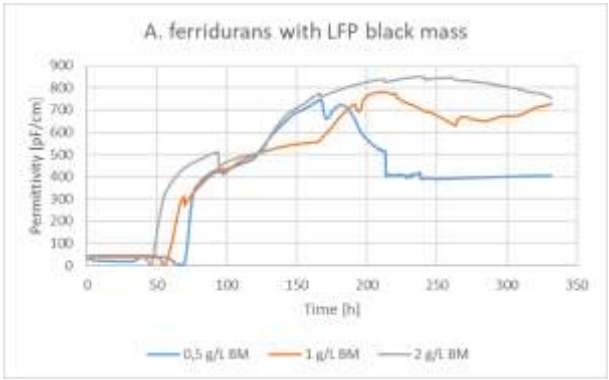

Fig.3. Inhibition analysis results with Hamilton Bonaduz Incyte sensor for *A. ferridurans* with the presence of LFP black mass

Comparing population growth curves without and with black mass the upward shift in the permittivity and shift in the residence time can be indicated. It also proves that black mass from LFP-s enhances the population growth. On Fig.3 it can be seen, that at 2g/L concentration, the growth curve fits better the echte cultured case, so it was decided to apply this concentration as the lowest when bioleaching experiments performed.

3.2 Bioleaching experiments

Based on the results of bioleaching experiments of the LPF battery BM, particulary on the average lithum concentrations measured in filtrates of parallel experiments after 14 days, it can be drawn, that at 2g/L and 5 g/L solid concentrations, the lithium recovery was about the same (near 55% for *A. ferrooxidans* and 42% for *A. ferridurans*), but increasing the solid concentration from 5g/L to 10g/L the lithium recovery increased, as it can be seen from Fig. 4. This predicts, that in this system, besides possible inhibitory elements like Li, Al and Cu, there are ions, presumably iron and phosphate which could play a role of additional substrates in bacterial growth and bioleaching performance. But further research should be done to reveal the mechanism.

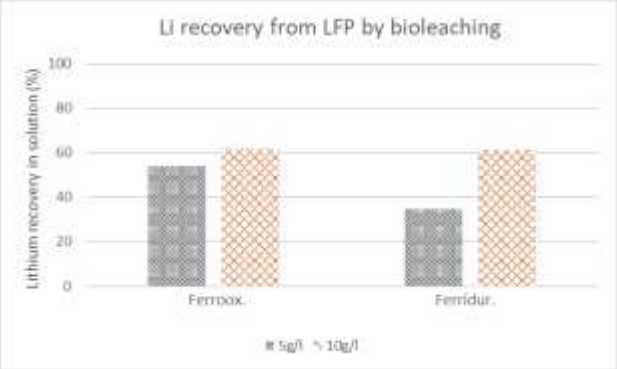

Fig.4. Li recovery in solution at 5g/L and 10 g/L solid concentration after bioleaching

In case of NMC battery bioleaching, highest metal recovery was reached, when 5g/L solid concentration was used. According to the data can be seen from Fig. 5 bioleaching was as efficient as HCl leaching at this solid concentration for Li and was sufficient for Mn, but for Ni and especially for Co, recovery was poor.

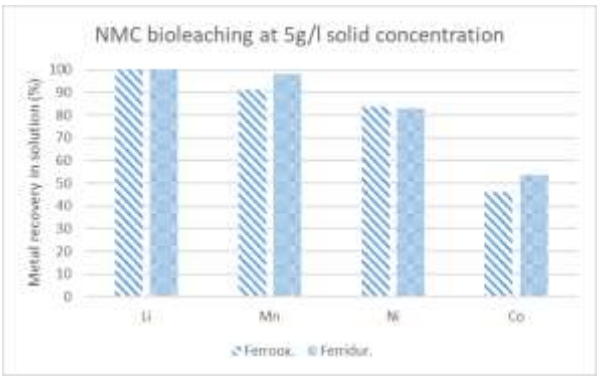

Fig. 2. Recovery of valuable metals in solutions after bioleaching NMC battery black mass at 5g/L solid concentration

Metal recovery decreased when solid concentration was raised above 5g/L. Li recovery reduced to around 85% for 20g/L and around 53% for 52.5g/L. In case of other metals, the same tendency was observed.

4 Conclusions

Preliminary experiments were carried out to investigate *Acidithiobacillus ferrooxidans* and *Acidithiobacillus ferridurans* bacteria assisted leaching as a possible process for the recycling of electronic vehicle batteries. Black masses produced by mechanical pretreatment at Institute of Raw Material Preparation and Environmental Technology were used for inhibitory analyses in case of LFP type battery and for bioleaching preliminary experiments for both LFP and NMC type.

It was revealed, that both strains are able to solubilise metals from both types of LIBs. Li-recovery in case of LFP is lower than at NMC. It was further revealed that although lithium recovery from NMC type battery was higher at 5g/L concentration, than from LFP, above 5g/L solid concentration, in case of NMC lithium (and other metals) dissolution were hindered, while in case of LFP type black mass, higher pulp density resulted higher metal lithium recovery. An explanation for this paradoxon can be the overall positive effect of the existing ions in LPF system, such as iron and phosphate as a contrast with the inhibiting effect of ions releasing from NMC batteries. These findings narrow down the possible recycling routes for NMC-type batteries, but opens the way for bio-recovery in the LFP line. For such considerations, the production and use of LFP can be declared as preferable from point of view of their recycling by bioleaching.

Authors would like to thank István Illés research & development manager at Metal Shredder PLC for chemical analysis of black mass and solutions. This project is funded by the European Union's Horizon Europe program under grant no. 101079354.

References

Chen, T-L., Kim, H., Pan, S-Y., Tseng, P-C, Liu Y-P., Chiang, P-C. (2020) Implementation of green chemistry principles in circular economy system towards sustainable development goals: Challenges and perspectives. *Science of the Total Environment*, Vol. 716; 136998

Hedrik, S and Johnson, D. B. (2013) Acidithiobacillus ferridurans sp. nov, an acidophilic iron-, sulphur-, and hydrogen metabolizing chemolitotrophic gammaproteobacterium.". *International Journal of Systematic and Evolutionary Microbiology*, 4018-4025.

Roy, J. J., Madhavi, S., Cao, B. (2021) Metal extraction from spent lithium-ion based batteries (LIBs) at high pulp density by envrionmentally freindly bioleaching process. *Journal of Cleaner Production 280,124242, 1-9*

Kovalenko T. V., Karavaiko, G.I, and Piskunov V.P. (1982) Effect of Fe3+ ions in the oxidation of ferrous iron by *Thiobacillus ferrooxidans* at various temperatures. *Mikrobiologiya 51:156-160.*

Mádainé Üveges, V. (2022) Some innovative applications of reaction-techniques and bio-process engineering in waste management. PhD dissertation (in Hungarian). Mikoviny Sámuel Doctoral School of Earth Sciences, University of Miskolc

Tawonezvi, T., Nomnqa, M., Petrik, L. and Bladegroen B.J. (2023) Recovery and recycling of valuable metals from spent Lithium-ion batteries: a comprehensive review and analysis. *Energies, 16, 1365, 1-35.*

web1: https://tradingeconomics.com/commodities

Xin, Y., Guo, X, Chen, S., Wang, J., Wu, F. and Xin, B. (2016) Bioleaching of valuable metals: Li, Co, Ni and Mn from spent electric vehicle Li-ion batteries for the purpose of recovery. *Journal of Cleaner Production, Vol 116, 249-25*

N2: INVESTIGATION OF HEAT AND MASS TRANSFER OF CASSON FLUID FLOW OVER STRETCHING AND SHRINKING SHEET

K. N. Sneha[1], *U. S.* Mahabaleshwar[1], Payman Jalali[2] and *Gabriella* Bognár[3, *]

[1]Faculty of Engineering, Davangere University, Davangere, India
[2]School of Energy Systems, Lappeenranta-Lahti University of Technology, Lappeenranta, Finland
[3]Faculty of Mechanical Engineering and Informatics, University of Miskolc, Miskolc-Egyetemváros, Hungary

Abstract. The current study examines an magnetohydrodynamic effect of non-Newtonian fluid flow and heat transfer over a stretching/shrinking sheet with velocity slip and temperature jump in the thermo-hydrodynamic attribution of boundary layer flow of an incompressible liquid with two types of carbon nanotubes (CNT), namely single wall carbon nanotubes and multi wall carbon nanotubes taking into account the mass transpiration and radiation impact. As a result, the carbon nanotubes (CNTs) used are analyzed with favourable prospects for applications involving heat transfer.

1 Introduction

The stretching/shrinking sheet determines how the boundary layer moves around the surface. Here, we saw how the magnetic boundary layer affected fluid motion. In the large field of engineering applications, heat, and transport in accelerating sheets are thoroughly studied. A few examples of industrial applications include glass fiber synthesis, hot rolling, wire drawing, polymer extrusion, and thin-film fabrication. Energy and mass transmission are key factors in determining the desired outcome in an accelerating sheet. Analytical studies on boundary-layer flows concentrate on continuous accelerating sheets with magnetohydrodynamic (MHD) effects. The research on the boundary layer flow of a continuously stretching surface was first carried out by Sakiadis (1961a, 1961b), then by Crane (1970), who was successful in providing exact solutions to the two-dimensional Navier-Stokes equations regulating the flow of a stretching plane. Then, Gupta and Gupta (1979) investigated Crane's flow for surface suction or injection. For MHD flow and slip flow over a stretching surface, Andersson (1995, 2002) provided exact solutions. New impermeable and permeable solutions for stretching sheets were introduced by Liao (2005, 2007). In a two-dimensional stretched plane flow with velocity slip and wall suction, Wang (2009) examined a closed-form solution.

The novelty of the current research is that we investigate the MHD fluid flow and heat transfer analogies as well as significance-based nanofluids' flow along stretching/shrinking surfaces. The Casson fluid, containing CNTs with MHD effects through momentum and temperature profiles is examined by an analytical technique. The effects of physical parameters on the graphical representations of the profiles, such as Casson fluid, mass transpiration, the magnetic parameter, and first- and second-order parameters are also discussed using various plots.

2 Problem formulation

In the presence of a homogeneous magnetic field, the Casson fluid flows through first and second-order slips brought on by the linearly stretching/shrinking sheet is investigated. A second-order derivative of the velocity and temperature profile can explain MHD effects. Heat transfer research involves the use of nanoparticles in Casson fluid flow. Assume a continuous laminar flow across a stretching or shrinking surface that lies in a porous medium along $y > 0$, with the x-axis running along the surface and the y-axis measuring normal to it. The ambient fluid temperature is T_∞. The quantity $d = \frac{\alpha_1}{c}$, is the stretching/shrinking parameter with $u_w = \alpha_1 x$. A two-dimensional incompressible fluid flow in Cartesian coordinates (x, y) with its origin at the surface of the wall is used to describe the fluid flow. The suggested model is as follows (see Bognár & Mahabaleshwar (2024):

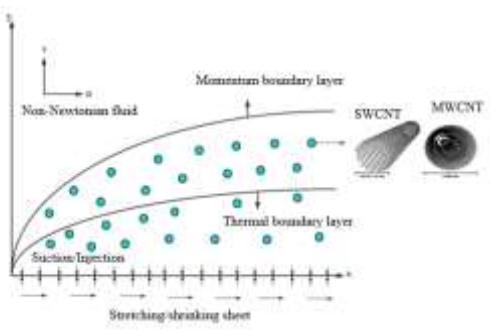

Fig. 1. Physical model of the stretching/shrinking surface.

* Corresponding author: gabriella.v.bognar@uni-miskolc.hu

$$\frac{\partial u}{\partial x}+\frac{\partial u}{\partial y}=0, \quad (1)$$

$$u\frac{\partial u}{\partial x}+v\frac{\partial u}{\partial y}=\nu_{nf}\left(1+\frac{1}{\Lambda}\right)\frac{\partial^2 u}{\partial y^2}-\frac{\sigma_{nf}{B_0}^2}{\rho_{nf}}u, \quad (2)$$

$$u\frac{\partial T}{\partial x}+v\frac{\partial T}{\partial y}=\frac{\kappa_{nf}}{(\rho C_P)_{nf}}\frac{\partial^2 T}{\partial y^2}-\frac{1}{(\rho C_P)_{nf}}\frac{\partial q_r}{\partial y}+\frac{Q_0(T-T_\infty)}{(\rho C_P)_{nf}}. \quad (3)$$

The boundary conditions associated with the above equation are given by

$$u(x,\infty)=0, v(x,0)=v_w,$$
$$u(x,0)=u_w(x)+b_1\frac{\partial u}{\partial y}+b_2\frac{\partial^2 u}{\partial y^2},$$
$$T(x,\infty)=T_\infty, T(x,0)=T_w(x)+a\frac{\partial T}{\partial y}. \quad (4)$$

Suitable similarity transformations are given by

$$\eta=\sqrt{\frac{c}{\nu_f}}y, u=cxf'(\eta), v=-\sqrt{c\nu_f}f(\eta). \quad (5)$$

with some constant *c*. After using Eq. (5) in Eqs. (1) to (3), the following ordinary differential equations can be derived

$$\varepsilon_1\left(1+\frac{1}{\Lambda}\right)f_{\eta\eta\eta}(\eta)+\varepsilon_2\left(f(\eta)f_{\eta\eta}(\eta)-{f_\eta}^2(\eta)\right)-\varepsilon_3 M f_\eta(\eta)=0, \quad (6)$$

with boundary conditions associated as

$$f(0)=V_C, f_\eta(0)=d+\alpha f_{\eta\eta}(0)+\beta f_{\eta\eta\eta}(0), \eta\to 0,$$
$$f_\eta(\infty)=0, \eta\to\infty. \quad (7)$$

Here, $M=\frac{\sigma_f B_0^2}{\rho_f c}$ is the magnetic parameter, $V_c=-\frac{v_w}{\sqrt{cx}}$ represents the mass transpiration, *d* denotes the stretching/shrinking surface, v_w is the wall suction/injection, and $\varepsilon_1=\frac{\mu_{nf}}{\mu_f}, \varepsilon_2=\frac{\rho_{nf}}{\rho_f}$ and $\varepsilon_3=\frac{\sigma_{nf}}{\sigma_f}$ are non-dimensional parameters.

The thermophysical characteristics of carbon nanofluids are obtained from the models available in the literature. The effective dynamic viscosity, density and heat capacity are given by the classical expressions as

$$\mu_{nf}=\frac{\mu_f}{(1-\varphi)^{2.5}},$$
$$\rho_{nf}=(1-\varphi)\rho_f+\varphi\rho_{CNT},$$
$$(\rho C_p)_{nf}=(1-\varphi)(\rho C_p)_f+\varphi(\rho C_p)_{CNT}.$$

The electrical conductivity is

$$\sigma_{nf}=\sigma_f\left\{1+\left[3\varphi\left(\frac{\sigma_{CNT}}{\sigma_f-1}\right)\right]\left[\frac{\sigma_{CNT}}{\sigma_f}-2-\left(\frac{\sigma_{CNT}}{\sigma_f-1}\right)\varphi\right]^{-1}\right\}.$$

Let us assume the analytical solution for the momentum equation of Eq. (6) and Eq. (7) is of the form

$$f(\eta)=A+B\exp(-\lambda\eta). \quad (8)$$

We note that $f(\eta)$ is

$$f(\eta)=V_C+\frac{d[1-exp(-\lambda\eta)]}{\lambda(1+\alpha\lambda-\beta\lambda^2)}. \quad (9)$$

Boundary conditions in (7) are satisfied with the choice of

$$A=V_C+\frac{d}{\lambda(1+\alpha\lambda-\beta\lambda^2)}, \quad B=\frac{-d}{\lambda(1+\alpha\lambda-\beta\lambda^2)}.$$

Then, the velocity and wall shear stress are obtained from Eq. (9) as

$$f_\eta(\eta)=\frac{d[1-exp(-\lambda\eta)]}{1+\alpha\lambda-\beta\lambda^2}, \quad (9a)$$

$$f_{\eta\eta}(0)=-\frac{d\lambda}{1+\alpha\lambda-\beta\lambda^2}. \quad (9b)$$

By using solutions (8) and (9) in Eq. (6), we get the following fourth order equation for λ

$$\varepsilon_1\left(1+\frac{1}{\Lambda}\right)\beta\lambda^4-\left(\varepsilon_1\left(1+\frac{1}{\Lambda}\right)\alpha+\varepsilon_2 V_C\beta\right)\lambda^3-\left(\varepsilon_1\left(1+\frac{1}{\Lambda}\right)-\varepsilon_2 V_C\alpha+\varepsilon_3 M\beta\right)\lambda^2$$

$$-(\varepsilon_2 V_C+d\varepsilon_2-\varepsilon_3 M\alpha)\lambda+(\varepsilon_2 d+\varepsilon_3 M)=0. \quad (10)$$

To extend the results of this study, consider the skin friction parameter C_f defined as $C_f=\frac{\tau_w}{\rho_f {u_w}^2}$, and

$$f_{\eta\eta}(0)=-\frac{d\lambda}{1+\alpha\lambda-\beta\lambda^2}. \quad (11)$$

Here, $Re_x=\frac{cx^2}{\nu_f}$ is called a local Reynolds number.

Using Rosseland's approximation

$$q_r=-\frac{4\sigma^*}{3k^*}\frac{\partial T^4}{\partial y}, \quad (12)$$

the term T^4 can be expanded by using Taylor's series and ignoring higher-order terms to get

$$T^4\cong -3T_\infty^4+4T_\infty^3 T. \quad (13)$$

By using Eqs. (12), (13), Eq. (3) reduces to

$$uT_x+vT_y=\frac{1}{(\rho C_p)_{nf}}\left(\kappa_{nf}+\frac{16\sigma^* T_\infty^3}{3k^*}\right)T_{yy}+\frac{Q_0(T-T_\infty)}{(\rho C_p)_{nf}}. \quad (14)$$

The boundary conditions are as follows

$$T(x,\infty)=T_\infty, T(x,0)=T_w(x)+c_1\frac{\partial T}{\partial y}. \quad (15)$$

In this section, we employ the temperature variable that alters the temperature equation, $T=T_\infty+xT_0\theta(\eta)$. Using Eqs (14) the following ODE can be derived

$$(\varepsilon_5+N_R)\theta_{\eta\eta}+Pr\varepsilon_4(f\theta_\eta-f_\eta\theta)+N_I Pr\theta=0. \quad (16)$$

Similarly, the effective d

where $\varepsilon_4=\frac{(\rho C_p)_{nf}}{(\rho C_p)_f}$, and $\varepsilon_5=\frac{\kappa_{nf}}{\kappa_f}$.

The thermal conductivity of nanofluids, if considered on a limited scale, applies to particles that resemble the shape of a circle or an ellipse. This, however, does not qualify to show the required properties of spatial distribution. Suggested carbon nanotube model yields the ratio of thermal conductivities

$$\frac{\kappa_{nf}}{\kappa_f}=\frac{1+\varphi+2\varphi\frac{\kappa_{CNT}}{\kappa_{CNT}-\kappa_f}log\left[\frac{\kappa_{CNT}+\kappa_f}{2\kappa_f}\right]}{1+\varphi+2\varphi\frac{\kappa_f}{\kappa_{CNT}-\kappa_f}log\left[\frac{\kappa_{CNT}+\kappa_f}{2\kappa_f}\right]}.$$

Here, $Pr=\frac{\mu C_P}{\kappa_f}$, is the Prandtl number, $N_R=\frac{16\sigma^* T_\infty^3}{3k^*\kappa_f}$ is the radiation, $\alpha=\frac{a}{b}$ is the stretching/shrinking

parameter, and $N_I = \frac{Q_0}{(\rho C_P)_f c}$ is the heat source/sink parameter. The quantity $d = \frac{\alpha_1}{a}$ indicates the stretching/shrinking sheet parameter. Additionally, the above system $\alpha = b_1\sqrt{\frac{a}{\nu_f}}, \beta = b_2\left(\frac{a}{\nu_f}\right)$, and $\gamma = c\sqrt{\frac{a}{\nu_f}}$ indicates first and second-order slips and temperature jumps, respectively.
Nanofluid quantities are given in Table 1.

Table 1. Characteristics of water and CNT.

Physical properties	MWCNT	SWCNT	H_2O
C_p (J kg^{-1} K^{-1})	796	425	4179.0
ρ (kg m^{-3})	1600	2600	997.1
κ (W m^{-1} K^{-1})	3000	6600	0.613
σ (Ω m^{-1})	3.8×10^7	4.8×10^7	0.05

We define the variable ξ to obtain the findings of Eq. (16) as follows

$$\xi = \frac{Pr}{\lambda^2} exp(-\lambda\eta). \tag{17}$$

To generate the following equation, substitute this new variable defined in Eq. (17) into Eq. (16).

$$\xi\frac{\partial^2\theta}{\partial\xi^2} + (k_1 - k_2\xi)\frac{\partial\theta}{\partial\xi} + \left(k_2 + \frac{\delta}{\lambda^2\xi}\right)\theta = 0, \tag{18}$$

where the following constants are applied

$$k_1 = 1 - \frac{\chi\left(d+V_C\lambda(1+\alpha\lambda-\beta\lambda^2)\right)}{\lambda^2(1+\alpha\lambda-\beta\lambda^2)}, k_2 = \frac{\chi d}{\lambda^2(1+\alpha\lambda-\beta\lambda^2)},$$
$$\chi = \frac{Pr\,\varepsilon_4}{(\varepsilon_5+N_R)}, \delta = \frac{N_I Pr}{(\varepsilon_5+N_R)}\text{a}$$

The boundary conditions associated with Eq. (15)-(16) are also reduced to

$$\frac{Pr}{\lambda}\theta_\eta(-1) = \gamma\left(1-\theta(-1)\right), \theta(0) = 0. \tag{19}$$

The singular point of the transformation (17) is $\xi = 0$. As a result, the Frobenius method is used to analyze the power solutions of Eq. (18)

$$\theta(\xi) = \sum_{r=0}^{\infty} a_r \xi^{m+r}, \tag{20}$$

to obtain the following derivatives

$$\theta_\eta(\xi) = \sum_{r=0}^{\infty} a_r (m+r)\xi^{m+r-1},$$
$$\theta_{\eta\eta}(\xi) = \sum_{r=0}^{\infty} a_r (m+r)(m+r-1)\xi^{m+r-2}. \tag{21}$$

To acquire the following analytical answers by plugging Eqs. (20) and (21) into Eq. (18), the solution is given by the Kummers function F[a, b, exp(-λη)] as follows

$$\theta(\eta) = \frac{exp[-m\lambda\eta]\gamma F\left(m,1+n,-d\varepsilon_4\frac{Pr}{\lambda^2}exp[-m\lambda\eta]\right)}{(\gamma+m\alpha)M\left(m,1+n,-d\varepsilon_4\frac{pr}{\lambda^2}\right)\frac{m\lambda\varepsilon_4 Pr}{(1+n)}F\left(m-1,2+n,-d\varepsilon_4\frac{Pr}{\lambda^2}exp[-m\lambda\eta]\right)} \tag{22}$$

where

$$\text{m} = \frac{1}{2}\left((1\text{-k}_1) + \sqrt{(1\text{-k}_1)^2 - \frac{4\text{N}_\text{I}\text{Pr}}{(\varepsilon_5+\text{N}_\text{R})\lambda^2}}\right), \text{n} = \frac{1}{2}\left(\sqrt{(1\text{-k}_1)^2 - \frac{4\text{N}_\text{I}\text{Pr}}{(\varepsilon_5+\text{N}_\text{R})\lambda^2}}\right).$$

Using Eq. (22), the Nusselt number can be calculated.

3 Results and discussion

The MHD flows with mass transpiration and a heat source/sink parameter is considered. Analytical solutions are provided for the fluid motion of CNT-water nanofluid via the MHD fluid flow described above. The solid volume of CNT nanoparticles can be used to produce better heat transfer. After solving the ODE (6) for λ analytically, the reduced momentum equation (16) is solved to investigate the solution domain. The solution of the temperature profile expressed by Kummer's function with a temperature jump condition also makes use of this solution domain. The outcomes reflect the dual nature of the behavior namely, upper branch solution and lower branch solution. For many governing parameters, such as magnetic parameters, first and second-order slips, mass transpiration, thermal radiation, heat source/sink parameter, and temperature jump condition, two branches of the solution are apparent. The velocity and temperature results for fluid water-based CNTs nanofluid are displayed in Figs. 2-5.

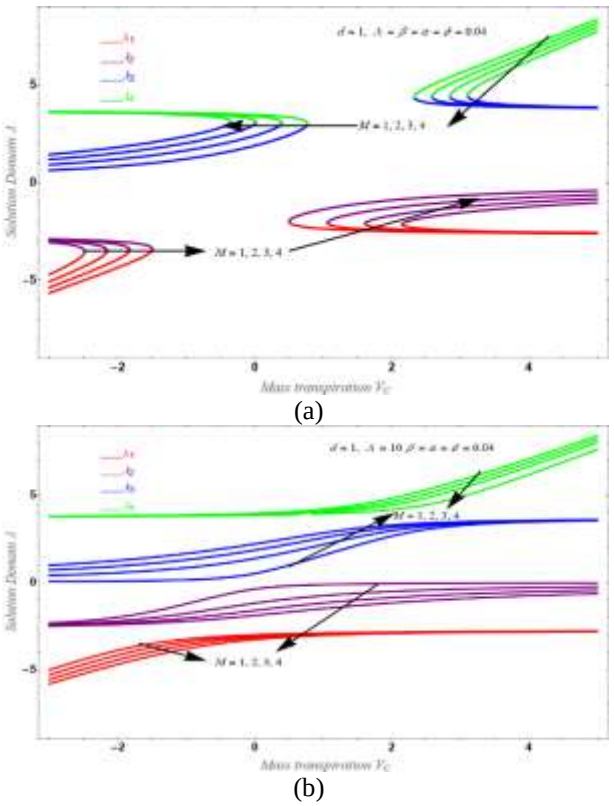

(a)

(b)

Fig. 2. Effect of M on the solution domainλ versus mass transpiration V_c for (a) stretching surface (b) shrinking surface

On the base of the plots we can summarize our conclusions as follows:

- It can be seen that the axial velocity profile decreases with increasing magnetic field.
- The suspended particles slow down the flow's velocity, which accelerates the surface cooling rate.
- As the volume fraction of nanoparticles increases, heat transmission at the surface typically increases.
- the temperature gradient increases in both nanofluids.
- The rate of heat transfer at the surface increases as the suction parameter increases in both nanofluids.
- The physical and chemical conditions are better for effective boundary layer flow cooling.

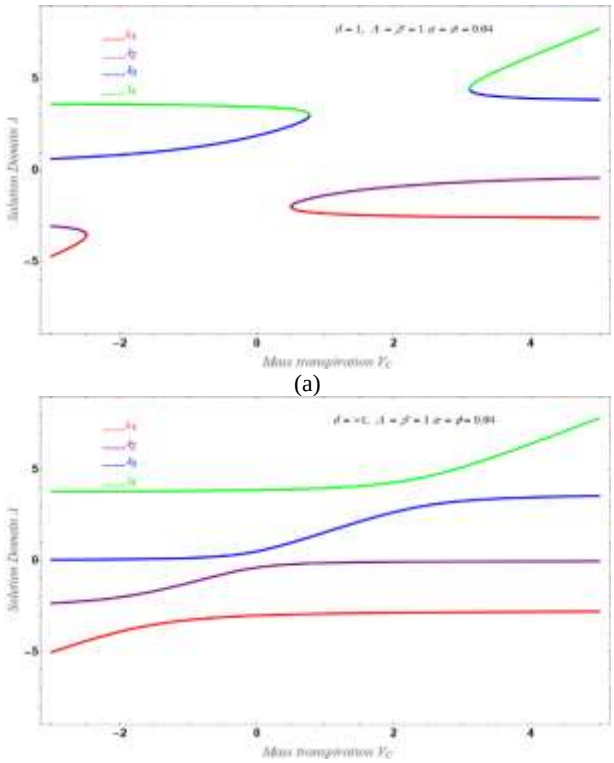

(a)

(b)

Fig. 3. Effect of Mon the solution domainλ versus mass transpiration V_c (a) stretching surface (b) shrinking surface.

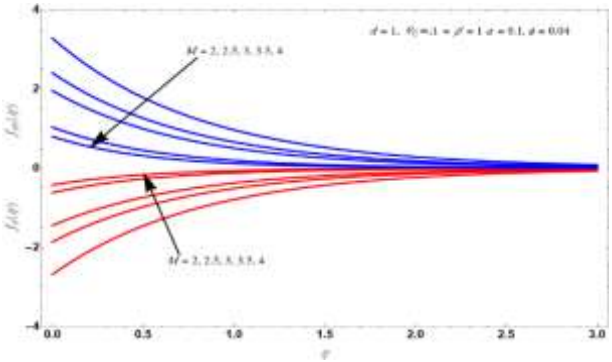

Fig. 4. Effect of magnetic parameter M on $f_\eta(\eta)$ and $f_{\eta\eta}(\eta)$ used real solution of λ_1.

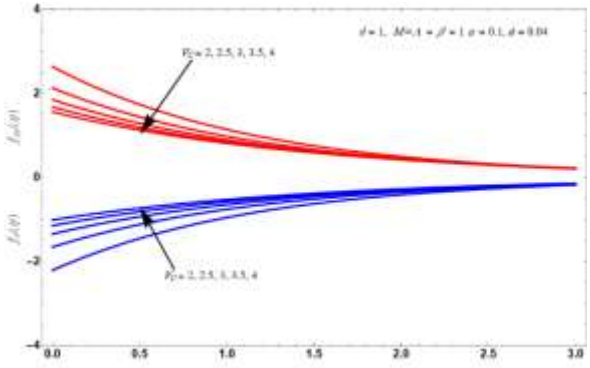

Fig. 5. Effect of V_C on $f_\eta(\eta)$ and $f_{\eta\eta}(\eta)$ used real solution ofλ_1.

This project is funded by the European Union's Horizon Europe program under grant no. 101079354.

References

Sakiadis, B.C., (1961a) Boundary layer behavior on continuous solid surfaces. *AICHE, J.*, 7, 26–28.

Sakiadis, B.C., (1961b) Boundary layer behavior on continuous solid surfaces: I. Boundary layer on a continuous flat surface. *AICHE, J.*, 7, 221–225.

Crane, L.J., (1970) Flow past a stretching plate. *Z. Angew. Math. Phys.*, 21 (4): 645–647.

Gupta, P.S., & Gupta, A.S., (1979) Heat and mass transfer on a stretching sheet with suction or blowing. *Can. J. Chem. Eng.*, 55, 744–746.

Andersson, H.I., (1995) An exact solution of the Navier-Stokes equations for magnetohydrodynamic flow. *Acta Mech.*, 113, 241–244.

Andersson, H.I., (2002) Slip flow past a stretching surface. *Acta Mech.*, 158, 121–125.

Liao, S.J., (2005) A new branch of solutions of boundary-layer flows over a stretching flat plate. *Int. J. Heat Mass Transf.*, 49 (12) (20): 2529–2539.

Liao, S.J. (2007) A new branch of solution of boundary-layer flows over a permeable stretching plate. *Int. J. Non-Linear Mech.*, 42, 819–830.

Wang, C.Y., (2009) Analysis of viscous flow due to a stretching sheet with surface slip and suction. *Nonlinear Anal. Real World Appl.*, 10, 375–380.

Bognár, G., & Mahabaleshwar, U.S., (2024) Series solution for MHD fluid flow due to nonlinear accelerating surface with suction/injection. *AIP Conference Proceedings*, 3034 Paper 020011

N3: Processing of Concrete Construction and Demolition Waste

[1]*Cornelius* Ngandu [1,2,*], *John Kwame* Bediako[3], *Gábor* Mucsi[1]

[1]Faculty of Earth and Environmental Science and Engineering, University of Miskolc, Miskolc, Hungary
[2]Faculty of Engineering and Technology, Egerton University, Egerton, Nakuru, Kenya
[3]Department of Separation Science, School of Engineering Science, Lappeenranta-Lahti University of Technology (LUT), Finland

Abstract. Large scale up-cycle and value addition for construction and demolition waste (CDW) can significantly promote environmental sustainability, economic returns, reduced carbon emissions and ensure quality control. To optimize the benefits, proper and effective preparation and processing techniques are vital. This study presents a systematic preparation and processing of CDW. Crushing was done by jaw and impact crushers. The reduction ratios and particles sizes showed a reduction of sizes for 50% and 80% fractions. Visually, there was change in morphology of aggregates after impact crushing, becoming more regular shaped, with reduced sharp edges. Though some size fractions were not within the curve limit, this study shows that with further treatment, the CDW I and CDW III can be considered for production of 20 mm recycled coarse aggregate and CDW III for 10 mm recycled coarse aggregate materials. The research shows the importance of undertaking preliminary systematic studies for preparing and adequately characterizing recyled aggregates for potential adoption and reuse in a circular economy context. Other quality control tests are recommended for the treated recycled aggregates.

1 Introduction

There has been an increased interest at a global level regarding the reuse and recycle of construction and demolition wastes (CDWs) (Contreras-Llanes *et al.* 2021). According to the European Environmental Agency (2021-last updated), CDW had high recovery rate in the EU. Besides, management practices indicated that CDW recovery was largely based on backfilling operations and low-grade recovery, there is a big potential for making CDW management truly circular. To increase the value and feasibility for CDW application, there is a need to develop proper up-cycling techniques. Extensive work has shown that plain and reinforced concrete debris can be crushed by primary or secondary crushers to produce recycled concrete aggregates within acceptable quality to BS 882 requirements (Limbachiya 2010).

The "equiaxed" nature for impact breaker is advantageous in concrete aggregates (Tarján 1981). The advantage of vertical shaft impact (VSI) crusher is ability to produce cubicle shapes, however this shape result to significance quantities of fines (Bengtsson and Evertsson 2006). In Bengtsson and Evertsson (2006) study, the flakiness index (FI) from VSI crushed particles were around ½ those from cone crusher, and VSI speed have influence on the FI, higher speed producing lower FI. Also, higher velocity increase the proportions of finer particles produced as compared to lower velocity VSI.

This paper systematically examined the impact of crushing on three fractions of concrete CDW in Hungary. Preparations and analysis were conducted at the university of Miskolc. Crushing was done be jaw and impact crushing. The aim of this research is to systematically process and classify CDW for concrete recycled aggregates and geopolymer precursor materials.

2 Materials and Method

Three CDW waste size fractions were classified based on raw particles size (feed sizes) and denoted as CDW I for the 45 - 80 mm, CDW II for the 22 - 45 mm and CDW III for the 0 - 22 mm.

X-ray fluorescence (XRF) was used to determine the chemical composition and loss of ignition (LOI), and the result is presented in Table 1.

Table 1 Chemical composition and LOI for the CDW materials by XRF.

	CDW III	**CDW II**	**CDW I**	**< 4mm, jaw crusher**
SiO_2	53.85	52.87	52.71	53.24
Al_2O_3	5.2	5.19	4.47	5.82
MgO	1.2	1.36	1.29	1.26
CaO	20.64	22.04	22.94	20.83
Na_2O	0.56	0.55	0.5	0.61
K_2O	1.28	1.21	1	1.44
Fe_2O_3	1.51	1.41	1.2400	1.62
MnO	0.087	0.103	0.1020	0.101
TiO_2	0.159	0.162	0.1490	0.187
P_2O_5	0.084	0.081	0.0780	0.086
S	0.749	0.915	0.905	0.818
LOI	14.47	14.2	14.41	14.34

* Corresponding author: CORNELIUS.NGUNJIRI.NGANDU@student.uni-miskolc.hu

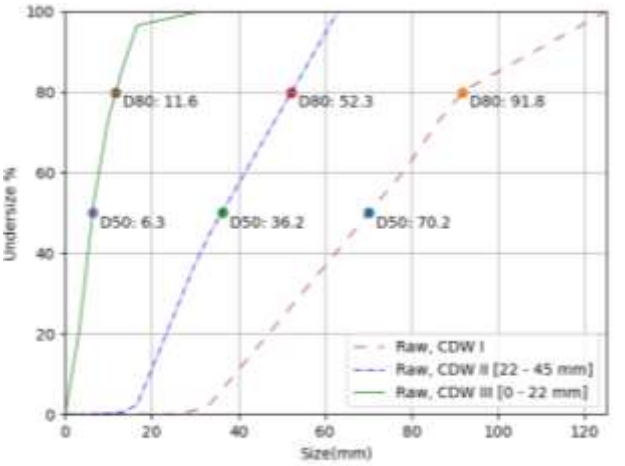

Fig. 1. Particle size distribution for the CDW raw materials,sieve sizes 125 to 31.5 mm, 4 fractions for CDW I, 63 to 8 mm, 4 fractions for CDW II and 63 to 0.063 mm, 11 fractions for CDW III

2.1 Sampling of the CDWs

In order to make the homogenized samples, quartering and/or mechanical splitting sampling techniques were employed based on the sizes, to obtain representative samples for both shorter- and longer-term usage. Quartering was initially conducted for the 3 categories of concrete CDW, then mechanical splitting was performed for the CDW III sample. The general procedure, based on ASTM C702 and AASTHO R 76, was followed as described by Gilson Company Inc. Based on AASHTO R 76, described in Washington state department of transportation (2023), the minimum width of the splitter chutes should be 50% larger than the largest particles. Hence, only CDW III sizes qualified for mechanical splitting using 50 mm width splitter.

2.2 Crushing and particle size distribution

The use of sections to divide the text of the paper is optional and left as a decision for the author. Where the author wishes to divide the paper into sections the formatting shown in Table 1 should be used.The raw CDW II & CDW III particle size distributions were done by seives of < 63 mm based on ISO-3310.2 and ISO-3310.1, and DIN EN 933-2: 1996 (https://labsieves.com/blau-metall/test-sieves-for-particle-size-distribution-analysis-in-aggregates/). Seives of upto 125 mm were used for CDW I, due to larger sizes. Fig. 1 illustrates the raw material particle size distributions. The CDW I and CDW II were crushed by jaw crusher and impact crusher at 30 m/s, CDW III was crushed only by 30 m/s impact crusher. The type and level of crushing was chosen based on the size-dependent classification. In other words, the CDW III was crushed only by impact crusher due its relatively small average particle size.

General crushing and classification steps are illustrated in Fig. 2

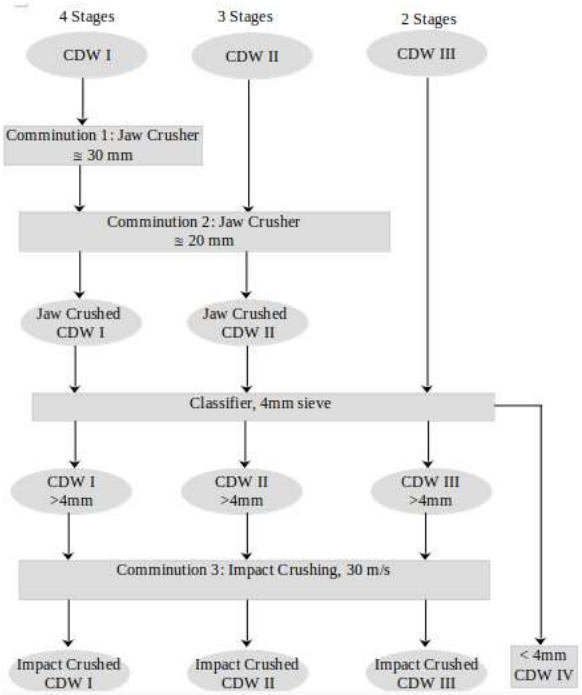

Fig. 2. Crushing and classification process for CDW I (45-80 mm size), CDW II (22- 45 mm size) & CDW III (0 – 22 mm size)

3 Results

Particle size distribution for the impact crushing products are illustrated in Fig. 3 and Fig. 4, for CDW I, CDW II, and CDW III after impact crushing with BS 882 limits. In addition, Fig. 5 is the CDW IV size distrubution a mixture of CDW I, II & III for sizes < 4 mm, sieved from the impact crusher feed.

Reduction ratios for 50% passing (r_{50}) and 80% passing (r_{80}), for the jaw crusher and impact crusher (30m/s) are as illustrated in Table 2. Fig. 6 shows the jaw crushed sample and Fig. 7 illustrates the samples after impact crushing, with a visible size reduction.

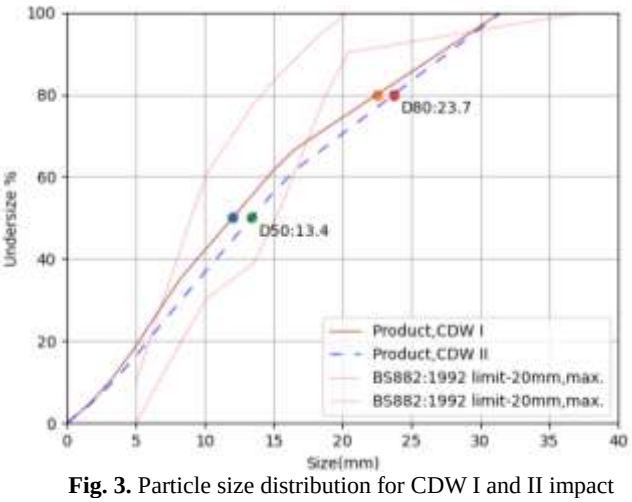

Fig. 3. Particle size distribution for CDW I and II impact crushing product, seive sizes 31.5 to 0.063 mm, 10 size fractions.

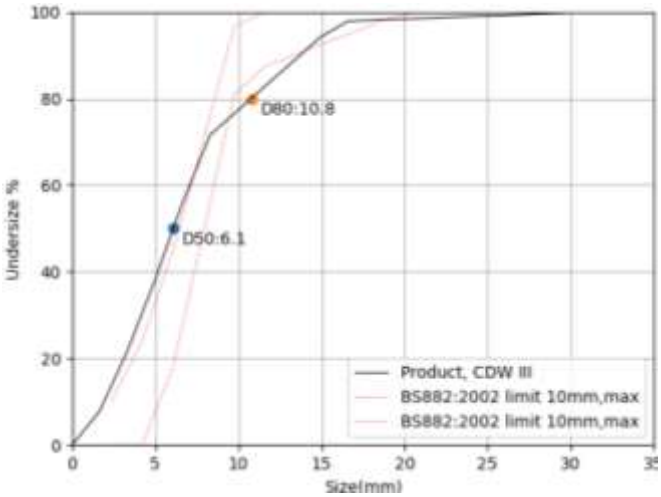

Fig. 4. Particle size distribution, CDW III products after impact crushing sizes 31.5 to 0.063 mm, 10 size fractions.

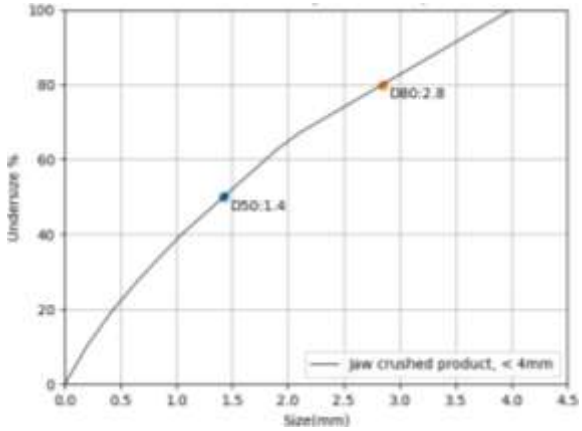

Fig. 5. Particle size distribution for CDW IV, <4mm from impact feed, sieve sizes 8 to 0.063 mm, 8 size fractions

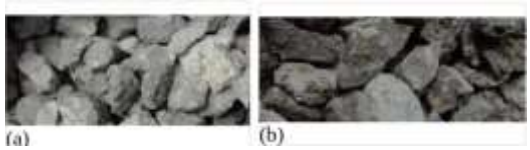

Fig. 6. Jaw crushed concrete waste sample a) CDW II, b) CDW I

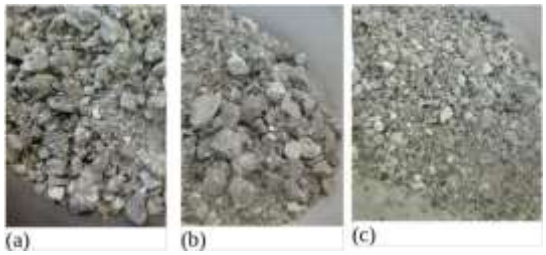

Fig. 7. Impact crushed concrete waste at 30 m/s sample a) CDW I, b) CDW II, c) CDW III

Table 2 Reduction ratios for jaw and impact crushers.

	CDW I		**CDW II**		**CDW III**	
	r_{50}	**r_{80}**	**r_{50}**	**r_{80}**	**r_{50}**	**r_{80}**
Jaw Crushed	3.7*	3.4*	1.8	1.9		
Impact Crushed	1.9	1.2	1.6	1.1	1.3	1.2
****Total**	**7.1**	**4.1**	**2.9**	**2.2**	**1.3**	**1.2**

*2 passes; ** 4 mm classifier before feeding to the impact crusher, hence the feed, >4 mm

4 Discussion and Conclusions

Sampling for the CDW enhanced the material consistency. Furthermore, size reductions were achieved after crushing the CDW samples. The CDW I and CDW II reduction ratios were 7.1 and 4.1 for jaw crushing, 4 mm classifier and impact crushing of D_{50} and D_{80} respecively. This can be attributed to the higher raw material sizes for the CDW I. There was not much difference between the CDW I and CDW II product sizes, with the CDW II producing marginally higher sizes. The CDW I and II lower and higher fractions were not within the 20 mm maximum limit curve ranges, however, the D_{50} were within the range. The CDW III was marginary not within the 10 mm maximum limit curves range.

The aggregates produced by the impact crusher had fairly regular shapes, with reduced sharp edges. The advantage of VSI is ability to produce cubicle shapes, however this result to significant quantities of fines (Bengtsson and Evertsson 2006). According to a study by Ulsen *et al.* (2013), impact crushing affected the sphericity of CDW-sand and rock-to-rock crushing, resulting in improved morphology.

This study underscores the significance of initial systematic preparation and characterization of recycled aggregates, however, there is a need to pursue further studies. Further treatment and selective material sizing will be considered for the CDW 10 mm and 20 mm coarse aggregate production.

However, further treatment is required, due to the adhering mortar. In Qiu *et al.* (2014) study with microbial carbonate precipitate treatment and Li *et al.* (2019) study, with carbonation treatment, both resulted to reduced water absorption of treated coarse aggregates.

The CDW fines (< 4 mm) from the classifier will be further processed for concrete binder utilization research. In Mucsi *et al.* (2021) study, ground fine CDW impoved the 28 days compressive strength of concrete, attributed to high reactivity, with the 30% cement replacement attaining 53 MPa, and a strength activity index (SAI) of 126%.

According to Moreno-Juez (2021), higher LOI for CDW in comparison to cement was attributed to calcite content in the CDW. According to ASTM C618-92a, requirement, maximum LOI at 6%, for fly ash or natural pozzolans as a portland cement admixture as described by the Federal Highway Administration Research and Technology (USA). In this study, the LOI values are in the range of 14 – 15 %, significantly higher than the ordinary portland cement (OPC) allowable limits.

This project is funded by the European Union's Horizon Europe program under grant no. 101079354.

References

Bengtsson, M., & Evertsson, C. (2006) Measuring characteristics of aggregate material from vertical shaft impact crushers. *Minerals Engineering*, 19 (2006) ,1479 – 1486.

Contreras-Llanes, M., Romero, M., Gázquez, M.J., & Bolívar, J.P. (2021) Recycled aggregates from construction and demolition waste in the manufacture of urban pavements. *Materials* 2021, 14(21),6605.

European Environmental Agency. (2021-last updated). https://www.eea.europa.eu/publications/construction-and-demolition-waste-challenges

Federal highway administration research and technology. https://www.fhwa.dot.gov/publications/research/infrastructure/structures/97148/cfa53.cfm

Li Y., Zhang S., Wang R., Zhao Y., and Men C., Effect of carbonation treatment on the crushing characteristics of recycled coarse aggregates. Construction and building materials, 201(2019), 408-420

Limbachiya, M.C., (2010) Recycled aggregates: Production, properties and value-added sustainable applications. *Journal of Wuhan university of technology-material science edition*, Dec.2010.

Moreno-Juez, I.J., Vegas, M.F., Rojas, R.V., Villa, E. Guede-Vazquez (2021) laboratory-scale study and semi-industrial validation of viability of inorganic CDW fine fractions as SCMs in blended cements. *Construction and building materials*, 271 (2021) 121823.

Mucsi G., Papné N.H., Ulsen C., Figueiredo P.O., and Kristály F. (2021) Mechanical activation of construction and demolition waste in order to improve its pozzolanic reactivity. *ACS Sustainable Chemistry and Engineering*, 2021,9,9

Qiu J., Tng D.Q.S., and Yang E-H., Surface treatment of recycled concrete aggregates through microbial carbonate precipitation. *Construction and building materials*, 57(2014), 144-150

Reducing bulk samples to testing sizes by quartering(ASTM C702 and AASTHO R 76), Gilson Company Inc.

Ulsen, C., Kahn, H., Hawlitschek, G., Masini, E.A., Angulo, S.C., (2013) Production of recycled sand from construction and demolition waste. *Construction and building materials*, 40(2013), 1168 – 1173.

Washington state department of transportation (2023) *WSDOT material manual M 46-01.42*, January 2023. Washington state department of transportation.

Tarján G. (1981) Mineral processing, Volume I: Fundamentals, comminution, sizing and classification. Akadémiai Kiadó.

Test sieves for particle size distribution analysis in aggregates, Blau-Metall, online: https://labsieves.com/blau-metall/test-sieves-for-particle-size-distribution-analysis-in-aggregates/

N4: Mechanical activation of waste glass for geopolymer and cementitious applications: a review

Maen Alwahsh[1], Gábor Mucsi[2]*

[1,2] Institute of Raw Material Preparation and Environmental Technology, University of Miskolc, Miskolc, Hungary

Abstract. The focus on waste management in the glass industry has led to extensive exploration of utilizing waste glass in building materials to mitigate environmental impact and reduce production costs. Studies have highlighted the potential of waste glass in cementitious and geopolymer applications, emphasizing its role in enhancing sustainability and performance. Mechanical activation techniques have been investigated to improve the reactivity of waste glass, with findings indicating enhanced mechanical properties and durability in resulting materials. Additionally, incorporation of fine-ground waste glass in geopolymer formulations has shown promise in improving mechanical strength and sustainability in construction practices, although effects on properties vary depending on specific compositions. Similarly, in cementitious systems, the addition of waste glass has demonstrated positive impacts on workability, hydration kinetics, and mechanical properties, while also addressing issues like alkali-silica reaction. However, further research is needed to fully understand and optimize its potential in these applications.

Introduction

The increasing concern about waste management and the environmental impact of different types of glass has led to a focus on reclamation options and the potential for waste glass to be used in building materials. The need for waste management in the glass industry has been highlighted, with a call for the recycling of waste to minimize energy requirements and reduce production costs (Adekomaya & Majozi, 2021). Waste glass has been identified as a potential solution for the high greenhouse gas emissions and intensive use of energy and natural resources in the cement and glass industries, with a review of its use in cement and concrete production (Jani & Hogland, 2014). The use of waste glass as a supplementary material in geopolymer and cementitious applications (SCM) has been extensively explored. Federico and Chidiac (2009) and Jiang et al. (2019) highlight the potential of waste glass powder (GP) as an eco-friendly material in cement-based and extended construction materials, with Federico noting the importance of particle size and percent addition in controlling ASR expansion. Rivera et al. (2018) presents a specific application of waste glass in the production of geopolymeric tiles, demonstrating the feasibility and environmental benefits of this approach. These studies collectively underscore the promising role of waste glass in enhancing the sustainability and performance of geopolymer and cementitious materials. It was concluded by Aphale and Sahare (2016) after reviewing the work done by various researchers to investigate the effect of glass on strength of concrete that, as the particle size of waste glass reduces it helps in enhancing strength of concrete. Provided that, particle size less than 75 microns show pozzolanic activity, however, an increase in glass content as cement replacement material decreases the workability of concrete. However, Draganovska and Sicakova (2015) noted that while specific grinding parameters can be verified, the strength activity index of fine-grained waste glass may not always meet the required limit values for certain applications. Therefore, it is necessary to investigate systematically the effect of grinding fineness on SCM and concrete properties.

Characterization of waste glass

Waste glass, a byproduct of various industries, has a complex composition and diverse properties. It is characterized by a low leach rate, tolerance to changes in waste composition, and low surface area. The particle size distribution of waste glass varies depending on the source, with some studies reporting a range of 0.1 mm to 21.118 μm (Ayadi et al., 2011). The amorphous content of waste glass, which is crucial for its reactivity, has been studied in the context of its use in concrete. Moreover, the chemical composition of waste glass can also be tailored for specific applications, as demonstrated in the production of glasses and glass ceramics using industrial wastes (Kara, 2013). A range of methods have been used to characterize waste glass, including X-ray diffraction (XRD), scanning electron

* Corresponding author: maenalwahsh@hotmail.com

microscopy (SEM), and Fourier-transform infrared spectroscopy (FTIR). Erol (2004) used DTA, XRD, and SEM to investigate the crystallization behavior of glasses produced from industrial wastes.

Mechanical activation techniques

A range of techniques have been explored for mechanical activation by fine grinding of waste glass. Fóris and Mucsi (2022) found that the drum mill is the most energy-efficient for grinding container glass bottles, while Yoon and Yun (2005) used a disk type ball mill for recycling fly ash and waste glass. Zeng and Gan (2011) discussed the importance of controlling the grinding mode for hard and brittle glasses, and the potential of ultra-precision grinding and electrolytic in-process dressing. Fähnle and Hauser (2011) analyzed various fine-grinding techniques in terms of achievable surface qualities. These studies collectively highlight the importance of selecting the appropriate grinding technique based on the specific properties and intended use of the waste glass. Research on the principles of fine grinding and mechanical activation of waste glass has revealed several key findings. Chen et al. (2020) found that the specific surface area and activity index of waste glass powder increase with prolonged mechanical activation, indicating that mechanical grinding can effectively enhance the reactivity of waste glass. Boldyrev et al. (1996) further supports this, suggesting that the size reduction and amorphization of waste glass particles are key outcomes of fine grinding and mechanical activation.

3.1 Effects of Fine Grinding on Reactivity

A range of studies have explored the impact of fine grinding on the reactivity of waste glass in geopolymer and cementitious systems. Wang et al. (2020) found that wet-ground superfine waste glass powder significantly improved the workability of cement pastes and accelerated the reaction of cement. Mirzahosseini and Riding (2015) and Nwaubani (2013) highlighted the potential of waste glass powder to enhance the compressive strength and pozzolanic reactivity of concrete, with the latter emphasizing the role of particle size in this reactivity. Afshinnia and Rangaraju (2015) further demonstrated the ability of fine ground recycled glass to mitigate alkali-silica reaction in mortars, particularly when used as an aggregate replacement material. These findings collectively suggest that fine grinding can enhance the reactivity of waste glass in geopolymer and cementitious systems, leading to improved performance in these materials.

1.2 Geopolymer Applications

Recent research has shown the potential of incorporating fine-ground waste glass into geopolymer formulations. Manikandan and Vasugi (2021) highlight the use of waste glass powder (WGP) as an aluminosilicate source material in geopolymer concrete, emphasizing its eco-friendly and sustainable properties. Toniolo et al. (2018) further explores the extensive reuse of soda-lime waste glass in fly ash-based geopolymers, demonstrating its ability to improve mechanical strength and immobilize heavy metal ions. Novais et al. (2016) and Arulrajah et al. (2017) investigate the incorporation of waste glass from end-of-life fluorescent lamps and recycled glass, respectively, into geopolymers, with Novais et al. (2016) finding that curing conditions are the most influential factor and Arulrajah et al. (2017) showing that higher recycled glass contents lead to higher strength values. The addition of waste glass to geopolymers can have varying effects on their properties. Alomayri (2017) reported that the appropriate addition of glass microfibers can enhance the mechanical properties of geopolymer composites, including flexural strength and impact strength. However, Kawalu et al. (2022) observed a decrease in compressive strength when using glass-waste aggregate in fly ash-based geopolymer mortars. Marcin et al. (2018) noted an improvement in the mechanical properties of slag-based geopolymers with the addition of waste glass. These studies collectively suggest that the effects of waste glass addition on workability, setting time, compressive strength, and durability of geopolymers can be positive and negative, depending on the specific type of waste glass and the composition of the geopolymer.

3.3 Cementitious Applications

The use of fine-ground waste glass as a supplementary material in cementitious systems, including Portland cement concrete and alkali-activated binders, has been explored in several studies. Shi and Zheng (2007) highlight the potential for controlling alkali-silica reaction (ASR) and achieving suitable strength and durability in concrete mixtures that use waste glass as an aggregate. Nwaubani (2013) further emphasizes the positive influence of waste glass powder fineness on the properties of cement mortars, particularly in enhancing compressive strength. Bueno et al. (2020) provide a comprehensive review of the use of ground waste glass as a supplementary cementitious material, noting its potential as a pozzolan and its ability to reduce expansion caused by ASR. However, the review also points out the need for further research in this area. The incorporation of waste glass in cementitious composites has been found to have several positive effects. Gao et al. (2020) and Chang et al. (2015) observed improvements in workability and hydration kinetics, with . Gao et al. (2020) also noting a beneficial impact on the microstructure. Aly et al. (2012) reported enhanced mechanical properties, specifically attributing this to the presence of colloidal nano-silica. These findings collectively suggest that waste

glass can positively influence the hydration kinetics, microstructure development, and mechanical properties of cementitious composites.

Summary

In summary, the utilization of waste glass in building materials to address environmental concerns and reduce production costs in the glass industry was reviewed in this paper. In addition, it highlights the potential of waste glass in both cementitious and geopolymer applications, emphasizing its ability to enhance sustainability and performance of construction materials. Mechanical activation technique was investigated to show how it improves the reactivity of waste glass, leading to enhanced mechanical properties and durability in resulting materials. In geopolymer formulations, incorporating finely ground waste glass has shown promise in improving mechanical strength and sustainability in construction practices. However, the effects on properties can vary depending on specific compositions. Similarly, in cementitious systems, adding waste glass has demonstrated positive impacts on workability, hydration kinetics, and mechanical properties while addressing issues like alkali-silica reaction. The article emphasizes the need for further research to fully understand and optimize the potential of waste glass in these applications. Various studies referenced in the article highlight the importance of particle size, percentage of addition, and grinding parameters in controlling properties like compressive strength, workability, and durability of cementitious and geopolymer materials when incorporating waste glass. This review underscores the promising role of waste glass in improving the sustainability and performance of geopolymer and cementitious materials, while also pointing out areas requiring additional investigation to optimize its use effectively.

This project is funded by the European Union's Horizon Europe program under grant no. 101079354.

References

Adekomaya, O. and Majozi, T. (2021) 'Mitigating environmental impact of waste glass materials: review of the existing reclamation options and future outlook', Environmental Science and Pollution Research, 28(9), pp. 10488–10502. Available at: https://doi.org/10.1007/s11356-020-12263-0.

Afshinnia, K. and Rangaraju, P.R. (2015) 'Influence of fineness of ground recycled glass on mitigation of alkali-silica reaction in mortars', Construction and Building Materials, 81, pp. 257–267. Available at: https://doi.org/10.1016/j.conbuildmat.2015.02.041.

Alomayri, T. (2017) 'Effect of glass microfibre addition on the mechanical performances of fly ash-based geopolymer composites', Journal of Asian Ceramic Societies, 5(3), pp. 334–340. Available at: https://doi.org/10.1016/j.jascer.2017.06.007.

Aly, M. et al. (2012) 'Effect of colloidal nano-silica on the mechanical and physical behaviour of waste-glass cement mortar', Materials and Design, 33(1), pp. 127–135. Available at: https://doi.org/10.1016/j.matdes.2011.07.008.

Aphale, A.S. and Sahare, S.A. (2016) 'Effect of Particle Size of Recycled Glass on Concrete Properties-a Review', International Journal of Advances in Mechanical and Civil Engineering, (3), pp. 2394–2827. Available at: www.wrap.org.uk/downloads/ConGlassCrete1Final.

Arulrajah, A. et al. (2017) 'Recycled glass as a supplementary filler material in spent coffee grounds geopolymers', Construction and Building Materials, 151, pp. 18–27. Available at: https://doi.org/10.1016/j.conbuildmat.2017.06.050.

Ayadi, A. et al. (2011) 'Elaboration and characterization of porous granules based on waste glass', Powder Technology, 208(2), pp. 423–426. Available at: https://doi.org/10.1016/j.powtec.2010.08.038.

Boldyrev, V. V., Pavlov, S. V. and Goldberg, E.L. (1996) 'Interrelation between fine grinding and mechanical activation', International Journal of Mineral Processing, 44–45(SPEC. ISS.), pp. 181–185. Available at: https://doi.org/10.1016/0301-7516(95)00028-3.

Bueno, E.T. et al. (2020) 'A review of ground waste glass as a supplementary cementitious material: A focus on alkali-silica reaction', Journal of Cleaner Production, 257, p. 120180. Available at: https://doi.org/10.1016/j.jclepro.2020.120180.

Chang, X. et al. (2015) 'Influence of Glass Powder on Hydration Kinetics of Composite Cementitious Materials', Advances in Materials Science and Engineering, 2015. Available at: https://doi.org/10.1155/2015/713415.

Chen, Z. et al. (2020) 'Grinding kinetics of waste glass powder and its composite effect as pozzolanic admixture in cement concrete', Construction and Building Materials, 239, p. 117876. Available at: https://doi.org/10.1016/j.conbuildmat.2019.117876.

Draganovska, M. and Sicakova, A. (2015) 'Verification of specific grinding parameters and strength activity index of glass and clay brick', Pollack Periodica, 10(3), pp. 153–163. Available at: https://doi.org/10.1556/606.2015.10.3.16.

Erol, M. (2004) 'Characterization of glass-ceramics produced from waste materials', Key Engineering

Materials, 264–268(III), pp. 1883–1886. Available at: https://doi.org/10.4028/www.scientific.net/kem.264-268.1883.

Fähnle, O. and Hauser, K. (2011) 'Analysis of fine-grinding techniques in terms of achievable surface qualities', Optical Manufacturing and Testing IX, 8126, p. 81260J. Available at: https://doi.org/10.1117/12.894393.

Federico, L.M. and Chidiac, S.E. (2009) 'Waste glass as a supplementary cementitious material in concrete - Critical review of treatment methods', Cement and Concrete Composites, 31(8), pp. 606–610. Available at: https://doi.org/10.1016/j.cemconcomp.2009.02.001.

Fóris, I. and Mucsi, G. (2022) 'Comparative investigation of glass waste grinding in various mills', Rudarsko Geolosko Naftni Zbornik, 37(3), pp. 33–41. Available at: https://doi.org/10.17794/rgn.2022.3.3.

Gao, X. et al. (2020) 'Assessing the modification efficiency of waste glass powder in hydraulic construction materials', Construction and Building Materials, 263. Available at: https://doi.org/10.1016/j.conbuildmat.2020.120111.

Jani, Y. and Hogland, W. (2014) Waste glass in the production of cement and concrete - A review, Journal of Environmental Chemical Engineering. Elsevier. Available at: https://doi.org/10.1016/j.jece.2014.03.016.

Jiang, Y. et al. (2019) 'A critical review of waste glass powder – Multiple roles of utilization in cement-based materials and construction products', Journal of Environmental Management, 242(May), pp. 440–449. Available at: https://doi.org/10.1016/j.jenvman.2019.04.098.

Kawalu, N., Naghizadeh, A. and Mahachi, J. (2022) 'The effect of glass waste as an aggregate on the compressive strength and durability of fly ash-based geopolymer mortar', MATEC Web of Conferences, 361, p. 05007. Available at: https://doi.org/10.1051/matecconf/202236105007.

Manikandan, P. and Vasugi, V. (2021) 'A Critical Review of Waste Glass Powder as an Aluminosilicate Source Material for Sustainable Geopolymer Concrete Production', Silicon, 13(10), pp. 3649–3663. Available at: https://doi.org/10.1007/s12633-020-00929-w.

Marcin, M., Sisol, M. and Brezani, I. (2018) 'Effect of waste glass addition on mechanical properties of slag based geopolymers', IOP Conference Series: Materials Science and Engineering, 379(1), pp. 0–7. Available at: https://doi.org/10.1088/1757-899X/379/1/012013.

Mirzahosseini, M. and Riding, K.A. (2015) 'Influence of different particle sizes on reactivity of finely ground glass as supplementary cementitious material (SCM)', Cement and Concrete Composites, 56, pp. 95–105. Available at: https://doi.org/10.1016/j.cemconcomp.2014.10.004.

Novais, R.M. et al. (2016) 'Waste glass from end-of-life fluorescent lamps as raw material in geopolymers', Waste Management, 52, pp. 245–255. Available at: https://doi.org/10.1016/j.wasman.2016.04.003.

Rivera, J.F. et al. (2018) 'Novel use of waste glass powder: Production of geopolymeric tiles', Advanced Powder Technology, 29(12), pp. 3448–3454. Available at: https://doi.org/10.1016/j.apt.2018.09.023.

Shi, C. and Zheng, K. (2007) 'A review on the use of waste glasses in the production of cement and concrete', Resources, Conservation and Recycling, 52(2), pp. 234–247. Available at: https://doi.org/10.1016/j.resconrec.2007.01.013.

Toniolo, N. et al. (2018) 'Extensive reuse of soda-lime waste glass in fly ash-based geopolymers', Construction and Building Materials, 188, pp. 1077–1084. Available at: https://doi.org/10.1016/j.conbuildmat.2018.08.096.

Wang, Y. et al. (2020) 'Effects of wet-grinded superfine waste glass on the fresh properties and reaction characteristic of cement pastes', Construction and Building Materials, 247, p. 118593. Available at: https://doi.org/10.1016/j.conbuildmat.2020.118593.

Yoon, S. Do and Yun, Y.H. (2005) 'An advanced technique for recycling fly ash and waste glass', Journal of Materials Processing Technology, 168(1), pp. 56–61. Available at: https://doi.org/10.1016/j.jmatprotec.2004.10.012.

Zeng, X. and Gan, Y.X. (2011) 'A review of grinding technologies for glass machining', International Journal of Abrasive Technology, 4(3), pp. 223–239. Available at: https://doi.org/10.1504/IJAT.2011.042830.

P1: Active ingredient particle size stability effects for foamed pharmaceutical dosage form

András Szoboszlai[1], *Ádám* Haimhoffer[2], *and István* Budai[3*]

[1]Faculty of Materials Science and Engineering, University of Miskolc, Miskolc-Egyetemváros 3515 Miskolc, Hungary
[2]Faculty of Pharmacy, University of Debrecen, Nagyerdei körút 98, 4032 Debrecen, Hungary
[3]Faculty of Engineering, University of Debrecen, Ótemető utca 2-4, 4028 Debrecen, Hungary

Abstract. A prototype and a novel method are presented as a continuous technology for ultrasonic foaming of a melt suspension containing metronidazole particles of different sizes. It has been demonstrated that the particle size of the active ingredient influences the foaming rate. Above 180 microns, a sufficient density was achieved, with the apparent density of the compositions being less than that of gastric juice. By characterising the distribution of the trapped gas bubbles by the ratio d90/d10, it can be concluded that below the value of 100, the capsule will float. The preparations showed prolonged release and were capable of gastro-retention.

1 Introduction

Beyond the most common imaging applications (during pregnancy), it is also used for cell destruction Pitt et al (2004), gene therapy Walsh et al (2021), drug delivery Husseini et al (2008), and medical devices Naidu et al (2022). In the pharmaceutical industry, ultrasound is mostly used for particle size reduction, and research on ultrasound as a major production step in oral formulations is negligible. It is also used in many cases for digestion, extraction and to accelerate the preparation of solutions.

At present, apart from previous work, there is no technology in the literature that uses ultrasound to produce low-density, floating capsules Blynskaya et al (2022), even though metallic or metal foams are already known to be produced Mankovits et al (2014). The use of ultrasound has long been widespread in healthcare, but to date it has not yet been applied in continuous production processes to produce foamed, gastro-retentive dosage forms.

2 Materials and methods

2.1 Materials

Polyethylene glycol 4000 (PEG4000), stearic acid, type 50 (SA) and metronidazole (MNZ) were Ph. Eur. grade and purchased from Molar Chemicals Ltd. (Halásztelek, Hungary). Labrasol® was kindly gifted from Gattefossé (Saint- Priest, France). Other reagents were all of analytical grade and purchased from Sigma Aldrich Kft. (Budapest, Hungary

2.2 Foaming Device Setup

The apparatus can be divided into three main parts: a temperature-controlled vessel with a volume of 50 mL, a Bandelin Sonopuls HD4200 ultrasonic homogenizer with a TS103 sonotrode probe (BANDELIN Electronic GmbH & Co. KG, Berlin, Germany), and a gas injection device that converts the high-pressure gas to atmospheric pressure.

2.3 Preparation of Solid Foams

The metronidazole samples that contained 15% MNZ, 75% PEG 4000, and 10% stearic acid were foamed based on the method mentioned above. The independent variables were set to a gas flow rate of 3 mL/s, the sonotrode amplitude was 30%, and the foaming process carried out lasted 8 s.
A 50 g amount of melt was foamed by the following method. PEG 4000 and SA were measured and melted in the temperature-controlled vessel at 54 °C. Then, MNZ was dispersed in the melted mixture. Foaming was performed by ultrasonic sonication when adding gas into the molten mixture. For further investigations of the sample, the foamed and hot dispersion was molded into a steel mold (V = 1.027 mL)

2.4 Separation of the MDZ by particle size

The particles of the active substance were separated by RETSCH AS 200 vibratory sieve shakers (Retsch GmbH. Haan, German) with the following USP standard sieve sizes: 355, 250, 180, 125, 90 µm. The resulting fractions were collected and used for further analysis and production.

* Corresponding author: budai.istvan@eng.unideb.hu

2.5 Microtomography and size distribution of foam bubbles

A SkyScan 1272 compact desktop micro-CT system was used for the measurement. The scanning parameters were as follows: image pixel size: 5 microns, matrix size: 1344x2016 (rows x columns), Source Voltage= 50 kV; Source Current= 200 µA, Flat Field Correction, and Geometrical Correction were applied. After scanning, the SkyScan NRecon package (Version: 2.0.4.2) was used to reconstruct cross-sectional images from tomographic projection images. For 2D/3D analysis, the CTAn software was used. Based on the density analysis, we used Thresholding, ROI shrink-wrap, Reload, 2D and 3D Analysis plugins. The bubbles and drug particles were marked and coloured by a software evaluating the threshold values.

3 Results

The microCT results show that the cavities in the formulation are composed of closed cells and their number increases with increasing particle size. The bubbles within the formulation are homogeneously distributed and of variable size ranging from 200 to 800 µm in diameter on average. The formulations also contain the active substance homogeneously. The particle size of the active substance in the formulations after foaming is similar to that before foaming. Micro-CT images also confirm that the drug does not accumulate anywhere in the formulation, showing uniform distribution within the matrix.

The aim of the bubble distribution analysis is to understand the relationship between buoyancy and entrapped bubble distribution in products as well as the relationship between API size and bubble distribution. The analysis of the gas bubble distribution is based on micro-CT images. The analysis of the histograms shows that the proportion of d10 bubbles in the capsules is nearly the same. In contrast, comparing the diameters of d50 and d90 bubbles, this is no longer the case. Based on the density analysis it is known that products A, B, and C do not float, despite the high proportion of small bubbles in these samples. Product B has nearly 10% large bubbles. It can be concluded that it is not the relatively high number of small and/or large diameter bubbles that causes the capsule to float. It is supported by the higher proportion of small bubbles with a diameter of less than 0.22 mm in products F and G. The floating condition is that the density of the product is lower than the density of the medium in which it floats. This statement should be complemented by the fact that the distribution of bubbles in the products must be homogeneous. If this is not the case, the capsule will not be singly weighted. By characterizing the distribution of the entrapped gas bubbles with the d90/d10 ratio, it can be concluded that below a value of 100, the capsule will float.

References

Pitt, W.G., Husseini, G.A., Staples, B.J., (2004) Ultrasonic drug delivery – a general review, *Expert Opin. Drug Deliv.* 1 37–56.

Walsh, A.P.G., Gordon, H.N., Peter, K., Wang, X., (2021) Ultrasonic particles: An approach for targeted gene delivery, *Adv. Drug Deliv. Rev*. 179 113998.

Husseini, G.A., Pitt, W.G., (2008) Micelles and nanoparticles for ultrasonic drug and gene delivery, *Adv. Drug Deliv. Rev*., 60 1137–1152.

Naidu, H., Kahraman, O., Feng, H., (2022) Novel applications of ultrasonic atomization in the manufacturing of fine chemicals, pharmaceuticals, and medical devices, *Ultrason. Sonochem.* 86 105984.

Blynskaya, E. V., Tishkov, S. V., Vinogradov, V.P., Alekseev, K. V., Marakhova, A.I., Vetcher, A.A., (2022) Polymeric Excipients in the Technology of Floating Drug Delivery Systems, *Pharmaceutics.* 14

Mankovits, T., Budai, I., Balogh, G., Gábora, A., Kozma, I., S. Manó, S., Kocsis, I., (2014) Structural analysis and its statistical evaluation of a closed-cell metal foam, *Int. Rev. Appl. Sci. Eng*. 5 135–143.

P2: Activated carbon preparation from refuse-derived fuel via pyrolysis and steam gasification for phenol removal

Emese Sebe[1,*], *John Kwame* Bediako[2], and *Youssef* El Ouardi[2]

[1]Institute of Energy, Ceramic and Polymer Technology, University of Miskolc, Hungary
[2]Department of Separation Science, School of Engineering Science, Lappeenranta-Lahti University of Technology (LUT), FI-53850, Lappeenranta, Finland

Abstract. Water pollution poses a critical environmental challenge, necessitating effective wastewater treatment methodologies. In this regard, adsorption stands out as a common and efficient approach. Utilizing waste materials for adsorbent production provides an additional environmental benefit. This study focuses on converting refuse-derived fuel mixtures (composed of PS, PP, HDPE, paper, cardboard, cotton, and wood) into activated carbon through pyrolysis at 500 °C. The resulting chars underwent steam gasification at 900 °C for 60 min, with a steam flow rate of 5 $cm^3\ h^{-1}$. The physically activated chars were then systematically examined for their efficacy in removing phenol from 20 mg dm^{-3} solutions. The prevalence of phenolic compounds in various industrial wastewater, including those from pyrolysis and gasification plants, emphasizes the relevance and practical implications of this research in addressing water pollution challenges.

1 Introduction

Among the various adsorbent materials, activated carbons are widely utilized in water and gas treatment. Approximately 100.000 tonnes of activated carbon are produced annually (Heidarinejad et al., 2020). One characteristic that stands out compared to zeolites and polymer-based adsorbents is their resistance to toxic and corrosive environments. The most common raw materials for activated carbon production include wood, bituminous coal, lignite, and coconut. However, there is an increasing demand for utilizing various wastes as raw materials (Heidarinejad et al., 2020).

Municipal solid waste is rich in carbonaceous materials; therefore, it could serve as an alternative raw material for activated carbon production. The challenge with this waste lies in its heterogeneous and variable nature. However, the fluctuations in its characteristics can be significantly reduced through mechanical processing, such as converting it into refuse-derived fuel (RDF).

The production of activated carbon involves two main steps: carbonization and activation. Activation can be achieved through physical methods, chemical methods, or impregnation (Kapoor et al., 2021) When physical activation is conducted using steam, an additional product is generated, i.e., synthesis gas (syngas). This gas primarily comprises hydrogen and carbon-monoxide and may find application in the chemical industry.

In this study, activated carbons were produced under laboratory conditions using refuse-derived fuel mixtures with varying compositions, and their phenol adsorption capacities were investigated. Phenol was selected as the adsorbate due to its prevalence as the main component of effluents from biomass gasification. Additionally, phenolic wastewater is commonly generated across various industrial sectors, including polypropylene production, oil refineries, and the paper, pharmaceutical, and textile industries (Cunha and Aguiar, 2014; Hernández-Fernández et al., 2021; Ke et al., 2022; Wang et al., 2022).

2 Materials and methods

Model laboratory RDF mixtures with different compositions were prepared as presented in Table 1. The composition of RDF1 is based on an analysis of an RDF sample from an RDF production plant in Hejőpapi, Hungary (Ladányi, 2015).

Table 1. Composition of RDF mixtures [wt.%].

	RDF1	RDF2	RDF3
Cardboard	9.00	7.76	6.52
Office paper	49.50	42.67	35.84
PP	5.50	7.50	9.50
HDPE	16.50	22.50	28.50
PS	5.50	7.50	9.50
Wood	10.00	8.62	7.24
Cotton	4.00	3.45	2.90

A minor adjustment was made by excluding polyethylene terephthalate (PET), as there is an existing technology capable of effectively removing this

* Corresponding author: emese.sebe@uni-miskolc.hu

component. This step was deemed necessary for two reasons: firstly, by separating PET, it becomes available for recycling; secondly, the pyrolysis of PET can pose challenges, such as the formation of benzoic acid, which can lead to system blockages and likely organic acid pollution (Xayachak et al., 2022). In RDF2 and RDF3 samples, the total plastic content was increased by 10% and 20% by weight, respectively.

The RDF mixture was subjected to pyrolysis at 500 °C with an approximately 3.5 °C min^{-1} heating rate. Subsequently, the resulting pyrolysis chars underwent steam gasification at 900 °C for 1 h with 10 °C min^{-1} and a steam flow rate of 5 cm^3 h^{-1}.

The adsorption experiments were conducted using simulated phenol solutions with an initial concentration of 20 mg L^{-1}. A total of 100 mg of activated carbon was added to 100 mL of solution, and the mixtures were agitated on a shaker. After 40 h, the mixtures were filtered, and the residual phenol concentrations of the solutions were determined according to the ISO 6439:1990 standard titled, "*Water quality — Determination of phenol index — 4-Aminoantipyrine spectrometric method after distillation*". Activated carbon from Thermo Fisher Scientific with a particle size of ≤2 mm and an iodine number of 969 mg g^{-1} was used as a reference point for the experimental evaluations.

3 Results and discussion

Table 2 presents the ultimate analysis of the RDF1-3 activated carbon samples. The most notable difference is observed in the carbon content after pyrolysis, which increases as the ratio of plastic components in the initial RDF mixture increases.

Table 2. Ultimate analysis of the RDF chars.

Sample	RDF1	RDF2	RDF3
Ultimate analysis (wt.%)			
C	48.4	51.5	53.4
H	1.1	1.1	1.2
N	<0.3	<0.3	<0.3
S	<0.2	<0.2	<0.2
O (by diff.)	0.0	0.0	0.0
Ash	50.5	47.4	45.4
LHV (kJ kg^{-1})	16636.0	16814.9	17956.2

After each pyrolysis experiment, the weight of the produced chars was measured. Typically, during the degradation of most plastics, the predominant product is oil, resulting in less char compared to cellulosic and lignocellulosic materials. Consequently, increasing the plastic content of the RDF leads to a decrease in the amount of produced char. In this instance, the reduction occurred from 29.6±0.1 to 24.6±0.5 wt.%.

Evaluating the adsorption efficiency of activated carbons derived from individual components, an estimated uptake capacity (q_{est}) was calculated for the RDF1-3 chars. This estimation assumes no synergy between the components. Equation (1) outlines the calculation, where q_{est} represents the estimated value of phenol adsorptivity (wt.%), a_i (wt.%) denotes the ratio of the "i" component in the initial RDF mixture, r_i (wt.%) stands for the weight ratio of the remaining char during the pyrolysis of the "i" component, q_i (wt.%) indicates the adsorptivity of the activated carbon derived from component "i", and r_{RDF} (wt.%) represents the remaining char ratio of the RDF mixture.

$$q_{est} = \Sigma \frac{a_i \cdot r_i \cdot q_i}{r_{RDF} \cdot 100} \quad (1)$$

This adsorptivity value specifically applies to the investigated conditions: a 20 mg L^{-1} initial phenol concentration and a 1:1 (mg:mL) adsorbent-solution ratio.

Fig. 1. illustrates the comparison between estimated and actual adsorptivity values. Contrary to expectations, an inverse trend was observed. In other words, increasing the plastic content of the RDF resulted in improved adsorption efficiency. This could be due to a synergistic effect offered by the increasing presence of plastic in the RDF (Adeniyi et al., 2024). In the same conditions, the efficiency of RDF-based activated carbons is approximately 50-59% when compared to a commercial (Thermo Fisher) activated carbon.

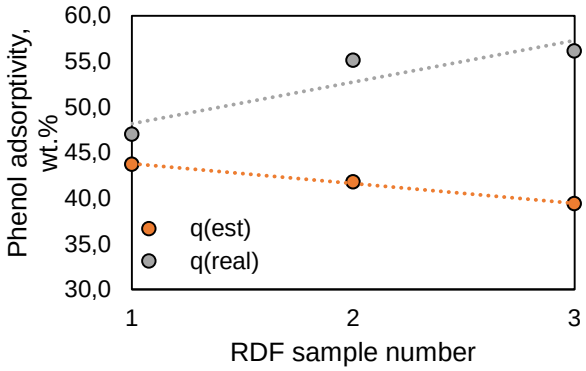

Fig. 1. Estimated and real adsorption efficiency.

Nitrogen physisorption measurements were performed under isothermal conditions, and the resulting adsorption and desorption isotherms are depicted in Fig. 2., revealing distinct hysteresis loops. These loops are common in materials with mesopores and indicate capillary condensation (Donohue and Aranovich, 1998). According to the International Union of Pure and Applied Chemistry (IUPAC) classification, an H3-type loop can be seen here, which suggests slit-shaped pores (Yurdakal et al., 2019).

Table 3. Gas adsorption analysis of RDF chars.

Parameter	Unit	RDF1	RDF2	RDF3
BET, meas.	m^2 g^{-1}	197.4	236.5	233.6
Total pore area	m^2 g^{-1}	136.8	153.5	142.25
Total pore vol.	m^3 g^{-1}	0.0631	0.0709	0.0658
Avr. pore diam.	nm	3.313	3.372	3.426

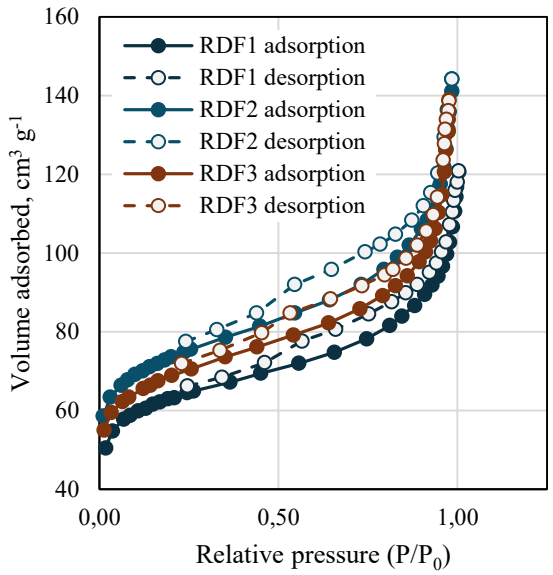

Fig. 2. Adsorption and desorption isotherms of RDF chars

The gas adsorption analysis results are presented in Table 3. The specific surface area determined by the Brunauer–Emmett–Teller (BET) method, as well as the micropore area and volume, reached their peak values for the RDF2 sample. This observation aligns with findings from Adeniyi et al. (Adeniyi et al., 2024), who noted a synergy in biomass-plastic mixtures leading to the production of biochar with a higher specific surface area compared to biochar produced solely from biomass. It is possible that a similar synergy occurred in this study, suggesting that the optimal biomass-plastic ratio was achieved with RDF2.

Unlike the specific surface area, the carbon content of the chars exhibited a stronger correlation with the adsorption efficiency (Fig. 3.). The surface area, pore size and carbon content all play crucial roles in the overall adsorptive capacity of activated carbons. Thus, the relatively higher adsorption efficiency trend from RDF1-3 could be attributed to factors such as the carbon content and average pore diameter rather than the surface area.

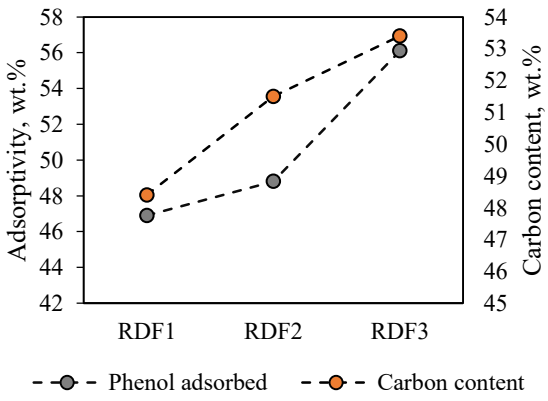

Fig. 3. Carbon content and adsorptivity of the samples.

The composition of the gases produced during the carbonization process was analyzed by using a gas chromatograph capable of identifying hydrogen, carbon monoxide, methane, carbon dioxide, ethene, and ethane (Fig. 4.). With this method, 52.8-55.2 vol.% of the gases was identified, while the remaining portion possibly consisted of other hydrocarbons and the nitrogen used for reactor flushing. Since apart from the additives, the polymeric components of this RDF composed of carbon and hydrogen atoms, increasing the plastic ratio in the RDF mixtures expectedly led to a higher proportion of hydrocarbons in the produced gas. Concurrently, the hydrogen, carbon monoxide, and carbon dioxide contents decreased. As a significant portion of the produced gas was unidentified, it was impossible to calculate its heating value. Nevertheless, the trends shown in Fig. 4. indicate that increasing the plastic content of the RDF correlates with an increase in the heating value of the produced gas.

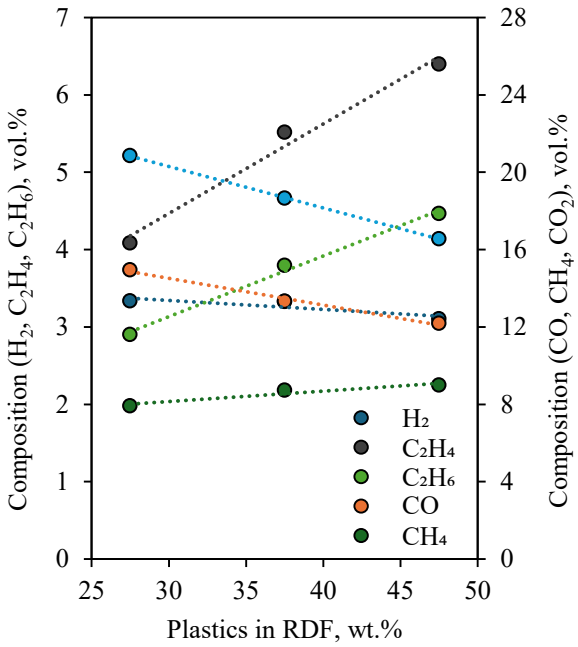

Fig. 4. Composition of pyrolysis gases.

The composition of the syngas produced during the steam activation process was also analyzed, where 89.4-94.0 vol% of the gases were identified. The effect of the initial composition of the RDF was not particularly significant in this case. The analyzed syngas consisted of 47.1-48.7 vol.% H_2, 30.6-34.6 vol.% CO, 1.5-2.1 vol.% CH_4, and 9.1-10.2 vol.% CO_2. The total CO and H_2 contents, which are crucial components for further utilization in the chemical industry, varied between 77.8 and 83.3 vol%.

4 Conclusion

The utilization of municipal solid waste through thermochemical methods often encounters challenges due to its highly heterogeneous composition, influenced by various factors such as location, climate, and living

standards. However, the conversion of this waste into refuse-derived fuel (RDF) offers a more manageable and uniform form for processing. Through appropriate high-treatment methods, the inherent unpredictability of RDF can be significantly reduced. Steam gasification presents a versatile approach, offering two potential directions depending on the desired end product: activated carbon or synthesis gas. This study focused on investigating the feasibility of preparing activated carbon from RDF and assessing the influence of RDF composition on product properties. The findings indicate that, within the examined compositional range, the produced chars exhibited approximately half the efficiency in phenol removal compared to high-quality commercial activated carbon. An increasing plastic content in the RDF mixture correlated with higher carbon content and adsorptivity of the activated carbons. Analysis of by-product gases revealed minor fluctuations in syngas composition, with at least 77.8 vol.% total H_2 and CO content. These results are promising, considering that even if double the amount of these activated carbons is required, it can still be cost-efficient, given that the raw material is waste requiring treatment regardless.

Acknowledgement

We acknowledge the support of the CIRCLETECH project (101079354) funded by the Horizon Europe programme of the European Commission.

References

Adeniyi, A.G., Iwuozor, K.O., Emenike, E.C., Ajala, O.J., Ogunniyi, S., Muritala, K.B., 2024. Thermochemical co-conversion of biomass-plastic waste to biochar: a review. Green Chemical Engineering 5, 31–49. https://doi.org/10.1016/j.gce.2023.03.002

Cunha, F., Aguiar, A., 2014. Methods for the Removal of Phenolic Derivatives from Aqueous Effluents. Revista Virtual de Química 6. https://doi.org/10.5935/1984-6835.20140052

Donohue, M.D., Aranovich, G.L., 1998. Adsorption Hysteresis in Porous Solids. Journal of Colloid and Interface Science 205, 121–130. https://doi.org/10.1006/jcis.1998.5639

Heidarinejad, Z., Dehghani, M.H., Heidari, M., Javedan, G., Ali, I., Sillanpää, M., 2020. Methods for preparation and activation of activated carbon: a review. Environ Chem Lett 18, 393–415. https://doi.org/10.1007/s10311-019-00955-0

Hernández-Fernández, J., Lopez-Martinez, J., Barceló, D., 2021. Quantification and elimination of substituted synthetic phenols and volatile organic compounds in the wastewater treatment plant during the production of industrial scale polypropylene. Chemosphere 263, 128027. https://doi.org/10.1016/j.chemosphere.2020.128027

Kapoor, R.T., Treichel, H., Shah, M.P., 2021. Biochar and its Application in Bioremediation. Springer.

Ke, P., Zeng, D., Wang, R., Cui, J., Li, X., Fu, Y., 2022. Magnetic carbon microspheres as a reusable catalyst in heterogeneous Fenton system for the efficient degradation of phenol in wastewater. Colloids and Surfaces A: Physicochemical and Engineering Aspects 638, 128265. https://doi.org/10.1016/j.colsurfa.2022.128265

Ladányi, R., 2015. Hejőpapi mechanikai-optikai előkezelő mű.

Wang, Q., Shi, Y., Zhao, Y., Ning, P., 2022. Design of solvent mixtures for removal of phenol from wastewater using a non-linear programming model with a multi-start method. Emerging Contaminants 8, 39–45. https://doi.org/10.1016/j.emcon.2021.11.001

Xayachak, T., Haque, N., Parthasarathy, R., King, S., Emami, N., Lau, D., Pramanik, B.K., 2022. Pyrolysis for plastic waste management: An engineering perspective. Journal of Environmental Chemical Engineering 10, 108865. https://doi.org/10.1016/j.jece.2022.108865

Yurdakal, S., Garlisi, C., Özcan, L., Bellardita, M., Palmisano, G., 2019. (Photo)catalyst Characterization Techniques, in: Heterogeneous Photocatalysis. Elsevier, pp. 87–152. https://doi.org/10.1016/B978-0-444-64015-4.00004-3

P3: Adsorptive treatment of potential mine tailings using bio-derived activated carbons

John Kwame Bediako[1,2,*], *Sebe* Emese[3], *Brighton Emmanuel* Maburutse[4], and *Eveliina* Repo[1]

[1]Department of Separation Science, School of Engineering Science, LUT University, Lappeenranta, Finland
[2]Department of Food Process Engineering, School of Engineering Sciences, University of Ghana, Legon, Accra, Ghana
[3]Institute of Energy, Ceramics and Polymer Technology, University of Miskolc, Miskolc, Hungary
[4]Department of Animal Production Sciences, Marondera University of Agricultural Sciences and Technology, Marondera, Zimbabwe

Abstract. In this study, an attempt to addressing the environmental challenges associated with mine wastewater was explored via treatment with waste biomass-derived activated carbons (ACs). The study involves the synthesis of ACs from bio-based precursors obtained from food wastes and evaluating their adsorption performances in treating heavy metals in acid mine drainages (AMDs). The AMDs containing various toxic heavy metals were simulated and studied through batch adsorption experiments. The best adsorption capacities were recorded by $ZnCl_2$-AC, KOH-AC and NaOH-AC, with estimated equilibrium uptakes of 526.31±50.52, 26.14±0.23, 426.62±20.68, 164.24±11.54, 129.95±6.31 and 141.75±26.01, for Hg(II), As(IV), Pb(II), Cd(II), Cu(II) and Co(II), respectively. The adsorption kinetics was found to be faster for the smaller size metals than the larger ones. The study highlights the potential of these ACs as sustainable and effective adsorbents for mitigating the impact of mining activities on water quality. The findings may contribute valuable insights to the field of environmental remediation and sustainable mining.

1 Introduction

Toxic heavy metal pollution from the mining industry is one of many environmental problems facing today's world. Mining contributes immensely into the economic coffers of many countries across the globe; however, mining activities also lead to the generation of acid mine drainages (AMD), which are always laden with numerous toxic heavy metals such as As, Hg, Pb, Cd, Cu, Co, Ni, Cr, Al, Fe, etc. (Oyewo et al., 2018). Heavy metal toxicity can cause serious carcinogenic and other adverse health problems even at low concentrations Bediako et al., 2017). This is because they are easily accumulated by aquatic organisms, which can be passed on to human beings via the food chain; hence they must be properly treated (Li et al., 2015; Oyewo et al., 2018).
Among several treatment methods, adsorption is one of the best options owing to its simplicity, low-cost, eco-friendliness, and efficiency for dilute concentrations (Bediako et al., 2016). Moreover, several classes of adsorbents have been developed and tested. Adsorption using activated carbon (AC) is one of the most widely known options; however, a major issue confronting its patronage is the high costs of commercial ACs, which are usually sourced from coal, coir, and petroleum residues (Yagsi, 2004; Bediako et al., 2018). Recent studies have suggested the use of food waste-derived ACs as alternatives, which have received considerable acceptance owing to the ready availability and abundance of food waste precursors such as fruit peels, shells, nuts, and seeds. Thus, in this study, fruit peels were employed as precursors for the syntheses of low-cost ACs and their evaluations for heavy metal removal from potential AMDs. The study offers important perspectives for advancing environmental remediation and fostering sustainable mining practices through effective treatment of mining wastewater.

2 Materials and methods

2.1 Reagents and AC synthesis method

Metal complexes, viz., $HNa_2AsO_4.7H_2O$, $Pb(NO_3)_2$, $Cd(NO_3)_2.4H_2O$, $Cu(NO_3)_2.3H_2O$, $Co(NO_3)_2.6H_2O$, and $HgCl_2$, and reagents including H_2SO_4, KOH, NaOH, H_3PO_4, $ZnCl_2$ and HCl, were procured from Daejung Chemicals and Metals Co., Ltd. and Sigma-Aldrich Ltd. Dry orange peels were first pre-carbonized at 400 ^oC for 1 h. After that, they were soaked in activation agents including KOH, NaOH, H_2SO_4, H_3PO_4, and $ZnCl_2$ in 3:1 weight ratios for 24 h, followed by activation at 800^oC for 1 h under continuous N_2 purging. In all, five types of activation agent-based ACs were produced. These ACs were washed with distilled water (DW) and dried in an oven kept at 70 ^oC for 24 h pending adsorption evaluation. The synthesized ACs were characterized as previously reported (Bediako et al., 2018).

2.2 Adsorption studies

The adsorption studies were performed in batch modes using the prepared metal solutions of As(V), Hg(II),

* Corresponding author: john.bediako@lut.fi

Pb(II), Cd(II), Cu(II), and Co(II) as representatives of the heavy metals that usually accompany AMDs. Stock solutions (~1000 mg/L) were prepared from the respective metal complexes and diluted into working solutions. First, each of the five ACs was evaluated against each of the six heavy metal ions. After that, the best AC for each of the metal species was selected to run adsorption isotherm studies at pH 6 with initial concentrations ranging from 0–1000 mg/g. Approximately 10 mg of each AC sample was weighed into a 50 mL falcon tube and 20 mL of each metal solution was added. The mixtures were placed in a multi-shaking incubator whirling at 120 rpm and 25±2 °C for 24 h. After equilibrium, the solutions were centrifuged at 12000 rpm for 5 min and diluted for analysis of the residual concentrations of metal ions. Next, adsorption kinetics were carried out with multi-metal mixtures of all the metals. About 300 mL of 100 mg/L metal solutions were filled into glass beakers covered with aluminum foils and placed on multi-purpose magnetic stirrers with stirring bars. AC dozes of 0.1 g were then added to the solutions and timers were set to start counting. Small portions (~ 1 mL) were drawn from the bulk of each solution at various time intervals for 24 h and then analyzed for residual concentrations. An inductively coupled plasma-atomic emission spectrometer (Thermo Scientific, iCAP 7000 series, ICP Spectrometer, USA) was used for the analyses, and the uptakes were calculated according to the expression:

$$q = \frac{(C_i V_i - C_e V_e)}{M} \quad (1)$$

where C_i and C_e are the initial and equilibrium metal concentrations in mg/L, V_i and V_e are the initial and equilibrium volumes in L, and M is the dry weight of ACs in g.

3 Results and discussion

3.1. Evaluation of heavy metal removal capacities

Initial adsorption tests were conducted to evaluate the adsorption affinity of each of the synthesized ACs towards the heavy metal ions, and to select the best adsorbent for each metal ion. The metal uptakes by the ACs using 100 mg/L initial concentrations of each metal are plotted in Fig. 1. As can be seen, the adsorption capacities differed according to the types of activation agents used. The As(V) and Co(II) uptakes had been relatively low for all the ACs; however, the $ZnCl_2$-AC and NaOH-AC showed differences by recording significantly high uptakes of 15.30 and 38.58 mg/g, respectively for the aforementioned metals. The best adsorbents for Pb(II) and Hg(II) were identified to be the KOH-AC and $ZnCl_2$-AC, which exhibited uptakes reaching 210.17 and 194.32 mg/g, respectively. The Cd(II) and Cu(II) appeared to be best adsorbed by the H_3PO_4-AC, which recorded uptakes of 151.37 and 161.96 mg/g, respectively; however, careful observations of the supernatants revealed that large amounts of precipitations had occurred. For this reason, the next best adsorbent, i.e., NaOH-AC was considered for the subsequent adsorption tests for these two metals. A summary of the selected best ACs and their respective heavy metal uptakes are given in Table 1.

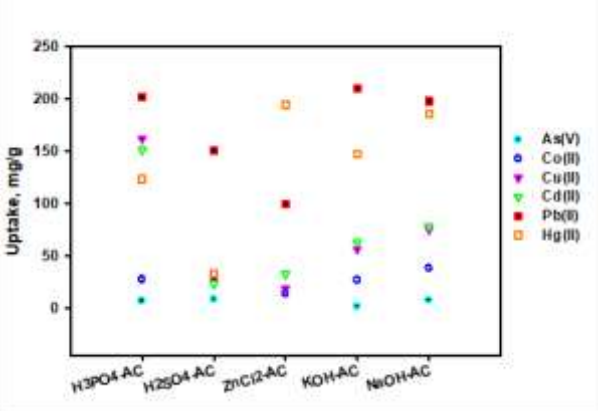

Fig. 1. Activation agent-based carbons and their heavy metal uptakes. Experimental conditions: 10 mg AC in 20 mL of 100 mg/L metal solutions at pH 6, 120 rpm, and 25±2 °C for 24 h.

Table 1. Summary of best AC adsorbents for the representative heavy metals.

Adsorbent	Metal specie	Uptake (mg/g)
ZnCl2-AC	As(V)	15.30
NaOH-AC	Co(II)	38.58
NaOH-AC	Cu(II)	75.49
NaOH-AC	Cd(II)	78.65
KOH-AC	Pb(II)	210.17
ZnCl2-AC	Hg(II)	194.32

3.2. Adsorption isotherm evaluation

Following Table 1, adsorption isotherm studies were performed using the selected best ACs for each of the respective target heavy metals. The isotherm experiments were carried out to obtain the maximum equilibrium uptake of each metal by the ACs. It could be observed from Fig. 2 that all the uptakes followed the usual adsorption phenomenon where the adsorption capacity increases but removal efficiency decreases comparatively with increasing initial concentrations (Abudaia et al., 2013; Bediako et al., 2016). In other words, the isotherm data points rose steadily and reached near plateau-like shapes at equilibrium. Each data was modeled by the two most utilized isotherm models; the Langmuir and Freundlich models, to estimate the maximum equilibrium uptakes and intensities of interactions. These models are presented in the following equations.

Langmuir model:

$$q_e = q_m \frac{bC_e}{1 + bC_e} \quad (2)$$

Freundlich model:

$$q_e = K{C_e}^{1/n} \quad (3)$$

where q_m is the maximum equilibrium uptake given in mg/g, b is the coefficient concerning the affinity between

the ACs and heavy metal ions, q_e is the equilibrium uptake (mg/g) at any time, C_e is the equilibrium metal ion concentration (mg/L), K and n are the Freundlich constants depicting the relative adsorption capacity and adsorption intensity, respectively.

The Langmuir model provided better fits to the isotherm data with high R^2 values than the Freundlich model (Table 2). Moreover, the Langmuir model's predicted order of maximum equilibrium uptakes was consistent with that from the experiments. The order was $ZnCl_2$-AC-Hg > KOH-AC-Pb > NaOH-AC-Cd > NaOH-AC-Co > NaOH-AC-Cu > $ZnCl_2$-AC-As. Although the $ZnCl_2$-AC recorded the highest adsorption capacity of 526.31±50.52 mg/g for Hg(II), the KOH-AC showed the strongest affinity of 1.029±0.39 L/mg for Pb(II). This means that the KOH-AC could be very efficient for Pb(II) removal from very dilute AMDs (Oyewo et al., 2018).

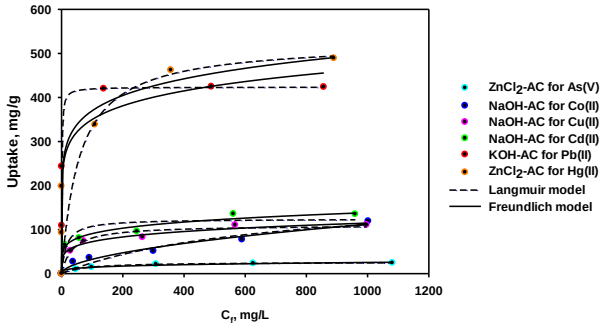

Fig. 2. Isotherms of heavy metal adsorption based on the best suitable AC for each target metal. Experimental conditions: 10 mg AC in 20 mL of 0 – 1000 mg/L metal solutions at pH 6, 120 rpm, and 25±2 °C for 24 h.

Table 2. Parameters of fitted data to isotherm models.

Adsorbent-metal	Langmuir Model		
	q_{max} (mg/g)	b (L/mg)	R^2
$ZnCl_2$-Hg	526.31±50.52	0.017±0.002	0.976
$ZnCl_2$-As	26.14±0.23	0.013±0.0005	0.999
KOH-Pb	426.62±20.68	1.029±0.39	0.993
NaOH-Cd	164.24±11.54	0.063±0.03	0.990
NaOH-Cu	129.95±6.31	0.028±0.008	0.986
NaOH-Co	141.75±26.01	0.002±0.0001	0.989
Adsorbent-metal	Freundlich Model		
	k (L/g)$^{1/n}$	n	R^2
$ZnCl_2$-Hg	204.12±22.47	4.74±1.12	0.977
$ZnCl_2$-As	4.64±1.20	4.06±0.69	0.971
KOH-Pb	198.92±39.54	8.15±2.29	0.918
NaOH-Cd	39.16±6.42	5.47±0.83	0.979
NaOH-Cu	28.95±5.06	5.02±0.73	0.981
NaOH-Co	2.72±1.28	1.86±0.25	0.973

To provide information on the tendency of the adsorption process by the AC adsorbents, the dimensionless constant, R_L in Eq. (4) was derived from the Langmuir model and applied (Bediako et al., 2016; Yan et al., 2012).

$$R_L = \frac{1}{1 + bC_0} \quad (4)$$

where C_0 is the initial metal concentration (mg/L). The adsorption process can be described as either favorable ($0 < R_L < 1$), unfavorable ($R_L > 1$), linear ($R_L = 1$), or irreversible ($R_L = 0$) (Bediako et al., 2016; Yan et al., 2012). Generally, smaller values of R_L ranging between 0 and 1 signify favorable adsorption with good binding affinity. The values obtained in this study were $0.1 < R_L < 0.9$ for the isotherm concentration range evaluated, i.e., 0 – 1000 mg/L, indicating that the adsorption process was favorable for the entire range of concentrations. The Freundlich model's n values further affirmed that the binding affinities were good and favorable, especially at higher initial concentrations (Yan et al., 2012).

3.3. Kinetics of competitive adsorption in multi-metal mixtures

Kinetics of competitive adsorptions in multi-metal solutions were conducted to estimate the rates of adsorption and identify any likely displacement mechanisms among the metal ions (Liu et al., 2008). Here, As was omitted due to its inducement of precipitation of other metal ions in the mixture. Similar to the isotherm results, the uptakes of Hg(II) and Pb(II) were significantly more compared to Cd(II), Cu(II) and Co(II). However, the adsorption rates were much faster in the case of the latter group, reaching equilibria within an average of ~1 h, whereas the equilibria of Hg(II) and Pb(II) were achieved between 5–10 h (Fig. 3). This adsorption kinetics phenomenon could be understood to be probably due to the smaller atomic sizes of the latter group than the former group.

In a previous study using diethylenetriamine(DETA)-functionalized polymeric adsorbent, it was observed that initially adsorbed Pb(II) were displaced by subsequently adsorbed copper ions, likely because of the greater electronegativity of Cu(II) than Pb(II) (Liu et al., 2008). It was speculated that the displacement mechanism was possibly through the repulsion of Pb(II) and the adjacent attachment of Cu(II). However, this phenomenon was not observed in the present study. All the ACs were observed to show rising data points of uniform and increasing metal uptakes until equilibria were reached.

The kinetics data for each metal adsorption was fitted through the pseudo-first-order and pseudo-second-order models given by the following equations.

Pseudo-first-order:

$$q_t = q_1(1 - exp(-k_1 t)) \quad (5)$$

Pseudo-second-order:

$$q_t = \frac{q_2^2 k_2 t}{1 + q_2 k_2 t} \quad (6)$$

where q_1 and q_2 are the uptakes at equilibrium given in mg/g; q_t is the adsorption capacity at time, t (mg/g); k_1 is the first-order equilibrium rate constant (min^{-1}), and k_2 is the second-order equilibrium rate constant (g/mg min).

The two kinetic models closely fitted the data with relatively similar R^2 values in most cases; however, the pseudo-second-order provided relatively better fittings. The ranges of R^2 values are summarized in Table 3. The similarities in the model fits depicted a combination of physisorption and chemisorption mechanisms by the ACs (Bediako et al., 2016). Furthermore, the estimated equilibrium uptakes were comparable, especially for the lowly adsorbed metals; however, in some cases, the predictions were underestimations probably due to the rising trends of the data points.

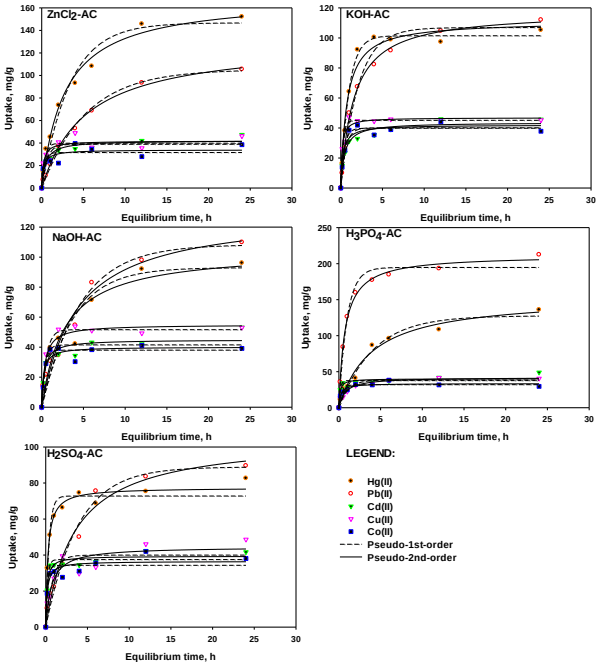

Fig. 3. Kinetics of heavy metal adsorption in competitive metal mixtures. Experimental conditions: 0.1 mg ACs in 300 mL of 100 mg/L metal solutions at 120 rpm and 25±2 ^{o}C for 24 h.

Table 3. Ranges of R^2 values for fitted kinetics data from competitive adsorption.

Metal	R^2 pseudo-first-order	R^2 pseudo-second-order
Hg(II)	0.895 – 0.996	0.925 – 0.998
Pb(II)	0.964 – 0.995	0.969 – 0.998
Cd(II)	0.833 – 0.953	0.922 – 0.968
Cu(II)	0.783 – 0.975	0.846 – 0.976
Co(II)	0.763 – 0.962	0.829 – 0.965

4 Conclusion

The adsorptive treatment of heavy metal ions contained in mining wastewater (AMD) using food waste bio-derived ACs was studied. $ZnCl_2$-AC, KOH-AC, NaOH-AC, H_3PO_4-AC, and H_2SO_4-AC were effective for the removal of Hg(II), As(IV), Pb(II), Cd(II), Cu(II) and Co(II). The order of best adsorption capacity was $ZnCl_2$-AC for Hg(II) > KOH-AC for Pb(II) > NaOH-AC for Cd(II) > NaOH-AC for Co(II) > NaOH-AC for Cu(II) > $ZnCl_2$-AC for As(V) according to the isotherm studies. The kinetics of Cd(II), Cu(II), and Co(II) adsorption were faster than Hg(II) and Pb(II) likely because of the larger atomic sizes of the latter pair. The pseudo-second-order model provided a relatively better fit to the kinetic data. The study could be helpful for promoting sustainable mining through the adoption of effective AMD treatment strategies.

Acknowledgement

The authors wish to acknowledge support from the Research Hub on Sustainable Circular Economy, CiRCLETECH Hub project (101079354) funded by the European Commission through the Horizon Europe programme.

References

Abudaia, J. A., Sulyman, M. O., Elazaby, K. Y., & Ben-Ali, S. M. (2013). Adsorption of Pb (II) and Cu (II) from aqueous solution onto activated carbon prepared from dates stones. *International Journal of Environmental Science and Development*, *4*(2), 191.

Bediako, J. K., & Yun, Y. S. (2018). Adsorption of aurocyanide onto KOH-activated orange peel carbons: optimisation of the activated carbon yield and adsorption capacity through central composite design. In *5th UMaT Biennial International Mining and Mineral Conference. Ghana Min. J.* (pp. 62-67). University of Mines and Technology Tarkwa, Ghana.

Bediako, J. K., Kim, S., Wei, W., & Yun, Y. S. (2016). Adsorptive separation of Pb (II) and Cu (II) from aqueous solutions using as-prepared carboxymethylated waste Lyocell fiber. *International journal of environmental science and technology*, *13*, 875-886.

Li, Z., Kong, Y., & Ge, Y. (2015). Synthesis of porous lignin xanthate resin for Pb2+ removal from aqueous solution. *Chemical Engineering Journal*, *270*, 229-234.

Liu, C., Bai, R., & San Ly, Q. (2008). Selective removal of copper and lead ions by diethylenetriamine-functionalized adsorbent: behaviors and mechanisms. *Water research*, *42*(6-7), 1511-1522.

Oyewo, O. A., Agboola, O., Onyango, M. S., Popoola, P., & Bobape, M. F. (2018). Current methods for the remediation of acid mine drainage including continuous removal of metals from wastewater and mine dump. In *Bio-geotechnologies for mine site rehabilitation* (pp. 103-114). Elsevier.

Yağşi, N. U. (2004). *Production and characterization of activated carbon from apricot stones* (Master's thesis, Middle East Technical University).

Yan, H., Yang, L., Yang, Z., Yang, H., Li, A., & Cheng, R. (2012). Preparation of chitosan/poly (acrylic acid) magnetic composite microspheres and applications in the removal of copper (II) ions from aqueous solutions. *Journal of hazardous materials*, *229*, 371-380.

P4: Nanomilling of copper sulphide (CuS) for immunotherapy

Zdenka Lukáčová Bujňáková[1,*], *Aneta* Salayová[2], *Erika* Tóthová[1], *Matej* Baláž[1], and *Erika* Dutková[1]

[1]Institute of Geotechnics, Slovak Academy of Sciences, Košice, Slovakia
[2]Department of Chemistry, Biochemistry and Biophysics, University of Veterinary Medicine and Pharmacy, Košice, Slovakia

Abstract. Currently, there is a growing interest in cancer immunotherapy research. The use of nanoparticles (NPs) as carriers of antibodies (Ab) and inhibitors represents a novel therapeutic approach, however, it is not yet sufficiently explored. The mechanochemical preparation of CuS NPs and the modification of the surface by mechanical activation to obtain effective conjugation to Ab was researched in this paper. Mechanochemical synthesis and mechanical activation have been performed in the laboratory mills working in dry and wet milling modes. The surface and bulk properties of the obtained samples have been characterized by a broad spectrum of experimental techniques. Future studies will involve *in vitro* and *ex vivo* experiments on multiple myeloma to assess the immunotherapeutic efficacy of the synthesized products.

1 Introduction

Many inorganic NPs (e.g. CuS, CuSe, ZnS) have interesting physicochemical properties, such as electrical conductivity, paramagnetism, or catalytic activity. Due to these properties they have found applications also in medicine, e.g. in diagnosis, treatment or in the field of regenerative medicine (Pelaz et al., 2017). However, if we want to use them for medical applications, they need to be biocompatible, which can be achieved by coating with inorganic or organic substances (Hernandez-Hernandez et al., 2020). By modifying the surface, we can control their size and shape, prevent oxidation, also reduce their cytotoxic effect, or bind them to the desired substance for the so-called targeted treatment.

CuS NPs have low toxicity and they can be easily synthesized. In an acidic environment, copper ions are released from CuS and can catalyze the formation of reactive oxygen species and subsequently lead to the destruction of tumor cells. In the field of therapeutics, they are successfully studied in photothermal therapy, as a nanocarrier, and also as an excipient in chemotherapy, radiotherapy, or immunotherapy (Feng et al., 2016). A synergistic effect in photothermal properties when combining the drug and CuS NPs was discovered (Wang et al., 2015).

The modern approach in cancer treatment is represented by the development of a compact new generation drug system for the targeted treatment, which would include individual components for localization, treatment as well as diagnosis of the disease with minimal side effects. Currently, there is a growing interest in cancer immunotherapy research. The principle is the activation of the immune system, which guarantees an antitumor reaction. The use of NPs as carriers of antibodies and inhibitors represents a novel therapeutic approach, however, it is not yet sufficiently explored.

2 Results and discussion

Firstly, CuS NPs were prepared by mechanochemical synthesis from elemental copper and sulphur in reaction stoichiometry 1:1 in a planetary ball mill using 80 mL ZrO_2 chamber and 18 balls. The weight of the product was 3 grams. The process of the pure phase formation was monitored using X-ray diffraction and the final covellite phase was identified (ICDD 3-0724, Fig. 1a). This phase was obtained after 15 minutes of milling at milling speed 400 rpm. The reaction is proceeds via the formation of digenite (Cu_2S and $Cu_{2-x}S$) intermediate phases.

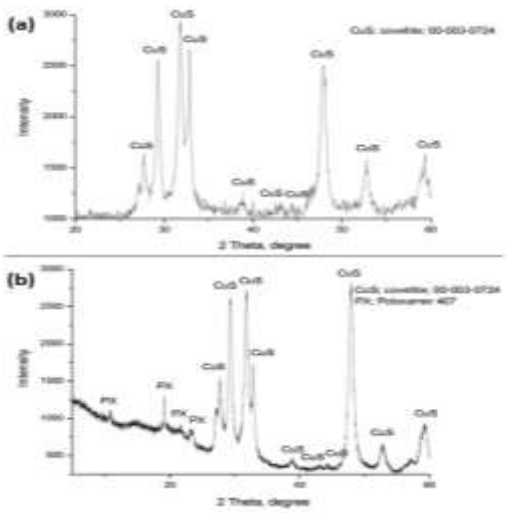

Fig. 1. XRD patterns of (a) CuS and (b) CuS-poloxamer

Under certain conditions, the reaction of copper and sulphur belongs to the so-called mechanically induced self-propagating reactions. This type of reaction is characterized by the fact that after a certain activation

* Corresponding author: bujnakova@saske.sk

time, when no reaction has yet taken place, a sudden increase in temperature and pressure is observed in the milling chamber with the subsequent formation of the resulting product. The time during which a sudden increase in temperature and pressure can be observed is called ignition time (t_{ig}). This phenomenon was recorded by using a special device that monitors temperature changes inside the milling chamber during milling and the dependence of the ignition time on the supplied milling energy was monitored, i.e. rotation speed changes (from 200 to 400 rpm). It was observed that higher supplied energy resulted in shorter t_{ig}. The results are in accordance with (Baláz et al., 2017).

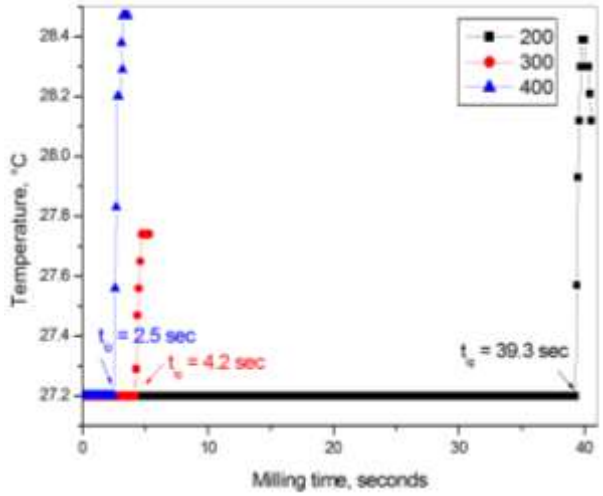

Fig. 2. Milling time vs. increase of temperature in milling chamber at different milling speeds (200-400 rpm) and determination of ignition time (t_{ig}) for CuS

Since the intended use of the prepared NPs is in the field of medicine, the solubility of these nanoparticles in various simulated body fluids was studied. Almost no solubility was detected at a temperature of 36.5 °C for 2 hours in neither of the fluids, except in the case of simulated lung fluid, when 0.15% solubility of copper into the solution was achieved. The results confirm the high stability of the prepared NPs. Their stability was also proven by thermal analysis methods in both inert (Ar) and oxidizing atmospheres (air), when CuS decomposes between 400-500 °C.

Subsequently, the stabilization of NPs in an aqueous solution was studied by coating of the surface with polyethylene glycol (PEG) and poloxamer (PX) with different concentrations and different lengths of polymer chains. It has been demonstrated that both a hydrophilic and a hydrophobic component are required for successful stabilization, i.e. PX is more suitable. A circulation mill was used to prepare stable solutions, and by subsequent centrifugation it was possible to prepare nanosuspensions with a unimodal distribution of particles up to 200 nm in size. The XRD pattern of CuS-poloxamer sample (CuS-PX) is shown in Fig. 1b. As can be seen PX reflexes are clearly visible suggested its amorphous contribution. The reflections corresponding to CuS are retained.

The samples were subsequently immobilized with antibodies (Ab). They were bound to CuS-PX NPs in two different ways; one was conducted by direct reaction of Ab, and the other was carried out in the presence of 1-ethyl-3-(3-dimethylaminopropyl)carbodiimide (EDC). The mixtures were shaken for 2 hours at 25°C. Then, the suspensions were centrifuged for 10 minutes at 6 000 rpm, and the resulting supernatant and precipitate were used for Ab determination by the colorimetric Bradford method at 590 nm (Bradford, 1976). The preliminary results are shown in Fig. 3. As can be seen, by using EDC, Ab were bound to CuS NPs. After optimizing the conditions, samples will be further prepared for in vitro and ex vivo experiments.

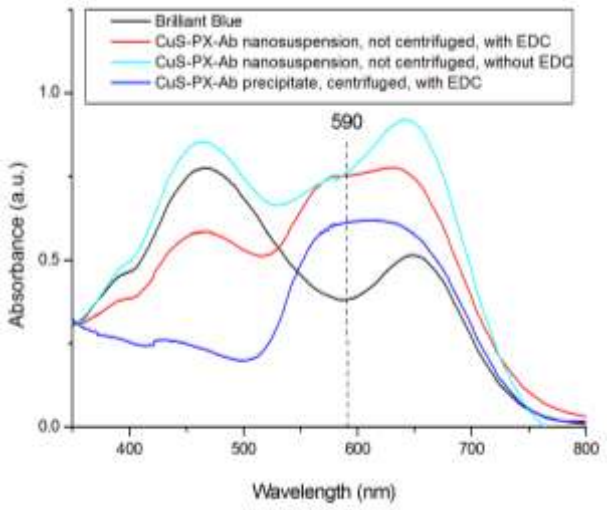

Fig. 3. UV/Vis absorption spectra of Coomassie Brilliant Blue and CuS-PX-Ab nanosuspensions and precipitate with and without EDC

This work was supported by the grant of the Slovak Academy of Sciences (Project Scheme for Parents Returning to Work after Maternity and/or Parental Leave).

References

Baláz, M., A. Zorkovská, J. S. Blazquez, N. Daneu & P. Baláz (2017) Mechanochemistry of copper sulphides: phase interchanges during milling. *Journal of Materials Science*, 52, 11947-11961.

Bradford, M. M. (1976) Rapid and Sensitive Method for Quantitation of Microgram Quantities of Protein Utilizing Principle of Protein-Dye Binding. *Analytical Biochemistry*, 72, 248-254.

Feng, Q. H., Y. Y. Zhang, W. X. Zhang, X. N. Shan, Y. J. Yuan, H. L. Zhang, L. Hou & Z. Z. Zhang (2016) Tumor-targeted and multi-stimuli responsive drug delivery system for near-infrared light induced chemo-phototherapy and photoacoustic tomography. *Acta Biomaterialia*, 38, 129-142.

Hernandez-Hernandez, A. A., G. Aguirre-alvarez, R. Carino-Cortes, L. H. Mendoza-Huizar & R. Jimenez-Alvarado (2020) Iron oxide nanoparticles: synthesis,

functionalization, and applications in diagnosis and treatment of cancer. *Chemical Papers,* 74, 3809-3824.

Pelaz, B., C. H. Alexiou, R. A. Alvarez -Puebla, F. Alves, A. M. Andrews, S. Ashraf, L. P. Balogh, L. Ballerini, A. Bestetti, C. Brendel, S. Bosi, M. Carril, W. C. W. Chan, C. Y. Chen, X. D. Chen, X. Y. Chen, Z. Cheng, D. X. Cui, J. Z. Du, C. Dullin, A. Escudero, N. Feliu, M. Y. Gao, M. George, Y. Gogotsi, A. Grunweller, Z. W. Gu, N. J. Halas, N. Hampp, R. K. Hartmann, M. C. Hersam, P. Hunziker, J. Jian, X. Y. Jiang, P. Jungebluth, P. Kadhiresan, K. Kataoka, A. Khademhosseini, J. Kopecek, N. A. Kotov, H. F. Krug, D. S. Lee, C. M. Lehr, K. W. Leong, X. J. Liang, M. L. Lim, L. M. Liz-Marzan, X. M. Ma, P. Macchiarini, H. Meng, H. Mohwald, P. Mulvaney, A. E. Nel, S. M. Nie, P. Nordlander, T. Okano, J. Oliveira, T. H. Park, R. M. Penner, M. Prato, V. Puntes, V. M. Rotello, A. Samarakoon, R. E. Schaak, Y. Q. Shen, S. Sjoqvist, A. G. Skirtach, M. G. Soliman, M. M. Stevens, H. W. Sung, B. Z. Tang, R. Tietze, B. N. Udugama, J. S. VanEpps, T. Weil, P. S. Weiss, I. Willner, Y. Z. Wu, L. L. Yang, Z. Yue, Q. Zhang, Q. Zhang, X. E. Zhang, Y. L. Zhao, X. Zhou & W. J. Parak (2017) Diverse Applications of Nanomedicine. *Acs Nano,* 11, 2313-2381.

Wang, H., Z. Liu, Y. Gou, Y. Qin, Y. Xu, J. Liu & J.-Z. Wu (2015) Apoptosis and necrosis induced by novel realgar quantum dots in human endometrial cancer cells via endoplasmic reticulum stress signaling pathway. *International Journal of Nanomedicine,* 10, 5505-5512.

P5: Mechanochemical synthesis of $CuInSe_2/TiO_2$ nanocomposite for solar cell applications

Erika Dutková[1*], *Matej* Baláž[1], *Jaroslav* Kováč[2], *Adelia* Kashimbetova[3], *Jaroslav* Briančin[1], *Jaroslav* Kováč, Jr.[2], and *Ladislav* Čelko[3]

[1]Institute of Geotechnics, Slovak Academy of Sciences, Košice, Slovakia
[2]Institute of Electronics and Photonics, Slovak University of Technology, Bratislava, Slovakia
[3]Central European Institute of Technology, Brno University of Technology, Brno, Czech Republic

Abstract. This study demonstrates synthesis of $CuInSe_2/TiO_2$ nanocomposite by a simple, low-cost mechanochemical synthesis. The structural and microstructural characterization of synthesized $CuInSe_2/TiO_2$ nanocomposite was studied using X-ray diffraction, which confirmed the nanocrystalline character of all components of the nanocomposite. Raman spectroscopy also confirmed the crystalline nanoparticles formation of the synthesized nanocomposite. Surface and morphological properties were characterized by SEM and nitrogen adsorption measurement. The surface chemical composition was analyzed by XPS method. Optical properties using UV-Vis and micro-photoluminescence spectroscopy were also investigated. Photoresponse of $CuInSe_2/TiO_2$ nanocomposite was verified by I-V measurements under dark and light illumination.

1 Introduction

Ternary chalcogenide semiconductors of I–III–VI group with promising applications in electronics, optics, and catalysis have been intensively studied in recent years. However, majority of the best investigated sulphide-based semiconductors contain toxic heavy metals, which seriously limit their potential application.

$CuInSe_2$ is also one of the promising semiconductive ternary materials applicable in high-efficiency solar cells and photocatalysis due to its large absorption coefficient, suitably small bandgap, large conversion efficiency and radiation stability (Guo et al., 2008; Kang et al., 2009). It is beneficial to couple $CuInSe_2$, a small bandgap semiconductor (its bulk bandgap is 1.05 eV) with the material with larger bandgap, like TiO_2 (its bulk bandgap is 3.2 eV). The coupling these two components can improve the optical properties due to the elimination of surface non-radiative recombination defects. $CuInSe_2/TiO_2$ nanocomposite can be an excellent alternative for the solar cell applications (Yu et al., 2011; Das et al., 2017) as well as for the photocatalytic degradation of dyes in visible light region. There are several synthetic procedures for the preparation of $CuInSe_2/TiO_2$ nanomaterial, including thermal and microwave assisted hybridization, oxidative chemical polymerization method, electrodeposition technique, colloidal synthesis, electrophoretic deposition technique, simple (SILAR) method, spin coating method, electrochemical anodic oxidation, solvothermal synthesis, etc.

Mechanochemistry as environmentally friendly alternative to the traditional preparation methods is well-applicable in the field of materials science. The high-energy milling process is used either as a synthesis step to prepare inorganic nanomaterials applicable in advanced applications or to introduce defects into the crystalline structure, which can dramatically improve the application potential (Baláž et al., 2017).

To the best of our knowledge, the $CuInSe_2/TiO_2$ nanocomposite has not been prepared by mechanochemical synthesis so far. The novelty of this work is the simple and environmentally friendly mechanochemical method of $CuInSe_2/TiO_2$ nanocomposite (a suitable material for solar cell applications) preparation in a very short time, and at ambient pressure and temperature.

2 Experimental

2.1 Materials

The $CuInSe_2/TiO_2$ nanocomposite was synthesized from elemental copper (99.7%, Merck, Germany), indium (99.99%, Aldrich, Germany), selenium (99.5% Aldrich, Germany) and commercially available TiO_2 Degussa P25 (Degussa, Netherland) (75% anatase and 25% rutile).

2.1 Mechanochemical synthesis

$CuInSe_2/TiO_2$ nanocomposite was prepared by a two-step process. In the first step (Eq. 1), $CuInSe_2$ was prepared by milling 0.94 g of copper, 1.71 g of indium and 2.35 g of selenium. The milling was carried out in a

* Corresponding author: dutkova@saske.sk

planetary mill Pulverisette 6 (Fritsch, Germany) at 550 rpm using a tungsten carbide milling chamber (250 mL in volume) and 50 balls (360 g) with 10 mm in diameter, composed of the same material, during 60 min in an argon atmosphere according the procedure described in (Dutkova et al., 2016). The ball-to-powder ratio was 72:1. In the second step, 2.5 g of TiO_2 was introduced into milling with 2.5 g previously synthesized $CuInSe_2$. Co-milling (eq. 2) was also performed in a planetary mill Pulverisette 6 (Fritsch, Germany) in an argon atmosphere (>99.998%, Linde Gas group, Slovakia) for 30 min without break cooling due to shorter milling times. The milling chamber was vented with Ar gas for 3 min providing an inert atmosphere. The 250 mL tungsten carbide milling chamber with 50 tungsten carbide balls with 10 mm in diameter was used. Rotational speed of the planet carrier was 500 rpm. The ball-to-powder ratio was 72:1. Preparation of the $CuInSe_2/TiO_2$ 1:1 nanocomposite can be described by the following Eq. 1-2:

$$Cu+In+2Se \rightarrow CuInSe_2 \quad (1)$$

$$CuInSe_2+TiO_2 \rightarrow CuInSe_2/TiO_2 \quad (2)$$

2.3 Characterization

X-ray diffraction (XRD) measurements were performed using a D8 Advance diffractometer (Bruker, Germany) equipped with a θ-θ goniometer, CuK_α radiation (40 kV, 40 mA), a secondary graphite monochromator, and a scintillation detector. All samples were scanned from 15° to 80° with the step 0.03° and 12 s counting time. Diffracplus Eva software was used for phase analysis according to the ICDD - PDF2 database. The Rietveld refinement was performed using a TOPAS Academic software. Morphology was investigated using a field emission-scanning electron microscope (FE-SEM, Mira 3, Tescan, Czech Republic) coupled with an EDX analyzer (Oxford Instruments). The values of the specific surface area were obtained by using a NOVA 1200e Surface Area & Pore Size Analyzer (Quantachrome Instruments, USA). Absorption spectra were recorded using a UV-Vis spectrophotometer Helios Gamma (Thermo Electron Corporation, UK) in a quartz cell by dispersing the synthesized particles in absolute ethanol by ultrasonic stirring. The bandgap energy (E_g) was determined by utilization of Tauc equation (3)

$$(\alpha h\nu)^{(1/n)}=A(h\nu-E_g) \quad (3)$$

where α is the absorption coefficient, A is a constant, h = Planck's constant, ν = frequency and n is a constant associated with different kinds of electronic transitions (0.5 for a direct allowed, 2 for an indirect allowed, 1.5 for a direct forbidden and 3 for an indirect forbidden). The optical bandgap, E_g was estimated by plotting $(\alpha h\nu)^2$ as a function of the photon energy hν. Extrapolating the straight line portion of the Tauc plot for zero absorption coefficient (α = 0) gives optical bandgap energy.

The current-voltage (I-V) characteristics were measured using semiconductor parameter analyzer Agilent 4155C under dark and focused halogen white light illumination (illumination intensity of ~ 600 mW/cm^2). The measured sample was separated from crushing pellets to small pieces (thin stripe with dimensions ~ 200-500 μm) and transferred onto insulating pad. The sample contacts were made by small droplet of silver paste and then annealed together with wiring to the socket.

3 Results

Structural characterization

The XRD patterns of mechanochemically prepared $CuInS_2$, commercial TiO_2 and mechanochemically synthesized $CuInS_2/TiO_2$ nanocomposite are shown in Fig. 1.

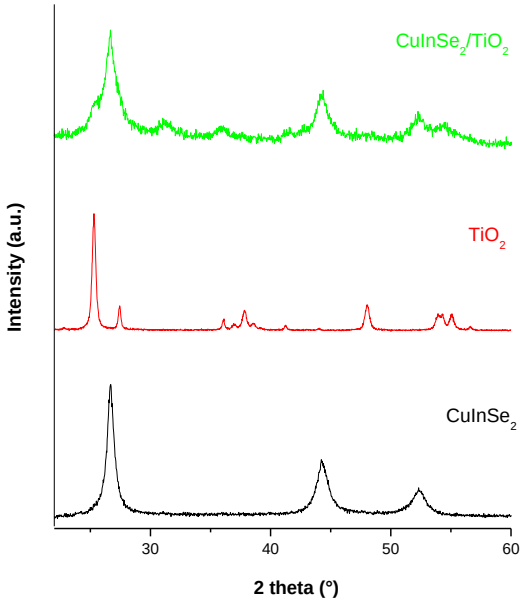

Fig. 1. XRD patterns of $CuInSe_2$, TiO_2, and $CuInSe_2/TiO_2$ nanocomposite.

The diffractions of both components of the composite can be well-seen in the figure. Surprisingly, the reflections corresponding to tetragonal $CuInSe_2$, the content of which is same with content of TiO_2, are more intensive that of TiO_2. This means that the crystallite size of selenide seems to be larger than in the case of titanium dioxide. With regards to TiO_2, commercial Degussa P25 with the 75% content of anatase and 25% of rutile has been used. However, the reflections corresponding to the rutile phase are more pronounced, so it seems that the anatase-to-rutile phase transformation took place during milling, which has been previously observed (Kostova and Dutkova, 2016). According to Rietveld refinement, the estimated crystallite size of $CuInSe_2$ is 18±5 nm and the detected microstrain is 2.1±0.4 %. For titanium dioxide phases, the estimated crystallite size is 5±1 and 8±1 nm for rutile and anatase, respectively, which confirms the presence

of very fine crystallites and broad diffractions with low intensity detected for TiO_2 in the XRD pattern.

Surface and morphological characterization

The specific surface area (S_A) values belong to some of the most important characteristics of milled samples (Baláž et al., 2013). The S_A of pure $CuInSe_2$, from which the studied nanocomposite was prepared, is 2.9 m^2g^{-1} and that of pure TiO_2 P25 is 28.7 m^2g^{-1} as was reported in (Dutkova et al., 2016). In the present study, the co-milling with TiO_2 led to a considerable increase of the specific surface area of the sample $CuInSe_2/TiO_2$ (13 m^2g^{-1}) in comparison with pure $CuInSe_2$. The achieved value of S_A for $CuInSe_2/TiO_2$ is far lower than in the other reports on a similar system applying different synthetic approaches (Kshirsagar et al., 2017).

The morphology of synthesized nanocomposite was studied by the means of scanning electron microscopy (SEM). SEM micrograph of the prepared $CuInSe_2/TiO_2$ nanocomposite is shown in Fig. 2. SEM image displays polydispersed particles, where the agglomerates exhibit the size in micrometers, however, smaller units with the sizes in the nanometer range can be clearly distinguished.

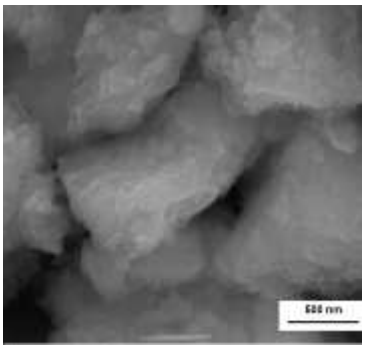

Fig. 2. SEM image of $CuInSe_2/TiO_2$ nanocomposite

Optical properties

The optical properties of $CuInSe_2$, TiO_2 and mechanochemically synthesized $CuInSe_2/TiO_2$ nanocomposite were investigated using UV-Vis spectroscopy. The optical bandgaps were determined by plotting $(\alpha h\nu)^2$ against $(h\nu)$ and extrapolating the slope in the band edge region to zero (Eq. 3) as shown in insets of Fig. 3.

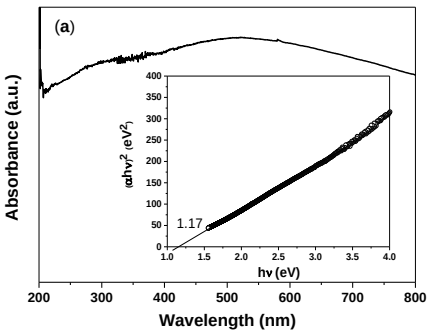

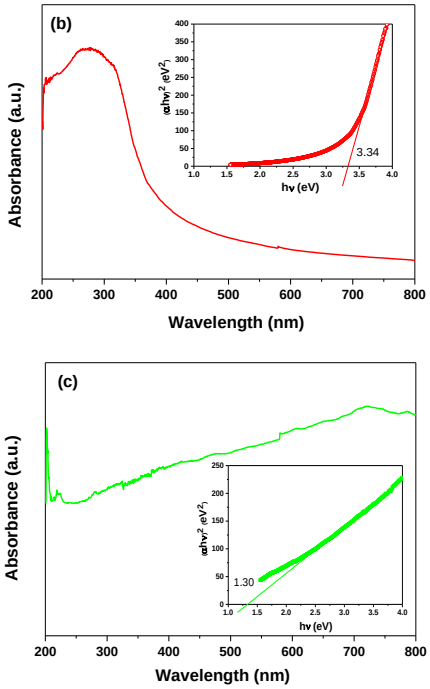

Fig. 3. UV-Vis spectra and Tauc plots (inset) for $CuInSe_2$ (a), TiO_2 (b) and $CuInSe_2/TiO_2$ nanocomposite (c).

The calculated bandgap of $CuInSe_2$, TiO_2 and $CuInSe_2/TiO_2$ nanocomposite was determined to be 1.17, 3.34 and 1.30 eV, respectively. The optical bandgap of TiO_2 was lightly blue-shifted in comparison with the previous reports (Kostova and Dutkova, 2016). The optical bandgap of $CuInSe_2$ was also blue-shifted compared to the bulk $CuInSe_2$ with bandgap of 1.05 eV (Eisener et al., 1999). The observed bandgap value of the nanocomposite is between those of pure $CuInSe_2$ and TiO_2 and mixing of both semiconducting materials are expected to show absorption pattern bearing the signature of both components. In comparison with pure $CuInSe_2$, the obtained $CuInSe_2/TiO_2$ nanocomposite exhibits lightly enhanced absorption in visible light region.

Optoelectrical properties

To verify the optoelectrical properties of the mechanochemically synthesized $CuInSe_2/TiO_2$ nanocomposite, the current-voltage (I-V) characteristics were measured in the dark and under illumination. The measured I-V characteristics in dark (Fig. 4) show sufficient conductivity and are almost linear, which confirms the formation of an ohmic contact on the prepared nanocomposite. After illuminating the sample, the number of generated charge carriers in the $CuInSe_2/TiO_2$ nanocomposite increases, causing an increase in the photocurrent. The results showed a photosensitivity of 4.8% for $CuInSe_2/TiO_2$ at an applied voltage of 2 V compared to the current in the dark. Overall, in the nanocomposite $CuInSe_2/TiO_2$ compared to $CuInSe_2$, there was an increase in the current by 57%. This suggests that the structure formed between $CuInSe_2$ and TiO_2 can increase the photoelectron transfer rate and

promote the separation of photogenerated carriers as reported in the literature (Yang et al., 2022). The above-mentioned measurements of optoelectrical properties confirm the suitability of using this material for the absorber layer in solar cells.

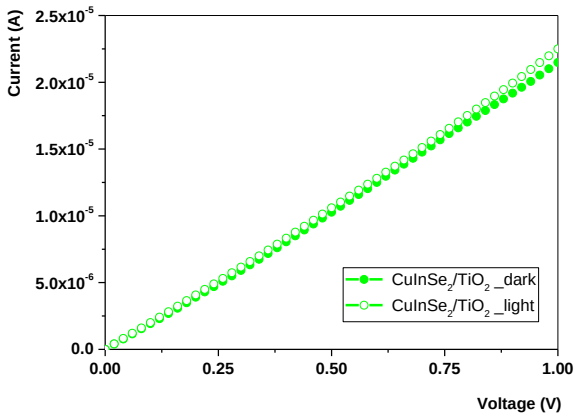

Fig. 4. I-V characteristics of $CuInSe_2/TiO_2$ nanocomposite in the dark and under light illumination

4 Conclusions

$CuInSe_2/TiO_2$ nanocomposite has been prepared by a simple, low-cost mechanochemical route. X-ray diffraction has confirmed the nanocrystalline character of all the components of the nanocomposite, the crystallite size for $CuInSe_2$ (18 nm) being larger than in the case of both TiO_2 phases (5 and 8 nm for rutile and anatase, respectively). The morphology characterization using SEM demonstrated the homogeneity of the prepared nanocomposite. The surface properties investigated by the low-temperature nitrogen adsorption showed that the nanocrystallites are agglomerated into micron-scale particles and co-milling $CuInSe_2$ with TiO_2 led to a considerable increase of the specific surface area of $CuInSe_2/TiO_2$ (13 m^2g^{-1}) in comparison with standalone $CuInSe_2$. Mechanochemically synthesized $CuInSe_2/TiO_2$ nanocomposite exhibits stronger absorption from the ultraviolet to visible region with the determined optical bandgap 1.3 eV. The current increased by 57% in $CuInSe_2/TiO_2$ nanocomposite compared to $CuInSe_2$. This investigation has shown the possibility to prepare nanocomposite material with potential applications in optoelectronics by an environmentally friendly manner.

This work was supported by the Slovak Research and Development Agency under the contracts No. APVV-18-0357, APVV-20-0437 and by the Slovak Grant Agency VEGA (project 2/0112/22 and 2/0084/23).

References

Baláž, P., Achimovičová, M., Baláž, M., Billik, P., Cherkezova-Zheleva, Z., Criado, J. M., Delogu, F., Dutková, E., Gaffet, E., Gotor, F. J., Kumar, R., Mitov, I., Rojac, T., Senna, M., Streletskii, A. & Wieczorek-Ciurowa, K. (2013) Hallmarks of mechanochemistry: from nanoparticles to technology. *Chemical Society Reviews,* 42, 7571-7637.

Baláž, P., Baláž, M., Achimovičová, M., Bujňáková, Z. & Dutková, E. (2017) Chalcogenide mechanochemistry in materials science: insight into synthesis and applications (a review). *Journal of Materials Science,* 52, 11851-11890.

Das, S., Sopha, H., Krbal, M., Zazpe, R., Podzemna, V., Prikryl, J. & Macak, J. M. (2017) Electrochemical Infilling of $CuInSe_2$ within TiO_2 Nanotube Layers and Subsequent Photoelectrochemical Studies. *Chemelectrochem,* 4, 495-499.

Dutkova, E., Sayagues, M. J., Kovac, J., Kovac, J., Bujnakova, Z., Briancin, J., Zorkovska, A., Balaz, P. & Ficeriova, J. (2016) Mechanochemically synthesized nanocrystalline ternary $CuInSe_2$ chalcogenide semiconductor. *Materials Letters,* 173, 182-186.

Eisener, B., Wagner, M., Wolf, D. & Muller, G. (1999) Study of the intrinsic defects in solution grown $CuInSe_2$ crystals depending on the path of crystallization. *Journal of Crystal Growth,* 198, 321-324.

Guo, Q., Kim, S. J., Kar, M., Shafarman, W. N., Birkmire, R. W., Stach, E. A., Agrawal, R. & Hillhouse, H. W. (2008) Development of $CuInSe_2$ nanocrystal and nanoring inks for low-cost solar cells. *Nano Letters,* 8, 2982-2987.

Kang, F., Ao, J. P., Sun, G. Z., He, Q. & Sun, Y. (2009) Structure and photovoltaic characteristics of $CuInSe_2$ thin films prepared by pulse-reverse electrodeposition and selenization process. *Journal of Alloys and Compounds,* 478, L25-L27.

Kostova, N. & Dutkova, E. (2016) Mechanochemical synthesis and properties of ZnS/TiO_2 composites. *Bulgarian Chemical Communications,* 48, 161-166.

Kshirsagar, A. S., Gautam, A. & Khanna, P. K. (2017) Efficient photo-catalytic oxidative degradation of organic dyes using $CuInSe_2/TiO_2$ hybrid hetero-nanostructures. *Journal of Photochemistry and Photobiology a-Chemistry,* 349, 73-90.

Yang, Z. Y., Li, H., Cui, X. Q., Zhu, J. K., Li, Y. H., Zhang, P. F. & Li, J. R. (2022) Highly Efficient $CuInSe_2$ Sensitized TiO_2 Nanotube Films for Photocathodic Protection of 316 Stainless Steel. *Coatings,* 12.

Yu, Y. Y., Chien, W. C., Ko, Y. H. & Chen, S. H. (2011) Preparation and characterization of $P_3HT:CuInSe_2:TiO_2$ thin film for hybrid solar cell applications. *Thin Solid Films,* 520, 1503-1510.

P6: Investigating the suitability of K-feldspar modified by milling for CO_2 sequestration

Marcela Achimovičová[1,*], *Erika* Tóthová[1], *Matej* Baláž[1], *Anton* Zubrik[1], *Murat* Erdemoğlu[2], *Mustafa* Birinci[2], *Sema* Erdemoğlu[2] and *Hikmet* Sis[2]

[1]Institute of Geotechnics, Slovak Academy of Sciences, Watsonova 45, 04001 Košice, Slovakia
[2]Mining Engineering Department, Inönü University, Elazig Yolu 15. km, 44280 Battalgazi/Malatya, Türkiye

Abstract. Nowadays, carbon dioxide (CO_2) emissions are one of the main factors of global warming and climate change. Controlling CO_2 levels in the atmosphere and limiting global warming requires urgent action. However, some minerals can be used to capture and store CO_2 from the air or other sources. Mechanochemically modified K-feldspar (with KOH, $Ca(OH)_2$, and CaO) was used for *in situ* and *ex situ* CO_2 capture. In the *ex situ* experiment (in a thermoanalytical apparatus at 150 °C, 5 h), infrared spectroscopy indicated that mechanochemically modified feldspar caused CO_2 sequestration via carbonate formation. The *in situ* CO_2 capture experiment consists of two steps. The first step involved the mechanochemical modification of feldspar using $Ca(OH)_2$ and CaO. The second phase consisted of direct *in situ* CO_2 sequestration in the milling chamber. X-ray diffraction patterns demonstrated the formation of the calcite phase, and elemental analysis confirmed the binding of approximately 1.4% carbon.

1 Introduction

K-Feldspar, $KAlSi_3O_8$, is an insoluble potash ore from the aluminosilicate group of minerals, whose occurrence and large amount of reserves from a global point of view are considerable, e.g. in China or Türkiye. It is well-known that CO_2 is the most abundant of the greenhouse gases and is, therefore, the largest contributor to the greenhouse effect. In the last decade, the need and various activities to reduce CO_2 emissions to pre-industrial levels have greatly intensified (2019).

Mineral carbonation is a natural weathering process in which alkaline earth metals, mainly Ca and Mg react with CO_2 to form stable carbonates. These reactions are exothermic, but in nature, they take place slowly during the weathering of silicate minerals (2007; Seifritz, 1990). O´Connor and coworkers developed an aqueous process of direct carbonation of silicate minerals (olivine, serpentine, enstatite) using pressure and temperature above 150°C as a method for CO_2 storage in solid form (O'Connor et al, 2002). Wang et al. studied carbonation using natural K-feldspar calcined with phosphogypsum (Wang et al, 2014). The first attempts to use mechanical activation (high-energy milling) of various silicate minerals for CO_2 sequestration were performed already 20 years ago (Kalinkin et al, 2003; Kalinkin et al, 2004; Kalinkina et al, 2001a; b). Later Turianicová and coworkers investigated the carbonation of olivine and vermiculite using mechanical activation (Turianicová et al, 2013; Turianicová et al, 2014). It is known from the literature that mechanical activation causes grain comminution, increases the specific surface area of the minerals and even breaks their crystal structure by the formation of lattice defects, which increases their overall reactivity in subsequent reactions (Baláž, 2008).

The aim of our study was to demonstrate the potential CO_2 sequestration strategies within mineral carbonation of abundant aluminosilicate K-feldspar. Ex-situ and in-situ capture of CO_2 on mechanochemically additive-modified K-feldspar during high-energy milling was elaborated, characterized and quantified.

2 Experimental

2.1 Materials

Feldspar ore used as input material for the experiments was provided by Kale Seramik Company, Turkey with the following chemical analysis: 70.87 SiO_2, 16.33 Al_2O_3, 0.34% CaO, 0.15% Fe_2O_3, 0.04% MgO, 1.99% Na_2O, 10.6% K_2O, 0.05% TiO_2, 0.06% P_2O_5, 0.01% SrO, 0.14% BaO. Apart from K-feldspar or microcline ($KAlSi_3O_8$), the X-ray diffraction analysis (XRD) showed quartz (SiO_2) and albite ($NaAlSi_3O_8$) as well. Its particle size d_{90}, d_{50}, and d_{10} values were 518, 293, and 121 μm, respectively. For mechanochemical modification of feldspar pure chemicals p.a. KOH, $Ca(OH)_2$, and CaO (all from Centralchem, Slovakia) were used.

2.1.1 Mechanochemical modification of feldspar

Mechanochemical modification of feldspar ore was performed in the laboratory planetary ball mill Pulverisette 6 (Fritsch, Germany) with the addition of 1

* Corresponding author: achimovic@saske.sk

M of KOH, and $Ca(OH)_2$ (Table 1) under the following conditions: volume of milling chamber-250 mL, loading of the mill-50 balls (10 mm in diameter), the material of milling chamber and balls- tungsten carbide, WC, the total mass of the milling charge-20.18 g, ball-to-powder ratio-20:1, milling atmosphere-air, rotation speed 600 rpm, and milling time 90 min (each cycle of milling lasting 30 min was followed by a cooling break of 15 min).

Table 1. The amounts of added materials for mechanochemical modification of feldspar by milling.

Sample	Mass of feldspar [g]	Mass of added material + H_2O [g]
Feldspar	20.18	—
Feldspar/ KOH	16.79	3.39
Feldspar/ $Ca(OH)_2$	15.94	4.24
Feldspar/ $Ca(OH)_2$ wet	16.85	2.24 + 1.1

2.2 CO_2 sequestration of feldspar

2.2.1 Ex situ CO_2 sequestration

Feldspar and mechanochemically modified samples of feldspar were subjected to *ex situ* sequestration using thermoanalytical apparatus STA 449 F3 Jupiter (Netzsch, Germany) under dynamic conditions in CO_2 (50 $cm^3.min^{-1}$) by heating up to 150 °C for 5 h.

2.2.2 In situ CO_2 sequestration

The mechanochemically modified samples according to the conditions in *2.1.1* were *in situ* sequestrated using laboratory planetary ball mill Pulverisette 6 (Fritsch, Germany) according to the following conditions: volume of milling chamber-250 ml, loading of the mill-50 balls (10 mm in diameter), the material of milling chamber and balls-tungsten carbide, WC, the total mass of the milling charge-20.18 g, the addition of 10.1 ml H_2O, ball-to-powder ratio-20:1, milling atmosphere-CO_2 (5 $L.min^{-1}$, 3 min flushing), rotation speed 450 rpm, and milling time 30 min.

2.3 Characterization techniques

X-ray diffraction measurements (XRD) were carried out in the Bragg-Brentano geometry using a D8 Advance diffractometer (Bruker, Germany), working with CuK_α radiation and a scintillation detector. ICDD-PDF2 was used for phase matching.

Fourier-transform infrared (FT-IR) spectra were measured using the Tensor 29 (Bruker, Germany) in the frequency range of 4000–400 cm^{-1} with the KBr pellet method. KBr was dried before the analysis at 100°C for 1 h.

Thermogravimetric measurements were carried out using STA 449 Jupiter thermal analyzer (Netzsch, Germany) coupled with a QMS 430C Aëolos mass spectrometer (Netzsch, Germany). The measurements were performed at steady air flow from 45 °C up to 1000 °C with a heating rate of 10 °C/min. Changes in the sample weight and m/z signals (m/z = 18 (H_2O) and m/z = 44 (CO_2)) were constantly monitored.

CHNS analysis was performed by elementary analyser Vario MACRO cube (Elementar Analysensysteme GmbH, Germany) using a thermal conductivity detector. Helium (purity 99.995%, intake pressure 2 bar) was chosen as the carrier gas in all analyses. The purity of oxygen for combustion was 99.995% with an intake pressure of 2 bar A combustion tube was set up at 1150 °C and a reduction tube at 850 °C. Sulphanilamide (C=41.81%, N=16.26%, H=4.65%, S=18.62%) was used as the CHNS standard.

3 Results and discussion

The first *ex situ* CO_2 capture tests using mechanically activated feldspar without modification were unsuccessful. Therefore, the feldspar was subjected to mechanochemical modification with the addition of KOH and $Ca(OH)_2$ in order to create new phases that would be able to capture CO_2 gas. By evaluating the XRD patterns (Fig. 1) of such modified feldspar was found, that during 90 min of milling, only the amorphization of microcline and albite phases was detected and no new phases were formed. In the case of milling with $Ca(OH)_2$ in the liquid state, a WC phase appeared originating from the wear of the milling chamber and balls.

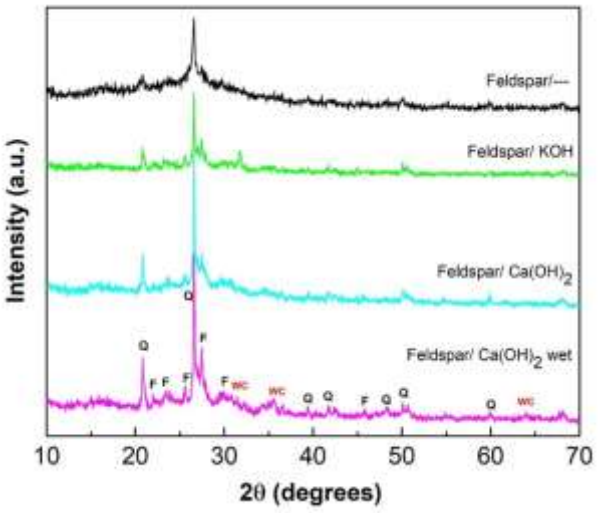

Fig. 1. XRD patterns of mechanically activated feldspar and mechanochemically modified feldspar with KOH and $Ca(OH)_2$. F - $KAlSi_3O_8$, Q - SiO_2.

Ex situ CO_2 sequestration of such modified samples was monitored using TG/DTA analysis for 5 h at 150 °C in a CO_2 atmosphere. The curves in Fig. 2 revealed that at the beginning of the experiment, a slight weight increase was observed in the case of feldspar/ KOH and $Ca(OH)_2$ mixtures. This increase in weight might be due

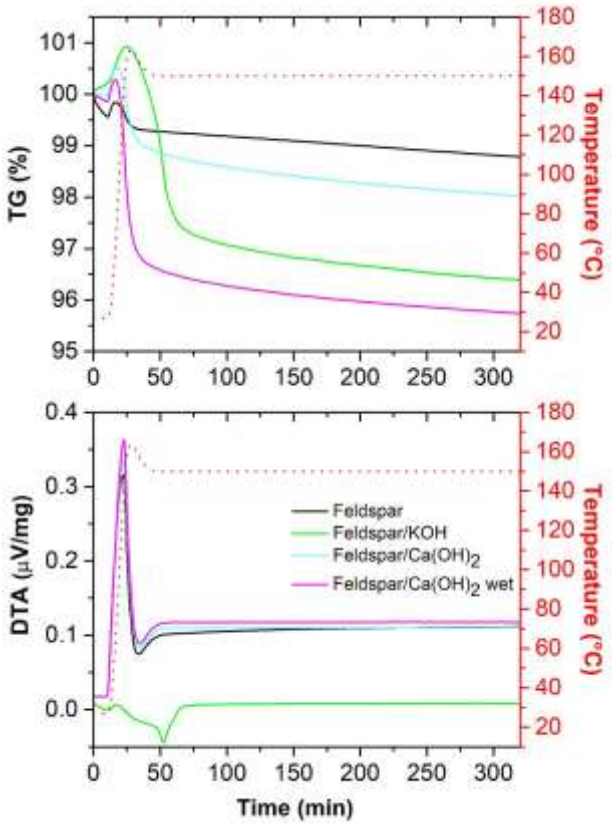

Fig. 2. TG and DTA curves of mechanically activated feldspar (black line) and mechanochemically modified feldspar with KOH and $Ca(OH)_2$ during *ex situ* CO_2 sequestration.

to the carbonization process; however, no other effects were detected.

The FT-IR spectra of the samples modified with KOH, $Ca(OH)_2$ under dry and wet conditions after CO_2 exposure in Fig. 3 showed evidence of CO_2 binding and carbonate phase formation, which can be determined by the peak in the wavenumber region of 1600-1300 cm^{-1}, characteristic for CO_3^{2-} vibrations (Nakamoto, 2008).

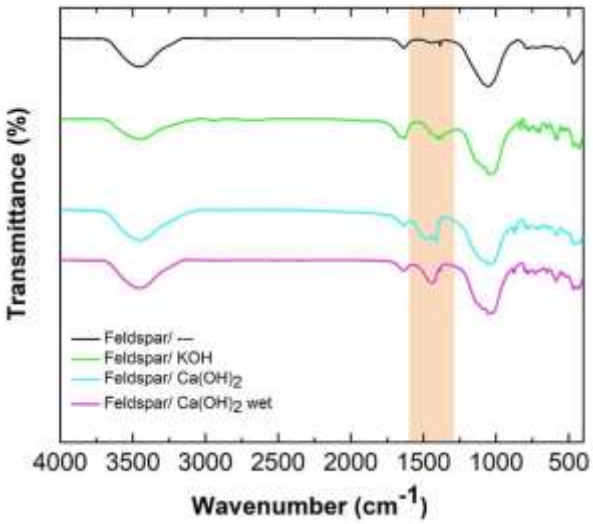

Fig. 3. FT-IR spectra of mechanically activated feldspar (black line) and mechanochemically modified feldspar with KOH and $Ca(OH)_2$ after *ex situ* CO_2 sequestration.

The same behaviour is not detected in the case of feldspar without modification. It means, that $CaCO_3$ and K_2CO_3 were formed during mentioned conditions in the case of feldspar modified by KOH and $Ca(OH)_2$. However, we assume that the binding of CO_2 proceeds only due to the presence of KOH and $Ca(OH_)2$ and feldspar is inactive.

Therefore, to intensify CO_2 capture by modified feldspar, another investigation strategy was chosen- two-step milling. In the first step, the milling with the addition of $Ca(OH)_2$ and CaO, respectively, chemically altered feldspar, and then in the subsequent second step, *in situ* CO_2 sequestration was realized. XRD analysis in Fig. 4 confirmed the formation of the calcite phase, $CaCO_3$. This is the evidence that there is a chemical bond between CO_2 and Ca^{2+} during *in situ* sequestration, i.e. 30 min of milling in a CO_2 atmosphere.

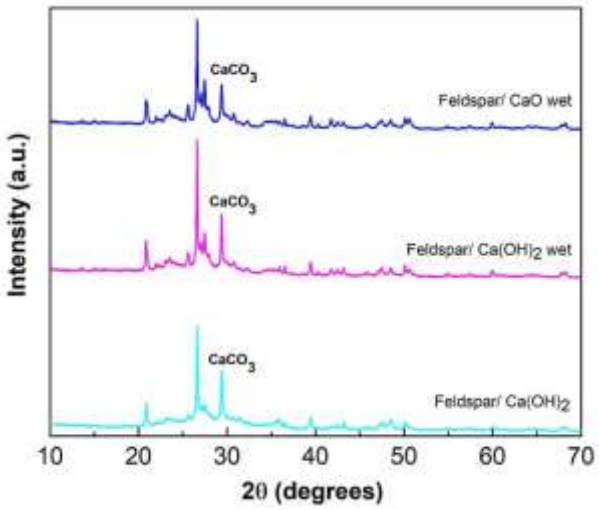

Fig. 4. XRD patterns of feldspar after two-step milling: mechanochemical modification with $Ca(OH)_2$ and CaO and subsequent *in situ* CO_2 sequestration.

With the aim to confirm $CaCO_3$ formation during milling in a CO_2 atmosphere, the thermal decomposition accompanied by the evolution of gases from the calcium carbonate-containing samples was monitored. Fig. 5 compares the thermal behaviour of feldspar modified with $Ca(OH)_2$ and CaO after *in situ* mechanochemical carbonation.

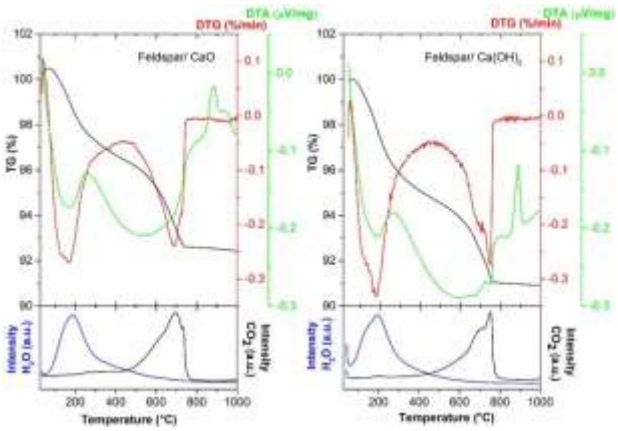

Fig. 5. TG/DTG-DTA curves with mass spectrometry analysis of feldspar after two-step milling: mechanochemical modification with $Ca(OH)_2$ and CaO and subsequent *in situ* CO_2 sequestration.

As can be seen, in both cases, the TG/DTG-DTA curves are similar. As expected, the evolution of H_2O and CO_2 gases has been observed in both cases. While dehydration occurred in the range of 25-400 °C, decarbonization occurred in the range of 500-850 °C, which confirms the decomposition of the mechanochemically formed calcite phase.

The results of CHNS elemental analysis of the samples after *in situ* CO_2 sequestration are summarised in Table 2. According to the amounts of carbon they refer to the binding of around 1.2-1.36% of C for modified samples against unmodified feldspar. The values of N and S were under the calibration range.

Table 2. CHNS elemental analysis of feldspar after two-step milling: mechanochemical modification with $Ca(OH)_2$ and CaO and subsequent *in situ* CO_2 sequestration.

Sample	C [%]	H [%]	N [%]	S [%]
Feldspar	0.27	1.59	0.19	0.08
Feldspar/ CaO wet	1.50	0.71	0.15	0.03
Feldspar/ $Ca(OH)_2$ wet	1.63	0.82	0.18	0.02
Feldspar/ $Ca(OH)_2$	1.47	0.76	0.17	0.02

The present investigation was supported by ERA-MIN3 POTASSIAL 27 project and the Scientific and Technological Research Council of Türkiye (Project 122N039). The authors are grateful to the group of Prof. Emmerling from the Federal Institute of Materials Research and Testing in Berlin, Germany for making XRD analysis available.

References

(2007) *Synthesis Report. Contribution of Working Groups I, II and III to the Fourth Assessment Report of the Intergovernmental Panel on Climate Change.* Geneva, Switzerland.

(2019) *What is carbon neutrality and how can it be achieved by 2050?* , 2019. Available online: https://www.europarl.europa.eu/news/en/headlines/society/20190926STO62270/what-is-carbon-neutrality-and-how-can-it-be-achieved-by-2050 [Accessed June 13, 2023].

Baláž, P. (2008) *Mechanochemistry in Nanoscience and Minerals Engineering.* Springer, Berlin.

Kalinkin, A., Boldyrev, V., Politov, A., Kalinkina, E., Makarov, V. & Kalinnikov, V. (2003) Investigation into the mechanism of interaction of calcium and magnesium silicates with carbon dioxide in the course of mechanical activation. *Glass Physics and Chemistry*, 29(4), 410-414.

Kalinkin, A., Kalinkina, E., Politov, A., Makarov, V. & Boldyrev, V. (2004) Mechanochemical interaction of Ca silicate and aluminosilicate minerals with carbon dioxide. *Journal of Materials Science*, 39(16-17), 5393-5398.

Kalinkina, E., Kalinkin, A., Forsling, W. & Makarov, V. (2001a) Sorption of atmospheric carbon dioxide and structural changes of Ca and Mg silicate minerals during grinding - I. Diopside. *International Journal of Mineral Processing*, 61(4), 273-288.

Kalinkina, E., Kalinkin, A., Forsling, W. & Makarov, V. (2001b) Sorption of atmospheric carbon dioxide and structural changes of Ca and Mg silicate minerals during grinding - II. Enstatite, akermanite and wollastonite. *International Journal of Mineral Processing*, 61(4), 289-299.

Nakamoto, K. (2008) *Infrared and Raman Spectra of Inorganic and Coordination Compounds: Part A: Theory and Applications in Inorganic Chemistry*, 6th. edition. John Wiley & Sons, Inc.

O'Connor, W., Dahlin, D., Rush, G., Dahlin, C. & Collins, W. (2002) Carbon dioxide sequestration by direct mineral carbonation: process mineralogy of feed and products. *Minerals & Metallurgical Processing*, 19(2), 95-101.

Seifritz, W. (1990) CO_2 disposal by means of silicates. *Nature*, 345 (6275), 486-486.

Turianicová, E., Baláž, P., Tuček, L., Zorkovská, A., Zeleňák, V., Németh, Z., Šatka, A. & Kováč, J. (2013) A comparison of the reactivity of activated and non-activated olivine with CO_2. *International Journal of Mineral Processing*, 123, 73-77.

Turianicová, E., Obut, A., Tuček, E., Zorkovská, A., Girgin, I., Baláž, P., Németh, Z., Matik, M. & Kupka, D. (2014) Interaction of natural and thermally processed vermiculites with gaseous carbon dioxide during mechanical activation. *Applied Clay Science*, 88-89, 86-91.

Wang, C., Yue, H., Li, C., Liang, B., Zhu, J. & Xie, H. (2014) Mineralization of CO_2 using natural K-feldspar and industrial solid waste to produce soluble potassium. *Industrial & Engineering Chemistry Research*, 53(19), 7971-7978.

P7: Investigating the effect of milling parameters on the comminution of the rice husk in a planetary ball mill

Imelda Octa Tampubolon[1], *Róbert* Džunda[2], *Radovan* Bureš[2], *Giacomo* Marra[3], *Paz* Sebastiá Luna[3], *Ana* Mangas Roca[3] and *Matej* Baláž[1,*]

[1]Institute of Geotechnics, Slovak Academy of Sciences, Slovakia
[2]Institute of Materials Research, Slovak Academy of Sciences, Slovakia
[3]AIMPLAS Technological Institute of Plastics, Spain

Abstract. Rice husk has been extensively studied, utilized in various applications, and contributed to developing a circular bio-economy due to its content of lignocellulosic compounds and silica. Its valorisation has become one of the recent research interests. This study aims to investigate the effect of the planetary ball milling conditions on its particle size and morphology, which significantly influences the subsequent isolation of lignin cellulose, hemicellulose and silica. It was found that changing the milling vessel and balls material from zirconium oxide to tungsten carbide and prolonging the milling process had a beneficial effect on the comminution of rice husk, as evidenced by the SEM images and the analysis of mean particle size distribution. The original structure of the rice husk was disrupted during milling, resulting in its transformation into a powdered form characterized by smoother textures. Remarkably, milling rice husk for 60 min using ZrO_2 demonstrates a particle size distribution akin to that achieved by milling with WC for 30 minutes, with respective median particle sizes of around 13 and 17 μm. These findings underscore the intricate relationship between milling parameters and material properties, thereby informing strategies for the effective pretreatment for the valorisation of rice husk within scientific and industrial contexts.

1 Introduction

Rice production reaches up to 750 million tons annually, generating excessive rice husk as a by-product (150 million tons). However, rice husk has been reported to contain valuable organic compounds, 25–35% of cellulose, 18–21% of hemicellulose, 26–31% of lignin, and 15–25% of silica. (Beaino et al., 2022), Hence, this waste valorisation has been studied extensively and transformed into valuable products for some potential applications, namely as catalysts for transesterification of fatty acids to give biodiesel (Akhter et al., 2023), fuel source, ceramic industries, cosmetic, activated carbon, and metal and dye adsorbent (Goodman, 2020).

The first step for valorisation is a pretreatment. Lignocellulosics can be extracted through a series of processes by delignification techniques without cellulose-fibrils destruction (Zanuncio and Colodette, 2011) and can overcome the recalcitrant nature of lignocellulosic biomass, reducing cellulose crystallinity index; hence improving the effectiveness of the enzymatic processes (Rajamani et al., 2023).

Mechanical and mechanochemical activation of biomass in a high-energy ball mill has been reported as an efficient method for the delignification of biomass, with the advantages of offering an appropriate particle size dimension, producing low levels of fermentation inhibitors, and reducing losses of hemicelluloses and structural changes in the lignin compared to steam explosion. This benefit comes from the activation that accelerates the reaction rates and leverages energy via localized pressures and frictional heating, which improves the efficiency and economy of biomass valorisation (Baláž, 2021; Calcio Gaudino et al., 2021).

Recent studies in the mechanochemical treatment of biomass have demonstrated its capacity to induce distinct degrees of particle size reduction and diverse mechanochemical effects, including depolymerization and acetylation. Such milling treatments are pivotal in reducing particle size, influencing the broader biomass-to-product process chains. In the present investigation, multiple milling parameters were systematically varied to elucidate their impact on the morphology and particle size distribution of rice husks subjected to milling treatment.

2 Material and methods

2.1 Material

Rice husk was obtained from the AIMPLAS company, with a particle size of <1mm.

2.2 Milling experiments

* Corresponding author: balazm@saske.sk

Rice husk was milled using a Pulverisette 6 planetary ball mill (Fritsch, Germany) under the air atmosphere. Further milling conditions are stated in Table 1. Six milling experiments were performed altogether, starting with the initial experiment RH-1 and always changing one parameter (namely, milling time, milling rotation speed, material of milling media, ball-to-mass of powder ratio, and sample mass) while keeping the others constant. Subsequently, the samples were kept in the plastic seal for further analysis.

Particle size measurement was done using a particle size laser diffraction analyzer Mastersizer 2000E (Malvern, Malvern, UK) in the dry mode. Three measurements were conducted for each sample. Lyra3 (Tescan, Czech Republic) scanning electron microscope (SEM) was used to visualize the surface characteristics with scanning voltages of 3 keV and in secondary electron (SE) mode. Before analysis, the sample was affixed onto double-sided adhesive carbon tape and coated with a 40 nm thick carbon layer using a Leica EM ACE600 sputter coater (Leica Microsystems, Germany).

2.3 Characterization techniques

Table 4. Design of milling conditions for the rice husk

Code	Milling time (min)	Sample mass (g)	Rotation speed (rpm)	Ball diameter (mm)	Milling material
RH-1	30	5	550	10	ZrO_2
RH-2	30	5	550	5	ZrO_2
RH-3	30	5	300	10	ZrO_2
RH-4	30	10	550	10	ZrO_2
RH-5	60	5	550	10	ZrO_2
RH-6	30	5	550	10	WC
RH-7	Untreated rice husk				

3 Results and discussion

2.1 Morphology of the rice husk

SEM analysis gives information about the morphology of the rice husk after being subjected to certain milling parameters. Among other parameters, rotation speed of planet carrier, material of milling media, milling time, and sample mass contribute to these structural changes. A comparison of images of RH-1 (Fig. 1a) and RH-3 (Fig. 1c), with the milling speed of 500 and 300 rpm, respectively, reveals a significant difference in the morphology. At 300 rpm, the morphology is only slightly changed in comparison with the starting RH. However, when using 500 rpm, harsher collisions between the ball and the sample take place, resulting in the finer rice husk powder and an increased degree of depolymerization. Increasing sample mass to 10 g (RH-4, Fig. 1d) led to a lower extent of comminution in comparison with using 5 g (RH-1, Fig. 1a). Observation of SEM images of RH-1 (Fig. 1a) and RH-5 (Fig. 1e) unveils significant surface changes upon extending milling time from 30 min to 60 min, with the latter exhibiting smoother particle surfaces. Fig 1 also illustrates the changes in the rice husk when milling with the balls of different size, namely the particles are larger when using 5 mm balls (RH-2, Fig. 1b) than when using the ones with diameter 10 mm (RH-1, Fig. 1a). Employing tungsten carbide as milling media transformed rice husk into finer powder (RH-6, Fig. 1f).

Additionally, Fig. 1(g) depicts that the surface of the untreated rice husk is highly ridged and abundant in protuberances, as previously observed (Park et al., 2003; Yang et al., 2021). These results indicate that the structural changes in the morphology were induced by milling treatment, with certain parameters facilitating the breakdown of the rice husk structure into fine powder.

2.2 Particle size distribution

The data on particle size distribution supported the morphology and structural changes of the rice husk detected by SEM. The median particle size (d_{50}) of treated and untreated rice husks is presented in Fig. 2. There is a correlation between the structural changes and the particle size after milling treatment. The d_{50} of the rice husks decreased from 89 to 13 μm when the milling duration in ZrO_2 was prolonged from 30 (RH-1) to 60 min (RH-5). Previous experiments verified that extending the milling duration significantly increases the collision frequencies between the balls and particles (Borhan et al., 2012; Ye et al., 2020), generating energy and reducing particle size. Changing the milling material from ZrO_2 (RH-1) to WC (RH-6) significantly reduces the d_{50} particle size from 89 μm to 17 μm with the same milling time. The density of the WC and ZrO_2 is 14.8 and 5.5 g/cm^3, respectively (Kudaka et al., 2000). With the same number of 10 mm balls of WC and ZrO_2, the energy generated using WC is higher than ZrO_2. Changing the ball diameter from 10 mm (RH-1) to 5 mm (RH-2) resulted in d_{50} value increasing from 89 to 228 μm. Small balls might be effective in grinding the fine powder; however, in the case of rice husk; in the coarse form, the larger balls have more kinetic energy and can break larger particles, resulting in the smaller particle size obtained. d_{50} of untreated rice husk (RH-7)

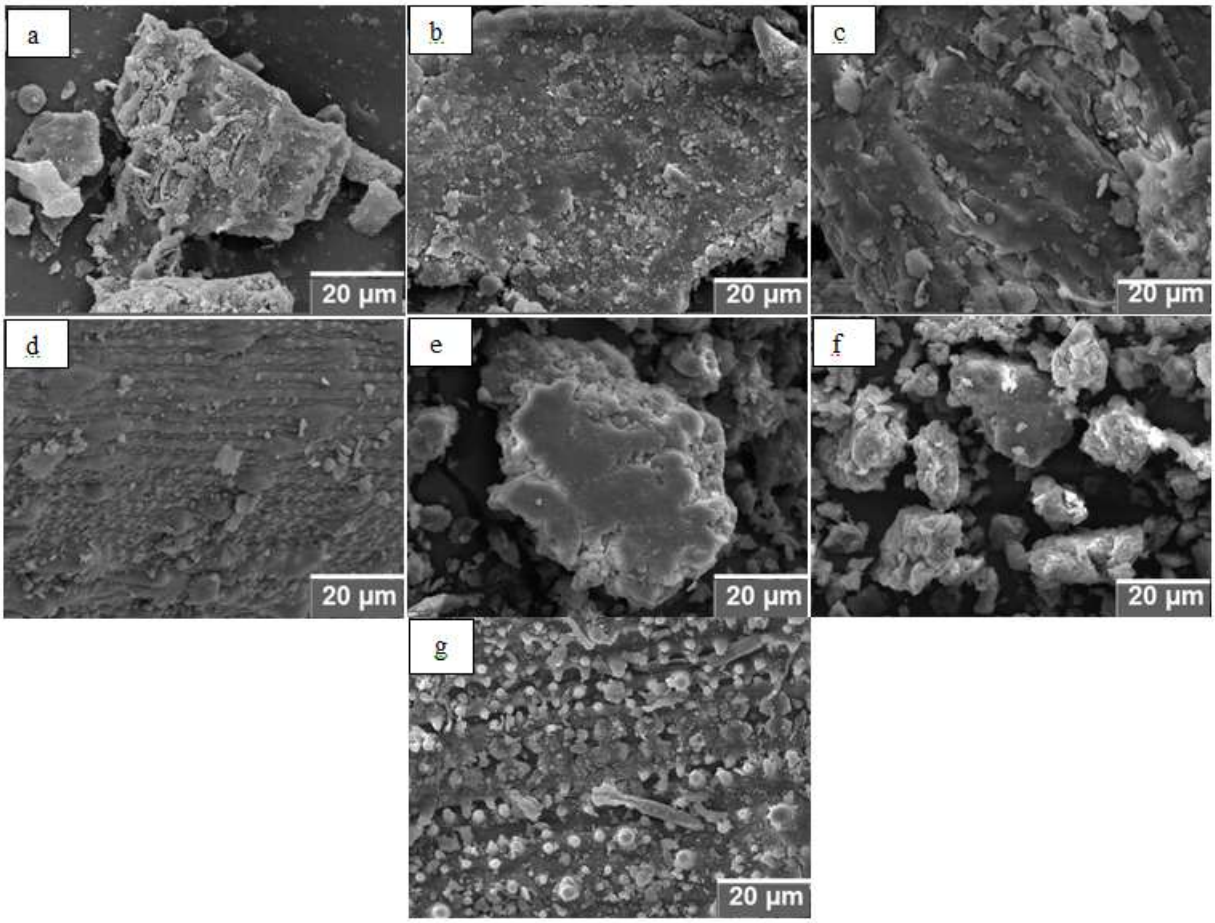

Fig. 1. SEM images of samples a) RH-1, b) RH-2, c) RH-3, d) RH-4, e) RH-5, f) RH-6 and g) RH-7

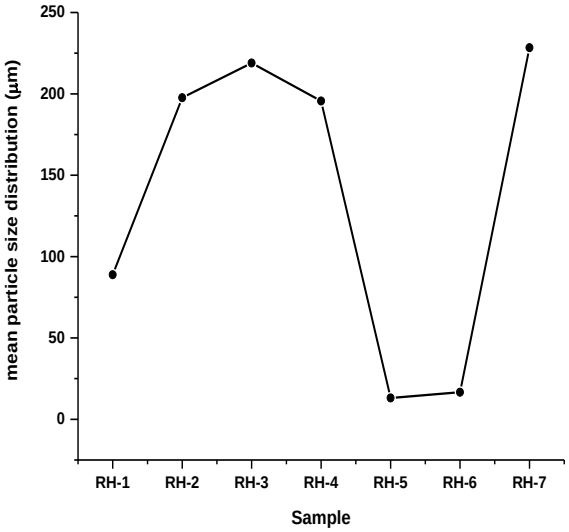

Fig. 2. d_{50} values for rice husk treated under different milling conditions

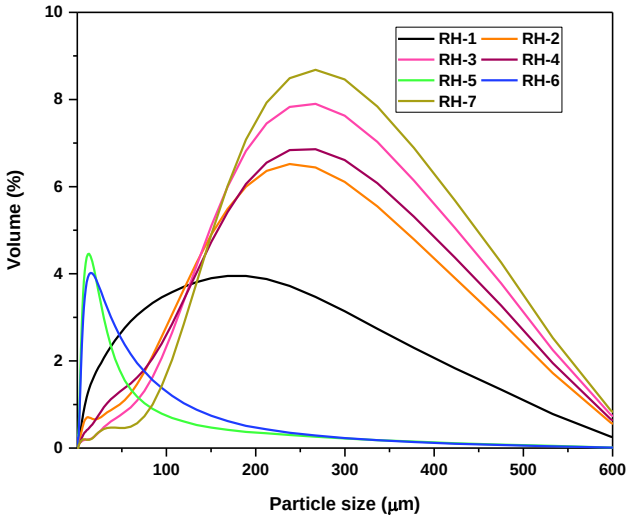

Fig. 3. Particle size distribution of mechanically-activated and untreated rice husk

are equal to 228 µm is similar to that of the RH-2, RH-3 and RH-4, (d_{50} = 228, 198, 219, and 195 µm, respectively. Fig. 3. displays the overview of particle size of all the samples. In general, a significant particle size reduction in comparison with starting RH-7 sample was achieved for RH-1, RH-5 and RH-6 samples.

Conclusion

Mechanically activating rice husk in a high-energy planetary ball mill under specific conditions enhances the degree of depolymerisation, breaks down the lignocellulosics, and leads to structural changes and particle size reduction of the rice husk. Milling 5 g of rice husk for 60 min using ZrO_2 vessel and for 30 min using WC vessel and balls resulted in similar results.

Thus, increasing milling duration and changing milling material for denser one improve the efficient comminution of rice husk into fine powder, resulting in d_{50} particle sizes of 13 and 16 μm, respectively, in comparison with 228 μm of untreated rice husk and 89 μm for the reference experiment. Other parameters, such as sample mass, milling speed and ball diameter, had negligible impact under the given conditions. A proper selection of milling conditions can facilitate the valorisation of rice husk, leading to a more efficient subsequent processing (e.g. delignification or enzymatic hydrolysis).

This work was supported by the Scientific Grant Agency of Education, Research and Sport of the Slovak Republic (project 2/0112/22).

References

Akhter, F., Soomro, S.A., Jamali, A.R., Chandio, Z.A., Siddique, M., Ahmed, M., 2023. Rice husk ash as green and sustainable biomass waste for construction and renewable energy applications: a review. Biomass Conversion and Biorefinery 13, 4639–4649.

Baláž, M., 2021. Environmental mechanochemistry: Recycling waste into materials using high-energy ball milling. Springer.

Beaino, S., Hage, P. El, Sonnier, R., Seif, S., Hage, R. El, 2022. Novel Foaming-Agent Free Insulating Geopolymer Based on Industrial Fly Ash and Rice Husk. Molecules 27, 1–19.

Borhan, M.Z., Ahmad, R., Rusop, M., Abdullah, S., 2012. Influence of milling time on fineness of Centella Asiatica particle size produced using planetary ball mill. AIP Conference Proceedings 1502, 454–463.

Calcio Gaudino, E., Cravotto, G., Manzoli, M., Tabasso, S., 2021. Sono- And mechanochemical technologies in the catalytic conversion of biomass. Chemical Society Reviews 50, 1785–1812.

Goodman, B.A., 2020. Utilization of waste straw and husks from rice production: A review. Journal of Bioresources and Bioproducts 5, 143–162.

Kudaka, K., Iizumi, K., Sasaki, T., Izumi, H., 2000. Effect of milling media on the reaction kinetics of the mechanochemical synthesis of pentatitanium trisilicide. Journal of the American Ceramic Society 83, 2887–2889.

Park, B.D., Gon Wi, S., Ho Lee, K., Singh, A.P., Yoon, T.H., Soo Kim, Y., 2003. Characterization of anatomical features and silica distribution in rice husk using microscopic and micro-analytical techniques. Biomass and Bioenergy 25, 319–327.

Rajamani, S., Kolla, S.S.N., Gudivada, R., Raghunath, R., Ramesh, K., Jadhav, S.A., 2023. Valorisation of Rice Husk to Value-Added Chemicals and Functional Materials. International Journal of Environmental Research 17, 1–20.

Yang, Y., Pang, Y., Zhang, W., Xia, R., Li, Y., Liu, Y., Guo, H., 2021. Effects of desilication pretreatment on rice husk/high-density polyethylene bio-composites. Polymer Composites 42, 1429–1439.

Ye, M., Pan, J., Guo, Z., Liu, X., Chen, Y., 2020. Effect of ball milling process on the photocatalytic performance of CdS/TiO2composite. Nanotechnology Reviews 9, 558–567.

Zanuncio, A.J.V., Colodette, J.L., 2011. Correlation between levels of lignin and uronic acids in the wood and cellulose pulp of Eucalyptus. Revista Arvore 35, 341–347.

P8: Experimental investigation of the effect of the powder and the suspension rheology on grindability

Katalin Bohács[1*], *Roland* Romenda[1], *Ádám Rácz*[1], *Teemu* Kinnarinen[2], *Nazila* Bolourieh[2], *József* Faitli[1], *Barnabás* Csőke[1]

[1]Institute of Raw Materials Preparation and Environmental Technology, University of Miskolc, Hungary
[2]LUT School of Engineering Sciences, Lappeenranta-Lahti University of Technology LUT, Lappeenranta, Finland

Abstract. The grindability of raw materials is a key parameter of mineral processing. It is also very important for some kinds of secondary raw materials, such as the demolition and construction wastes. The Institute of Raw Materials Preparation and Environmental Technology of the University of Miskolc has been dealing with this topic for a long time. The Universal Hardgrove Mill and the Universal Bond Mill had been developed. With these devices the grindability can be measured at so called universal circumstances, namely at high temperature in any (acidic or alkali or neutral) medium. The rheological behaviour of the ground slurry or suspension evidently affects grinding because of the well-known viscous dampening effect. However, the grindability of materials as function of the moisture content and rheology has not been studied on-line. Therefore, the grindability of a soft adhesive (limestone) and a hard non-adhesive (quartz) material was examined in the Universal Hardgrove Mill during room temperature dry and wet (in tap water) grinding. The powder flow behaviour of the dry ground samples was measured in an FT4 powder rheometer, while the rheological properties of the wet ground suspensions were measured in a rotational rheometer.

1 Introduction and aim

The issue of the high energy demand of comminution is widely known in the literature and continuous research is ongoing in this field. On the other hand, the process engineering design of crushing and grinding units is typically carried out by using different kinds of grindability indices characterising the given raw material. This is the reason why the fundamental research of grindability test methodology development and the development of the auxiliary complementary test methodology is so important. At the Institute of Raw Materials Preparation and Environmental Technology of the University of Miskolc, it has a long tradition, the Universal Hardgove Mill and the Universal Bond Mill had been developed by with grindability can be measured at so called universal circumstances, namely at high temperature and in any kind of (neutral, acidic, alkali) media (Csőke et al., 2003; Mucsi et al., 2006).

Beyond these, lack of knowledge about the effect of the moisture content on grindability can be found in the literature and another current issue is the questions of viscous dampening in comminution machines (Ding et. al., 2007a and 2007b; He et. al., 2006; He, 2007; Jankovic, 2003). Therefore, two model materials, - a soft and adhesive material the limestone and a hard and non-adhesive material the quartz - were selected. After preparation of the taken samples the so called dry (< 20 m/m% moisture content) and wet (> 50 m/m%) grindability tests were carried out in the Universal Hardgrove Mill. At this time auxiliary tests had been carried out also. Powder flow features were measured in a powder rheometer and suspension rheology was measured in a rotational rheometer.

2 Materials and Methods

The limestone samples - with a material density of 2680 kg/m^3 (measured by liquid pycnometer in water) were taken in Tornanádaska, Hungary. The quartz samples - with a material density of 2631 kg/m^3 (measured by liquid pycnometer in water) were taken in Alsózsolca, Hungary. The Hardgrove grindability index was measured by the earlier developed Universal Hardgrove Mill (Figure 1 and 2).

According to the standard Hardgrove protocol 50 g prepared sample, namely only the x = 590… 1190 µm particle size fraction is fed into the grinding chamber. There are eight 25.4 mm diameter balls in there. The vertical force on the grinding balls is set constant to be 290 N. The constant revolution number of the rotor is 20 1/min and a round of grinding lasts until 60 full revolutions. After grinding, the ground solids is removed and sieved in a Retsch sieving machine for 20 minutes using a 0.075 mm opening size screen. The mass of the fine fraction (m_{75}) is measured in gram unit and the Hardgrove index is calculated by Equation 1 left. However, the Hardgrove index (H) is widely used in the industry, this index characterises the required specific energy only indirectly. (Csőke et al., 2013) suggested a

* Corresponding author: katalin.bohacs@uni-miskolc.hu

simple conversion equation (Equation 1 right) by with the Bond index ($W_{B,H}$) can be calculated from the Hardgrove index.

$$^0H = 16 + 6.93 \cdot m_{75} \qquad W_{B,H} = \frac{468}{H^{0,82}} \tag{1}$$

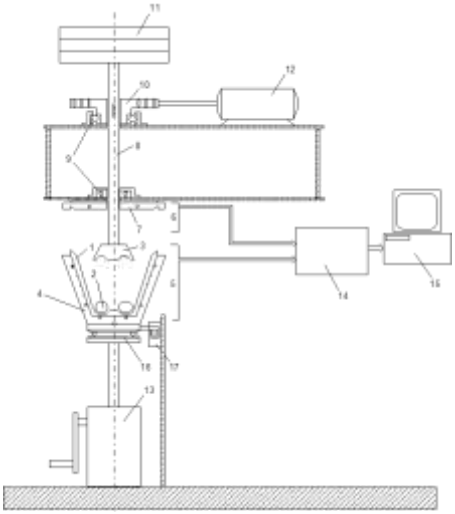

Fig. 1. Schematics of the Universal Hardgrove mill.

1. Grinding balls, 2. Shaped closing assembly for pushing down the balls, 3. Grinding crucible, 4. Crucible furnace: heat-insulating enclosure with three 230 V/500 W heating wires and three PT100 platinum thermal resistors, 5. Electric connection field for connecting the heating wires and thermal resistors, 6. Electric connection field for connecting the heating wire and thermal resistor, 7. Cover of crucible furnace: heat-insulating enclosure with one 230 V/500 W heating wire and one PT100 platinum thermal resistor, 8. Axially moving shaft with bearing, 9. Bearing, 10. Worm-gear drive, 11. Weight, 12. Asynchronous motor, 13. Lever, 14. Measurement electronics, 15. Measurement data acquisition and A/D card, measuring and controlling computer, measuring and controlling software, 16, Axial bearing, 17. Force measuring transducer.

Fig. 2. Photo of the upgraded Universal Hardgrove mill.

Powder flow properties were measured in a FreemanTech FT4 powder rheometer according to the so-called Specific Energy (SE) protocol. SE is a measure of how powder flows in an unconfined or low stress environment. It is calculated from the energy required to establish a particular flow pattern in a conditioned, precise volume of powder. This flow pattern is an upward clockwise motion of the blade, generating gentle lifting and low stress flow of the powder. The powder samples were placed into the 25 mm diameter and 60 mm height sample holder. The shape of the blade is shown in Figure 3.

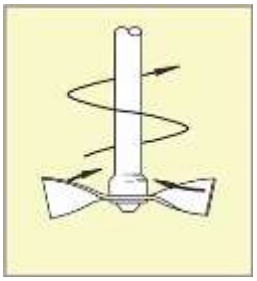

Fig. 3. Shape of blade of SE tests.

During each SE tests 8 test cycles were done, and the tip speed of the blade was always constant 100 mm/s. One test cycle contained first a total down and an upward moving of the blade into the powder bed for conditioning purposes without measurements. Afterward the blade moved down again, and measurement started when the blade started to move up again. Since the revolution number and torque were measured, the total energy required for moving the blade totally upward was calculated by the data acquisition software by numerical integration. The measured SE values as function of the 8 consecutive test cycles can be considered as the function of powder flow and cohesion and friction angle can be determined as the energy axis intersect and slope of the fitted straight line.

The rheological properties of the suspensions were measured in an Anton-Paar Physica MCR51 rotational rheometer using a cylinder – cylinder measuring system with a 40 mm diameter bob and 0.5 mm Couette gap when the necessary sample quantity for one test was 50 cm^3. The revolution number of the bob was set when the shear rate was gradually decreased from 1000 1/s down to 100 1/s.

3 Results and Discussion

During the systematic tests two different materials, limestone (LS) and quartz (QA) and five initial moisture contents were tested. Moisture contents of 0, 10 and 20 m/m% can be considered as dry grindability tests and the ones of 50 and 70 m/m% can be considered as wet tests. The exact moisture contents were set by drying and wetting before the Hardgrove tests. After the Hardgrove tests the ground samples were dried at 105 °C for mass equilibrium, because without this, sieving with the 0.075 mm opening size screen was not feasible. This simple operation just shows the reason why the moisture content

is not taken into account during regular Hardgrove testing. Results of the Hardgrove tests are shown in Table 1.

After the Hardgrove testing, the entire fine (<0.075 mm) and coarse fractions were mixed again and the Specific Energy (SE) tests were performed. Figure 4 shows the sample holder of the FT4 powder rheometer with a quartz sample when the blade was rotated in it.

Fig. 4. Sample holder of SE testing.

Figure 4 well illustrates what was the problem with the SE tests of quartz. The particulate system was a little too coarse for the device and the powder was gradually dug up by the blade. The carrying out of quartz SE tests was not feasible, but with limestone it was without problems. Figure 5 shows the measured powder flow points and fitted flow curves of the limestone SE tests.

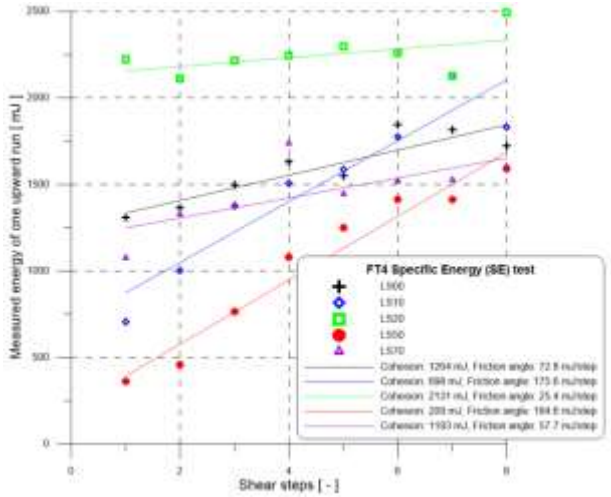

Fig. 5. Specific energy as function of test cycles of limestone SE tests.

The measured Hardgrove indices, cohesions and friction angle values are shown in Table 1. According to Table 1, grindability is strongly influenced by the initial moisture content. It is well known in the literature that sieving at 5-15 m/m% moisture content is critical because the capillary force between the adjacent particles is the highest in such cases, practically materials with such moisture content cannot be sieved (Tarján, 1981 and 1986). Above 20 m/m% moisture content, wet sieving is considered to be occurred. According to practical experience the most effective grinding happens when the raw material is dried below about 5 m/m% lower critical moisture content or just the opposite, the raw material is moistened above the upper critical moisture content (15-20 m/m%). At the so-called dry grinding range (0 and 10 m/m%) of quartz the measured Bond grindability indices are considerably higher because the particles with themselves and with the balls are bonded by the capillary forces. At wet quartz grinding (20, 50 and 70 m/m%) the required energy is lower, because the inter-particle bond decreases but the particles still can be bonded to the surface of the balls.

Table 1. Results of the Hardgrove and SE tests.

Mark of sample	H index -	$W_{B,H}$ Wh/t	Spec. work Ws/50g	Coh. mJ	Frict. angle mJ/step
LS00	58.48	16.7	26.8	1264	72.8
LS10	57.93	16.8	26.8	698	175.6
LS20	70.26	14.3	26.8	2131	25.4
LS50	71.51	14.1	26.7	209	184.6
LS70	70.75	14.2	26.8	1193	57.7
QA00	47.05	19.9	26.7	-	-
QA10	42.47	21.6	26.7	-	-
QA20	51.07	18.6	26.7	-	-
QA50	54.05	17.7	26.8	-	-
QA70	53.70	17.9	26.8	-	-

Probably grinding also deteriorates at extremely high moisture contents because particles cannot be bonded to the balls anymore. From these observations the conclusion must be drawn that the Hardgrove grindability testing should be carried out at the actual moisture content of industrial grinding, especially when the measured values are used for on-line grinding regulation. Regarding the limestone grindability tests, similar conclusions can be drawn except that the adhesive limestone can be efficiently ground at 70 m/m% moisture content too, because limestone can be bonded to the balls still.

Table 2. Results of rheological tests of limestone samples.

Original sample	Volumetric concentration %	Absolute viscosity mPas	Absolute viscosity (repeated) mPas
finer than 0.16 mm			
LS10	2.2	4.0	3.9
	4.4	4.0	4.1
LS20	2.2	4.0	4.0
	4.4	4.2	4.1
	6.7	4.4	4.4
LS70	2.2	3.9	4.0
	4.4	4.0	4.0
	6.7	4.3	4.3
finer than 0.5 mm			
LS70	16.3	4.6	4.4

After the powder flow tests, the same material was used for the rotational rheometer tests. Because of the Couette gap width (0.5 mm) between the cylinders and according

to our earlier experiences, particles typically coarser than 0.16 mm cannot be measured in the MCR51 rotational rheometer with this measurement system. Therefore, the solids were sieved again, but now with a 0.16 mm aperture size screen. Unfortunately, this method decreased the quantity of fine solids; therefore, only low solids concentrations could be measured. There is one exception, in the case of the LS70 solids, a higher concentration and the <0.5 mm fraction was measured successfully.

Table 2 shows the results of rheological tests of limestone samples; these low concentration suspensions were Newtonian fluids with low absolute viscosity values. Table 3 shows the results of rheological tests of quartz samples.

Table 3. Results of rheological tests of quartz samples.

Original sample	Volumetric concentration %	Absolute viscosity mPas	Absolute viscosity (repeated) mPas
finer than 0.16 mm			
QA00	2.2	4.0	4.0
	4.4	4.0	4.0
QA10	2.2	4.1	4.1
	3.0	4.1	4.1
QA20	2.2	4.1	4.1
	4.4	4.1	4.1
QA50	2.2	4.0	4.0
QA70	2.2	4.0	4.0

It is well seen that the many sample operations with the ground solids (drying, sieving, SE testing, sieving, mixing) probably destroyed the original effect of Hardgrove testing or there is no such effect in this case. The measured absolute viscosity values follow the well-known Einstein concentration-viscosity relation for dilute fine suspensions.

4 Conclusion

The carried out wet mode grindability testing has proved that the moisture content is also a very important technological parameter. Two important phenomena were revealed, namely that the capillary force acting among the particles and among the particles and balls are important and controversial effect. The particle-particle bonds are typically not advantageous because it deteriorates grinding; however, particle-ball bonds are advantageous because in ball and ring mills it helps forming more stressing events. It was also concluded that on-line grindability testing for technological regulation should be done at the same moisture content.

This study also has revealed that further measurement methodology development is also necessary. Just think about the problem when Hardgrove grindability is measured in the 10-20 m/m% moisture content range, but sieving at this range is impossible, because of the high capillary forces. Measurement techniques difficulties were also found at the powder flow and the rotational rheometer testing, but it is thought that this initial work can pave the way for later developments.

This project is funded by the European Union's Horizon Europe program under grant no. 101079354.

References

Csőke B., Faitli J., Hatvani Z., Solymár K., Papanastassiou D.: (2003) New test method for investigation of grindability in alkaline media at high temperature. In: Leon, Lorenzen (ed.) Proceedings of the XXII International Mineral Processing Congress, South African Institute of Mining and Metallurgy (SAIMM) pp. 434-441.

Csőke B., Rácz Á., Mucsi G. (2013) Determination of the Bond work index of binary mixtures by different methods. *International Journal of Mineral Processing*. Vol. 123. pp. 78-86.

Ding, H.., Lu, S., Deng, Y., Du, G., Mechano-activated surface modification of calcium carbonate in wet stirred mill and its properties, Transactions of Nonferrous Metals Society of China, 17 (2007a), pp. 1100-1104

Ding, Z., Yin, Z., Liu, L., Chen, Q., Effect of grinding parameters on the rheology of pyrite-heptane slurry in a laboratory stirred media mill, Minerals Engineering, 20 (2007b), pp. 701-709.

Faitli J., Bohács K., Mucsi G. (2016) Online Rheological Monitoring of Stirred Media Milling. *Powder Technology*. Vol. 308. pp. 20-29.

He, M., Wang, Y., Forssberg, E., Parameter effects on wet ultrafine grinding of limestone through slurry rheology in a stirred media milling, Powder Technology, 161 (2006), pp. 10-21

He, M., Slurry Rheology of Industrial Minerals and Its Effects on Wet Ultra-fine Grinding, Thesis, Luleå University of Technology, Sweden, 2007

Jankovic, A., Variables affecting the fine grinding of minerals using stirred mills, Minerals Engineering, 16 (2003), pp. 337-345

Jankovic, A., Sinclair, S. The shape of product size distributions in stirred mills, Minerals Engineering, 19 (2006), pp. 1528-1536

Mucsi G., Csőke B., Faitli J., Solymár K.: (2006) Grindability tests in heated Bond mill. In: Önal, Güven (ed.) Proceedings of the XXIII. International Mineral Processing Congress. Istanbul, Turkey. pp. 87-90.

Tarján G.: (1981 and 1986) Mineral processing 1 and 2. Akadémiai Kiadó, Budapest. ISBN 963-05-2243-8

Toraman, O.Y., Katircioglu, D., A study on the effect of process parameters in stirred ball mill, Advanced Powder Technology, 22 (2011), pp. 26-30

P9: End of Life organic light-emitting diodes (OLEDs) processing – Review

Sándor Márton Nagy[1,*], *Izabella Rebeka* Márkus[1], *Manivannan* Sethurajan[2] and *John* Bediako[2]

[1]Faculty of Earth and Environmental Sciences and Engineering, University of Miskolc, Miskolc, HU
[2]LUT School of Engineering Science, Lappeenranta-Lahti University of Technology, Lappeenranta, FIN

Abstract. The OLED displays are nowadays the second popular ones behind the LED/LCD displays. The average life expectancy of computers are 3 years, mobile phone 2 year and television 5 years, thus the quantity of OLED in the e-waste in the near future will show an inevitable increase. The OLED technology uses less non-organic compound in comparison with LCD technology, however some elements like In, Sn, Co, Ga, Au, Ag, Sr etc. are still indispensable for their production. Due to environmental risk and a worldwide shortage of metals, recycling and recovering valuable metals from the waste OLEDs is an urgent task and has started to gain vivid attention in the last years. The application of bioleaching in the recovering of the metals from waste OLED panels, the use of different bacteria and optimizing the influencing factors like pH, substrates (ferrous sulfate and elemental sulphur), and solid content led to promising results in the metal recovery. And other promising research trend and recycling possibility is the use of glass material from e-waste as secondary raw material in cement and concrete production.

1 Introduction

Electrical and electronic equipment (EEE) is strongly linked to widespread global economic development, its production and usage can be very resource demanding. Based on the statistics of The Global E-waste Monitor 2020, the world generated 53.6 Mt of e-waste in 2019 and based on the actual trends it is expected to reach 74.7 Mt in 2030. The quantity of screens and monitors e-in waste in 2019 was 4.7 Mt, showing a -1% decrease in comparison to the previous years which can be explained by the decreasing quantity of the heavy cathode ray tube (CRT) monitors from the waste stream (Forti et al., 2020).

There are various types of screens and monitors present in the market: liquid crystal display (LCD), organic light-emitting diode (OLED), active-matrix organic light-emitting diode (AMOLED) etc. The OLEDs are becoming widespread, replacing the liquid LCDs since they are thinner and lighter. Moreover the power consumption of OLEDs is 20-80% of that of LCDs, they provide higher contrast and truer colours, higher brightness, wider viewing angles, better temperature tolerance, faster response times and can be deposited onto almost any substrate, both rigid and flexible (Borchardt, 2004). The use of OLED based lighting sources started to gain popularity in the last few years due to its energy saving potential, and other physiological features like foldability and transparency (Swayamprabha et al., 2021), however this sector is less significant. Based on the global technological and market trends the dominance of OLED displays in the near future is unquestionable, leading to the production of large quantities of OLED.

2 OLED panel production capacity

Based on the global technological and market trends the dominance of OLED displays in the near future is unquestionable, leading to the production of large quantities of OLED with total revenue numbers rising from 135 million U.S. dollars in 2016 to nearly 1.1 billion by 2022. The OLED penetration of the display market was around 1.0% in 2017 (Vidal-Abraca et al, 2020). The global OLED market has grown rapidly in the last decade (Fig. 1), the increase speeding up in the last years and a speedy growth is to be expected in the next decade.

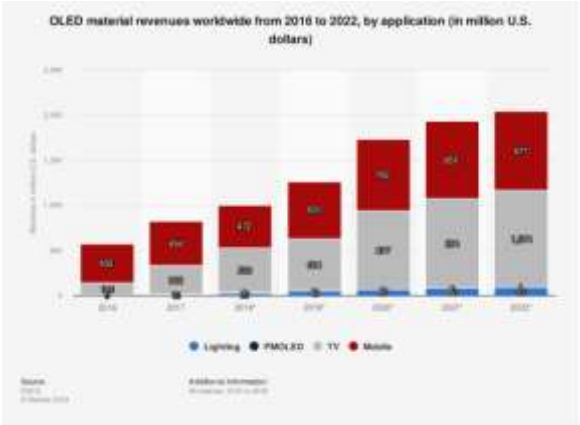

Fig. 1. OLED revenue worldwide (Source: www.statista.com)

The production is concentrated in Asia-Pacific region, with China, South Korea and Japan being the leading manufacturers and also being the largest market

* Corresponding author: sandor.nagy@uni-miskolc.hu

for OLED displays due to the presence of major manufacturers such as Samsung and LG. China's OLED display production capacity is 43.7 % of the global production, while that of Korea 54.9 % (https://www.businesskorea.co.kr).

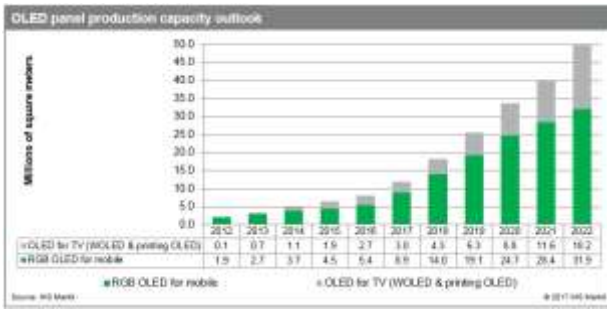

Fig. 2. OLED production capacity (Source: https://sst.semiconductor-digest.com)

The production of OLED for TVs and mobile phones in 2012 was around 2 million of square meters, and mainly used in phone production. In 2022 this quantity reached 50-53 million square meters (https://sst.semiconductor-digest.com, www.statista.com), the phone producers being still the main end users with intake amount of 31-32 millions square meters, however the TV manufacturing sector became notable and reached around 18-19 millions square meters in 2022 (Fig. 2).

3 OLED anatomy

In a typical OLED, on a transparent surface, which can be either glass or a flexible plastic substrate, an anode, such as indium tin oxide (ITO) or $(In_2O_3)_{0.9}(SnO_2)_{0.1}$ is placed (Fig. 3). This is followed by two conducting layers, a hole injection layer containing metal complexes based on Co(III) and Ga(III) and an electron transport layer such as Al-poly(phenylenevinylene), which sandwich the emissive organic layer. The structure is topped with a reflective metal cathode of Mg-Ag alloy or Li-Al. The thickness of these five layers is ~300 nm, but most of the weight and thickness of the OLED comes from the substrate (Borchardt, 2004).

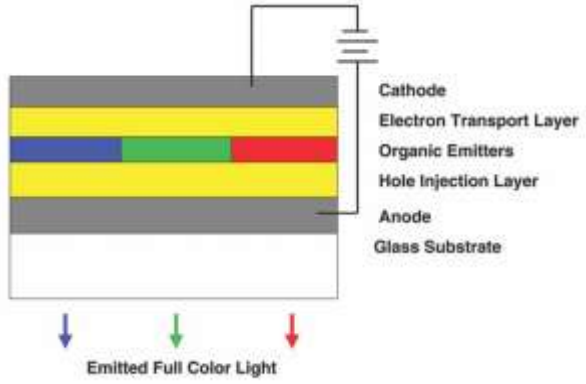

Fig. 3. Schematic structure of an OLED (Borchardt, 2004)

Structure of mobile phone OLED was investigated, and the thin-film transistors (TFTs) for pixels can be observed on Fig. 4. (Magyar et al., 2018).

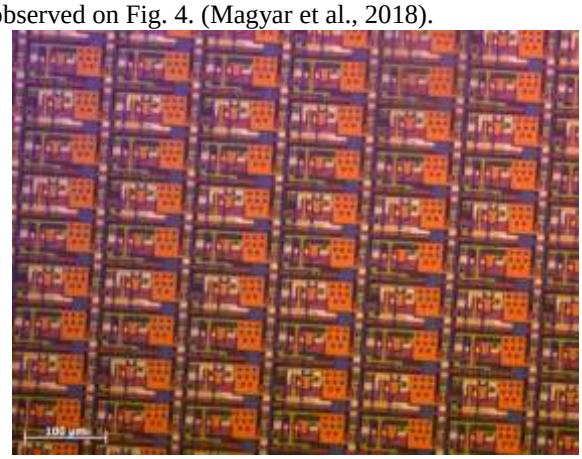

Fig. 4. OLED TFTs (optical microscopy) (Magyar et al., 2018)

4 OLED chemistry

From a material design perspective, EEE is very complex. Up to 69 elements from the periodic table can be found in EEE, including precious metals (e.g. gold, silver, copper, platinum, palladium, ruthenium, rhodium, iridium, and osmium) (Forti et al., 2020). The OLED technology uses less non-organic compound in comparison with LCD technology, however some elements like In, Sn, Co, Ga, Ag etc. are still indispensable for their production. That is, the exact chemical composition varies depending on the OLED type. Although OLED consists mostly of organic substances, because it was developed to reduce the consumptions of rare and precious metals, OLED display has a possibility to contain more metal-based components than LCD (Yeom et al. 2018); for instance, a pixel circuit for OLED needs two TFTs, whereas that for LCD requires only one (Yeom et al. 2018). Moreover, problem with availability of rare metals, especially indium, is leading to a major issue that is limiting the growth of the OLED market. Thus, the future industrial mass-market applications of OLEDs arises the question of raw material supply shortage.

5 OLED recycling

Considering the issues related to primary mining, market price fluctuations, material availability, and access to resources, the improvement of secondary resources mining has become vital in sustaining the raw material supply chain. Forti et al. (2020) highlights that only 17.4% of e-waste is documented to be formally collected and recycle because the recycling sector is often confronted with high costs of recycling and challenges in recycling the materials. The recovery of some materials such as germanium and indium is challenging because of their dispersed use in products, and the products are neither designed nor assembled with recycling principles been taken into account.

Although OLED displays are beneficial from the point of energy consumption reduction (Fernandez et al.,

2015), their relative short life span will result in the discarding of the end-of-life (EoL) OLED displays to solid-waste streams. Based on Robinson (2009), the average life expectancy of computers are 3 years, mobile phone 2 years and television 5 years. Thus, the relatively shorter life spans of these gadgets corroborate the growing expectations that the amount of OLED-based e-wastes will witness a sharp increase in the near future.

The recycling of screens and monitors involves multiple steps, which includes collection, sorting, disassembling, and mechanical processing. The critical metals are concentrated in size fractions (< 1 mm), which are subsequently processed through pyro- and hydrometallurgy. In the case of OLED screens and monitors, due to their different structure compared to LCD, the steps may vary, and the technology for recycling and the recovery of the critical metals are still in the phase of research and development.

5.1 Metal recovery by bioleaching

The application of bioleaching in the recovering of the metals found in the OLED panels has started to gain attention in recent years. Pourhossein et al. (2021, 2022), Golzar-Ahmadi et al. (2021) have assessed the bioleaching of metals Ag, Mo, Cu and In from OLED panels using *Bacillus foraminis* and *Acidithiobacillus ferrooxidans*, optimizing the influencing factors and obtaining promising results as they achieved near complete recovery of indium. Pourhussein et al. (2021) has studied the effect of variables such as pH, ferrous sulfate, elemental sulfur, and solid content and their interactions on indium and strontium recovery using adapted *Acidithiobacillus ferrooxidans*. The most efficient conditions for indium extraction were, ferrous sulfate concentration of 13 g/L, the elemental sulfur concentration of 5.63 g/L, solid content of 3 g/L, and initial pH of 1.1 resulting in maximal indium recovery. In the case of the strontium the best result was 5% extraction efficiency but even so the high concentration of the solid resulted in concentration of 3000 mg/L in the solution. Golzar-Ahmadi and Mousavi, (2021) used the alkali-tolerant *Bacillus foraminis* with the aim to reduce the heterotrophs bioleaching duration and prevent the production of highly acidic leachate in conjunction with obtaining an efficient removal of toxic metals. The results suggested that the organic acid secreted by the alkali-tolerant bacteria could be utilized as an innocuous leaching agent for the efficient extraction of Ag, Mo, and Cu (100, 56.8, and 41.4%, respectively) at a high pulp density of 7%. The extraction of these metals was also without applying hazardous chemical agents such as H_2SO_4, HCN, and H_2O_2. In addition, as bioleaching by the alkaliphilic bacteria occurs at near-neutral pH, the risk of equipment corrosion and soil quality damage by acidic leachate decreases, and safe disposal of the leachate is accessible.

5.2 Use of OLED glass as secondary raw material

The use of glass material from e-waste as secondary raw material in cement and concrete production is a widely researched topic, Yang et al. (2021) and Hanif (2023) have demonstrated that the addition of glass waste sourced from OLED has resulted in the improvement of the mechanical strength of concrete attributed to the pozzolanic activity due to high amounts of alumina and amorphous silica. Yang et al. (2021) used glass wastes from OLED as supplementary cementing material in concrete, substituting 10 wt%, 20 wt%, and 30 wt% of the Portland cement in the concrete mix. The resulting mechanical properties, hydration attributes, and microstructural features were studied at various ages, up to one year. Superior mechanical properties were shown after 28-day age for blended concretes; however, much profound improvement in compressive and flexural strength was observed at 1-year age. The replacement of cement with 20 wt% OLED glass waste has been found as the optimal value of cement replacement. The findings of Hanif (2023) were similar to Yang et al. (2021) regarding the strength improvement of the concretes, highlighting the great significance of the particle size of added OLED glass on the concrete, with finer particles improving reactivity in the cementitious matrix. The superior durability and mechanical properties of OLED-incorporated concrete are mainly due to the dense microstructure with pore structure.

5.3 Eco-design

The development of products for eco-designed and green devices that allow recycling of all the components and recovering of the valuable materials through sustainable methods are a relatively new research direction, i.e. Cocchi et al. (2021) giving insights on the future application on the use of biodegradable materials in OLED production. Considering the high economic values but also due to environmental risk and a worldwide shortage of metals, recycling and recovery of the valuable metals in waste OLED displays is an urgent task. Yeaom et al. (2018) highlights that although OLEDs are considered more eco-friendly in comparison to LCDs, their research result demonstrated that OLED has higher resource depletion and toxicity potentials than the LCD, due to the high concentrations of gold, arsenic, cadmium, chromium, and antimony. Thus, their effective recycling and recovery will ultimately address the dual issues of resource sustainability and environmental management.

6 Conclusion

Nowadays, OLED panels are the second most relevant materials on the display market behind LCD panels. Processing of EoL OLEDs is a crucial task due to environmental protection and resource harnessing to address the pending worldwide metal shortage. Collection of EoL equipment and the removal of display panels should be done before processing. The method should be different from the LCDs, because OLED has different structure and composition. Application of bioleaching in the recovering of the metals seems to be a promising approach to achieving high efficiency of

valuable metals. Other recycling possibility of waste OLED is its use as a glass raw material for cement and concrete production.

Funding

The research was funded by the Sustainable Development and Technologies National Programme of the Hungarian Academy of Sciences (FFT NP FTA). This project is funded by the European Union's Horizon Europe program under grant no. 101079354.

References

Forti, V., Baldé, C.P., Kuehr, R. & Bel, G. (2020) The Global E-waste Monitor 2020 Quantities, flows, and the circular economy potential, 117

Robinson, B. H. (2009) E-waste: An assessment of global production and environmental impacts, *Science of the Total Environment*, 408, 183-191.

Borchardt, J. K. (2004) Developments in organic displays, *Materials Today*, 7 (9), 42–46

Swayamprabha, S. S., Dubey, D. K, Shahnawaz, Yadav, R. A. K, Nagar, M. R., Sharma, A., Tung, F. C. & Jou, J.H. (2021) Approaches for Long Lifetime Organic Light Emitting Diodes, *Advanced Science*, 8(1), 2002254

T. Magyar, S. Nagy, J. Őrsi, R. Z. Papp: Chemical and material characterization of smartphones with special regards to OLED screens for recovery of valuable elements. ECOTERRA: JOURNAL OF ENVIROMENTAL RESEARCH AND PROTECTION 15: (1) pp. 18-26. (2018)

Vidal-Arbaca, C., Dodd, N.& Wolf, O. (2020) JRC Science and Policy Report-Revision of EU Ecolabel Criteria for Electronic Displays (previously Television)-Final Technical Report: Final criteria, European Commission Joint Research Centre Institute for Energy and Transport, 75

Fernández, M. R., Casanova, E. Z. & Alonso, I. G. (2015) Review of Display Technologies Focusing on Power Consumption, *Sustainability*, 7, 10854-10875

Pourhossein, F., Mousavi, S. M. & Beolchini, F. (2022) Innovative bio-acid leaching method for high recovery of critical metals from end-of-life light emitting diodes, *Resources, Conservation & Recycling*, 182, 106306

Pourhossein, F., Rezaei, O., Mousavi, S. M. & Beolchini, F. (2021) Bioleaching of critical metals from waste OLED touch screens using adapted acidophilic bacteria, *Journal of Environmental Health Science and Engineering*, 19, 893–906

Golzar-Ahmadi, M., Mousavi, S. M. (2021) Extraction of valuable metals from discarded AMOLED displays in smartphones using Bacillus foraminis as an alkali-tolerant strain, *Waste Management*, 131, 226–236

Yang, H.bJ., Lee, H., Wang, L. & Hanif, A. (2022) Hydration characteristics and microstructure evolution of concrete with blended binders from LCD and OLED wastes, *European Journal of Environmental and Civil Engineering*, 27 (1), 174-193

Cocchi, M., Bertoldo, M., Seri, M., Maccagnani, P., Summonte, C., Buoso, S., Belletti, G., Dinelli, F. & Capelli, R. (2021) Fully Recyclable OLEDs Built on a Flexible Biopolymer Substrate, *ACS Sustainable Chem. Eng.*, 9, 12733–1273

Yeom, J. M., Jung, H. J., Choi, S. Y., Lee, D. S. & Lim, Y-S. (2018) Environmental Effects of the Technology Transition from Liquid–Crystal Display (LCD) to Organic Light-Emitting Diode (OLED) Display from an E-Waste Management Perspective, *Int J Environ Res*, 12, 479–488

https://www.businesskorea.co.kr/news/articleView.html?idxno=119156 Date of information: 9th nov. 2024

https://sst.semiconductor-digest.com/2017/10/global-amoled-panel-production-capacity-set-to-more-than-quadruple-over-next-five-years/ Date of information : 9th nov. 2024

https://www.statista.com/topics/3288/display-technology/#topicOverview Date of information : 13th march 2024.

EDITED BY
J. FAITLI AND Á. RÁCZ

NyKI 1923

EFCE

MKE